GEOPHYSICAL MONOGRAPH SERIES

AGU
ADVANCING EARTH
AND SPACE SCIENCE

Crustal Magmatic System Evolution

Anatomy, Architecture, and Physico-Chemical Processes

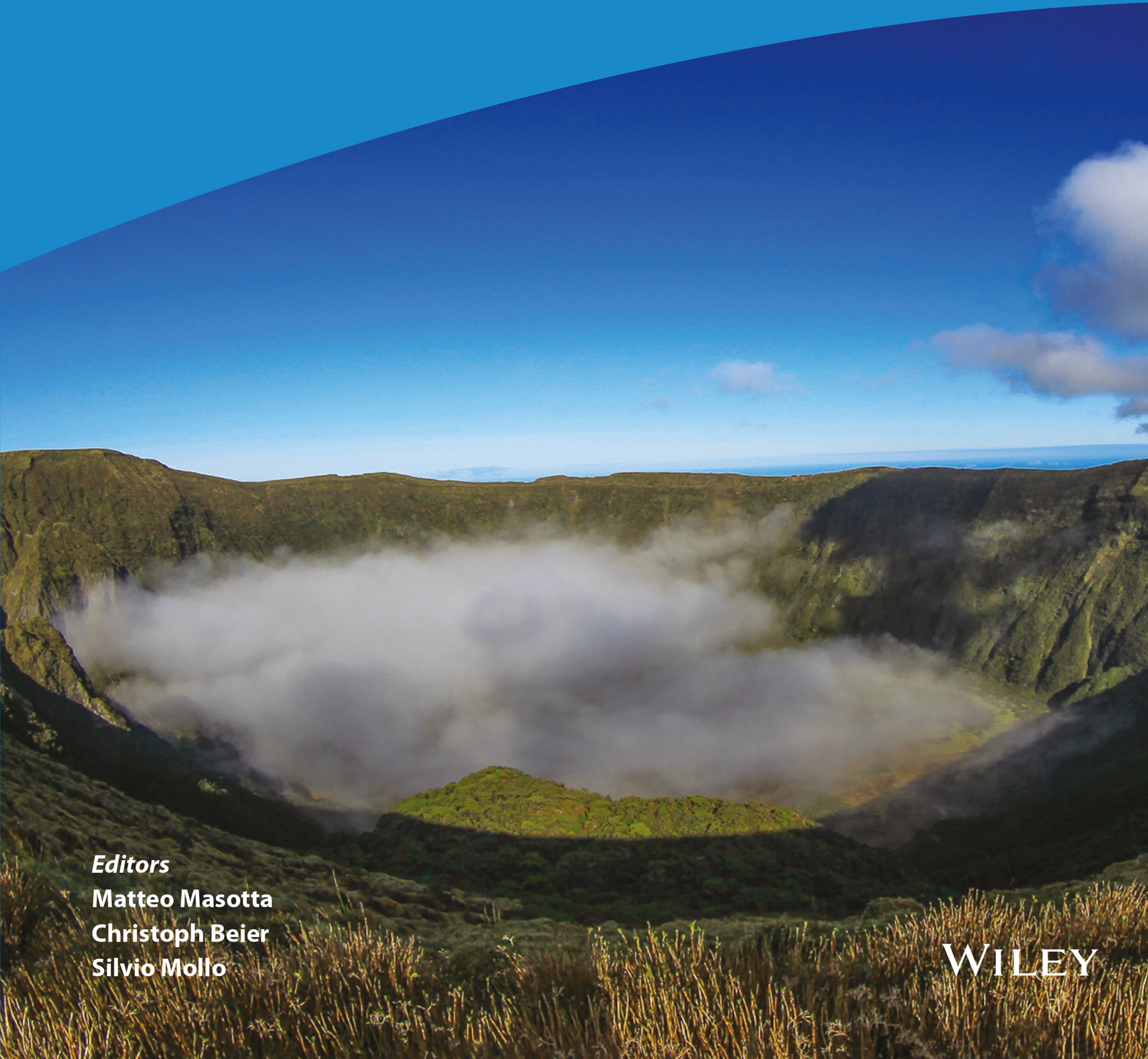

Editors
Matteo Masotta
Christoph Beier
Silvio Mollo

WILEY

GEOPHYSICAL MONOGRAPH SERIES

Crustal Magmatic System Evolution

Anatomy, Architecture, and Physico-Chemical Processes

Matteo Masotta, University of Pisa, Italy
Christoph Beier, University of Helsinki, Finland
Silvio Mollo, Sapienza University of Rome, Italy

The composition of igneous rocks – their minerals, melts, and fluids – reveals the physical and chemical conditions under which magmas form, evolve, interact, and move from the Earth's mantle through the crust. These magma dynamics affect processes on the surface including crustal growth and eruptive behaviour of volcanoes.

Crustal Magmatic System Evolution: Anatomy, Architecture, and Physico-Chemical Processes uses analytical, experimental, and numerical approaches to explore the diversity of crustal processes from magma differentiation and assimilation to eruption at the surface.

Volume highlights include:

- Physical and chemical parameterization of crustal magmatic systems
- Experimental, theoretical and modelling approaches targeting crustal magmatic processes
- Timescales of crustal magmatic processes, including storage, recharge, and ascent through volcanic conduits

---

The American Geophysical Union promotes discovery in Earth and space science for the benefit of humanity. Its publications disseminate scientific knowledge and provide resources for researchers, students, and professionals.

Cover Design: Wiley
Cover Image: View into the Caldeira Volcano
of the ocean island of Faial, Azores; © Christoph Beier,
University of Helsinki, Finland

www.wiley.com

WILEY

Also available
as an e-book

AGU ADVANCING EARTH AND SPACE SCIENCE

ISBN 978-1-119-56445-4
90000
9 781119 564454

Geophysical Monograph Series

Geophysical Monograph Series

212 **The Early Earth: Accretion and Differentiation** *James Badro and Michael Walter (Eds.)*
213 **Global Vegetation Dynamics: Concepts and Applications in the MC1 Model** *Dominique Bachelet and David Turner (Eds.)*
214 **Extreme Events: Observations, Modeling and Economics** *Mario Chavez, Michael Ghil, and Jaime Urrutia-Fucugauchi (Eds.)*
215 **Auroral Dynamics and Space Weather** *Yongliang Zhang and Larry Paxton (Eds.)*
216 **Low-Frequency Waves in Space Plasmas** *Andreas Keiling, Dong- Hun Lee, and Valery Nakariakov (Eds.)*
217 **Deep Earth: Physics and Chemistry of the Lower Mantle and Core** *Hidenori Terasaki and Rebecca A. Fischer (Eds.)*
218 **Integrated Imaging of the Earth: Theory and Applications** *Max Moorkamp, Peter G. Lelievre, Niklas Linde, and Amir Khan (Eds.)*
219 **Plate Boundaries and Natural Hazards** *Joao Duarte and Wouter Schellart (Eds.)*
220 **Ionospheric Space Weather: Longitude and Hemispheric Dependences and Lower Atmosphere Forcing Timothy Fuller-Rowell,** *Endawoke Yizengaw, Patricia H. Doherty, and Sunanda Basu (Eds.)*
221 **Terrestrial Water Cycle and Climate Change Natural and Human-Induced Impacts** *Qiuhong Tang and Taikan Oki (Eds.)*
222 **Magnetosphere-Ionosphere Coupling in the Solar System** *Charles R. Chappell, Robert W. Schunk, Peter M. Banks, James L. Burch, and Richard M. Thorne (Eds.)*
223 **Natural Hazard Uncertainty Assessment: Modeling and Decision Support** *Karin Riley, Peter Webley, and Matthew Thompson (Eds.)*
224 **Hydrodynamics of Time-Periodic Groundwater Flow: Diffusion Waves in Porous Media** *Joe S. Depner and Todd C. Rasmussen (Auth.)*
225 **Active Global Seismology** *Ibrahim Cemen and Yucel Yilmaz (Eds.)*
226 **Climate Extremes** *Simon Wang (Ed.)*
227 **Fault Zone Dynamic Processes** *Marion Thomas (Ed.)*
228 **Flood Damage Survey and Assessment: New Insights from Research and Practice** *Daniela Molinari, Scira Menoni, and Francesco Ballio (Eds.)*
229 **Water-Energy-Food Nexus – Principles and Practices** *P. Abdul Salam, Sangam Shrestha, Vishnu Prasad Pandey, and Anil K Anal (Eds.)*
230 **Dawn–Dusk Asymmetries in Planetary Plasma Environments** *Stein Haaland, Andrei Rounov, and Colin Forsyth (Eds.)*
231 **Bioenergy and Land Use Change** *Zhangcai Qin, Umakant Mishra, and Astley Hastings (Eds.)*
232 **Microstructural Geochronology: Planetary Records Down to Atom Scale** *Desmond Moser, Fernando Corfu, James Darling, Steven Reddy, and Kimberly Tait (Eds.)*
233 **Global Flood Hazard: Applications in Modeling, Mapping and Forecasting** *Guy Schumann, Paul D. Bates, Giuseppe T. Aronica, and Heiko Apel (Eds.)*
234 **Pre-Earthquake Processes: A Multidisciplinary Approach to Earthquake Prediction Studies** *Dimitar Ouzounov, Sergey Pulinets, Katsumi Hattori, and Patrick Taylor (Eds.)*
235 **Electric Currents in Geospace and Beyond** *Andreas Keiling, Octav Marghitu, and Michael Wheatland (Eds.)*
236 **Quantifying Uncertainty in Subsurface Systems** *Celine Scheidt, Lewis Li, and Jef Caers (Eds.)*
237 **Petroleum Engineering** *Moshood Sanni (Ed.)*
238 **Geological Carbon Storage: Subsurface Seals and Caprock Integrity** *Stephanie Vialle, Jonathan Ajo-Franklin, and J. William Carey (Eds.)*
239 **Lithospheric Discontinuities** *Huaiyu Yuan and Barbara Romanowicz (Eds.)*
240 **Chemostratigraphy Across Major Chronological Eras** *Alcides N.Sial, Claudio Gaucher, Muthuvairavasamy Ramkumar, and Valderez Pinto Ferreira (Eds.)*
241 **Mathematical Geoenergy:Discovery, Depletion, and Renewal** *Paul Pukite, Dennis Coyne, and Daniel Challou (Eds.)*
242 **Ore Deposits: Origin, Exploration, and Exploitation** *Sophie Decree and Laurence Robb (Eds.)*
243 **Kuroshio Current: Physical, Biogeochemical and Ecosystem Dynamics** *Takeyoshi Nagai, Hiroaki Saito, Koji Suzuki, and Motomitsu Takahashi (Eds.)*
244 **Geomagnetically Induced Currents from the Sun to the Power Grid** *Jennifer L. Gannon, Andrei Swidinsky, and Zhonghua Xu (Eds.)*
245 **Shale: Subsurface Science and Engineering** *Thomas Dewers, Jason Heath, and Marcelo Sánchez (Eds.)*
246 **Submarine Landslides: Subaqueous Mass Transport Deposits From Outcrops to Seismic Profiles** *Kei Ogata, Andrea Festa, and Gian Andrea Pini (Eds.)*
247 **Iceland: Tectonics, Volcanics, and Glacial Features** *Tamie J. Jovanelly*
248 **Dayside Magnetosphere Interactions** *Qiugang Zong, Philippe Escoubet, David Sibeck, Guan Le, and Hui Zhang (Eds.)*
249 **Carbon in Earth's Interior** *Craig E. Manning, Jung-Fu Lin, and Wendy L. Mao (Eds.)*
250 **Nitrogen Overload: Environmental Degradation, Ramifications, and Economic Costs** *Brian G. Katz*
251 **Biogeochemical Cycles: Ecological Drivers and Environmental Impact** *Katerina Dontsova, Zsuzsanna Balogh-Brunstad, and Gaël Le Roux (Eds.)*
252 **Seismoelectric Exploration: Theory, Experiments, and Applications** *Niels Grobbe, André Revil, Zhenya Zhu, and Evert Slob (Eds.)*
253 **El Niño Southern Oscillation in a Changing Climate** *Michael J. McPhaden, Agus Santoso, and Wenju Cai (Eds.)*
254 **Dynamic Magma Evolution** *Francesco Vetere (Ed.)*
255 **Large Igneous Provinces: A Driver of Global Environmental and Biotic Changes** *Richard. E. Ernst, Alexander J. Dickson, and Andrey Bekker (Eds.)*
256 **Coastal Ecosystems in Transition: A Comparative Analysis of the Northern Adriatic and Chesapeake Bay** *Thomas C. Malone, Alenka Malej, and Jadran Faganeli (Eds.)*
257 **Hydrogeology, Chemical Weathering, and Soil Formation** *Allen Hunt, Markus Egli, and Boris Faybishenko (Eds.)*
258 **Solar Physics and Solar Wind** *Nour E. Raouafi and Angelos Vourlidas (Eds.)*
259 **Magnetospheres in the Solar System** *Romain Maggiolo, Nicolas André, Hiroshi Hasegawa, and Daniel T. Welling (Eds.)*
260 **Ionosphere Dynamics and Applications** *Chaosong Huang and Gang Lu (Eds.)*
261 **Upper Atmosphere Dynamics and Energetics** *Wenbin Wang and Yongliang Zhang (Eds.)*
262 **Space Weather Effects and Applications** *Anthea J. Coster, Philip J. Erickson, and Louis J. Lanzerotti (Eds.)*
263 **Mantle Convection and Surface Expressions** *Hauke Marquardt, Maxim Ballmer, Sanne Cottaar, and Jasper Konter (Eds.)*
264 **Crustal Magmatic System Evolution: Anatomy, Architecture, and Physico-Chemical Processes** *Matteo Masotta, Christoph Beier, and Silvio Mollo (Eds.)*

Geophysical Monograph 264

Crustal Magmatic System Evolution

Anatomy, Architecture, and Physico-Chemical Processes

Matteo Masotta
Christoph Beier
Silvio Mollo
Editors

This Work is a co-publication of the American Geophysical Union and John Wiley and Sons, Inc.

AGU
ADVANCING EARTH
AND SPACE SCIENCE

WILEY

This edition first published 2021
© 2021 American Geophysical Union

All rights reserved. No part of this publication may be reproduced, stored in a retrieval system, or transmitted, in any form or by any means, electronic, mechanical, photocopying, recording or otherwise, except as permitted by law. Advice on how to obtain permission to reuse material from this title is available at http://www.wiley.com/go/permissions.

The right of Matteo Masotta, Christoph Beier, and Silvio Mollo to be identified as the editors of this work has been asserted in accordance with law.

Published under the aegis of the AGU Publications Committee

Brooks Hanson, Executive Vice President, Science
Carol Frost, Chair, Publications Committee
For details about the American Geophysical Union visit us at www.agu.org

Registered Office
John Wiley & Sons, Inc., 111 River Street, Hoboken, NJ 07030, USA

Editorial Office
111 River Street, Hoboken, NJ 07030, USA

For details of our global editorial offices, customer services, and more information about Wiley products visit us at www.wiley.com.

Wiley also publishes its books in a variety of electronic formats and by print-on-demand. Some content that appears in standard print versions of this book may not be available in other formats.

Limit of Liability/Disclaimer of Warranty
While the publisher and authors have used their best efforts in preparing this work, they make no representations or warranties with respect to the accuracy or completeness of the contents of this work and specifically disclaim all warranties, including without limitation any implied warranties of merchantability or fitness for a particular purpose. No warranty may be created or extended by sales representatives, written sales materials or promotional statements for this work. The fact that an organization, website, or product is referred to in this work as a citation and/or potential source of further information does not mean that the publisher and authors endorse the information or services the organization, website, or product may provide or recommendations it may make. This work is sold with the understanding that the publisher is not engaged in rendering professional services. The advice and strategies contained herein may not be suitable for your situation. You should consult with a specialist where appropriate. Further, readers should be aware that websites listed in this work may have changed or disappeared between when this work was written and when it is read. Neither the publisher nor authors shall be liable for any loss of profit or any other commercial damages, including but not limited to special, incidental, consequential, or other damages.

Library of Congress Cataloging-in-Publication Data
Names: Masotta, Matteo, 1984- editor. | Beier, Christoph, 1977- editor. | Mollo, Silvio, 1975- editor.
Title: Crustal magmatic system evolution : anatomy, architecture, and physico-chemical processes / Matteo Masotta, Christoph Beier, Silvio Mollo, editors.
Description: Hoboken, NJ : Wiley-American Geophysical Union, [2021] | Includes bibliographical references and index.
Identifiers: LCCN 2020055759 (print) | LCCN 2020055760 (ebook) | ISBN 9781119564454 (cloth) | ISBN 9781119564478 (adobe pdf) | ISBN 9781119564461 (epub)
Subjects: LCSH: Magmatism. | Magmas. | Volcanoes. | Geological time. | Geochemistry. | Earth (Planet)–Crust.
Classification: LCC QE461 .C88 2021 (print) | LCC QE461 (ebook) | DDC 552/.03–dc23
LC record available at https://lccn.loc.gov/2020055759
LC ebook record available at https://lccn.loc.gov/2020055760

Cover Design: Wiley
Cover Image: View into the Caldeira Volcano of the ocean island of Faial, Azores; © Christoph Beier, University of Helsinki, Finland

Set in 10/12pt Times New Roman by SPi Global, Pondicherry, India

10 9 8 7 6 5 4 3 2 1

CONTENTS

LIST OF CONTRIBUTORS

Abigail K. Barker
Department of Earth Sciences
Uppsala University
Uppsala, Sweden;
and
Centre of Natural Hazards and Disaster Sciences
Uppsala, Sweden

Lukas P. Baumgartner
Institute of Earth Sciences
University of Lausanne
Lausanne, Switzerland

Jon D. Blundy
School of Earth Sciences
University of Bristol
Bristol, United Kingdom

Wendy A. Bohrson
Department of Geological Sciences
Central Washington University
Ellensburg, Washington, USA;
and
Geology and Geological Engineering Department
Colorado School of Mines
Golden, Colorado, USA

Marco Brenna
Department of Geology
University of Otago
Dunedin, New Zealand

Gianmarco Buono
Istituto Nazionale di Geofisica e Vulcanologia
Sezione di Napoli-Osservatorio Vesuviano
Naples, Italy;
and
Dipartimento di Scienze della Terra
dell'Ambiente e delle Risorse
Università degli Studi di Napoli Federico II
Naples, Italy

Katharine V. Cashman
School of Earth Sciences
University of Bristol
Bristol, United Kingdom

Antonio Castro
Instituto Andaluz de Ciencias de la Tierra
Consejo Superior de Investigaciones
Científicas–Universidad de Granada
Granada, Spain

Flavio Di Stefano
Department of Earth Sciences
Sapienza – University of Rome
Rome, Italy

Juan Díaz-Alvarado
Departamento de Ciencias de la Tierra
Universidad de Huelva
Huelva, Spain

Carlos Fernández
Departamento de Ciencias de la Tierra
Universidad de Huelva
Huelva, Spain

Riikka Fred
Department of Geosciences and Geography
University of Helsinki
Helsinki, Finland

Olga García-Moreno
Departamento de Geología
Universidad de Oviedo
Oviedo, Spain

Jussi S. Heinonen
Department of Geosciences and Geography
University of Helsinki
Helsinki, Finland

Aku Heinonen
Department of Geosciences and Geography
University of Helsinki
Helsinki, Finland

Kieran A. Iles
Department of Geosciences and Geography
University of Helsinki
Helsinki, Finland;
and
Finnish Museum of Natural History
University of Helsinki
Helsinki, Finland

Paul A. Jarvis
Department of Earth Sciences
University of Geneva
Geneva, Switzerland

Heidy M. Mader
School of Earth Sciences
University of Bristol
Bristol, United Kingdom

Martin F. Mangler
Department of Earth Sciences
The Natural History Museum
London, United Kingdom;
and
Department of Earth Sciences
Durham University
Durham, United Kingdom

Silvio Mollo
Department of Earth Sciences
Sapienza – University of Rome
Rome, Italy;
and
Istituto Nazionale di Geofisica e Vulcanologia
Rome, Italy

Alexander R. L. Nichols
Department of Geological Sciences
University of Canterbury
Christchurch, New Zealand

Lucia Pappalardo
Istituto Nazionale di Geofisica e Vulcanologia
Sezione di Napoli-Osservatorio Vesuviano
Naples, Italy

Chiara Maria Petrone
Department of Earth Sciences
The Natural History Museum
London, United Kingdom

Mattia Pistone
Department of Geology
University of Georgia
Athens, Georgia, USA;
and
Institute of Earth Sciences
University of Lausanne
Lausanne, Switzerland

Alessio Pontesilli
Department of Geology
University of Otago
Dunedin, New Zealand

Carmen Rodríguez
Departamento de Ciencias de la Tierra
Universidad de Huelva
Huelva, Spain;
and
Geosciences Barcelona (formerly ICTJA)
Consejo Superior de Investigaciones Cientificas
Barcelona, Spain

Elin M. Rydeblad
Department of Earth Sciences
Uppsala University
Uppsala, Sweden;
and
Department of Earth Science and Engineering
Imperial College London
London, United Kingdom

Piergiorgio Scarlato
Istituto Nazionale di Geofisica e Vulcanologia
Rome, Italy

Alexia Secretan
Institute of Earth Sciences
University of Lausanne
Lausanne, Switzerland

Sónia M. D. M. Silva
Faculty of Science and Technology
University of Cape Verde
Praia, Cape Verde

Frank J. Spera
Department of Earth Science and Earth Research Institute
University of California Santa Barbara
Santa Barbara, California, USA

Chenguang Sun
Department of Geological Sciences
The University of Texas at Austin
Austin, Texas, USA

Teresa Ubide
School of Earth and Environmental Sciences
The University of Queensland
Brisbane, Australia

Ville J. Virtanen
Department of Geosciences and Geography
University of Helsinki
Helsinki, Finland

Luca Ziberna
Department of Mathematics and Geosciences
University of Trieste
Trieste, Italy

PREFACE

Magmatism in the continental and oceanic lithosphere contributes to the rejuvenation of Earth's crust and is fundamental for the evolution of life on our planet. After their formation, magmas crystallize, differentiate, degas, mix with other magmas, and interact with the surrounding lithologies over a wide range of pressures and temperatures. The petrological and geochemical signatures of volcanic and plutonic rocks reflect the diversity of the petrogenetic processes. Deciphering these signatures has fundamental implications for elucidating the eruptive behavior of volcanoes and quantifying the mass fluxes related to the generation and growth of the crust.

Volcanoes are the most spectacular expression of magmatism, and for this reason they have attracted the interest of different disciplines in Earth Sciences, such as mineralogy, petrology, geochemistry, and geophysics. The rapid advancement of analytical and modeling methods and experimental techniques has contributed significantly to the common objective of unveiling the processes that underlie the surface expression of magmatism on Earth.

In this context, the textural and petrochemical analysis of natural rock samples and the new findings from experimental and modeling works represent the basis of modern studies modeling the architecture of volcanic plumbing systems. Specifically, minerals, melts, and fluids contained in natural rock samples represent archives of the physical and chemical conditions under which magmas are generated and evolve, whereas laboratory experiments are pivotal to extract such information at temperatures and pressures relevant to different tectonic environments.

This monograph provides a comprehensive overview of the spatiotemporal variations in magma production, transport pathway, storage, and differentiation related to the lifetime of active volcanoes. The volume is organized into three parts. Part I focuses on the physical and chemical parameterization of crustal magmatic systems, based on the petrological and geochemical investigation of igneous rocks from different types of geodynamic settings. Part II presents an overview of the experimental, theoretical, and modeling approaches that allow evaluating and constraining magmatic processes, such as magma differentiation, contamination, and mixing. Part III is dedicated to the timescales of magmatic processes, including storage, recharge, and ascent through volcanic conduits.

These different petrologic themes provide a comprehensive picture of the architecture of crustal magmatic systems by comparing and integrating analytical, experimental, and numerical aspects. Our expectation is that the present book will help to better elucidate the close interaction between magma generation at depth and subsequent differentiation and ascent in the crust, offering to the reader food for thought fostering future research on the topic of crustal processes.

The editors acknowledge the effort of the authors and reviewers who have contributed to the success of this volume. The AGU editorial team is also acknowledged for their support and help.

Matteo Masotta
Department of Earth Sciences,
University of Pisa, Italy
Christoph Beier
Department of Geosciences and Geography,
University of Helsinki, Finland
Silvio Mollo
Department of Earth Sciences,
Sapienza – University of Rome, Italy

Part I

Architecture of Crustal Magmatic Systems

1

Geothermobarometry of Mafic and Ultramafic Xenoliths: Examples From Hualalai and Mauna Kea Volcanoes, Hawaii

Luca Ziberna

ABSTRACT

Xenoliths of plutonic rocks sporadically torn off by erupting magmas are known to carry valuable information about volcano plumbing systems and the lithosphere in which they are emplaced. One of the main steps in the interpretation of such information is to quantify the pressure and temperature conditions at which the xenolith mineral assemblages last equilibrated. This chapter discusses some aspects of geothermobarometry of mafic and ultramafic rocks using the xenolith populations of the Hualalai and Mauna Kea volcanoes, Hawaii, as case studies. Multiple-reaction geobarometry, recently revisited for olivine + clinopyroxene + plagioclase ± spinel assemblages, provides the most precise pressure estimates (uncertainties as low as 1.0 kbar). An example is shown that integrates these estimates with the calculated seismic velocities of the xenoliths and the available data from seismic tomography. The results make it possible to better constrain some kilometer-scale horizontal and vertical heterogeneities in the magmatic system beneath Hawaii. Ultramafic xenoliths at Hualalai are the residuals of magma crystallization at 16–21 km depth, below the pre-Hawaiian oceanic crust. The few available gabbronorites and diorites record instead lower pressures and likely represent conduits or small magma reservoirs crystallized at 0–8 km depth. At Mauna Kea, on the other hand, a significant portion of the xenolith record is composed of olivine-gabbros, which crystallized almost over the entire crustal thickness (3–18 km). Ultramafic xenoliths are less abundant and might represent the bottom of the same magma reservoirs that crystallized in the deeper portion of the magmatic systems (11–18 km). Some unresolved issues remain in the geothermometry of mafic and ultramafic rocks representing portions of magma reservoirs that cooled and recrystallized under subsolidus conditions. This suggests that further experimental and theoretical work is needed to better constrain the thermodynamics and kinetics of peridotitic and basaltic systems at low (<1000°C) temperatures.

1.1. INTRODUCTION

The geothermobarometry of magmatic rocks is well known to be one of the key tools used to interpret the processes within volcanic systems. This is why much effort has been put in since the first pioneering studies in petrology (e.g., Bowen, 1928; Green & Ringwood, 1967; Tuttle & Bowen, 1958; Wells, 1977) to perform experimental and theoretical work constraining the relationships between the mineralogy and chemistry of magmatic rocks and the temperatures and pressures at which their constituent phases formed. It was clear since then that the complexity of volcanic processes and the compositional variability of the erupted magmas and their lithic fragments make it difficult to develop geothermobarometers that are both accurate and precise for any sample, but considerable progress has been made in the last three decades. Considering only published work on magmatic systems relevant for crustal processes, more than 6,000 phase equilibrium laboratory experiments have been performed so far (based on the LEPR database at http://lepr.ofm-research.org and additional literature). These experiments led to the development of geothermobarometers

---

Department of Mathematics and Geosciences, University of Trieste, Trieste, Italy

Crustal Magmatic System Evolution: Anatomy, Architecture, and Physico-Chemical Processes, Geophysical Monograph 264, First Edition.
Edited by Matteo Masotta, Christoph Beier, and Silvio Mollo.

DOI: 10.1002/9781119564485.ch1

and forward thermodynamic simulations (e.g., Ghiorso & Sack, 1995; Gualda et al., 2012; Jennings & Holland, 2015; Masotta et al., 2013; Mollo et al., 2018; Putirka, 2008, 2016; Ziberna et al., 2017) that can now be used to model the differentiation paths of magmas.

The most common inverse-modeling approach to estimating the pressure (*P*) and temperature (*T*) of volcanic systems is geothermobarometry based on mineral-liquid equilibria (see Putirka, 2008, for an exhaustive discussion). It is usually applied to porphyric lava samples, using whole-rock chemical analyses (as representative of liquid compositions) in combination with the chemistry of phenocrysts. As a rule, measured partition coefficients [e.g., $K_D(\text{Fe-Mg})^{\text{mineral-liquid}}$] is compared to experimental values to demonstrate equilibrium (e.g., Putirka, 2008). For basaltic to andesitic and trachytic rocks, clinopyroxene-liquid geothermometry and geobarometry proved to be the most precise methods when tested against experimental data, producing model errors as small as 28 °C and 1.4 kbar (Masotta et al., 2013; Neave & Putirka, 2017; Putirka, 2008). The success of such methods lies in the large entropy and volume change of the reactions used as geothermometers and geobarometers, respectively (Putirka, 2008), and in the ubiquity of clinopyroxene in many basaltic systems. Other common methods are plagioclase-liquid geothermometry (e.g., Lange et al., 2009; Putirka, 2008), amphibole-liquid geothermometry and geobarometry (Molina et al., 2015; Putirka, 2016), and mineral-mineral equilibria like two-pyroxene geothermometers and geobarometers (e.g., Lindsley, 1983; Putirka, 2008; Wells, 1977), amphibole-plagioclase geothermometers (Blundy & Holland, 1990; Holland & Blundy, 1994) and geobarometers (Molina et al., 2015), Ca-in-olivine geothermometers (Shejwalkar & Coogan, 2013) or two-oxide geothermometers (Ghiorso & Evans, 2008). Furthermore, new methods based on the partitioning of rare earth elements (REEs) are the two-pyroxene thermometer of Liang et al. (2013) and the plagioclase-clinopyroxene thermometer of Sun and Liang (2017).

Phenocryst assemblages in volcanic rocks often show complex intra- and inter-mineral variations in major and trace element compositions (i.e., zoning and grain-to-grain heterogeneities), which are known to reflect possible changes in *P*, *T*, oxygen fugacity (fO_2), undercooling, degassing, crystallization, and interaction with other magmas or crustal rocks. Application of mineral-liquid geothermobarometers to such assemblages is not a straightforward task, but recent careful studies taking into account the textural relationships in lavas and the required care for assessing equilibrium have shown that these methods can help in investigating the complex architecture of magmatic systems (e.g., Erdmann et al., 2014; Giacomoni et al., 2016; Mollo et al., 2015, 2020; Neave et al., 2019; Putirka, 1997; Stock et al., 2018).

Erupted lavas, however, represent only a part of volcano plumbing systems and do not provide direct information about the residua of crystal fractionation (i.e., cumulates) or the plutonic rocks derived from isochemical solidification of magmas at depth. Such information is rather provided by plutonic or cumulate xenoliths that are occasionally brought to the surface by the erupted magmas. These are valuable samples that can be studied in combination with volcanic rocks to unravel magmatic processes at depth and help constrain the crustal structure beneath volcanoes. In most cases, classical mineral-liquid geothermobarometers cannot be applied to these rocks, either because the liquid composition is not well constrained or because the system re-equilibrated at subsolidus conditions. The available methods are therefore based on either single reactions between mineral phases (e.g., two-pyroxene geothermobarometry; Putirka, 2008; olivine-plagioclase-pyroxene geobarometry; Fumagalli et al., 2017), REE partitioning (Liang et al., 2013; Sun & Liang, 2015; Sun & Liang, 2017); or on multiple-reaction approaches (e.g., Powell & Holland, 1994) using as many mineral phases as those present in the assemblage and for which thermodynamic data are available.

Obtaining accurate pressure estimates for mafic and ultramafic xenolith has always been hampered by the lack of suitable geobarometers with sufficiently large volume change of their reactions. Although the problem still remains for rocks with high-variance assemblages, like pure dunites, clinopyroxenites, wehrlites, and troctolites with no accessory phases, recent work has shown that obtaining accurate and precise pressure estimates for lower-variance assemblages is possible by means of either a single-reaction ($Mg_2SiO_4^{\text{olivine}} + CaAl_2Si_2O_8^{\text{plagioclase}} = CaAl_2SiO_6^{\text{clinopyroxene}} + Mg_2Si_2O_6^{\text{orthopyroxene}}$; Fumagalli et al., 2017) or a multiple-reaction approach (three or six reactions in the assemblage olivine + clinopyroxene + plagioclase ± spinel; Ziberna et al., 2017). The multiple-reaction approach relies on an internally consistent set of thermodynamic data for mineral end-members (e.g., Holland & Powell, 2011) and a set of mixing models for phases. In principle, it allows for all the phases in a rock to be used for P calculations and is based on an algorithm (i.e., average *P*, *avP*, originally developed for metamorphic rocks; Powell & Holland, 1994) that combines all the thermodynamic information and takes into account the uncertainties and correlations of the input data (mineral composition, thermodynamic properties) to produce an average value of *P*. The *avP* method has been tested and refined for olivine-bearing igneous rocks and has been shown to accurately reproduce the pressure of phase equilibrium experiments and produce *P* estimates for natural samples with 1σ uncertainties on the order of 1 kbar (Ziberna et al., 2017).

The objective of this chapter is to show how geobarometry can help constrain the depth of formation of mafic and ultramafic xenoliths brought to the surface at basaltic volcanoes. As an example application, I selected the Hualalai and Mauna Kea volcanoes of the island of Hawaii, from which erupted a large quantity of ultramafic and mafic xenoliths that have been variably characterized by the petrological community. I will illustrate some advantages and limitations of some available geothermobarometers and how their results can be reconciled with the seismic structure of the crust beneath hot spot volcanoes.

1.2. GEOLOGICAL AND PETROLOGICAL BACKGROUND

Hualalai and Mauna Kea are two of the five volcanoes that build up the island of Hawaii (Figure 1.1). Similarly to other volcanoes from this island, their erupting activity can mainly be subdivided into a tholeiitic shield stage and an alkalic post-shield or post-caldera stage (Clague, 1987). The tholeiitic shield stage produced most of the erupted volumes and at Mauna Kea is suggested to have started at ~600 ka (Frey et al., 1990). The shield to post-shield transition is dated around 370 ka for Mauna Kea (Huang & Frey, 2003; Vazquez et al., 2007) and between 130 and 100 ka for Hualalai (Cousens et al., 2003). The most recent erupted products are some lava flows of the Laupahoehoe volcanics (~4 ka) at Mauna Kea (Wolfe et al., 1997) and the 1800–1801 Huehue and Kaupulehu lava flows at Hualalai (Clague et al., 1980). Reviews on Mauna Kea and Hualalai volcanism can be found in Frey et al. (1990, 1991), Moore et al. (1987), and Wolfe et al. (1997).

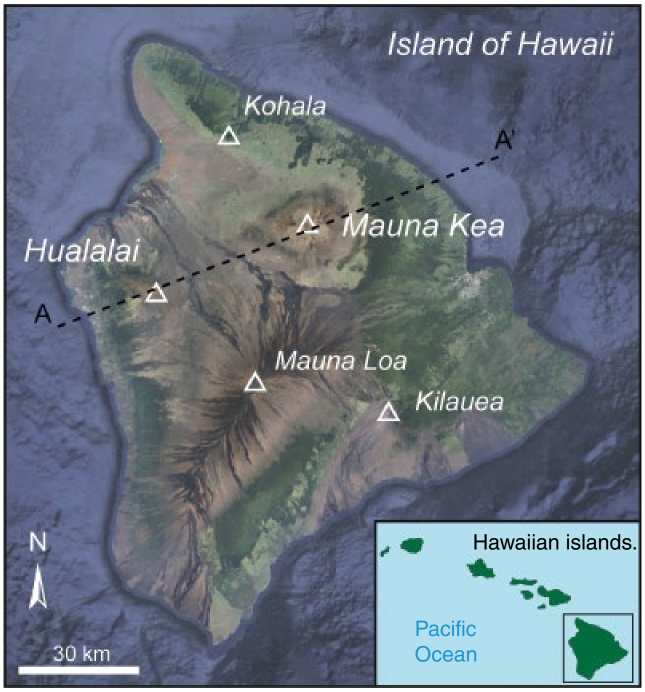

Figure 1.1 Location of Hualalai and Mauna Kea volcanoes, Island of Hawaii. Background map is from Google Earth®, version 7.3.2.5776, imagery date 14 December 2015, eye altitude 265 km. Dashed line A-A′ shows the position of the cross section in Figure 1.5.

Both Hualalai and Mauna Kea eruptions of the post-shield stage brought to the surface crustal and more rarely mantle xenoliths that have been variably characterized by the petrological community (e.g., Bohrson & Clague, 1988; Chen et al., 1992; Fodor & Galar, 1997; Jackson et al., 1981, 1982; Shamberger & Hammer, 2006). More than 4,000 xenoliths, ranging in size from ~1 cm to more than 40 cm, have been reported so far; rock types include dunites, wehrlites, clinopyroxenites, gabbros, gabbronorites, troctolites and minor anorthosites, diorites, and tonalites (e.g., Chen et al., 1992; Clague & Bohrson, 1991; Fodor, 2001; Fodor & Vandermeyden, 1988; Gao et al., 2016; Jackson et al., 1981, 1982; Shamberger & Hammer, 2006). Only a small part has been characterized for detailed petrography and mineral chemistry. With the exception of few diorites and gabbros (Fodor, 2001; Gao et al., 2016; Shamberger & Hammer, 2006), all xenoliths have been interpreted as fragments of cumulates derived by crystallization of Hawaiian tholeiitic and/or alkalic magmas (Bohrson & Clague, 1988; Fodor & Galar, 1997; Fodor & Vandermeyden, 1988). Based on Sr and Pb isotopic compositions and mineral chemistry of the xenoliths, derivation from the pre-Hawaiian oceanic crust has been excluded for most of the xenoliths (Bohrson & Clague, 1988; Fodor & Galar, 1997; Shamberger & Hammer, 2006). Most of the ultramafic xenoliths show evidence of annealing or recrystallization (Fodor & Galar, 1997), but this is not the case for the leucocratic and most of the gabbroic types (Shamberger & Hammer, 2006). The textures and composition of the ultramafic xenoliths suggest that they formed in the bottoms of reservoirs from magmas having 10–15 wt% MgO (Fodor & Galar, 1997).

Previous work generally suggests that both small- and large-scale modal, grain size and phase layering is a common feature of magma reservoirs beneath Hawaii (e.g., Fodor & Galar, 1997). Although small (centimeter)-scale layering is evidenced by the occurrence of composite xenoliths (c.f. Fodor & Galar, 1997; Hoover & Fodor, 1997), possible large (kilometer)-scale layering is more difficult to constrain. In principle, precise pressure estimates of the xenoliths could provide insights into this inferred layering, and more generally on the architecture of the magmatic system beneath Hawaii. However, most common geobarometers applicable to the xenoliths are affected by uncertainties of ~3 kbar (e.g., two-pyroxene barometers; Putirka et al., 2008), which propagate to depth uncertainties of ~10 km. Considering that the crustal thickness in Hawaii is lower than 20 km (Park et al., 2009; Zucca et al., 1982), such uncertainties are too high to well constrain any kilometer-scale heterogeneity. The recently refined multiple-reaction geobarometer for clinopyroxene + olivine + plagioclase assemblages (Ziberna et al., 2017), which has been shown to have pressure uncertainties as small as 1.0 kbar, might provide a new opportunity to overcome this problem.

1.3. REVISED GEOTHERMOBAROMETRY OF MAUNA KEA AND HUALALAI XENOLITHS

1.3.1. Rationale and Data Selection

There are several considerations to bear in mind when selecting a set of geothermometers and geobarometers to be applied to a xenolith population:

1. The selection is clearly restricted to algorithms involving phases that are present in the xenolith assemblage. For a xenolith suite composed of different lithologies, this often leads to the application of different geothermometers or geobarometers. If these were calibrated on different experimental data sets, their application might produce potentially inconsistent results.
2. The compositions of the phases have to be reasonably assumed to represent equilibrium conditions.
3. When the thermodynamic data of a given thermobarometric algorithm have been simplified to few parameters and these parameters have been calibrated from experiments in a specific range of pressures, temperatures, compositions and phase assemblages, then its application outside this range must be approached with caution.
4. Model errors (i.e., errors calculated from regression statistics on a test experimental data set) of a thermobarometer derived as in (3) represent only minimum errors when the algorithm is applied to natural assemblages. Additional, potentially quantifiable errors might result from propagation of analytical errors that are higher than the average errors of the experimental data set used for calibration. Further, unquantifiable errors might instead arise if compositions do not represent complete equilibrium conditions, despite assumption (2), and if simplified thermodynamic equations are applied outside the P-T-x range of experimental calibration [aspect (3)]. Notably, the concept of model errors as defined above is not applied to a multiple-reaction approach such as the *avP* method (Powell & Holland, 1994; Ziberna et al., 2017). In this case, errors are calculated by propagation of uncertainties with respect to both the mineral compositions and thermodynamic properties of the end-members of phases, taking into account the correlations between reactions that share end-members.

The method that was recently shown to predict the pressures of phase equilibrium experiments with sufficient accuracy and that can be applied to a discrete part of the xenolith suite from Hualalai and Mauna Kea is the *avP* method refined for olivine-bearing assemblages (Ziberna et al., 2017). Pressures have therefore been calculated with this method, with a major focus on spinel + clinopyroxene + olivine + plagioclase (SCOlP) assemblages, which allows six reactions to be used in the averaging procedure (Ziberna et al., 2017). Temperatures have been calculated with Ca-in-olivine geothermometry, which is convenient for applications to olivine+clinopyroxene-bearing assemblages. Available algorithms include those of Köhler and Brey (1990), which, however, were calibrated in peridotitic systems with olivines with $Fo_{87–100}$, not resembling the compositions of the Hawaiian xenoliths examined in this study (Fo_{67-86}). Moreover, their data set used for calibration includes experiments performed at P = 10–60 kbar (with the exception of one experiment at 2 kbar), which is outside the P range expected for Hawaiian xenoliths (P = 0–8 kbar; e.g., Bohrson & Clague, 1988; Shamberger & Hammer, 2006). I have therefore selected the method of Shejwalkar and Coogan (2013), which was calibrated in basaltic systems for olivines with $Fo_{70–100}$, which is closer to the compositional range of Hawaiian xenoliths. Still, their experiments used for calibrations are at P = 0.001 kbar and T = 1170–1322 °C, and therefore the results must be taken with caution [see aspect (3) above and the discussion in section 1.3.2]. For the sake of comparison, pressures and temperatures have also been calculated using the two-pyroxene geobarometer and geobarometer of Putirka (2008; his equations 36 and 39).

For this geothermobarometric study, I selected all the available published data sets on the Hualalai and Mauna Kea xenoliths that include both petrographic characterization and electron microprobe analyses of minerals (Bohrson & Clague, 1988; Chen et al., 1992; Clague & Bohrson, 1991; Fodor, 2001; Fodor & Galar, 1997; Fodor & Vandermeyden, 1988; Hoover & Fodor, 1997; Schamberger & Hammer, 2006). This collection of data includes 85 samples from Hualalai and 123 xenoliths from Mauna Kea. A first screening selected the xenolith containing the appropriate phases for geothermobarometry (i.e., olivine + clinopyroxene + plagioclase, clinopyroxene + orthopyroxene, or both) and for which the chemical compositions of these phases are available. Further screening discarded 13 xenoliths which were described in the source papers as showing evidence of textural disequilibrium, or that are characterized by large intra-sample compositional variations of pyroxenes {> 0.03 mg#[(Mg/(Mg+Fe^{2+}), Fe^{2+} calculated after Droop, 1987] units}, olivine (> 0.03 mg# units), and/or plagioclase (>10 mol% of anorthite component). This screening produced a data set of 31 xenoliths from Hualalai and 50 xenoliths from Mauna Kea.

1.3.2. Temperature Estimates

For Hualalai, temperatures calculated with the Ca-in-olivine thermometer ($T_{\text{Ca-in-ol}}$; eq. 12 in Shejwalkar & Coogan, 2013) range from 997 °C to 1168 °C (with a major cluster at 1040–1117 °C) for the ultramafic xenoliths, and from 841 °C to 904 °C for gabbroic xenoliths (see Supplementary material and Figures 1.2a, 1.3a). For Mauna Kea, on the other hand, the calculated temperatures are indistinguishable between the ultramafics and the gabbroic rocks and are in the range 744–1103 °C (see Supplementary material and Figures 1.2a, 1.3a). Two-pyroxene temperatures ($T_{\text{cpx-opx}}$) show a similar relative difference between Hualalai and Mauna Kea (Figures 1.2c,d). However, Figures 1.2 and 1.3a show that at lower temperatures (<1050 °C) two-pyroxene geothermometry produce significantly higher values (up to 230 °C; 125 °C on average) than Ca-in-olivine geothermometry.

Here I infer that the discrepancy between the two-pyroxene and Ca-in-olivine temperatures could be related to the slower diffusion of Mg-Fe^{2+} in pyroxenes compared to Ca-in-olivine (Chakraborty, 2010; Cherniak & Dimanov, 2010; Coogan et al., 2005; Müller et al., 2013), which would in principle make the Ca-in-olivine method more suitable for applications to cumulate rocks that underwent cooling below subsolidus temperatures. As a matter of fact, the source of the deviations seen in Figure 1.3a is less likely to be related to the calibration strategies of either methods, because a test on a large experimental data set shows that both methods appear to overestimate experimental values at low temperatures (with more pronounced overestimation by the Ca-in-olivine method; Figures 1.3b,c). This is also true when using a tentative equation for Ca-in-olivine geothermometry that accounts for its pressure dependency (eq. 13 in Shejwalkar & Coogan, 2013; Figures 1.3c,d). The sudden change in the deviations of $T_{\text{Ca-in-ol}}$ from T_{exp} shown in Figure 1.3c could be related to a change in the solubility mechanism of Ca-in-olivine at low temperatures (Köhler & Brey, 1990). Note that the test in Figures 1.3c,d is shown only as a first, preliminary evaluation, because the experimental data set does not include data obtained with analytical conditions optimized for analysis of Ca content in olivine, which is indeed reflected by the large deviations of Ca-in-olivine temperatures from the experimental values. In addition, there are scarce experimental data at $T < 1000$°C, and no data at all at $T < 900$ °C, which are the temperatures of interest for investigating the subsolidus conditions of mafic and ultramafic cumulates during cooling.

1.3.3. Pressure Estimates

For Hualalai, pressures calculated with *avP* ($\bar{P}$) on SCOlP assemblages, at temperatures $T_{\text{Ca-in-ol}}$, vary in the range $\bar{P}$ = 5.5–6.7 kbar ($\sigma_{\bar{P}}$ = 0.9–1.2 kbar) for the ultramafic xenoliths, $\bar{P}$ = −0.6–2.6 kbar ($\sigma_{\bar{P}}$ = 1.0–2.0 kbar) for gabbronorites and dioritic xenoliths, and $\bar{P}$ = 5.4 kbar ($\sigma_{\bar{P}}$ = 1.0 kbar) for one gabbro xenolith. For Mauna Kea, the calculated pressures of the different lithologies overlap within the range $\bar{P}$ = 0.6–5.9 kbar ($\sigma_{\bar{P}}$ = 1.0–2.8 kbar). Calculations produced diagnostic σ_{fit} values (Powell & Holland, 1994) that are generally higher for samples from Mauna Kea (σ_{fit} = 1.2–2.7) with respect to Hualalai (σ_{fit} = 0.4–1.8). The cutoff value provided by the χ^2 test, representing 95% confidence of the average P calculations (Powell & Holland, 1994), is $\sigma_{\text{fit}} <$ 1.49. However, higher values could still be considered acceptable, because $\sigma_{\bar{P}}$ is increased by a factor equal to σ_{fit} when the χ^2 test fails (Ziberna et al., 2017), as shown by the generally higher uncertainties for Mauna Kea samples (Figure 1.2b).

Compared to the results of *avP*, application of the two-pyroxene geobarometer at temperatures $T_{\text{cpx-opx}}$ generally provides higher pressures for Hualalai samples ($P^{\text{cpx-opx}}$ = 6.2–10.9 kbar for ultramafic xenoliths; 1.4–6.3 kbar for gabbroic and dioritic xenoliths) and similar ranges of pressures for Mauna Kea ($P^{\text{cpx-opx}}$ = −1.7–6.4 kbar). The model error for this geobarometer, as reported by Putirka (2008), is 2.8 kbar (if clinopyroxene mg# > 0.75, which is the case for the data set considered in this work). Note that, because *avP* and two-pyroxene geobarometers are based on two different assemblages, they were applied to two partially different subsets of xenoliths. Figure 1.4 avoids possible misleading interpretations by showing the results of each barometer for the individual xenoliths. This plot confirms that for Hualalai xenoliths the two-pyroxene geobarometer produces higher pressures than *avP*, as evidenced by the xenolith containing the assemblage olivine + clinopyroxene + orthopyroxene + plagioclase + spinel. On the other hand, pressures estimated with two-pyroxene and *avP* methods on Mauna Kea xenoliths do not show systematic differences.

To evaluate the effect of temperature on the pressures estimated with *avP*, Figure 1.4 also includes values of $\bar{P}$ calculated with temperatures from two-pyroxene thermometry, where possible. With few exceptions, the differences are smaller than 1.2 kbar and are not systematic (Figure 1.4). Furthermore, Figure 1.4 includes the results of *avP* using the COlP assemblage at $T_{\text{Ca-in-ol}}$, because some of the olivine-bearing gabbroic xenoliths do not contain spinel. The results are comparable, with a slight P overestimation compared to the pressures obtained using the SCOlP assemblage, consistent with

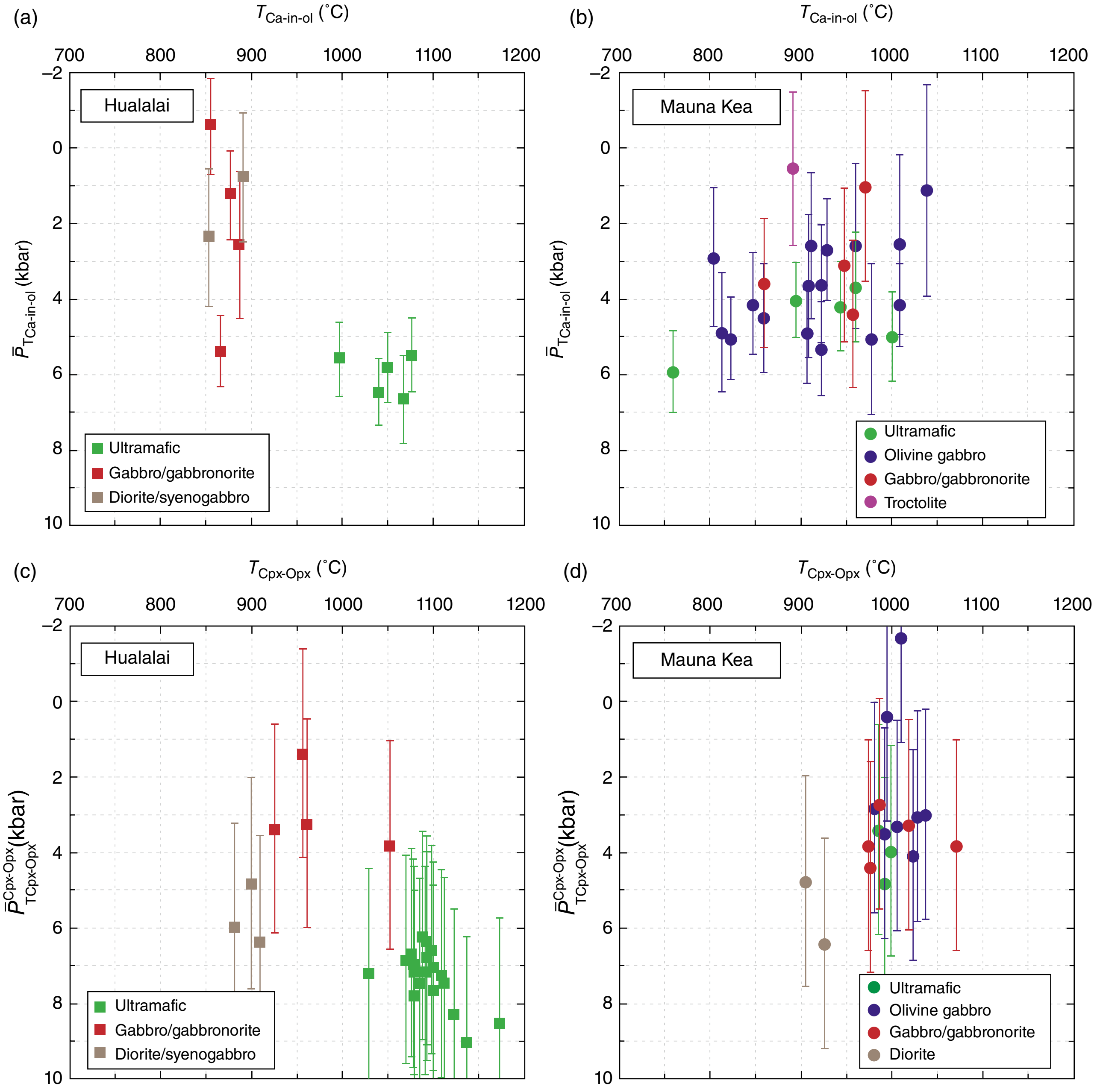

Figure 1.2 Pressure and temperature estimates for (a,c) Hualalai and (b,d) Mauna Kea xenoliths using either (a,b) the *avP* method refined for SCOlP assemblage (Ziberna et al., 2017) ($\bar{P}$) combined with the Ca-in-olivine geothermometer of Shejwalkar and Coogan (2013) ($T_{\text{Ca-in-ol}}$) or (c,d) the two-pyroxenes geothermometer and geobarometer of Putirka (2008) (his eqs. 39 – $P^{\text{Cpx-Opx}}$ and 36 – $T_{\text{Cpx-Opx}}$). Error bars in (a,b) are uncertainties ($\sigma_{\bar{P}}$) calculated through the *avP* algorithm, while errors in (c,d) are model errors as reported in Putirka (2008). Rock nomenclatures follow Streckeisen (1976).

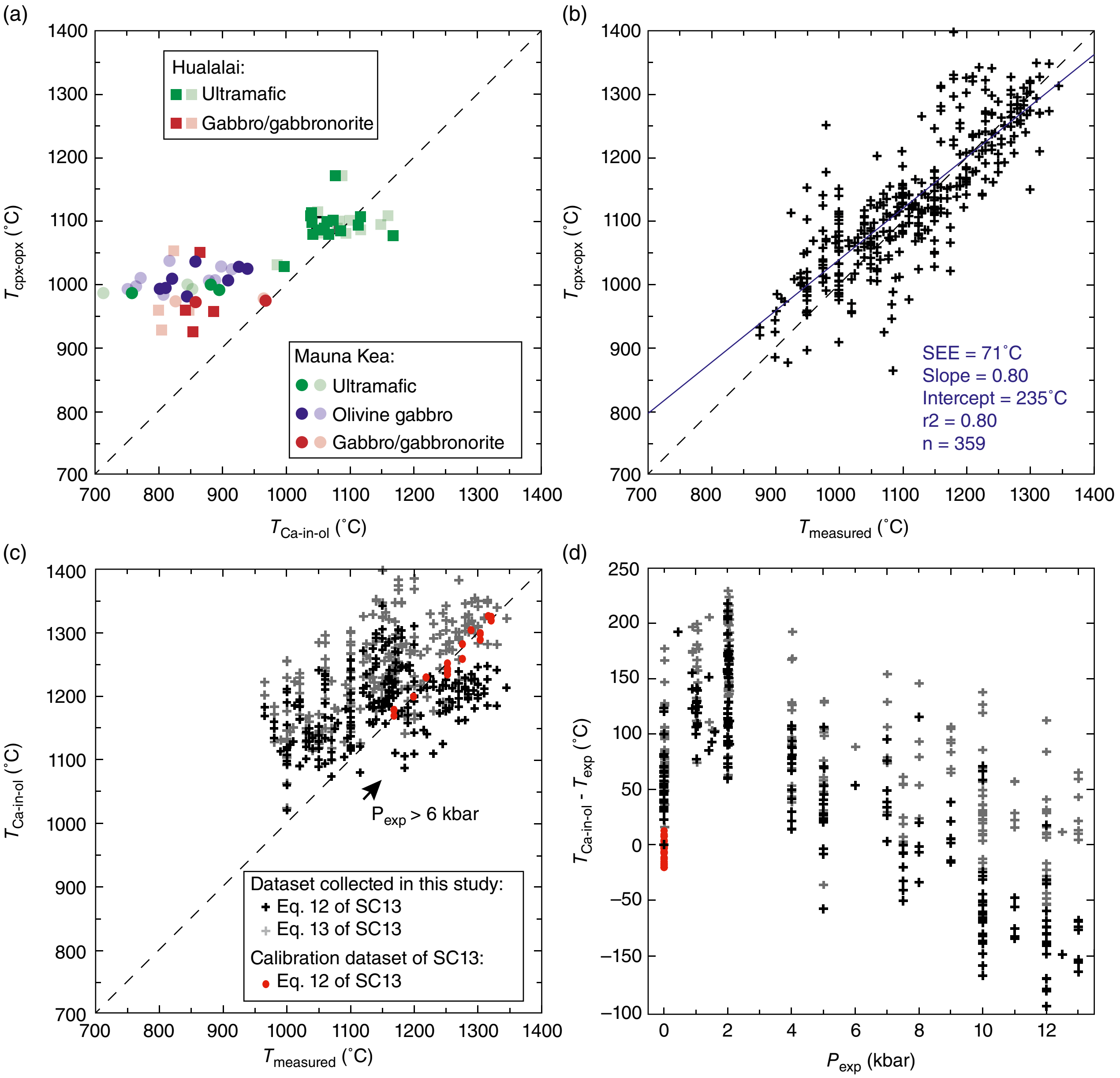

Figure 1.3 Comparison between the results of Ca-in-olivine ($T_{\text{Ca-in-ol}}$; Shejwalkar & Coogan, 2013; SC13) and two-pyroxene geothermometry ($T_{\text{cpx-opx}}$; Putirka, 2008). (a) Application to the xenoliths from Mauna Kea and Hualalai, using eq. 36 in Putirka (2008) and either eq. 12 (solid symbols) or eq. 13 (transparent symbols) in Shejwalkar and Coogan (2013). (b) Test of eq. 36 in Putirka (2008) and (c) Ca-in-olivine geothermometers using the experimental data set collected in this study (Baker & Eggler, 1987; Baker & Stolper, 1994; Bartels et al., 1991; Blatter et al., 2013; Borghini et al., 2010; Chalot-Prat et al., 2010, 2013; Di Carlo et al., 2006; Feig et al., 2006, 2010; Gaetani & Grove, 1998; Gaetani et al., 1994; Grove & Juster, 1989; Grove et al., 1997; Grove & Bryan, 1983; Hamada & Fuji, 2008; Husen et al., 2016; Kinzler & Grove, 1992; Lambart et al., 2009; Lanzo et al., 2016; Laporte et al., 2004; Melekhova et al., 2015; Nandedkar et al., 2014; Parat et al., 2014; Pichavant & MacDonald, 2007; Sisson & Grove, 1993; Stamper et al., 2014; Tormey et al., 1987; Yang et al., 1996); only clinopyroxene+olivine-bearing experimental products were considered. (d) Deviations of Ca-in-olivine from experimental temperatures as a function of experimental pressures, for the same experimental data set.

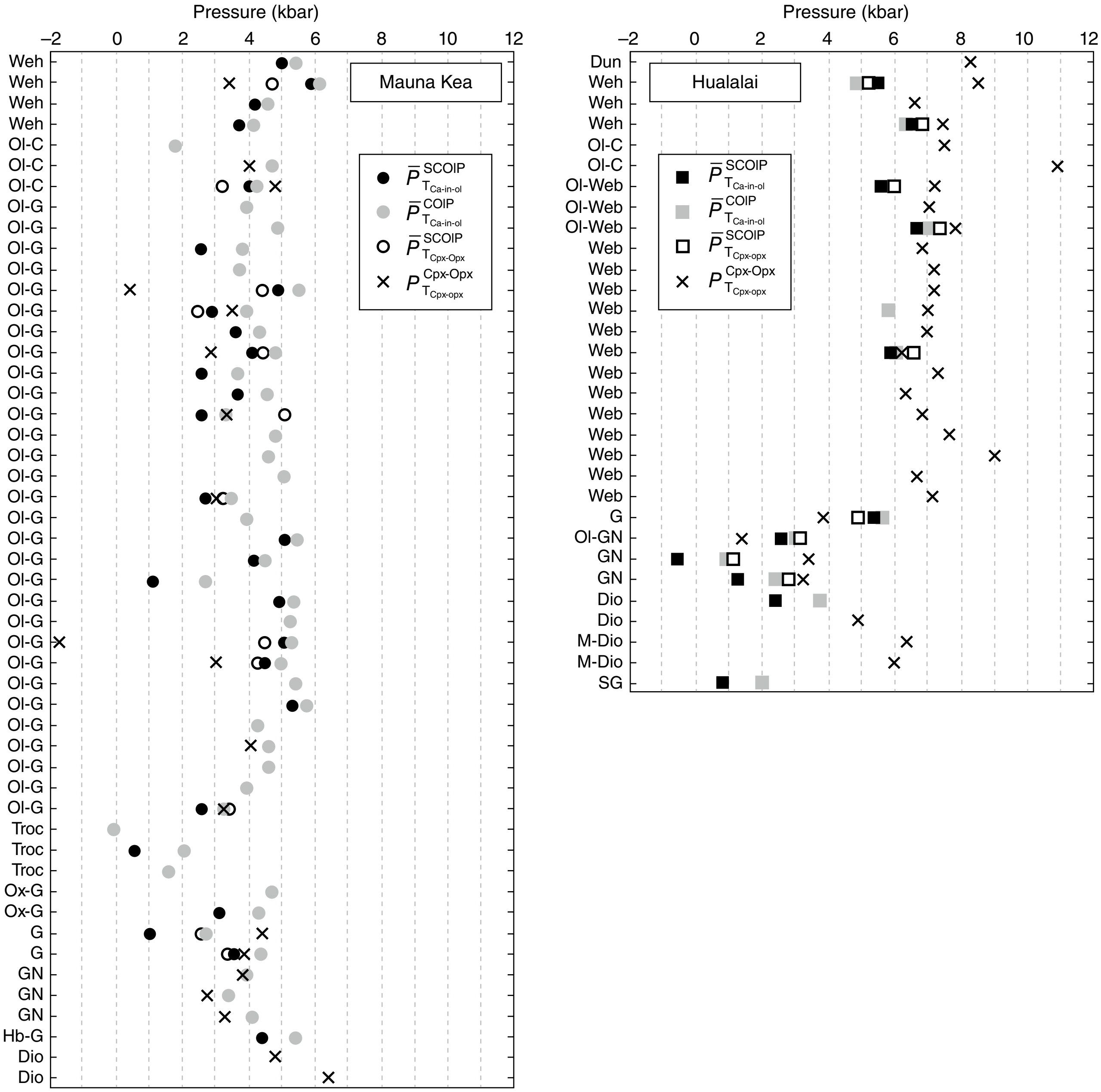

Figure 1.4 Pressure estimates for each Mauna Kea and Hualalai xenolith based on different sets of geothermobarometers. Errors are not shown for the sake of clarity of the plot. Dun – Dunite, Weh – Wehrlite, Ol-C – Olivine-clinopyroxenite, Ol-Web – Olivine-websterite, Ol-G, Olivine-gabbro, Troc – Troctolite, Ox-G – Oxide-gabbro, G – Gabbro, GN – Gabbronorite, Ol-GN – Olivine-gabbronorite, Hb-G – Hornblende-gabbro, Dio – Diorite, M-Dio – Monzodiorite, SG – Syenogabbro.

the observations of Ziberna et al. (2017). Despite the fact that using a SCOlP assemblage is considered more reliable, because it allows an independent set of six reactions to be used instead of three (Ziberna et al., 2017), the results of *avP* using the COlP assemblage are useful for showing that troctolites from Mauna Kea record among the lowest pressures of the xenolith suite (Figure 1.4).

1.4. DISCUSSION

1.4.1. Comparisons with Previous Estimates and Implications of the Results

Compared to the previous estimates on Hawaiian xenoliths, the results obtained with the *avP* method allow for more precise quantification of their pressure of

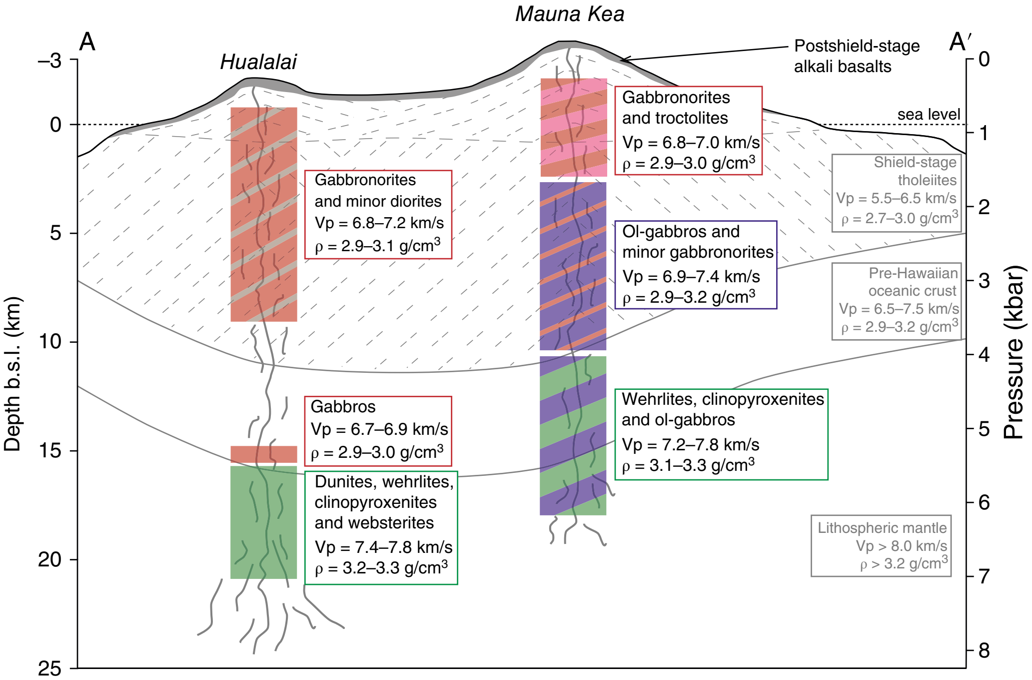

Figure 1.5 Schematic cross section of the island of Hawaii along the profile A-A′ in Figure 1.1 and tentative representation of the lithological variations beneath Hualalai and Mauna Kea (colored boxes), based on *avP* calculations on the available xenoliths containing the assemblage SCOlP (see text). The color code of the lithologies is the same as in Figures 1.2 and 1.3. The range of calculated P-wave velocities and densities of each group of lithologies are also reported. The approximate ranges of Vp and ρ for tholeiites, oceanic crust, and lithospheric mantle are from Christensen and Mooney (1995) and Manghnani and Woollard (1968). The gray cap on Hualalai and Mauna Kea does not represent the actual thickness of the postshield alkali basalts and is only shown as a sketch representation. The surface topography and depths of pre-Hawaiian oceanic crust are from Wolfe et al. (1997). Depths have been calculated from $\overline{P}$ assuming a constant density value of 3.0 g/cm^3. Sources: Christensen and Mooney (1995); Manghnani and Woollard (1968); Wolfe et al. (1997).

formation and for the xenolith data to be placed in the context of the crustal structure of the Hawaiian crust. Based on the model of Wolfe et al. (1997), the top of the ~5 km-thick Pacific oceanic crust beneath the island of Hawaii is mostly covered by a ~12 km-thick unit of shield-stage tholeiites. This is illustrated in Figure 1.5, a schematic cross section of the crust beneath the Hualalai and Mauna Kea volcanoes. The results of *avP* calculations of each xenolith have been grouped and schematically represented as colored boxes in Figure 1.5, in order to allow a direct comparison between the depth estimates for the xenoliths to the modeled structure of the crust. This comparison might be oversimplified for an in-depth investigation, and it is shown here only to demonstrate the potential of precise pressure estimates on xenoliths from active magmatic systems.

Previous estimates for the ultramafic xenoliths from Hualalai were only semi-quantitative and indicated a pressure range of 4.5–9.0 kbar, based on a comparison between the mineralogy of the xenoliths and the results of phase equilibrium experiments and on the minimum trapping pressure of CO_2 inclusions in olivines (Bohrson & Clague, 1988; Chen et al., 1992). *AvP* calculations on the available xenolith data agree with these estimates, but suggest a much narrower range ($\overline{P}$ = 5.5–6.7 kbar), with calculated errors for each xenolith smaller than 1.2 kbar. This pressure range translates to a depth range of 16–21 km b.s.l. (Figure 1.5), which is consistent with the presence of a pile of ultramafic cumulates derived from fractionation of basaltic magmas at or below the base of the Pacific oceanic crust, as already suggested by Bohrson and Clague (1988).

For the gabbronorites and diorites from Hualalai, Shamberger and Hammer (2006) suggested that their pressure of formation falls anywhere between 2.5 and 7.5 kbar, based on the application of the single-clinopyroxene method of Nimis (1999) and qualitative comparisons between natural and experimental clinopyroxene compositions. These pressures are higher than the results of *avP* calculations, which rather indicate a pressure range of 0.0–2.6 kbar, and translate to a depth range of 0–8 km (Figure 1.5). Because diorites xenoliths are considered parental to the Hualalai trachytes (Shamberger & Hammer, 2006), this depth range supports the hypothesis of trachytes formed by crystal fractionation in shallow (3–7 km; Clague, 1987; Cousens et al., 2003) rather than deep (10–23 km; Shamberger & Hammer, 2006) reservoirs during the shield to post-shield transition. It is worth noting, however, that two-pyroxene geothermobarometry on olivine-free diorites (Figure 1.2c) suggests significantly higher pressures ($P^{\text{cpx-opx}}$ = 4.9–6.5 kbar) than the *avP* calculation on the only available olivine-bearing diorite ($\bar{P}$ = 2.2 kbar). Further work will be needed to understand if this difference is related to the possible inconsistency of the geothermobarometric methods or to an actual difference in the pressure of formation of olivine-free and olivine-bearing diorites.

As already noted by Clague (1987) and Fodor and Galar (1997), although at Hualalai most of the xenoliths are ultramafic, at Mauna Kea the majority of xenoliths are gabbroic. They suggested that this might reflect lower magma production rates at Mauna Kea, which allowed for more extensive fractionation and production of magmas with FeO/MgO > 2. Fodor and Galar (1997) suggested that the gabbroic and ultramafic xenoliths at Mauna Kea record similar pressures, following the observation of similar $\text{Al}^{\text{iv}}/\text{Al}^{\text{vi}}$ ratios in clinopyroxene. Based on the absence of Mg-rich cumulus orthopyroxene, they also suggested that these pressures are less than ~5 kbar. These qualitative estimates are supported by two-pyroxene geobarometry (this work and Putirka, 2017) and *avP* calculations. The latter method also appears to detect a possible lithological variation with pressure. Looking closely at the *avP* results, ultramafic xenoliths are among those that record the highest pressures, troctolites and gabbronorites record the lowest pressures, and estimates for the olivine-gabbros span almost over the entire range (Figures 1.2b and 1.4). This translates to a sequence of ultramafic xenoliths and olivine-gabbros from 18 km to 11 km b.s.l., olivine-gabbros and minor gabbronorites from ~11 km to ~3 km b.s.l. and gabbronorites and troctolites from ~3 km b.s.l. to the subsurface beneath the summit (Figure 1.5).

1.4.2. Geobarometry of Xenoliths as One of the Links between Petrology and Geophysics

Seismic velocity and gravity modeling are indispensable to investigate the deep structure and physical properties of active magmatic systems and the lithosphere in which they are emplaced. They are known, however, to provide non-univocal solutions regarding the thermal state, chemistry, and phase assemblages of the imaged geophysical bodies. The number of solutions can be significantly decreased if there is a xenolith cargo in the erupted lavas that can be combined with the geophysical information. Recent work on the Lesser Antilles and Aleutian arcs, for example, proved the potential of integrating the petrology of xenoliths with the seismic information (Kiddle et al., 2010; Melekhova et al., 2019; Shillington et al., 2004). In the following, I show a brief and simplified exercise comparing the xenolith data from Hualalai and Mauna Kea to one of the existing seismic models of the crust beneath Hawaii. In this exercise, it is important to bear in mind that xenoliths likely represent conduits and reservoirs with dike, sill, laccolith, or batholith shapes and variable sizes (Fodor & Galar, 1997), which might or might not be sufficiently large to be detected by seismic methods. For the sake of this exercise, it is also assumed that the xenolith populations are, to some extent, representative of most of the lithologies in such conduits and reservoirs.

Seismic properties (P-wave velocity – Vp, density – ρ) have been calculated for each xenolith using the model of Abers and Hacker (2016), at the temperatures $T_{\text{Ca-in-ol}}$ and pressures $\bar{P}$ calculated in this work. Their model calculates the physical properties of mineral assemblages at high pressures and temperature by applying Voigt–Reuss–Hill and Hashin–Shtrikman averages to the pure end-members of minerals. Melt, vapor phase, or porosity is not considered, and the calculations do not take into account possible anisotropy and anelastic or physical dispersion effects for finite-frequency signals (Abers & Hacker, 2016). The proportions of end-members were calculated from mineral proportions and compositions, and therefore the calculations were limited to the xenoliths for which this information is available in the literature (Bohrson & Clague, 1988; Fodor & Galar, 1997; Fodor & Vandermeyden, 1988; Hoover & Fodor, 1997; Schamberger & Hammer, 2006). Results of the calculations are shown in Figure 1.6. The calculated Vp values vary in the range 6.8–7.2 km/s for gabbros, gabbronorites, and diorites; 6.9–7.7 km/s for olivine-gabbros; and 7.4–7.9 km/s for ultramafic xenoliths.

Figure 1.6 also compares 1D seismic profiles beneath southwestern Hualalai and southern Mauna Kea, extrapolated from the seismic tomography model of Park et al. (2009), to an ideal seismic profile built from room-temperature and high-pressure laboratory data of rock seismic properties (gray areas). The latter profile represents an ideal, end-member case in which the Hawaiian crust would be composed solely of shield-stage tholeiites on the top of the pre-Hawaiian oceanic crust (Figure 1.5). If this accurately depicted what lies beneath Hualalai and Mauna Kea, then the observed 1D seismic profiles should correspond to this ideal profile. Any positive variation from ideality might indicate the presence of intrusions with higher Vp velocities, and the Vp–depth relationships of the xenoliths can help constrain the nature of these intrusions. Note that higher temperatures and the

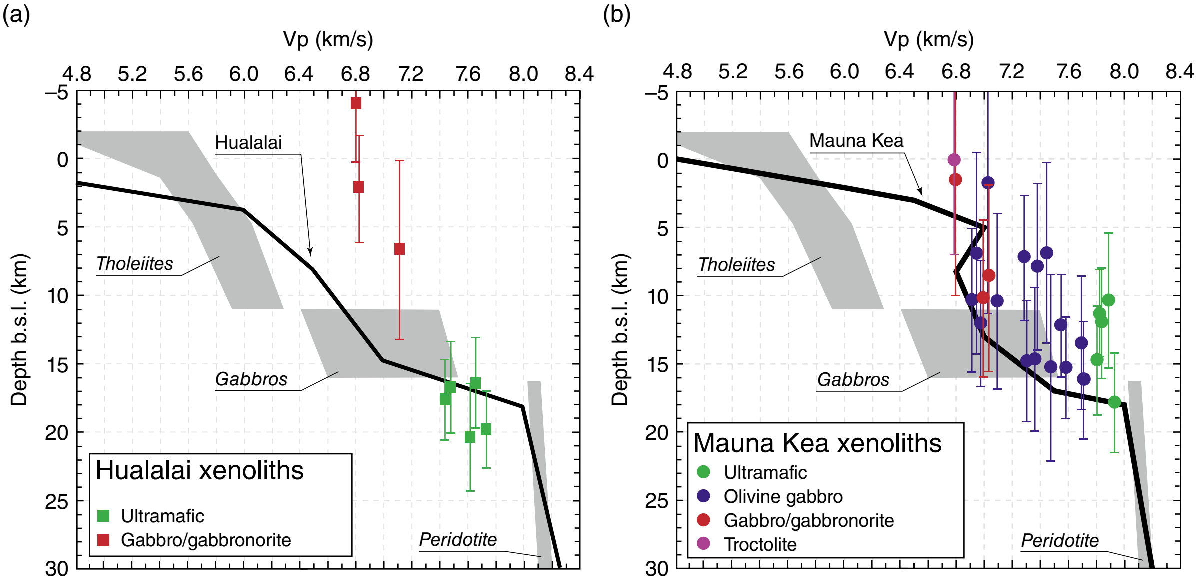

Figure 1.6 Calculated P-wave velocities (Vp) versus depth for the xenoliths from (a) Hualalai and (b) Mauna Kea. The depths have been calculated as in Figure 1.5. Solid curves are 1D seismic profiles beneath south-eastern Hualalai and southern Mauna Kea extrapolated from the seismic tomography model of Park et al. (2009). Gray areas show the range of Vp values measured in laboratory experiments (Behn & Kelemen, 2003; Khazanehdari et al., 2000; Manghnani & Woollard, 1968) for the rock types that are assumed to constitute the hypothetical cross section in Figure 1.5, devoid of the cumulates represented by the xenoliths. Sources: Park et al. (2009); Behn and Kelemen (2003); Khazanehdari et al. (2000); Manghnani and Woollard (1968).

presence of melts or porosities would only decrease Vp with respect to the experimental data.

At ~5–11 km depth beneath Hualalai, the seismic data of Park et al. (2009) show velocities that are higher than those expected for Hawaiian tholeiites (Manghnani & Woollard, 1968), but lower than those calculated for the gabbro and gabbronorite xenoliths from similar depths (Figure 1.6a). This might suggest that the depth interval 5–11 km beneath Hualalai is composed of shield-stage tholeiites variably intruded by gabbros and gabbronorite cumulates. Clearly, more gabbroic xenoliths need to be sampled and characterized to better define this depth interval. Figure 1.6a also shows that the calculated Vp–depth relationship of the ultramafic xenoliths from Hualalai (7.4–7.8 km/s) is consistent with the seismic tomography model of Park et al. (2009). This agreement supports the hypothesis that the dense, high-velocity bodies observed beneath the oceanic crust of Hawaiian islands (Watts et al., 1985) is indeed composed of intrusions of ultramafic cumulates (Clague, 1987; Richards et al., 2013). In the case of Hualalai, this intrusion might be as thick as ~3 km.

The depth interval 3–11 km beneath Mauna Kea shows a more pronounced disagreement between ideal (5.6–6.2 km/s) and observed (6.2–7.0 km/s) P-wave velocities (Figure 1.6b). The latter are much more consistent with the calculated velocities of xenoliths from the same depths (6.8–7.4 km/s), suggesting that a significant portion of the crust beneath Mauna Kea at 3–11 km depths have been intruded by basaltic magmas that fractionated to produced olivine-gabbros and minor gabbronorite cumulates. These lithologies could therefore be considered as the source of the high-velocity anomalies typically observed at these depths beneath Hawaiian volcanoes (e.g., Lin et al., 2014; Park et al., 2009). The presence of olivine-gabbro and ultramafic xenoliths at 11–16 km depth suggests that the pre-Hawaiian oceanic crust at Mauna Kea has been more pervasively intruded by shield or post-shield Hawaiian magmas, as opposed to Hualalai. However, the good agreement between observed and ideal seismic velocities and the significantly higher calculated velocities of the ultramafic lithologies suggest that ultramafic cumulates are volumetrically less significant in this depth interval.

1.5. CONCLUSIONS AND FUTURE PERSPECTIVES

Mafic and ultramafic xenoliths in magmatic rocks are sporadic but valuable carriers of information about the physical and chemical structure of volcano plumbing systems. If on the one hand they do not directly provide the spatial relationships of magmatic units as in the case of fossil crustal sections exposed at the surface (e.g., Ivrea-Verbano zone, southern Alps; Fountain & Salisbury, 1981;

Quick et al., 2009), on the other hand they represent the only direct samples of deep solidified intrusions in active volcanic systems. This reason alone justifies the past and future petrological and geophysical studies characterizing the available xenoliths and the effort to model the temperatures and pressures recorded by their phase assemblages. The geothermobarometric study shown in this work is a small and simplified example of how this modeling can be approached.

Application of the *avP* method (Powell & Holland, 1994; Ziberna et al., 2017) to the gabbroic and ultramafic xenoliths from Hualalai and Mauna Kea produced pressure estimates with calculated uncertainties as low as 1.0 kbar, which allowed detection of some lithological variations with depth in these two volcanic systems (Figure 1.5). Such estimates also allowed the xenolith data to be integrated with the available seismic models. Altogether, the results suggest that at Hualalai, ultramafic xenoliths likely represent fragments of one or more cumulate bodies intruded below the pre-Hawaiian oceanic crust. At Mauna Kea, on the other hand, ultramafic cumulate bodies might be less significant. Xenoliths of olivine-gabbros and ultramafic assemblages represent magmas that intruded and fractionated at shallower depths, within and above the pre-Hawaiian oceanic crust. A more in-depth work on a larger number of xenoliths will have to be performed to test these scenarios.

Despite this and other recent works (Cooper et al., 2019; Melekhova et al., 2017, 2019; Ziberna et al., 2017) which demonstrate that conventional geothermobarometry of xenoliths can help unravel important aspects about crustal magmatic systems, there are still problems that will need to be tackled in the future. For example, comparison between the results of two-pyroxene and Ca-in-olivine geothermometry showed significant disagreement at low temperatures (<1000°C), which suggests that more experimental and theoretical work is needed to refine the phase equilibrium and diffusion models for mafic and ultramafic systems at subsolidus conditions. Differential diffusion of elements could influence not only the results of the above geothermometers, but also the results of a multiple-reaction method involving a significant number of elements with potentially different diffusivities. At the same time, more work is needed to expand the application of the *avP* method to olivine-free magmatic rocks. This would allow the application of mutually consistent geothermobarometers to different xenoliths from the same populations and avoid possible inconsistency (compare Figures 1.2a,b to Figures 1.2c,d). These observations confirm once again that geothermobarometry is a continuously developing research field. Experimental and theoretical work refining the geothermobarometric models must proceed in parallel with their application to magmatic rocks and their xenoliths. Such an approach allows identification and potential resolution of relevant problems in geothermobarometry and therefore improves our knowledge of the complex architecture of magmatic systems.

ACKNOWLEDGMENTS

I thank the editors for their patience and helpful editorial handling, and I am grateful to an anonymous reviewer for the constructive review. I also thank Angelo De Min and Francesco Narduzzi for the useful discussions.

REFERENCES

Abers, G. A., & Hacker, B. R. (2016). A MATLAB toolbox and Excel workbook for calculating the densities, seismic wave speeds, and major element composition of minerals and rocks at pressure and temperature. *Geochemistry, Geophysics, Geosystems*, *17*, 616–624. doi:10.1002/2015GC006171.

Baker, D. R., & Eggler, D. H. (1987). Compositions of anhydrous and hydrous melts coexisting with plagioclase, augite, and olivine or low-Ca pyroxene from 1 atm to 8 kbar: Application to the Aleutian volcanic center of Atka. *American Mineralogist*, *72*, 12–28.

Baker, M. B., & Stolper, E. M. (1994). Determining the composition of high-pressure mantle melts using diamond aggregates. *Geochimica et Cosmochimica Acta*, *58*, 2811–2827. https://doi.org/10.1016/0016-7037(94)90116-3.

Bartels, K. S., Kinzler, R. J., & Grove, T. L. (1991). High pressure phase relations of primitive high-alumina basalts from Medicine Lake volcano, northern California. *Contributions to Mineralogy and Petrology*, *108*, 253–270. https://doi.org/10.1007/BF00285935.

Behn, M. D., & Kelemen, P. B. (2003). Relationship between seismic P-wave velocity and the composition of anhydrous igneous and meta-igneous rocks. *Geochemistry Geophysics Geosystems*, *4*, 1–57. https://doi:10.1029/2002GC000393.

Blatter, D. L., Sisson, T. W., & Hankins, W. B. (2013). Crystallization of oxidized, moderately hydrous arc basalt at mid- to lower-crustal pressures: Implications for andesite genesis. *Contributions to Mineralogy and Petrology*, *166*, 861–886. https://doi.org/10.1007/s00410-013-0920-3.

Blundy, J. D., & Holland, T. J. B. (1990). Calcic amphibole equilibria and a new amphibole-plagioclase geothermometer. *Contributions to Mineralogy and Petrology*, *104*, 208–224.

Bohrson, W. A., & Clague, D. A. (1988). Origin of ultramafic xenoliths containing exsolved pyroxenes from Hualalai Volcano, Hawaii. *Contributions to Mineralogy and Petrology*, *100*(2), 139–155.

Borghini, G., Fumagalli, P., & Rampone, E. (2010). The stability of plagioclase in the upper mantle: Subsolidus experiments on fertile and depleted lherzolite. *Journal of Petrology*, *51*, 229–254. https://doi.org/10.1093/petrology/egp079.

Bowen, N. L. (1928). *The evolution of igneous rocks*. Princeton, NJ: Princeton Univ. Press.

Chakraborty, S. (2010). Diffusion coefficients in olivine, wadsleyite and ringwoodite. *Reviews in Mineralogy & Geochemistry*, *72*(1), 603–639. https://doi.org/10.2138/rmg.2010.72.13.

Chalot-Prat, F., Falloon, T. J., Green, D. H., and &, W.O. (2010). An experimental study of liquid compositions in equilibrium with plagioclase + spinel lherzolite at low pressures (0.75 GPa). *Journal of Petrology*, *51*, 2349–2376. https://doi.org/10.1093/petrology/egq060.

Chalot-Prat, F., Falloon, T. J., Green, D. H., and &, W.O. (2013). Melting of plagioclase + spinel lherzolite at low pressures (0.5 GPa): An experimental approach to the evolution of basaltic melt during mantle refertilisation at shallow depths. *Lithos*, *172–173*, 61–80. https://doi.org/10.1016/j.lithos.2013.03.012.

Chen, C., Presnall, D. C., & Stern, R. J. (1992). Petrogenesis of ultramafic xenoliths from the 1800 Kaupulehu flow, Hualalai volcano, Hawaii. *Journal of Petrology*, *33*(1), 163–202. https://doi.org/10.1093/petrology/33.1.163.

Cherniak, D. J., & Dimanov, A. (2010). Diffusion in pyroxene, mica and amphibole. *Reviews in Mineralogy & Geochemistry*, *72*(1), 641–690. https://doi.org/10.2138/rmg.2010.72.14.

Christensen, N. I., & Mooney, W. D. (1995). Seismic velocity structure and composition of the continental crust: A global view. *Journal of Geophysical Research*, *100*(B6): 9761–9788. https://doi.org/10.1029/95JB00259.

Clague, D. A. (1987). Hawaiian xenolith populations, magma supply rates and development of magma chambers. *Bulletin of Volcanology*, *49*(4), 577–587. https://doi.org/10.1007/BF01079963.

Clague, D. A., & Bohrson, W. A. (1991). Origin of xenoliths in the trachyte at Puu Waawaa, Hualalai Volcano, Hawaii. *Contributions to Mineralogy and Petrology*, *108*(4), 439–452. https://doi.org/10.1007/BF00303448

Clague, D. A., Jackson, E. D., & Wright, T. L. (1980). Petrology of Hualalai Volcano, Hawaii: Implication for mantle composition. *Bulletin Volcanologique*, *43*(4), 641–656. https://doi.org/10.1007/BF02600363.

Coogan, L. A., Hain, A., Stahl, S., & Chakraborty, S. (2005). Experimental determination of the diffusion coefficient for calcium in olivine between 900 °C and 1500 °C. *Geochimica et Cosmochimica Acta 69*(14), 3683–3694. https://doi.org/10.1016/j.gca.2005.03.002

Cooper, G. F., Blundy, D. J., Macpherson, C. G., Humbphreys, M. C. S., & Davidson, J. P. (2019). Evidence from plutonic xenoliths for magma differentiation, mixing and storage in a volatile-rich crystal mush beneath St. Eustatius, Lesser Antilles. *Contributions to Mineralogy and Petrology*, *174*, 39. https://doi.org/10.1007/s00410-019-1576-4.

Cousens, B. L., Clague, D. A., & Sharp, W. D. (2003). Chronology, chemistry, and origin of trachytes from Hualalai Volcano, Hawaii. *Geochemistry Geophysics Geosystems*, *4*(9), https://doi.org/10.1029/2003GC000560.

Di Carlo, I., Pichavant, M., Rotolo, S., & Scaillet, B. (2006). Experimental crystallization of a high-K arc basalt: The Golden Pumice, Stromboli Volcano (Italy). *Journal of Petrology*, *47*, 1317–1343. https://doi.org/10.1093/petrology/egl011.

Droop, G. T. R. (1987) A general equation for estimation of Fe^{3+} concentrations in ferromagnesian silicates and oxides from microprobe analysis, using stoichiometry criteria. *Mineralogical Magazine*, *51*, 431–435.

Erdmann, S., Martel, C., Pichavant, M., & Kushnir, A. (2014) Amphibole as an archivist of magmatic crystallization conditions: Problems, potential, and implications for inferring magma storage prior to the paroxysmal 2010 eruption of Mount Merapi, Indonesia. *Contributions to Mineralogy and Petrology*, *167*, 1016. https://doi.org/10.1007/s00410-014-1016-4.

Feig, S. T., Koepke, J., & Snow, J. E. (2006). Effect of water on tholeiitic basalt phase equilibria: An experimental study under oxidizing conditions. *Contributions to Mineralogy and Petrology*, *152*, 611–638. https://doi.org/10.1007/s00410-006-0123-2.

Feig, S. T., Koepke, J., & Snow, J. E. (2010). Effect of oxygen fugacity and water on phase equilibria of a hydrous tholeiitic basalt. *Contributions to Mineralogy and Petrology*, *160*, 551–568. https://doi.org/10.1007/s00410-010-0493-3.

Fodor, R. V. & Galar, P. (1997). A view into the subsurface of Mauna Kea volcano, Hawaii: crystallization processes interpreted through the petrology and petrography of gabbroic and ultramafic xenoliths. *Journal of Petrology*, *38* (5), 581–624. https://doi.org/10.1093/petroj/38.5.581.

Fodor, R. V., & Vandermeyden, H. J. (1988). Petrology of gabbroic xenoliths from Mauna Kea volcano, Hawaii. *Journal of Geophysical Research*, *93*, 4435–4452. https://doi.org/10.1029/JB093iB05p04435.

Fodor, R. V. (2001). The role of tonalite and diorite in Mauna Kea Volcano, Hawaii, magmatism: Petrology of summit-region leucocratic xenoliths. *Journal of Petrology*, *42*, 1685–1704. https://doi.org/10.1093/petrology/42.9.1685.

Fountain, D. M., & Salisbury, M. H. (1981). Exposed cross-sections through the continental crust: Implications for crustal structure, petrology, and evolution. *Earth and Planetary Science Letters*, *56*, 263–277. https://doi.org/10.1016/0012-821X(81)90133-3.

Frey, F. A., Garcia, M. O., Wise, W. S., Kennedy, A., Gurriet, P., & Albarede, F. (1991). The evolution of Mauna Kea volcano, Hawaii: Petrogenesis of tholeiitic and alkalic basalts. *Journal of Geophysical Research*, *96*, 14347–14375. https://doi.org/10.1029/91JB00940.

Frey, F. A., Wise, W. S., Garcia, M. O., West, H., Kwon, S. T., & Kennedy, A. (1990). Evolution of Mauna Kea volcano, Hawaii: Petrologic and geochemical constraints on postshield volcanism. *Journal of Geophysical Research*, *95*, 1271–1300. https://doi.org/10.1029/JB095iB02p01271.

Fumagalli, P., Borghini, G., Rampone, E., & Poli, S. (2017). Experimental calibration of Forsterite–Anorthite–Ca-Tschermak–Enstatite (FACE) geobarometer for mantle peridotites. *Contributions to Mineralogy and Petrology*, *172*, 38. https://doi.org/10.1007/s00410-017-1352-2.

Gaetani, G. A., & Grove, T. L. (1998). The influence of water on melting of mantle peridotite. *Contributions to Mineralogy and Petrology*, *131*, 323–346. https://doi.org/10.1007/s004100050396.

Gaetani, G. A., Grove, T. L., & Bryan, W. B. (1994). Experimental phase relations of basaltic andesite from Hole 839B under hydrous and anhydrous conditions. In J. Hawkins, L. Parson, J. Allan, et al. (Eds.), *Proceedings of the Ocean Drilling Program, Scientific Results*, *135*.

Gao, R., Lassiter, J. C., Barnes, J. D., Clague, D. A., & Bohrson, W. A. (2016). Geochemical investigation of Gabbroic Xenoliths from Hualalai Volcano: Implications for lower oceanic crust accretion and Hualalai Volcano magma storage system. *Earth and Planetary Science Letters*, *442*, 162–172. http://dx.doi.org/10.1016/j.epsl.2016.02.043.

Ghiorso, M. S., & Sack, R. O. (1995). Chemical mass transfer in magmatic processes, IV, A revised and internally consistent thermodynamic model for the interpolation and extrapolation of liquid-solid equilibria in magmatic systems at elevated temperatures and pressures. *Contributions to Mineralogy and Petrology*, *119*(2–3), 197–212. https://doi.org/10.1007/BF00307281.

Ghiorso, M. S., & Evans, B. W. (2008). Thermodynamics of rhombohedral oxide solid solutions and a revision of the Fe-Ti two-oxide geothermometer and oxygen-barometer. *American Journal of Science*, *308*(9), 957–1039. https://doi.org/10.2475/09.2008.01.

Giacomoni, P. P., Coltorti, M., Bryce, J. G., Fahnestock, M. F., & Guitreau, M. (2016). Mt. Etna plumbing system revealed by combined textural, compositional, and thermobarometric studies in clinopyroxene. *Contributions to Mineralogy and Petrology*, *171*, 34. https://doi.org/10.1007/s00410-016-1247-7.

Green, D. H., & Ringwood, A. E. (1967). The genesis of basaltic magmas. *Contributions to Mineralogy and Petrology*, *15*, 103. https://doi.org/10.1007/BF00372052.

Grove, T. L., & Bryan, W. B. (1983). Fractionation of pyroxene-pyric MORB at low pressure: An experimental study. *Contributions to Mineralogy and Petrology*, *84*, 293–309. https://doi.org/10.1007/BF01160283.

Grove, T. L., & Juster, T. C. (1989). Experimental investigations of low-Ca pyroxene stability and olivine–pyroxene–liquid equilibria at 1-atm in natural basaltic and andesitic liquids. *Contributions to Mineralogy and Petrology*, *103*, 287–305. https://doi.org/10.1007/BF00402916.

Grove, T. L., Donnelly-Nolan, J. M., & Housh, T. (1997). Magmatic processes that generated the rhyolite of Glass Mountain, Medicine Lake volcano, N. California. *Contributions to Mineralogy and Petrology*, *127*, 205–223. https://doi.org/10.1007/s004100050276.

Gualda, G. A. R., Ghiorso, M. S., Lemons, R. V., & Carley, T. L. (2012). Rhyolite- MELTS: A modified calibration of MELTS optimized for silica-rich, fluid-bearing magmatic systems. *Journal of Petrology*, *53*(5), 875–890. https://doi.org/10.1093/petrology/egr080.

Hamada, M., & Fuji, T. (2008). Experimental constraints on the effects of pressure and H_2O on the fractional crystallization of high-Mg island arc basalt. *Contributions to Mineralogy and Petrology*, *155*, 767–790. https://doi.org/10.1007/s00410-007-0269-6.

Holland, T. J. B., & Powell, R. (2011). An improved and extended internally-consistent thermodynamic dataset for phases of petrological interest, involving a new equation of state for solids. *Journal of Metamorphic Geology*, *29*(3), 333–383. https://doi.org/10.1111/j.1525-1314.2010.00923.x.

Holland, T., & Blundy, J. (1994). Non-ideal interactions in calcic amphiboles and their bearing on amphibole-plagioclase thermometry. *Contributions to Mineralogy and Petrology*, *116*, 433–447. https://doi.org/10.1007/BF00310910.

Hoover, S. R., & Fodor, R. V. (1997). Magma-reservoir crystallization processes: Small-scale dikes in cumulate gabbros, Mauna Kea volcano, Hawaii. *Bulletin of Volcanology*, *59*(3), 186–197. https://doi.org/10.1007/s004450050185.

Huang, S., & Frey, F. A. (2003). Trace element abundances of Mauna Kea basalt from phase 2 of the Hawaii Scientific Drilling Project: Petrogenetic implications of correlations with major element content and isotopic ratios. *Geochemistry, Geophysics, Geosystems*, *4*, paper 2002GC000322. https://doi.org/10.1029/2002GC000322.

Husen, A., Almeev, R. R., & Holtz, F. (2016). The effect of H_2O on pressure and multiple saturation and liquid line of descent in basalt from the Shatsky Rise. *Journal of Petrology*, *57*, 309–344. https://doi.org/10.1093/petrology/egw008.

Jackson, E. D., Beeson, M. H., & Clague, D. A. (1982). Xenoliths in volcanics from Mauna Kea Volcano, Hawaii. USGS Open-File Report, 82–201. https://doi.org/10.3133/ofr82201.

Jackson, E. D., Clague, D. A., Engleman, E., Friesen, W. F., & Norton, D. (1981). Xenoliths in the alkalic basalt flows from Hualalai Volcano, Hawaii. USGS *Open-File Report, 81-1031*. https://doi.org/10.3133/ofr811031.

Jennings, E. S. & Holland, T. J. B. (2015). A simple thermodynamic model for melting of peridotite in the system NCFMASOCr. *Journal of Petrology*, *56*, 869–892. https://doi.org/10.1093/petrology/egv020.

Khazanehdari, J., Rutter, E. H., & Brodie, K. H. (2000). High-pressure-high-temperature seismic velocity structure of the midcrustal and lower crustal rocks of the Ivrea-Verbano zone and Serie dei Laghi, NW Italy. *Journal of Geophysical Research*, *105*(B6), 13843–13858. https://doi.org/10.1029/2000JB900025.

Kiddle, E. J., Edwards, B. R., Loughlin, S. C., Petterson, M., Sparks, R. S. J., & Voight, B. (2010). Crustal structure beneath Montserrat, Lesser Antilles, constrained by xenoliths, seismic velocity structure and petrology. *Geophysical Research Letters*, *37*(19). https://doi.org/10.1029/2009GL042145.

Kinzler, R. J., & Grove, T. L. (1992). Primary magmas of Mid-Ocean Ridge Basalts 1. Experiments and methods. *Journal of Geophysical Research*, *97*, 6885–6906.

Köhler, T. P., & Brey, G. P. (1990). Calcium exchange between olivine and clinopyroxene calibrated as a geothermobarometer for natural peridotites from 2 to 60 kbar with applications. *Geochimica et Cosmochimica Acta*, *54*, 2375–2388.

Lambart, S., Laporte, D., & Schiano, P. (2009). An experimental study of focused magma transport and basalt–peridotite interactions beneath mid-ocean ridges: Implications for the generation of primitive MORB compositions. *Contributions to Mineralogy and Petrology*, *157*, 429–451. https://doi.org/10.1007/s00410-008-0344-7.

Lange, R. A., Frey, H. M., & Hector, J. (2009). A thermodynamic model for the plagioclase-liquid hygrometer/thermometer. *American Mineralogist*, *94*(4), 494–506. https://doi.org/10.2138/am.2009.3011.

Lanzo, G., Di Carlo, I., Pichavant, M., Rotolo, S. G., & Scaillet, B. (2016). Origin of primitive ultra-calcic arc melts at crustal conditions — Experimental evidence on the La Sommata basalt, Vulcano, Aeolian Islands. *Journal of Volcanology and Geothermal Research*, *321*, 85–101. http://dx.doi.org/10.1016/j.jvolgeores.2016.04.032.

Laporte, D., Toplis, M. J., Seyler, M., & Devidal, J.-L. (2004). A new experimental technique for extracting liquids from peridotite at very low degrees of melting: Application to partial melting of depleted peridotite. *Contributions to Mineralogy and Petrology*, *146*, 463–484. https://doi.org/10.1007/s00410-003-0509-3.

Liang, Y., Sun, C. & Yao, L. (2013). A REE-in-two-pyroxene thermometer for mafic and ultramafic rocks. *Geochimica et Cosmochimica Acta*, *102*, 246–260. https://doi.org/10.1016/j.gca.2012.10.035.

Lin, G., Shearer, P. M., Matoza, R. S., Okubo, P. G., & Amelung, F. (2014). Three-dimensional seismic velocity structure of Mauna Loa and Kilauea volcanoes in Hawaii from local seismic tomography. *Journal of Geophysical Research Solid Earth*, *119*, 4377–4392, doi:10.1002/2013JB010820.

Lindsley, D. (1983). Pyroxene thermometry. *American Mineralogist*, *68*(5–6), 477–493.

Manghnani, M. H., & Woollard, G. P. (1968). Elastic wave velocities in Hawaiian rocks at pressures to ten kilobars. *American Geophysisical Union Geophysical Monographs*, *12*, 501–516. https://doi.org/10.1029/GM012p0501.

Masotta, M., Mollo, S., Freda, C., Gaeta, M., & Moore, G. (2013). Clinopyroxene–liquid thermometers and barometers specific to alkaline differentiated magmas. *Contributions to Mineralogy and Petrology*, *166*, 1545–1561. https://doi.org/10.1007/s00410-013-0927-9.

Melekhova, E., Blundy, J., Martin, R., Arculus, R., & Pichavant, M. (2017). Petrological and experimental evidence for differentiation of water-rich magmas beneath St. Kitts, Lesser Antilles. *Contributions to Mineralogy and Petrology*, *172*, 98. https://doi.org/10.1007/s00410-017-1416-3.

Melekhova, E., Blundy, J., Robertson, R., & Humphreys, M. C. S. (2015). Experimental evidence for polybaric differentiation of primitive arc basalt beneath St. Vincent, Lesser Antilles. *Journal of Petrology*, *56*, 161–192. https://doi.org/10.1093/petrology/egu074.

Melekhova, E., Schlaphorst, D., Blundy, J., Kendall, J. M., Connolly, C., McCarthy, A., & Arculus, R. (2019). Lateral variation in crustal structure along the Lesser Antilles arc from petrology of crustal xenoliths and seismic receiver functions. *Earth and Planetary Science Letters*, *516*, 12–24. https://doi.org/10.1016/j.epsl.2019.03.030.

Molina, J. F., Moreno, J. A., Castro, A., Rodruiguez, C., & Fershtater, G. B. (2015). Calcic amphibole thermobarometry in metamorphic and igneous rocks: New calibrations based on plagioclase/amphibole Al-Si partitioning and amphibole-liquid Mg partitioning. *Lithos*, *232*, 286–305. https://doi.org/10.1016/j.lithos.2015.06.027.

Mollo, S., Blundy, J., Scarlato, P., De Cristofaro, S. P., Tecchiato, V., Di Stefano, F., Vetere, F., Holtz F., & Bachmann, O. (2018). An integrated P-T-H_2O-lattice strain model to quantify the role of clinopyroxene fractionation on REE+Y and HFSE patterns of mafic alkaline magmas: Application to eruptions at Mt. Etna. *Earth-Science Reviews*, *185*, 32–56. https://doi.org/10.1016/j.earscirev.2018.05.014.

Mollo, S., Giacomoni, P. P., Coltorti, M., Ferlito, C., Iezzi, G., & Scarlato, P. (2015). Reconstruction of magmatic variables governing recent Etnean eruptions: Constraints from mineral chemistry and P-T-fO_2-H_2O modelling. *Lithos*, *212–215*, 311–320. https://doi.org/10.1016/j.lithos.2014.11.020.

Mollo, S., Ubide, T., Di Stefano, F., Nazzari, M. & Scarlato, P. (2020). Polybaric/polythermal magma transport and trace element partitioning recorded in single crystals: A case study of a zoned clinopyroxene from Mt. Etna. *Lithos*. https://doi.org/10.1016/j.lithos.2020.105382.

Moore, R. B., Clague, D. A., Meyer, R., & Bohrson, W. A. (1987). Hualālai Volcano: A preliminary summary of geologic, petrologic and geophysical data. In R. W. Decker, T. L. Wright, P. H. Stauffer (Eds.), *Volcanism in Hawaii*. USGS Professional Paper 1350, 571–585.

Müller, T., Dohmen, R., Becker, H. W., ter Heege, J. H., & Chakraborty, S. (2013). Fe–Mg interdiffusion rates in clinopyroxene: Experimental data and implications for Fe–Mg exchange geothermometers. *Contributions to Mineralogy and Petrology*, *166*(6), 1563–1576. https://doi.org/10.1007/s00410-013-0941-y.

Nandedkar, R. H., Ulmer, P., & Müntener, O. (2014). Fractional crystallization of primitive, hydrous arc magmas: An experimental study at 0.7 GPa. *Contributions to Mineralogy and Petrology*, *167*, 1015. https://doi.org/10.1007/s00410-014-1015-5.

Neave, D. A., & Putirka, K. D. (2017). A new clinopyroxene-liquid barometer, and implications for magma storage pressures under Icelandic rift zones. *American Mineralogist*, *102*(4), 777–794. https://doi.org/10.2138/am-2017-5968.

Neave, D. A., Bali, E., Guðfinnsson, G. H., Halldórsson, S. A., Kahl, M., Schmidt, A.-S., & Holtz, F. (2019). Clinopyroxene–liquid equilibria and geothermobarometry in natural and experimental tholeiites: The 2014–2015 Holuhraun eruption, Iceland, *Journal of Petrology, egz042*, https://doi.org/10.1093/petrology/egz042.

Nimis, P. (1999). Clinopyroxene geobarometry of magmatic rocks: Part 2—structural geobarometers for basic to acid, tholeiitic and mildly alkaline magmatic systems. *Contributions to Mineralogy and Petrology*, *135*(1), 62–74. https://doi.org/10.1007/s004100050498.

Parat, F., Streck, M. J., Holtz, F., & Almeev, R. (2014). Experimental study into the petrogenesis of crystal-rich basaltic to andesitic magmas at Arenal volcano. *Contributions to Mineralogy and Petrology*, *168*, 1040. https://doi.org/10.1007/s00410-014-1040-4.

Park, J., Morgan, J. K., Zelt, C. A., & Okubo, P. G. (2009). Volcano-tectonic implications of 3-D velocity structures derived from joint active and passive source tomography of the island of Hawaii, *Journal of Geophysical Research*, *114*, B09301, https://doi.org/10.1029/2008JB005929.

Pichavant, M., & Macdonald, R. (2007). Crystallization of primitive basaltic magmas at crustal pressures and genesis of the calc-alkaline igneous suite: Experimental evidence from St Vincent, Lesser Antilles arc. *Contributions to Mineralogy and Petrology*, *154*, 535–558. https://doi.org/10.1007/s00410-007-0208-6.

Powell, R., & Holland, T. J. B. (1994). Optimal geothermometry and geobarometry. *American Mineralogist*, *79*(1–2), 120–133.

Putirka, K. D. (2008). Thermometers and barometers for volcanic systems. *Reviews in Mineralogy and Geochemistry*, *69*, 61–120. https://doi.org/10.2138/rmg.2008.69.3

Putirka, K. (1997). Magma transport at Hawaii: Inferences from igneous thermobarometry. *Geology*, *25*, 69–72. https://doi.org/10.1130/0091-7613(1997)025<0069.

Putirka, K. (2016). Amphibole thermometers and barometers for igneous systems and some implications for eruption mechanisms of felsic magmas at arc volcanoes. *American Mineralogist*, *101*(4), 841-858. https://doi.org/10.2138/am-2016-5506.

Putirka, K. (2017). Down the crater: Where magmas are stored and why they erupt. *Elements*, *13*, 11–16. https://doi.org/10.2113/gselements.13.1.11

Quick, J. E., Sinigoi, S., Peressini, G., Demarchi, G., Wooden, J. L. & Sbisà, A. (2009). Magmatic plumbing of a large Permian caldera exposed to a depth of 25 km. *Geology 37*, 603–606. https://doi.org/10.1130/G30003A.1.

Richards, M., Contreras-Reyes, E., Lithgow-Bertelloni, C., Ghiorso, M., & Strixrude, L. (2013). Petrological interpretation of deep crustal intrusive bodies beneath oceanic hotspot provinces. *Geochemistry, Geophysics, Geosystems*, *14*(3), 604–619, https://doi.org/10.1029/2012GC004448.

Shamberger, P. J., & Hammer, J. E. (2006). Leucocratic and gabbroic xenoliths from Hualalai Volcano, Hawaii. *Journal of Petrology*, *47*(9), 1785–1808. https://doi.org/10.1093/petrology/egl027.

Shejwalkar, A., & Coogan, L. A. (2013). Experimental calibration of the roles of temperature and composition in the Ca-in-olivine geothermometer at 0.1 MPa. *Lithos*, *177*, 54-60. https://doi.org/10.1016/j.lithos.2013.06.013.

Shillington, D. J., Van Avendonk, H. J. A., Holbrook, W. S., Kelemen, P. B., & Hornbach, M. J. (2004). Composition and structure of the central Aleutian island arc from arc-parallel wide-angle seismic data. *Geochemistry, Geophysics, Geosystems*, *5*(10), https://doi.org/10.1029/2004GC000715.

Sisson, T. W., & Grove, T. L. (1993). Experimental investigations of the role of H_2O in calc-alkaline differentiation and subduction zone magmatism. *Contributions to Mineralogy and Petrology*, *113*, 143–166. https://doi.org/10.1007/BF00283225.

Stamper, C. C., Melekhova, E., Blundy, J. D., Arculus, R. J., Humphreys, M. C. S., & Brooker, R. A. (2014). Oxidised phase relations of a primitive basalt from Grenada, Lesser Antilles. *Contributions to Mineralogy and Petrology*, *167*, 1–20. https://doi.org/10.1007/s00410-013-0954-6.

Stock, M. J., Bagnardi, M., Neave, D. A., Maclennan, J., Bernard, B., Buisman, I., et al. (2018). Integrated petrological and geophysical constraints on magma system architecture in the western Galápagos Archipelago: Insights from Wolf volcano. *Geochemistry, Geophysics, Geosystems*, *19*, 4722–4743. https://doi.org/10.1029/2018GC007936.

Streckeisen, A. (1976). To each plutonic rock its proper name. *Earth Science Reviews*, *12*(1), 1–33.

Sun, C., & Liang, Y. (2015). A REE-in-garnet-clinopyroxene thermobarometer for eclogites, granulites and garnet peridotites. *Chemical Geology*, *393*, 79–92. https://doi.org/10.1016/j.chemgeo.2014.11.014.

Sun, C., & Liang, Y. (2017). A REE-in-plagioclase–clinopyroxene thermometer for crustal rocks. *Contributions to Mineralogy and Petrology*, *172*, 24. https://doi.org/10.1007/s00410-016-1326-9.

Tormey, D. R., Grove, T. L., & Bryan, W. B. (1987). Experimental petrology of normal MORB near the Kane Fracture Zone: 22°–25°, mid-Atlantic ridge. *Contributions to Mineralogy and Petrology*, *96*, 121–139. https://doi.org/10.1007/BF00375227.

Tuttle, O. F., & Bowen, N. L. (1958). The origin of granite in the light of experimental studies in the system $NaAlSi_3O_8$-$KAlSi_3O_8$-SiO_2-H_2O. *Geological Society of America*, *74*. https://doi.org/10.1130/MEM74.

Vazquez, J. A., Shamberger, P. J., & Hammer, J. E. (2007). Plutonic xenoliths reveal the timing of magma evolution at Hualalai and Mauna Kea, Hawaii. *Geology*, *35*(8), 695–698. https://doi.org/10.1130/G23495A.1.

Watts, A. B., ten Brink, U. S., Buhl, P., & Brocher, T. M. (1985). A multichannel seismic study of lithospheric flexure across the Hawaiian-Emperor seamount chain. *Nature*, *315*, 105–111.

Wells, P. R. A. (1977). Pyroxene thermometry in simple and complex systems. *Contributions to Mineralogy and Petrology*, *62*(2), 129–139.

Wolfe, E. W., Wise, W. S., & Dalrymple, G. B. (1997). The geology and petrology of Mauna Kea volcano, Hawaii—a study of postshield volcanism. *US Geological Survey Professional Paper 1557*. https://doi.org/10.3133/pp1557.

Yang, H.-J., Kinzler, R. J., & Grove, T. L. (1996). Experiments and models of anhydrous, basaltic olivine-plagioclase-augite saturated melts from 0.001 to 10 kbar. *Contributions to Mineralogy and Petrology*, *124*, 1–18. https://doi.org/10.1007/s004100050169.

Ziberna, L., Green, E. C. R., & Blundy, J. D. (2017). Multiple-reaction geobarometry for olivine-bearing igneous rocks. *American Mineralogist*, *102*, 2349–2366. http://dx.doi.org/10.2138/am-2017-6154.

Zucca, J. J., Hill, D. P., & Kovach, R. L. (1982). Crustal structure of Mauna Loa volcano, Hawaii, from seismic refraction and gravity data. *Bulletin of the Seismological Society of America*, *72*(5), 1535–1550.

2

Trace Element Geothermometry and Geospeedometry for Cumulate Rocks: Quantitative Constraints on Thermal and Magmatic Processes During Igneous Crust Formation

Chenguang Sun

ABSTRACT

Cumulate rocks record the magmatic and cooling processes during formation of Earth's igneous crust. Extracting the information of these two processes from mineral records, however, is often complicated by various extents of diffusive resetting during cooling subsequent to the main stages of crystallization. Accordingly, for cumulate rocks at diffusive closure, the apparent "equilibrium" temperatures derived from geothermometers are generally lower than the crystallization temperatures. Using analytical or numerical models, geospeedometers can extract cooling rates from the closure temperatures (or profiles), but only if the initial temperatures are determined independently. Here, I summarize the general framework of geothermometry and geospeedometry from a trace element perspective. The Mg- and REE-based exchange geothermometers for mafic cumulate rocks are reviewed as examples of the geothermometer design. Based on the observed differential diffusive closures of Mg and REE in oceanic gabbros, I outline a general approach to uniquely determine the initial crystallization temperature and cooling rate of a cumulate rock. This concept is further demonstrated using the recently developed Mg–REE coupled geospeedometer for mafic cumulate rocks. Finally, I use the Hess Deep gabbros as a case study to show that this two-element coupled geospeedometer is particularly useful for delineating the igneous accretion and cooling styles during crust formation. This two-element (or multi-element) coupled approach outlined here can also be readily extended for decoding comprehensive thermal histories of other petrological systems at various geological settings or other rocky planetary bodies.

2.1. INTRODUCTION

Earth's crust is mainly composed of cumulate rocks, which are mafic beneath the oceans and vary from mafic to silicic at continents. Formation of Earth's igneous crusts generally involves generation, transport, emplacement, and differentiation of magmas that are primarily derived from partial melting of mantle and/or crustal materials (e.g., Bachmann & Huber, 2016; Nicolas et al., 1988; Phipps Morgan & Chen, 1993; Quick & Denlinger, 1993). Through buoyancy-driven migration, these melts could be transported to shallower depths and build up magma bodies/chambers at crustal levels. In the cold crustal environment, these magma bodies/chambers (Figure 2.1) gradually solidify and evolve through fractional crystallization, melt replenishment, magma mixing, wall-rock assimilation, and/or volcanic eruption (e.g., Bachmann & Bergantz, 2004; DePaolo, 1981; Edmonds et al., 2019; Hildreth, 1979; Lee et al., 2014; Maclennan, 2019; Spera & Bohrson, 2004; Wark et al., 2007). Depending on the styles of magma supply (e.g., singular, pulsive, or continuous) and cooling (e.g., conductive or convective), these crustal magma bodies/chambers may undergo various solidification paths

---

Department of Geological Sciences, The University of Texas at Austin, Austin, Texas, USA

Crustal Magmatic System Evolution: Anatomy, Architecture, and Physico-Chemical Processes, Geophysical Monograph 264, First Edition.
Edited by Matteo Masotta, Christoph Beier, and Silvio Mollo.

DOI: 10.1002/9781119564485.ch2

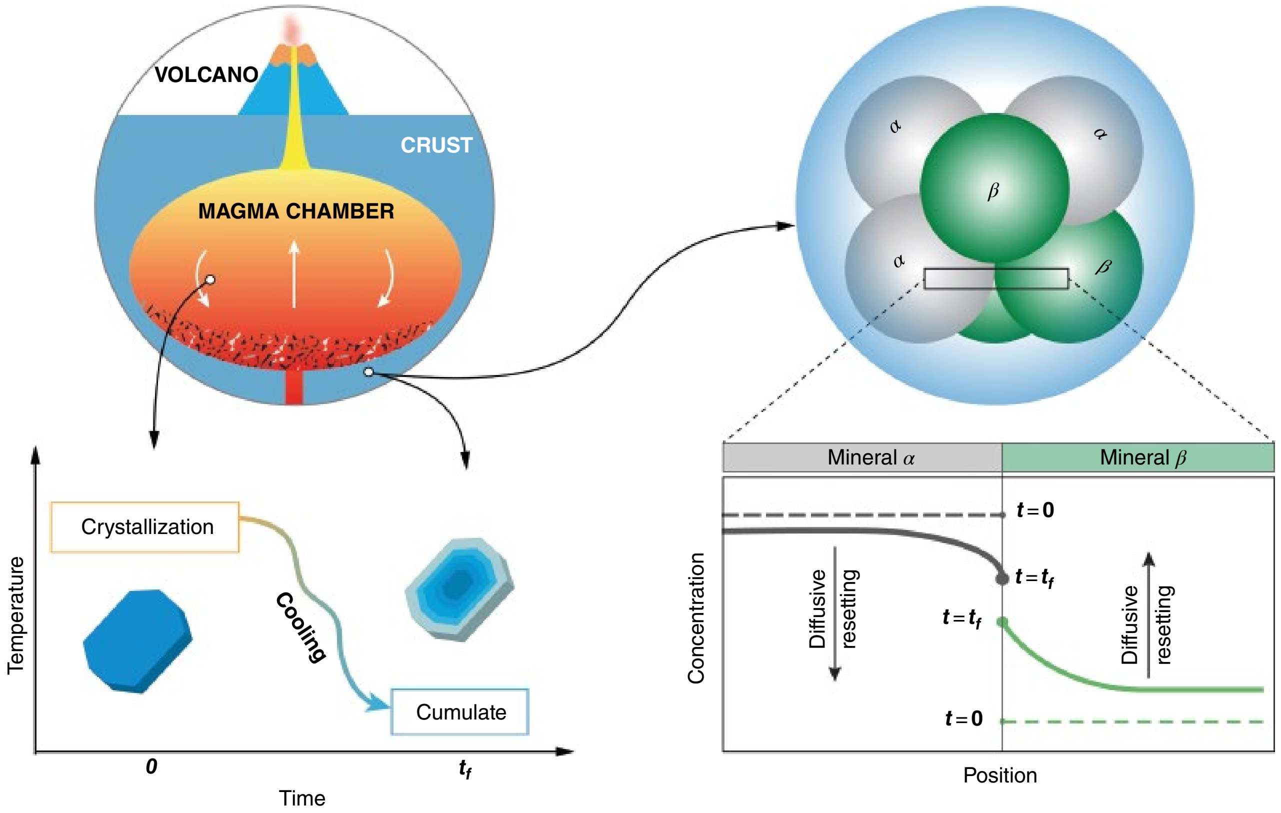

Figure 2.1 Schematic diagram showing the crystallization and cooling of cumulate rocks in a crustal magma chamber as well as the mineral responses to cooling after the main stages of crystallization. The magma chamber solidifies continuously in the cold crustal environment and evolves dynamically through melt replenishment, wall-rock assimilation, fractional crystallization, and perhaps volcanic eruption. These magmatic processes are recorded in cumulate rocks during solidification of the evolving magma chamber. Subsequent cooling, however, can alter the crystallization records in cumulate rocks to various extents by diffusive resetting.

generating evolved melts and crystalline cumulates with diverse compositions. In this context, cumulate rocks can provide continuous records of magma solidification as a unique tool for unraveling the magmatic and thermal histories during igneous crust formation at different tectonic settings.

Primary questions on magma chamber processes concern (a) the compositions of parental and differentiated magmas, (b) the igneous accretion and melt emplacement for building the crustal magma body, and (c) the cooling style and crustal environment of the solidifying magma body. Conventional approaches to deciphering these questions mostly rely on the chemical and isotopic compositions of the cumulate rocks (e.g., Ashwal et al., 2005; McBirney, 2003; Namur & Humphreys, 2018; Tecchiato et al., 2018; Tegner et al., 2009; VanTongeren & Mathez, 2013; Veksler et al., 2018; S. H. Yang et al., 2019) as well as forward simulations of magma crystallization and cooling using petrological models (e.g., Bohrson et al., 2014; Lee et al., 2014; Spera & Bohrson, 2004) or high-temperature experiments (e.g., Green & Ringwood, 1968; Grove et al., 1982; Koepke et al., 2018; Morse et al., 2004). Given that most magma bodies are open to various extents of melt influx and wall-rock assimilation, petrological modeling and experimental simulation of the magma chamber behaviors are complicated by the unknown compositions and temperatures of parental and influx melts. Major element compositions of cumulate minerals/rocks are often used as petrological indexes (e.g., Mg# = 100×Mg/(Mg+Fe), and An# = 100×Ca/(Ca+Na+K) in moles) to qualitatively track fractional crystallization of the magma chamber and replenishment of melts with distinct compositions (e.g., Ashwal et al., 2005; Cawthorn & Walraven, 1998; Tegner et al., 2009; VanTongeren & Mathez, 2013; S. H. Yang et al., 2019). When the residual magmas have significant interactions with crustal wall rocks, the primitive melt influx may also be differentiable through changes in isotopic compositions of the cumulate rocks (e.g., DePaolo, 1985; Kruger, 2005). These conventional approaches have significantly improved our knowledge of magmatic processes but are inadequate to constrain the igneous accretion and cooling histories of the magma bodies.

The crystallization temperatures and cooling rates of cumulate rocks are the two fundamental variables that pinpoint the extents of solidification, melt influx events, cooling histories, and residence times of the crustal magma bodies/chambers. These two variables can be determined by geothermometers and geospeedometers that are calibrated based on the temperature-dependent chemical equilibrium and diffusion between coexisting phases (e.g., minerals or melts), respectively. Many thermometers have been developed to determine the crystallization temperatures of minerals in silicate melts (e.g., Masotta et al., 2013; Mollo et al., 2011; Putirka, 2005, 2008; Waters & Lange, 2015), but without knowledge of equilibrium melt compositions, these thermometers are invalid for cumulate rocks. Upon crystallization, the cumulate minerals undergo subsequent cooling and diffusive exchange with their surroundings (Figure 2.1). The diffusive response to changes in temperature complicates the estimation of crystallization (or initial) temperatures through geothermometers but enables the quantitative extraction of thermal histories from rock records using geospeedometers. Major challenges to resolving the thermal and magmatic histories of cumulate rocks thus include (a) development of relevant geothermometers, (b) quantitative characterization of diffusion behaviors of the key elements used in the geothermometers, and ultimately (c) accurate extraction of the crystallization temperature and cooling rate from a given cumulate rock.

With recent advance in the studies of trace element partitioning and diffusion in minerals, I here provide a trace element approach toward a general resolution for the magmatic and cooling histories of cumulate rocks. This chapter is organized as follows: I first introduce the advantages of the trace element approach to decoding thermal-magmatic processes from mineral records in section 2.2, and then outline the theoretical bases, calibration methods, and implementations of trace element geothermometers and geospeedometers in sections 2.3 and 2.4. As a case study, in section 2.5, I discuss the application of the Mg–REE coupled geospeedometer to oceanic gabbros and its implications for formation of fast-spreading lower oceanic crust. Using the recent developments of trace element geothermometry and geospeedometry for mafic cumulates, this chapter aims to set up an integrated framework that could be extended for understanding comprehensive thermal histories of petrological systems in general.

2.2. A TRACE ELEMENT PERSPECTIVE FOR DECODING THERMAL AND MAGMATIC RECORDS IN MINERALS

2.2.1. Equilibrium Exchange

Partitioning describes the equilibrium distribution of a chemical species between two coexisting phases (α and β) and is quantitatively measured by the partition coefficient (K):

$$K_i = C_i^\alpha / C_i^\beta, \tag{2.1}$$

where C denotes the concentration of species i in each phase. Thermodynamically, the partition coefficient is derived from the equilibrium constant ($K^\ominus$) for an exchange reaction between the two phases:

$$K^\ominus = \frac{a_i^\alpha}{a_i^\beta} = \frac{C_i^\alpha \gamma_i^\alpha}{C_i^\beta \gamma_i^\beta} = K_i \frac{\gamma_i^\alpha}{\gamma_i^\beta}, \tag{2.2}$$

where a and γ are the thermodynamic activity and activity coefficient of the chemical species, respectively. The equilibrium constant can be expressed as

$$\ln K^\ominus = -\frac{\Delta G}{RT} = -\frac{\Delta H}{RT} + \frac{\Delta S}{R} - \frac{P\Delta V}{RT}, \tag{2.3}$$

where ΔG, ΔH, ΔS, and ΔV are the changes in Gibbs free energy, enthalpy, entropy, and volume for the exchange reaction, respectively; R is the gas constant; T is temperature; and P is pressure.

According to equations (2.2–2.3), the thermodynamic expression of geothermometers can be generally written as

$$T = \frac{\Delta H + P\Delta V}{\Delta S - R\left(\ln K_i + \ln \gamma_i^\alpha - \ln \gamma_i^\beta\right)}. \tag{2.4}$$

Note that in equation (2.4), the partition coefficient defined by chemical concentration ratios (cf. equation (2.1)) is the only variable that can be directly measured from natural samples, whereas all others demand calibrations through systematic laboratory experiments. As major elements constitute the crystal lattice or melt structure, their equilibrium exchange between different minerals or between minerals and melts often involves other major elements (or components) to adjust the changes in crystal or melt structure. For instance, Mg partitioning between coexisting mafic minerals (e.g., olivine, pyroxene and/or garnet) is generally considered coupling with Fe exchange (e.g., Ellis & Green, 1979; O'Neill & Wood, 1979); Al exchange between peridotite minerals and partial melts in the mantle appears to be coupled with Mg distribution (Sun & Dasgupta, 2020). In addition, the activity coefficients of major elements, for their non-Henry's law behaviors, depend on their concentrations as well as other components in the minerals or melts. With Henry's law behaviors, however, trace elements are expected to have activity coefficients independent of their concentrations, which practically reduces the complexity in geothermometer calibration.

2.2.2. Chemical Diffusion

The intra-crystalline diffusive redistribution of an element is driven by the gradient of chemical potential. The corresponding diffusion coefficient (i.e., chemical diffusivity, D^*) is related to the intrinsic (i.e., tracer or self-) diffusion coefficient (D) through the following expression:

$$D^* = D\left(1+\frac{\partial \ln \gamma}{\partial \ln C}\right), \tag{2.5}$$

where $(1+\partial\ln\gamma/\partial\ln C)$ is the thermodynamic factor varying as a function of the concentration (C) and activity coefficient (γ) of the diffusing species (Darken, 1948). Distinct from the chemical diffusion, self- (or tracer-) diffusion takes place through spontaneous mixing driven by the gradient of isotopic ratios (or trace element abundance) in the crystal instead of the chemical potential gradient. Because of their Henry's law behaviors, trace elements have thermodynamic factors of unity, and thus their chemical diffusivities are effectively self- (or tracer-) diffusion coefficients. In light of these considerations, the experimentally determined D values for trace element cations can be directly used to model their diffusive exchanges in natural systems.

Because the equilibrium distribution of a major element between mineral pairs involves the exchange of additional major elements, the chemical diffusion of major elements in natural systems often behaves as a binary or multi-component diffusion process. Binary diffusion, also called interdiffusion, is used to describe diffusion in a binary system, whereas multi-component diffusion involves three or more components in the system (e.g., Lasaga, 1979; Liang, 2010; Watson & Baxter, 2007; Y. Zhang, 2010). For instance, Fe-Mg diffusion in olivine is an interdiffusion process (e.g., Chakraborty, 1997; Wang et al., 2004), given that olivine can be regarded as a binary solid solution of forsterite (Mg_2SiO_4) and fayalite (Fe_2SiO_4). Many other minerals are solid solutions of multiple components, such as the pyroxene solid solution composed of enstatite, ferrosilite, hedenbergite, and diopside components. For stoichiometry, diffusive redistribution of one major component in the mineral often requires concurrent diffusive exchange of other components. Therefore, the chemical diffusion of a major element in binary or multi-component diffusion processes depends on the intrinsic diffusivity and thermodynamic behavior (i.e., activity coefficients) of this major element component as well as those of the coupling components in the system (e.g., Darken, 1948; Lasaga, 1979; Liang, 2010).

The coefficients of tracer and effective binary diffusion have been measured for major element cations in multicomponent minerals (e.g., pyroxenes) under laboratory conditions; however, the two types of diffusivities could be distinct from each other by up to about one order of magnitude in minerals with similar compositions, such as Ca and Mg in clinopyroxene with 93–96 mol% diopside (e.g., Cherniak & Dimanov, 2010; X. Zhang et al., 2010) (Figure 2.2). The significant differences are likely attributed to the non-Henry's law behaviors of major element components in the minerals in addition to the coupled diffusion of Ca-Mg-Fe in clinopyroxene. Therefore, tracer (or self-) diffusion coefficients should be used with great caution to model chemical diffusion of major elements in natural systems. It is also important to note that binary diffusion coefficients of an element couple may vary with the mineral composition. For example, the interdiffusion coefficients of Ca-(Mg+Fe) differ by about one and a half orders of magnitude in clinopyroxenes (Brady & McCallister, 1983; Müller et al., 2013) with different amounts of diopside components (52 vs. 93 mol%;

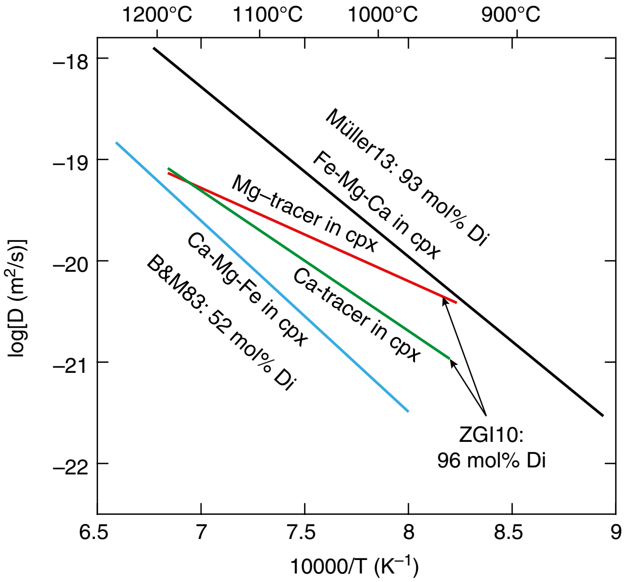

Figure 2.2 Comparison of diffusion data in clinopyroxene parallel to *c*-axis. The Mg and Ca tracer diffusivities were taken from Zhang (2010; ZGl10) and measured for clinopyroxene (cpx) with 96 mol% diopside (Di) components. The Ca-(Mg+Fe) interdiffusion coefficients from Brady and McCallister (1983; B&M83) were determined for cpx with 52 mol% diopside components, whereas those from Müller et al. (2013) were measured for cpx with 93 mol% diopside components. Sources: Zhang (2010); Brady and McCallister (1983); Müller et al. (2013).

Figure 2.2). Given these complexities in major element diffusion, modeling trace element diffusion appears to be more straightforward for extracting cooling histories from rock records.

2.3. TRACE ELEMENT GEOTHERMOMETRY

As outlined in section 2.2, the calibration of geothermometers is based on the partitioning of a chemical species or exchange of two coupled species between equilibrium phases. To provide an overview of trace element geothermometry, in this section I first summarize the theoretical bases of different trace element geothermometers, briefly discuss the mechanism of trace element partitioning in minerals for thermometer calibration, and then review the trace element geothermometers for mafic cumulate rocks.

2.3.1. Theoretical Basis

According to equations (2.2–2.3), the partition (or exchange) coefficient (*K*) for a chemical species *i* between two phases (α and β) can be described by the thermodynamic expression

$$\ln K_i = -\frac{\Delta G}{RT} - \ln\left(\frac{\gamma_i^\alpha}{\gamma_i^\beta}\right) = \frac{\Delta S}{R} - \frac{\Delta H + P\Delta V}{RT} - \ln\left(\frac{\gamma_i^\alpha}{\gamma_i^\beta}\right). \quad (2.6)$$

For simplicity, equation (2.6) could also be written in a general form:

$$\ln K_i = A_i + \frac{B_i - f(P)}{T}, \quad (2.7)$$

where A and B are coefficients dependent on mineral major element compositions, and $f(P)$ is a pressure correction term for the exchange reaction. Although temperature in general is one of the intensive parameters controlling the exchange reaction, not all chemical exchanges are temperature sensitive. Hence, a major challenge in the design of a new geothermometer is to find the exchange reaction with a strong temperature dependence. Well-controlled laboratory experiments are subsequently required to calibrate A, B and $f(P)$ in equation (2.7). After testing by independent experiments or well-characterized field samples, equation (2.7) could then be turned into a geothermometer to determine the temperatures of natural samples.

Trace element geothermometers are usually calibrated using one exchange reaction or the partitioning of a single element between two coexisting minerals. For instance, the Ti-in-zircon and Ti-in-quartz thermometers are calibrated based on Ti partitioning in zircon and quartz, respectively, with coexisting rutile (e.g., Wark & Watson, 2006; Watson et al., 2006), and the Mg-in-plagioclase thermometer is based on Mg partitioning between plagioclase and clinopyroxene (Faak et al., 2013; Sun & Lissenberg, 2018a). A generic expression for single element geothermometers follows the form of equation (2.4):

$$T = \frac{B_i - f(P)}{\ln K_i - A_i}. \quad (2.8)$$

Considering a group of geochemically similar elements (e.g., REE: rare earth elements), we can define their partition coefficients using the system of equations

$$\begin{bmatrix} \ln K_1 \\ \ln K_2 \\ \cdots \\ \ln K_n \end{bmatrix} = \begin{bmatrix} A_1 \\ A_2 \\ \cdots \\ A_n \end{bmatrix} + \frac{1}{T}\begin{bmatrix} B_1 \\ B_2 \\ \cdots \\ B_n \end{bmatrix} - \frac{f(P)}{T}, \quad (2.9a)$$

where 1, 2, . . ., n denote the number of elements. Rearranged in a linear form, equation (2.9a) can be written as

$$\begin{bmatrix} B_1 \\ B_2 \\ \cdots \\ B_n \end{bmatrix} = T\begin{bmatrix} \ln K_1 - A_1 \\ \ln K_2 - A_2 \\ \cdots \\ \ln K_n - A_n \end{bmatrix} + f(P). \quad (2.9b)$$

As presented in Sun and Liang (2017), equation (2.9b) can be written as a vector expression:

$$\vec{\mathrm{B}} = T\left(\ln \vec{\mathrm{K}} - \vec{\mathrm{A}}\right) + f(P), \quad (2.10)$$

where $\vec{\mathrm{B}}$, $\vec{\mathrm{K}}$, and $\vec{\mathrm{A}}$ are column vectors of B_i, K_i, and A_i, respectively. In the ($\ln K - A$) versus B diagram (Figure 2.3a), all elements in the group should define a straight line with the slope and intercept corresponding to the equilibrium temperature and $f(P)$, respectively. Thus, equation (2.10) provides a new approach to geothermometer calibration, which has been implemented in orthopyroxene-clinopyroxene (Liang et al., 2013), garnet-clinopyroxene (Sun & Liang, 2015), and plagioclase-clinopyroxene systems (Sun & Liang, 2017).

It is important to note that the equilibrium temperature and pressure can be obtained simultaneously from equation (2.10) when their effects on the partition coefficients are both significant (cf. the red line in Figure 2.3a). Accurate determination of pressures becomes difficult if the pressure effect is negligible or relatively small (i.e., $f(P) \approx 0$). In this case, $f(P)$ can be integrated into the coefficient B, and then equation (2.10) can be simplified as

$$\vec{\mathrm{B}} = T\left(\ln \vec{\mathrm{K}} - \vec{\mathrm{A}}\right). \quad (2.11)$$

Accordingly, all elements in the plot of ($\ln K - A$) versus B should define a straight line (cf. the blue line in Figure 2.3a) passing through the origin, the slope of

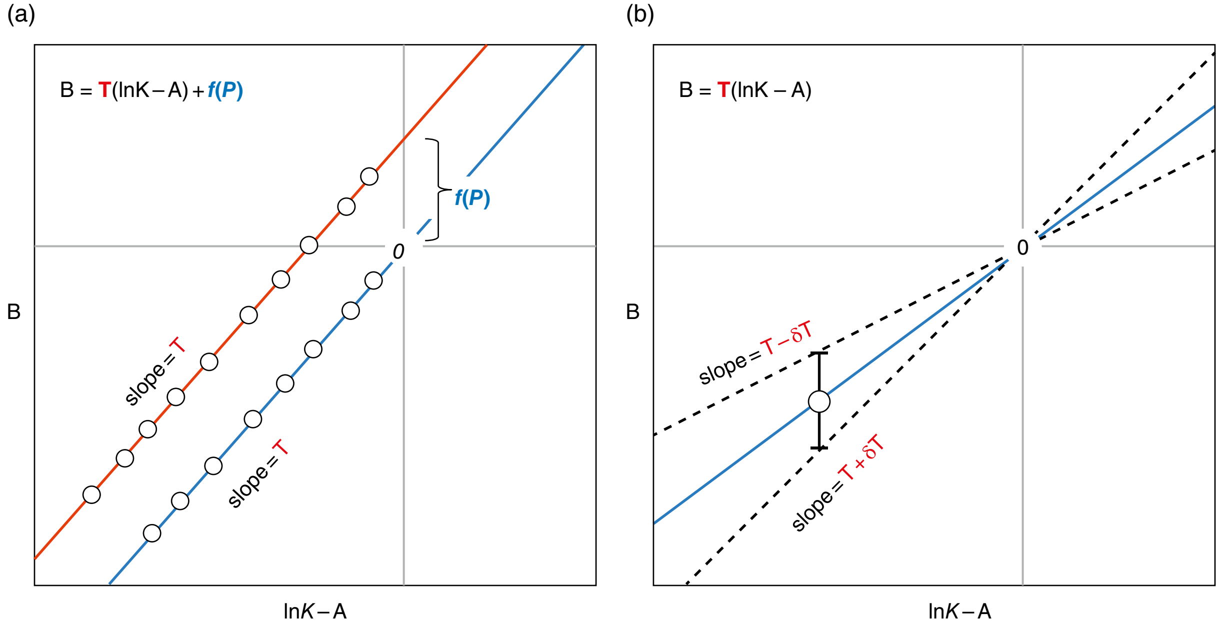

Figure 2.3 Schematic diagrams showing thermometers based on (a) multiple elements and (b) a single element. The multi-element approach can potentially reduce the uncertainties of temperature calculations through statistical analyses of all relevant partitioning data.

which determines the equilibrium temperature. Distinct from the approach used with the single-element thermometers, this multi-element approach requires linear regression analyses of the partition coefficients of multiple elements. An obvious advantage of this multi-element approach is that it could make use of all the geochemically similar elements to determine temperatures (and pressures) with statistical confidence, even if some of the elements may appear as anomalies in the system due to alteration by later processes (e.g., metasomatism). When only one element is available, this multi-element approach recovers the single-element geothermometer, which effectively determines the temperature by a straight line through this element and the origin (Figure 2.3b). As this line is effectively defined by one element, the accuracy of the temperature determination strongly relies on the analytical uncertainties of this element in the coexisting minerals.

2.3.2. Trace Element Partitioning

Trace elements are generally regarded as impurities substituting the major element cations in the crystal lattice site. As a major interest in petrology, trace element partitioning in various crystal-melt systems has been experimentally studied for magmatic processes (e.g., Gaetani & Grove, 1995; Le Roux et al., 2011; Mollo et al., 2018; Sun, 2018; Tiepolo et al., 2007; van Westrenen & Draper, 2007; Wood & Blundy, 2013 and references therein). Substitution of a trace element cation into the crystal lattice site (Figure 2.4) needs to overcome the strain energy changes (ΔG_{strain}) in the crystal and other coexisting phase (χ; crystal or melt) in addition to the Gibbs free energy change (ΔG_0) for strain-free exchange of an ideal isovalent cation (Brice, 1975). The overall changes in Gibbs free energy can be described as

$$\Delta G = \Delta G_0 - \Delta G_{\text{strain}}^{\text{crystal}} + \Delta G_{\text{strain}}^{\chi}, \tag{2.12}$$

$$\Delta G_{\text{strain}}^{\text{crystal}} = 4\pi E N_A \left[\frac{r_0}{2}(r_0 - r_i)^2 - \frac{1}{3}(r_0 - r_i)^3 \right], \tag{2.13}$$

where r_i is the ionic radius of the trace element cation (i) often taken from Shannon (1976) for the relevant coordination number, r_0 is the radius of an "ideal" or strain-free cation site in the crystal lattice, E is the apparent Young's modulus for the lattice site, and N_A is Avogadro's number.

When the crystal coexists with a melt, ΔG_{strain} of the melt can be neglected because the melt structure is much more relaxed than the crystal. Combining equation (2.6) with equations (2.12–2.13) enables one to derive a general expression to describe the partition coefficient of a trace element in this crystal-liquid system:

$$K_i^{\text{crystal/melt}} = K_0^{\text{crystal/melt}} \exp\left\{ -\frac{4\pi E N_A}{RT} \left[\frac{r_0}{2}(r_0 - r_i)^2 - \frac{1}{3}(r_0 - r_i)^3 \right] \right\}, \tag{2.14}$$

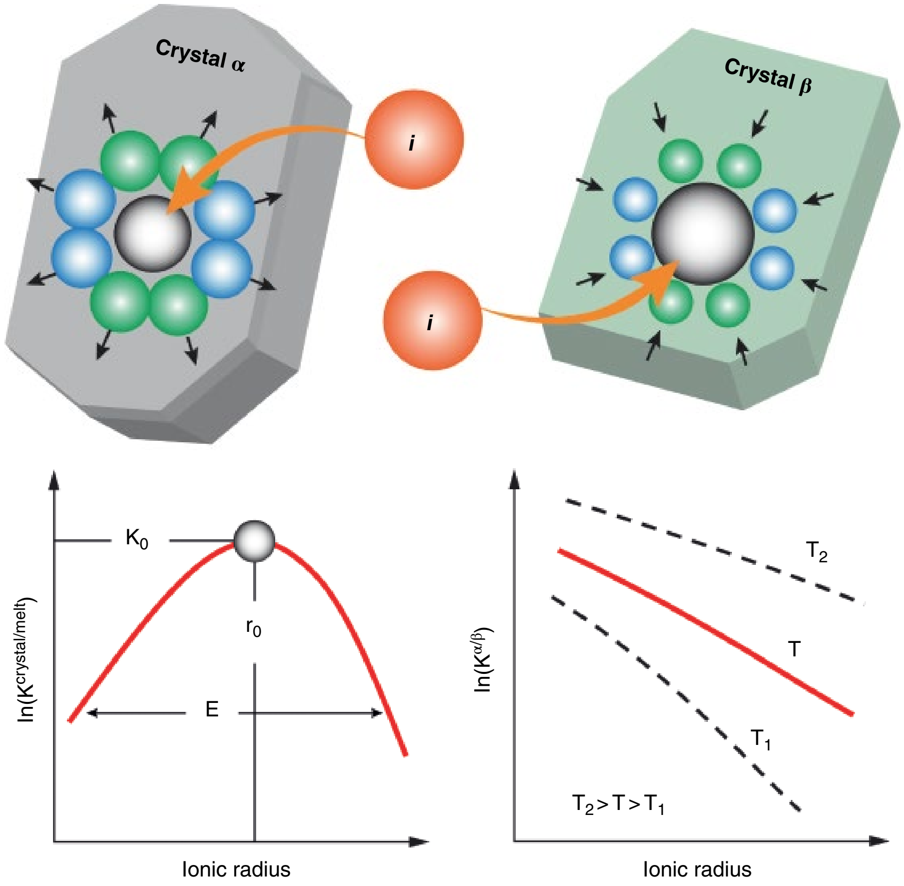

Figure 2.4 Cartoon drawings of trace element partitioning in crystals. The substitution of a trace element into the crystal lattice sites has to overcome the change in lattice strain energy, which depends on the relative size difference between the trace element cation and the ideal lattice site. In the crystal-melt system, partition coefficients of isovalent trace element cations follow a parabolic pattern in the Onuma diagram (Onuma et al., 1968) and are controlled by the three lattice strain parameters, K_0, E, and r_0 (modified after Sun, 2018). However, in the two-mineral system, partition coefficients of isovalent cations on a log scale generally manifest linear patterns with their ionic radii and vary systematically with the change in equilibrium temperatures.

$$\ln K_0^{\text{crystal/melt}} = \frac{\Delta S_0}{R} - \frac{\Delta H_0 + P\Delta V_0}{RT} - \ln\left(\frac{\gamma_0^{\text{crystal}}}{\gamma_0^{\text{melt}}}\right), \quad (2.15)$$

where K_0 is the strain-free partition coefficient of the ideal cation and varies as a function of temperature, pressure, and composition. Equation (2.14) is sometimes called the Brice equation or lattice strain model (Blundy & Wood, 1994) for quantifying the parabolic relation between the crystal-melt partition coefficients of isovalent trace element cations and ionic radii in the Onuma diagram (Figure 2.4). Through nonlinear least-squares regression analyses, the three lattice strain parameters (K_0, r_0, and E) can be inverted from the crystal-melt partition coefficients of isovalent cations.

When the two coexisting phases are crystals (α and β), ΔG_{strain} has to be considered for both crystals (Figure 2.4). Thus, in this mineral-mineral system, the partition coefficient of a trace element can be described by the following expression (Lee et al., 2007; Liang et al., 2013; Sun & Liang, 2014):

$$K_i^{\alpha/\beta} = K_0^{\alpha/\beta} \exp\left\{-\frac{4\pi E^{\alpha} N_A}{RT}\left[\frac{r_0^{\alpha}}{2}\left(r_0^{\alpha} - r_i\right)^2 - \frac{1}{3}\left(r_0^{\alpha} - r_i\right)^3\right] + \frac{4\pi E^{\beta} N_A}{RT}\left[\frac{r_0^{\beta}}{2}\left(r_0^{\beta} - r_i\right)^2 - \frac{1}{3}\left(r_0^{\beta} - r_i\right)^3\right]\right\}, \quad (2.16)$$

$$\ln K_0^{\alpha/\beta} = \ln\left(\frac{K_0^{\alpha/\text{melt}}}{K_0^{\beta/\text{melt}}}\right) = \frac{\Delta S_0^{\alpha/\beta}}{R} - \frac{\Delta H_0^{\alpha/\beta} + P\Delta V_0^{\alpha/\beta}}{RT} - \ln\left(\frac{\gamma_0^{\alpha}}{\gamma_0^{\beta}}\right). \quad (2.17)$$

As shown in equations (2.16–2.17), E and r_0 of the two crystals are identical to those in the two crystal-melt systems, whereas K_0 of the mineral-mineral system is equivalent to the ratios of K_0's in two crystal-melt systems. Although one may expect the crystal-melt K_0 to depend on melt compositions (i.e., γ_0^{melt}; equation (2.15)), the effect of melt composition, if any, can be cancelled out between $K_0^{\alpha/\text{melt}}$ and $K_0^{\beta/\text{melt}}$. For the calibration of single-element geothermometers, it is not necessary to determine all six lattice strain parameters in equation (2.16). However, for the calibration of multi-element geothermometers, understanding the systematic partitioning behaviors of isovalent cations is an important first step.

Given the nonlinear trade-off between the six lattice strain parameters in equation (2.16), it is challenging to invert them directly from the measured partition coefficients between two coexisting minerals. Because these lattice strain parameters are effectively the same as those in the lattice strain model for crystal-melt systems (equation (2.14)), the experimentally determined mineral-melt partition coefficients can be used to invert the lattice strain parameters for individual minerals at a broad range of pressures and temperatures. The lattice strain parameters can then be parameterized as a function of temperature, pressure, and/or mineral composition. Substituting these models of lattice strain parameters into equation (2.16), one could obtain a generalized expression as a new geothermometer. Following this approach, previous studies have calibrated several multi-element geothermometers (Liang et al., 2013; Sun & Liang, 2015, 2017) using REE partitioning models for different mineral-melt systems (Sun & Liang, 2012, 2013a, 2013b; Sun et al., 2017; Yao et al., 2012).

2.3.3. Geothermometers for Mafic Cumulates

Plagioclase and clinopyroxene are the main rock-forming minerals co-crystallizing in mafic to intermediate magmas over an extended temperature interval (e.g., Grove & Bryan, 1983; Sisson & Grove, 1993). Thus, geothermometers for plagioclase-clinopyroxene systems are particularly useful to quantitatively constrain the equilibrium or crystallization temperatures of cumulate rocks. Recent studies have developed two types of geothermometers based on the exchange of multiple elements (REE: Sun & Liang, 2017) or a single element (Mg: Faak et al., 2013; Sun & Lissenberg, 2018a) between plagioclase and clinopyroxene. With the theoretic background outlined in sections 2.3.1 and 2.3.2, here I briefly review the recently developed geothermometers for mafic cumulate rocks.

REE-in-Plagioclase-Clinopyroxene Thermometer

The REE-in-plagioclase-clinopyroxene geothermometer (Sun & Liang, 2017) was established from the lattice strain models for clinopyroxene-melt (Sun & Liang, 2012) and plagioclase-melt systems (Sun et al., 2017). These lattice strain parameters were calibrated using 43 partitioning experiments for clinopyroxene-melt systems and 29 experiments for plagioclase-melt systems. The 43 clinopyroxene-melt partitioning experiments were conducted at 1042–1470 °C and 0.0001–4 GPa and crystalized clinopyroxene with Mg# of 54–100. The 29 plagioclase-melt partitioning experiments cover temperatures of 1127–1410 °C, pressures of 0.0001–1.5 GPa, and a wide range of plagioclase compositions (An# = 41–98).

The lattice strain parameters for REE partitioning between clinopyroxene and melt can be described by the following expressions from Sun and Liang (2012):

$$\ln K_0^{\text{cpx}} = -7.14 + \frac{7.19\times10^4}{RT} + 4.37X_{\text{Al}}^{\text{T,cpx}} + 1.98X_{\text{Mg}}^{\text{M2,cpx}} - 0.91X_{\text{H}_2\text{O}}^{\text{melt}}, \tag{2.18}$$

$$r_0^{\text{cpx}}(\text{Å}) = 1.066 - 0.104X_{\text{Al}}^{\text{M1,cpx}} - 0.212X_{\text{Mg}}^{\text{M2,cpx}}, \tag{2.19}$$

$$E^{\text{cpx}}(\text{GPa}) = \left(2.27r_0^{\text{cpx}} - 2.00\right)\times10^3, \tag{2.20}$$

where $X_{\text{Al}}^{\text{T,cpx}}$ is the Al content in the tetrahedral site of clinopyroxene (cpx) per formula unit; $X_{\text{Al}}^{\text{M1,cpx}}$ is the Al content in the M1 site; $X_{\text{Mg}}^{\text{M2,cpx}}$ is the Mg content in the M2 site assuming a random distribution of Fe-Mg in the M1 and M2 sites; $X_{\text{H}_2\text{O}}^{\text{melt}}$ is the molar fraction of H_2O in the melt; and T is the temperature in Kelvin. Iron is assumed as Fe^{2+} for pyroxene formula calculations.

The lattice strain parameters for REE partitioning between plagioclase and melt are expressed as follows (Sun et al., 2017):

$$\ln K_0^{\text{plg}} = 16.05 - \frac{19.45 + 1.17P^2}{RT}\times10^4 - 5.17\left(X_{\text{Ca}}^{\text{plg}}\right)^2, \tag{2.21}$$

$$r_0^{\text{plg}}(\text{Å}) = 1.179, \tag{2.22}$$

$$E^{\text{plg}}(\text{GPa}) = 196, \tag{2.23}$$

where $X_{\text{Ca}}^{\text{plg}}$ is the cation fraction of Ca in plagioclase (plg), and P is the pressure in GPa. Uncertainties of the coefficients in equations (2.18–2.23) were not shown for simplicity, but can be found in Sun and Liang (2012) and Sun et al. (2017). Although melt major element compositions appear to be unnecessary for the model calibration, they may indirectly affect REE partitioning through mineral-melt phase equilibria.

Together with these lattice strain parameters (equations (2.18–2.23)), equation (2.16) can then be used to quantify the effects of temperature, pressure, and composition on REE partitioning between plagioclase and clinopyroxene. The complete form of equation (2.16) can be rearranged to derive the REE thermometer for plagioclase-clinopyroxene systems:

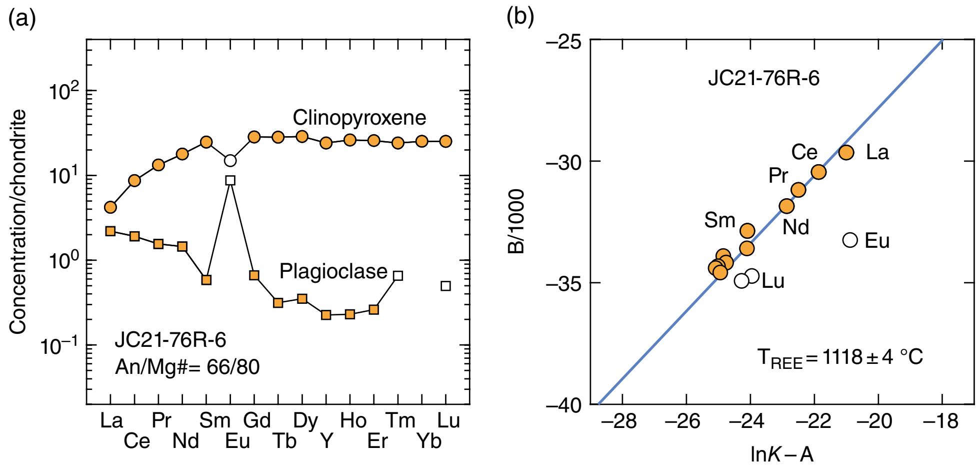

Figure 2.5 Temperature calculation using the REE-in-plagioclase-clinopyroxene thermometer for an oceanic gabbro (JC21-76R-6) from Hess Deep. Plot (a) shows the REE abundances in clinopyroxene and plagioclase normalized by chondrite compositions (Anders & Grevesse, 1989), and plot (b) displays the linear least-squares regression analysis of the REE partitioning data. The solid curve is the best-fit line passing through the origin. The temperature error was obtained from the regression analysis without considering the analytical uncertainties. In the temperature calculation, Eu was excluded for its divalent behavior, and heavy REE in plagioclase were also excluded because of their large analytical uncertainties.

$$B_i = T\left(\ln K_i^{\mathrm{plg/cpx}} - A\right), \tag{2.24}$$

$$A = 23.19 - 5.17\left(X_{\mathrm{Ca}}^{\mathrm{plg}}\right)^2 - 4.37X_{\mathrm{Al}}^{\mathrm{T,cpx}} - 1.98X_{\mathrm{Mg}}^{\mathrm{M2,cpx}} + 0.91X_{\mathrm{H_2O}}^{\mathrm{melt}}, \tag{2.25}$$

$$B_i = -32.04\times10^3 - 1.41\times10^3 P^2 + 909.85G\left(r_i\right), \tag{2.26}$$

$$G\left(r_i\right) = -E^{\mathrm{plg}}\left(\frac{r_0^{\mathrm{plg}}}{2}\left(r_0^{\mathrm{plg}} - r_i\right)^2 - \frac{1}{3}\left(r_0^{\mathrm{plg}} - r_i\right)^3\right) + E^{\mathrm{cpx}}\left(\frac{r_0^{\mathrm{cpx}}}{2}\left(r_0^{\mathrm{cpx}} - r_i\right)^2 - \frac{1}{3}\left(r_0^{\mathrm{cpx}} - r_i\right)^3\right). \tag{2.27}$$

Note that G is the correction for changes in the lattice strain energy and can be calculated using E and r_0 from equations (2.19–2.20) and (2.22–2.23). For anhydrous magmatic conditions or subsolidus mineral assemblages, $X_{\mathrm{H_2O}}^{\mathrm{melt}}$ in equation (2.25) should be neglected; for hydrous magmatic conditions, ±2 wt% of the melt water contents yield an uncertainty of about ±10 °C in the calculated temperatures (Sun & Liang, 2017). If the major and trace element compositions are provided for coexisting plagioclase and clinopyroxene, the temperature can be obtained through linear least-squares regression analyses of K_{REE} in the plot of ($\ln K$–A) versus B (Figure 2.3) and is given by the slope of the straight line passing through the origin. For interested readers, Sun and Liang (2017) provided an Excel® spreadsheet to automate the temperature calculation using the REE-in-plagioclase-clinopyroxene thermometer.

Figure 2.5 shows an example of the temperature calculation for a gabbro sample (JC21-76R-6; Sun & Lissenberg, 2018a) from Hess Deep at the East Pacific Rise. In the spider diagram (Figure 2.5a), heavy REE in plagioclase are close to or below detection limits because of their high incompatibility in plagioclase, and Eu is significantly apart from other REE due to its divalent behavior. Therefore, these elements should be excluded for accurate determination of the temperature. Through robust linear least-squares regression analyses, the remaining REE can define a straight line passing through the origin (Figure 2.5b), the slop of which determines the temperature at 1118 ± 4 °C, similar to the crystallization temperatures of mid-ocean ridge basalts (e.g., Grove & Bryan, 1983). As an independent test, Sun and Liang (2017) also applied their REE thermometer to 12 volcanic rocks with coexisting plagioclase and clinopyroxene phenocrysts reported in the literature. They noted that the temperatures of these samples derived from the REE thermometer are in good agreement with the plagioclase crystallization temperatures calculated using the plagioclase-melt thermometers (e.g., Putirka, 2005; Waters & Lange, 2015). This demonstrates that this REE thermometer can record the crystallization temperatures of plagioclase in pre-eruptive magmatic conditions.

Mg-in-Plagioclase-Clinopyroxene Thermometer

The Mg equilibrium exchange between plagioclase and clinopyroxene can be described through various chemical reactions, given the multiple end-members in the two minerals and the multi-phase assemblages in natural petrological systems. The preferred reaction in Faak et al. (2013) is

$$[\mathrm{MgSiO_3}]_{\mathrm{cpx}} + [\mathrm{SiO_2}] + [\mathrm{Al_2O_3}] = [\mathrm{MgAl_2Si_2O_8}]_{\mathrm{plg}}, \quad (2.28)$$

where $MgSiO_3$ and $MgAl_2Si_2O_8$ are end-member components in clinopyroxene (cpx) and plagioclase (plg), respectively, and SiO_2 and Al_2O_3 may not be directly linked to any phases. In contrast, Sun and Lissenberg (2018a) suggested that the Mg exchange could be coupled together with Ca,

$$\begin{aligned}&[\mathrm{Mg_2Si_2O_6}]_{\mathrm{cpx}} + [\mathrm{CaAl_2Si_2O_8}]_{\mathrm{plg}} \\ &= [\mathrm{CaMgSi_2O_6}]_{\mathrm{cpx}} + [\mathrm{MgAl_2Si_2O_8}]_{\mathrm{plg}}, \quad (2.29)\end{aligned}$$

where $Mg_2Si_2O_6$ and $CaMgSi_2O_6$ can be replaced by other Mg and Ca end-member components in clinopyroxene (e.g., $MgAl_2SiO_6$ and $CaAl_2SiO_6$). Alternatively, the Mg exchange may also take place by reactions with other coexisting minerals (Sun & Lissenberg, 2018b):

$$\begin{aligned}&[\mathrm{MgSiO_3}]_{\mathrm{cpx}} + 2[\mathrm{MgSiO_3}]_{\mathrm{opx}} + [\mathrm{Al_2O_3}] \\ &= [\mathrm{Mg_2SiO_4}]_{\mathrm{ol}} + [\mathrm{MgAl_2Si_2O_8}]_{\mathrm{plg}}, \quad (2.30)\end{aligned}$$

where opx and ol denote orthopyroxene and olivine, respectively.

Given these multiple choices of Mg exchange between plagioclase and clinopyroxene, chemical reactions need to be carefully selected to reduce the complexities for thermometer calibration and application. Thermometers derived from equation (2.28) require independent constraints on SiO_2 and Al_2O_3 activities, whereas those calibrated using equation (2.30) are only applicable to rocks with four coexisting minerals (i.e., ol, opx, cpx, and plg) and known Al_2O_3 activities. With the aforementioned limitations, these types of exchange reactions are not practical for thermometer applications to natural samples. On the other hand, equation (2.29) appears to be more promising as it postulates minimal assumptions regarding the coexisting mineral assemblages and the knowledge of SiO_2 and/or Al_2O_3 activities. Although additional minerals and activities of SiO_2 or Al_2O_3 are not included in equation (2.29), they may still indirectly influence the Mg–Ca coupled exchange through the compositions of major elements in plagioclase and clinopyroxene. For instance, changing the SiO_2 activity can potentially modify the anorthite component in plagioclase ($CaAl_2Si_2O_8$) and the Ca-Tschermak component in clinopyroxene ($CaAl_2SiO_6$) and, in turn, affect Mg partitioning through the Mg–Ca coupled exchange reaction (equation (2.29)).

Many phase equilibria experiments in the literature have produced plagioclase and clinopyroxene coexisting with silicate melts (e.g., Feig et al., 2006; Grove & Bryan, 1983; Grove et al., 2003; Sack et al., 1987; Sisson & Grove, 1993; Takagi et al., 2005; Thy et al., 1998; Villiger et al., 2004; H.-J. Yang et al., 1996). Unfortunately, because the qualities of Mg data in plagioclase are highly variable, the existing phase equilibria experiments cannot be used directly for the Mg thermometer calibration. Similar to the multi-element approach for thermometer calibration (section 2.3.2), Sun and Lissenberg (2018a) calculated plagioclase-clinopyroxene K_{Mg} for existing phase equilibria experiments by combining the previously calibrated plagioclase-melt K_{Mg} model (Sun et al., 2017) with the measured clinopyroxene-melt K_{Mg} from the phase equilibria experiments. These phase equilibria experiments cover a wide range of temperatures (800–1430 °C), pressures (0.0001–2.7 GPa), and compositions (e.g., An# = 28–100 in plagioclase). Through multiple linear least-squares regression analyses of the plagioclase-clinopyroxene K_{Mg} data, Sun and Lissenberg (2018a) calibrated a new thermometer using the Mg–Ca coupled exchange (equation (2.29)):

$$T(K) = \frac{14265 + 487P^2}{5.15 - \ln\left(C_{\mathrm{MgO}}^{\mathrm{plg}} / C_{\mathrm{MgO}}^{\mathrm{cpx}}\right) + 0.75\left(X_{An}\right)^2}, \quad (2.31)$$

where C_{MgO} is the weight fraction of MgO in plagioclase (plg) or clinopyroxene (cpx), and X_{An} is the molar fraction of anorthite in plagioclase [X_{An} = Ca/(Ca+Na+K) in mole]. The uncertainties of the coefficients in equation (2.31) can be found in Sun and Lissenberg (2018a). The regression analyses yield a standard error of ±29 °C for this thermometer. As demonstrated in Sun and Lissenberg (2018a), the plagioclase-clinopyroxene K_{Mg} data from the diffusion experiments of Faak et al. (2013) further validate the accuracy of this Mg-based thermometer.

Applications of the Mg- and REE-based geothermometers to oceanic gabbros from Hess Deep indicate systematic differences in the temperatures recorded by Mg and REE (Figure 2.6a). The calculated REE temperatures (T_{REE} = 1040–1283 °C) are similar to the crystallization temperatures of mid-ocean ridge basalts (e.g., Grove & Bryan, 1983) and are also positively correlated with the anorthite content in plagioclase (An#) that has been widely used as a qualitative index to track magma crystallization. However, the calculated Mg temperatures (T_{Mg} = 904–1128 °C) are generally about 39–320 °C lower than T_{REE} and do not correlate with An#, indicating extensively diffusive resetting of Mg at lower temperatures after the main stages of crystallization. Given that the two different thermometers were applied to the same cumulate rocks, the most possible causes for the systematic differences between T_{Mg} and T_{REE} are the differential diffusive responses of Mg and REE to changes in temperature after crystallization of the cumulus minerals.

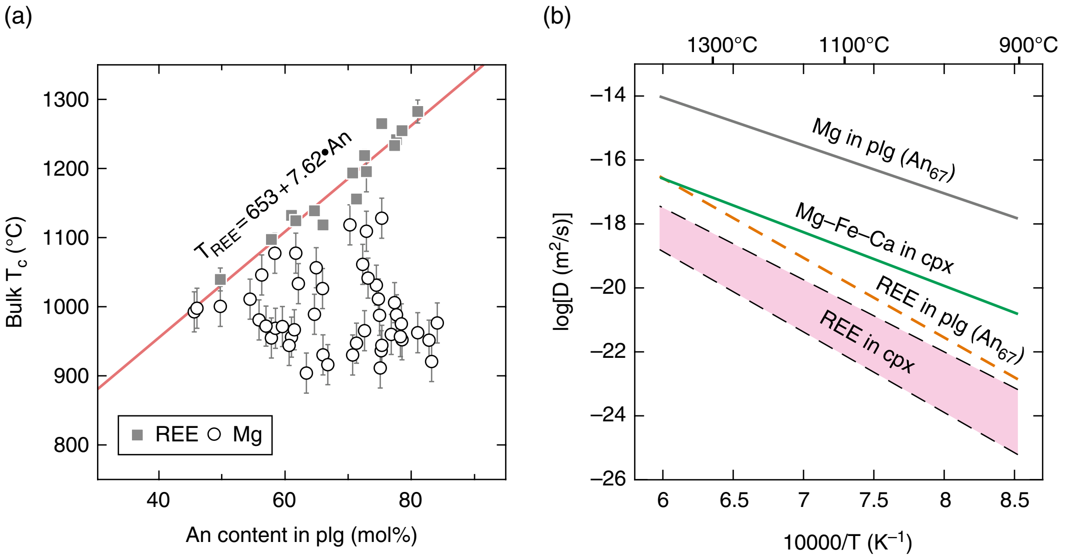

Figure 2.6 Plots showing (a) the thermometer-derived Mg and REE bulk closure temperatures of Hess Deep samples and (b) the experimentally determined diffusion coefficients of Mg and REE in plagioclase and in clinopyroxene. The solid line in (a) displays the strong positive correlation between REE closure temperatures and plagioclase anorthite contents (Sun & Lissenberg, 2018a). Errors in Mg closure temperatures were taken from the Mg-exchange thermometer calibration (±29 °C). The diffusion coefficients of REE in clinopyroxene were calculated at 2 kbar using the diffusion parameters from Van Orman et al. (2001), whereas those of REE in plagioclase (X_{An} = 0.67) were calculated using the diffusion parameters of Nd from Cherniak (2003). Mg diffusion coefficients in plagioclase were taken from Van Orman et al. (2014), and those in clinopyroxene were taken from Müller et al. (2013).

As shown in Figure 2.6b, the diffusion coefficients of Mg in plagioclase are about 2–4 orders of magnitude greater than those of REE in plagioclase, supporting the faster diffusive resetting of Mg in the plagioclase-clinopyroxene system. Thus, for mafic cumulate rocks, the REE-based exchange thermometer can potentially record temperatures at or close to the crystallization of cumulate minerals, whereas the Mg-based exchange thermometer is likely more sensitive to diffusive redistribution during cooling.

2.4. TRACE ELEMENT GEOSPEEDOMETRY

Extraction of thermal histories from rock records by geospeedometers relies on the quantitative measurement of mineral diffusive responses to changes in temperature. Without significant crystal overgrowth after the main stages of crystallization, such diffusive response manifests in the compositional variation. Major controls of the compositional variation include the rate of temperature changes, the initial conditions of temperature and concentration, and the diffusion coefficient of the element of interest in the mineral, as well as a number of other factors, such as the partition coefficient of the element between the mineral and surroundings, the size of the mineral grain, and the relative phase proportions of the mineral assemblage (e.g., Dodson, 1973, 1986; Ehlers & Powell, 1994; Eiler et al., 1992; Ganguly & Tirone, 1999; Lasaga, 1983; Lasaga et al., 1977; Liang, 2015; Sun & Lissenberg, 2018a; Watson & Cherniak, 2015; Yao & Liang, 2015). Thus, the design and application of geospeedometers are not as straightforward as those of geothermometers. In this section, I first provide a general overview of diffusion and geospeedometry in petrological systems, then outline the basic idea of geospeedometer design, and lastly present the recent progress in geospeedometry for mafic cumulate rocks.

2.4.1. Diffusion and Geospeedometry

A Brief Overview

According to the phenomenological analysis of Darken (1948), the diffusive flux (J) of a trace element of interest can be described as

$$J = -D^{*}\frac{\partial C}{\partial x} = -D\left(1+\frac{\partial \ln \gamma}{\partial \ln C}\right)\frac{\partial C}{\partial x}, \tag{2.32}$$

where x is the spatial coordination. The intrinsic diffusivity (D) can be determined in diffusion experiments through the Arrhenius equation

$$D = D_0 \exp\left(-\frac{E_A}{RT}\right), \tag{2.33}$$

where E_A is the activation energy, and D_0 is the pre-exponential factor indicating the maximum diffusion coefficient at infinite temperature. When the activity coefficient (γ) of a trace element is independent of its concentration (C), its diffusive flux reduces to

$$J = -D\frac{\partial C}{\partial x}. \tag{2.34}$$

However, when γ varies with the concentration of a major element (X), the diffusive flux of this trace element is expressed as follows:

$$J = -D\left(\frac{\partial C}{\partial x} + \frac{\partial \ln\gamma}{\partial x}C\right) = -D\left(\frac{\partial C}{\partial x} + \frac{\partial \ln\gamma}{\partial X}\frac{\partial X}{\partial x}C\right). \tag{2.35}$$

As shown in equation (2.35), the major element, if manifesting zonation ($\partial X/\partial x \neq 0$), can enhance or reduce the diffusive flux of the trace element, depending on the sign of $\partial \ln\gamma/\partial X$ and the major element zoning pattern ($\partial X/\partial x$) (Sun & Lissenberg, 2018b). Additional influence of the major element may arise from D when it is dependent on X.

Assuming chemical diffusion is the only mass transport process in the system (e.g., no radiogenic decay/ingrowth, or extensive crystal overgrowth), the concentration of a given chemical species varies with time (t), and the net diffusive flux can be described through the continuity equation:

$$\frac{\partial C}{\partial t} + \nabla\cdot J = 0. \tag{2.36}$$

By substituting equation (2.35) into equation (2.36), a general expression can be obtained to describe the isotropic diffusion of a trace element in a crystal:

$$\frac{\partial C}{\partial t} = \frac{1}{r^{n-1}}\frac{\partial}{\partial r}\left[r^{n-1}D\left(\frac{\partial C}{\partial r} + \frac{\partial \ln\gamma}{\partial X}\frac{\partial X}{\partial r}C\right)\right], \tag{2.37}$$

where r is the spatial coordinate from the center of the crystal, and n indicates the geometries (1 – plane sheet, 2 – cylinder, and 3 – sphere) approximating crystal shapes in one-, two-, and three-dimensional spaces. Assuming negligible effects of major elements on γ, equation (2.37) can be simplified to the familiar diffusion equation:

$$\frac{\partial C}{\partial t} = \frac{1}{r^{n-1}}\frac{\partial}{\partial r}\left[r^{n-1}D\frac{\partial C}{\partial r}\right]. \tag{2.38}$$

Assuming that the cooling system starts from chemical equilibrium, the initial (C_0) and boundary concentrations (C_b) are determined by the partition coefficient (K) between this crystal (α) and its surrounding phase (β):

$$C_0^\alpha = K(T_0)\cdot C_0^\beta, \tag{2.39}$$

$$C_b^\alpha = K(T)\cdot C_b^\beta, \tag{2.40}$$

where $K(T_0)$ and $K(T)$ denote partition coefficients at the initial (T_0) and instantaneous temperatures (T), respectively. The temperature dependence of partition coefficients can be experimentally calibrated using equation (2.7) or (2.16). If the system is approximately closed, an additional boundary constraint comes from the balance of total diffusive flux between this crystal and its surrounding phase:

$$\phi^\alpha \frac{D^\alpha}{L^\alpha}\frac{\partial C^\alpha}{\partial r}\bigg|_{r=L^\alpha} = \phi^\beta \frac{D^\beta}{L^\beta}\frac{\partial C^\beta}{\partial r}\bigg|_{r=L^\beta}, \tag{2.41}$$

where ϕ denotes the modal abundance, and L is the effective grain radius. However, this boundary constraint becomes unnecessary when the surrounding phase has no compositional responses to diffusion in the crystal; that is, phase β has a constant and homogeneous concentration profile. In this case, the surrounding phase behaves as a homogeneous infinite reservoir, and accordingly the initial and boundary conditions defined in equations (2.39) and (2.40) are sufficient to solve diffusion in the single crystal.

In a cooling petrological system (Figure 2.7), the crystal boundary responds instantaneously to temperature changes and thus causes a concentration gradient driving diffusion between the interior and the boundary. If chemical disequilibrium is imposed initially as zonation in the crystal (e.g., stepwise profiles) due to different stages of formation, diffusion could commence immediately within the crystal. Because D decreases exponentially with temperature (equation (2.33)), chemical diffusion effectively reaches closure at a lower temperature, leaving a stabilized concentration profile, that is, the closure profile (Dodson, 1986) in the crystal (Figure 2.7). The corresponding temperature is called the closure temperature (Dodson, 1973). Applying the relevant geothermometers to the mean or local concentration of the closure profile, one could obtain two types of closure temperatures, that is, the bulk and local closure temperatures (Dodson, 1973, 1986). Accordingly, cooling rates can be estimated using the grain-scale diffusion approach based on the local closure profile (or local closure temperature) or using the bulk diffusion approach based on the mean concentration of the crystal (or bulk closure temperature). Through analytical and numerical analyses of equation (2.38) or its approximate forms, both approaches have been widely used to model cooling histories of various petrological systems (e.g., Dodson, 1973, 1986; Ehlers & Powell, 1994; Eiler et al., 1992; Ganguly & Tirone, 1999; Lasaga, 1983; Lasaga et al., 1977; Liang, 2015; Sun & Lissenberg, 2018a; Watson & Cherniak, 2015; Yao & Liang, 2015).

Single Crystals Within Infinite Reservoirs

A simple scenario formulated in the seminal works of Dodson (1973, 1986) is a single crystal within an infinite

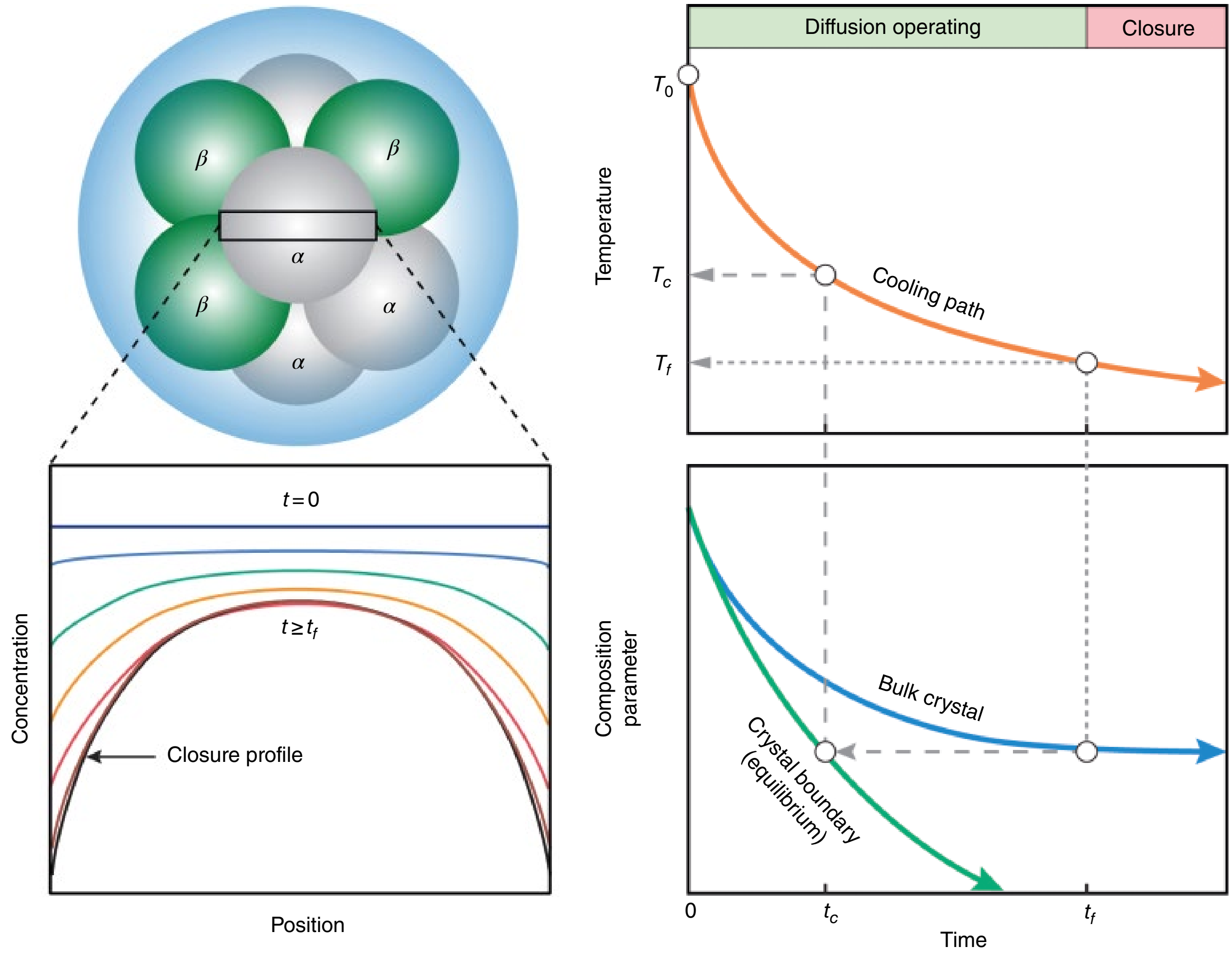

Figure 2.7 Schematic diagrams showing the closure profile and temperature of a cooling petrological system. During cooling, the crystal surface remains in chemical equilibrium with the surroundings, which generates a concentration gradient to drive diffusion. Due to diffusive interaction with the surroundings, the initial concentration profile of the crystal becomes progressively concave through time (t), but will be effectively locked at a certain point ($t = t_f$), marking the closure of diffusion in the crystal. The locked concentration profile is called the closure profile (Dodson, 1986). Similarly, the chemical composition of the crystal or other equivalent parameters (e.g., concentration ratios with the surroundings) would also become asymptotically invariant after a certain time. The invariant value is directly measurable from natural petrological systems at diffusive closure ($t \geq t_f$) and can then be related to an equilibrium temperature at an earlier time ($t = t_c$). This "equilibrium" temperature, called the closure temperature (T_c) by Dodson (1973), is apparently lower than the initial temperature (T_0) and greater than the ambient temperature (T_f) at the time of diffusive closure ($t = t_f$).

reservoir, in which the relative proportions of individual minerals can be omitted. To linearize this diffusion problem, Dodson (1973, 1986) assumed that both the reciprocal temperature ($1/T$) and boundary concentration (C_b) vary uniformly with time (t):

$$\frac{E_A}{RT} = \frac{E_A}{RT_0} + t/\tau, \tag{2.42}$$

$$C_b = C_0 + bt/\tau, \tag{2.43}$$

where τ is the characteristic time for an e-folding decrease of diffusivity (cf. equation (2.33)) during cooling, and b is a random constant. The characteristic time (τ) is related to the absolute cooling rate (dT/dt) at an instantaneous temperature (T) as follows:

$$\tau = -\frac{RT^2}{E_A\left(dT/dt\right)}. \tag{2.44}$$

Using an analytical approach, Dodson (1973, 1986) derived a simple expression relating the closure temperature (T_c) to the instantaneous cooling rate (dT/dt) at T_c:

$$T_c = \frac{E_A / R}{\ln\left[-\tau D_0 / L^2\right] + \Gamma} = \frac{E_A / R}{\ln\left[\dfrac{R T_c^2 D_0}{E_A \left(dT/dt\right) L^2}\right] + \Gamma}, \qquad (2.45)$$

where Γ is the closure function depending upon crystal geometry and location in the crystal. Interested readers are referred to Table 2 in Dodson (1986) for the spatially variable Γ that enables the calculation of a local closure temperature profile using equation (2.45). The spatially weighted average of Γ is 4.0066 for a sphere, 3.29506 for a cylinder, and 2.15821 for a plane sheet, which give rise to the bulk closure temperatures for the corresponding geometries.

According to Dodson's formulation (equation (2.45)), the closure temperature for diffusion in a single crystal is positively correlated with the cooling rate and grain size but increases with the decrease in diffusivity (Mg vs. REE; Figure 2.8a). The cooling rate (dT/dt) and the square of the grain radius (L^2) can be conveniently treated together by their product as a single term, that is, the *effective cooling rate*. As shown in Figure 2.8b, the bulk closure temperature derived from Dodson's formulation for a given element always follows a single curve as a function of the effective cooling rate, regardless of the initial conditions. This is due to the simplification adopted by Dodson (1973, 1986) that only takes account of cases with extensive diffusion and complete loss of the initial conditions (i.e., T_0 and C_0) in the crystal. If the assumptions of Dodson (1973, 1986) regarding the extensive diffusion and infinite reservoir can be justified for natural single-crystal systems, equation (2.45) could then be applied to estimate the rate of cooling using either the bulk closure temperature or the closure (temperature) profile of the crystal.

To incorporate an arbitrary small amount of diffusion in Dodson's formulation, Ganguly and Tirone (1999) introduced a numerical correction term for the closure function (Γ) in equation (2.45) that depends on the initial temperature and crystal geometry. Closure temperatures from the two formulations are consistent for systems with slow cooling rates and/or small grain radii. However, for systems with rapid cooling rates and/or large grain sizes, closure temperatures derived from the formulation of Ganguly and Tirone (1999) remain close to the corresponding initial temperatures (Figure 2.8b), indicating the necessity for correction of the closure function. Notably, the closure temperatures of slower-diffusing species (e.g., REE) are more resistant to diffusive resetting of the initial condition than those of faster-diffusing species (e.g., Mg). Given the potential effect of the initial conditions on the closure temperatures, estimation of

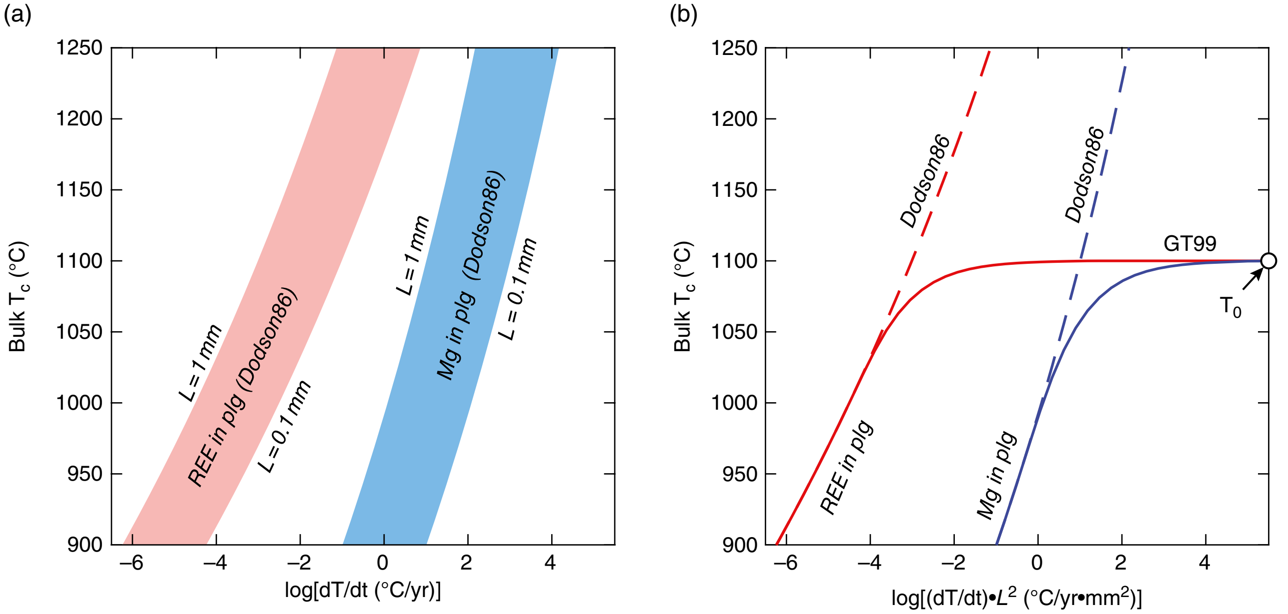

Figure 2.8 Comparison of bulk closure temperatures derived from the formulations of Dodson (1986) and Ganguly and Tirone (1999; GT99) for REE and Mg in spherical plagioclase crystals within a homogeneous infinite reservoir. The cooling rates in (a) are absolute cooling rates, whereas those in (b) are the effective cooling rates, that is, the products of grain radius squares (L^2) and cooling rates (dT/dt). Two different grain radii (0.1 and 1 mm) were used in the closure temperature calculations. See Figure 2.6 for the references of Mg and REE diffusion data.

cooling rates using the formulation of Ganguly and Tirone (1999) for natural single-crystal systems thus demands a prior assumption or an independent determination of the equilibrium initial conditions. In particular, for single-crystal systems with stepwise initial concentration profiles, Watson and Cherniak (2015) developed a simple parameterization from their numerical solutions to constrain the cooling history.

Two- or Multi-Mineral Assemblages

For cooling petrological systems with two or more minerals, simple analytical expressions have not been obtained following the approach of Dodson (1973, 1986). Using a second-order polynomial approximation for the diffusion profile of each crystal in the bi-mineral system, Liang (2015) simplified the familiar diffusion equation (equation (2.38); i.e., first-order derivative in time and second-order derivative in space) to the first-order transport equation (i.e., first-order derivatives in both time and space). Assuming that the system has not been open to mass transfer with their surrounding media during cooling, Liang (2015) constructed an analytical expression to describe the bulk closure temperature of a trace element in cooling bi-mineral systems:

$$\frac{\phi_\beta E_{\mathrm{A},\alpha} L_\alpha^2 \left(dT/dt\right)_{T_c} / D_{\alpha,T_c} + \phi_\alpha E_{\mathrm{A},\beta} L_\beta^2 \left(dT/dt\right)_{T_c} K_{T_c} / D_{\beta,T_c}}{\left(\phi_\alpha K_{T_c} + \phi_\beta\right) R T_c^2} + \frac{\phi_\beta \phi_\alpha K_{T_c} E_K}{\left(\phi_\alpha K_{T_c} + \phi_\beta\right)^2 R T_c^2} \left(\frac{L_\alpha^2}{D_{\alpha,T_c}} - \frac{L_\beta^2}{D_{\beta,T_c}}\right) \left(dT/dt\right)_{T_c} = \exp\left(\Gamma\right), \tag{2.46}$$

where quantities with subscript T_c indicate that they are evaluated at T_c, Γ is the spatially averaged closure function from the formulation of Dodson (1973, 1986) (equation (2.45)), and E_K is the activation energy of partitioning ($= B \bullet R$; B is defined in equation (2.10)). Because the corrected closure function (Γ) of Ganguly and Tirone (1999) for diffusion in single crystals is not applicable to bi-mineral systems, an arbitrary small amount of diffusion was not taken into account in equation (2.46) to incorporate the effects of large grain sizes and initial temperatures. Thus, direct estimation of cooling rates using equation (2.46) can only be made for bi-mineral systems with complete loss of the initial conditions.

This analytical expression (equation (2.46)) of Liang (2015) enables scale analysis on the relative importance of individual minerals for determining the bulk closure temperature of a trace element in the cooling bi-mineral system. Introducing two shorthand notations (Θ and ω), Sun and Liang (2017) rewrote the above equation as a Dodson-type expression:

$$T_c = \frac{E_{\mathrm{A},\alpha}/R}{\ln\left[\dfrac{R T_c^2 D_{0,\alpha}}{E_{\mathrm{A},\alpha}\left(dT/dt\right) L_\alpha^2}\right] + \Gamma + \ln\left(\Theta\right)}, \tag{2.47}$$

$$\Theta = \frac{1 + \left(\phi_\alpha/\phi_\beta\right) K_{T_c}}{1 + \left(\phi_\alpha/\phi_\beta\right) \omega K_{T_c}}, \tag{2.48}$$

$$\omega = \frac{D_{\alpha,T_c}}{D_{\beta,T_c}} \frac{L_\beta^2}{L_\alpha^2} \left(\frac{E_{\mathrm{A},\beta} + E_K}{E_{\mathrm{A},\alpha}}\right) - \frac{E_K}{E_{\mathrm{A},a}}, \tag{2.49}$$

where Θ is a correction factor for the effects of diffusion, partitioning, and relative proportions of the coexisting minerals (α and β), and ω denotes the relative diffusion rates in the two minerals. It is important to note that due to various effects from the surrounding phase, the closure temperature of a bi-mineral system cannot be simply taken as that of a single crystal. As shown in equation (2.48), the relative diffusion rate (ω) is the primary factor controlling the bulk effect (Θ) of the surrounding phase. When the two minerals have comparable diffusion rates ($\omega = 1$), the bulk effect of the surrounding phase becomes negligible ($\Theta = 1 \rightarrow \ln(\Theta) = 0$), which reduces equation (2.47) to the formulation (equation (2.45)) of Dodson (1973, 1986). In this case, the surround phase β effectively becomes an infinite reservoir for diffusion in mineral α, and thus the closure temperature formulations for single-crystal systems (e.g., equation (2.45)) likely remain valid. However, when the relative diffusion rates in the two minerals are distinct from each other ($|\omega - 1| >> 0$), the bulk effect of the surrounding phase can exert sufficient influences ($|\ln(\Theta)| >> 0$) to make the bi-mineral closure temperature significantly deviate from that of the single crystal. Under this condition, a numerical analysis of equation (2.38), as shown in previous studies (e.g., Ehlers & Powell, 1994; Eiler et al., 1992; Lasaga et al., 1977; Sun & Lissenberg, 2018a; Yao & Liang, 2015), is necessary for a more comprehensive understanding of the cooling histories.

2.4.2. Basic Idea of Geospeedometer Design

The goal of geospeedometry is to conveniently extract the cooling history information from the diffusive relaxation of petrological systems that can be measured through closure temperatures (i.e., equivalent to closure profiles). As discussed in section 2.4.1, the closure temperature (T_c) of the system can be described in general as

$$T_c = f\left(T_0, dT/dt, \Omega\right), \tag{2.50a}$$

$$\Omega = \left\{D, K, \phi, L\right\}, \tag{2.50b}$$

where f denotes an unspecified expression defined by the analytical or numerical solution of the diffusion equation, and Ω is a set of directly measurable variables including the diffusion coefficients (D), phase proportions (ϕ), grain radii (L), and partition coefficient(s) (K) of the mineral(s) in the petrological system. If the system starts cooling from disequilibrium concentration profiles, the initial concentration (C_0) should also be considered as an additional variable. In addition to the cooling rate (dT/dt), the initial condition (i.e., T_0 and C_0) can significantly influence the closure temperatures (or profiles) for systems with relatively rapid cooling rates and/or large grain radii. As shown in Figure 2.8b for a single crystal in a homogeneous infinite reservoir, without knowing the relevant T_0, it is easy to mistakenly underestimate the cooling rate by several orders of magnitude using the observed closure temperatures. Moreover, as the initial point of the cooling path (Figure 2.7), T_0 is also important for estimation of the cooling timescale for the petrological system.

Because cumulate rocks have simple monotonic cooling paths after the main stages of crystallization, T_0's of cumulate rocks are effectively the mean temperatures of cumulus crystallization and hence are especially important for understanding magmatic histories of cumulate parental melts. Estimation of T_0 for cumulate rocks depends not only on the precision of geothermometers but also on the extent of diffusive resetting (i.e., equivalent to closure temperatures) of key elements used in the geothermometers. In general, slowly diffusing elements tend to have small extents of diffusive relaxation and thus likely record closure temperatures near the condition of mineral crystallization (e.g., Liang et al., 2013; Sun & Liang, 2015, 2017; Wark & Watson, 2006; Watson et al., 2006). However, at smaller effective cooling rates ($L^2 \bullet dT/dt$; equation (2.45)), elements with slow diffusivities (e.g., REE) could also be extensively reset to lower temperatures (Figure 2.8). Given the codependent relation between closure temperatures and cooling histories (i.e., T_0 and dT/dt; equation (2.50a)), it is challenging to determine the full cooling path (including both T_0 and dT/dt) from the measured closure temperatures (or profiles) of single elements.

A promising resolution to this problem is the combination of two or multiple elements with distinct geochemical behaviors in diffusion and/or partitioning. Following equation (2.50a), the closure temperatures of two elements (i vs. j) can be written as

$$T_c^i = f\left(T_0, dT/dt, \Omega_i\right), \qquad (2.51a)$$

$$T_c^j = g\left(T_0, dT/dt, \Omega_j\right), \qquad (2.51b)$$

Given their distinct geochemical behaviors, the two elements have unique Ω's and explicit formulas (f vs. g) for closure temperatures. From the measured closure temperatures of each element, one may obtain a family of solutions for T_0 and dT/dt; however, when considered together, the two families of solutions may intersect at a singular point that determines both T_0 and dT/dt for the petrological system (Figure 2.9). This approach has been detailed recently in the framework of differential responses of bulk closure temperatures by Sun and Lissenberg (2018a), and similar ideas were also suggested in several previous studies (e.g., Costa & Dungan, 2005; Morgan & Blake, 2006; Sun & Liang, 2017; Watson & Cherniak, 2015; Watson & Harrison, 1984).

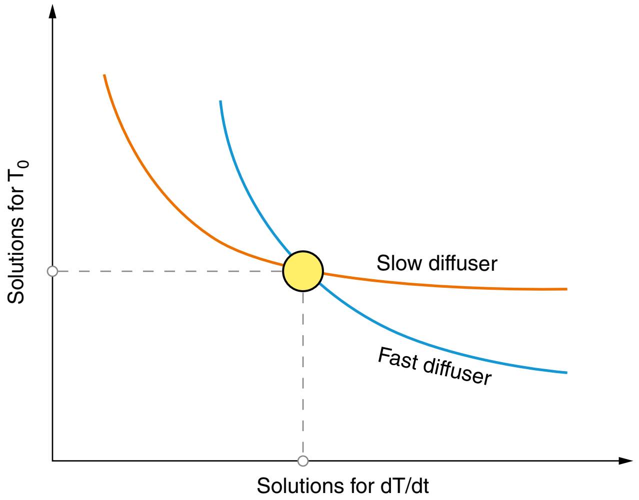

Figure 2.9 Schematic illustration showing the determination of initial temperature (T_0) and cooling rate (dT/dt) for a cooling petrological system. As T_0 and dT/dt both affect the measured closure temperatures, one may find a family of possible solutions for T_0 and dT/dt using the closure temperatures of single elements. The combination of two elements with distinct partitioning and diffusion behaviors could simultaneously constrain the two unknowns (T_0 and dT/dt) from the intersection between the two series of solutions.

2.4.3. The Mg–REE Coupled Geospeedometer for Mafic Cumulates

For mafic cumulate rocks, two different geothermometers have been calibrated based on the partitioning of REE and Mg, respectively, between plagioclase and clinopyroxene (see section 2.3.3). As shown in Figure 2.6a, the closure temperatures of REE and Mg derived from the two thermometers appear to be systematically distinct from each other for oceanic gabbros, which can be explained by the relative differences in their diffusivities (Figure 2.6b). Following the concept outlined in section 2.4.2, the differential diffusive closures of Mg and REE in plagioclase-clinopyroxene systems are suitable for constructing a generalized geospeedometer to determine the full cooling path of mafic cumulate rocks (Sun & Lissenberg, 2018a). In addition to the two geothermometers, however, implementation of this idea also requires establishing the exact expressions of the closure temperatures (equation (2.50a)) from analytical or numerical solutions of the diffusion equation.

Diffusion Model

Mafic cumulate rocks with plagioclase and clinopyroxene as the major cumulus phases can be effectively treated as two-mineral aggregates for diffusion modeling. Given their significantly different diffusivities (Figure 2.6b), plagioclase and clinopyroxene in this two-mineral system have distinct diffusion rates of Mg or REE ($\omega >> 1 \rightarrow \ln(\Theta) << 0$; see equation (2.47)) and thus cannot be considered simply as a single crystal in an infinite reservoir that has been formulated previously with analytical solutions (e.g., Dodson, 1973, 1986; Ganguly & Tirone, 1999). Accordingly, numerical models are required to build the explicit expressions for Mg and REE closure temperatures in this two-mineral system. As both minerals are important for determining the measured closure temperatures or profiles, the grain-scale diffusion approach has to consider the closure profiles of individual crystals in the plagioclase-clinopyroxene aggregate to obtain the representative cooling information. Because cross-sectional analysis of trace elements requires more dedicated protocols and analytical facilities, often one or two selected profiles are measured for grain-scale diffusion modeling, which apparently introduces a significant bias for this two-mineral diffusion system. Instead, the bulk diffusion approach is more practical, because the averaged mineral compositions can be routinely measured through in situ analyses of cores and rims in multiple representative grains of each mineral.

Numerical modeling of trace element diffusion commonly solves the familiar diffusion equation (equation (2.38)) through finite difference methods. For bulk diffusion simulations of a trace element (i.e., Mg and REE), the plagioclase-clinopyroxene system can be approximated as an aggregate of two types of spherical mineral grains, and chemical diffusion has to be solved simultaneously in both plagioclase and clinopyroxene along a prescribed cooling path. Similar to Dodson (1973, 1986), the monotonic cooling profile of cumulate rocks can be described as a reciprocal function of time in the diffusion simulations:

$$1/T = 1/T_0 + \eta \cdot t, \tag{2.52a}$$

$$\eta = \left(dT/dt\right)_{T_0} / \left(T_0\right)^2 = \left(dT/dt\right)_{T_c} / \left(T_c\right)^2, \tag{2.52b}$$

where η is a cooling constant determined by the absolute initial cooling rate. As shown in equation (2.52b), the (absolute) cooling rates decrease at lower temperatures and can be adjusted for instantaneous temperatures. The initial and boundary conditions of the two types of minerals are constrained by equations (2.39–2.41), the temperature-dependent partition coefficients (K_{REE}: equations (2.24–2.27); K_{Mg}: equation (2.31)), and the temperature-dependent diffusion coefficients in plagioclase (equations (A14 and A15) in Sun & Lissenberg, 2018a) and in clinopyroxene (Müller et al., 2013; Van Orman et al., 2001). Note that equations (A14) and (A15) in Sun and Lissenberg (2018a) are parameterized Arrhenius equations using the Mg diffusion data of Faak et al. (2013) and Van Orman et al. (2014) and the REE diffusion data of Cherniak (2003), respectively. The closure of diffusive exchange, following Dodson (1973, 1986), can be defined by the asymptote of apparent bulk partition coefficients. Interested readers are referred to Appendix A in Sun and Lissenberg (2018a) for details of the numerical methods and calculations of bulk closure temperatures.

It has been suggested that the anorthite zonation in plagioclase can influence the diffusive relaxation of Mg in plagioclase (e.g., Costa et al., 2003). According to equation (2.35), additional diffusive fluxes may come from the effect of major elements on activity coefficients. Although rigorous activity models have not been constructed for trace elements in minerals, they could be inferred from the partitioning model or its equivalents (e.g., exchange geothermometers) according to the scaling relation between the activity coefficient and relevant major elements. Incorporating the effect of anorthite zoning, Sun and Liang (2017) solved the more complete form of diffusion equation (equation (2.37)) for Mg and REE diffusion in two representative aggregates with normally zoned plagioclase. However, their simulation results indicate negligible influences on the calculated bulk closure temperatures. Given that natural cumulate rocks likely have various types of zoning patterns in plagioclase, the integrated effects of anorthite zoning, if any, are anticipated to be insignificant for the bulk diffusion in the two-mineral aggregate.

Determination of the Cooling Path

Figure 2.10 shows an example of the numerical calculations for Mg and REE diffusion in a cooling plagioclase-clinopyroxene aggregate with a uniform grain radius and equal mineral mode. The imposed cooling paths were defined by four equilibrium initial temperatures (1000, 1100, 1200, and 1300 °C) and a wide range of effective cooling rates (10^{-7}–10^{3} °C/yr·mm^2). The calculated bulk closure temperatures of REE (T_{REE}; solid curves) and Mg (T_{Mg}; dashed curves) define two regimes, a slow- and a fast-cooling regime (Figure 2.10a). The boundaries of these two regimes are controlled by the "Dodson limit" corresponding to bulk closure temperatures for a "sufficiently high initial temperature" but, importantly, varying as a function of Ω (see equation (2.50a); Sun & Lissenberg, 2018a). Within the two regimes, the differential

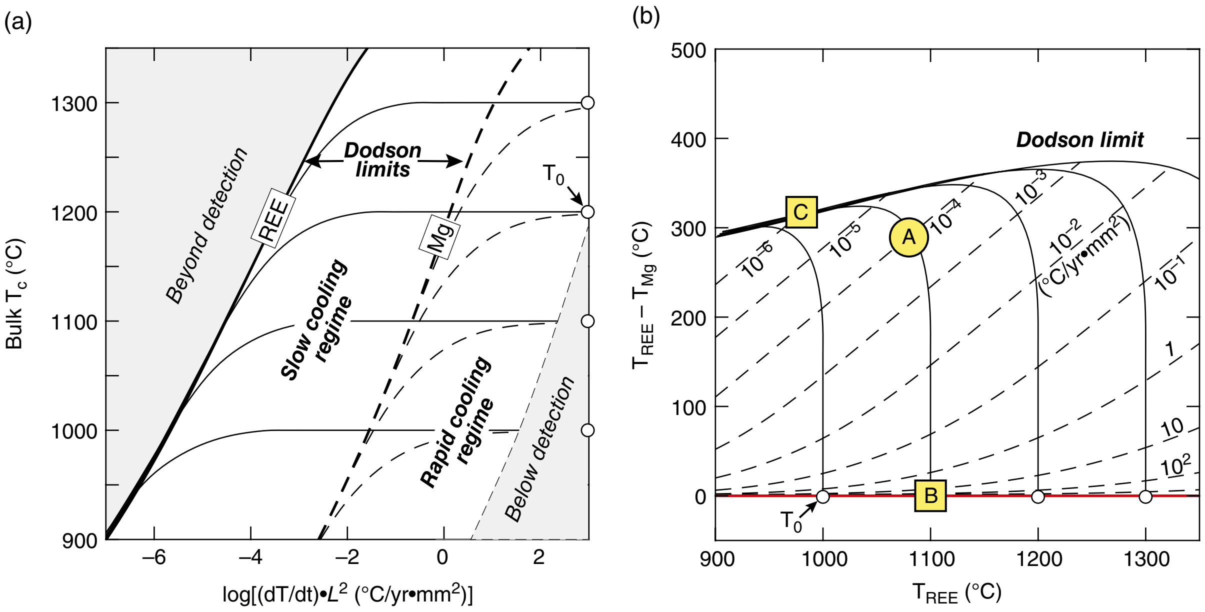

Figure 2.10 Numerical simulation results of REE (T_{REE}) and Mg (T_{Mg}) bulk closure temperatures for a plagioclase–clinopyroxene assemblage with a uniform grain radius and equal mineral mode (Sun & Lissenberg, 2018a). Plot (a) shows T_{REE} (solid curves) and T_{Mg} (dashed curves) as functions of effective cooling rates and initial temperatures, and plot (b) illustrates the simultaneous inversion of the cooling rate (dT/dt) and initial temperature (T_0) for a given sample by intersecting the two isopleths (the dashed and solid curves for dT/dt and T_0, respectively). Given the observed compositional dependences (Cherniak, 2003; Faak et al., 2013; Van Orman et al., 2014; Sun & Liang, 2017; Sun & Lissenberg, 2018a), the diffusion and partition coefficients of REE and Mg in plagioclase need be calculated for different anorthite contents. The simulation here used plagioclase An_{65}.

responses of T_{REE} and T_{Mg} to the same cooling path enable one to establish their explicit expressions (equation (2.50a)) and, further, to uniquely constrain both T_0 and dT/dt of the cooling path. However, for extremely slow cooling, both T_{REE} and T_{Mg} may lose the memory of the initial conditions and fall on their Dodson limits; for very rapid cooling, both T_{REE} and T_{Mg} likely remain at T_0 and thus are unable to determine dT/dt.

The simultaneous inversion of T_0 and dT/dt could be visualized by plotting the differences between T_{REE} and T_{Mg} as a function of T_{REE} (Figure 2.10b). The maximum differences between T_{REE} and T_{Mg} define the upper boundary in Figure 2.10b and are equivalent to the Dodson limit of REE. The background curves in Figure 2.10b are two families of contours for the numerically calculated bulk closure temperatures: The dashed curves are isopleths of dT/dt, whereas the solid curves are isopleths of T_0. The two families of isopleths intersect at singular points that uniquely define T_0 and dT/dt. For instance, T_{REE} (1080 °C) and T_{Mg} (800 °C) of a hypothetical sample place it at the intersection of two isopleths (point A; Figure 2.10b), which determines dT/dt at 10^{-4} °C/yr•mm^2 and T_0 at 1100 °C. If samples have identical T_{Mg} and T_{REE} (e.g., point B in Figure 2.10b), T_{Mg} and T_{REE} could only determine T_0 and the lower limits of dT/dt; if samples reach the upper boundary (e.g., point C in Figure 2.10b), T_{Mg} and T_{REE} can only constrain dT/dt and the lower limits of T_0. However, samples may also go beyond the upper limit or below the zero-horizontal line in Figure 2.10b, as a result of inaccurate estimations of closure temperatures or complex thermal histories; for these samples, no solutions can be obtained from this two-element-coupled geospeedometer.

The aforementioned inversion approach is based on the numerical simulations of Mg and REE diffusion for a plagioclase-clinopyroxene aggregate with a specified grain radius, mineral mode, and plagioclase composition. Given that natural mafic cumulate samples likely have a wide range of grain sizes, mineral modes, and plagioclase compositions, a substantial number of numerical simulations will thus be needed to establish the exact expressions for T_{Mg} and T_{REE} and to further invert dT/dt and T_0 for individual samples. For convenience, Sun and Lissenberg (2018a) compiled their numerical solutions from 1.575×10^5 diffusion simulations in a multidimensional grid that can be used to interpolate the expressions for T_{Mg} and T_{REE} over a wide range of plagioclase compositions, mineral proportions, and grain radii.

Using the MATLAB® program provided in Sun and Lissenberg (2018a), interested users could readily automate the inverse calculations of T_0 and dT/dt for a batch of mafic cumulate samples.

2.5. A CASE STUDY ON OCEANIC CRUST FORMATION

The cumulate section of the oceanic crust is mainly composed of gabbros and gabbronorites that solidify from mantle-derived magmas beneath the spreading mid-ocean ridges. For oceanic crust formation at fast-spreading mid-ocean ridges, the existing models remain highly debated as to whether oceanic cumulates crystalize mainly in a shallow melt lens (e.g., Coogan et al., 2007; Faak et al., 2015; Phipps Morgan & Chen, 1993; Quick & Denlinger, 1993; Sleep, 1978) or largely in situ from various magma sills in the lower crust (e.g., Kelemen et al., 1997; Lissenberg et al., 2004; Maclennan et al., 2005; Natland & Dick, 2009; Nicolas et al., 1988; VanTongeren et al., 2008, 2015). The former implies that oceanic cumulates underwent near-conductive cooling in the deeper crust; however, the latter suggests that oceanic cumulates experienced rapid cooling, perhaps due to crustal-scale hydrothermal circulations. Hence, these two models can be distinguished by the cooling histories recorded in oceanic cumulate rocks.

The oceanic crust at Hess Deep rift valley is a reference section for fast-spreading oceanic crust and has been mapped and sampled in several previous studies (e.g., Karson et al., 2002; Lissenberg et al., 2013). Recently, a suite of gabbroic samples from Hess Deep has been reported with mineral compositions, detailed petrographic descriptions, and reconstructed stratigraphy (Lissenberg et al., 2013). Through dedicated analysis on representative samples, Sun and Lissenberg (2018a) further confirmed the reliability of MgO data in plagioclase from Lissenberg et al. (2013). To correct for the effects of grain size, Sun and Lissenberg (2018a) also measured the average grain sizes of plagioclase and clinopyroxene from these samples. This provides a total of 46 well-characterized samples from a reconstructed section of 4.35 km below the dike-gabbro transition (DGT) at Hess Deep. Among them, only 15 samples have REE data. However, the 15 samples define a strong positive linear relationship between the calculated REE closure temperatures and plagioclase An# (Figure 2.6a), which can be used to empirically estimate the REE closure temperatures of other Hess Deep samples.

Applying the Mg–REE coupled geospeedometry (section 2.4.3) to the Hess Deep samples, Sun and Lissenberg (2018a) successfully calculated the initial temperatures and cooling rates for 44 of the 46 samples. The inverted initial temperatures (998–1353 °C) are slightly greater than T_{REE} (998–1294 °C), but the overall differences are small, indicating small extents of diffusive redistribution of REE in Hess Deep gabbros. As shown in Figure 2.11a, near the DGT, the initial temperatures (998–1125 °C) vary over ~130 °C within 56 m, which suggests that the axial magma chamber is likely dominated by continuous influx and fractional crystallization of evolved melts from the deeper crust. The highly evolved temperatures near the DGT are consistent with the petrological evidence on Hess Deep samples (Natland & Dick, 1996). Although with the largest uncertainty (± 60 °C), the highest temperature (1353 °C) at 3523 m is comparable with the primary melt temperatures at mid-ocean ridges (1300–1400 °C; e.g., Lee et al., 2009). Similar temperatures (1261–1289 °C) also arise at 2066–3568 m, indicating emplacement of mantle-derived partial melts at various depths of the lower oceanic crust. The overall upward decrease of initial temperatures along the stratigraphy (Figure 2.11a) suggests that the deeper crustal section (>2000 m) likely confines the overall temperatures of migrating melts in crystal mushes. Given the small-scale temperature variations in the deeper section, accumulation and in situ solidification of replenished melts likely proceed in small magma bodies at various depths, perhaps about tens to hundreds of meters in thickness, which is also supported by a recent magnetic anisotropy study (Morris et al., 2019).

Notably, the inverted cooling rates agree well with the cooling rates inferred from the hydrothermal cooling models of Maclennan et al. (2005) and are generally greater than those from Maclennan et al.'s conductive cooling model by about one to two orders of magnitude (Figure 2.11b). This supports the previous notion of deep hydrothermal cooling of the lower oceanic crust (e.g., Maclennan et al., 2005; VanTongeren et al., 2008) and also appears to be compatible with the estimated cooling profiles of the uppermost mantle section in Oman ophiolite (Dygert et al., 2017). More importantly, with a comprehensive coverage of the oceanic crust profile, the cooling rate results enable a systematic assessment of stratigraphic variations. Near the DGT, the inverted cooling rates vary over two orders of magnitude (0.024–2.26 °C/yr) within about 56 m, indicating efficient heat extraction at the axial magma chamber. The five samples at 2198–3193 m appear to have anomalously rapid cooling rates (0.372–10.2 °C/yr), indicative of more efficient heat extraction at localized regions of the lower oceanic crust. Such rapid cooling zones can be attributed to high hydrothermal flows at regional depths and/or to later intrusion of magma bodies into colder off-axial regions. Both mechanisms likely involve brittle-ductile transition in the lower oceanic crust. However, the latter appears to be favored by recent seismic observations at East Pacific Rise (e.g., Canales et al., 2012; Han et al., 2014). In addition,

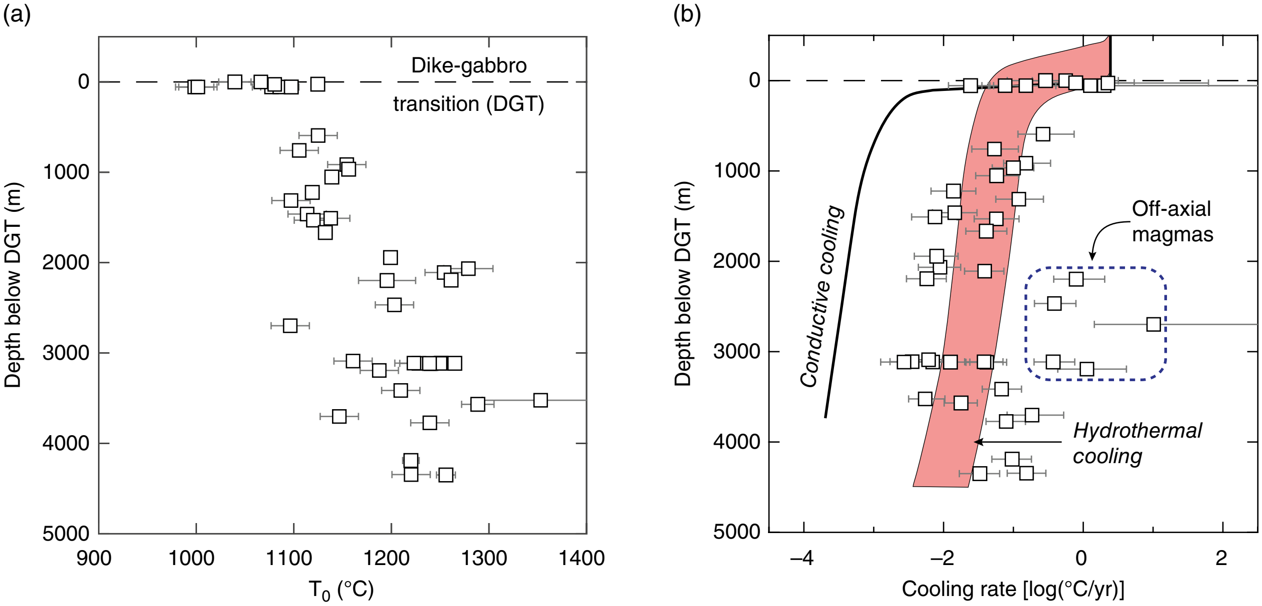

Figure 2.11 Stratigraphic variations of (a) the initial temperatures (T_0) and (b) cooling rates (dT/dt) derived from the Mg–REE coupled geospeedometer for the Hess Deep gabbros (Sun & Lissenberg, 2018a). Modeling results of Maclennan et al. (2005) for two different thermal models (conductive vs. hydrothermal) are shown in (b) for comparison with the inverted cooling rates.

most of the high-temperature samples (T_0 > 1260 °C; about 2066–3568 m) show relatively slow cooling rates (≤0.01 °C/yr) and thus solidified at extended time intervals that are consistent with multiple replenishments of mantle melts in the deeper crustal section.

The geospeedometry results of Hess Deep samples, together with previous evidence in petrology and seismology, lead Sun and Lissenberg (2018a) toward a new model for oceanic crust formation at fast-spreading mid-ocean ridges (see their Figure 2.7). They suggested that the crust formation zone consists of a crustal-scale magma mush, off-axial magma bodies, and a shallow axial magma lens. According to the thermal structure from Dunn et al. (2000), the mush region may extend to ~1.5–3.5 km off the ridge axis, which is mainly constrained by crustal-scale hydrothermal circulations and mantle melt influx. As suggested by recent observations at Oman ophiolite (Zihlmann et al., 2018), the deep circulations of hydrothermal fluids may involve off-axial faulting in the lower crust. The replenished melts likely transport reactively through the mush and partly accumulate as small magma bodies at various depths. In situ crystallization and replenishment of these magma bodies can disturb the stratigraphic variations of crystallization temperatures and cooling rates recorded in the cumulate rocks. Along the brittle-ductile transition, melts may escape from the mush zone and segregate in the off-axial region. These off-axial magma bodies, if there is no continuous melt supply, likely solidify on timescales of hundreds to thousands of years (see equation (2.52a)), according to the calculated cooling rates and crystallization temperatures (Figure 2.11). However, the shallow axial magma lens is dynamically stable during crustal formation because of the continuous melt replenishment from the deeper mush zone.

2.6. CONCLUDING REMARKS

The general framework of trace element geothermometry and geospeedometry was outlined in this chapter and discussed with the recently developed geothermometers and geospeedometers for mafic cumulate rocks. I emphasized that trace elements, with relatively simple behaviors of partitioning and diffusion, have unique advantages over major elements for constructing new geothermometers and geospeedometers. Through lattice strain analyses of trace element partitioning, I showed that two-mineral exchange geothermometers can be calibrated using crystal-melt partitioning data for individual minerals. In particular, the lattice strain model also enables a new approach to geothermometer calibration by making use of the systematic partitioning behaviors of multiple trace elements with the same valent state (e.g., REE^{3+}). Yet independent tests of the geothermometers are strongly required before application to natural rocks.

Although designed to determine the equilibrium temperatures, geothermometers can only decode closure temperatures from the natural mineral records. Due to cooling after the rock formation, mineral compositions have been reset to various extents by diffusive exchange with the surroundings. As shown by the Mg and REE thermometry of oceanic gabbros, such diffusive resetting mainly depends on the diffusion coefficients and causes the closure temperatures to deviate from the initial temperatures. Thus, the meaning of thermometer-determined closure temperatures has to be interpreted using relevant geospeedometers in the context of cooling histories, that is, cooling rates and initial temperatures. The two cooling parameters are equally important for understanding the thermal histories of a rock system but are challenging to constrain together. However, the differential diffusive responses of two or multiple elements with distinct geochemical behaviors provides a general resolution to this problem, using the closure temperatures (or profiles) of these elements in the same petrological system.

As an example, I showed that coupling Mg and REE diffusive closures in plagioclase-clinopyroxene systems can be used to simultaneously determine the crystallization temperatures and cooling rates of mafic cumulate rocks. Coupled with stratigraphic information, the speedometry results enable one to establish a comprehensive record of igneous accretion and cooling styles during igneous crust formation, which was demonstrated by the case study on Hess Deep gabbros from the fast-spreading East Pacific Rise. This Mg–REE coupled geospeedometer could be applied to mafic cumulate rocks from other geological settings, such as slow-spreading ridges and ophiolites, for comparative studies on the formation and thermal structures of oceanic crusts. In addition, it could also be used to delineate the first-order information on crustal formation at other rocky planetary bodies (e.g., Moon, Vesta, and Mars) through returned samples or meteorites despite the lack of geological contexts.

ACKNOWLEDGMENTS

Many collaborators and colleagues have inspired the author's interests in trace element partitioning, geothermobarometry, geospeedometry, ocean ridge processes, and experimental petrology in general over the years, including in particular Yan Liang, Bruce Watson, Nobu Shimizu, Henry Dick, Johan Lissenberg, Lijing Yao, Cin-Ty Lee, and Rajdeep Dasgupta. Detailed comments from Flavio Di Stefano and an anonymous reviewer helped the author to improve the presentation of this chapter and are greatly appreciated. The author is also grateful to Matteo Masotta and Silvio Mollo for their editorial advice. The geospeedometry work was supported by the Devonshire postdoctoral scholarship at WHOI and NSF grant OCE-1637130.

REFERENCES

Anders, E., & Grevesse, N. (1989). Abundances of the elements: Meteoritic and solar. *Geochimica et Cosmochimica Acta*, *53*(1), 197–214. https://doi.org/10.1016/0016-7037(89)90286-X

Ashwal, L. D., Webb, S. J., & Knoper, M. W. (2005). Magmatic stratigraphy in the Bushveld Northern Lobe: Continuous geophysical and mineralogical data from the 2950 m Bellevue drillcore. *South African Journal of Geology*, *108*(2), 199–232. https://doi.org/10.2113/108.2.199

Bachmann, O., & Bergantz, G. W. (2004). On the origin of crystal-poor rhyolites: Extracted from batholithic crystal mushes. *Journal of Petrology*, *45*(8), 1565–1582. https://doi.org/10.1093/petrology/egh019

Bachmann, O., & Huber, C. (2016). Silicic magma reservoirs in the Earth's crust. *American Mineralogist*, *101*, 2377–2404. https://doi.org/10.2138/am-2016-5675

Blundy, J., & Wood, B. (1994). Prediction of crystal-melt partition coefficients from elastic moduli. *Nature*, *372*(6505), 452–454. https://doi.org/10.1038/372452a0

Bohrson, W. A., Spera, F. J., Ghiorso, M. S., Brown, G. A., Creamer, J. B., & Mayfield, A. (2014). Thermodynamic model for energy-constrained open-system evolution of crustal magma bodies undergoing simultaneous recharge, assimilation and crystallization: The magma chamber simulator. *Journal of Petrology*, *55*(9), 1685–1717. https://doi.org/10.1093/petrology/egu036

Brady, J. B., & McCallister, R. H. (1983). Diffusion data for clinopyroxenes from homogenization and self-diffusion experiments. *American Mineralogist*, *68*, 95–105. Retrieved from http://www.minsocam.org/ammin/AM68/AM68_95.pdf

Brice, J. C. (1975). Some thermodynamic aspects of the growth of strained crystals. *Journal of Crystal Growth*, *28*(2), 249–253. https://doi.org/10.1016/0022-0248(75)90241-9

Canales, J. P., Carton, H., Carbotte, S. M., Mutter, J. C., Nedimović, M. R., Xu, M., et al. (2012). Network of off-axis melt bodies at the East Pacific Rise. *Nature Geoscience*, *5*(4), 279–283. https://doi.org/10.1038/ngeo1377

Cawthorn, R. G., & Walraven, F. (1998). Emplacement and crystallization time for the Bushveld Complex. *Journal of Petrology*, *39*(9), 1669–1687. https://doi.org/10.1093/petroj/39.9.1669

Chakraborty, S. (1997). Rates and mechanisms of Fe-Mg interdiffusion in olivine at 980°-1300°C. *Journal of Geophysical Research: Solid Earth*, *102*(B6), 12317–12331. https://doi.org/10.1029/97jb00208

Cherniak, D. J. (2003). REE diffusion in feldspar. *Chemical Geology*, *193*(1–2), 25–41. https://doi.org/10.1016/S0009-2541(02)00246-2

Cherniak, D. J., & Dimanov, A. (2010). Diffusion in pyroxene, mica and amphibole. *Reviews in Mineralogy and Geochemistry*, *72*(1), 641–690. https://doi.org/10.2138/rmg.2010.72.14

Coogan, L. A., Jenkin, G. R. T., & Wilson, R. N. (2007). Contrasting cooling rates in the lower oceanic crust at fast- and slow-spreading ridges revealed by geospeedometry. *Journal of Petrology*, *48*(11), 2211–2231. https://doi.org/10.1093/petrology/egm057

Costa, F., Chakraborty, S., & Dohmen, R. (2003). Diffusion coupling between trace and major elements and a model for calculation of magma residence times using plagioclase. *Geochimica et Cosmochimica Acta*, *67*(12), 2189–2200. https://doi.org/10.1016/S0016-7037(02)01345-5

Costa, F., & Dungan, M. (2005). Short time scales of magmatic assimilation from diffusion modeling of multiple elements in olivine. *Geology*, *33*(10), 837–840. https://doi.org/10.1130/G21675.1

Darken, L. S. (1948). Diffusion, mobility and their interrelation through free energy in binary metallic systems. *Transactions of the Metallurgical Society of AIME*, *175*, 184–201. https://doi.org/10.1007/s11661-010-0177-7

DePaolo, D. J. (1981). Trace element and isotopic effects of combined wallrock assimilation and fractional crystallization. *Earth and Planetary Science Letters*, *53*(2), 189–202. https://doi.org/10.1016/0012-821X(81)90153-9

DePaolo, D. J. (1985). Isotopic studies of processes in mafic magma chambers: I. The Kiglapait intrusion, labrador. *Journal of Petrology*, *26*(4), 925–951. https://doi.org/10.1093/petrology/26.4.925

Dodson, M. H. (1973). Closure temperature in cooling geochronological and petrological systems. *Contributions to Mineralogy and Petrology*, *40*(3), 259–274. https://doi.org/10.1007/BF00373790

Dodson, M. H. (1986). Closure profiles in cooling systems. *Materials Science Forum*, *7*, 145–154. https://doi.org/10.4028/www.scientific.net/msf.7.145

Dunn, R. A., Toomey, D. R., & Solomon, S. C. (2000). Three-dimensional seismic structure and physical properties of the crust and shallow mantle beneath the East Pacific Rise at 9°30'N. *Journal of Geophysical Research: Solid Earth*, *105*(B10), 23537–23555. https://doi.org/10.1029/2000jb900210

Dygert, N., Kelemen, P. B., & Liang, Y. (2017). Spatial variations in cooling rate in the mantle section of the Samail ophiolite in Oman: Implications for formation of lithosphere at mid-ocean ridges. *Earth and Planetary Science Letters*, *465*, 134–144. https://doi.org/10.1016/j.epsl.2017.02.038

Edmonds, M., Cashman, K. V., Holness, M., & Jackson, M. (2019). Architecture and dynamics of magma reservoirs. *Philosophical Transactions of the Royal Society A: Mathematical, Physical and Engineering Sciences*, *377*. https://doi.org/10.1098/rsta.2018.0298

Ehlers, K., & Powell, R. (1994). An empirical modification of Dodson's equation for closure temperature in binary systems. *Geochimica et Cosmochimica Acta*, *58*(1), 241–248. https://doi.org/10.1016/0016-7037(94)90461-8

Eiler, J. M., Baumgartner, L. P., & Valley, J. W. (1992). Intercrystalline stable isotope diffusion: A fast grain boundary model. *Contributions to Mineralogy and Petrology*, *112*(4), 543–557. https://doi.org/10.1007/BF00310783

Ellis, D. J., & Green, D. H. (1979). An experimental study of the effect of Ca upon garnet-clinopyroxene Fe-Mg exchange equilibria. *Contributions to Mineralogy and Petrology*, *71*(1), 13–22. https://doi.org/10.1007/BF00371878

Faak, K., Chakraborty, S., & Coogan, L. A. (2013). Mg in plagioclase: Experimental calibration of a new geothermometer and diffusion coefficients. *Geochimica et Cosmochimica Acta*, *123*, 195–217. https://doi.org/10.1016/j.gca.2013.05.009

Faak, K., Coogan, L. A., & Chakraborty, S. (2015). Near conductive cooling rates in the upper-plutonic section of crust formed at the East Pacific Rise. *Earth and Planetary Science Letters*, *423*, 36–47. https://doi.org/10.1016/j.epsl.2015.04.025

Feig, S. T., Koepke, J., & Snow, J. E. (2006). Effect of water on tholeiitic basalt phase equilibria: An experimental study under oxidizing conditions. *Contributions to Mineralogy and Petrology*, *152*(5), 611–638. https://doi.org/10.1007/s00410-006-0123-2

Gaetani, G. A., & Grove, T. L. (1995). Partitioning of rare earth elements between clinopyroxene and silicate melt Crystal-chemical controls. *Geochimica et Cosmochimica Acta*, *59*(10), 1951–1962. https://doi.org/10.1016/0016-7037(95)00119-0

Ganguly, J., & Tirone, M. (1999). Diffusion closure temperature and age of a mineral with arbitrary extent of diffusion: Theoretical formulation and applications. *Earth and Planetary Science Letters*, *170*(1–2), 131–140. https://doi.org/10.1016/S0012-821X(99)00089-8

Green, T. H., & Ringwood, A. E. (1968). Genesis of the calc-alkaline igneous rock suite. *Contributions to Mineralogy and Petrology*, *18*(2), 105–162. https://doi.org/10.1007/BF00371806

Grove, T. L., & Bryan, W. B. (1983). Fractionation of pyroxene-phyric MORB at low pressure: An experimental study. *Contributions to Mineralogy and Petrology*, *84*(4), 293–309. https://doi.org/10.1007/BF01160283

Grove, T. L., Elkins-Tanton, L. T., Parman, S. W., Chatterjee, N., Müntener, O., & Gaetani, G. A. (2003). Fractional crystallization and mantle-melting controls on calc-alkaline differentiation trends. *Contributions to Mineralogy and Petrology*, *145*(5), 515–533. https://doi.org/10.1007/s00410-003-0448-z

Grove, T. L., Gerlach, D. C., & Sando, T. W. (1982). Origin of calc-alkaline series lavas at Medicine Lake Volcano by fractionation, assimilation and mixing. *Contributions to Mineralogy and Petrology*, *80*(2), 160–182. https://doi.org/10.1007/BF00374893

Han, S., Carbotte, S. M., Carton, H., Mutter, J. C., Aghaei, O., Nedimović, M. R., & Canales, J. P. (2014). Architecture of on- and off-axis magma bodies at EPR 9°37-40'N and implications for oceanic crustal accretion. *Earth and Planetary Science Letters*, *390*, 31–44. https://doi.org/10.1016/j.epsl.2013.12.040

Hildreth, W. (1979). The Bishop Tuff: Evidence for the origin of compositional zonation in silicic magma chambers. *Geological Society of America Special Paper*, *180*, 43–76. https://doi.org/10.1130/spe180-p43

Karson, J. A., Klein, E. M., Hurst, S. D., Lee, C. E., Rivizzigno, P. A., Curewitz, D., et al. (2002). Structure of uppermost fast-spread oceanic crust exposed at the Hess Deep Rift: Implications for subaxial processes at the East Pacific Rise. *Geochemistry, Geophysics, Geosystems*, *3*. https://doi.org/10.1029/2001GC000155

Kelemen, P. B., Koga, K., & Shimizu, N. (1997). Geochemistry of gabbro sills in the crust-mantle transition zone of the Oman ophiolite: Implications for the origin of the oceanic lower crust. *Earth and Planetary Science Letters*, *146*(3–4), 475–488. https://doi.org/10.1016/S0012-821X(96)00235-X

Koepke, J., Botcharnikov, R. E., & Natland, J. H. (2018). Crystallization of late-stage MORB under varying water activities and redox conditions: Implications for the formation of highly evolved lavas and oxide gabbro in the ocean crust. *Lithos*, *323*, 58–77. https://doi.org/10.1016/j.lithos.2018.10.001

Kruger, F. J. (2005). Filling the Bushveld Complex magma chamber: Lateral expansion, roof and floor interaction, magmatic unconformities, and the formation of giant chromitite, PGE and Ti-V-magnetitite deposits. *Mineralium Deposita*, *40*(5), 451–472. https://doi.org/10.1007/s00126-005-0016-8

Lasaga, A. C. (1979). Multicomponent exchange and diffusion in silicates. *Geochimica et Cosmochimica Acta*, *43*(4), 455–469. https://doi.org/10.1016/0016-7037(79)90158-3

Lasaga, A. C. (1983). Geospeedometry: An Extension of Geothermometry. In *Kinetics and equilibrium in mineral reactions*(pp. 81–114). https://doi.org/10.1007/978-1-4612-5587-1_3

Lasaga, A. C., Richardson, S. M., & Holland, H. D. (1977). The mathematics of cation diffusion and exchange between silicate minerals during retrograde metamorphism. In *Energetics of Geological Processes* (pp. 353–388). https://doi.org/10.1007/978-3-642-86574-9_15

Le Roux, V., Dasgupta, R., & Lee, C. T. A. (2011). Mineralogical heterogeneities in the Earth's mantle: Constraints from Mn, Co, Ni and Zn partitioning during partial melting. *Earth and Planetary Science Letters*, *307*(3–4), 395–408. https://doi.org/10.1016/j.epsl.2011.05.014

Lee, C.-T. A., Harbert, A., & Leeman, W. P. (2007). Extension of lattice strain theory to mineral/mineral rare-earth element partitioning: An approach for assessing disequilibrium and developing internally consistent partition coefficients between olivine, orthopyroxene, clinopyroxene and basaltic melt. *Geochimica et Cosmochimica Acta*, *71*(2), 481–496. https://doi.org/10.1016/j.gca.2006.09.014

Lee, C.-T. A., Lee, T. C., & Wu, C. T. (2014). Modeling the compositional evolution of recharging, evacuating, and fractionating (REFC) magma chambers: Implications for differentiation of arc magmas. *Geochimica et Cosmochimica Acta*, *143*, 8–22. https://doi.org/10.1016/j.gca.2013.08.009

Lee, C. T. A., Luffi, P., Plank, T., Dalton, H., & Leeman, W. P. (2009). Constraints on the depths and temperatures of basaltic magma generation on Earth and other terrestrial planets using new thermobarometers for mafic magmas. *Earth and Planetary Science Letters*, *279*(1–2), 20–33. https://doi.org/10.1016/j.epsl.2008.12.020

Liang, Y. (2010). Multicomponent diffusion in molten silicates: Theory, experiments, and geological applications. *Reviews in Mineralogy and Geochemistry*, *72*(1), 409–446. https://doi.org/10.2138/rmg.2010.72.9

Liang, Y. (2015). A simple model for closure temperature of a trace element in cooling bi-mineralic systems. *Geochimica et Cosmochimica Acta*, *165*, 35–43. https://doi.org/10.1016/j.gca.2015.05.028

Liang, Y., Sun, C., & Yao, L. (2013). A REE-in-two-pyroxene thermometer for mafic and ultramafic rocks. *Geochimica et Cosmochimica Acta*. https://doi.org/10.1016/j.gca.2012.10.035

Lissenberg, C. J., Bédard, J. H., & van Staal, C. R. (2004). The structure and geochemistry of the gabbro zone of the Annieopsquotch ophiolite, Newfoundland: Implications for lower crustal accretion at spreading ridges. *Earth and Planetary Science Letters*, *229*(1–2), 105–123. https://doi.org/10.1016/j.epsl.2004.10.029

Lissenberg, C. J., MacLeod, C. J., Howard, K. A., & Godard, M. (2013). Pervasive reactive melt migration through fast-spreading lower oceanic crust (Hess Deep, equatorial Pacific Ocean). *Earth and Planetary Science Letters*, *361*, 436–447. https://doi.org/10.1016/j.epsl.2012.11.012

Maclennan, J. (2019). Mafic tiers and transient mushes: Evidence from Iceland. *Philosophical Transactions of the Royal Society A: Mathematical, Physical and Engineering Sciences*, *377*. https://doi.org/10.1098/rsta.2018.0021

Maclennan, J., Hulme, T., & Singh, S. C. (2005). Cooling of the lower oceanic crust. *Geology*, *33*(5), 357–360. https://doi.org/10.1130/G21207.1

Masotta, M., Mollo, S., Freda, C., Gaeta, M., & Moore, G. (2013). Clinopyroxene-liquid thermometers and barometers specific to alkaline differentiated magmas. *Contributions to Mineralogy and Petrology*, *166*(6), 1545–1561. https://doi.org/10.1007/s00410-013-0927-9

McBirney, A. R. (2003). The Skaergaard layered series, Part VII: Sr and Nd Isotopes. *Journal of Petrology*, *44*(4), 757–771. https://doi.org/10.1093/petrology/44.4.757

Mollo, S., Blundy, J., Scarlato, P., De Cristofaro, S. P., Tecchiato, V., Di Stefano, F., et al. (2018). An integrated P-T-H_2O-lattice strain model to quantify the role of clinopyroxene fractionation on REE+Y and HFSE patterns of mafic alkaline magmas: Application to eruptions at Mt. Etna. *Earth-Science Reviews*, *185*, 32–56. https://doi.org/10.1016/j.earscirev.2018.05.014

Mollo, S., Putirka, K., Iezzi, G., Del Gaudio, P., & Scarlato, P. (2011). Plagioclase-melt (dis)equilibrium due to cooling dynamics: Implications for thermometry, barometry and hygrometry. *Lithos*, *125*(1–2), 221–235. https://doi.org/10.1016/j.lithos.2011.02.008

Morgan, D. J., & Blake, S. (2006). Magmatic residence times of zoned phenocrysts: Introduction and application of the binary element diffusion modelling (BEDM) technique. *Contributions to Mineralogy and Petrology*, *151*(1), 58–70. https://doi.org/10.1007/s00410-005-0045-4

Morris, A., Meyer, M., Anderson, M. W., & MacLeod, C. J. (2019). What do variable magnetic fabrics in gabbros of the Oman ophiolite reveal about lower oceanic crustal magmatism at fast spreading ridges? *Geology*, *47*(3), 275–278. https://doi.org/10.1130/G45442.1

Morse, S. A., Brady, J. B., & Sporleder, B. A. (2004). Experimental petrology of the Kiglapait Intrusion: Cotectic trace for the Lower Zone at 5 kbar in graphite. *Journal of Petrology*, *45*(11), 2225–2259. https://doi.org/10.1093/petrology/egh054

Müller, T., Dohmen, R., Becker, H. W., ter Heege, J. H., & Chakraborty, S. (2013). Fe-Mg interdiffusion rates in clinopyroxene: Experimental data and implications for Fe-Mg exchange geothermometers. *Contributions to Mineralogy and Petrology*, *166*(6), 1563–1576. https://doi.org/10.1007/s00410-013-0941-y

Namur, O., & Humphreys, M. C. S. (2018). Trace element constraints on the differentiation and crystal mush solidification in the Skaergaard intrusion, Greenland. *Journal of Petrology*, *59*(3), 387–418. https://doi.org/10.1093/petrology/egy032

Natland, J. H., & Dick, H. J. B. (1996). Melt migration through high-level gabbroic cumulates of the East Pacific Rise at Hess Deep: The origin of magma lenses and the deep crustal structure of fast-spreading ridges. *Proceedings of the Ocean Drilling Program, 147 Scientific Results*(pp. 21–58). https://doi.org/10.2973/odp.proc.sr.147.002.1996

Natland, J. H., & Dick, H. J. B. (2009). Paired melt lenses at the East Pacific Rise and the pattern of melt flow through the gabbroic layer at a fast-spreading ridge. *Lithos*, *112*(1–2), 73–86. https://doi.org/10.1016/j.lithos.2009.06.017

Nicolas, A., Reuber, I., & Benn, K. (1988). A new magma chamber model based on structural studies in the Oman ophiolite. *Tectonophysics*, *151*(1–4), 87–105. https://doi.org/10.1016/0040-1951(88)90242-9

O'Neill, H. S. C., & Wood, B. J. (1979). An experimental study of Fe-Mg partitioning between garnet and olivine and its calibration as a geothermometer. *Contributions to Mineralogy and Petrology*, *70*(1), 59–70. https://doi.org/10.1007/BF00371872

Onuma, N., Higuchi, H., Wakita, H., & Nagasawa, H. (1968). Trace element partition between two pyroxenes and the host lava. *Earth and Planetary Science Letters*, *5*, 47–51. https://doi.org/10.1016/s0012-821x(68)80010-x

Phipps Morgan, J., & Chen, Y. J. (1993). The genesis of oceanic crust: Magma injection, hydrothermal circulation, and crustal flow. *Journal of Geophysical Research: Solid Earth*, *98*(B4), 6283–6297. https://doi.org/10.1029/92jb02650

Putirka, K. D. (2005). Igneous thermometers and barometers based on plagioclase + liquid equilibria: Tests of some existing models and new calibrations. *American Mineralogist*, *90*, 336–346. https://doi.org/10.2138/am.2005.1449

Putirka, K. D. (2008). Thermometers and barometers for volcanic systems. *Reviews in Mineralogy and Geochemistry*, *69*, 61–120. https://doi.org/10.2138/rmg.2008.69.3

Quick, J. E., & Denlinger, R. P. (1993). Ductile deformation and the origin of layered gabbro in ophiolites. *Journal of Geophysical Research: Solid Earth*, *98*(B8), 14015–14027. https://doi.org/10.1029/93jb00698

Sack, R. O., Walker, D., & Carmichael, I. S. E. (1987). Experimental petrology of alkalic lavas: constraints on cotectics of multiple saturation in natural basic liquids. *Contributions to Mineralogy and Petrology*, *96*(1), 1–23. https://doi.org/10.1007/BF00375521

Shannon, R. D. (1976). Revised effective ionic radii and systematic studies of interatomic distances in halides and chalcogenides. *Acta Crystallographica Section A*, *32*, 751–767.

Sisson, T. W., & Grove, T. L. (1993). Experimental investigations of the role of H_2O in calc-alkaline differentiation and subduction zone magmatism. *Contributions to Mineralogy and Petrology*, *113*(2), 143–166. https://doi.org/10.1007/BF00283225

Sleep, N. H. (1978). Thermal structure and kinematics of mid-oceanic ridge axis, some implications to basaltic volcanism. *Geophysical Research Letters*, *5*(6), 426–428. https://doi.org/10.1029/GL005i006p00426

Spera, F. J., & Bohrson, W. A. (2004). Open-system magma chamber evolution: An energy-constrained geochemical model incorporating the effects of concurrent eruption, recharge, variable assimilation and fractional crystallization (EC-E′RAχ FC). *Journal of Petrology*, *45*(12), 2459–2480. https://doi.org/10.1093/petrology/egh072

Sun, C. (2018). Partitioning and partition coefficients. In W. M. White (Ed.), *Encyclopedia of Geochemistry. Encyclopedia of Earth Sciences Series*. https://doi.org/10.1007/978-3-319-39193-9_347-1

Sun, C., & Dasgupta, R. (2020). Thermobarometry of CO_2-rich, silica-undersaturated melts constrains cratonic lithosphere thinning through time in areas of kimberlitic magmatism. *Earth and Planetary Science Letters*, *550*, 116549. https://doi.org/10.1016/j.epsl.2020.116549

Sun, C., Graff, M., & Liang, Y. (2017). Trace element partitioning between plagioclase and silicate melt: The importance of temperature and plagioclase composition, with implications for terrestrial and lunar magmatism. *Geochimica et Cosmochimica Acta*, *206*, 273–295. https://doi.org/10.1016/j.gca.2017.03.003

Sun, C., & Liang, Y. (2012). Distribution of REE between clinopyroxene and basaltic melt along a mantle adiabat: Effects of major element composition, water, and temperature. *Contributions to Mineralogy and Petrology*, *163*(5), 807–823. https://doi.org/10.1007/s00410-011-0700-x

Sun, C., & Liang, Y. (2013a). Distribution of REE and HFSE between low-Ca pyroxene and lunar picritic melts around multiple saturation points. *Geochimica et Cosmochimica Acta*, *119*, 340–358. https://doi.org/10.1016/j.gca.2013.05.036

Sun, C., & Liang, Y. (2013b). The importance of crystal chemistry on REE partitioning between mantle minerals (garnet, clinopyroxene, orthopyroxene, and olivine) and basaltic melts. *Chemical Geology*, *358*, 23–36. https://doi.org/10.1016/j.chemgeo.2013.08.045

Sun, C., & Liang, Y. (2014). An assessment of subsolidus re-equilibration on REE distribution among mantle minerals olivine, orthopyroxene, clinopyroxene, and garnet in peridotites. *Chemical Geology*, *372*, 80–91. https://doi.org/10.1016/j.chemgeo.2014.02.014

Sun, C., & Liang, Y. (2015). A REE-in-garnet-clinopyroxene thermobarometer for eclogites, granulites and garnet peridotites. *Chemical Geology*, *393–394*, 79–92. https://doi.org/10.1016/j.chemgeo.2014.11.014

Sun, C., & Liang, Y. (2017). A REE-in-plagioclase–clinopyroxene thermometer for crustal rocks. *Contributions to Mineralogy and Petrology*, *172*(4). https://doi.org/10.1007/s00410-016-1326-9

Sun, C., & Lissenberg, C. J. (2018a). Formation of fast-spreading lower oceanic crust as revealed by a new Mg–REE coupled geospeedometer. *Earth and Planetary Science Letters*, *487*, 165–178. https://doi.org/10.1016/j.epsl.2018.01.032

Sun, C., & Lissenberg, C. J. (2018b). Caveats and challenges in geospeedometry: A reply to Faak et al.'s critique of the Mg–REE coupled geospeedometry. *Earth and Planetary Science Letters*, *502*, 287–290. https://doi.org/10.1016/j.epsl.2018.08.044

Takagi, D., Sato, H., & Nakagawa, M. (2005). Experimental study of a low-alkali tholeiite at 1-5 kbar: Optimal condition for the crystallization of high-An plagioclase in hydrous arc tholeiite. *Contributions to Mineralogy and Petrology*, *149*(5), 527–540. https://doi.org/10.1007/s00410-005-0666-7

Tecchiato, V., Gaeta, M., Mollo, S., Bachmann, O., Quadt, A. Von, & Scarlato, P. (2018). Snapshots of primitive arc magma evolution recorded by clinopyroxene textural and compositional variations: The case of hybrid crystal-rich enclaves from Capo Marargiu Volcanic District (Sardinia, Italy). *American Mineralogist*, *103*(6), 899–910. https://doi.org/10.2138/am-2018-6446

Tegner, C., Thy, P., Holness, M. B., Jakobsen, J. K., & Lesher, C. E. (2009). Differentiation and compaction in the Skaergaard intrusion. *Journal of Petrology*, *50*(5), 813–840. https://doi.org/10.1093/petrology/egp020

Thy, P., Lesher, C. E., & Fram, M. S. (1998). Low pressure experimental constraints on the evolution of basaltic lavas from Site 917, southeast Greenland Continental Margin. *Proceedings of the Ocean Drilling Program: Scientific Results*, *152*, 359–372.

Tiepolo, M., Oberti, R., Zanetti, A., Vannucci, R., & Foley, S. F. (2007). Trace-Element Partitioning Between Amphibole and Silicate Melt. *Reviews in Mineralogy and Geochemistry*, *67*(1), 417–452. https://doi.org/10.2138/rmg.2007.67.11

Van Orman, J. A., Cherniak, D. J., & Kita, N. T. (2014). Magnesium diffusion in plagioclase: Dependence on composition, and implications for thermal resetting of the 26Al-26Mg early solar system chronometer. *Earth and Planetary Science Letters*, *385*, 79–88. https://doi.org/10.1016/j.epsl.2013.10.026

Van Orman, J. A., Grove, T. L., & Shimizu, N. (2001). Rare earth element diffusion in diopside: influence of temperature, pressure, and ionic radius, and an elastic model for diffusion in silicates. *Contributions to Mineralogy and Petrology*, *141*(6), 687–703. https://doi.org/10.1007/s004100100269

van Westrenen, W., & Draper, D. S. (2007). Quantifying garnet-melt trace element partitioning using lattice-strain theory: New crystal-chemical and thermodynamic constraints. *Contributions to Mineralogy and Petrology*, *154*(6), 717–730. https://doi.org/10.1007/s00410-007-0222-8

VanTongeren, J. A., Hirth, G., & Kelemen, P. B. (2015). Constraints on the accretion of the gabbroic lower oceanic crust from plagioclase lattice preferred orientation in the Samail ophiolite. *Earth and Planetary Science Letters*, *427*, 249–261. https://doi.org/10.1016/j.epsl.2015.07.001

VanTongeren, J. A., Kelemen, P. B., & Hanghøj, K. (2008). Cooling rates in the lower crust of the Oman ophiolite: Ca in olivine, revisited. *Earth and Planetary Science Letters*, *267*(1–2), 69–82. https://doi.org/10.1016/j.epsl.2007.11.034

VanTongeren, J. A., & Mathez, E. A. (2013). Incoming magma composition and style of recharge below the pyroxenite marker, eastern Bushveld Complex, South Africa. *Journal of Petrology*, *54*(8), 1585–1605. https://doi.org/10.1093/petrology/egt024

Veksler, I. V., Sedunova, A. P., Darin, A. V., Anosova, M. O., Reid, D. L., Kaufmann, F. E. D., et al. (2018). Chemical and textural re-equilibration in the UG2 chromitite layer of the Bushveld Complex, South Africa. *Journal of Petrology*, *59*(6), 1193–1216. https://doi.org/10.1093/petrology/egy058

Villiger, S., Ulmer, P., Müntener, O., & Thompson, A. B. (2004). The liquid line of descent of anhydrous, mantle-derived, tholeiitic liquids by fractional and equilibrium crystallization – An experimental study at 1·0 GPa. *Journal of Petrology*, *45*(12), 2369–2388. https://doi.org/10.1093/petrology/egh042

Wang, Z., Hiraga, T., & Kohlstedt, D. L. (2004). Effect of H+ on Fe–Mg interdiffusion in olivine, (Fe,Mg)2SiO4. *Applied Physics Letters*, *85*(2), 209–211. https://doi.org/10.1063/1.1769593

Wark, D. A., Hildreth, W., Spear, F. S., Cherniak, D. J., & Watson, E. B. (2007). Pre-eruption recharge of the Bishop magma system. *Geology*, *35*(3), 235–238. https://doi.org/10.1130/G23316A.1

Wark, D. A., & Watson, E. B. (2006). TitaniQ: A titanium-in-quartz geothermometer. *Contributions to Mineralogy and Petrology*, *152*(6), 743–754. https://doi.org/10.1007/s00410-006-0132-1

Waters, L. E., & Lange, R. A. (2015). An updated calibration of the plagioclase-liquid hygrometer-thermometer applicable to basalts through rhyolites. *American Mineralogist*, *100*(10), 2172–2184. https://doi.org/10.2138/am-2015-5232

Watson, E. B., & Baxter, E. F. (2007). Diffusion in solid-Earth systems. *Earth and Planetary Science Letters*, *253*(3–4), 307–327. https://doi.org/10.1016/j.epsl.2006.11.015

Watson, E. B., & Cherniak, D. J. (2015). Quantitative cooling histories from stranded diffusion profiles. *Contributions to Mineralogy and Petrology*, *169*(6). https://doi.org/10.1007/s00410-015-1153-4

Watson, E. B., & Harrison, T. M. (1984). Accessory minerals and the geochemical evolution of crustal magmatic systems: a summary and prospectus of experimental approaches. *Physics of the Earth and Planetary Interiors*, *35*(1–3), 19–30. https://doi.org/10.1016/0031-9201(84)90031-1

Watson, E. B., Wark, D. A., & Thomas, J. B. (2006). Crystallization thermometers for zircon and rutile. *Contributions to Mineralogy and Petrology*, *151*(4), 413–433. https://doi.org/10.1007/s00410-006-0068-5

Wood, B. J., & Blundy, J. D. (2013). Trace element partitioning: The influences of ionic radius, cation charge, pressure, and temperature. In *Treatise on Geochemistry: Second Edition* (Vol. 3, pp. 421–448). https://doi.org/10.1016/B978-0-08-095975-7.00209-6

Yang, H.-J., Kinzler, R. J., & Grove, T. L. (1996). Experiments and models of anhydrous, basaltic olivine-plagioclase-augite saturated melts from 0.001 to 10 kbar. *Contributions to Mineralogy and Petrology*, *124*(1), 1–18. https://doi.org/10.1007/s004100050169

Yang, S. H., Maier, W. D., Godel, B., Barnes, S. J., Hanski, E., & O'Brien, H. (2019). Parental magma composition of the Main Zone of the Bushveld complex: Evidence from in situ LA-ICP-MS trace element analysis of Silicate minerals in the cumulate rocks. *Journal of Petrology*, *60*(2), 359–392. https://doi.org/10.1093/petrology/egy115

Yao, L., & Liang, Y. (2015). Closure temperature in cooling bi-mineralic systems: I. Definition and with application to REE-in-two-pyroxene thermometer. *Geochimica et Cosmochimica Acta*, *162*, 137–150. https://doi.org/10.1016/j.gca.2015.03.041

Yao, L., Sun, C., & Liang, Y. (2012). A parameterized model for REE distribution between low-Ca pyroxene and basaltic melts with applications to REE partitioning in low-Ca pyroxene along a mantle adiabat and during pyroxenite-derived melt and peridotite interaction. *Contributions to Mineralogy and Petrology*, *164*(2), 261–280. https://doi.org/10.1007/s00410-012-0737-5

Zhang, X., Ganguly, J., & Ito, M. (2010). Ca-Mg diffusion in diopside: Tracer and chemical inter-diffusion coefficients. *Contributions to Mineralogy and Petrology*, *159*(2), 175–186. https://doi.org/10.1007/s00410-009-0422-5

Zhang, Y. (2010). Diffusion in minerals and melts: Theoretical background. *Reviews in Mineralogy and Geochemistry*, *72*(1), 5–59. https://doi.org/10.2138/rmg.2010.72.2

Zihlmann, B., Müller, S., Coggon, R. M., Koepke, J., Garbe-Schönberg, D., & Teagle, D. A. H. (2018). Hydrothermal fault zones in the lower oceanic crust: An example from Wadi Gideah, Samail ophiolite, Oman. *Lithos*, *323*, 103–124. https://doi.org/10.1016/j.lithos.2018.09.008

3

Magma Storage at Ocean Islands: Insights From Cape Verde

Abigail K. Barker[1,2], Elin M. Rydeblad[1,3], and Sónia M. D. M. Silva[4]

ABSTRACT

The Cape Verde archipelago is a group of ocean islands in the Central Atlantic that forms two chains of islands trending northwest and southwest. Several of the islands are considered to be volcanically active, with frequent eruptions on Fogo. We examine the mineral chemistry and thermobarometry of the southern islands—Santiago, Fogo, and Brava—together with the Cadamosto Seamount. Our objective is to explore the magmatic storage system and implications for volcanic eruptions and associated hazards at Cape Verde. The volcanic rocks at Cape Verde are alkaline and dominantly mafic, whereas the island of Brava and the Cadamosto Seamount are unusually felsic. Clinopyroxene compositions range from 60 to 90 Mg# at Santiago and Fogo. In contrast, at Brava and the Cadamosto Seamount, the clinopyroxene compositions are 5 to 75 Mg#. Mineral chemistry and zonation records fractional crystallization, recharge, aggregation of crystals, magma mixing, and variations in thermal conditions of the magma at temperatures from 925 to 1250 °C. Magma storage depths at Santiago, Fogo, Brava, and the Cadamosto Seamount are between 12 and 40 km, forming deep sub-Moho magma storage zones. Transient magma storage in the crust is suggested by fluid inclusion re-equilibration and pre-eruption seismicity. A global compilation of magma storage at ocean islands suggests that deep magma storage is a common feature, and volcanic eruptions are often associated with rapid magma ascent through the crust. Shallow magma storage is more variable and likely reflects local variations in crustal structure, sediment supply, and tectonics. Petrological constraints on the magma plumbing system at Cape Verde and elsewhere are vital to integrate with deformation models and seismicity in order to improve understanding and mitigation of the volcanic hazards.

3.1. INTRODUCTION

Ocean islands occur in all of the world's oceans and are formed by intraplate volcanism. Several ocean islands are volcanically active with eruptions at Reunion, Canary Islands, Cape Verde, and Hawaii between 2007 and 2020 (e.g., Di Muro et al., 2014; Liu et al., 2018; Longpré et al., 2014; Worsley, 2015). Many of the ocean islands are inhabited and have lucrative tourist industries, which put people directly at risk from the volcanic hazards associated with eruptions. Moreover, submarine and subaerial eruptions can also be hazardous for the shipping and aviation industries, respectively (Di Muro et al., 2014; O'Mongain et al., 2007). Consequently, understanding the magma plumbing systems from the magma storage zones to the volcanic centers is imperative for assessing and monitoring the volcanic hazards. We present insights into the magma storage at Cape Verde to explore the nature of the volcanically active parts of the archipelago, which is motivated by the recent eruptions at Fogo (Ribeiro, 1960; Worsley, 2015).

The Cape Verde archipelago is an ocean island group built upon the Cape Verde Rise (Ramalho et al., 2010a, 2010b). The older and now heavily eroded islands of Maio,

---

[1] *Department of Earth Sciences, Uppsala University, Uppsala, Sweden*

[2] *Centre of Natural Hazards and Disaster Sciences, Uppsala, Sweden*

[3] *Department of Earth Science and Engineering, Imperial College London, London, United Kingdom*

[4] *Faculty of Science and Technology, University of Cape Verde, Praia, Cape Verde*

Crustal Magmatic System Evolution: Anatomy, Architecture, and Physico-Chemical Processes, Geophysical Monograph 264, First Edition.
Edited by Matteo Masotta, Christoph Beier, and Silvio Mollo.

DOI: 10.1002/9781119564485.ch3

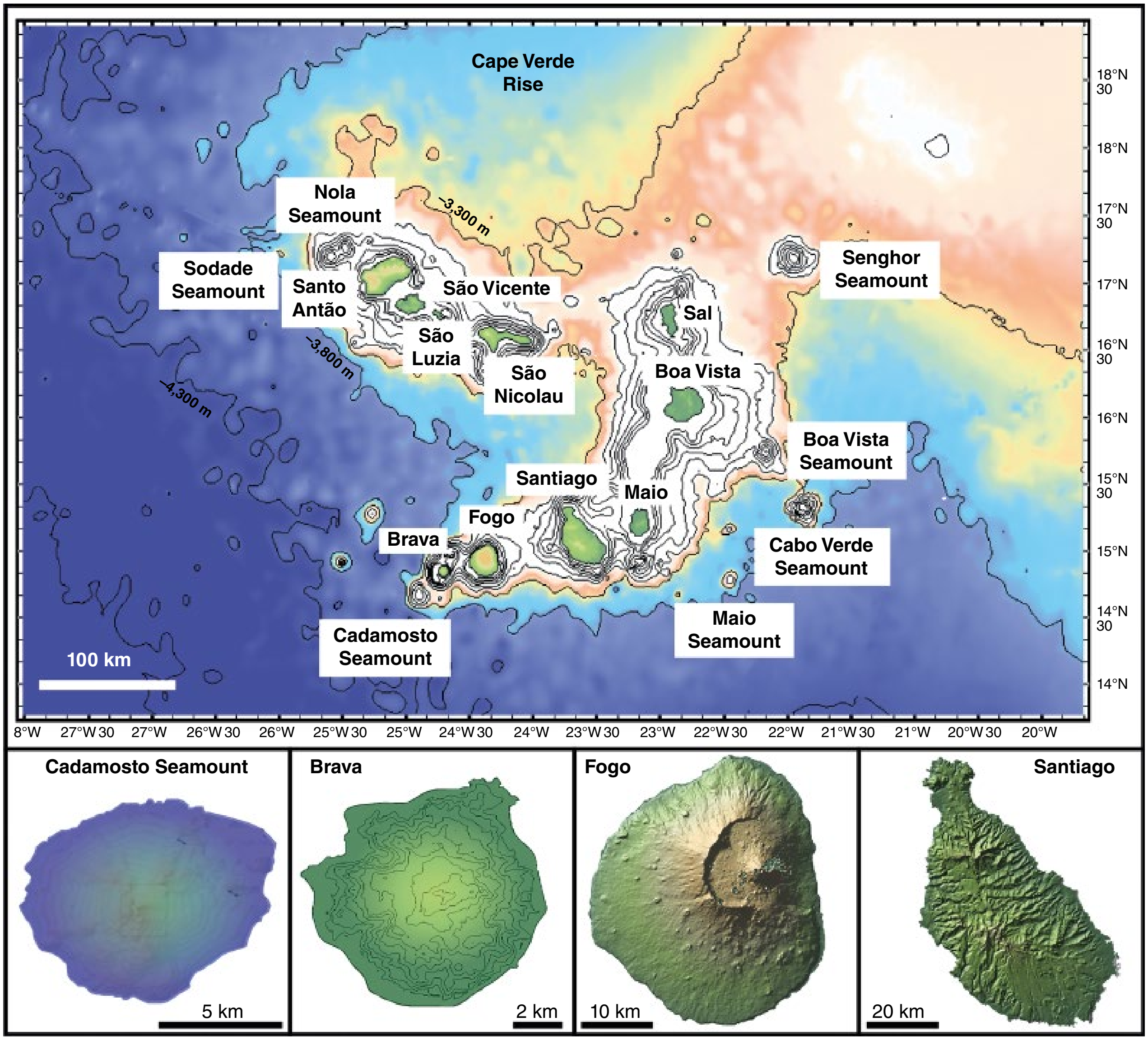

Figure 3.1 Bathymetric and topographic map of the Cape Verde Archipelago, which shows the Cadamosto Seamount, and islands of Brava, Fogo, and Santiago. Note the existence of a "northern chain" composed of the islands of Santo Antão, São Vicente, Santa Luzia and islets, and São Nicolau, and seamounts, plus a "southern chain" composed of the islands Santiago, Fogo, and Brava and the Cadamosto Seamount. Relatively deep water separates most islands. Sources: Ryan et al. (2009); Hansteen et al. (2014).

Sal, and Boa Vista are found in the east, from where two volcanic chains emerge. The northern chain consists of São Nicolau, Santa Luzia, São Vicente, and Santa Antão. The islands of Santiago, Fogo, and Brava as well as the Cadamosto Seamount form the southern island chain (Figure 3.1). The island of Fogo displays the iconic Pico do Fogo, peaking at 2829 m above sea level, located inside the Bordeira, on the Chã das Caldeiras, where the historic eruption sites are found; the latest eruption occurred from November 2014 to February 2015 (Fernandes & Faria, 2015; González et al., 2015; Jenkins et al., 2017; Richter et al., 2016; Silva et al., 2015; Worsley, 2015). Prior to that, nine eruptions occurred at Fogo between 1760 and 1995, with a total of 28 eruptions since settlement in the 15th century (Nascimento, 2015; Ribeiro, 1960). Brava and the Cadamosto Seamount have no historical record of volcanic activity. However, Holocene volcanic activity is documented at Brava, and the Cadamosto Seamount records eruption ages of 21 ka (Faria & Fonseca, 2014; Madeira et al., 2010; Samrock et al., 2019). Further, seismicity extends from Fogo to the Cadamosto Seamount, suggesting that Brava and the Cadamosto Seamount are also underlain by active magmatic systems (Grevemeyer et al., 2010; Heleno et al., 2006).

The volcanic hazards on Fogo are in the form of ash and lapilli associated with Strombolian activity and lava flows as well as occasional sub-Plinian to Plinian eruptions (Eisele et al., 2015; Torres et al., 1997). The residents of Fogo are vulnerable to the direct volcanic hazards associated with an eruption, especially the approximately one thousand who live and work inside the Bordeira close to Pico do Fogo, followed by the 11,000 residents of the East Coast of Fogo (Faria & Fonseca, 2014). The eruptions in 1995 and 2014/2015 led to large-scale evacuation as well as significant damage to property, agricultural land, and buildings (Jenkins et al., 2017; Silva et al., 2015; Worsley 2015). Potential volcanic hazards at Brava are connected to pyroclastic and phreatomagmatic eruptions and endanger the 6,000 inhabitants (Faria & Fonseca, 2014).

In addition, the onshore and offshore geological record of the Cape Verde archipelago shows evidence for flank collapses and landslide deposits (Barrett et al., 2020; Masson et al., 2002, 2008; Paris et al., 2018). The Bordeira cliffs of Fogo were potentially exposed by a huge landslide (Day et al., 1999; Foeken et al., 2009; Martínez-Moreno et al., 2018; Ramalho et al., 2015). Tsunami deposits have been used to constrain the associated flank collapse and landslide to approximately 73 ka (Ramalho et al., 2015). Furthermore, tsunami deposits associated with local flank collapses are found, among other locations, on Santiago and Maio (Madeira et al., 2019; Paris et al., 2011, 2018; Ramalho et al., 2015). Therefore, the Cape Verde islands are associated with multiple natural hazards that may pose a threat to the population both locally and farther afield.

Monitoring of the volcanism is the responsibility of the National Institute for Metrology and Geophysics. In addition, the University of Cape Verde has been conducting geochemical monitoring in partnership with national and international institutions (Barrancos et al., 2015; Dionis et al., 2015a, b; Fonseca et al., 2003; Pérez et al., 2015). Seismicity and deformation are monitored throughout Cape Verde with 15 seismometers and a geodetic network (Faria & Fonseca, 2014). The Fogo-Brava seismic network consists of seven seismometers on Fogo and two on Brava, and Fogo hosts three geodetic stations. Additional monitoring targets volcanic gas emissions with semi-frequent measurements of CO_2 and SO_2 emissions and fumerole temperatures (Faria & Fonseca, 2014; Worsley, 2015). The National Institute for Metrology and Geophysics works with the National Civil Protection service to provide risk communication (Faria & Fonseca, 2014).

The magmatic system can be investigated through minerals in the erupted products. The minerals capture the compositional signature of the host magma during growth; therefore, they respond to variations in magma composition. Consequently, minerals provide a chronological record of magma evolution (Davidson et al., 2007). On this basis, mineral thermobarometry offers a petrological method to estimate the crystallization conditions of magma chambers, including the temperature and pressure of crystal growth (e.g., Putirka, 2008). Igneous thermobarometers have been widely applied in many settings such as volcanic arcs (e.g., Lai et al., 2018; Till, 2017) and to investigate continental magmatism (Putirka et al., 2003; Putirka & Condit, 2003). Clinopyroxene-melt thermobarometers have also been applied in ocean island settings to explore tholeiitic to alkaline systems, for example, Hawaii, Cape Verde, Canary Islands (e.g., Aulinas et al., 2010; Hildner et al., 2011, 2012; Klügel et al., 2000, 2005; Longpré et al., 2014; Mata et al., 2017; Nikogosian et al., 2002; Putirka, 1997). Despite large uncertainties associated with crystallization pressure estimates, thermobarometry offers several advantages that complement geophysical methods for determining magma chamber depth location (Magee et al., 2018). First, a magma pocket requires significant dimensions to be detected by seismic arrays, even at dense seismic station distribution (e.g., Gudmundsson, 2012). Second, seismicity picks up differences in seismic velocities, and thereby requires magma pockets to be melt rich; if they are mush zones with a significant proportion of crystals, then the melt-to-solid ratio may not be high enough to observe variations in seismic wave velocities (e.g., Gudmundsson, 2012). In addition, studies of deformation often employ petrological data as inputs to estimate the shape, size, and depth of the point source, to model the inflation of a magma chamber (e.g., Amelung & Day, 2002; González et al., 2015). Petrological techniques can thus provide crucial information on magma storage for integration with geophysical models (Magee et al. 2018). Geophysical methods, on the other hand, are not only useful for investigating the magma storage system but also have distinct advantages in real-time monitoring of magma movement prior to eruptions (Magee et al., 2018).

Furthermore, thermobarometry determines the pressure and temperature of mineral growth and is often sensitive to crystals growing in small magma pockets (e.g., Geiger et al., 2016; Stock et al., 2018). In many cases, these magma pockets are not detected until earthquakes trace magma ascent prior to an eruption. Several cases have shown that other methods confirm the models for magma plumbing systems developed from thermobarometry (e.g., Barker et al., 2019; Longpré et al., 2014). However, thermobarometry is not without limitations, restricted by the minerals present as well as magma compositions and experimental conditions of calibrations (e.g., Putirka, 2008). For instance, although clinopyroxene crystallizes over wide temperature, pressure and compositional ranges, the felsic magmas in many settings evolve beyond clinopyroxene crystallization (e.g., Weidendorfer et al., 2016). Therefore, other minerals or features such as fluid inclusions and volatile solubility in glass are required to trace the more evolved parts of the magmatic system (e.g., Jeffery et al., 2016; Schwarz & Klügel 2004).

All volcanic activity is fed from the magma plumbing system; therefore, it is important to understand magma storage, magmatic processes, and where they occur as well as the processes that lead to magma ascent (Cooper, 2017; Putirka, 2017; Sparks & Cashman, 2017). To address the connection between the magmatic system and volcanic hazards at Cape Verde, we will discuss magmatic processes recorded by mineral chemistry and the magma plumbing system derived from thermobarometric modeling for the southern Cape Verde archipelago. Mineral chemistry from the islands of Santiago, Fogo, Brava, and the Cadamosto Seamount will be examined to provide insights into magmatic processes. These examples have been selected based on the availability of mineral chemistry and geophysical data as well as relevance from a volcanic hazard perspective. Mineral–melt equilibrium thermobarometry for Santiago, Fogo, Brava, and the Cadamosto Seamount will be integrated into a model for the magmatic plumbing systems in southern Cape Verde. Evidence for the shallower parts of the magma plumbing systems and the volcanic hazards at Fogo will be reviewed. Finally, the magma plumbing system for Cape Verde will be compared with other ocean islands globally.

3.2. THE CAPE VERDE ARCHIPELAGO

The Cape Verde Rise is situated 2000 km east of the Mid-Atlantic Ridge in the Central Atlantic, between 15 and 17°N and approximately 500 km west of Dakar, Senegal (Figure 3.1). The Cape Verde Rise forms a gigantic bathymetric swell reaching about 2 km above the surrounding ocean crust and covers an area of more than 0.3 million km^2 (Brown et al., 2009; Crough, 1982; Holm et al., 2008; Jørgensen & Holm, 2002; Lodge and Helffrich, 2006; Masson et al., 2008; McNutt, 1988). The Cape Verde islands and seamounts are located in the Southwest of the Cape Verde Rise (Figure 3.1; Dash et al., 1976; Egloff, 1972; Rona, 1971). The islands are arranged in a semicircle opening to the west, with older heavily eroded islands occurring in the east and two subparallel chains of islands in the north and south, which extend westwards (Figure 3.1; Gerlach et al., 1988).

The northern and southern island chains are subparallel to the fracture zones found to the west of the Cape Verde archipelago (Figure 3.2; Jacobi & Hayes, 1982). Therefore, fracture zones may influence the orientation of the island chains (Doucelance et al., 2003; Klerkx et al., 1974; Le Pichon & Fox, 1971). Evidence for fracture zone offsets is documented by magnetic lineations and gravity anomalies (Figure 3.2; Ali et al., 2003; Dash et al., 1976; Hayes & Rabinowitz, 1975; Roest et al. 1992;Verhoef et al. 1991; Williams et al. 1990). In addition, brittle deformation through normal, reverse, and transverse faults has formed horst and graben structures on the Cape Verde Rise (Figure 3.2b; Efimov & Skolotnev, 2006; Skolotnev et al., 2007, 2009).

The Cretaceous ocean crust, formed at the Mid-Atlantic Ridge, is overlain by a several kilometer thick sequence of hemipelagic sediments (Figure 3.3; Ali et al., 2003; Courtney & White, 1986; Dash et al., 1976; Müller et al., 2008; Pim et al., 2008; Williams et al., 1990). The oceanic lithosphere is approximately 85 km thick, confirmed by elevated seismic velocities extending to about 80 km and a Lower Velocity Zone that appears at 90±6 km depth (Cazenave et al., 1988; Lodge & Helffrich, 2006). Although the ocean crust beneath Cape Verde has normal thicknesses of 7 to 8 km, the islands are underlain by a thickened crust (Pim et al., 2008; Wilson et al., 2010, 2013). The Moho beneath individual islands decreases westwards from >20 km beneath Maio, to 17 to 18 km beneath Santiago and to 12 to 14 km beneath Fogo (Lodge & Helffrich, 2006; Pim et al., 2008; Wilson et al., 2010, 2013). The sedimentary stratigraphy observed at Deep Sea Drilling Project (DSDP) Site 368 is composed of marl and nannofossil ooze, underlain by clay, claystone and minor chert associated with turbidites, plus black shale interbedded with dikes below (Faugères et al., 1989; Lancelot et al., 1978).

The Cape Verde islands display core complexes composed of intrusive carbonatite to alkaline assemblages as well as submarine pillow basalts (Davies et al., 1989; De Paepe et al., 1974; Gerlach et al., 1988; Madeira et al., 2010; Ramalho et al., 2010b; Serralheiro, 1970; Serralheiro, 1976; Stillman et al., 1982). The extrusives are dominantly mafic as exemplified by nephelinites and basanites at Santiago and Fogo (Barker et al., 2009; Davies et al., 1989; Gerlach et al., 1988; Hildner et al., 2011, 2012). However, several volcanic centers such as the island of Brava and the Cadamosto Seamount exhibit largely felsic assemblages (Assunção et al., 1965; Barker et al., 2012; Machado et al., 1968; Madeira et al., 2008, 2010; Samrock et al., 2019; Weidendorfer et al., 2016). Cape Verde is one of the few ocean island groups hosting carbonatites, which are widespread on Brava with minor exposures on Fogo, Santiago, and São Vicente (e.g., Assunção et al., 1965; Hoernle et al., 2002; Jørgensen & Holm, 2002; Mata et al., 2010; Mourão et al., 2010; Silva et al., 1981; Turbeville et al., 1987).

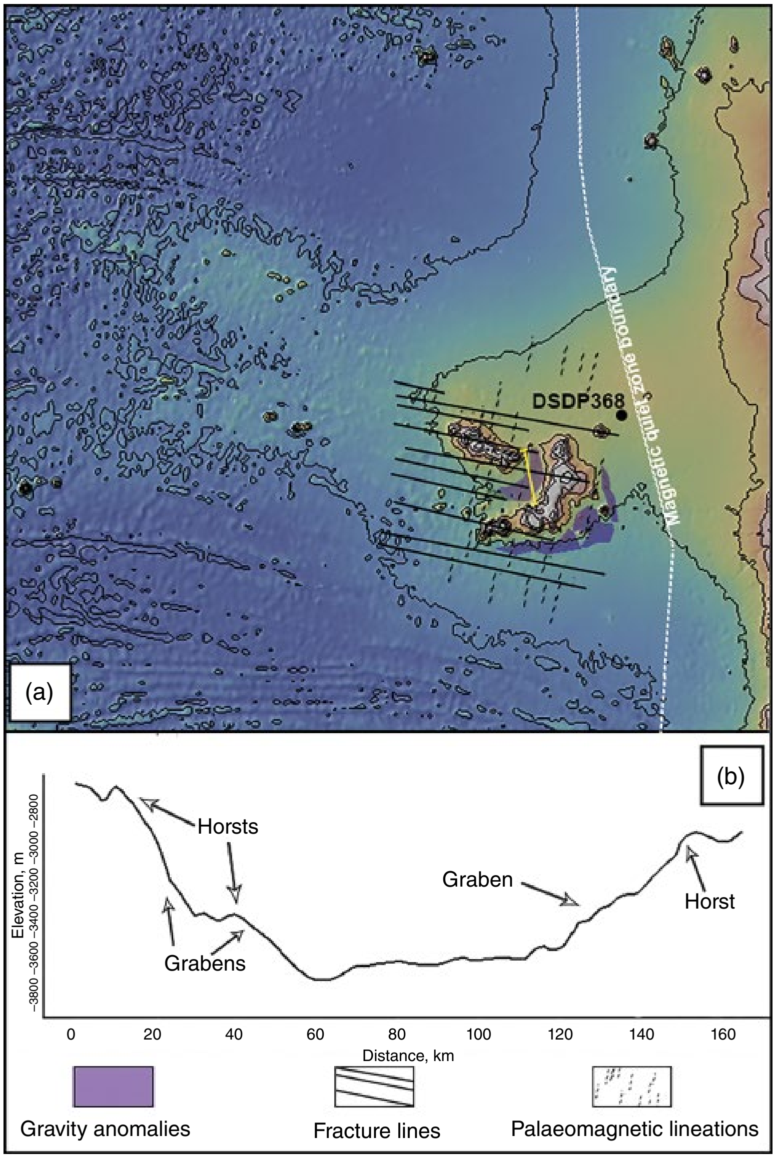

Figure 3.2 (a) Map showing fractures zones, magnetic lineations, gravity, and magnetism of the Cape Verde Rise. Black lines show fracture zones as mapped by Williams et al. (1990). Magnetic lineations of M4–M25 are plotted after Klitgord and Schouten (1987). The satellite-derived free-air gravity anomalies are shown (Sandwell & Smith, 1997). DSDP Site 368 is labeled. Magnetic quiet zone boundary is from Hayes and Rabinowitz (1975). (b) Schematic cross section NNW to SSE across the Cape Verde Rise following the yellow line (Stillman et al., 1982; Ryan et al., 2009; www.geomapapp.org).

3.2.1. Geochronology of the Cape Verde Archipelago

The Cape Verde islands exhibit a general age progression from the early Miocene for the oldest exposures, which decrease westwards to the presently volcanically active parts of the archipelago (Figure 3.4; Bernard-Griffiths et al., 1975; Duprat et al., 2007; Dyhr & Holm, 2010; Foeken et al. 2009; Holm et al. 2008; Jørgensen & Holm 2002; Madeira et al. 2010; Mitchell et al. 1983; Plesner et al. 2003; Samrock et al., 2019; Stillman et al., 1982; Torres et al., 2002). The older islands in the east are highly eroded, displaying a relatively flat and low topography in contrast to the shield volcanoes that occur further west. The earliest age of the eastern islands is recorded by submarine pillow basalts from the island of Sal at 26 Ma (Torres et al., 2002). The volcano-magmatic activity continues until approximately 1 Ma at Sal (Figure 3.4; Dyhr & Holm, 2010; Holm et al., 2008;

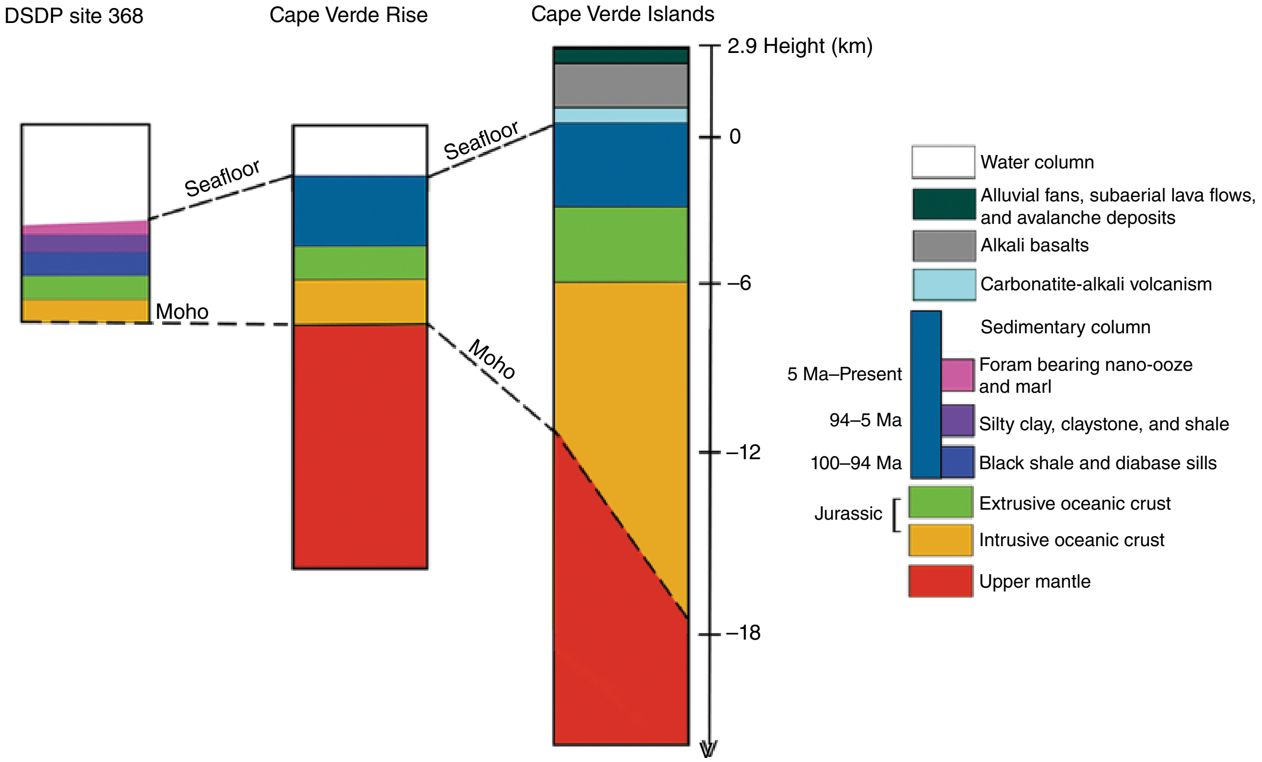

Figure 3.3 Compiled stratigraphy of the Deep Sea Drilling Project DSDP Site 368, the Cape Verde Rise, and the Cape Verde islands. Several kilometer thick sequences of sediment are found above the ocean crust throughout the region (Dash et al. 1976; Lancelot et al., 1978; Pim et al., 2008). The Moho is thickened beneath the islands and occurs at depths of 12 to 18 km, becoming deeper toward the East (Dash et al. 1976; Lancelot et al., 1978; Ali et al., 2003; Lodge & Helffrich, 2006; Pim et al., 2008).

Mitchell et al., 1983; Torres et al., 1997). The northern islands show volcanic activity from approximately 8 to 10 Ma to between 100,000 and 300,000 years ago at São Nicolau to Santa Antão (Figure 3.4; Duprat et al., 2007; Holm et al., 2008; Plesner et al., 2003). Seismic activity beneath Santa Antão suggests that this region continues to be volcanically active (Faria & Fonseca, 2014).

There is evidence that volcanism in the southern islands commenced at Santiago approximately 11 Ma ago (Figure 3.4; Ali et al., 2003; Mitchell et al., 1983; Stillman et al., 1982; Torres et al., 2002). The majority of the volcano-magmatic activity on the southern islands emerges from 5.5 Ma at Santiago, 4.5 Ma at Fogo, and 2.3 Ma at Brava (Foeken et al., 2009; Holm et al., 2008; Madeira et al., 2010; Ramalho et al., 2010c). The most recent volcanic eruptions from Santiago are dated to 740,000 years ago and from Brava to 300,000 years ago (Holm et al., 2008; Madeira et al., 2010). The islands typically show multiple stages of volcanism interrupted by periods of quiescence (Figure 3.4; Foeken et al., 2009; Holm et al., 2008; Madeira et al., 2010; Ramalho et al., 2010a, 2010b, 2010c). Volcanic activity at the Cadamosto Seamount appears to occur in the last 20,000 to 100,000 years (Samrock et al., 2019). The island of Fogo displays historical volcanism with around 30 eruptions since discovery and settlement in 1460 including recent eruptions in 1995 and 2014 to 2015 (Da Silva et al., 1999; Fernandes & Faria, 2015; Hildner et al., 2011, 2012; Ribeiro, 1960; Silva et al., 2015; Worsley, 2015). In addition, Fogo, Brava, and the Cadamosto Seamount display ongoing seismic activity (Faria & Fonseca, 2014; Grevemeyer et al., 2010; Heleno et al., 2006).

3.2.2. The Geology of Santiago

The island of Santiago is composed of an intrusive complex, followed by submarine and subaerial volcanics (Figures 3.5 and 3.6; Bebiano, 1932; Ramalho, 2011; Serralheiro, 1976). The Complexo Antigo consists of alkaline silicate intrusives and carbonatites. The submarine stage is represented by the Flamengos Formation and exhibits pillow lavas embedded in hyaloclastite with eruption ages of 4.0 to 5.5 Ma (Figures 3.4–3.6; Barker et al., 2009; Holm et al., 2008; Ramalho, 2011; Ramalho

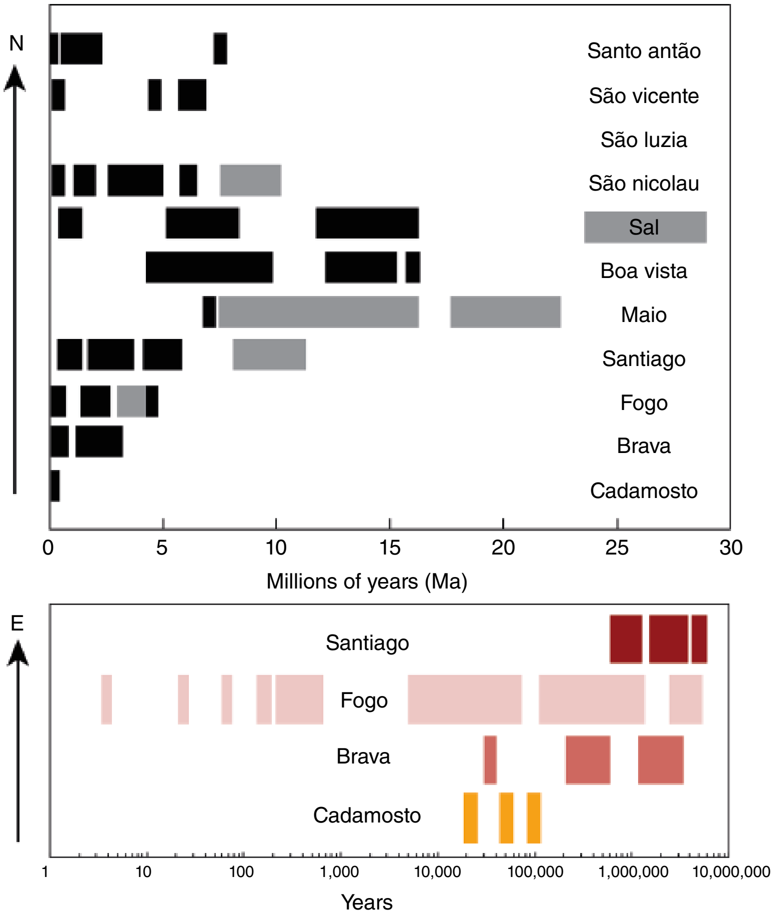

Figure 3.4 Age distribution of exposed volcanic and intrusive products across the Cape Verde Archipelago. Black bars mark $^{40}Ar/^{39}Ar$ geochronology and He exposure dating, whereas gray bars show K/Ar geochronology and other geological inferences. Note the tentative age progression of the oldest exposed rocks in the east to the youngest in the west. The lower part focuses on the southern chain comparing geochronology of Santiago, Fogo, Brava and the Cadamosto Seamount. Modified from Holm et al. (2008) and based on the geochronological data of Bernard-Griffiths et al. (1975); Mitchell et al. (1983); Torres et al. (2002); Plesner et al. (2003); Jørgensen and Holm (2002); Duprat et al., (2007); Holm et al. (2008); Foeken et al. (2009); Dyhr and Holm (2010); Madeira et al. (2010); Ramalho et al. (2010c); Samrock et al. (2019).

et al., 2010c; Serralheiro, 1976). The shield stage is formed by subaerial lavas of the Pico da Antónia Formation between 1.5 and 3.2 Ma (Figures 3.4–3.6; Barker et al., 2010; Holm et al., 2008; Ramalho et al., 2010c; Serralheiro, 1976). Occasional carbonatite lava flows belong to the Pico da Antónia Formation (Jørgensen & Holm, 2002). The Assomada and Monte das Vacas formations erupted post-erosional lavas and scoria cones between 0.7 and 1.1 Ma (Figures 3.4 and 3.6; Barker et al., 2010; Holm et al., 2008; Ramalho et al., 2010c; Serralheiro, 1976). In addition, a sliver of the Jurassic ocean crust has been uplifted and emplaced at Baía de Angra, and uplifted sediments are found at Tarrafal (Gerlach et al., 1988; Ogg, 1995; Ramalho, 2011; Serralheiro, 1976).

3.2.3. The Geology of Fogo

The geology of Fogo can be divided into four units. The stratigraphy begins with the submarine stage composed of carbonatites and alkaline basalts from approximately 4.5 Ma (Figure 3.4; Day et al., 1999; Madeira et al., 2010). The emergence of Fogo as an island is recorded by the subaerial lavas of the Monte Barro

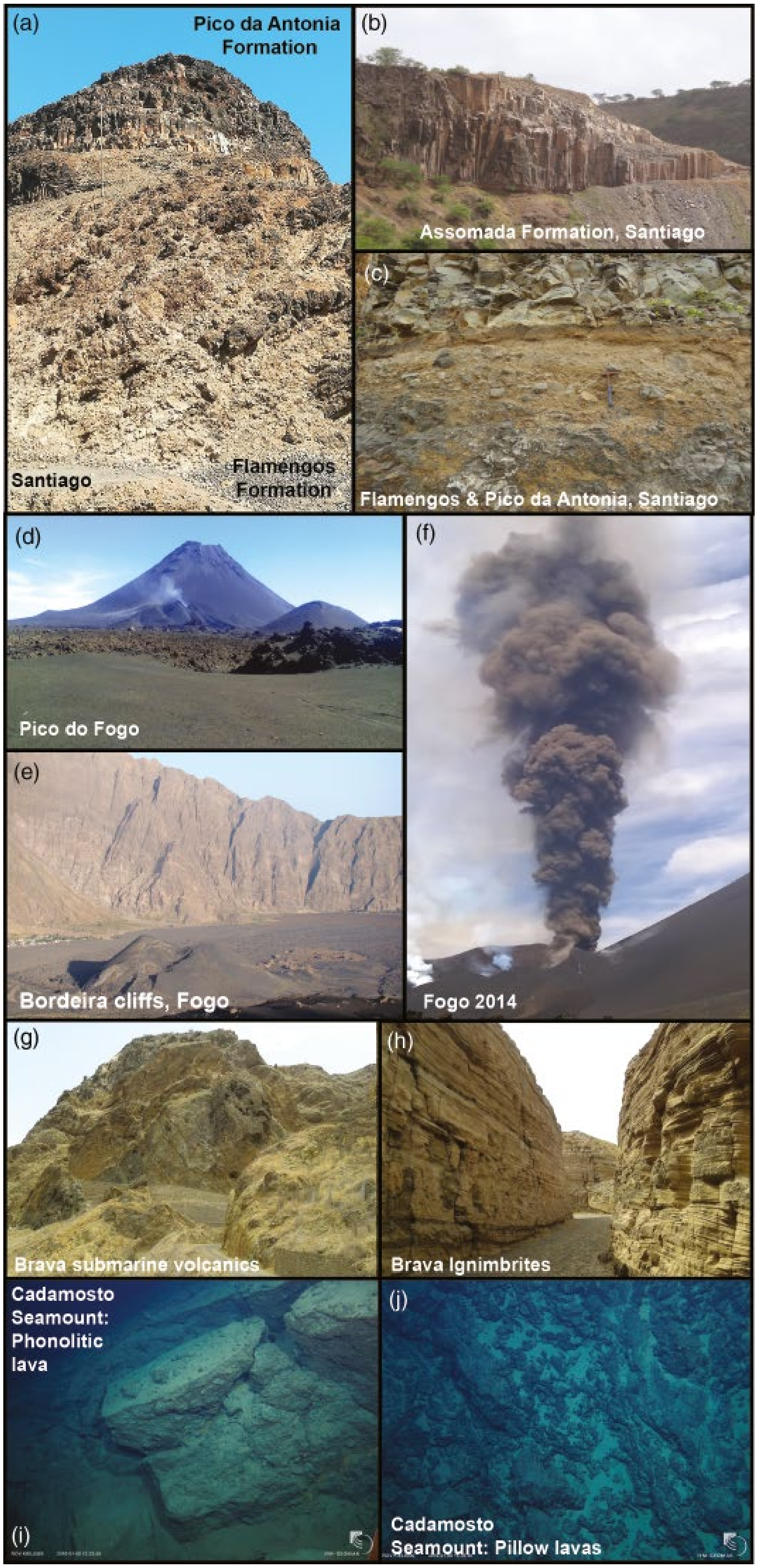

Figure 3.5 Photographs from the islands of Santiago, Fogo, and Brava and the Cadamosto Seamount, (a) hyaloclastite from the submarine Flamengos Formation overlain by subaerial lavas of the Pico de Antónia Formation, Santiago, (b) the Assomada Formation, Santiago, (c) pillow lavas in hyaloclastite from the Flamengos Formation overlain by a beach conglomerate followed by lavas of the Pico de Antónia Formation, Santiago, (d) the iconic Pico do Fogo standing on the Chã das Caldeiras plateau, Fogo, (e) Bordeira cliffs that surround the western part of the Chã das Caldeiras, Fogo, (f) the volcanic eruption at Fogo in November 2014, (g) pillow lavas and hyaloclastites intruded by dike swarms, Brava, (h) sequence of ignimbrites, Brava, (i) phonolitic lava near the summit of the Cadamosto Seamount (M80/3-033ROV), and (j) steep cliffs of a crater at the Cadamosto Seamount (M80/3-033ROV).

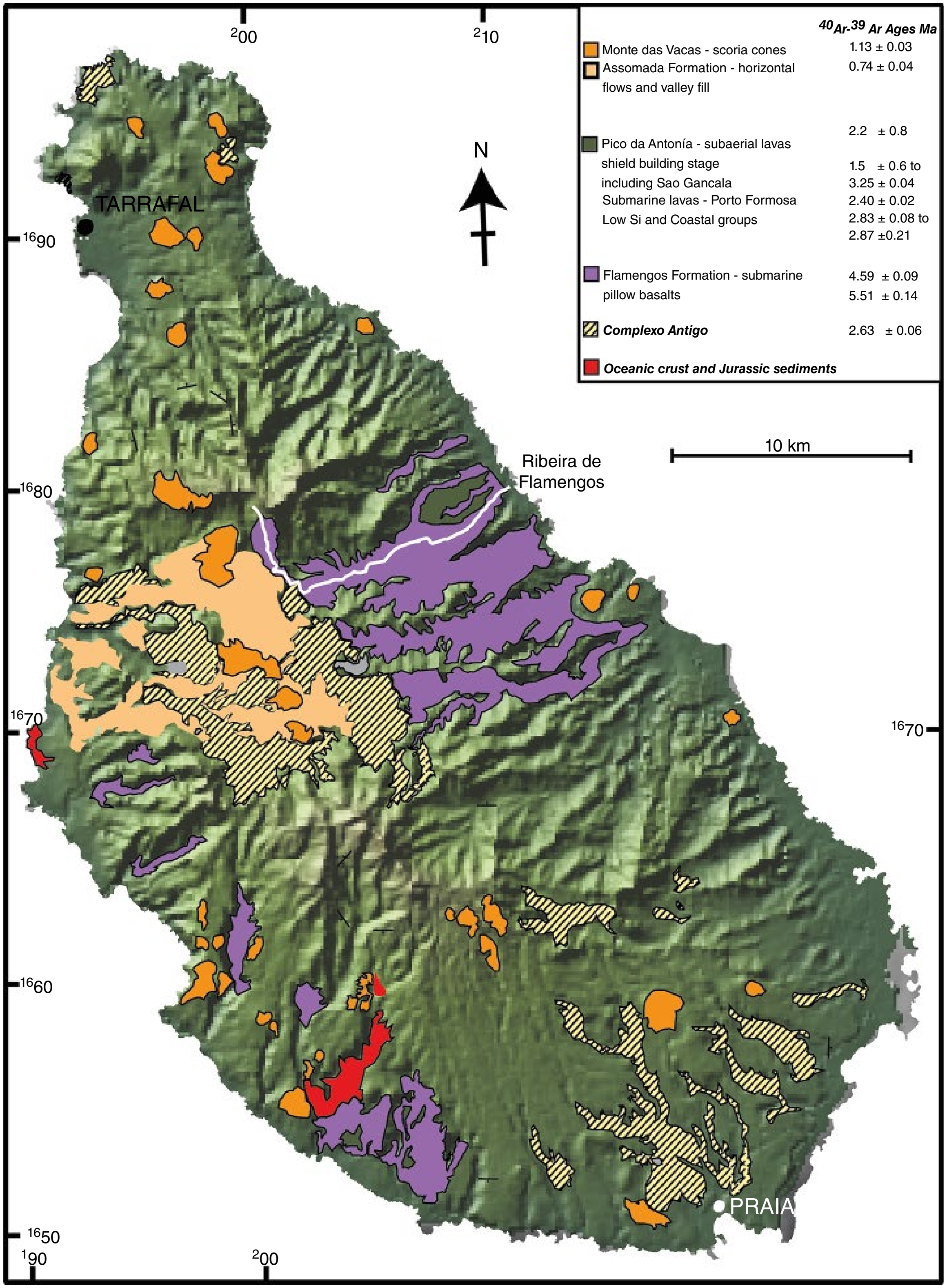

Figure 3.6 Geological and topographic map of Santiago after Serralheiro, 1976; Ryan et al., 2009; www.geomapapp.org. The Flamengos Formation is exposed along river valleys and in highly eroded areas. The Pico da Antonía Formation is widespread and represents the shield building stage of volcanism. An erosional phase was followed by lavas of the Assomada Formation, which flowed into valleys, and the Monte das Vacas scoria cones.

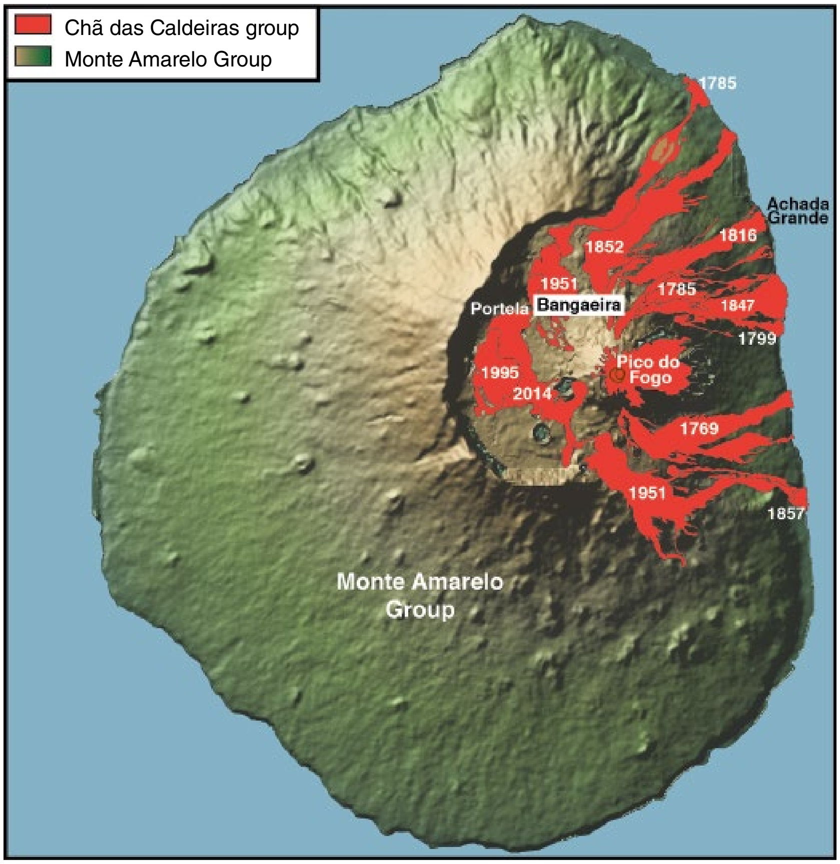

Figure 3.7 Geological and topographic map of Fogo after Torres et al., 1998; Ryan et al., 2009; www.geomapapp.org; Carracedo et al., 2015. The shield volcano is composed of the Monte Amarelo Group volcanism, and a large landslide created the Bordeira cliffs delineating the Chã das Caldeiras plateau that hosts the Pico do Fogo and recent volcanic eruptions.

Group (Day et al., 1999). Subsequently a large stratovolcano known as Monte Amarelo developed during the Quaternary, reaching up to 3 km above sea level (Figure 3.7; Day et al., 1999). A giant landslide occurred at approximately 73 ka, leaving the Bordiera cliffs as a remnant of the caldera wall or flank collapse scarp (Figure 3.5; Elsworth & Day, 1999; Foeken et al., 2009; Madeira et al., 2019; Masson et al., 2008; Paris et al., 2011, 2018; Ramalho et al., 2015). The associated structure is filled with volcanic materials to form a plateau known as the Chã das Caldeiras, which hosts the majority of the volcanic activity from 62 ka to present (Figures 3.4 and 3.7; Day et al., 1999; Foeken et al., 2009; Ribeiro, 1960; Torres et al., 1997). The spectacular Pico do Fogo, rising 2829 m above sea level, is formed by Hawaiian and Strombolian activity that produced basanite to tephrite lapilli and lava (Figures 3.5 and 3.7; Torres et al., 1997). Historic eruptions emanated from the base of Pico do Fogo, the eastern flank of Pico do Fogo or from vents on the Chã das Caldeiras plain. The eruptions have typical durations of two months, and the last eruption occurred from 23 November 2014 to 7 February 2015 (Figure 3.5; Fernandes & Faria, 2015; Silva et al., 2015; Worsley, 2015). The eight previous eruptions occurred in 1785, 1799, 1816, 1847, 1852, 1857, 1951, and 1995 (Figure 3.4; Day et al., 1999; Ribeiro, 1960; Torres et al., 1997).

3.2.4. The Geology of Brava

Brava is smaller than Fogo and Santiago, with an area of 64 km^2, located 18 km from Fogo on the Brava-Fogo platform, which is only 1400 m below sea level (mbsl) (Figure 3.1; Da Silva et al., 1999; Madeira et al., 2010). The geology was first investigated by Bebiano (1932) and later by Machado et al. (1968). Recent work by Madeira et al. (2010) has divided the stratigraphy into three units. The submarine volcanism consists of hyaloclastite and pillow basalt breccias and flows that radiate from the center of the island (Figure 3.8; Madeira et al., 2010). They are intruded by N-S and E-W oriented dikes. Subsequently the intrusive complex was emplaced in the

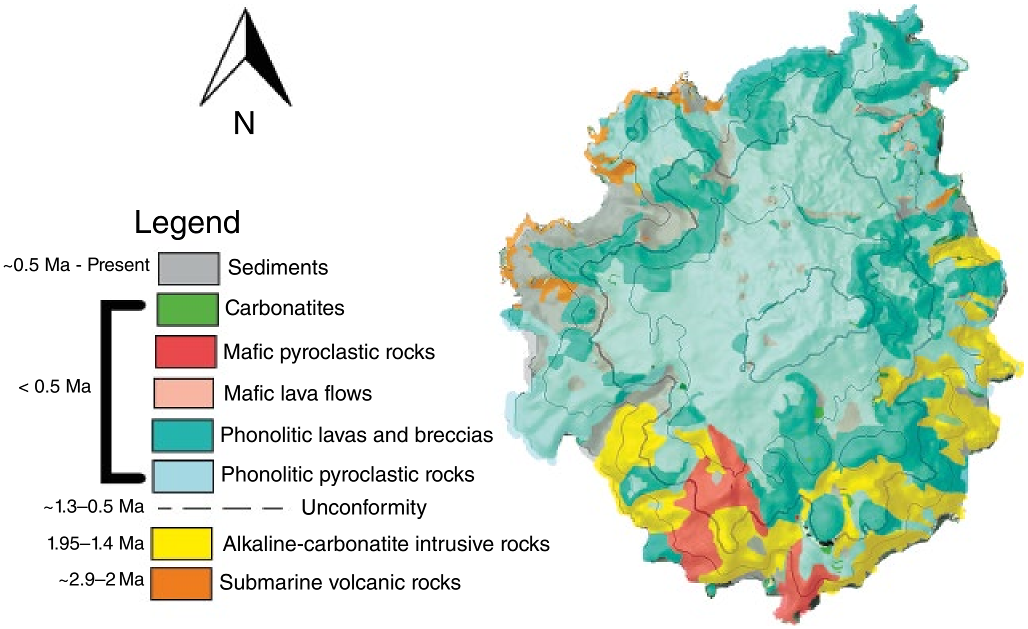

Figure 3.8 Geological and topographic map of Brava after Madeira et al., 2010; Ryan et al., 2009; www.geomapapp.org. The island core complex is composed of alkaline and carbonatite intrusive rocks, whereas the volcanic rocks are mostly nephelinite to phonolite.

submarine volcanics. The alkaline-carbonatite intrusives are represented by pyroxenites, ijolite-melteigites-urites, and nepheline syenites plus carbonatites (Figure 3.8; Madeira et al., 2010; Mourão et al., 2010). Post-erosional volcanism is dominantly phonolitic and ranges from ignimbrites and tephra deposits due to phreatomagmatic eruptions, to phonolite lava flows and domes (Figures 3.5 and 3.8). Mafic volcanism is rare in the post-erosional sections; however, carbonatites in the form of ignimbrites and lava flows are not uncommon (Figure 3.8; Madeira et al., 2010). Seismicity, particularly NE and SE of Brava associated with volcanic cones on the Brava-Fogo platform, indicate that Brava is magmatically active. Seismic swarms at depths of 2 to 10 km, along with seismic tremor, suggest volcano-tectonic events related to submarine intrusions (Faria & Fonseca, 2014).

3.2.5. The Cadamosto Seamount

The Cadamosto Seamount is a large circular submarine volcano, with a diameter of approximately 15 km, and a height of 3 km, reaching water depths of up to 1380 m below sea level (mbsl) (Figure 3.1; Hansteen et al., 2014). The seamount has three main craters in the summit area, where pillow and sheet flows have been observed (Figure 3.5). The samples are mainly phononephelinites to phonolites, with occasional basaltic samples (Barker et al., 2012; Hansteen et al., 2014; Samrock et al., 2019). New ^{40}Ar-^{39}Ar geochronology gives eruption ages of 20 to 97 ka, confirming the young nature of the seamount (Samrock et al., 2019). In addition, the Cadamosto Seamount is seismically active with notable earthquakes of magnitudes 4.9 and 4.3 recorded in 1998 and 2004, respectively (Grevemeyer et al., 2010). The seismicity is attributed to brittle rock failure resulting from submarine intrusion (Grevemeyer et al., 2010).

3.2.6. Volcanic Eruptions and Hazards at Fogo

The natural hazards faced by the population of Fogo are weather related, such as droughts that lead to famine, as well as flash floods and related landslides that destroy roads and buildings. Less common and therefore considered less of a risk are volcanic eruptions and associated earthquakes. The volcanic eruptions pose a hazard to the communities living in the Chã das Caldeiras area (964 people) plus potentially the towns on the East Coast of Fogo (11,000 people). Lava flows are the greatest hazard; however, volcanic gases and tephra also contribute to the volcanic hazards (Nascimento, 2015; Richter et al., 2016; Silva et al., 2015, 2017; Texier-Teixeira et al., 2014).

There have been 28 eruptions on Fogo since the discovery of the island by Portuguese sailors in 1460 (Ribeiro, 1960). The most recent eruption commenced on 22 November 2014 and continued for 77 days, finally ceasing on 7 February 2015. The eruption consisted of a 6-km-high eruption cloud causing tephra deposits in eight villages and towns, as well as other islands such as

Brava to the west and São Vicente to the north (Nascimento, 2015). The lava flows rapidly cut off the road access to Chã das Caldeiras and went on to destroy the villages of Portela and Bandaeira, including 75% of the buildings in the Chã das Caldeiras area and 25% of the agricultural land and water storage facilities (Jenkins et al., 2017).

The volcano monitoring activities carried out by the Institute of National Meteorology and Geophysics and the University of Cape Verde are essential to volcanic crisis management. Regular automated monitoring covers seismicity and deformation of the volcano (Dionis et al., 2015a, 2015b; Faria & Fonesca, 2014; Fernandes & Faria, 2015; Fonseca et al., 2003). During the eruption in 1995, volcanic tremor and seismic swarms occurred between 1 and 5 km depths (Da Silva et al., 1999). Approximately seven weeks prior to the eruption in 2014–2015, earthquakes were detected originating at depths of >15 km (Fernandes & Faria, 2015). Additional geochemical monitoring of the volcanic gases is manual, and therefore sampling is conducted during specific campaigns and does not provide a continuous record of volcano degassing (Dionis et al., 2015a, 2015b; Pérez et al., 2015). For instance, air quality was monitored during the 2014–2015 eruption by the deployment of an instrument at one station in São Filipe on the west coast of Fogo (Nascimento, 2015).

3.3. MAGMATIC PROCESSES

We use mineral chemistry from Cape Verde to explore the magmatic processes recorded by clinopyroxene (Davidson et al., 2007). The advantages of focusing on clinopyroxene include crystallization over a wide temperature range and during a large extent of magmatic differentiation. The volcanic rocks from Santiago and Fogo are classified as basanite, tephrite, alkali basalt, nephelinite and melanephelinite, with minor tephriphonolite occurring at Fogo. However, those from Brava and the Cadamosto Seamount are dominantly phonolite and phonotephrite combined with the presence of intrusive syenite at Brava (Figure 3.9; Barker et al., 2009, 2012; Hildner et al., 2011, 2012; Mata et al., 2017; Samrock et al., 2019; Weidendorfer et al., 2016).

Clinopyroxene from Santiago and Fogo is classified as diopside-augite, whereas Brava and the Cadamosto

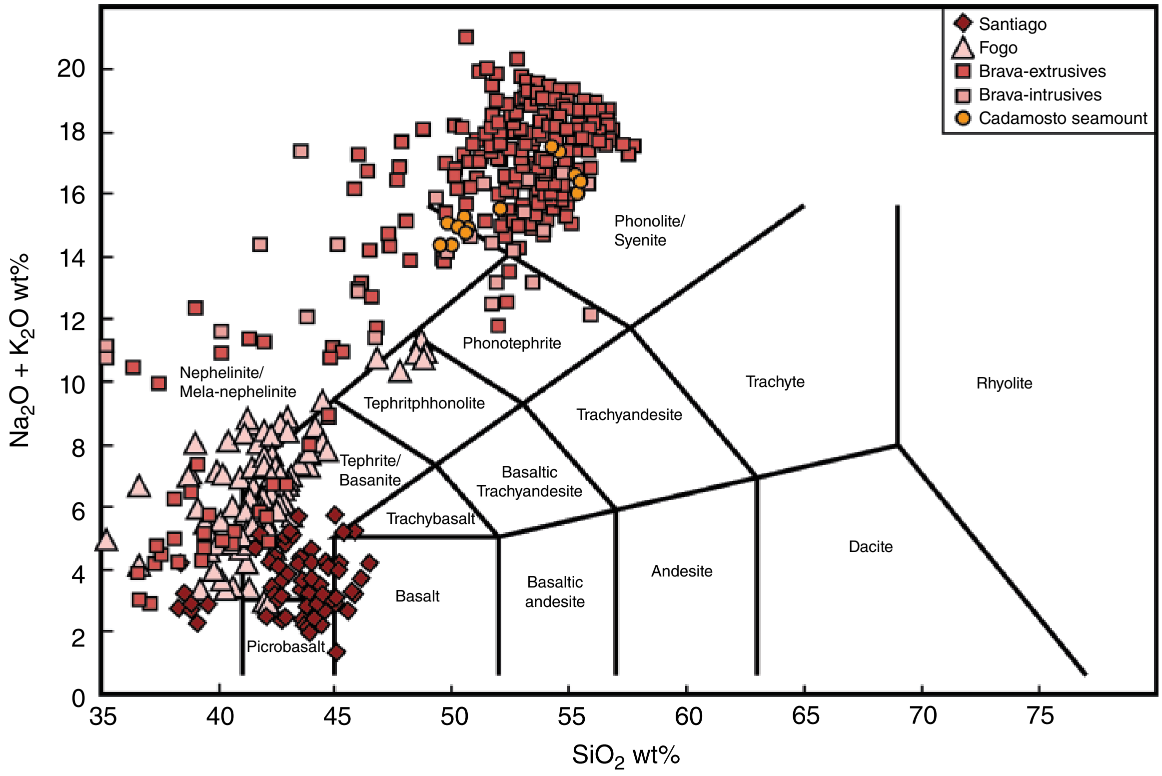

Figure 3.9 Compositional classification of the volcanic rocks from Santiago, Fogo, Brava, and the Cadamosto Seamount after LeMaitre et al. 2002. Santiago and Fogo host (mela)nephelinite, basanite, and tephrite to basalt and even tephriphonolite at Fogo. By contrast, Brava and the Cadamosto Seamount host dominantly phonolite and syenite. Data are unnormalized. Sources: Kokfelt et al. (1998); Barker et al. (2009, 2012); Hildner et al. (2011, 2012); Magnusson (2016); Weidendorfer et al. (2016).

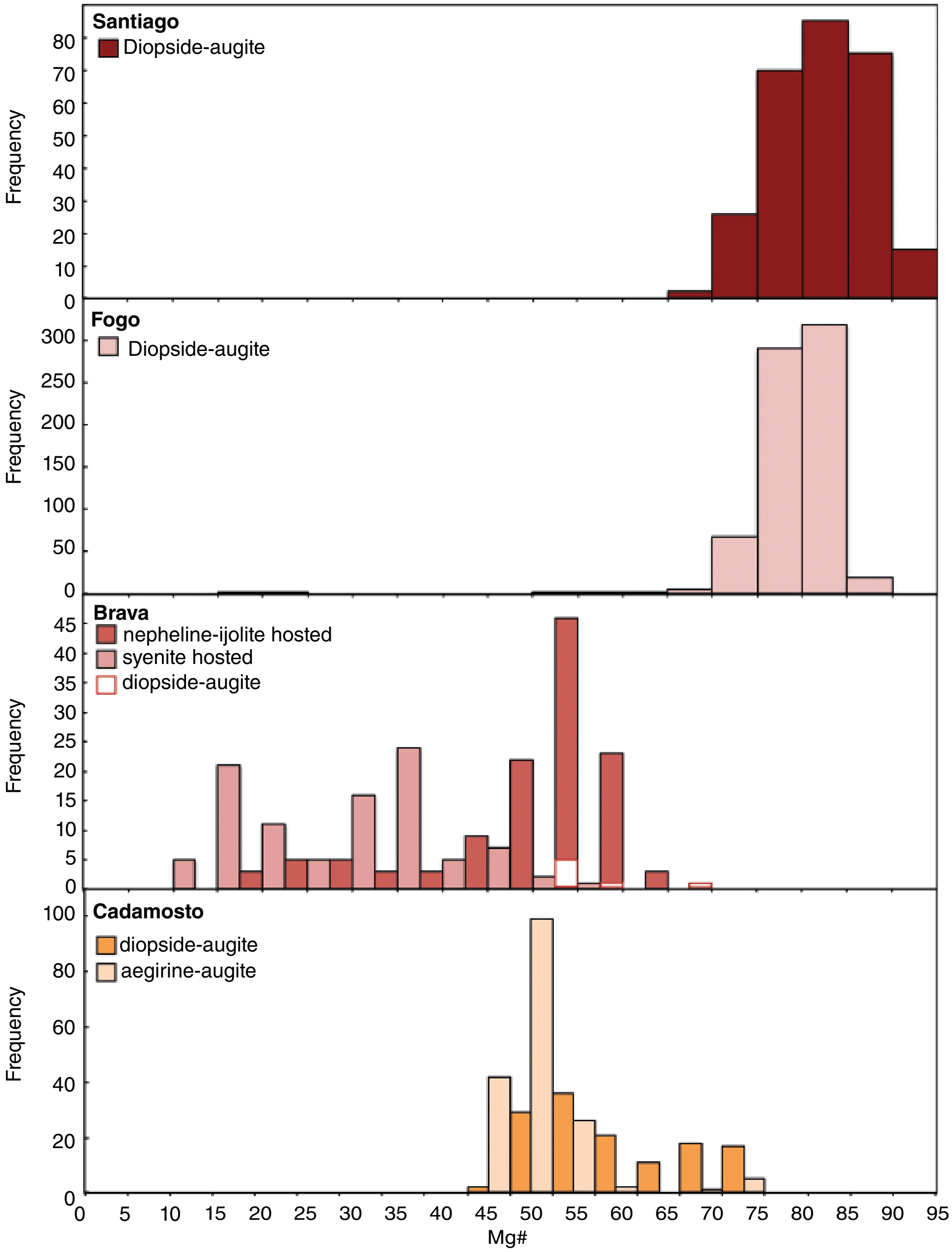

Figure 3.10 Clinopyroxene Mg# histograms for Santiago, Fogo, Brava, and the Cadamosto Seamount. All locations host diopside-augite, whereas Brava and the Cadamosto Seamount display highest abundances of aegirine-augite. Sources: Barker et al. (2009, 2012); Hildner et al. (2011, 2012); Weidendorfer et al. (2016); Rydeblad (2018).

Seamount host both diopside-augite and green aegirine-augite (Barker et al., 2009, 2012; Hildner et al., 2011, 2012; Rydeblad, 2018; Weidendorfer et al., 2016). Clinopyroxene from Santiago and Fogo display compositions of dominantly 60 to 90 Mg# and 60 to 85 Mg#, respectively (Figure 3.10; Mg# mol% = (Mg/Mg + Fe^{total}). The samples from Fogo also show minor abundances of clinopyroxene at 10 to 20 Mg# and 45 to 60 Mg#. Analyzed clinopyroxene from Brava are dominantly aegirine-augite that display a much wider range of compositions from 5 to 65 Mg# (Figure 3.10). The nephelinites and ijolites host clinopyroxene with the highest frequency between 35 and 55 Mg#, whereas the syenites host clinopyroxene with 10 to 35 Mg# (Figure 3.10). The seven diopside-augite analyses have 45 to 65 Mg#. Clinopyroxene from the Cadamosto Seamount shows a skewed distribution with a range of 40 to 75 Mg# and mode at 40 to 55 Mg# (Figure 3.10). When the diopside-augite and aegirine-augite are distinguished, they range from 41 to 74 Mg# and 42 to 72 Mg#, respectively (Figure 3.10). The high Fe^{3+}/Fe^{total} observed for volcanic rocks from Cape Verde indicates crystallization under oxidizing conditions with high oxygen fugacity (Duprat et al., 2007; Holm et al., 2006; Mata et al., 2017). This may increase the Mg# of the clinopyroxene and would likely have a more significant effect as the iron content increases, thereby having the greatest influence on the clinopyroxene compositions from Brava and the Cadamosto Seamount (Freise et al., 2003). Moreover, the presence of häuyne and high sulfur contents in the Brava and Cadamosto Seamount samples would further contribute to higher Mg# contents in clinopyroxene (Andújar et al., 2008; Barker et al., 2012; Weidendorfer et al., 2016). The clinopyroxene compositions reflect the overall composition of the volcanic centers with a restricted range of mafic volcanic rocks found at Santiago and Fogo with high clinopyroxene Mg#; therefore, differentiation has played a limited role in these locations. At Brava and the Cadamosto Seamount, the volcanic centers become more felsic with wider compositional ranges and lower clinopyroxene Mg#. Consequently, the clinopyroxene compositions exhibit wider ranges or skewed distributions recording the influence of extensive fractional crystallization.

More detailed examination of the mineral chemistry shows that clinopyroxene from Santiago and Fogo display increasing Al_2O_3, TiO_2, and low but increasing Na_2O and MnO with decreasing Mg# (Figure 3.11). In contrast, the clinopyroxene crystals from Brava and the Cadamosto Seamount form a different trend with low and decreasing Al_2O_3 and TiO_2 with decreasing Mg#. The clinopyroxene crystals from Brava exhibit a high Na_2O content of 2.1 to 6.2 wt% compared to 0.3 to

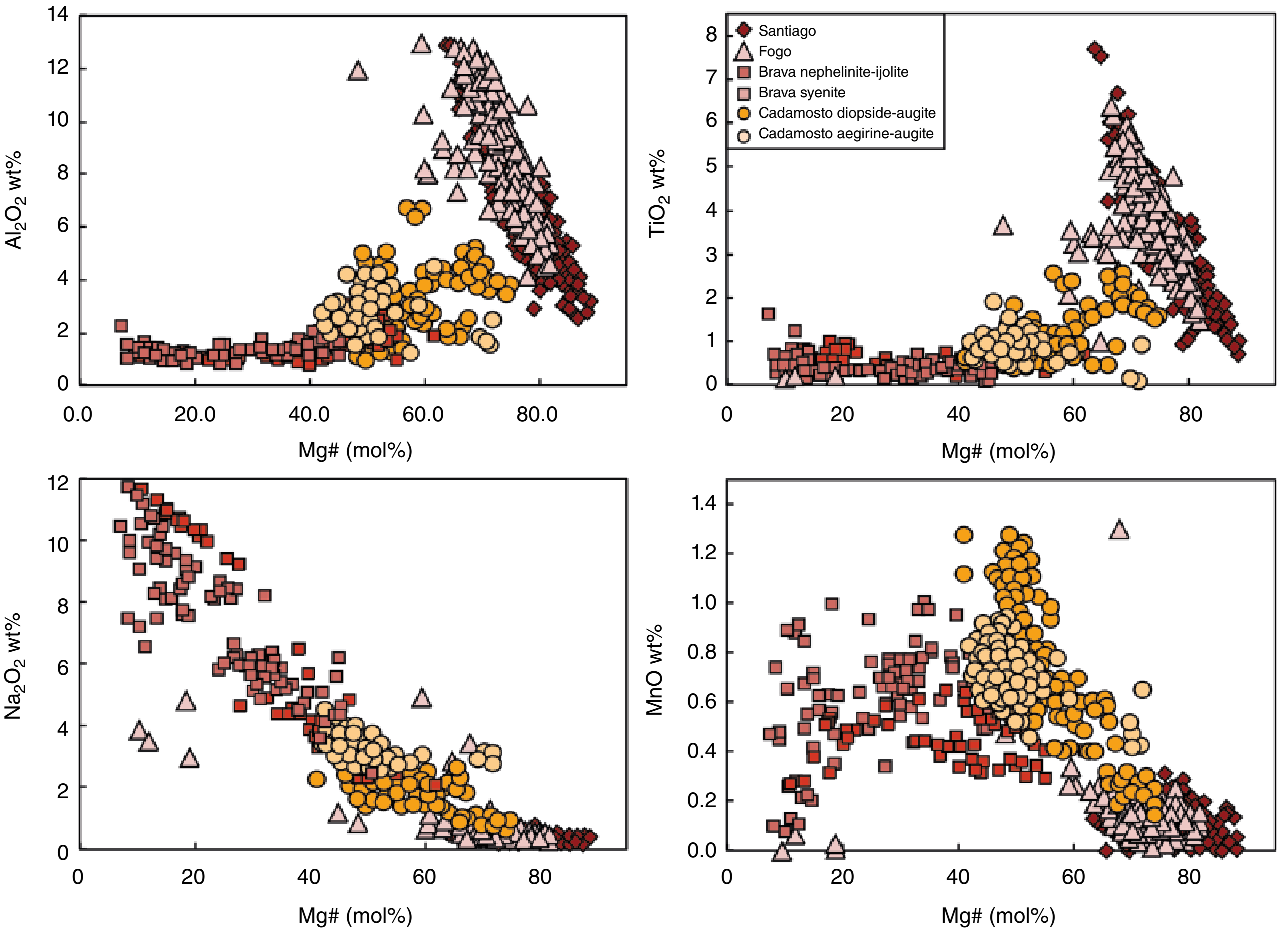

Figure 3.11 Clinopyroxene mineral chemistry for Santiago, Fogo, Brava, and the Cadamosto Seamount. The clinopyroxene crystals from Santiago and Fogo display a distinct trend from the clinopyroxene found at Brava and the Cadamosto Seamount. Sources: Barker et al. (2009, 2012); Hildner et al. (2011, 2012); Weidendorfer et al. (2016); Rydeblad (2018).

1.3 wt% Na_2O in the clinopyroxene from Santiago and Fogo. At the Cadamosto Seamount, Na_2O content increases from diopside-augite with 0.8 to 2.7 wt% to the aegirine-augite population with 2.7 to 4.5 wt% (Figure 3.11). The MnO content increases from 0.2 to 1.3 wt% in clinopyroxene with Mg# between 35 and 75 including all crystals from the Cadamosto Seamount (Figure 3.11). Clinopyroxene crystals with Mg# ≤35 from Brava show a decrease in MnO content from 1.0 to 0.1 wt% as Mg# decreases (Figure 3.11).

The majority of the clinopyroxene crystals from Santiago and Fogo display strong correlations, with only a relatively small proportion of clinopyroxene from Fogo plotting at lower Mg# for given Al_2O_3 and TiO_2 content (Figure 3.11). This suggests dominantly equilibrium growth during fractional crystallization of the magma and phenocryst formation (Mollo et al., 2013, 2018; Welsch et al., 2016). The extensive differentiation trends in the clinopyroxene chemistry and the liquid lines of descent observed in the whole rock geochemistry (Barker et al., 2009; Mata et al., 2017), suggest that equilibrium crystallization occurred during melt evolution (e.g., Mollo et al., 2018). Thus, much of the crystal population is in disequilibrium with the final host melt, and this disequilibrium is not homogenized by diffusion or mixing of magmas. Consequently, the erupted products host antecrysts crystallized under different conditions compared to the final melt compositions (e.g., Barker et al., 2009; Davidson et al., 2007; Klügel et al., 2020; Mollo et al., 2013, 2018; Welsch et al., 2016). At Brava and the Cadamosto Seamount, the clinopyroxene populations are more scattered, illustrating greater compositional diversity. The equilibrium mineral–melt pairs indicate that the diopside-augite population grew in equilibrium with low Na_2O melts (<8 wt% Na_2O), whereas the host rocks have much higher Na_2O content (8 to 14 wt% Na_2O; Barker et al., 2012; Weidendorfer et al., 2016). Therefore, despite their similar compositions, the diopside-augite and aegirine-augite populations were likely aggregated from different melts (Figure 3.11).

Whole rock geochemistry for Santiago, Fogo, and Brava confirms significant fractional crystallization. At Santiago, the full range of compositions indicates a total of 24% fractional crystallization of predominantly clinopyroxene (Barker et al., 2009). The Fogo lavas record significant fractional crystallization to produce the basanites and tephrites, which requires crystallization of up to 21% clinopyroxene and minor olivine, Fe-Ti-oxides, and apatite (Magnusson, 2016; Mata et al., 2017). Likewise, the magmatic system at Brava shows 15% olivine and 35% clinopyroxene crystallization, with subordinate Fe-Ti-oxides and apatite, which explains the ijolite and nephelinite compositions (Weidendorfer et al., 2016). Furthermore, a total of 90% fractional crystallization is required to produce the entire range of whole rock compositions (Weidendorfer et al., 2016). The lavas at Santiago and a few of those from Fogo display high MgO content, implying a role for aggregation of crystals (Barker et al., 2009; Magnusson, 2016; Mata et al., 2017). These accumulated crystals must have grown in very similar magmas following the liquid line of descent for clinopyroxene crystallization shown by their Mg# and Al_2O_3 content (Figure 3.11).

Now we consider zoning patterns in clinopyroxene crystals and the processes they reveal. Petrographically at Santiago we frequently observe patchy cores that are rounded by resorption. It is apparent in this example that the resorbed, patchy core passes into an area of concentric zonation, where oscillatory zoning emphasizes the different growth rates for different sectors of the crystal (Figure 3.12). The associated chemistry for the zoned clinopyroxene crystal from Santiago exhibits a plateau over the patchy core with only small variations. The outer oscillatory zonation displays trends of fractional crystallization with decreasing Mg# and MnO content simultaneous with increasing TiO_2 content (Figure 3.12; Streck, 2008). In addition, at Santiago, the oscillatory zonation records recharge events with increasing Mg# and MnO associated with a decrease in TiO_2 content. The behavior of Mg# and MnO are observed to be decoupled in some instances, which indicates the occurrence of magma mixing. The selected clinopyroxene crystal from Fogo also reveals a patchy core followed by two outer zones. The fractures highlight differences in resorption of the core. The zone surrounding the core shows oscillatory zoning and then passes into a relatively homogeneous rim (Figure 3.12). The patchy core shows small variations in Mg#, whereas the oscillatory zone exhibits large variations in Mg#, and the rim shows homogeneously high Mg# (Figure 3.12). The variations in TiO_2 and MnO content are not consistent with the variations in Mg#, and therefore much of the variation cannot be attributed to fractional crystallization or recharge events. Instead, the zonation records magma chamber dynamics associated with temperature and compositional differences causing convection and mixing (Figure 3.12; Rydeblad, 2018; Streck, 2008). The clinopyroxene crystal from the Cadamosto Seamount shows a resorbed core surrounded by two concentric outer zones (Figure 3.12). The concentric zones are homogeneous and incongruent with curved boundaries. In the associated chemical variations, we observe a decrease in both Mg# and TiO_2 in the outer zones of the crystal, reflecting differentiation in this felsic system (Figures 3.11 and 12). The variation in MnO content in the outer zones, despite the decrease in Mg#, suggests that MnO behaves differently in felsic alkali magmas than their mafic counter parts (Streck, 2008). However, the offset in composition of Mg# and TiO_2 in the two outer zones and the change in MnO also points toward

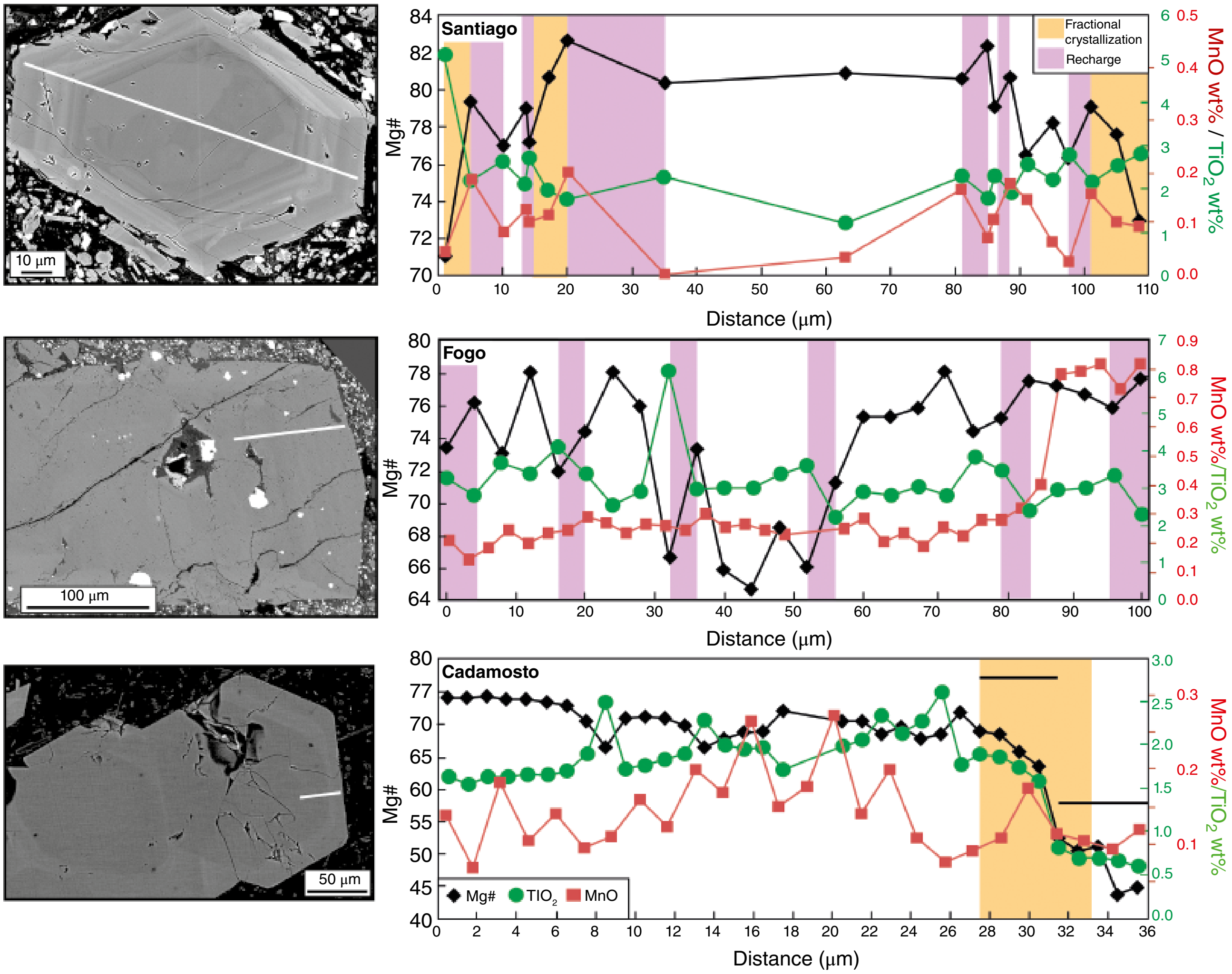

Figure 3.12 Zonation in clinopyroxene from Santiago, Fogo, and the Cadamosto Seamount, shown by Mg# (mol%), TiO_2, and MnO content. Santiago Coastal group of the Flamengos Formation (121-306; Barker et al., 2009); Fogo eruption 1847 (CVF07 pyroxene 11; Rydeblad, 2018); Cadamosto Seamount (D885 J1; Barker et al., 2012). The horizontal black lines mark the outer two zones.

magma mixing or variations in thermal conditions of the magma (>32 µm; Figure 3.12). The small variations in the inner part of the crystal (<27 µm) reflect variations in magma chamber compositional and thermal conditions. The zonation and textures of clinopyroxene crystals from southern Cape Verde indicate that the host magmas were not homogeneous in composition or temperature. This is traced by significant differences in behavior between the major cation species in the mineral structure such as MgO, FeO, and CaO and the trace elements TiO_2, MnO, and Al_2O_3. The latter record the chemical and thermal disequilibrium of the magma chamber (Mollo et al., 2013, 2018; Welsch et al., 2016).

3.4. MAGMA STORAGE IN SOUTHERN CAPE VERDE

The volcanics at Cape Verde are highly alkaline; by contrast, most thermobarometers for igneous minerals are calibrated for subalkaline tholeiitic and calc-alkaline systems (e.g., Neave & Putirka, 2017; Nimis, 1995; Putirka, 2008). The clinopyroxene thermobarometers that are appropriate for alkaline systems often target mafic and ultramafic compositions (Ashchepkov et al., 2011), and are therefore not suited to the range of differentiated compositions observed at Cape Verde. The only available clinopyroxene-melt thermobarometer that has been developed specifically for evolved alkaline systems is calibrated for relatively high K/Na (Masotta et al., 2013). Unfortunately, the lavas from Cape Verde are highly enriched in Na, giving a low K/Na ratio, and thus this formulation is not ideal for clinopyroxene from Cape Verde (Barker et al., 2012, 2019). The only thermobarometer that has been calibrated for a range of alkaline compositions, providing a method for intercomparison between all samples, is the clinopyroxene-melt equilibrium thermobarometer of Putirka (Putirka et al., 1996, 2003; Putirka, 2008). The Putirka clinopyroxene-melt thermobarometer has been widely applied in many alkaline settings (e.g., Klügel et al., 2000, 2005; Nikogosian et al., 2002). It has also been shown to be consistent with independent depth estimates such as seismic tomography, seismic reflection profiles, or earthquakes patterns (e.g., Barker et al., 2019; Longpré et al., 2014). Unfortunately, the data used by Putirka (2008) for calibration of evolved alkali compositions is sparse and therefore also not ideal (Putirka et al., 1996, 2003; Putirka 2008). Hence, we compare the results from the models of Masotta with those of Putirka (Masotta et al., 2013; Putirka et al., 1996, 2003; Putirka 2008). Therefore, we employ models A and B for pressure and temperature respectively from Putirka et al. (2003) for consistency with Hildner et al. (2011, 2012) and also for the evolved compositions equations P-alk and T-alk from Masotta et al. (2013).

The clinopyroxene-melt thermobarometer is based upon jadeite (NaAl) and diopside-hedenbergite (CaMgFe) exchange between clinopyroxene and melt for determination of temperature. The corresponding pressure is estimated from the distribution of the jadeite component (NaAl) between clinopyroxene and the equilibrium melt (Putirka, 2008). Employment of the clinopyroxene-melt equilibrium thermobarometer thus requires demonstration of equilibrium between the clinopyroxene and melt. There are two commonly used approaches to test for equilibrium. First, testing for equilibrium from Fe-Mg partitioning utilizing a Rhodes diagram, with Kd(Fe-Mg) of 0.275 ± 0.067 (Barker et al., 2009, 2012; Putirka, 2008;). A second approach is to employ the variations between clinopyroxene components as observed from the mineral chemistry and calculated from the melt composition (Mollo et al., 2013; Putirka, 2008). Typically, equilibrium is considered to be within ±0.06 DiHd, ±0.07 EnFs, and ±0.02 Jd of unity (Putirka, 1999). Mollo et al. (2013) proposed an additional multicomponent equilibrium test, expressed as ΔDiHd, and tested on the alkaline compositions characteristic of Mt. Etna. The multicomponent equilibrium test derives from a comparison between the clinopyroxene components calculated from the equilibrium with the melt and directly from the clinopyroxene composition.

Ideal mineral–melt pairs are considered to be analysis of groundmass glass and proximal crystal rims. However, it is rare to have much glass in lavas from Cape Verde, which tend to display a microcrystalline groundmass (Barker et al., 2009, 2012; Hildner et al., 2011, 2012). Glassy melt inclusions are typically modified during cooling of volcanic rocks and are therefore not suitable (Baker, 2008). Glass or groundmass separates would provide equilibrium melt compositions for crystal rims, representing the final growth from the melt. Consequently, whole rock compositions that include minerals and groundmass are more likely to represent core compositions (Barker et al., 2009). Employing the whole rock composition of a sample as nominal melts for testing clinopyroxene-melt equilibrium is therefore not only suitable but also necessary to understand the crystallization conditions of the entire crystal population. Equilibrium between clinopyroxene and melt can be further optimized by subtracting the compositions of the modal mineral content from the whole rock composition (Barker et al., 2009). Another approach to find an optimal equilibrium match between clinopyroxene and melt is to select equilibrium melt compositions from a related suite of volcanic rocks (Barker et al., 2015; Neave & Putirka, 2017). The minimum ΔDiHd for data from Santiago, Fogo, Brava, and the Cadamosto Seamount occurs at a temperature difference of 20 °C (Figure 3.13). The ΔDiHd ranges from +0.02 to +0.15; meanwhile, the temperature decreases to 0.4 °C at ΔDiHd of +0.03 and increases up to 75 °C as ΔDiHd increases to a maximum of +0.15. The multicomponent equilibrium appears to be equally good for evolved compositions such as at the Cadamosto Seamount as for the more mafic systems, for example, Fogo.

Evaluation of the oxygen fugacity for the most recent eruptions at Fogo suggests a fO_2 of +0.9 to +2.3 log ΔNNO with a Fe^{3+}/Fe^{total} of 0.21 (Mata et al., 2017). These relatively oxidized conditions are confirmed by ultramafic xenoliths with a fO_2 of up to +2.2 log ΔQFM (Ryabchikov et al., 1995). Other approaches have determined the Fe^{3+}/Fe^{total} as 0.19 to 0.26 at Santo Antão and São Nicolau (Duprat et al., 2007; Holm et al., 2006). Cape Verde, similar to many ocean island basalts, is apparently relatively oxidized compare to mid-ocean ridge basalts. Herzberg and Asimow (2008) calculated primary magma compositions for ocean island basalts globally and found a range in Fe^{3+}/Fe^{total} of 0.15 to 0.25. Their findings are consistent with estimates of oxygen fugacity and Fe^{3+}/Fe^{total} at Cape Verde that represent relatively oxidized conditions. The influence of oxidation on the clinopyroxene compositions may impact the equilibrium, especially those based on Mg# and clinopyroxene components that contain iron (Andújar et al., 2008; Freise et al., 2003). It is possible to vary Fe^{3+}/Fe^{total} in the thermobarometric modeling, and therefore we have adopted a Fe^{3+}/Fe^{total} of 0.21. However, the potential implications for the resulting crystallization conditions

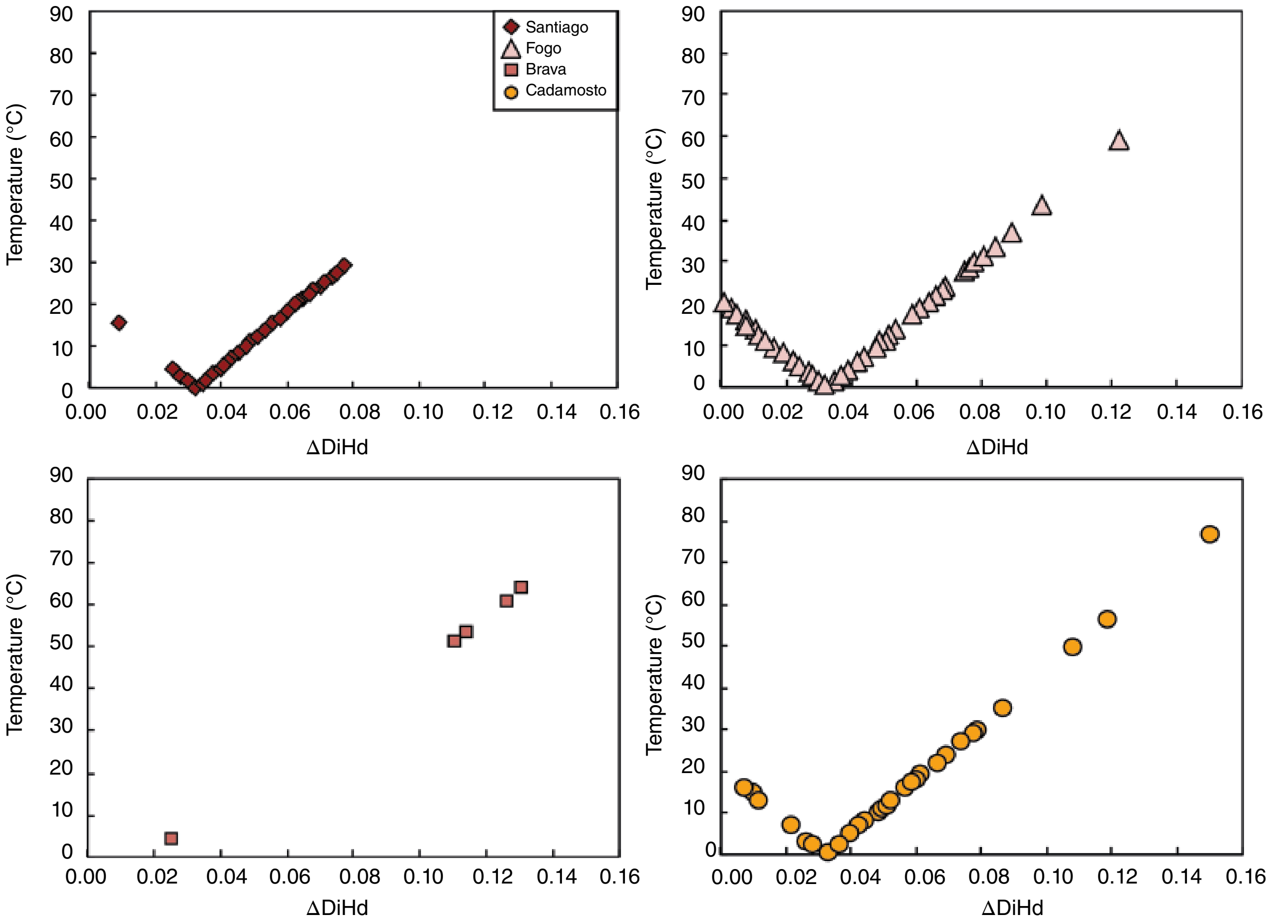

Figure 3.13 Multicomponent equilibrium ΔDiHd versus temperature for diopside-augite from Santiago, Fogo, Brava and the Cadamosto Seamount calculated after Mollo et al. (2013).

are unclear, and the applicability of the calibration data to such oxidized conditions is also uncertain.

Conversion of pressure to depth has been performed with a crustal density of 2800 kg/m^3 for the mafic ocean crust (Barker et al., 2009, 2012; Hildner et al., 2011, 2012). Uncertainties associated with the experimental calibration data are ±33 °C and ±0.17 GPa (SEE; Putirka, 2008), which equates to depths of ±6 km. Hence, much of the range in pressure estimates described below is within error of the method (Figure 3.14).

Turning now to southern Cape Verde, the equilibrium clinopyroxene crystals from Santiago display compositions of 75 to 90 Mg#. These clinopyroxene crystals belong to alkaline basalts, basanites, tephrites, and melanephelinites and are in equilibrium with whole rock compositions in the range of 52 to 65 Mg# (ΔDiHd of 0.01 to 0.08; Figures 3.9 and 3.13; Barker et al., 2009). The corresponding crystallization conditions are temperatures of 1165 to 1255 °C and pressures of 0.40 to 1.15 GPa (Figure 3.14; Barker et al., 2009).

From Fogo, the clinopyroxene mineral chemistry shows the highest frequency compositions between 60 and 85 Mg# (Figure 3.10). The host rocks are tephrite, basanite, foidite, and tephriphonolite, and the equilibrium melt compositions have between 30 and 54 Mg# (ΔDiHd of <0.12; Figures 3.9 and 3.13; Hildner et al., 2011, 2012; Rydeblad, 2018). The resulting crystallization conditions are 1010 to 1255 °C and 0.45 to 1.35 GPa, which compare well with existing data of 1010 to 1150 °C and 0.42 to 0.90 GPa for pre-eruptive magma storage conditions (Hildner et al., 2011, 2012; Klügel et al., 2020; Mata et al., 2017). Mata et al. (2017) further divide the crystallization conditions for the 2014–2015 eruption at Fogo by host magma into 1045 to 1065 °C and 0.56 to 0.78 GPa for phonotephrites and 1100 to 1145 °C at 0.70 to 0.90 GPa for tephrites. Additionally, Klügel et al. (2020) constrain rim crystallization associated with the 2014–2105 eruption to 1045 to 1052 °C at 0.42 to 0.70 GPa for phonotephrites and 1123 to 1134 °C at 0.60 to 0.82 GPa for tephrites. This study extends the range of crystallization

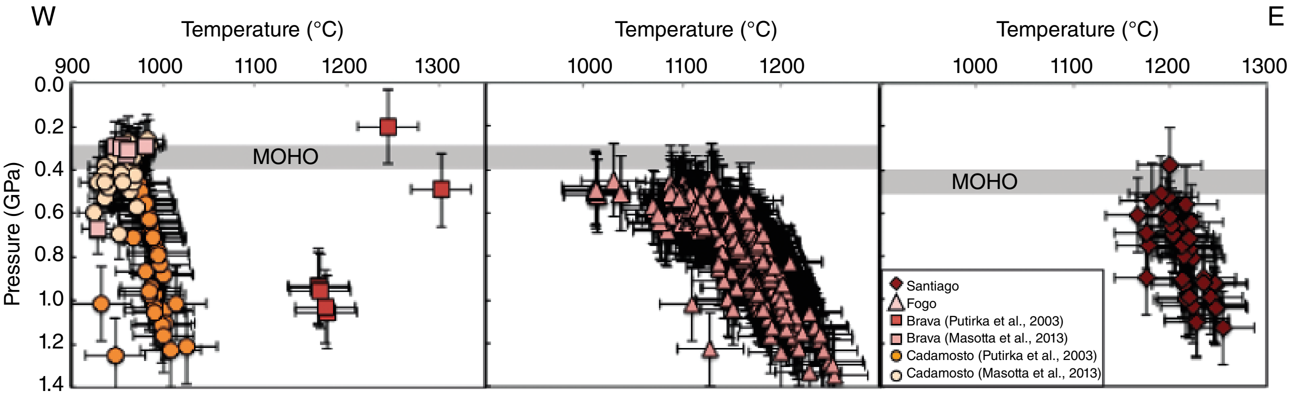

Figure 3.14 Thermobarometry for Santiago, Fogo, Brava, and the Cadamosto Seamount. The Moho is from Lodge & Helffrich 2006 and Pim et al. 2008. Sources: Barker et al. (2009, 2012); Hildner et al. (2011, 2012); Rydeblad (2018).

conditions to higher temperatures and pressures, thereby also characterizing the deeper part of the magma storage system (Figure 3.14; Hildner et al., 2011, 2012; Klügel et al., 2020; Mata et al., 2017).

There are only a few analyses of diopside-augite from Brava that are hosted by nephelinite with 47 to 62 Mg# (Weidendorfer et al., 2016). They show an equilibrium, ΔDiHd, of 0.02 to 0.13, with low Na melt compositions of Mg# 20 to 32 (Figures 3.10 and 3.13). The Putirka et al. (2003) models estimate crystallization at 1170 to 1300 °C and 0.2 to 1.0 GPa (Figure 3.14). In comparison, the Masotta et al. (2013) model indicates crystallization at lower temperatures of 930 to 980 °C and 0.29 to 0.67 GPa and shows less scatter than the estimate from Putirka et al. (2003).

Diopside-augite from the Cadamosto Seamount has Mg# 40 to 75 (Figure 3.10; Barker et al., 2012). The corresponding whole rocks are phonolite to phononephelinite, and equilibrium melt compositions are 29 to 37 Mg# with a ΔDiHd of 0.01 to 0.16 (Figures 3.9 and 3.13; Barker et al., 2012). The Putirka et al. (2003) model gives crystallization conditions of 970 to 1025 °C and 0.45 to 1.35 GPa, whereas the Masotta et al. (2013) model indicates 925 to 980 °C and 0.26 to 0.70 GPa (Figure 3.14). Hence, the results from the Masotta et al. (2013) model overlap with those estimated by the model of Putirka et al. (2003) and extend them to lower temperatures and pressures. These evolved magmas from Brava and the Cadamosto Seamount crystallized at lower temperatures compared to the clinopyroxene from Santiago and Fogo (Figure 3.14; Barker et al., 2012).

The clinopyroxene crystals feature significant zonation, through which we track the magma chamber dynamics for samples from Fogo. Rapid decreases in clinopyroxene Mg# occur under several scenarios, sometimes with no discernible temperature or pressure changes, suggesting mixing processes (Figure 3.15a). A second scenario observed in the zonation is a rapid decrease in clinopyroxene Mg# with a decrease in temperature on the order of 30 °C and simultaneous decrease in pressure suggesting convection and ascent within the magma reservoir (Figure 3.15b). By contrast, a rapid increase in clinopyroxene Mg# occurs with large variations in temperature (Figure 3.15b). This implies that the thermal and compositional gradients are not perfectly contemporaneous and that thermal and chemical mixing occur at different rates, although there are also examples of a gradual increase in clinopyroxene Mg# corresponding to slight increases in temperature and pressure (Figure 3.15c). In some places, the outer rims record a decrease in clinopyroxene Mg#, with simultaneous decreases in temperature and pressure (Figure 3.15d), indicating magma evolution during ascent within the magma reservoir.

Integrating the thermobarometry from the different locations, we find that crystallization was in the range of 12 to 40 km (Figures 3.14 and 3.16). Therefore, the magma storage beneath southern Cape Verde occurs below the Moho in the oceanic lithospheric mantle. At Santiago and Fogo, the highest frequency of crystallization is at 30 to 40 km (Figure 3.16; Barker et al., 2009; Hildner et al., 2011, 2012; Rydeblad, 2018). We also observe in the samples from Fogo that the rims crystallize with highest frequency between 20 and 30 km and extend to lower pressures approaching the Moho (Figure 3.14). This suggests that the more mafic magmas begin to crystallize clinopyroxene deep in the system and move upward toward the Moho as crystallization continues and zonation and final rim compositions progressively form (Figure 3.15d). Evolution of magma storage depths with differentiation is consistent with the increase in Al_2O_3 content up to 13 wt% as MgO content decreases, signaling magmatic differentiation associated with lower pressures

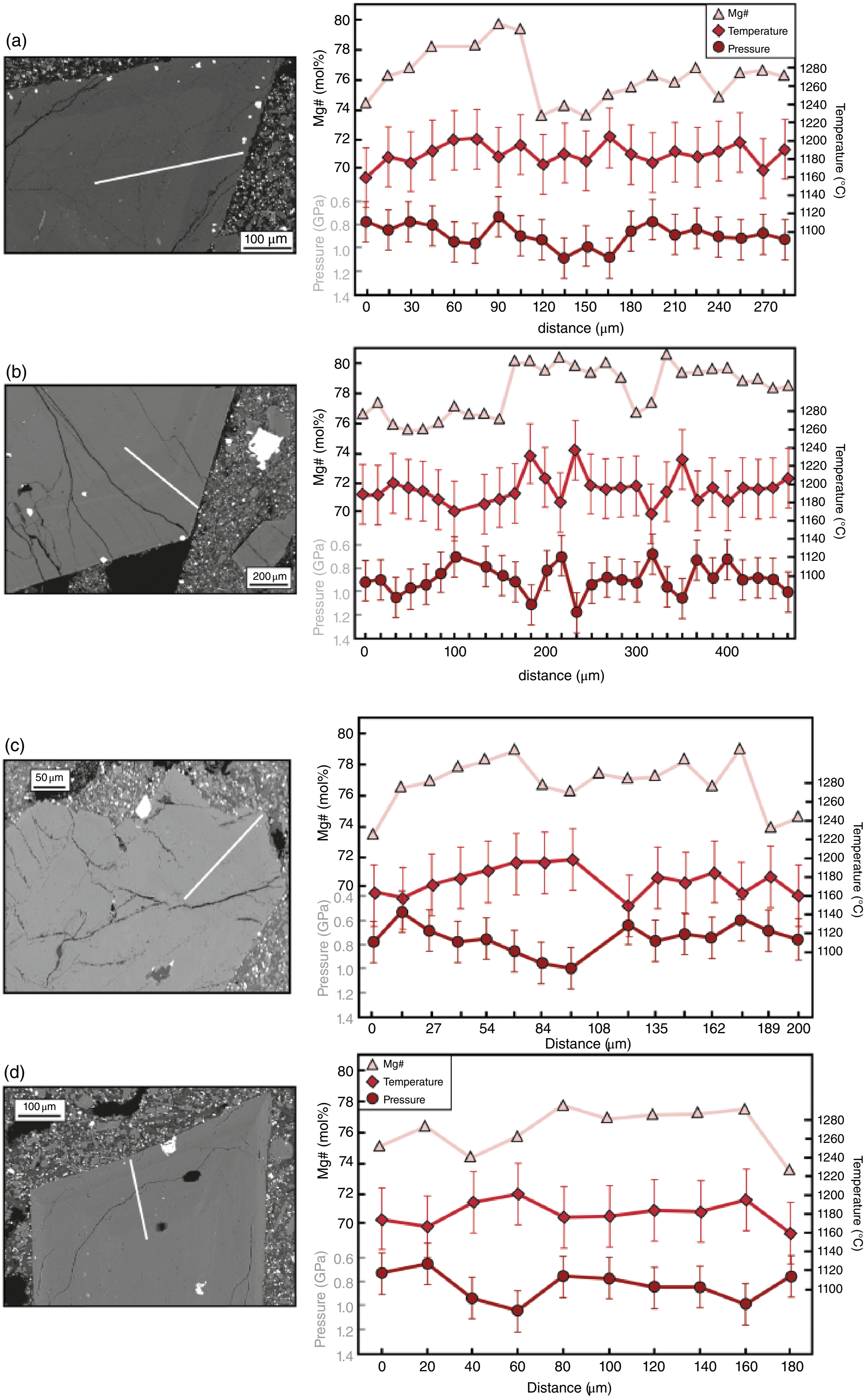

Figure 3.15 Crystallization conditions; temperature and pressure, with composition for zoned clinopyroxene from Fogo. (a) Prehistoric eruption CVF05 pyroxene 8, (b) eruption in 1785 CVF08 pyroxene 15, (c) eruption in 1799 CVF09 pyroxene 5, and (d) eruption in 1847 CVF06 pyroxene 7. Source: Rydeblad (2018).

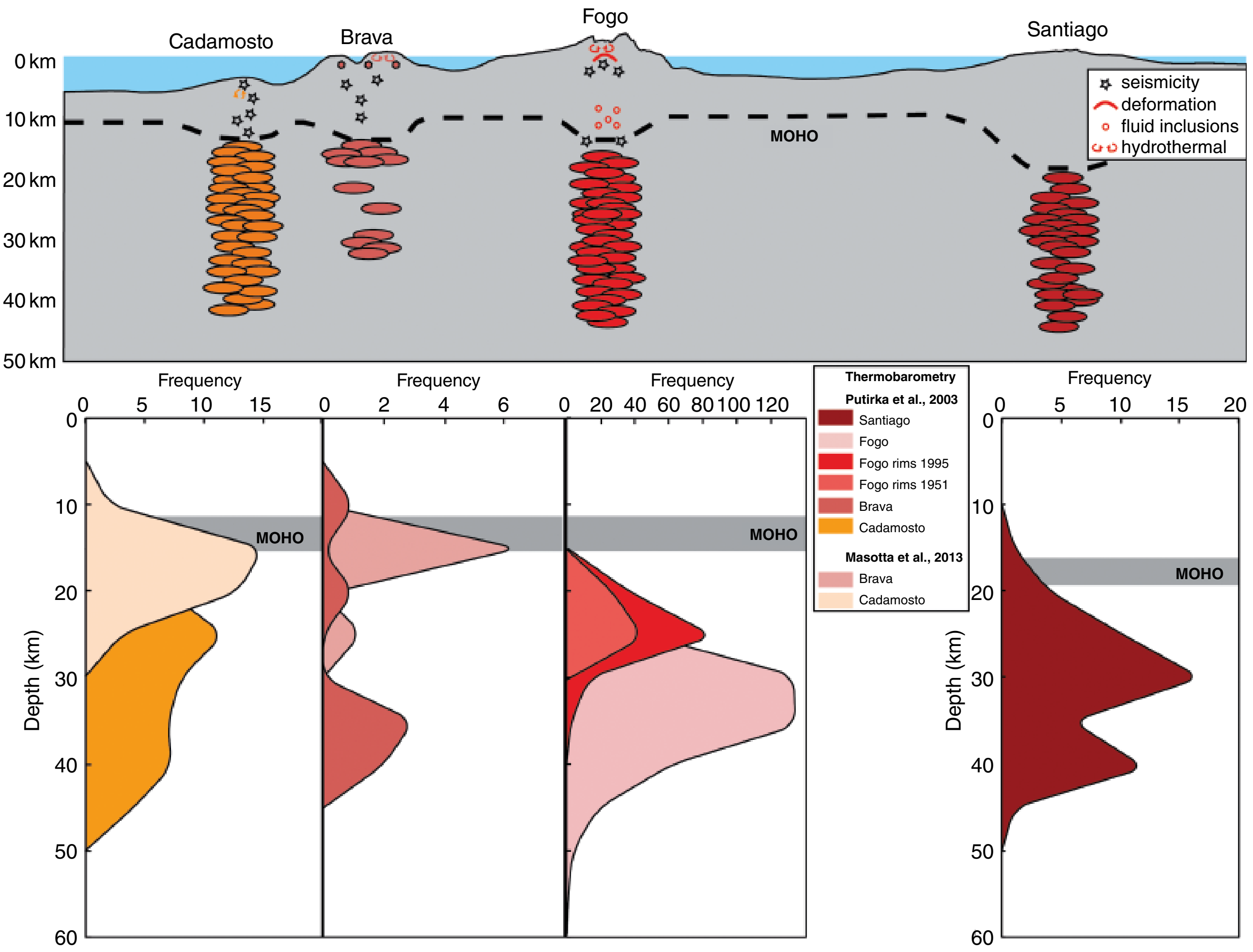

Figure 3.16 Crystallization depth and model for the magma plumbing system beneath Santiago, Fogo, Brava, and the Cadamosto Seamount. The shallow magma storage system is illustrated by fluid inclusion barometry as well as seismicity, deformation, and the active hydrothermal systems. Shallow crystallization is inferred at Brava. Data sources: Da Silva et al., 1999; Amelung & Day, 2002; Barker et al., 2009, 2012; Ryan et al., 2009; www.geomapapp.org; Heleno et al., 2006; Grevemeyer et al., 2010; Hildner et al., 2011, 2012; Faria & Fonseca, 2014; Rydeblad, 2018. The Moho is from Lodge & Helffrich 2006 and Pim et al. 2008.

of crystallization (Figure 3.11; Marianelli et al., 1999; Morgan et al., 2004). Hildner et al. (2012) proposed that the pre-eruptive magma storage conditions become shallower with time in the historic eruptions. However, no trends with time appear when we investigate the crystallization conditions of the whole range of clinopyroxene compositions. The absence of systematic temporal variations is confirmed by clinopyroxene from the 2014–2015 eruption recording pressures of 0.40 to 0.9 GPa, which are mostly deeper than for the 1995 and 1951 eruptions (Klügel et al., 2020; Mata et al., 2017).

The dominance of the deep magma storage zone indicates that the magmatic processes of differentiation, recharge, mixing, and potentially convection recorded by the crystal populations take place in this deep magma storage zone (Figures 3.12, 3.14, and 3.15). The accumulation of antecrysts and aggregation of crystal populations is likely to also occur in this deep magma storage zone before magmas ascend and erupt. Thus, the resorbed kaersutite crystals frequently found in lavas from Fogo probably crystallized in the oceanic lithospheric mantle, consistent with amphibole thermobarometry yielding pressures of approximately 0.6 GPa (Klügel et al., 2020; Mata et al., 2017). Subsequently they would have been incorporated into magmas with starkly different compositions, leading to their breakdown (Hildner et al., 2011, 2012).

3.4.1. Controls on the Depth of Magma Storage

The location of the magma storage is controlled by the crustal structure beneath the islands and seamounts of the southern Cape Verde archipelago. The islands and seamounts stand several kilometers above the seafloor at approximately 4000 m below sea level (mbsl), and beneath that is 1 to 2 km of sediments (Figure 3.3; Lancelot et al., 1978; Pim et al., 2008). The sediments overlie relatively old 130–135 Ma Central Atlantic ocean crust that extends down to the Moho at depths of 12 to 18 km, which decreases from east to west (Ali et al., 2003; Lodge & Helffrich, 2006; Pim et al., 2008). Hence, the deep mantle plume source generates magmas that ascend into the oceanic lithospheric mantle, where they stagnant below the mantle-crust boundary (Figure 3.16; Barker et al., 2009).

The density of the ocean islands and seamounts, as well as the ocean crust extending down to the crust–mantle boundary at 12 to 18 km beneath Cape Verde, is estimated to be 2750 to 2800 kg/m^3 (Ali et al., 2003; Lodge & Helffrich, 2006; Pim et al., 2008). The sediments would be expected to provide a low-density layer between the mafic ocean crust and the Cape Verde islands and seamounts (Pim et al., 2008). The expected upper mantle density is 3100 kg/m^3 (Tenzer et al., 2013). The density contrast between the upper mantle and the oceanic crust evidently controls the depth and pressures of magma storage (Figures 3.14 and 3.16). The basanite, tephrite, and melanephelinite at Fogo and Santiago have calculated densities of 2650 to 2800 kg/m^3 (Bottinga & Weill, 1970; Bottinga et al., 1982). This range is similar to the mafic ocean crust and extends to slightly lower densities, and therefore the mafic magmas would be expected to pool at the Moho or slowly ascend. However, the actual density of magma is a function of both the melt density and the crystal cargo. Many of the erupted basanitic lavas have crystal content of 5% to 20% and even more in ankaramite samples (Barker et al., 2009). Such crystal cargoes of dominantly clinopyroxene and olivine would increase the density of the magma, leading to a decrease in buoyancy and stagnation of the magma below the crust–mantle boundary.

Common magma storage depths, irrespective of magma composition and age, are likely associated with significant magma intrusion, solidification, and formation of crystal mush zones. This would serve to underplate the oceanic crust with mafic materials, building a magma storage zone of lower density than the surrounding upper mantle lithologies (Klügel et al., 2015, 2020). Evidence for this comes from Fogo lavas that host cumulate nodules, containing olivine, clinopyroxene, kaersutite, spinel, and phlogopite (Hildner et al., 2012). The spinel, kaersutite, and phlogopite are consistent with crystallization in the oceanic lithospheric mantle. Therefore, these nodules are likely sampling cumulates formed in the deep magma storage zone. Furthermore, crustal thickening associated with underplating and potentially shallower intrusions contributes to localized uplift on individual islands, such as observed on Santiago and Brava (Madeira et al., 2010; Ramalho et al., 2010a, 2010b).

The phonolites and syenites at Brava and the Cadamosto Seamount have calculated densities of 2350 to 2480 kg/m^3, and even the clinopyroxene-equilibrium melts show densities of 2450 to 2480 kg/m^3, consistent with recent experimental constraints (Bottinga & Weill, 1970; Bottinga et al., 1982; Seifert et al., 2013). Such densities for phonolitic magma carrying relatively low-density minerals should promote magma buoyancy and ascent through the ocean crust. Although the viscosity of magma would also change during differentiation and influence the magma dynamics, the resulting increase in viscosity of the magma plus the entrained crystal population potentially inhibit magma ascent. Crystal contents of 40% to 50% cause the magma to behave as a rigid crystal network, trapping it in the magma storage zone (Cooper, 2017). The crystal content ranges from 10% to 50% for the Cadamosto Seamount; thus, the crystal assemblages along with the magma evolution control the viscosity and thereby promote continued magma storage in the upper oceanic lithospheric mantle (Barker et al., 2012). However, it is likely that the host magma carrying the existing crystal cargo would have continued to evolve with a corresponding density change to 2350 kg/m^3. Such a change in density provides a larger density contrast between the mafic ocean crust and the most evolved phonolitic compositions that may have promoted magma ascent.

3.5. INSIGHTS INTO THE SHALLOWER MAGMATIC SYSTEM

Evidence of magmatic processes occurring shallower in the crust at Cape Verde is limited. At the Cadamosto Seamount, the majority of the diopside-augite crystallization occurs below the Moho in the deep magma storage zone (Figure 3.16). However, the magma differentiation and aegirine-augite crystallization is unaccounted for by this crystallization model. Furthermore, at the Cadamosto Seamount, the $\delta^{18}O$ for clinopyroxene (diopside-augite) have mantle-derived values of +5.3‰, whereas the feldspathoids show $\delta^{18}O$ of +6.3‰ to +7.1‰, elevated over the mantle equilibrium value of +6.25‰ ($\delta^{18}O$ SMOW; Barker et al., 2012; Zhao & Zheng 2003). In addition, the sulfur isotopes for whole rock powders gave $\delta^{34}S$ of +4.7‰ to +5.9‰, highly enriched compared to mantle values with $\delta^{34}S$ of +0.8‰± 0.2‰ (Barker et al., 2012;

Sakai et al. 1984). Barker et al. (2012) interpreted these feldsapathoid and whole rock isotope signatures to be caused by assimilation of a few percent of oceanic sediments and anhydrite. Hence, the magmas associated with the Cadamosto Seamount interact with the sedimentary crustal layer, which is likely located at 4 to 6 km below sea level (Figures 3.3 and 3.16; Lancelot et al., 1978; Pim et al., 2008). This evidence suggests that less differentiated magmas ascend from the deep magma storage zone and evolve to phonolitic compositions through assimilation during storage in the upper crust. Seismicity in the vicinity of the Cadamosto Seamount also records crustal magmatic activity at depths of 0.5 to 15 km, which is likely associated with shallow hydrothermal processes and slightly deeper volcano-tectonic events such as magma intrusion in the ocean crust (Figure 3.16; Grevemeyer et al., 2010). The volcano-tectonics events provide evidence for crustal magma storage, consistent with assimilation of sedimentary components by the magmas.

Brava hosts a carbonatite-silicate intrusive complex, where the silicate rock types are represented by ijolite, nephelinite, and nepheline syenite (Weidendorfer et al., 2016). Extreme fractional crystallization takes place, up to 90%, which is reflected in the large range of clinopyroxene compositions of 5 to 65 Mg# (Figure 3.10). The presence of clinopyroxene from 3% to 90% fractional crystallization is consistent with the wide range in clinopyroxene compositions (Figure 3.10). Significant crystallization may have occurred in the deep magma storage zone (<30%; Weidendorfer et al., 2016), in the presence of olivine, perovskite, and magnetite as illustrated by the crystallization of clinopyroxene with 47 to 62 Mg# at and below the Moho in the nephelinites from Brava (Figure 3.13). Given the challenges of mobilizing magmas containing more than 40% to 50% crystals (Cooper, 2017), deep crystallization is likely followed by magma ascent and intrusion into the upper crust beneath the volcanic edifice, where *in situ* differentiation and crystallization continue. The result is crystallization of the majority of the aegirine-augite and other phases of the syenite in the ocean crust. Persistent and relatively shallow magma storage is required to provide the heat source for the active geothermal system on Brava that contains a mixture of magmatic and biogenic gases (Dionis et al., 2015a). In addition, Brava is seismically active, recording volcano-tectonic events at depths of 2 to 10 km in the ocean crust and volcanic edifice (Figure 3.16; Faria & Fonseca, 2014). The seismicity is consistent with continued magma differentiation in the volcanic edifice.

There is evidence for temporary magma storage at Fogo, associated with magma ascent and eruption. Olivine and clinopyroxene hosted fluid inclusions from the eruptions in 1951, 1995 and 2014/2015 re-equilibrated at depths of 8 to 13 km in the lower crust (Figure 3.16; Hildner et al., 2011, 2012, Klügel et al., 2020) Hildner et al. (2011, 2012) report relatively rapid re-equilibration during stagnation at these lower crustal depths over timescales of hours to days. Hence, eruption-related temporary magma pooling occurs in the lower ocean crust. Seismicity associated with the 1995 eruption at Fogo locates depths of magma storage between 1 and 5 km in the volcanic edifice and oceanic crust (Figure 3.16; Da Silva et al., 1999). Furthermore, the surface deformation signals from the 1995 eruption have been explained by a 2-km-deep magma source, fed from a conduit that extends to depths of more than 16 km (Figure 3.16; Amelung & Day, 2002). Precursory seismicity to the 2014 eruption commenced in early October before the eruption on 23 November 2014 (Fernandes & Faria, 2015). The initial earthquakes were recorded at depths exceeding 15 km, associated with the sub-Moho magma storage zone. On 22 November, the seismicity was dominated by high-frequency and high-magnitude long-period earthquakes at depths of 2 to 4 km (Fernandes & Faria, 2015; Jenkins et al., 2017). The 2014/2015 surface deformation is consistent with a dike propagating vertically from sub-Moho depths and arriving below Pico do Fogo, where the magma flowed laterally toward the southwest before erupting (González et al., 2015). Therefore, the transient eruption-related magma pathways can be traced from the sub-Moho magma storage zone, through the lower ocean crust to magma pockets in the volcanic edifice feeding the magma to the eruption fissure.

Long-term magma storage in the crust is suggested by shallow seismicity and the sustained geothermal system. Fogo hosts a geothermal system with typical temperatures of 90–100 °C recorded at degassing fumeroles and values up to 130 to 190 °C reported in the months leading up to the 2014 eruption (Dionis et al., 2015b; Risby & Sandback 2014). The active degassing is composed of a mixture between magmatic and biogenic-atmospheric gases (Dionis et al., 2015b). Shallow seismicity at depths of 300 to 400 m below the Chã das Caldeiras plateau is confirmed by drilling to correspond to the geothermal system (Faria & Fonseca, 2014). This requires a relatively shallow long-term heat source to sustain the geothermal activity, although it has not yet been detected by geophysical methods (Caranova & Silva, 2012). The heat source may be associated with volcano-tectonic earthquakes at depths of up to 7 km, which would imply that these earthquakes are caused by magma intrusion (Faria & Fonseca, 2014).

This information on magma storage depths and magma ascent timescales provides vital information to scientists at the Institute of National Meteorology and Geophysics and the University of Cape Verde attempting to interpret seismicity, deformation, and volcanic gas geochemistry.

The information provided thus contributes to the decision making and communication with the National Civil Protection of Cape Verde in times of impending volcanic crisis (Dionis et al., 2015a,b; Faria & Fonsesa, 2014). Additional information on the volcanic hazards offered by Earth science comes in the form of volcanic hazard maps. Richter et al. (2016) have examined the probable pathways of lava flows following the 2014–2015 eruption. Their results suggest that the locations of Portela and Bangaeira continue to be a risk of future lava flows.

3.6. OCEAN ISLANDS GLOBALLY

The southern chain of the Cape Verde hotspot therefore exhibits a predominantly deep magma storage zone at depths of between 12 and 40 km traced by clinopyroxene thermobarometry, seismicity, and deformation (Figure 3.17). Magma ascent through the ocean crust is documented by fluid inclusions and seismicity. In addition, shallow crustal magma storage is found by seismicity and deformation in the upper 5 km of the oceanic crust and volcanic edifice. Prior to the eruption in 2014/2015, seismicity traced the magma ascent from below the Moho, through the crust to the upper crust in the months leading up to the eruption (Fernandes & Faria, 2015; González et al., 2015; Jenkins et al., 2017).

A comparison with the Canary Islands suggests that clinopyroxene-equilibrium thermobarometry and seismicity also display similarly deep magma storage relative to a Moho depth of 13 to 15 km (Figure 3.17; Ranero et al., 1995). Gran Canaria records magma storage below the Moho at depths of 15 to 36 km with a subsidiary zone at 3 to 4 km (Table 3.1; Aulinas et al., 2010). The island of Tenerife also shows deep magma storage at 20 to 45 km (Longpré et al., 2008). Estimates for magma storage at La Palma also range from 12 to 45 km, placing the magma storage within the oceanic lithospheric mantle (Barker et al., 2015; Galipp et al., 2006; Klügel et al., 2000; 2005; Nikogosian et al., 2002). Magma storage for the 2011 eruption at El Hierro has been reported to occur at depths of 17 to 24 km consistent with seismic activity (Longpré et al., 2014, and references therein). Fluid inclusions and deformation suggest magma storage in the lower crust (Longpré et al., 2014). Further, investigation of the deformation places a magma storage zone in the upper crust (Figure 3.17). In the 2011 eruption offshore El Hierro, the seismicity migrated upward, laterally tracking the movement of magma supplied from sub-Moho magma storage through the crust to eruption at the seafloor (González et al., 2013).

At Madeira, magma storage from clinopyroxene-equilibrium thermobarometry has been shown to occur at depths of 15 to 35 km and therefore deep relative to Moho depths of 14 to 15 km (Figure 3.17; Klügel & Klein, 2006; Schwarz & Klügel, 2004). Furthermore, fluid inclusions record temporary stagnation in the lower and upper crust (Klügel & Klein, 2006; Schwarz & Klügel 2004).

The Azores also record deep crystallization of clinopyroxene, olivine, and plagioclase as well as entrapment of primary fluid inclusions (Figure 3.17; Beier et al., 2006; Dias et al., 2007; Madureira et al., 2011; Renzulli & Santi, 2000; Zanon et al., 2013; Zanon & Pimentel 2015). In the lower crust, magma storage is recorded by continued crystallization of clinopyroxene, along with fluid inclusion equilibration and the appearance of seismicity (Beier et al., 2006; Dias et al., 2007; Madureira et al., 2011; Renzulli & Santi 2000; Silva et al 2012; Zanon et al., 2013; Zanon & Pimentel 2015). A shallow crustal magma pocket is picked out by seismicity, water solubility, and plagioclase-olivine experimental phase petrology (Jeffery et al., 2016; Renzulli & Santi 2000; Silva et al., 2012).

Clinopyroxene crystallization in basanites traces magma storage at Tristan da Cunha to the oceanic mantle lithosphere and for more evolved trachyandesite to the middle of the ocean crust (Figure 3.17; Weit et al., 2017). Earthquakes were felt on Tristan da Cunha commencing several months prior to the eruption in 1961 and again associated with the nearby submarine eruption in 2004 (O'Mongain et al., 2007). These earthquakes showed high signal-to-noise ratios on the nearest seismometers, and thus the earthquakes were deemed to have shallow epicenters, and the seismicity was employed to locate the eruption to 40 to 50 km south of Tristan da Cunha (O'Mongain et al., 2007).

Information on the magma storage system at Ascension is derived from melt inclusions, placing stagnation in the lower crust (Figure 3.17; Chamberlain et al., 2016). In addition, seismic data suggest volcano-tectonic events, some of which occur in the shallow crust of the Ascension rift zone (Hanson et al., 1996).

In the Pacific Ocean, the two hotspots with records of magma plumbing systematics are Hawaii and the Galapagos. Investigations at Hawaii record clinopyroxene crystallization in the oceanic lithosphere and through to the lower crust (Figure 3.17; Chatterjee et al., 2005; Hammer et al., 2016; Poland et al., 2015; Putirka et al. 1996; Putirka 1997). However, seismicity occurs in the upper crust beneath the central volcanoes and extends into the middle crust at rift zones. Wolf Island in the Galapagos shows clinopyroxene crystallization in the lower crust (Stock et al., 2018). Lower crustal magma storage is confirmed by deformation, which places magma storage at 6 to 9 km depth as well as in the volcanic edifice at approximately 1 km (Stock et al., 2018).

Reunion hotspot in the Indian Ocean hosts the Piton de la Fournaise volcano, which frequently displays

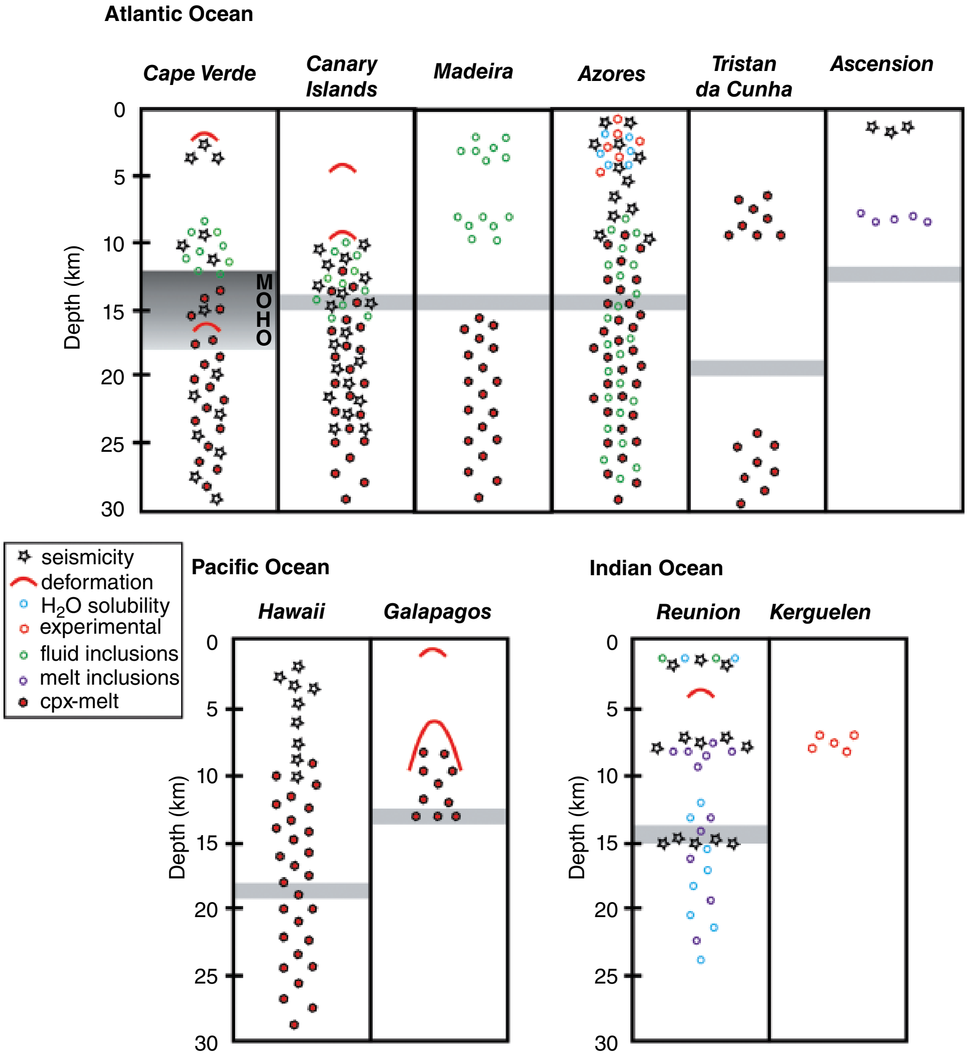

Figure 3.17 Schematic of the magma storage systems for ocean islands globally including results from clinopyroxene-melt thermobarometry, fluid inclusions, melt inclusions, experimental petrology deformation, and seismicity. Cape Verde: Da Silva et al 1999; Amelung & Day 2002; Lodge & Helffrich, 2006; Pim et al., 2008; Barker et al., 2009, 2012; Grevemeyer et al., 2010; Hildner et al., 2011, 2012; Faria & Fonseca 2014; Fernandes & Faria, 2015; Vales et al., 2015; Jenkins et al., 2017; Leva et al., 2019; Mata et al., 2017; this study. Canary Islands: Klügel et al., 2000; 2005; Galipp et al., 2006; Longpré et al., 2008, 2014; Aulinas et al., 2010; Barker et al., 2015; González et al., 2013. Madeira: Schwarz & Klügel 2004; Klügel & Klein, 2006. The Azores; Renzulli & Santi 2000; Beier et al., 2006; Dias et al., 2007; Silva et al 2012; Jeffery et al., 2016; Madureira et al., 2008; Zanon et al., 2013; Zanon & Pimentel 2015. Tristan da Cunha; Geissler et al., 2016; Weit et al., 2017. Ascension: Klingelhöfer et al., 2001; Hanson et al., 1996; Chamberlain et al., 2016. Hawaii; Putirka et al. 1996, Putirka 1997; Chatterjee et al., 2005; Poland et al., 2015; Hammer et al., 2016. Galapagos: Stock et al., 2018. Reunion: Bureau et al., 1998; Famin et al., 2009; Peltier et al. 2009; Di Muro et al., 2014; Fontaine et al., 2014. Kerguelen: Freise et al., 2003.

volcanic activity, including an eruption in 2007. Magma storage at the Moho and below is traced by seismicity, as well as by melt inclusions and volatile solubility, which extend to much greater depths (Figure 3.17; Bureau et al., 1998; Di Muro et al., 2014; Peltier et al. 2009). Mid-crustal magma stagnation is indicated by melt inclusions and seismicity, whereas shallow magma storage below the volcanic edifice is shown by fluid inclusions, volatile solubility, and seismicity above a deformation zone (Figure 3.17; Bureau et al., 1998; Di Muro et al., 2014; Famin et al., 2009; Fontaine et al., 2014; Peltier et al., 2009). Notably for the 2007 eruption at the Piton de la

Table 3.1 Compilation of Magma Storage Data for Ocean Islands

Atlantic Ocean					
Cape Verde	Canary Islands	Madeira	Azores	Tristan da Cunha	Ascension
1 to 5 km seismicity, deformation	4.5 km deformation	2 to 4 km fluid inclusions	2 to 4 km water solubility, fractionation, seismicity	2 to 4 km water solubility, fractionation, seismicity	1.5 to 2 km seismicity
8 to 13 km fluid inclusions, seismicity	10 to 16 km fluid inclusions, deformation	8 to 10 km fluid inclusions	>8 km fluid inclusions, cpx-melt, seismicity	6 to 10 km cpx-melt	8.5 km melt inclusions
12 to 18 km Moho	14 km Moho	14 to 15 km Moho	14 km Moho	19 km Moho	12 to 13 km Moho
13 to 46 km cpx-melt, seismicity, deformation	12 to 45 km cpx-melt, seismicity	15 to 35 km cpx-melt	<30 km cpx-melt, fsp-ol melt, fluid inclusions	24 to 36 km cpx-melt	
Da Silva et al., 1999; Amelung & Day, 2002; Lodge & Helffrich, 2006; Pim et al., 2008; Barker et al., 2009, 2012; Grevemeyer et al., 2010; Hildner et al., 2011, 2012; Faria & Fonseca 2014; Fernandez & Faria, 2015; Vales et al., 2015; Jenkins et al., 2017; Leva et al., 2019; Mata et al., 2017; this study.	Klügel et al., 2000, 2005; Galipp et al., 2006; Longpré et al., 2008, 2014; Aulinas et al., 2010; Barker et al., 2015; González et al., 2013.	Schwarz et al., 2004; Klügel & Klein, 2006	Renzulli & Santi, 2000; Beier et al., 2006; Dias et al., 2007; Silva et al., 2012; Jeffery et al., 2016; Madureira et al., 2008; Zanon et al., 2013; Zanon & Pimentel, 2015	Geissler et al., 2016; Weit et al., 2017	Klingelhöfer et al., 2001; Hanson et al., 1996; Chamberlain et al., 2016

Pacific Ocean		Indian Ocean	
Hawaii	Galapagos	Reunion	Kerguelen
2 to 4 km (<10 km) seismicity	1 km deformation	0.5 to 2.5 km water solubility, melt inclusions, seismicity	
9 to 18 km cpx-melt	8 to 13 km cpx-melt, deformation	7 to 14 km water solubility, melt inclusions, seismicity	6 to 8 km experimental
18 to 19 km Moho	13 km Moho	14 to 15 km Moho	
19 to 46 km cpx-melt		15 to 24 km water solubility, melt inclusions, seismicity	
Putirka et al., 1996; Putirka 1997; Chatterjee et al., 2005; Poland et al., 2015; Hammer et al., 2016	Stock et al., 2018	Bureau et al., 1998; Famin et al., 2009; Peltier et al., 2009; Di Muro et al., 2014; Fontaine et al., 2014	Freise et al., 2003

Fournaise volcano, the seismicity started shallow and penetrated downward with time, as the eruption was fed from progressively deeper (Massin et al., 2011).

Studies of the magma plumbing system associated with the volcanic islands of the Kerguelen archipelago are scarce, partly due to their inaccessibility and relatively evolved character often hosting phonolites (e.g., Freise et al., 2003; Quilty & Wheller, 2000). However, several islands seem to be volcanically active, as observed by passing vessels on long ocean voyages (Quilty & Wheller, 2000). Volcanic eruptions have been reported from Heard Island in 1910, 1948 to 1954, 1985 to 1987, and 1996, and a submarine eruption likely occurred in 1992. An eruption was reported from McDonald Island in 1997, and satellite images show evidence for an eruption in 2001 (Stephenson et al., 2005; Quilty & Wheller, 2000; Wunderman, 2003). The only constraints on the magma storage suggest mid-crustal magma evolution of phonolitic magmas based on experimental petrology (Figure 3.17; Freise et al., 2003). Given the recent history of eruptions in the Kerguelen archipelago and potential hazard for shipping, we recommend detailed investigation into the magma storage system. Sample material exists from several of the islands that can be used for petrological investigation (Barling et al., 1994; Freise et al., 2003), and InSAR would provide useful insights into the shallow magma storage system without the need for an expedition or deployment of equipment.

This comparison shows that deep magma storage is common to ocean islands; however, the shallow crustal magma storage systems vary considerably and are therefore likely controlled by local factors opposed to the tectonic setting (Figure 3.17). Magma storage in the crust may be controlled by density differences such as the transition between the ocean crust and sediments, the presence of which will vary depending on the supply of sedimentary materials to the ocean islands. Sedimentary layers provide a low-density zone between the mafic ocean crust and the base of the volcano, hence creating an opportunity for magmas to stall. Evidence for magma–sediment interaction is observed in lavas from Cape Verde, and seismicity, plus intrusions at this level, likely contribute to local uplift at Santiago and Brava (Barker et al., 2012; Da Silva et al., 1999; Fernandes & Faria, 2015; Ramalho et al., 2010a, 2010b). Magmas stalling deeper in ocean crust may be influenced by the gabbro–dike or lava–dike transitions, where porosity and permeability change. Furthermore, at these contacts, the ocean crust changes from massive gabbro to vertically aligned dikes and then to horizontal lava flows and random orientations of pillow lavas in the volcanic pile. Such changes, which potentially modify the relationship between the magma and crust, lead to readjustment of magma flow. The characteristics of magmatic conduits will also influence magma ascent, with high permeability associated with fractures or faults aiding direct magma ascent, whereas sealing of previous pathways may enforce stalling of magma. Some ocean islands, such as Tenerife, Canary Islands, have well-developed rift zones, which may promote magma ascent (Carracedo et al., 2007). The regional fracture zones that potentially control the alignment of volcanic islands in Cape Verde likely provide effective pathways for magma ascent (Jacobi & Hayes, 1982; Klerkx et al., 1974; Le Pichon & Fox, 1971). Furthermore, magmatic properties may also influence magma dynamics on ascent through the crust, with magma buoyancy affected by density contrasts with the wall rock as well as viscosity associated with the crystal cargo and magma composition (Bottinga & Weill, 1970; Bottinga et al., 1982; Cooper, 2017; Seifert et al., 2013). This may explain storage of mafic magmas in the lower crust, as the magma density may have changed just enough for magma to ascend above the Moho and then stall in the lower crust, where a similar density is encountered.

3.7. CONCLUSIONS AND RECOMMENDATIONS

Globally at ocean islands, we observe that clinopyroxene crystallization tends to occur deep in the magmatic system: in the oceanic lithosphere and sometimes up into the lower crust. Therefore, clinopyroxene captures the magmatic processes and magma storage that occur deep in these relatively mafic volcanic islands. Recent, well-monitored eruptions of Fogo [Cape Verde (2014–2015)] and El Hierro [Canary Islands (2011)] have been fed from deep magma storage zones, and seismicity traced the ascent of magma through the crust to the eruption site (González et al., 2013, 2015). By contrast, the eruption at Piton de la Fournaise [Reunion (2007)] appears to have started with fracturing of the shallow magma storage zone followed by magma ascent from progressively deeper to feed the ongoing eruption (Massin et al., 2011).

Therefore, knowledge of the deep magma storage system from clinopyroxene crystallization is appropriate for volcanoes where eruptions are fed from deep magma chambers, allowing monitoring teams to interpret enhanced deep seismicity. However for others such as Piton de la Fournaise, it is essential to understand the shallow magma storage system. The presence of such long-lived shallow magmatic systems may influence the eruption style, and therefore the presence or absence of protracted shallow magma storage may be a useful indicator of likely eruptive behavior. To investigate the temporary as well as long-term shallow magma storage zones, a combination of methods is recommended. Petrological methods that lend themselves to investigating the shallower magmatic system are water solubility, experimental studies, glassy melt inclusions, and to some extent fluid inclusions depending on the timescales available for re-equilibration (Di Muro et al., 2014; Famin et al., 2009; Freise et al., 2003; Jeffery et al., 2016; Renzulli & Santi 2000; Zanon et al., 2013). Ideally seismicity and deformation data are used both for developing models of the magma storage system as well as real-time monitoring (Magee et al., 2018).

Investigation of timescales of magmatic processes that provide indications of typical timescales for magma ascent from a magma storage zone to eruption are also important. Such indications may be assessed on a case-by-case basis from the extent of re-equilibration of fluid inclusions (Hildner et al., 2011, 2012). Further information about magmatic timescales that may give insights into the magma ascent processes involved in volcanic eruptions may be gleaned by exploring diffusion between compositional zones within crystals. An example of olivine diffusion chronometry from Fogo, Cape Verde, suggests rapid ascent of magmas and corresponding eruptions on the order of 3 to 12 hr (Hildner et al., 2011). We recommend integration of all types of petrological data, to provide indications of magmatic processes and their location and timescales, with geophysical methods, such as seismicity to track magma storage and transport, as well as InSAR and geodetics to reveal deformation patterns and assess source location and geometry (Magee et al., 2018).

ACKNOWLEDGMENTS

We are particularly grateful to the editors Matteo Massotta, Silvio Mollo, and Christoph Beier, for the invitation to contribute to this volume and their professional editorial handling. We are grateful to Andreas Klügel, David Neave, and Ricardo Ramalho for constructive reviews that helped improve this contribution.

REFERENCES

Ali, M. Y., Watts, A. B., & Hill, I. (2003). Structure of Mesozoic oceanic crust in the vicinity of the Cape Verde Islands from seismic reflection profiles. *Marine Geophysical Researches*, 24(3–4): 329–343.

Ali, M. Y., & Watts, A. B., (2003). A seismic reflection profile study of lithospheric flexure in the vicinity of the Cape Verde Islands. *Journal of Geophysical Research*, 108(B5), 2239–2263.

Amelung, F., & Day, S. (2002). InSAR observations of the 1995 Fogo, Cape Verde, eruption: Implications for the effects of collapse events upon island volcanoes. *Geophysical Research Letters*, 29(12), 47–1.

Andújar, J., Costa, F., Martí, J., Wolff, J. A., and Carroll, M. R., (2008). Experimental constraints on pre-eruptive conditions of phonolitic magma from the caldera-forming El Abrigo eruption, Tenerife (Canary Islands). *Chemical Geology*, 257(3–4), 173–191.

Ashchepkov, I. V., André, L., Downes, H., & Belyatsky, B. A. (2011). Pyroxenites and megacrysts from Vitim picrite-basalts (Russia): Polybaric fractionation of rising melts in the mantle? *Journal of Asian Earth Sciences*, 42, 14–37.

Assunção, C. F. T., Machado, F., & Gomes, R. A. D. (1965). On the occurrence of carbonatites in the Cape Verde Islands. *Boletim da Sociedade Geológica de Portugal*, 16, 179–188.

Aulinas, M., Gimeno, D., Fernandez-Turiel, J. L., Pérez-Torrado, F. J., Rodriguez- González, A., & Gasperini, D. (2010). The Plio-Quaternary magmatic feeding system beneath Gran Canaria (Canary Islands, Spain): Constraints from thermobarometric studies. *Journal of the Geological Society*, 167, 785–801.

Baker, D. R. (2008). The fidelity of melt inclusions as records of melt composition. *Contributions to Mineralogy and Petrology*, 156, 377–395.

Barker, A. K., Nilsson, D., & Hansteen, T. (2019). Unravelling the crustal architecture of Cape Verde; the xenolith record. Special Issue: Mineral Textural and Compositional Variations as a Tool for Understanding Magmatic Processes editor: Silvio Mollo. *Minerals*, 9(2), 90.

Barker, A. K., Troll, V. R., Carracedo, J. C., & Nicholls, P. (2015). The magma plumbing system for the 1971 Tenguía eruption, La Palma, Canary Islands. *Contributions to Mineralogy and Petrology*, 170(5). doi: 10.1007/s00410-015-1207-7

Barker, A. K., Troll, V. R., Ellam, R. M., Hansteen, T. H., Harris, C., Stillman, C. J., & Andersson, A. (2012). Magmatic evolution of the Cadamosto Seamount, Cape Verde: Beyond the spatial extent of EM1. *Contributions to Mineralogy and Petrology*, 163, 949–965. doi: 10.1007/s00410-011-0708-2.

Barker, A. K., Holm, P. M., Peate, D. W., & Baker, J. A. (2010). A five million year record of compositional variations in mantle sources to magmatism on Santiago, southern Cape Verde archipelago. *Contributions to Mineralogy and Petrology.* 160, 133–154. doi: 10.1007/s00410-009-0470-x

Barker, A., Holm, P., Peate, D., & Baker, J., (2009). A 5 million year record of compositional variations in mantle sources to magmatism on Santiago, southern Cape Verde archipelago. *Mineralogy & Petrology*, 160, 33–154.

Barling, J., Goldstein, S. L., & Nucholls, I. A. (1994). Geochemistry of Heard Island (southern Indian Ocean): Characterization of an enriched mantle component and implications for enrichment of the sub-Indian Ocean mantle. *Journal of Petrology*, 35(4), 1017–1053.

Barrancos, J., Dionis, S., Quevedo, R., Fernandes, P., Rodríguez, F., Pérez, N., et al. (2015). Sulphur dioxide (SO2) emissions during the 2014–15 Fogo eruption, Cape Verde. *Geophysical Research Abstracts*, 17, 2015. EGU General Assembly 2015.

Bebiano, J., (1932). A geologia do Arquipélago de Cabo Verde. *Comunicações dos Serviços Geológicos de Portugal*, 18, 167–187.

Beier, C., Haase, K. M., & Hansteen, T. H. (2006). Magma evolution of the Sete Cidades volcano, São Miguel, Azores. *Journal of Petrology*, 47(7), 1375–1411.

Bernard-Griffiths, J., Cantagrel, J.-M., Alves, C., Mendes, F., Serralheiro, A., & Macedo, J. (1975). Geochronologie: Donnés radiometriques potassium-argon sur quelques formations magmatiques des îlles de l'archipel du Cap Vert. *Comptes rendus de l'Académie des Sciences Série D.*, 280, 2429–2432.

Bottinga, Y., & Weill, D. F. (1970). Densities of liquid silicate systems calculated from partial molar volumes of oxide components. *American Journal of Science*, 269(2), 169–182.

Bottinga, Y., Weill, D., & Richet, P. (1982). Density calculations for silicate liquids. I. Revised method for aluminosilicate compositions. *Geochimica et Cosmochimica Acta*, 46(6), 909–919.

Brown, M. C., Singer, B. S., Knudsen, M. F., Jicha, B. R., Finnes, E., & Feinberg, J. M. (2009). No evidence for Brunhes age excursions, Santo Antão, Cape Verde. *Earth and Planetary Science Letters*, 287(1–2), 100–115.

Bureau, H., Pineau, F., Me¤ trich, N., Semet, M. P. & Javoy, M. (1998). A melt and fluid inclusion study of the gas phase at Piton de la Fournaise volcano (Reunion Island). *Chemical Geology*, 147, 115–130.

Caranova, R., & Silva, R. P. (2012). Geothermal resource assessment in volcanic islands-Fogo Island, Cape Verde.

Carracedo, J.-C., Perez-Torrado, F., Rodriguez- Gonzalez, A., Paris, R., Troll, V. R., & Barker, A. K. (2015) Volcanic and structural evolution of Pico do Fogo, Cape Verde. *Geology Today*, 31(4), 146–152. 10.1111/gto.12101

Carracedo, J. C., Rodríguez Badiola, E., Guillou, H., Paterne, M., Scaillet, S., Pérez Torrado, F. J., et al. (2007). Eruptive and structural history of Teide volcano and rift zones of Tenerife, Canary Islands. *Geological Society of America Bulletin*, 19, 1027–1051. http://dx.doi.org/10.1130/B26087.1.

Cazenave, A., Dominh, K., Rabinowicz, M., & Ceuleneer, G. (1988). Geoid and depth anomalies over ocean swells and troughs: evidence of an increasing trend of the geoid to depth ratio with age of plate. *Journal of Geophysical Research: Solid Earth*, 93(B7), 8064–8077.

Chamberlain, K. J., Barclay, J., Preece, K., Brown, R. J., & Davidson, J. P. (2016). Origin and evolution of silicic magmas at ocean islands: Perspectives from a zoned fall deposit on Ascension Island, South Atlantic. *Journal of Volcanology and Geothermal Research*, 327, 349–360.

Chatterjee, N., Bhattacharji, S., & Fein, C. (2005). Depth of alkalic magma reservoirs below Kolekole cinder cone, Southwest rift zone, East Maui, Hawaii. *Journal of Volcanology and Geothermal Research*, 145(1–2), pp.1–22.

Cooper, K. M. (2017). What does a magma reservoir look like? The "crystal's-eye" view. *Elements*, 13(1), 23–28.

Courtney, R. C., & White, R.S. (1986). Anomalous heatflow and geoid across the Cape Verde Rise: Evidence for dynamic support from a thermal plume in the mantle. *Geophysical Journal of the Royal Astronomical Society*, 87, 815–867.

Crough, S. (1982). Geoid height anomalies over the Cape Verde Rise. *Marine Geophysical Researches*, 5, 263–271.

Da Silva, S. H., Day, S. J., & Fonseca, J. F. B. D. (1999). Fogo Volcano, Cape Verde Islands: Seismicity-derived constraints on the mechanism of the 1995 eruption. *Journal of Volcanology and Geothermal Research*, 94(1–4), 219–231.

Dash, P., Ball, M. M., King, G. A., Butler, L. W., & Rona, P. A. (1976). Geophysical investigation of the Cape Verde Archipelago. *Journal of Geophysical Research*, 81(29), 5249–5259.

Davidson, J. P., Morgan, D. J., & Charlier, B. L. (2007). Isotopic microsampling of magmatic rocks. *Elements*, 3(4), 253–259.

Davies, G., Norry, M., Gerlach, D., & Cliff, R. (1989). A combined chemical and Pb.Sr.Nd isotope study of the Azores and Cape Verde hot spots, the geodynamic implications. In A.D. Saunders, M. J. Norry (Eds.), *Magmatism in the ocean basins* (Vol. 42, pp. 231–255). Geological Society, Special Publications, London.

Day, S., Heleno, S., & Fonseca, J. (1999). A past giant lateral collapse and present day flank instability of Fogo, Cape Verde Islands. *Journal of Volcanology and Geothermal Research*, 94, 191–218.

De Paepe, P. D., Klerkx, J., Hertogen, J., & Plinke, P. (1974). Oceanic tholeiites on Cape Verde Islands – petrochemical and geochemical evidence. *Earth and Planetary Science Letters*, 22(4), 347–354.

Di Muro, A., Métrich, N., Vergani, D., Rosi, M., Armienti, P., Fougeroux, T., et al. (2014). The shallow plumbing system of Piton de la Fournaise Volcano (La Reunion Island, Indian Ocean) revealed by the major 2007 caldera-forming eruption. *Journal of Petrology*, 55(7), 1287–1315.

Dias, N. A., Matias, L., Lourenço, N., Madeira, J., Carrilho, F., & Gaspar, J. L. (2007). Crustal seismic velocity structure near Faial and Pico Islands (AZORES), from local earthquake tomography. *Tectonophysics*, 445(3–4), 301–317.

Dionis, D., Melián, G., Rodríguez, R., Hernández, P., Padrón, E., Pérez, N., et al. (2015b). Diffuse volcanic gas emission and thermal energy release from the summit crater of Pico do Fogo, Cape Verde. *Bulletin of Volcanology*, 77, 10.

Dionis, S., Pérez, N., Hernández, P., Melián, G., Rodríguez, F., Padrón, E., et al. (2015a). Diffuse CO_2 degassing and volcanic activity at Cape Verde islands, West Africa. *Earth, Planets and Space*, 67, 48.

Doucelance, R., Escrig, S., Moreira, M., Gariépy, C., & Kurz, M. D. (2003). Pb-Sr-He isotope and trace element geochemistry of the Cape Verde Archipelago. *Geochimica et Cosmochimica Acta*, 67(19), 3717–3733.

Duprat, H., Friis, J., Holm, P., Grandvuinet, T., & Sørensen, R. (2007). The volcanic and geochemical development of São Nicolau, Cape Verde Islands: Constraints from field and 40Ar/39Ar evidence. *Journal of Volcanology and Geothermal Research*, 162(1–2), 1–19.

Dyhr, C. T., & Holm, P. M. (2010). A volcanological and geochemical investigation of Boa Vista, Cape Verde Islands; 40Ar/39Ar geochronology and field constraints. *Journal of Volcanology and Geothermal Research*, 189, 19–32.

Efimov, V. N., & Skolotnev, S. G. (2006). New data on the structure of sedimentary cover at the Cape Verde Seamount and the Cape Verde Basin (central Atlantic) based on continuous seismic profiling data. In *Doklady earth sciences* (Vol. 407, No. 2, pp. 376–380). MAIK Nauka/Interperiodica.

Egloff, J. (1972). Morphology of ocean basin seaward of northwest Africa: Canary Islands to Monrovia, Liberia. *AAPG Bulletin*, 56(4), 694–706.

Eisele, S., Reißig, S., Freundt, A., Kutterolf, S., Nürnberg, D., Wang, K. L., & Kwasnitschka, T. (2015). Pleistocene to Holocene offshore eruptions from the southwestern Cape Verde Archipelago. *Marine Geology*, 369, 233–250.

Elsworth, D., & Day, S. J. (1999). Flank collapse triggered by intrusion: The Canarian and Cape Verde Archipelagoes. *Journal of Volcanology and Geothermal Research*, 94(1–4), 323–340.

Famin, V., Welsch, B., Okumura, S., Bachèlery, P., & Nakashima, S. (2009). Three differentiation stages of a single magma at

Piton de la Fournaise volcano (Reunion hot spot). *Geochemistry, Geophysics, Geosystems*, 10, Q01007. doi:10.1029/2008GC002015.

Faria, B., & Fonseca, J.F.B.D. (2014). Investigating volcanic hazard in Cape Verde Islands through geophysical monitoring: Network description and first results. *Natural Hazards and Earth System Sciences*, *v*.14, 485–494.

Faria, B. (2010). *Monitorização Geofísica do Vulcão do Fogo e Níveis de Alerta*. Ph.D thesis. Universidade Técnica de Lisboa (in Portuguese).

Faugères, J., Legigan, P., Maillet, N., & Latouche, C., (1989). Pelagic, turbiditic, and contouritic sequential deposits on the Cape Verde Plateau (Leg 108, Site 659, Northwest Africa): Sediment record during Neogene time: Proceedings of the Ocean Drilling Program. *Scientific Results*, *v*. 108, 311–327.

Fernandes, R., & Faria, B. (2015). FOGO-2014: monitoring the Fogo 2014 eruption, Cape Verde. In *EGU General Assembly Conference Abstracts*, Vol. 17 id.12709.

Foeken, J., Day, S., & Stuart, F. (2009). Cosmogenic 3He exposure dating of the Quaternary basalts from Fogo, Cape Verdes: Implications for rift zone and magmatic reorganisation. *Quaternary Geochronology*, 4(1), 37–49.

Fonseca, J. F., Faria, B. V., Lima, N. P., Heleno, S. I., Lazaro, C., d'Oreye, N. F., et al. (2003). Multiparameter monitoring of Fogo Island, Cape Verde, for volcanic risk mitigation. *Journal of Volcanology and Geothermal Research*, 125(1–2), 39–56.

Fontaine, F. R., Roult, G., Michon, L., Barruol, G., & Muro, A. D. (2014). The 2007 eruptions and caldera collapse of the Piton de la Fournaise volcano (La Réunion Island) from tilt analysis at a single very broadband seismic station. *Geophysical Research Letters*, 41(8), 2803–2811.

Freise, M., Holtz, F., Koepke, J., Scoates, J., & Leyrit, H., (2003). Experimental constraints on the storage conditions of phonolites from the Kerguelen Archipelago. *Contributions to Mineralogy and Petrology*, 145(6), 659–672.

Galipp, K., Klügel, A., & Hansteen, T. H. (2006). Changing depths of magma fractionation and stagnation during the evolution of an oceanic island volcano: La Palma (Canary Islands). *Journal of Volcanology and Geothermal Research*, 155, 285–306.

Geiger, H., Barker, A. K., & Troll, V. R. (2016). Locating the depth of magma supply for volcanic eruptions, insights from Mt. Cameroon. *Scientific Reports*, 6, 33629. doi: 10.1038/srep33629

Geissler, W. H., Jokat, W., Jegen, M., & Baba, K. (2016). Thickness of the oceanic crust and the mantle transition zone in the vicinity of the Tristan da Cunha hot spot estimated from ocean-bottom and ocean-island seismometer receiver functions. Tectophysics this volume.

Gerlach, D. C., Cliff, R. A., Davies, G. R., Norry, M., & Hodgson, N. (1988). Magma sources of the Cape-Verdes Archipelago – isotopic and trace-element constraints. *Geochimica Et Cosmochimica Acta*, 52(12), 2979–2992.

González, P. J., Bagnardi, M., Hooper, A. J., Larsen, Y., Marinkovic, P., Samsonov, S. V., & Wright, T. J. (2015). The 2014–2015 eruption of Fogo volcano: Geodetic modeling of Sentinel-1 TOPS interferometry. *Geophysical Research Letters*, 42(21), 9239–9246.

González, P. J., Samsonov, S. V., Pepe, S., Tiampo, K. F., Tizzani, P., Casu, F., et al. (2013). Magma storage and migration associated with the 2011–2012 El Hierro eruption: Implications for crustal magmatic systems at oceanic island volcanoes. *Journal of Geophysical Research: Solid Earth*, 118(8), 4361–4377.

Grevemeyer, I., Helffrich, G., Faria, B., Booth-Rea, G., Schnabel, M., & Weinrebe, R. W. (2010). Seismic activity at Cadamosto seamount near Fogo Island, Cape Verdes—formation of a new ocean island? *Geophysical Journal International*, 180, 552–558. doi:10.1111/j.1365-246X. 2009. 04440.x

Gudmundsson, A. (2012). Magma chambers: Formation, local stresses, excess pressures, and compartments. *Journal of Volcanology and Geothermal Research*, 237, 19–41.

Hammer, J., Jacob, S., Welsch, B., Hellebrand, E., & Sinton, J. (2016). Clinopyroxene in postshield Haleakala ankaramite: 1. Efficacy of thermobarometry. *Contributions to Mineralogy and Petrology*, 171(1), 7.

Hanson, J. A., Given, H. K., & Berger, J. (1996). Earthquake activity near Ascension Island, South Atlantic Ocean, as seen by a combined seismic/hydrophone array. *Geothermics*, 25(4–5), 507–519.

Hansteen, T., Kwasnitschka, T., & Klügel, A. (2014). *Cape Verde Seamounts – Cruise No. M80/3: December 29, 2009 - February 1, 2010 - Dakar (Senegal) – Las Palmas de Gran Canaria (Spain)*. DFG-Senatskommission für Ozeanographie, Bremen, 1–42. doi:10.2312/cr_m80_3, 42 pp.

Hayes, D. E., & Rabinowitz, P. D. (1975). Mesozoic magnetic lineations and the magnetic quiet zone off northwest Africa. *Earth and Planetary Science Letters*, 28, 105–115.

Heleno, S. I. N., Faria, B. V. E., Bandomo, Z., & Fonseca, J. F. B. D. (2006). Observations of high-frequency harmonic tremor in Fogo, Cape Verde Islands. *Journal of Volcanology and Geothermal Research*, 158, 361–379.

Herzberg, C., & Asimow, P. D. (2008). Petrology of some oceanic island basalts: PRIMELT2. XLS software for primary magma calculation. *Geochemistry, Geophysics, Geosystems*, 9, Q09001. doi:10.1029/2008GC002057.

Hildner, E., Klügel, A., & Hansteen, T. (2012). Barometry of lavas from the 1951 eruption of Fogo, Cape Verde Islands: Implications for historic and prehistoric magma plumbing systems. *Journal of Volcanology and Geothermal Research*, 217–218, 73–90.

Hildner, E., Klügel, A., & Hauff, F. (2011). Magma storage and ascent during the 1995 eruption of Fogo, Cape Verde archipelago. *Contributions to Mineralogy and Petrology*, 162, 751–772. doi:10.1007/s00410-011-0623-6.

Hoernle, K., Tilton, G., Le Bas, M. J., Duggen, S., & Garbe-Schönberg, D. (2002). Geochemistry of oceanic carbonatites compared with continental carbonatites: mantle recycling of oceanic crustal carbonate. *Contributions to Mineralogy and Petrology*, 142(5), 520–542.

Holm, P. M., Grandvuinet, T., Friis, J., Wilson, J. R., Barker, A. K., & Plesner, S., (2008). An 40Ar/39Ar study of the Cape Verde hot spot: Temporal evolution in a semistationary plate environment. *Journal of Geophysical Research: Solid Earth (1978 – 2012)*, 113(B8).

Holm, P. M., Wilson, J. R., Christensen, B. P., Hansen, L., Hansen, S. L., Hein, K. H., et al. (2006). Sampling the Cape Verde mantle plume: Evolution of melt compositions on Santo Antão, Cape Verde Islands. *Journal of Petrology*, 47, 145–189.

Jacobi, R. D., & Hayes, D. E. (1982). Bathymetry, microphysiography and reflectivity characteristics of the West African margin between Sierra Leone and Mauritania. In *Geology of the Northwest African continental margin* (pp. 182–212). Springer, Berlin, Heidelberg.

Jeffery, A. J., Gertisser, R., O'Driscoll, B., Pacheco, J. M., Whitley, S., Pimentel, A., & Self, S. (2016). Temporal evolution of a post-caldera, mildly peralkaline magmatic system: Furnas volcano, São Miguel, Azores. *Contributions to Mineralogy and Petrology*, 171(5), 42.

Jenkins, S. F., Day, S. J., Faria, B. V. E., & Fonseca, J. F. B. D. (2017). Damage from lava flows: Insights from the 2014–2015 eruption of Fogo, Cape Verde. *Journal of Applied Volcanology*, *6*(1), 6.

Jørgensen, J., & Holm, P. (2002). Temporal variation and carbonatite contamination in primitive ocean island volcanic from São Vicente. Cape Verde Islands. *Chemical Geology*, 192, 249–267.

Klerkx, J., Deutsch, S., & De Paepa, P. (1974). Rubidium, strontium content and strontium isotopic composition of strongly alkalic basaltic rocks from the Cape Verde Islands. *Contributions to Mineralogy and Petrology*, 45, 107–118.

Klingelhöfer, F., Minshull, T. A., Blackman, D. K., Harben, P., & Childers, V., (2001). Crustal structure of Ascension Island from wide-angle seismic data: implications for the formation of near-ridge volcanic islands. *Earth and Planetary Science Letters*, 190(1–2), 41–56.

Klitgord, K., & Schouten, H. (1987). Plate kinematics of the Central Atlantic. In B. E. Tucholke, P. R. Vogt (Eds.), *The Geology of North America: The Western Atlantic Region: Geological Society of America, Decade of North American Geology*.

Klügel, A., & Klein, F. (2006). Complex magma storage and ascent at embryonic submarine volcanoes from Madeira Archipelago. *Geology*, 34, 337–340.

Klügel, A., Day, S., Schmid, M., & Faria, B. (2020). Magma plumbing during the 2014–2015 eruption of Fogo (Cape Verde Islands). *Frontiers in Earth Science*, 8, 157. doi: 10.3389/feart.2020.00157.

Klügel, A., Longpré, M. A., García-Cañada, L., & Stix, J. (2015). Deep intrusions, lateral magma transport and related uplift at ocean island volcanoes. *Earth and Planetary Science Letters*, 431, 140–149.

Klügel, A., Galipp, K., & Hansteen, T. H. (2005). Magma storage and underplating beneath Cumbre Vieja volcano, La Palma (Canary Islands). *Earth and Planetary Science Letters*, 236, 211–226.

Klügel, A, Hoernle, K. A., Schmincke, H. U., & White, J. D. L. (2000). The chemically zoned 1949 eruption on La Palma (Canary Islands): Petrologic evolution and magma supply dynamics of a rift-zone eruption. *Journal of Geophysical Research*, 105(B3), 5997–6016

Kokfelt, T. F., Holm, P. M., Hawkesworth, C. J., & Peate, D. W. (1998). A lithospheric mantle source for the Cape Verde Island magmatism: Trace element and isotopic evidence from the Island of Fogo. *Mineralogical Magazine*, 62A, 801–802.

Lai, Z., Zhao, G., Han, Z., Huang, B., Li, M., Tian, L., & Bu, X. (2018). The magma plumbing system in the Mariana Trough back-arc basin at 18° N. *Journal of Marine Systems*, 180, 132–139.

Lancelot, Y., Seibold, E., Cepek, P., Dean, W., Eremeev, V., Gardner, J., et al. (1978). Site 368: Cape Verde Rise. In Y. Lancelot et al. (Eds.),. *Initial Reports of the Deep Sea Drilling Project* (Vol. 41, pp. 233–326). Washington (U.S. Government Printing Office).

Le Maitre, R. W., Streckeisen, A., Zanettin, B., Le Bas, M. J., Bonin, B., Bateman, P., et al. (2002). *Igneous rocks. A classification and glossary of terms, Recommendations of the IUGS subcommission on the systematics of igneous rocks*. Cambridge University Press, Cambridge, UK

Le Pichon, X.L., & Fox, P.J., (1971). Marginal offsets, fracture zones and the early opening of the North Atlantic. *Journal of Geophysical Research*, 75, 6294–6307.

Leva, C., Rümpker, G., Link, F., & Wölbern, I., (2019). Seismological evidence for subcrustal magmatic injection beneath Fogo volcano, Cape Verde hotspot. EarthArXiv 10.31223/osf.io/f6zdp

Liu, C., Lay, T., & Xiong, X. (2018). Rupture in the 4 May 2018 MW 6.9 earthquake seaward of the Kilauea east rift zone fissure eruption in Hawaii. *Geophysical Research Letters*, 45(18), 9508–9515.

Lodge, A., & Helffrich, G. (2006). Depleted swell root beneath the Cape Verde Islands. *Geology*, 34(6): 449–452.

Longpré, M. A., Klügel, A., Diehl, A., & Stix, J. (2014). Mixing in mantle magma reservoirs prior to and during the 2011–2012 eruption at El Hierro, Canary Islands. *Geology*, 42(4), 315–318.

Longpré, M. A., Troll, V. R., & Hansteen, T. H. (2008). Upper mantle magma storage and transport under a Canarian shield-volcano, Teno, Tenerife (Spain). *Journal of Geophysical Research: Solid Earth*, 113(B8).

Machado, F., Azeredo Leme, J., Monjardino, J., & Seita, M. F. (1968). Carta geológica de Cabo Verde, notícia explicativa da Ilha Brava e dos Ilhéus Secos. *Garcia de Orta*, 16, 123–130

Madeira, J., Ramalho, R. S., Hoffmann, D. L., Mata, J., & Moreira, M. (2019). A geological record of multiple Pleistocene tsunami inundations in an oceanic island: The case of Maio, Cape Verde. *Sedimentology*. https://doi.org/10.1111/sed.12612

Madeira, J., Mata, J., Mourão, C., da Silveira, A. B., Martins, S., Ramalho, R., & Hoffmn, D. L. (2010). Volcano-stratigraphy and structural evolution of Brava Island (Cape Verde) based on 40Ar/39Ar, U-Th and field constraints. *Journal of Volcanology and Geothermal Research*, 196, 219–235.

Madeira, J., Brum da Silveira, A., Mata, J., Mourão, C., & Martins, S. (2008). The role of mass movements on the geomorphologic evolution of island volcanoes: Examples from Fogo and Brava in the Cape Verde archipelago. *Comunicações Geológicas*, 95, 93–106.

Madureira, P., Mata, J., Mattielli, N., Queiroz, G., & Silva, P. (2011). Mantle source heterogeneity, magma generation and magmatic evolution at Terceira Island (Azores archipelago):

Constraints from elemental and isotopic (Sr, Nd, Hf, and Pb) data. *Lithos*, 126, 402–418.

Madureira, P., Mata, J., & Moreira, M. (2008). The Ne isotopic signature of Terceira lavas (Azores): Evidence for Ne recycling?. *e-Terra*, 5(11).

Magee, C., Stevenson, C. T., Ebmeier, S. K., Keir, D., Hammond, J. O., Gottsmann, J. H., & O'Driscoll, B. (2018). Magma plumbing systems: A geophysical perspective. *Journal of Petrology*, 59(6), 1217–1251.

Magnusson, E. (2016). Temporal evolution of historic mafic lavas from Fogo, Cape Verde. Examensarbete vid Institutionen för geovetenskaper,ISSN1650–6553;365.urn:nbn:se:uu:diva-296417

Marianelli, P., Metrich, N., & Sbrana, A. (1999) Shallow and deep reservoirs involved in magma supply of the 1944 eruption of Vesuvius. *Bulletin of Volcanology*, 61, 48–63

Martínez-Moreno, F. J., Santos, F. M., Madeira, J., Pous, J., Bernardo, I., Soares, A., et al. (2018). Investigating collapse structures in oceanic islands using magnetotelluric surveys: The case of Fogo Island in Cape Verde. *Journal of Volcanology and Geothermal Research*, 357, 152–162.

Masotta, M., Mollo, S., Freda, C., Gaeta, M., & Moore, G. (2013). Clinopyroxene–liquid thermometers and barometers specific to alkaline differentiated magmas. *Contributions to Mineralogy and Petrology*, 166(6), 1545–1561.

Massin, F., Ferrazzini, V., Bachèlery, P., Nercessian, A., Duputel, Z., & Staudacher, T. (2011). Structures and evolution of the plumbing system of Piton de la Fournaise volcano inferred from clustering of 2007 eruptive cycle seismicity. *Journal of Volcanology and Geothermal Research*, 202(1–2), 96–106.

Masson, D. G., Le Bas, T. P., Grevemeyer, I., & Weinrebe, W. (2008). Flank collapse and large-scale landsliding in the Cape Verde Islands, off West Africa. *Geochemistry, Geophysics, Geosystems*, 9, Q07015. doi:10.1029/ 2008GC001983.

Masson, D. G., Watts, A. B., Gee, M. J. R., Urgeles, R., Mitchell, N. C., Le Bas, T. P., & Canals, M. (2002). Slope failures on the flanks of the western Canary Islands. *Earth Science Reviews*, 57, 1–35. doi:10.1016/S0012-8252(01)00069-1.

Mata, J., Martins, S., Mattielli, N., Madeira, J., Faria, B., Ramalho, R. S., et al. (2017). The 2014–15 eruption and the short-term geochemical evolution of the Fogo volcano (Cape Verde): Evidence for small-scale mantle heterogeneity. *Lithos*, 288, 91–107.

Mata, J., Moreira, M., Doucelance, R., Ader, M., & Silva, L. C. (2010). Noble gas and carbon isotopic signatures of Cape Verde oceanic carbonatites: implications for carbon provenance. *Earth and Planetary Science Letters*, 291(1), 70–83.

McNutt, M. K. (1988) Thermal and mechanical properties of the Cape Verde Rise. *Journal of Geophysical Research*, 93, 2784–2794.

Mitchell, J. G., LeBas, M. J., Zielonka, J., & Furnes, H. (1983). On dating the magmatism of Maio, Cape Verde Islands. *Earth and Planetary Science Letters*, 64, 61–76.

Mollo, S., Blundy, J., Scarlato, P., De Cristofaro, S. P., Tecchiato, V., Di Stefano, F., et al. (2018). An integrated PT-H_2O-lattice strain model to quantify the role of clinopyroxene fractionation on REE+ Y and HFSE patterns of mafic alkaline magmas: Application to eruptions at Mt. Etna. *Earth-Science Reviews*, 185, 32–56.

Mollo, S., Putirka, K., Misiti, V., Soligo, M., & Scarlato, P. (2013). A new test for equilibrium based on clinopyroxene–melt pairs: clues on the solidification temperatures of Etnean alkaline melts at post-eruptive conditions. *Chemical Geology*, 352, 92–100.

Morgan, D. J., Blake, S., Rogers, N. W., DeVivo, B., Rolandi, G., Macdonald, R., & Hawkesworth, C. J. (2004). Timescales of crystal residence and magma chamber volume from modelling of diffusing profiles in phenocrysts: Vesuvius 1944. *Earth and Planetary Science Letters*, 222, 933–946. doi:10.1016/j.epsl.2004.03.030

Mourão, C., Mata, J., Doucelance, J., Madeira, J., Brum da Silveira, A., Silva, L. & Moreira, M. (2010). Quaternary extrusive calciocarbonatite volcanism on Brava Island (Cape Verde). *Journal of African Earth Sciences*, 55, 59–74.

Müller, R., Sdrolias, M., & Roest, W. (2008). Age, spreading rates and spreading symmetry of the world's ocean crust. *Geochemistry Geophysics Geosystems*, 9(Q04006).

Nascimento, A. (2015). Post disaster needs assessment: Fogo volcanic eruption 2014–2015. https://www.gfdrr.org/en/cape-verde-post-disaster-needs-assessment-volcano-eruption-2014-2015

Neave, D. A., & Putirka, K. D. (2017). A new clinopyroxene-liquid barometer, and implications for magma storage pressures under Icelandic rift zones. *American Mineralogist*, 102(4), 777–794.

Nikogosian, I. K., Elliott, T., & Touret, J. L. R. (2002). Melt evolution beneath thick lithosphere: a magmatic inclusion study of La Palma, Canary Islands. *Chemical Geology*, 183, 169–193.

Nimis, P. (1995). A clinopyroxene geobarometer for basaltic systems based on crystal-structure modelling. *Contributions to Mineralogy and Petrology*, 121, 115–125.

O'Mongain, A., Ottemoller, L., Baptie, B., Galloway, D., & Booth, D. (2007). Seismic activity associated with a probable submarine eruption near Tristan da Cunha, July 2004–July 2006. *Seismological Research Letters*, 78(3), 375–382.

Ogg, J. G. (1995). Magnetic polarity time scale of the Phanerozoic. In T. J. Ahrens (Ed.), *Global Earth Physics: A handbook of physical constants. AGU Ref. Shelf* (Vol. 1, pp. 240–270). Washington D.C.

Paris, R., Giachetti, T., Chevalier, J., Guillou, H., & Frank, N., (2011). Tsunami deposits in Santiago Island (Cape Verde archipelago) as possible evidence of a massive flank failure of Fogos volcano. *Sedimentary Geology*, 239(3–4), 129–145.

Paris, R., Ramalho, R. S., Madeira, J., Ávila, S., May, S. M., Rixhon, G., et al. (2018). Mega-tsunami conglomerates and flank collapses of ocean island volcanoes. *Marine Geology*, 395, 168–187.

Peltier, A., Bachèlery, P., & Staudacher, T. (2009). Magma transport and storage at Piton de La Fournaise (La Réunion) between 1972 and 2007: A review of geophysical and geochemical data. *Journal of Volcanology and Geothermal Research*, 184(1–2), pp.93–108.

Pérez, M., Dionis, S., Fernandes, P., Barrancos, J., Rodríguez, F., Bandomo, Z., et al. (2015). Precursory signals of the 2014–15 Fogo eruption (Cape Verde) detected by surface CO_2 emission and heat flow observations. *Geophysical Research Abstracts*, Vol. 17, 2015, EGU General Assembly 2015.

Pim, J., Peirce, C., Watts, A. B., Grevemeyer, I., & Krabbenhöft, A. (2008). Crustal structure and origin of the Cape Verde Rise. *Earth and Planetary Science Letters*, 272(1), 422–428.

Plesner, S., Holm, P. M., & Wilson, J. R. (2003). 40Ar–39Ar geochronology of Santo Antão, Cape Verde Islands. *Journal of Volcanology and Geothermal Research*, 120(1–2), 103–121.

Poland, M. P., Miklius, A., & Montgomery-Brown, E. K. (2015). Magma supply, storage, and transport at shield-stage. Charact. *Hawaii. Volcanoes*, 179(1801), 179–234.

Putirka, K. D. (2017). Down the crater: Where magmas are stored and why they erupt. *Elements*, 13(1), 11–16.

Putirka, K. (2008). Thermometers and barometers for volcanic systems. *Reviews in Mineralogy and Geochemistry*, 69, 61–120.

Putirka, K., Mikaelian, H., Ryerson, F. J., & Shaw, H. (2003). New clinopyroxene-liquid thermobarometers for mafic, evolved and volatile-bearing lava compositions, with applications to lavas from Tibet and the Snake River Plain, ID. *American Mineralogist*, 88, 1542–1554.

Putirka, K. (1999). Clinopyroxene + liquid equilibria to 100 kbar and 2450 K. *Contributions to Mineralogy and Petrology*, 135, 151–163.

Putirka, K. (1997). Magma transport at Hawaii: Inferences based on igneous thermobarometry. *Geology*, 25, 69–72.

Putirka, K., Johnson, M., Kinzler, R., Longhi, J., & Walker, D. (1996). Thermobarometry of mafic igneous rocks based on clinopyroxene-liquid equilibria, 0–30 kbar. *Contributions to Mineralogy and Petrology*, 123, 92–108.

Putirka, K., & Condit, C. (2003). A cross section of a magma conduit system at the margins of the Colorado Plateau. *Geology*, 31, 701–704.

Quilty, P. G., & Wheller, G. E. (2000). Heard Island and the McDonald Islands: A window into the Kerguelen Plateau. In *Papers and Proceedings of the Royal Society of Tasmania* (Vol. 133, No. 2, pp. 1–12).

Ranero, C. R., Torne, M., & Banda, E. (1995). Gravity and multichannel seismic reflection constraints on the lithospheric structure of the Canary Swell. *Marine Geophysical Research*, 17, 519–534.

Ramalho, R. S., Winckler, G., Madeira, J., Helffrich, G. R., Hipólito, A., Quartau, R., et al. (2015). Hazard potential of volcanic flank collapses raised by new megatsunami evidence. *Science Advances*, 1(9), e1500456.

Ramalho, R. A. dos Santos (2011). Vertical movements of ocean island volcanoes: Insights from a stationary plate. In *Building the Cape Verde Islands* (pp. 177–197). Springer, Berlin, Heidelberg.

Ramalho, R. S., Helffrich, G., Cosca, M., Vance, D., Hoffmann, D., & Schmidt, D. N. (2010c). Vertical movements of ocean island volcanoes: Insights from a stationary plate environment. *Marine Geology*, 275(1–4), 84–95.

Ramalho, R., Helffrich, G., Schmidt, D., & Vance, D. (2010b). Tracers of uplift and subsidence in the Cape Verde Archipelago. *Journal of Geological Society London*, 167, 519–538.

Ramalho, R., Helffrich, G., Cosca, M., Vance, D., Hoffmann, D. & Schmidt, D. (2010a). Episodic swell growth inferred from variable uplift of the Cape Verde hotspot islands. *Nature Geoscience*, 3, 774–777.

Renzulli, A., & Santi, P. (2000). Two-stage fractionation history of the alkali basalt-trachyte series of Sete Cidades volcano (São Miguel Island, Azores). *European Journal of Mineralogy*, 12(2), 469–494.

Ribeiro, O. (1960). *A ilha do Fogo e as suas Erupções.* Memórias Série Geográfica I. Lisboa: Junta de Investigações do Ultramar.

Richter, N., Favalli, M., de Zeeuw-van Dalfsen, E., Fornaciai, A., Fernandes, R. M. D. S., Pérez, N. M., et al. (2016). Lava flow hazard at Fogo Volcano, Cabo Verde, before and after the 2014–2015 eruption. *Natural Hazards & Earth System Sciences*, 16(8), 1925–1951.

Risby, O., & Sandback, B. (2014). Mapping report Fogo, Cape Verde. Uppsala University.

Roest, W. R., Danobeitia, J. J., Verhoef, J., & Collette, B. J. (1992). Magnetic anomalies in the Canary Basin and the Mesozoic evolution of the central North Atlantic. *Marine Geophysical Researches*, 14(1), 1–24.

Rona, P. A. (1971). Bathymetry off central northwest Africa. In *Deep Sea Research and Oceanographic Abstracts*, 18(3): 321–327. Elsevier.

Ryabchikov, J. D., Ntaflos, T., Kurat, G., & Kogarko, L. N. (1995). Glass-bearing xenoliths from Cape Verde: Evidence for a hot rising mantle jet. *Mineralogy and Petrology*, 55(4), 217–237.

Ryan, W. B., Carbotte, S. M., Coplan, J. O., O'Hara, S., Melkonian, A., Arko, R., et al. (2009). Global multi-resolution topography synthesis. *Geochemistry, Geophysics, Geosystems*, 10, 3.

Rydeblad, E. (2018). *Mineral Constraints on the Source Lithologies at Fogo, Cape Verde*. Unpublished MSc thesis, Uppsala University. ISSN 1650–6553; 433. urn:nbn:se:uu:diva-354077

Sakai, H, Des Marias, D. J., Ueda, A., & Moore, J. G. (1984). Concentrations and isotope ratios of carbon, nitrogen and sulfur in ocean-floor basalts. *Geochimica et Cosmochimica Acta*, 48, 2433–2441.

Samrock, L. K., Wartho, J-A., & Hansteen, T. H. (2019). ^{40}Ar-^{39}Ar dating of the active phonolitic Cadamosto Seamount (CapeVerde): Indications for periodic volcanic activity and a possible relationship to global sea level changes. *Lithos* 344–345, 464–481. doi 10.1016/j.lithos.2019.07.003

Sandwell, D. T., & Smith, W. H. (1997). Marine gravity anomaly from Geosat and ERS 1 satellite altimetry. *Journal of Geophysical Research: Solid Earth*, 102(B5), 10039–10054.

Schwarz, S., & Klügel, A. (2004). Melt extraction pathways and stagnation depths beneath the Maderia and Desertas rift zones (NE Atlantic) inferred from barometric studies. *Contributions to Mineralogy and Petrology*, 147. 228–240.

Serralheiro, A. (1976). A geologia da ilha de Santiago (Cabo Verde). *Boletim do museu e laboratório mineralógico e geológico da Faculdade de Ciências*, 14, 157–369.

Serralheiro, A., (1970). *Geologia da ilha de Maio (Cabo Verde)*. Junta de Investigações do Ultramar.

Seifert, R., Malfait, W. J., Petitgirard, S., & Sanchez-Valle, C. (2013). Density of phonolitic magmas and time scales of crystal fractionation in magma chambers. *Earth and Planetary Science Letters*, 381, 12–20.

Silva, L., Le Bas, M., & Robertson, A. (1981). An oceanic carbonatite volcano on Santiago, Cape Verde Islands. *Nature*, 294, 644–645.

Silva, R., Havskov, J., Bean, C., & Wallenstein, N., (2012). Seismic swarms, fault plane solutions, and stress tensors for São Miguel Island central region (Azores). *Journal of Seismology*, 16(3), pp.389–407.

Silva, S., Calvari, S., Hernandez, P., Pérez, N., Ganci, G., Alfama, V., et al. (2017). Tracking the hidden growth of a lava flow field: The 2014–15 eruption of Fogo volcano (Cape Verde). *Geophysical Research Abstracts*, Vol. 19, EGU 2017-14514, 201. EGU General Assembly 2017.

Silva, S., Cardoso, N., Alfama, A., Cabral, J., Semedo, H., Pérez, N., et al. (2015). Chronology of the 2014 volcanic eruption on the island of Fogo, Cape Verde. *Geophysical Research Abstracts*, Vol. 17, 2015 EGU General Assembly 2015.

Skolotnev, S. G., Turko, N. N., Sokolov, S. Y., Peyve, A. A., Tsukanov, N. V., Kolodyazhnyi, S. Y., & Eskin, A. E. (2007). New data on the geological structure of the junction of the Cape Verde rise, Cape Verde abyssal basin, and bathymetrists seamounts (Central Atlantic ocean). In *Doklady Earth Sciences* (Vol. 416, No. 1, pp. 1037–1041). MAIK Nauka/Interperiodica.

Skolotnev, S. G., Kolodyazhny, S. Y., Tsukanov, N. V., Chamov, N. P., & Sokolov, S. Y. (2009). Neotectonic morphotructures in the junction zone of the Cape Verde Rise and Cape Verde Abyssal Plain, Central Atlantic. *Geotectonics*, 43(1), 51–66.

Sparks, R. S. J., & Cashman, K. V. (2017). Dynamic magma systems: Implications for forecasting volcanic activity. *Elements*, 13(1), 35–40.

Stephenson, J., Budd, G. M., Manning, J., & Hansbro, P. (2005). Major eruption-induced changes to the McDonald Islands, southern Indian Ocean. *Antarctic Science*, 17(2), 259–266.

Stillman, C., Furnes, H., Le Bas, M., Robertson, A., & Zielonka, J. (1982). The geological history of Maio, Cape Verde Islands. *Journal of the Geological Society*, 139(3), 347–361. Londres.

Stock, M. J., Bagnardi, M., Neave, D. A., Maclennan, J., Bernard, B., Buisman, I., et al. (2018). Integrated petrological and geophysical constraints on magma system architecture in the western Galápagos Archipelago: insights from Wolf volcano. *Geochemistry, Geophysics, Geosystems*, 19(12), 4722–4743.

Streck, M. J. (2008). Mineral textures and zoning as evidence for open system processes. *Reviews in Mineralogy and Geochemistry*, 69(1), 595–622.

Tenzer, R., Bagherbandi, M., & Vajda, P. (2013). Global model of the upper mantle lateral density structure based on combining seismic and isostatic models. *Geosciences Journal*, 17(1), 65–73.

Texier-Teixeira, P., Chouraqui, F., Perrillat-Collomb, A., Lavigne, F., Cadag, J. R., & Grancher, D. (2014). Reducing volcanic risk on Fogo Volcano, Cape Verde, through a participatory approach: Which outcome?. *Natural Hazards and Earth System Sciences*, 14(9), 2347–2358.

Till, C. B. (2017). A review and update of mantle thermobarometry for primitive arc magmas. *American Mineralogist*, 102(5), 931–947.

Torres, P. C., Madeira, J., Silva, L. C., Brum da Silveira, A., Serralheiro, A., & Mota Gomes, A. (1997). Carta geológica das erupções históricas da Ilha do Fogo: revisão e actualização. In *A erupção vulcânica de 1995 na ilha do Fogo, Cabo Verde* (pp. 119–132). Edição do Instituto de Investigação Científica Tropical e Ministério da Ciência e Tecnologia.

Torres, P. C., Madeira, J., Silva, L. C., da Silveira, A. B., Serralheiro, A., & Gomes, A. M. (1998). Carta Geológica das Erupções Históricas da Ilha do Fogo (Cabo Verde): revisão e actualização. *Comunicações do Instituto Geológico e Mineiro*, 84, A193–196.

Torres, P., Silva, L., Serralheiro, A., Tassinari, C., & Munhá, J. (2002). Enquadramento geocronológico pelo método K/Ar das principais sequências vulcano-estratigráficas da Ilha do Sal - Cabo Verde. *Garcia de Orta, Serviços Geológicos*, 18(1–2), 9–13.

Turbeville, B. N., Wolff, J. A., & Le Bas, M. J. (1987). An oceanic nephelinite–phonolite–carbonatite association. Brava, Cape Verde Islands. *Eos*, 68, 1522.

Vales, D., Dias, N. A., Rio, I., Matias, L., Silveira, G., Madeira, J., et al. (2014). Intraplate seismicity across the Cape Verde swell: A contribution from a temporary seismic network. *Tectonophysics*, 636, pp.325–337.

Verhoef, J., Collette, B. J., Dañobeitia, J. J., Roeser, H. A., & Roest, W. R. (1991). Magnetic anomalies off West-Africa (20–38° N). *Marine Geophysical Research*, 13(2), 81–103.

Weidendorfer, D., Schmidt, M. W., & Mattsson, H. B. (2016). Fractional crystallization of Si-undersaturated alkaline magmas leading to unmixing of carbonatites on Brava Island (Cape Verde) and a general model of carbonatite genesis in alkaline magma suites. *Contributions to Mineralogy and Petrology*, 171(5), 43.

Weit, A., Trumbull, R. B., Keiding, J. K., Geissler, W. H., Gibson, S. A., & Veksler, I. V. (2017). The magmatic system beneath the Tristan da Cunha Island: Insights from thermobarometry, melting models and geophysics. *Tectonophysics*, 716, 64–76.

Welsch, B., Hammer, J., Baronnet, A., Jacob, S., Hellebrand, E., & Sinton, J. (2016). Clinopyroxene in postshield Haleakala ankaramite: 2. Texture, compositional zoning and supersaturation in the magma. *Contributions to Mineralogy and Petrology*, 171(1), 6.

Williams, C., Hill, I., Young, R., & White, R. (1990). Fracture zones across the Cape Verde Rise, NE Atlantic. *Journal of Geological Society of London*, 147(5), 851–857.

Wilson, D., Peirce, C., Watts, A., Grevemeyer, I., & Krabbenhoeft, A. (2010). Uplift at litho- spheric swells-I: Seismic and gravity constraints on the crust and uppermost mantle structure of the Cape Verde mid-plate swell. *Geophysical Journal International*, 182, 531–550.

Wilson, D., Peirce, C., Watts, A., & Grevemeyer, I. (2013). Uplift at lithospheric swells-II: Is the Cape Verde mid-plate swell supported by a lithosphere of varying mechanical strength? *Geophysical Journal International*, 193, 798–819.

Worsley, P. (2015). Physical geology of the Fogo volcano (Cape Verde Islands) and its 2014–2015 eruption. *Geology Today*, 31(4), 153–159.

Wunderman, R. (2003). Summary of recent volcanic activity. *Bulletin of Volcanology*, 65(6), 458–459.

Zanon, V., Kueppers, U., Pacheco, J. M., & Cruz, I. (2013). Volcanism from fissure zones and the Caldeira central volcano of Faial Island, Azores archipelago: Geochemical processes in multiple feeding systems. *Geological Magazine*, 150(3), 536–555.

Zanon, V., & Pimentel, A. (2015). Spatio-temporal constraints on magma storage and ascent conditions in a transtensional tectonic setting: The case of the Terceira Island (Azores). *American Mineralogist*, 100(4), 795–805.

Zhao, Z.-F., & Zheng, Y.-F. (2003). Calculation of oxygen isotope fractionation in magmatic rocks. *Chemical Geology*, 193, 59–80.

4

Anatomy of Intraplate Monogenetic Alkaline Basaltic Magmatism: Clues From Magma, Crystals, and Glass

Marco Brenna[1], Teresa Ubide[2], Alexander R. L. Nichols[3], Silvio Mollo[4,5], and Alessio Pontesilli[1]

ABSTRACT

Intraplate basaltic systems, often occurring as fields of small monogenetic volcanoes, are dominated by eruption of alkaline basaltic rocks, ranging from nephelinite/basanite to transitional/subalkaline. Their primitive erupted compositions imply limited crustal modification, thus providing an important probe into deep, lithospheric mantle processes. The whole-rock chemical variability within single eruptions is controlled by the characteristics of the primary melting source, as well as near-source percolative/reaction processes. Complex crystal textures and compositions have so far demonstrated that basaltic magmas are principally processed and modified within the lithospheric mantle with minor modification en route through the crust. Fractional crystallization and magma mixing modify melts throughout ascent, and can imprint secondary chemical intra-eruptive variability. Quantifiable temperature and pressure parameters constrain the depth of formation, and hence provide information about the role of different mineral phases in deep versus shallow chemical evolution. Volatile components in the melt can be quantified on glass and melt inclusions. These analyses may help to reconstruct initial dissolved volatile content to further constrain the source characteristics and magmatic ascent dynamics. Integrated studies of crystals and melt paint a picture of extended lithospheric mantle to minor crustal processing resulting from the complex deep plumbing of monogenetic basaltic systems. This highlights the need for improved resolution to characterize true primary signatures and hence elucidate the formation of intraplate alkaline basalts.

4.1. INTRODUCTION

Basalt is the most common rock in Earth's crust, although it is admittedly mostly submerged as the oceanic floor. Basalts (*sensu lato*) also represent the compositions of partial melts forming in the mantle (Green, 1973), and hence primary magmas from which many intermediate and silicic igneous rocks are derived. Basaltic rocks are therefore fundamental for developing our understanding of processes of magma formation and evolution. Mid-oceanic ridge basalts (MORBs) are generated where tectonic plates diverge and new crust is formed. Melting in these settings occurs by adiabatic decompression (Langmuir et al., 1992; Oxburgh & Turcotte, 1968), and despite local and regional variability (Shimizu et al., 2016; Wood, 1979), MORBs have a restricted compositional

---

[1] *Department of Geology, University of Otago, Dunedin, New Zealand*

[2] *School of Earth and Environmental Sciences, The University of Queensland, Brisbane, Australia*

[3] *Department of Geological Sciences, University of Canterbury, Christchurch, New Zealand*

[4] *Department of Earth Sciences, Sapienza – University of Rome, Rome, Italy*

[5] *Istituto Nazionale di Geofisica e Vulcanologia, Rome, Italy*

Crustal Magmatic System Evolution: Anatomy, Architecture, and Physico-Chemical Processes, Geophysical Monograph 264, First Edition.
Edited by Matteo Masotta, Christoph Beier, and Silvio Mollo.

DOI: 10.1002/9781119564485.ch4

range compared to intraplate oceanic island basalts (OIBs) (e.g., Pilet, 2015). Despite the misleading appellation of these latter magma types, rocks with OIB characteristics occur in continental as well as oceanic settings. Our understanding of the generation of these intraplate rock suites, and the associated mantle plume theory (Morgan, 1971), was originally developed using intraoceanic islands as type localities, notably Hawaii (Wilson, 1963), and hence the name. OIBs are predominantly understood to be produced by adiabatic decompression (Cawthorn, 1975; Green & Ringwood, 1967). If exotic (metasomatic) amphibole and/or phlogopite are present, they may break down and cause melting upon compression, such as during lithospheric delamination (Allen et al., 2013). OIBs may also not be derived directly from the partially molten portion of an upwelling mantle diapir, with post-melting processes such as chromatographic percolation, reactions with overlying lithosphere, and re-melting due to thermal perturbation contributing to final basalt magma formation (Godard et al., 1995; Harte et al., 1993; Mallik & Dasgupta, 2012; Menzies & Murthy, 1980; Pilet, 2015). The wide compositional spectrum (major and trace elements and isotopes) of OIBs implies that the process of melting and melt modification through crystallization involve a greater number of variables than those governing MORB generation. As a consequence, the tectonic and petrogenetic processes of intraplate rock suites are still hotly debated (Foulger & Jurdy, 2007; Foulger et al., 2005; Herzberg, 2010; Pilet et al., 2008).

Systems with OIB-like characteristics are associated with magma spanning a broad compositional spectrum from subalkaline (tholeiitic) basalt to basanite/nephelinite (and some lamprophyre), with rhyolite to phonolite being their evolved derivatives. They also occur in a variety of tectonic settings from oceanic and continental intraplate to some back-arc environments. In this chapter, we will focus particularly on continental intraplate basaltic suites consisting of multiple monogenetic magma batches with OIB-like alkaline basalt/basanite associations. We will extend the discussion to subalkaline basalts where they occur in the context of their alkaline correlatives. The rationale for focusing our attention on monogenetic alkaline basaltic rocks is that they generally provide a direct probe into the processes involved with magma generation and evolution, and they are ubiquitous in most continental intraplate settings. Intraplate monogenetic alkaline basalts often host inclusions of lithospheric peridotite, indicative of their relatively rapid ascent from the mantle (O'Reilly & Griffin, 2011; Spera, 1984). The lack of complex plumbing and storage has implications in terms of minimizing the potential processes of magma modification en route to the surface (McGee & Smith, 2016). The relatively limited crustal interaction makes monogenetic alkaline basaltic rocks a useful tool to investigate deep processes of partial melting and melt modification. Their generally elementary crystal cargo, often consisting of only olivine and clinopyroxene, is another beneficial aspect to help the reconstruction of primitive and parental melt characteristics. Occasional complex zonation patterns of crystals can help resolve deep to shallow plumbing processes (Coote & Shane, 2018; Duda & Schmincke, 1985; Jankovics et al., 2013; Jankovics et al., 2016) and hence improve the resolution of petrogenetic models. Here we summarize current geochemical and petrological tools employed in the interpretation of continental alkaline basaltic suites to elucidate the magmatic processes within the plumbing system of intraplate monogenetic volcanoes.

4.2. ORIGIN OF INTRAPLATE MONOGENETIC BASALTIC SYSTEMS

Within the framework of the plate tectonic theory, intraplate volcanoes erupt away from the direct influence of either convergent or divergent plate boundaries. In this context, subduction-related and intraplate volcanoes (arc versus OIB magmas) bear distinct chemical signatures (Pearce & Peate, 1995). Due to the input of fluids and residual mineralogy from subducting slabs, the former are enriched in large-ion-lithophile elements (LILEs), depleted in high-field-strength elements (HFSEs) and have generally flat patterns of rare earth elements (REEs) (Elliott et al., 1997; Hawkesworth et al., 1994; Kessel et al., 2005; Tatsumi et al., 1986). By contrast, magmas erupted in intraplate settings tend to be enriched in HFSEs and LILEs, also showing relatively high light/heavy REE ratios (LREEs/HREEs), frequently interpreted to indicate residual garnet in the source of the melts (Clague & Frey, 1982; Floyd, 1991; Sun & McDonough, 1989). Where the spatial distinction between these different rock suites is not obvious, the chemical characteristics become paramount for interpreting their genetic origins. For instance, intraplate alkaline volcanism due to variable asthenospheric flow and decompression occurs in the immediate vicinity of the volcanic arc in North Island, New Zealand (Briggs & McDonough, 1990; McGee et al., 2013; Smith et al., 1993), Kyushu, Japan (Mahony et al., 2011; Mashima, 2009; Sakuyama et al., 2009), the trans-Mexican volcanic belt (Ferrari et al., 2001; Márquez et al., 1999), and the Cascades, western United States (Strong & Wolff, 2003). For the purpose of this chapter, we consider continental intraplate basalts (*sensu lato*) as those rocks with the following chemical characteristics: (a) whole-rock compositions in the fields of basalt-trachybasalt-basanite/tephrite plotted on the total-alkali versus silica (TAS) diagram (Le Maitre et al., 2005) and (b) lack of negative Nb-Ta anomalies on a trace element normalized diagram, otherwise interpreted as direct subduction signatures (Sun & McDonough, 1989).

It is noteworthy that some continental intraplate suites occurring in association with OIB volcanism display an arc-like signature (e.g., Nb-Ta depletion) even when there is no proximal active subduction, thus revealing the characteristics of lithologies involved in magma genesis (Menzies et al., 1991). However, these are rare occurrences and will, therefore, not be treated in detail here.

Magmatic intraplate systems generally occur as fields of small monogenetic volcanoes on both continental and oceanic crust (Smith & Németh, 2017). Because of the spatially and temporally dispersed nature of eruptions and their relatively short duration (weeks to a few years), such systems do not generally construct large volcanic edifices. The lack of burial of early eruptions means that field-scale eruptive histories can be investigated comprehensively from the onset of activity (Condit & Connor, 1996; Leonard et al., 2017), revealing changes occurring within the magma source area over the lifetime of the volcanic field (Brenna et al., 2012a; Valentine & Perry, 2006). Individual small volcanoes often form single scoria or phreatomagmatic cones or maars with small lava fields (Valentine and Gregg, 2008) and erupted volumes <<1 km^3 (Kereszturi et al., 2013), implying low magmatic flux from the mantle (Valentine & Hirano, 2010; Valentine & Perry, 2007). Historical examples (with scientific reports) of monogenetic eruptions, albeit in arc settings, are the Ukinrek maars, Aleutian arc, Alaska (Kienle et al., 1980), the generation of Teishi Knoll during submarine eruptions off the Izu Peninsula, Japan (Yamamoto et al., 1991), and the basaltic andesite to andesite Paricutin cone and lava field in the Trans-Mexican volcanic belt (Larrea et al., 2017; Segerstrom, 1966). Recent examples of actual intraplate monogenetic basaltic eruptions, though without direct observational records, include Laoheishan and Huoshaoshan (1719–1721 CE), Wudalianchi Volcanic Field, China (Feng & Whitford-Stark, 1986), Rangitoto (ca. 1500 CE), Auckland Volcanic Field, New Zealand (Needham et al., 2011), and the Al-Madinah eruption (1256 CE), Kingdom of Saudi Arabia (Camp et al., 1987). Due to the long recurrence times, such eruptions are not perceived as major hazards, and hence human settlements are constructed on volcanic fields (e.g., Auckland). Nevertheless, even relatively small eruptions could result in considerable loss of life and infrastructure (McDonald et al., 2017).

Alkaline basalts are not just a modern occurrence and have been erupted throughout Earth's history (Manikyamba & Kerrich, 2011). In the Archean, however, alkaline basaltic rocks are less abundant than other basaltic rock types (such as subalkaline, tholeiites, or rocks related to hydrous melting), possibly due to poor preservation and/or non-ideal mantle conditions for their generation, such as high mantle potential temperatures and high degrees of melting (Blichert-Toft et al., 1996). Mantle metasomatism (Menzies & Hawkesworth, 1986) derived from subduction and recycling of ancient crustal components is likely to be a prerequisite to form alkaline basalts because of their commonly enriched mantle isotopic signatures (Davies & Rawlinson, 2014; Menzies & Murthy, 1980; Wass & Roge, 1980), consequently explaining the paucity of such magma types early in the Precambrian. The origin of the recycled crustal component is still a matter of debate. It may be linked to either mantle cycling of subducted plates (Kogiso & Hirschmann, 2006; Xu, 2014) or delaminated lower crustal material (Homrighausen et al., 2018; Weiss et al., 2016), and is increasingly recognized to involve a carbonated component (Zeng et al., 2010). The mineralogical make-up of the melting material is another aspect that has as yet not met consensus. This is in part due to heterogeneities in chemical signatures that, given the lack of well-constrained parameters (such as modal mineralogy and partitioning values), can be accounted for by different models. Deep melting, reactions, and crystallization processes that involve principally pyroxenes and hydrous mineral phases (Condamine & Médard, 2014; Robinson et al., 1998; Späth et al., 2001) produce competing chemical trends, and it may be impossible to distinguish them with confidence. For instance, Pilet (2015) proposed a model whereby primitive basanites/alkaline basalts melts are derived from the melting of metasomatically derived hornblendite and react with orthopyroxene in the lithosphere to produce a trend toward subalkaline compositions. Conversely, Mallik and Dasgupta (2012) formed alkaline compositions starting from eclogite-derived subalkaline melts and through reaction-crystallization of orthopyroxene in peridotite. Moreover, deep clinopyroxene crystallization during early magma ascent may generate trends toward an increasing apparent alkaline character (decreasing SiO_2 and increasing Na_2O and K_2O) (Re et al., 2017; Smith et al., 2008).

In addition to mantle metasomatism/reaction and/or deep crystallization affecting the composition of primitive alkaline magmas, other models advocate for melts derived from distinct lithologies and different degrees of partial melting within the asthenosphere/lithosphere (Beccaluva et al., 2007; Harangi et al., 2015; Kim et al., 2019; McGee et al., 2013; Peters et al., 2008; Timm et al., 2010). There is general consensus that the mantle is heterogeneous on all scales. Distinct lithologies, however, have very different solidus curves, separated by several

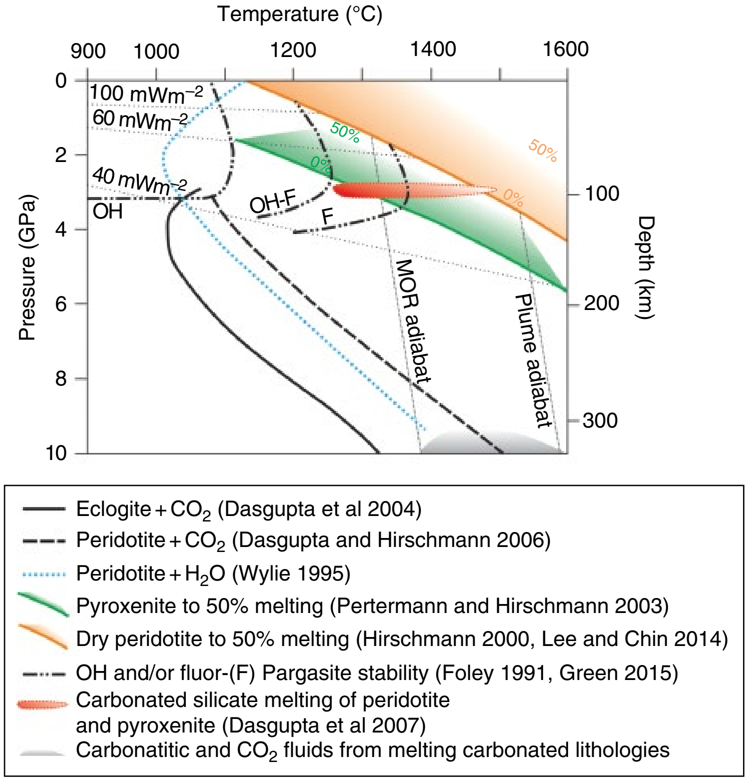

Figure 4.1 Summary of the solidus conditions of different mantle lithologies. It should be emphasized that distinct lithologies have very different melting temperatures and pressures. In the absence of clear indicators of thermal anomalies (i.e., mantle plumes), or vigorous mantle convection or upwelling, it is unlikely that unmetasomatized primitive mantle will partially melt because the base of continental lithosphere (e.g., 60 mWm^{-2} geotherm) intersects the mid-ocean ridge (MOR; normal) mantle adiabat at temperatures lower than the peridotite solidus.

hundreds of temperature degrees (Brey et al., 2009; Dasgupta & Hirschmann, 2006; Dasgupta et al., 2004; Kogiso & Hirschmann, 2006) (Figure 4.1). For instance, at 3 GPa, the solidus of carbonated eclogite is at <1100 °C, whereas that of dry peridotite is >1400 °C, and melting would generate widely differing liquids (Dasgupta et al., 2004). Therefore, models advocating for melting of different lithologies ought to be verified for consistency with the petrological and thermodynamic properties of the lithologies involved, and whether these can melt contemporaneously (and to the required degree) within a restricted spatial and temporal interval. Metasomatism and melt/mantle reactions may represent a continuum solution to explain distinct compositions (Pilet et al., 2005), often erupted within single small-volume monogenetic events (Brenna et al., 2010; Needham et al., 2011). Uncertainty remains large, and further and more advanced data-handling techniques may be necessary to produce models that can be applied generally.

The mechanisms responsible for the destabilization of the mantle source and its partial melting require further attention to better elucidate the origin of intraplate alkaline basaltic systems. Often, decompression melting is associated with upwelling in mantle plumes (Davies & Bunge, 2006; Kimura et al., 2018; Ritter et al., 2001). Peridotite upwelling can also result from other processes. For example, lithospheric delamination may lead to upwelling of asthenosphere, causing it to melt (Hoernle et al., 2006; Lustrino, 2005). Edge-driven asthenospheric flow may cause localized upwelling and decompression melting (Ballmer et al., 2015; Demidjuk et al., 2007) as could asthenospheric flow around slab tears (Rosenbaum et al., 2018). “Petit spots” resulting from lithospheric flexures and deformation could facilitate the ascent of existing asthenospheric melts (Harangi et al., 2013; Hirano et al., 2006; Valentine & Hirano, 2010) potentially formed by asthenospheric shear (Conrad et al., 2011). Alternative models require a multi-step process, whereby partial melts from the asthenosphere metasomatize the lower lithosphere, with subsequent thermodynamic destabilization of the latter generating alkaline magmas (Pilet et al., 2008; Pilet et al., 2005; Rooney et al., 2014). All models have their merits and flaws, but they are mostly based on the chemical characteristics of the erupted lavas.

The rheological and physical mechanisms involved in the upwelling of mantle peridotite have also been broadly constrained and provide an additional perspective to evaluate the feasibility of melting models. For instance, upwelling rates relating to continental intraplate volcanic areas have been estimated to be <1 cm a^{-1} in eastern Australia, New Zealand, and Northeast China (Demidjuk et al., 2007; McGee et al., 2011; Zou et al., 2008), and 10% partial melting of peridotite requires adiabatic decompression of ~35 km (Lee & Chin, 2014). Even conceding that alkaline basalts are likely to be generated by only a small percentage of peridotite partial melting, it would require >10 km upwelling over >1 Myr to form an alkaline melt. These timeframes are longer than the lifetime of some volcanic fields, and U-series indicate that partial melting is generally a fast process (Bourdon et al., 2005; Cohen & O'Nions, 1993; Williams & Gill, 1989), making decompression melting an unlikely sole and direct driver of intraplate volcanism. This is further emphasized in the case of contemporaneous eruption of alkaline and subalkaline magmas. Subalkaline magmas are generally modelled to require a greater degree of partial melting at a shallower level. If both compositions are erupted together (e.g., Brenna et al., 2010), it would imply that they had existed as independent magma batches for millions of years because fast contemporaneous melting is unlikely. In the case of melts generated by delamination or edge-driven flows, they would imply some serious irregularities (several tens of kilometers) in the lower lithosphere that ought to be reflected in surface topography. Hence, a robust model of the petrogenesis of intraplate alkaline basalts needs to marry chemical signatures with physical and timescale constraints.

Primarily, the study of intraplate basalts has obvious practical ramifications for society and the economy, in terms of the potential hazards associated with magma ascent and eruption. In this respect, post-sourcing differentiation processes have a more direct bearing on final eruption dynamics compared to the source mineralogy and mechanics. In the following we will focus on interpreting these processes based on rock, mineral, and glass chemistries.

4.3. INSIGHTS FROM WHOLE-ROCK CHEMICAL DATA

Intraplate alkaline basaltic rocks are the most common hosts of mantle xenoliths (Chen et al., 2007; Dalton et al., 2017; Pearson et al., 2003; Vaselli et al., 1995). Quantitative studies of magma ascent rates reveal that intraplate alkaline basalts rise from near-source mantle depths, where some storage may be involved, and ascend rapidly through the crust (Albert et al., 2015; Brenna et al., 2018; Demouchy et al., 2006; Harangi et al., 2013; Jankovics et al., 2013). Consequently, the effect of assimilation and crustal contamination do not generally plague the interpretation of chemical signatures in alkaline basalts, particularly those related to small-volume eruptions (McGee & Smith, 2016). Far from being dominated only by near-primary magmas, however, intraplate alkaline systems have often undergone considerable magmatic evolution to form trachyte/phonolite/rhyolite associations (Ablay et al., 1998; Brenna et al., 2012b; Crossingham et al., 2018; Harangi, 2001; Harangi et al., 1995; Melluso et al., 2018; Moufti et al., 2012). Such magma compositions generally occur in larger-volume central volcanoes that are associated with complex, multi-stage plumbing systems and result from magma stalling and evolving through fractional crystallization and assimilation processes. Nevertheless, nominally evolved magmas, such as trachyte and phonolite, can form broadly "monogenetic" eruptions, such as isolated domes, lava flows, and pyroclastic cones (Brenna et al., 2019; Paulick & Franz, 1997; Wörner & Schmincke, 1984). These could in some cases result from direct extraction of lithospheric peridotite melts (Laporte et al., 2014; Loges et al., 2019), particularly where they host mantle xenoliths (Irving & Price, 1981), although crustal storage and mixing may also explain unusual associations (Abratis et al., 2015; Schmitt et al., 2017). Because of the complexities introduced in the system by crustal storage, which end up obscuring primary magmatic signatures, we will not consider evolved intraplate alkaline series in this chapter.

The TAS (Figure 4.2) diagram (Le Maitre et al., 2005) provides a first-order visualization of the whole-rock chemical character of igneous suites. Considering single intraplate volcanic fields as whole magmatic entities, it is apparent that the range of erupted magmas spans a very broad spectrum, often from foidite/nephelinite to subalkaline basalt, as exemplified by the Auckland Volcanic Field (New Zealand; Figure 4.2a). Not every volcanic field, however, displays the same range and distribution of erupted compositions, likely reflecting heterogeneities in the primary melting mantle material, the degree of partial melting, the degree of percolative interaction, and the reacting lithologies. To constrain the deep processes that are occurring, focusing on single eruptions may facilitate greater sampling resolution and hence provide insightful information unattainable at the scale of entire fields.

The availability and interconnectivity of fertile material to produce melt and allow melt to percolate and be extracted (Katz et al., 2006) influence the volumes of individual melt pockets that eventually coalesce to produce a magma batch sufficient to sustain the opening and propagation of a dike to the surface (Rubin, 1995; Taisne & Tait, 2009). Such deep magma processing is recorded in

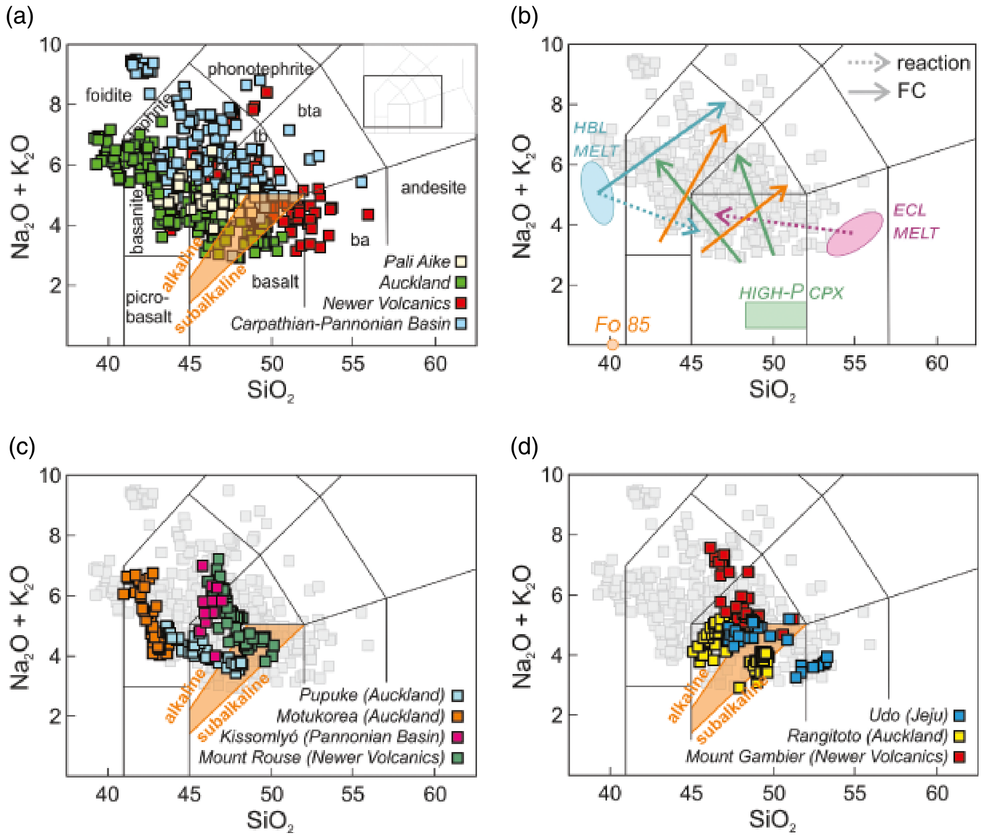

Figure 4.2 (a) TAS diagram with data from four representative intraplate basaltic volcanic fields (data from the GEOROC database: http://georoc.mpch-mainz.gwdg.de/georoc/). The illustrated portion of the TAS diagram is shown in the inset on top right. tb is trachybasalt, bta is basaltic trachyandesite, and ba is basaltic andesite. The distinctions between alkaline and subalkaline basalts and the field of overlap are as shown in Le Maitre et al. (2005) after Bellieni et al. (1983). (b) Possible mechanisms related to the compositional variability within the basaltic spectrum. Hornblendite (hbl) partial melts and melt/peridotite reactions (Pilet, 2015; Pilet et al., 2008). Eclogite (ecl) partial melts and melt/peridotite reactions (Mallik & Dasgupta, 2012). High-pressure clinopyroxene (acmite, Cr-diopside, and Al-augite) fractional crystallization (FC), compositional field from Duda and Schmincke (1985). Olivine FC, Fo 85 is representative of olivine crystallizing in primitive basaltic magmas. (c) and (d) Compositional variation within single monogenetic eruptions: (c) continuous trends from strongly alkaline to mildly alkaline or subalkaline compositions; and (d) alkaline/subalkaline compositional bimodality. Pupuke data from McGee et al. (2013), Motukorea data from McGee et al. (2012), Kissomlyó data from Jankovics et al. (2015), Mount Rouse data from Boyce et al. (2015), Udo data from Brenna et al. (2010), Rangitoto data from Needham et al. (2011), and Mount Gambier data from Van Otterloo et al. (2014). Sources: (a) Data from GEOROC database. (b) Pilet (2015); Pilet et al. (2008); Mallik and Dasgupta (2012); Duda and Schmincke (1985); (c) Data from McGee et al. (2012, 2013); Jankovics et al. (2015); Boyce et al. (2015); Brenna et al. (2010); Needham et al. (2011); Van Otterloo et al. (2014).

the chemical composition of the eruption products. For instance, it is not uncommon that single monogenetic eruptions show a continuous transition from strongly alkaline compositions (nephelinite/basanite) to mildly alkaline or subalkaline basalt, or subsets of this spectrum (Figure 4.2c). The extremes of the compositional spectrum within these eruptions generally have distinct trace element and isotopic characteristics, as seen, for instance, at Mount Rouse in the Newer Volcanic Province of Australia (Boyce et al., 2015) or Motukorea in the Auckland Volcanic Field (McGee et al., 2012). This has traditionally been interpreted to indicate that two distinct primary magma sources, such as peridotite and eclogite, or lithospheric and asthenospheric, exist and interact through mixing. However, the thermodynamics and thermal budget considerations involved in the independent melting of distinct lithologies make such a process unlikely, as noted earlier (Figure 4.1). Instead, in a metasomatic percolation scenario (Mallik & Dasgupta, 2012; Pilet, 2015), the spectrum may indicate melt extraction from porous mantle with interconnected melt channels. Complexly zoned olivine, clinopyroxene, and spinel phenocrysts and xenocrysts of Kissomlyó (Pannonian Basin, Hungary) (Jankovics et al., 2015) or olivine xenocrysts at Pupuke, Auckland Volcanic Field (Brenna et al., 2018), provide evidence that melts with diverse alkaline affinities interacted. These melts were proposed to have undergone different degrees of percolation and deep accumulation resulting in the broad compositional spectrum of those eruptions (Figure 4.2c). The extreme case of compositional diversity within monogenetic volcanoes is where two very distinct magma batches with different degrees of alkalinity are erupted within a single sequence (Figure 4.2d). The Udo tuff cone and lava field (Jeju Island, Korea) and Rangitoto scoria cone and lava (Auckland Volcanic Field) are two emblematic examples, where early erupted alkaline basalt was followed by subalkaline basalt (Brenna et al., 2010; Needham et al., 2011). Mount Gambier (Newer Volcanic Province, Australia) also erupted tephritic and trachybasaltic magmas with a distinct compositional gap (Van Otterloo et al., 2014). Such compositional records have generally been interpreted in terms of two distinct magma sources being tapped. This again raises the issue highlighted above of implausible contemporaneous melting at a range of degrees forming magmas with a range of alkalinity. The spatial and temporal constraints imposed by sequential eruption in a monogenetic volcano make a model involving melting of distinct portions of mantle or variable rates unlikely. Alternatively, the bimodality in the composition of eruption products may indicate the existence of two distinct areas of accumulated melt that are more or less percolated and reacted, and hence more or less alkaline in composition. One common characteristic of such bimodal systems is that the more alkaline magma batch is erupted first, followed by the less alkaline or subalkaline magma, likely indicating the opening of a path to the surface by the deeper-derived (less percolated) alkaline melts (Brenna et al., 2010). It is also observed that the initial alkaline magma is erupted explosively (phreatomagmatic/Strombolian), whereas the subsequent subalkaline magma is erupted effusively with minor Strombolian activity (Brenna et al., 2010, 2015). The overall compositional variation of small-volume eruptions can therefore provide a wealth of information on the deep (lithospheric mantle) plumbing architecture of monogenetic alkaline system and could also be linked to shallow eruption dynamics.

Intra-eruptive chemical variability is another aspect of monogenetic volcanoes that can provide insights into magma processing and ascent dynamics (Blondes et al., 2008; Reiners, 2002). For such investigations, it is necessary to know the stratigraphic order of collected sample suites, which is straightforward when sections are cut through cones by, for instance, wave erosion (Brenna et al., 2011; McGee et al., 2012; Sohn et al., 2012) (Figure 4.3). Stratigraphically ordered chemical variability can elucidate the sequence of magma input in the shallow plumbing and conduit of the ongoing eruption. Volcanic conduits are nevertheless very dynamic environments, and volcanic particles often fall back into the crater area (Graettinger et al., 2016). Hence, distinguishing truly juvenile particles can be challenging, particularly in phreatomagmatic deposits. Even so, there are physical properties of lapilli and bombs that can be employed to infer the degree of reworking and recycling of volcanic particles (D'oriano et al., 2014; Houghton & Smith, 1993). Particularly while sampling in the field, dense crystalline or mud coated clasts ought to be avoided as they likely represent recycled basement lithics or syn-eruptive reworked lapilli and bombs.

Identification of true chemical trends also require high-resolution sampling of as many eruptive beds as possible. Plotting of stratigraphically ordered compositions will reveal whether consistent and systematic trends emerge (Figure 4.3). Systematic trends imply that juvenile material was collected, because sampling of recycled clasts would impose a randomness to the compositional sequence. Smooth changes in chemical composition indicate an eruption that was likely fed by a single magma batch through one isolated dike or a set of interconnected dikes, such as Udo (Jeju) and Motukorea (Auckland Volcanic Field; Figures 4.3b,d,e) (Brenna et al., 2010; McGee et al., 2012). Abrupt switches in chemical composition may instead be indicative of renewed magma feeding by distinct dikes, such as at Ilchulbong and Songaksan (Jeju; Figures 4.3a,c,e) (Brenna et al., 2011; Sohn et al., 2012). Such switches often occur in association with lithic-rich horizons or evidence for brief eruption breaks or vent shifts. These events tend to be short-lived, recording single individual storm surges or tidal events, such as at Songaksan (Sohn & Sohn, 2019). Irregular or saw-toothed trends result from multiple dikes interacting in a chaotic fashion or alternatively that sampling included recycled material or lithic fragments.

A feature that is commonly observed in the chemical stratigraphy of individual eruptions is that the relatively more evolved magma (SiO_2-rich and MgO-poor) is ejected at the onset of the eruption, as pointed out by Smith et al. (2008) at Crater Hill (Auckland Volcanic Field). Data from Udo and Motukorea (Figures 4.3b,d) also show such a trend. This is likely to be related to the dynamics of dike tapping during the eruption. The tip of the feeder dike undergoes high degrees of crystallization due to strong undercooling associated with the opening of a path to the surface (Carrigan et al., 1992). Because of this intra-dike differentiation and the resulting tapping dynamics, a variety of chemical trends can be imposed on

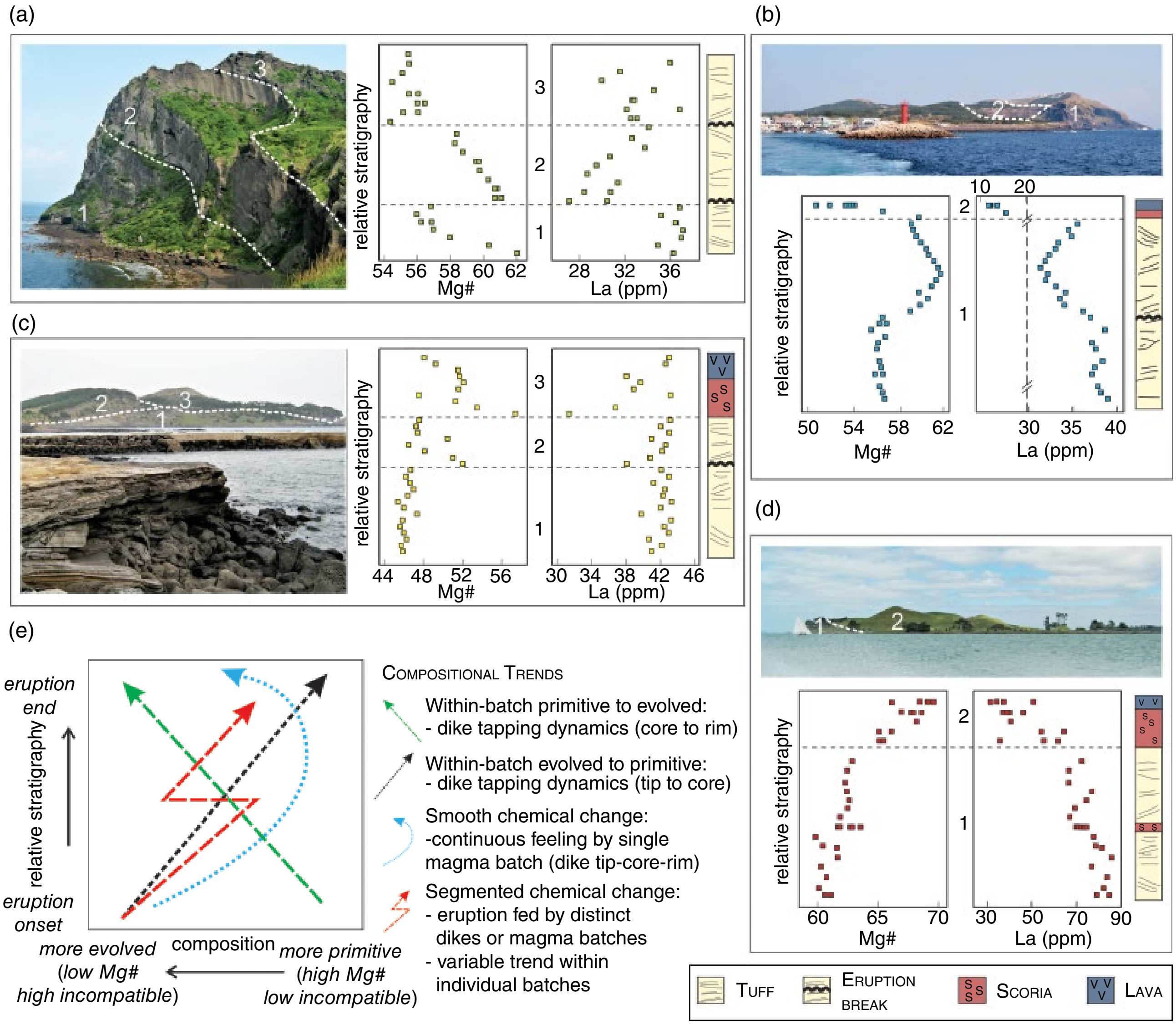

Figure 4.3 Trends in whole-rock compositions of small-volume alkaline basaltic eruptions. (a) Ilchulbong tuff cone (Jeju) was formed by three magma batches with analogous evolutionary trends (Sohn et al., 2012). (b) Udo tuff cone and lava field (Jeju) erupted alkaline and subalkaline magmas (Brenna et al., 2010). (c) Songaksan tuff ring, scoria, and lava consist of individual magma batches with various degrees of evolution (Brenna et al., 2011). (d) Motukorea (Auckland volcanic field) has constant variation from evolved to primitive compositions (McGee et al., 2012). Numbering 1 to 3 indicates eruption packages separated by collapse features, small erosional surfaces, or shifts in eruption styles. (e) Summary and possible interpretation of observed trends. Sources: Based on Sohn et al. (2011); Brenna et al. (2010, 2011); McGee et al. (2012).

the eruption products (Figure 4.3e). Relatively shallow effects on the magma composition are, however, distinct from deep, near-source crystallization and fractionation. Clinopyroxene tends to be the stable liquidus phase at lithospheric mantle depths, whereas olivine takes over in the crust (Bultitude & Green, 1971; Jakobsson & Holloway, 1986). The intra-suite variability of CaO, V, and Sc (compatible in clinopyroxene but not in olivine) usually indicates the involvement of clinopyroxene versus olivine fractionation. Clinopyroxene fractionation may be cryptic in basalts with principally olivine phenocrysts. This was observed at Crater Hill (Smith et al., 2008) and Udo (Brenna et al., 2010), where the chemical trends within the olivine basalt tuff have decreasing CaO, V, and Sc, with decreasing Mg# despite the lack of clinopyroxene as a phenocryst phase. In relatively hydrous alkaline melts, amphibole may also be involved in petrogenetic processes producing distinct chemical signatures, particularly in terms of the relative behavior of LILEs, LREEs, and HFSEs (Francis & Ludden, 1995; Mayer et al., 2014). Plagioclase tends to be a late crystallizing phase, generally only forming groundmass microlites or microphenocrysts upon cooling and eruption, or else, if present as an important phenocryst phase, implies considerable crustal processing (Giacomoni et al., 2014; Mollo et al., 2015; Ubide & Kamber, 2018). Early clinopyroxene and potentially amphibole fractionation implies that those trace element ratios commonly employed to interpret source characteristics, such as LREEs/HREEs, become unreliable. HREEs partition into both phases preferentially compared to LREEs (refer to the GERM partition coefficients database https://earthref.org/KDD/ for a comprehensive summary). The compositional changes that reflect clinopyroxene and amphibole crystallization play a major role in controlling the OIB signature of erupted magmas (Mollo et al., 2018; Scarlato et al., 2014). Primary LREEs/HREEs ratios can be changed, potentially imposing misleading "garnet signatures" on the melt (Bonadiman et al., 2005; Scott et al., 2016). In order to investigate true source signatures, it is therefore essential to unravel any near-source modification process, and focus on primitive (high-MgO) samples without crystal accumulation (Ubide et al., 2014b).

4.4. INSIGHTS FROM CRYSTAL COMPOSITIONS

The relative contribution of melting/metasomatism and fractional crystallization processes remains an enigmatic aspect of the chemical variability in basaltic products. Early-formed phenocrysts, antecrysts, or xenocrysts, however, witnessed deep processes and hence provide a first-hand look at the plumbing system of basaltic volcanoes. Alkaline basaltic rocks are relatively simple petrographically, consisting principally of a macrocryst assemblage dominated by olivine + clinopyroxene in a microlitic groundmass of olivine + clinopyroxene + plagioclase + oxide. Amphibole and phlogopite require H_2O-rich magmas, and with feldspathoids are confined to the SiO_2-poor end of the spectrum, as shown in H_2O-saturated experiments conducted on the melanephelinite from Kakanui (Waiareka-Deborah volcanics, New Zealand) (Merrill & Wyllie, 1975) and the nepheline mugearite of The Anakies (Newer Volcanic Province, Australia) (Irving & Green, 2008). Empirical hygrometry also suggests that H_2O content >3 wt% is required for amphibole and mica to be stable in the basanites and nephelinites with lamprophyric affinities at Jagged Rock (Hopi Buttes Volcanic Field, United States) (Re et al., 2017) and the Catalonian Coastal Range (Spain) (Ubide et al., 2014a). Plagioclase macrocrysts are prevalently segregated from SiO_2 saturated (subalkaline) magmas, such as those erupted in the Kaikohe-Bay of Islands Volcanic Field (New Zealand) (Coote et al., 2018). They also indicate relatively H_2O-poor melts or shallow degassing and crustal processes, with deviation from purely monogenetic basaltic systems (Crossingham et al., 2018; Giacomoni et al., 2014).

Detailed studies of the crystal cargo of alkaline basaltic rocks have, however, revealed a complex textural architecture (Coote & Shane, 2018; Duda & Schmincke, 1985; Jankovics et al., 2012; Jankovics et al., 2019; Re et al., 2017; Shane & Coote, 2018; Ubide et al., 2014a). For example, the occurrence of concentric zoning in clinopyroxene, as well as the development of sieve-textured and partially resorbed phenocrysts (Figure 4.4b), are indicative of disequilibrium processes including magma recharge and mixing (de Maisonneuve et al., 2016; Streck, 2008; Ubide et al., 2014a; Ubide & Kamber, 2018), whereas sector (hourglass) zoning is a response to crystal growth rates and undercooling phenomena (Masotta et al., 2020; Ubide et al., 2019). Concentric zonation can take on very different forms, from normal (more primitive core) to reverse (more evolved core), to oscillatory, patchy, or stepped (Figure 4.4). This generally means that antecrysts (crystals from preceding but genetically related magma batches) can be reincorporated and transported multiple times by subsequent magmas during ascent, similar to occurrences at more complex polygenetic volcanoes (Davidson et al., 2007). Several detailed case studies have been performed on the small alkaline volcanoes in the Carpathian-Pannonian Basin. Jankovics et al. (2015, 2019) identified up to five different types of olivine based on compositions and textures within single small eruptions. These were interpreted to represent crystal growth in storage areas within both the upper lithospheric mantle and the lower crust with subsequent magma mixing and crystal recycling (Figure 4.4a). Clinopyroxene crystals similarly display diverse zoning and distinct compositions (Figure 4.4b) in the Pannonian Basin volcanoes (Jankovics et al., 2016), as well as Eastern Austria (Dobosi et al., 1991), Jeju Island (Brenna et al., 2012a), the Hopi Buttes Volcanic Field (United States) (Re et al., 2017), and the Eifel Volcanic Field (Duda & Schmincke, 1985), for example. The occurrence of crystals derived from several levels within the plumbing systems and that have interacted with diverse magma batches implies that the plumbing system of even small-volume basaltic volcanoes is not as simple as the rock petrography may superficially suggest. Compositionally distinct accumulation and storage zones call into question the literal "monogenetic" character of some basaltic volcanoes. The deep portions of these feeding systems still require accurate investigation, in order to better resolve the different role played by partial melting and metasomatic source-related processes. For this reason, integrated studies dealing with bulk rock as well as phenocrysts and xenocrysts

(a) olivine

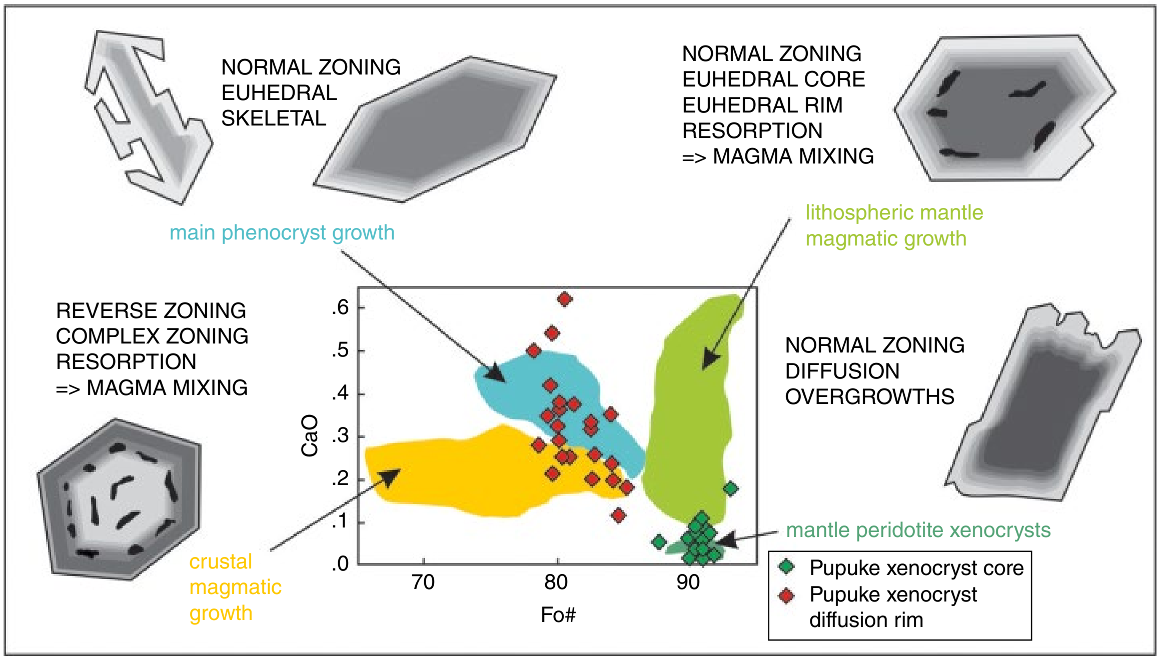

(b) clinopyroxene

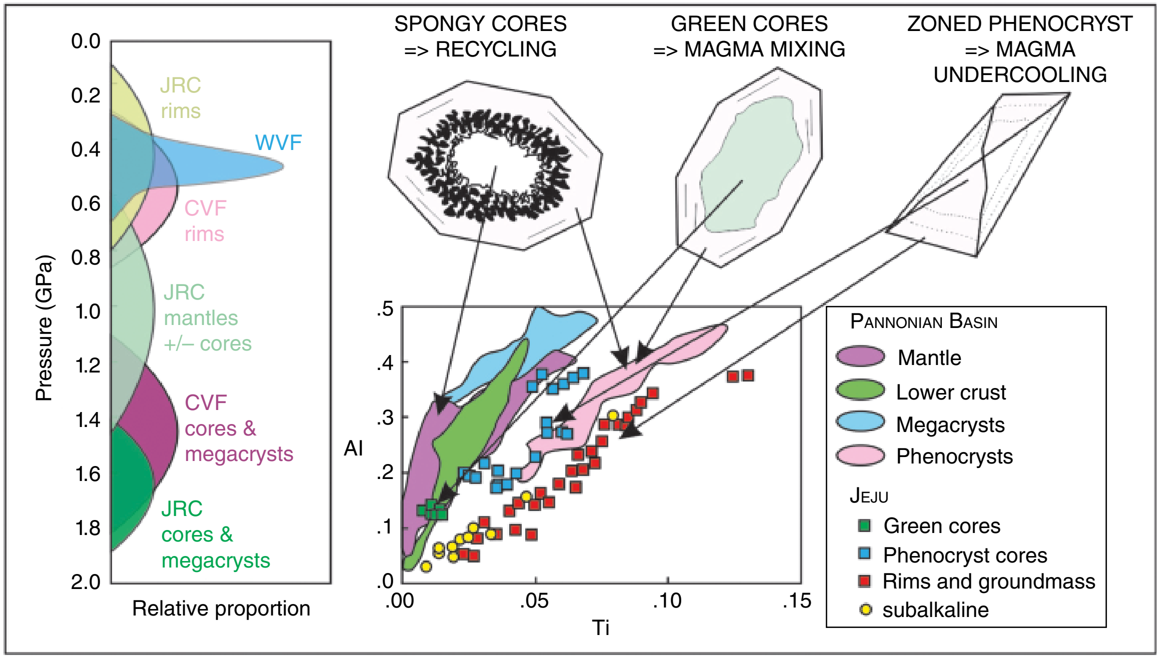

Figure 4.4 Summary of zoning patterns on olivine and clinopyroxene crystals in monogenetic alkaline basaltic systems. (a) Olivine textures and compositions indicative of complex magmatic processes involving diffusion and overgrowths (Shea et al., 2015). Grayscale olivine sketches indicate BSE response (dark = high Fo#, light = low Fo#). Compositional fields are from Jankovics et al. (2015), and Pupuke data are from Brenna et al. (2018). (b) Clinopyroxene textures and compositions are clear indicators of the conditions of crystallization, with spongy and green cores indicating crystal recycling and magma mixing (Duda and Schmincke, 1985; Ubide et al., 2014a) and sector zoning indicative of undercooling conditions (Masotta et al., 2020; Ubide et al., 2019). Ti and Al represent atoms per formula unit (considering 6 O). Pannonian Basin data from Jankovics et al. (2016), Jeju data from Brenna (2012). Clinopyroxene can be a useful geobarometer indicative of crystallization at various levels within the lithosphere. Jagged Rock Complex (JRC) pressures from Re et al. (2017), Calatrava Volcanic Field (CVF) pressures from Villaseca et al. (2019), and Whangarei Volcanic Field (WVF) pressures from Shane and Coote (2018). Sources: Shea et al. (2015); Jankovics et al. (2015); Brenna et al. (2018); Duda and Schmincke (1985); Ubide et al. (2019); Ubide et al. (2014a); Masotta et al. (2020); Jankovics et al. (2016); Brenna et al. (2012); Re et al. (2017); Villaseca et al. (2019); Shane and Coote (2018).

(or xenoliths) are necessary to elucidate the complex interplay between the original genetic signature of magmas and their differentiation through the upper mantle and crust.

Most of the open-system processes that can significantly change the compositions of magmas by shifting them toward intermediate and evolved terms are confined to crustal depths. For example, in the monogenetic volcanoes of the Kaikohe-Bay of Island Volcanic Field, intra-crystal isotopic zoning provides clues to the potential contribution of crustal contamination during the geochemical evolution of magmas (Coote et al., 2018). Complexly zoned plagioclase testifies to a crustal storage zone where assimilation occurred, contaminating the Sr isotopic signature of the mantle-derived magma. This can be compounded by mixing with stalled batches of magma from preceding diking events related to failed eruptions or unerupted magma from previous eruptions (Coote & Shane, 2018; Jankovics et al., 2019). Indeed, such crustal processing may be a precondition for the development of large volcanoes erupting trachytes and phonolites (Brenna et al., 2012b).

Different mineral phases have different stabilities in alkaline magmas, with clinopyroxene, rather than olivine, being the liquidus phase at >1.5–2 GPa (Bultitude & Green, 1971; Irving & Green, 2008; Jakobsson & Holloway, 1986). This also allows crystallization and fractionation within the lithospheric mantle to be distinguished from crystallization and fractionation within the crust (Dobosi et al., 1991). For a more quantitative approach concerning the depth of crystallization, there are now several updated thermometers, barometers, and hygrometers calibrated specifically for alkaline/subalkaline basaltic systems (Table 4.1), which can assist in constraining the crystallization conditions of magmas and identifying potential depths of magma storage. Several crystallization scenarios have been observed in intraplate monogenetic basaltic systems. Shane and Coote (2018) and Coote and Shane (2018) found that in the Whangarei and Kaikohe-Bay of Islands Volcanic Fields clinopyroxene crystallization occurs prevalently within the crust (Figure 4.4b). This is consistent with their investigation of plagioclase zoning, which also revealed a well-developed crustal storage system (Coote et al., 2018). However, in different systems, storage and crystallization may occur over a variety of different levels. Clinopyroxene thermobarometry revealed a bimodal distribution in the Calatrava Volcanic Field (Spain) (Villaseca et al., 2019). These authors interpreted the formation of cumulates within the lithospheric mantle as well as crystallization within the crust. Ubide et al. (2014a) obtained similar results, with principally two depths of storage within the upper mantle and lower crust in lamprophyres from the Catalonian Coastal Range (Spain). On the other hand, in the Springerville Volcanic Field (United States), Putirka and Condit (2003) found that clinopyroxene crystallization principally occurred at two levels in the crust (lower and upper), reflecting density and rheology boundaries. Crystallization may also be continuous during magma ascent from mantle depths, such as in the case of the Jagged Rock Complex, Hopi Buttes Volcanic Field (United States) (Re et al., 2017). Here, clinopyroxene cores mostly formed within the mantle, with crystal mantles forming from mantle to crust, and crystal rims formed within the crust.

Such variability bears similarities with active composite volcanoes, for which most thermobarometric models that apply to alkaline basaltic systems have been developed. For example, Mt. Etna (Sicily, Italy) is one of the most active and monitored volcanoes in the world, and although it is not *sensu stricto* a basaltic system (historically erupted compositions range up to trachyte) (Ferlito & Lanzafame, 2010), its ongoing basalt-dominated eruptions provide an outstanding opportunity to probe the plumbing dynamics on human timescales. The present-day activity at the volcano consists of trachybasaltic explosive and effusive products sharing a common mineral assemblage of plagioclase + clinopyroxene + olivine + titanomagnetite (Mollo et al., 2015). Mantle-derived magmas ascend toward shallower crustal reservoirs through complex crystallization-recharge processes (Kahl et al., 2011; Ubide & Kamber, 2018, and references therein). The crystallization of clinopyroxene is ubiquitous within the entire plumbing system, recording the entire decompression and cooling path of ascending magmas (Perinelli et al., 2018). On the other hand, the stability of olivine and plagioclase is restricted to the shallower portion of the plumbing system under the control of H_2O-saturated melt conditions and further degassing mechanisms (Mollo et al., 2015; Vetere et al., 2015), analogous to small-volume monogenetic basaltic centers in intraplate volcanic fields worldwide. Clinopyroxene compositional changes are dominantly controlled by the substitution of Mg + Fe^{2+} + Na with Ca + Fe^{3+} + Ti in octahedral sites, accounting for the replacement of Si by ^{T}Al in tetrahedral coordination (Figure 4.5a). These different crystallochemical configurations lead to variable proportions of jadeite (Jd), diopside (Di), hedenbergite (Hd), and Ca-Tschermak (CaTs) components in clinopyroxene (Figure 4.5b). Importantly, Jd-melt, Jd-Di+Hd and CaTs-Di+Hd equilibria define P-T-H_2O-sensitive exchange reactions governed by the physicochemical state of the system (Mollo et al., 2018; Perinelli et al., 2016). Thus, the geochemical evolution of clinopyroxene enables accurate tracking of the decompression, cooling, and degassing paths of mafic alkaline magmas rising from deep mantle regions to very shallow crustal levels (Figures 4.5c–d).

Table 4.1 Use of Different Minerals in Alkaline Basaltic Rocks to Interpret Magmatic Processes

Mineral	Technique	Interpretable mechanisms	References
Olivine	Thermometry	Crystallization temperature	Beattie (1993), Putirka (2008)
	Diffusion	Timing of crystallization and residence, magma ascent rates	Costa et al. (2008), Girona and Costa (2013)
	Mineral/melt partitioning	Estimate equilibrium melt compositions	GERM partition coefficients database
	Oxygen isotopes	Magma genesis, ascent and timing	Bindeman (2008)
Clinopyroxene	Thermobarometry	Crystallization temperature and pressure	Putirka (2008), Neave and Putirka (2017), Mollo et al. (2018)
	Hygrometry	Magma water content	Perinelli et al. (2016)
	Diffusion	Timing of crystallization	Brady (1995) and references therein
	Zoning	Magma mixing, crystallization dynamics	Streck (2008), Ubide and Kamber (2018)
	Mineral/melt partitioning	Estimate equilibrium melt compositions	GERM partition coefficients database, Mollo et al (2010), Putirka (1999)
Plagioclase	Thermometry	Crystallization temperature	Putirka (2005, 2008)
	Hygrometry	Magma water content	Waters and Lange (2015)
	Zoning	Magma mixing, assimilation, crystallization dynamics	Ustunisik et al. (2014), Coote et al. (2018)
	Mineral/melt partitioning	Estimate equilibrium melt compositions	GERM partition coefficients database, Namur et al. (2012)
Amphibole	Thermobarometry	Crystallization temperature and pressure	Ridolfi and Renzulli (2012), Putirka (2016)
	Hygrometry	Magma water content	Ridolfi and Renzulli (2012), Putirka (2016)
	Mineral/melt partitioning	Estimate equilibrium melt compositions	GERM partition coefficients database, Putirka (2016)
Ti-magnetite	Thermometry	Crystallization temperature	Aryaeva et al. (2018)
	Oxy-barometry	Magma oxygen fugacity	Aryaeva et al. (2018)
	Geospeedometry	Cooling rates during crystallization	Mollo et al. (2013)

Mantle-derived xenoliths and xenocrysts provide information on the deep magma dynamics of monogenetic volcanoes. These rock/crystal fragments give information on the lithological properties of the lithospheric mantle, testifying to heterogeneities on a range of scales. Mantle xenolith suites from broadly adjacent areas may have overall similar trace element and isotopic characteristics, but regional distinctions can be made, such as in northeast Asia, where there are spatial domains dominated by different types of enriched mantle (Choi et al., 2005). These result from metasomatic re-enrichment of depleted mantle (DMM) from asthenosphere-derived fluids. The signature can be imposed cryptically, such as in the Zealandia lithosphere recorded by LREEs re-enrichment of REE-depleted clinopyroxene in harzburgite and dunite xenoliths in the Dunedin Volcanic Group (Dalton et al., 2017), or explicitly such as in metasomatized, amphibole-veined peridotite in Transylvania (Vaselli et al., 1995) or Antarctica (Coltorti et al., 2004). Isotopic zoning in xenocrysts may indicate heterogeneities imposed by magmatic, hydro-, and carbothermal (CO_2-dominated) fluid percolation. The refractive nature of zircon makes it a useful tracer of such processes in the mantle over Myr timescales (Siebel et al., 2009). However, with respect to the original melting lithology, it is not clear how mantle metasomatic and chromatographic melt percolation may change the isotopic signatures of magmas. Isotopic zoning within mantle peridotite crystals, particularly clinopyroxene, may help to unravel some of these processes, but improved analytical techniques are required to pursue such an avenue.

Mantle-derived xenocrysts and deep plumbing phenocrysts and antecrysts displaying compositional zoning (elemental and/or isotopic) can also provide clues to the dynamics of magma ascent (Jankovics et al., 2013; Oeser et al., 2015). For example, intra-crystal elemental diffusion modeling on crystal cargoes (Costa & Morgan, 2011; Girona & Costa, 2013; Kahl et al., 2015) is a powerful tool to estimate the timescales of magma residence and ascent of alkaline basalts (Albert et al., 2015; Demouchy et al., 2006). Timescales of ascent from the last storage site within the upper mantle/lower crust for monogenetic

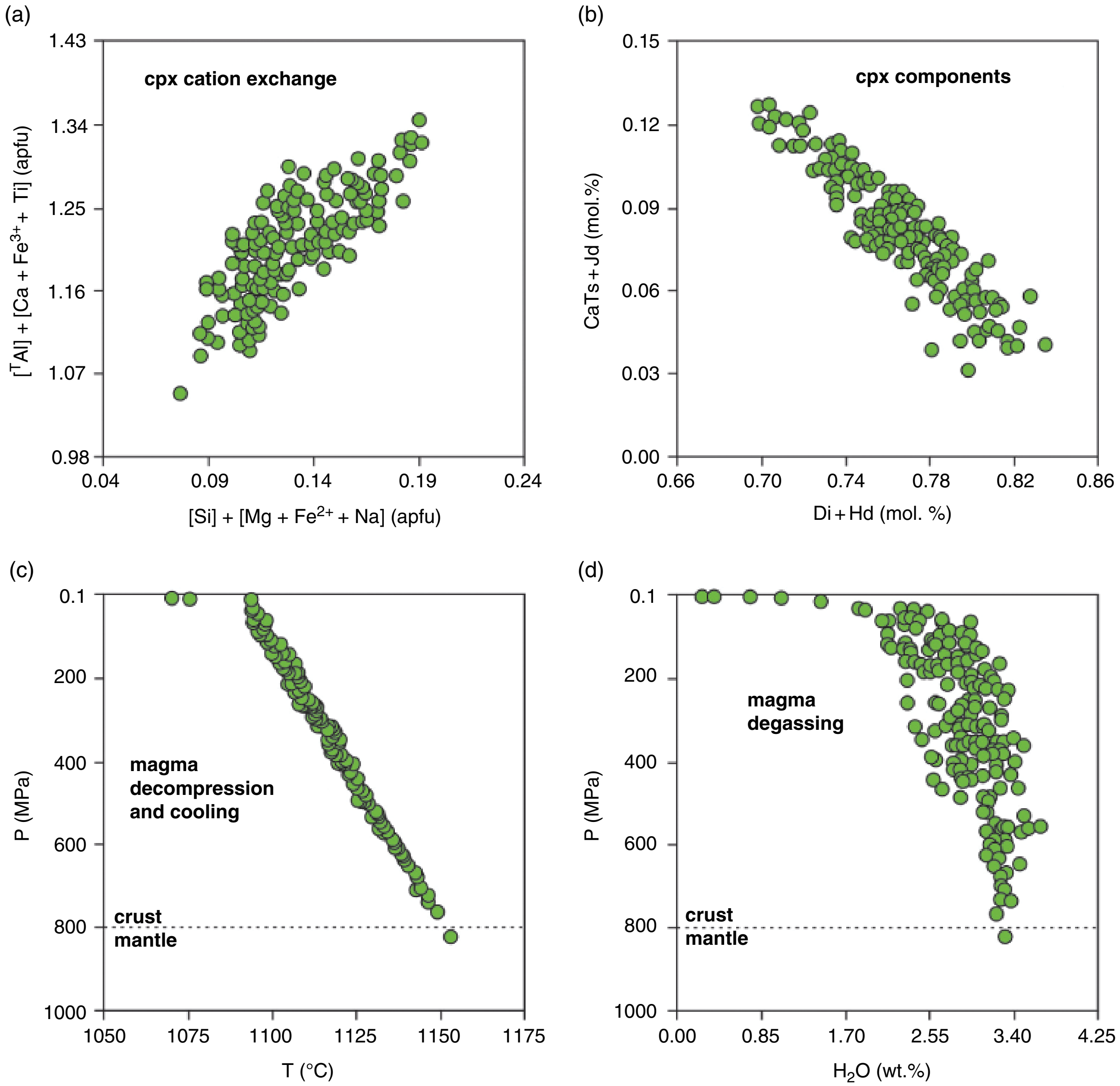

Figure 4.5 Clinopyroxene compositions from 2011–2013 trachybasaltic eruptions at Mt. Etna volcano, showing compositional changes in terms of (a) cations and (b) clinopyroxene components. Compositional variations record magma decompression and cooling (c), and degassing paths (d) (Mollo et al., 2018). Source: Based on Mollo et al. (2018).

basalts is generally estimated to be on the order of few hours to days or weeks depending on the method applied (Jankovics et al., 2013; Ray et al., 2016). A word of caution is warranted here regarding the technique used. Brenna et al. (2018) found that water diffusion time estimates tend to be faster than elemental (Fe-Mg) diffusion estimates, and attributed the discrepancy and fast timescales in the water signature to shallow degassing. They proposed that water loss from the melt starts the water diffusion chronometer instead of xenocryst entrainment within the mantle. Besides the attempted quantification of the rate of ascent of single magma batches, one insight arising from diffusion studies is that not all magmas rise from their source in one pulse. In the Perşani Volcanic Field (Romania), Harangi et al. (2013) found short diffusion rims and longer diffusion "mantles" in olivine xenocrysts. They interpreted these to represent a protracted period (>1 year) of magma stalling within the mantle followed by rapid ascent (few days) through the crust. In the Auckland Volcanic Field, Brenna et al. (2018) found hooked profiles in olivine xenocrysts, and implied that interaction between magmas with different degrees of alkalinity occurred within the deep plumbing also over protracted timeframes (months–years) prior to final ascent (days). These case studies provide evidence for the complex geometry of nominally simple deep plumbing systems. Undoubtedly, advances in analytical resolution will open new opportunities for multifaceted investigations accounting for the compositional changes recorded by the crystal cargo of intraplate basaltic magmas.

4.5. INSIGHTS FROM GLASS COMPOSITIONS

The last component of basalts that records plumbing system and eruptive processes is volcanic glass, that is, the portion of magma that was still liquid (i.e., the silicate melt) and carrying solids (crystals and xenoliths) at the time of eruption. Glass in volcanic products retains most of the physicochemical features of the melt, such as largely incompatible dissolved volatile species (e.g., H_2O, CO_2, SO_2) that do not partition strongly into anhydrous minerals, thus concentrating in the melt. The solubility of volatiles in silicate liquids is largely controlled by depth changes, as it decreases with decreasing pressure, but also depends on composition and temperature. Different volatile species and different mixtures of volatiles have different solubilities. For instance, CO_2-bearing melts become vapor-saturated at higher pressures than those in which CO_2 is absent. The higher the initial CO_2 and H_2O content, the deeper the pressure at which vapor saturation will be achieved (Dixon & Stolper, 1995). CO_2 solubility, in particular, is strongly dependent on composition in basaltic melts (Blank & Brooker, 1994; Dixon, 1997; Holloway & Blank, 1994). In alkaline basalts, the solubility of CO_2 is higher (Dixon, 1997), meaning vapor saturation occurs at lower pressures compared to subalkaline melts with the same initial volatile contents. Dixon (1997) used a seven-component empirical parameter, termed Π [$-6.50\times(\mathrm{Si}+\mathrm{Al}) + 20.17\times(\mathrm{Ca} + 0.8\times\mathrm{K} + 0.7\times\mathrm{Na} + 0.4\times\mathrm{Mg} + 0.4\times\mathrm{Fe})$], with each element in its molar concentration, to model the compositional dependence of H_2O-CO_2 solubility. The calculations of mixed H_2O-CO_2 saturation pressures for basaltic melts in the computer program VolatileCalc (Newman & Lowenstern, 2002) are based on this solubility model. This is to date the most widely used program to calculate mixed H_2O-CO_2 saturation pressures in basalts and rhyolites, largely owing to its ease of use, but it simplifies the compositional parameter in basalts to just SiO_2. However, neglecting the effect of alkalis on CO_2 solubility has been shown to severely overestimate CO_2 saturation pressures in alkaline basalts (Lesne et al., 2011; Vetere et al., 2011), making VolatileCalc not ideal for intraplate alkaline basaltic systems. In response to these discrepancies, Witham et al. (2012) developed the program SolEx to calculate H_2O-CO_2 solubilities and exsolved vapor compositions in basalts based on the parameterization of Dixon (1997), while also adding the other volatiles S and Cl. This model is calibrated for subalkaline basalts and alkaline basalts to nephelinites (<52 wt% SiO_2), and requires the seven oxide components in Π.

An alternative solubility model developed by Papale (1999) and Papale et al. (2006) is based on the multivariate regression of published H_2O and CO_2 solubility data, and produced a 29-component compositional and P-T parameterization. This allows the major oxides SiO_2, TiO_2, Al_2O_3, Fe_2O_3, FeO, MnO, MgO, CaO, Na_2O, and K_2O to be varied. H_2O solubilities are better constrained than CO_2 or mixed solubilities in this model due to the calibration dataset, and Moore (2008) concludes that although the Dixon (1997) model is the best option for tholeiitic melts, the Papale et al. (2006) model works better for calc-alkaline melts. The Papale et al. (2006) model can also deal with compositions that contain more than 52 wt.% SiO_2 and agrees more closely with high-pressure data (>300 MPa) in alkaline basalts (Witham et al., 2012), although the Dixon (1997) and Witham et al. (2012) parameterization is better at lower pressures. Following similar principles to the Papale et al. (2006) model, Duan (2014) developed a thermodynamically based H_2O-CO_2 solubility model for silicate melts using the chemical potential of volatile species in the melt and vapor phases and the Duan and Zhang (2006) equation of state for the vapor phase. The model is compared to existing experimental H_2O and CO_2 solubility data and calculates solubilities over a wide range of temperatures (660 to 1730 °C), pressures (up to 3 GPa), and compositions (ultramafic to silicic, metaluminous to peraluminous and subalkaline to peralkaline).

Another H_2O-CO_2 solubility model developed around the same time as SolEx was presented by Iacono-Marziano et al. (2012), who provided experimental data on a range of mafic melts (alkaline basalt, lamproite, and kamafugite) and used them to develop a semi-empirical model. They showed that alkalis bonded to non-bridging oxygens strongly enhance CO_2 solubility and that CO_2 solubility in mafic melts is more strongly affected by melt composition and silicate structure than H_2O solubility, which supports earlier studies (Blank & Brooker, 1994; Dixon, 1997; Holloway & Blank, 1994). Most recently, Burgisser et al. (2015) developed the D-Compress software, which models the pressure control of volatiles (H_2O, CO_2, and S in the systems O–H, S–O–H, C–S–O–H, C–S–O–H–Fe, and C–O–H) in the vapor and melt phases. The model was calibrated for basaltic, phonolitic, and rhyolitic compositions. The major oxides can be varied, and the solubility laws depend on the predefined (i.e., basalt, phonolite, rhyolite) composition selected.

D-Compress is intended to be used to model the chemical evolution of vapor and fluids phases when significant amounts of H_2O are present under moderately reducing conditions from 790 to 1400 °C, depending on composition and pressure up to 300 MPa. Currently, the models for which links to the operating software are still active are VolatileCalc (Newman & Lowenstern, 2002, at https://volcanoes.usgs.gov/observatories/yvo/jlowenstern/other/VolatileCalc_2.0.xls), the Papale model (Papale et al., 2006, at http://melts.ofm-research.org/CORBA_CTserver/Papale/Papale.php), and D-Compress [Burgisser et al., 2015, at https://ars.els-cdn.com/content/image/1-s2.0-S0098300415000503-mmc5.zip (Windows OS only)].

Volatile exsolution and subsequent magma expansion contribute to explosivity during eruption. The melt loses most of its volatiles during magma decompression and ascent prior to quenching to glass. Therefore, in most cases, melt inclusions within host macrocrysts are used to assess the volatile contents of melts prior to shallow degassing. Melt inclusions are portions of melts trapped during phenocryst growth at depth in the plumbing system. Volatile studies on alkaline basaltic rocks have demonstrated that H_2O and CO_2 can be dissolved at concentrations of several wt.% and thousands of ppm, respectively, together with other potentially important volatile species, such as S and Cl (Kamenetsky & Clocchiatti, 1996; Spilliaert et al., 2006). There is nevertheless a paucity of quantitative studies of the volatile content of alkaline basalt melt inclusions in continental intraplate monogenetic systems. Rowe et al. (2015) found <1 wt% H_2O and S and <2000 ppm Cl and F dissolved in alkaline to subalkaline basalt melt inclusions related to the Rio Grande Rift (United States). Cervantes and Wallace (2003) derived similar concentrations (1.3 wt% H_2O, <1000 ppm Cl and S, 370 ppm CO_2) dissolved in melt inclusions from the monogenetic Xitle volcano, which has OIB-like composition but sits within the supra-subduction Trans-Mexican Volcanic Belt. Such volatile abundances are lower than subduction-related systems (Figure 4.6); however, it is unclear to what degree these results represent partially degassed magmas. For example, Hidas et al. (2010) evaluated volatile content in melt inclusions hosted in clinopyroxenes from spinel lherzolite xenoliths from the Bakony–Balaton Highland Volcanic Field, part of the Pannonian Basin (western Hungary). They calculated H_2O contents of 3.1–4.5 wt% and CO_2 contents of 9000–12000 ppm when considering the contribution of the vapor bubble in addition to the volatiles dissolved in the surrounding glass of the silicate melt inclusion. Such high volatile contents suggest entrapment and crystallization under upper mantle conditions and reinforce the notion that metasomatism may be a precursor to intraplate volcanism. More studies are required to constrain recycled and metasomatic input in continental intraplate monogenetic basalts. Another aspect to consider when attempting volatile species quantification from melt inclusions is post-entrapment crystallization. This can significantly affect their concentrations with resulting discrepancies between pressures determined by volatile and mineral-melt geobarometers (Maclennan, 2017).

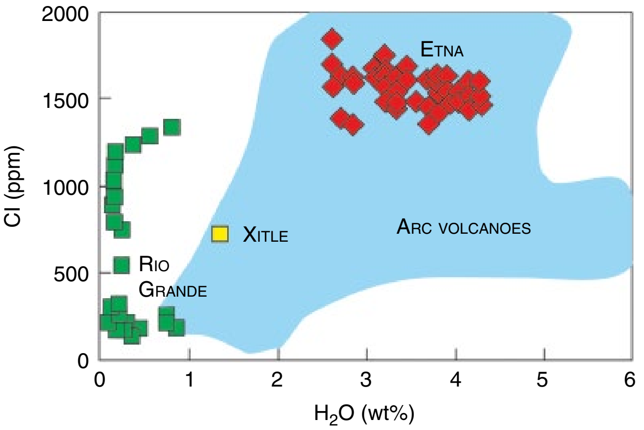

Figure 4.6 Volatile abundances in alkaline basalts related to monogenetic intraplate systems in the Rio Grande Rift (Rowe et al., 2015) and Xitle volcano (Cervantes & Wallace, 2003) tend to be lower than those in basalts from subduction arc systems (blue field; Métrich & Wallace, 2008). Etna data represent high-pressure, undegassed magma with >1000 ppm CO_2 (Spilliaert et al., 2006). Sources: Rowe et al. (2015); Cervantes and Wallace (2003); Métrich and Wallace (2008); Spilliaert et al. (2006).

Relying on the enhanced stability of olivine at lower pressure in alkaline basaltic systems, systematic melt inclusion studies can constrain the depth of magma storage and crystallization at shallow crustal levels (Spilliaert et al., 2006). This is made more effective by integrating whole-rock and melt inclusion data to provide insights into magma source and crystallization processes, such as in the Hainan (China) intraplate system (Liu et al., 2015). Rowe et al. (2011) identified shallow sedimentary basement contamination in the monogenetic Dotsero Volcano (United States) that shifted a basanitic magma composition (preserved in melt inclusions) toward alkaline basalt bulk compositions.

Finally, the composition of glass shards in tephra samples is used as a tool for fingerprinting tephra sources and cross-correlating eruptive records across individual volcanic fields (Hopkins et al., 2015; Shane & Smith, 2000). This method was successfully applied to provide a revised eruptive chronology in the Auckland Volcanic Field (Hopkins et al., 2017). In such investigations, comprehensive sampling and glass analyses are needed, given the potentially broad range of glass compositions found within single eruptive sequences, as in the case of Maungataketake, Auckland Volcanic Field (Agustín-Flores et al., 2014). The glass compositions tend to be broader than whole-rock analyses of analogous products, mostly due to shallow, syn-eruptive microlite crystallization (Verolino et al., 2018). Devitrification of older glass may also affect analytical precision.

4.6. SUMMARY AND CONCLUDING REMARKS

There is currently a breadth of knowledge that enables us to paint a conceptual picture of the complex plumbing architecture of continental intraplate monogenetic volcanic fields (Figure 4.7). The primary source area of magmatism is likely to contain fertile lithologies, such as recycled material from past subduction events or related to delamination. Localized slow upwelling due to broad asthenospheric circulation (or thermal anomalies) may cause these domains to partially melt. The derived fluids (silicate and/or carbonate melts) migrate through the lithospheric mantle and react, particularly with previously metasomatized domains. These processes cause the primary melts to undergo chemical contamination/differentiation through metasomatic/chromatographic processes altering their composition and alkaline character (Figure 4.7). Melt aggregation areas may form at different levels within the lithosphere, thus controlling the overall alkaline signature of ensuing magma batches. These percolation/aggregation volumes match the low-velocity anomalies that are generally identified beneath monogenetic volcanic systems (e.g., Horspool et al., 2006). Magma batches can be extracted without further interaction, or may mix and mingle with coeval or previously injected magmas to form bimodal or broad chemical spectra within single monogenetic eruptive episodes (Figure 4.7). Crustal involvement and contamination are essentially restricted to systems that show chemical evolution to intermediate compositions.

To better understand the origin and time/space evolution of monogenetic volcanoes, and their potential hazards, further constraints are needed, particularly regarding the deeper portion of the system and the percolation reactions that modify the *sensu stricto* primary partial melts. Magmas are complex mixtures of liquid, crystals, and gases. It is only through the integration of detailed studies of all these components that we will be able to gain a comprehensive understanding of natural magmatic systems. Future studies will need to employ a holistic approach focusing on the physicochemical mechanisms controlling the final textures and compositions of crystals and their host rocks. Additional studies are also needed to better constrain the deep storage portions of the plumbing systems that, in turn, control the availability of magmas to feed surface eruptions. In this context, the ensuing eruption characteristics are the consequence of the close interplay between deep (magma generation, fluid percolation, and metasomatism) and shallow (mixing, mingling, and fractionation processes) plumbing system dynamics.

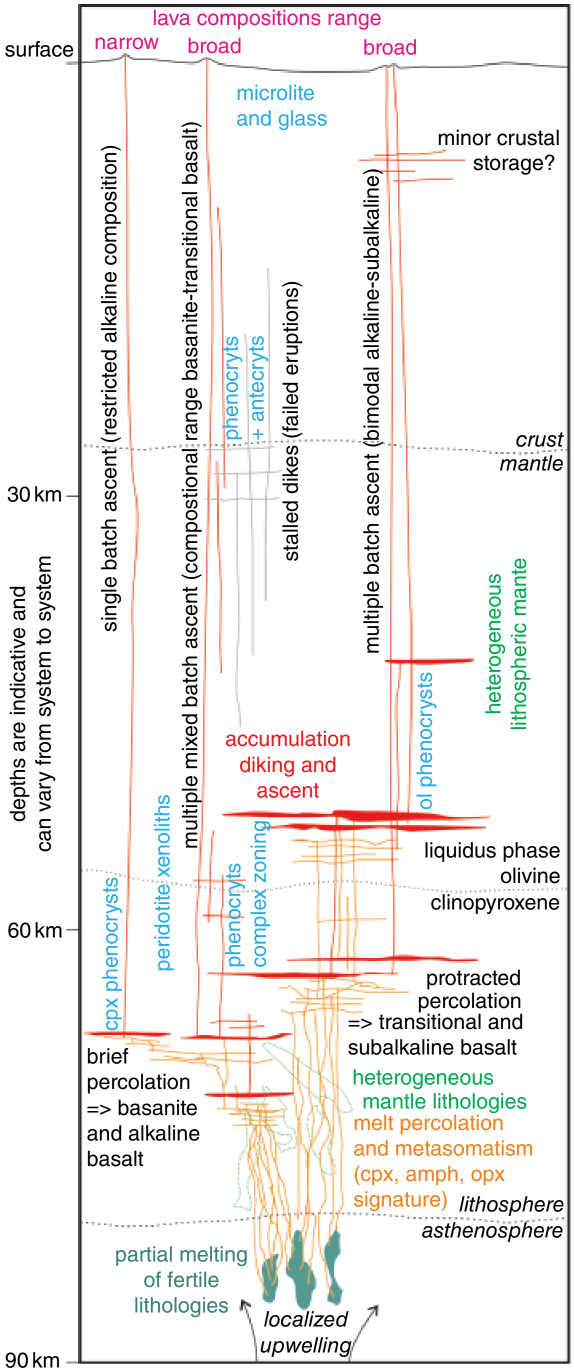

Figure 4.7 Conceptual model of continental intraplate monogenetic basaltic plumbing systems. In small volcanoes, the storage areas are not necessarily connected to the surface by conduits. A large portion of generated magmas may not actually erupt.

ACKNOWLEDGMENTS

We thank Szabolcs Harangi and Abigail Barker for constructive reviews and Matteo Masotta for editorial handling.

REFERENCES

Ablay, G., Carroll, M., Palmer, M., Martí, J., & Sparks, R. (1998). Basanite–phonolite lineages of the Teide–Pico Viejo volcanic complex, Tenerife, Canary Islands. *Journal of Petrology*, *39*, 905–936.

Abratis, M., Viereck, L., Pfänder, J. A., & Hentschel, R. (2015). Geochemical composition, petrography and 40 Ar/39 Ar age of the Heldburg phonolite: Implications on magma mixing and mingling. *International Journal of Earth Sciences (Geologische Rundschau)*, *104*, 2033–2055.

Agustín-Flores, J., Németh, K., Cronin, S. J., Lindsay, J. M., Kereszturi, G., Brand, B. D., & Smith, I. E. M. (2014). Phreatomagmatic eruptions through unconsolidated coastal plain sequences, Maungataketake, Auckland Volcanic Field (New Zealand). *Journal of Volcanology and Geothermal Research*, *276*, 46–63.

Albert, H., Costa, F., & Martí, J. (2015). Timing of magmatic processes and unrest associated with mafic historical monogenetic eruptions in Tenerife island. *Journal of Petrology*, *56*, 1945–1966.

Allen, M., Kheirkhah, M., Neill, I., Emami, M., & McLeod, C. (2013). Generation of arc and within-plate chemical signatures in collision zone magmatism: Quaternary lavas from Kurdistan Province, Iran. *Journal of Petrology*, *54*, 887–911.

Aryaeva, N., Koptev-Dvornikov, E., & Bychkov, D. (2018). A liquidus thermobarometer for modeling of the magnetite–melt equilibrium. *Moscow University Geology Bulletin*, *73*, 177–186.

Ballmer, M. D., Conrad, C. P., Smith, E. I., & Johnsen, R. (2015). Intraplate volcanism at the edges of the Colorado Plateau sustained by a combination of triggered edge-driven convection and shear-driven upwelling. *Geochemistry, Geophysics, Geosystems*, *16*, 366–379.

Beattie, P. (1993). Olivine-melt and orthopyroxene-melt equilibria. *Contributions to Mineralogy and Petrology*, *115*, 103–111.

Beccaluva, L., Bianchini, G., Bonadiman, C., Coltorti, M., Milani, L., Salvini, L., et al. (2007). Intraplate lithospheric and sublithospheric components in the Adriatic domain: Nephelinite to tholeiite magma generation in the Paleogene Veneto volcanic province, southern Alps. *Special Papers-Geological Society of America*, *418*, 131.

Bellieni, G., Justin Visentin, E., Le Maitre, R., Piccirillo, E., & Zanettin, B. (1983). Proposal for a division of the basaltic (B) field of the TAS diagram. *IUGS subcommission on the Systematics of Igneous Rocks*. Circular.

Bindeman, I. (2008). Oxygen isotopes in mantle and crustal magmas as revealed by single crystal analysis. *Reviews in Mineralogy and Geochemistry*, *69*, 445–478.

Blank, J. G., & Brooker, R. A. (1994). Experimental studies of carbon dioxide in silicate melts: Solubility, speciation and stable isotope behavior. *Reviews in Mineralogy and Geochemistry*, *30*, 157–186.

Blichert-Toft, J., Arndt, N. T., & Ludden, J. N. (1996). Precambrian alkaline magmatism. *Lithos*, *37*, 97–111.

Blondes, M. S., Reiners, P. W., Ducea, M. N., Singer, B. S., & Chesley, J. (2008). Temporal-compositional trends over short and long time-scales in basalts of the Big Pine Volcanic Field, California. *Earth and Planetary Science Letters*, *269*, 140–154.

Bonadiman, C., Beccaluva, L., Coltorti, M., & Siena, F. (2005). Kimberlite-like metasomatism and 'garnet signature' in spinel-peridotite xenoliths from Sal, Cape Verde Archipelago: Relics of a subcontinental mantle domain within the Atlantic oceanic lithosphere? *Journal of Petrology*, *46*, 2465–2493.

Bourdon, B., Turner, S. P., & Ribe, N. M. (2005). Partial melting and upwelling rates beneath the Azores from a U-series isotope perspective. *Earth and Planetary Science Letters*, *239*, 42–56.

Boyce, J. A., Nicholls, I. A., Keays, R. R., & Hayman, P. C. (2015). Variation in parental magmas of Mt Rouse, a complex polymagmatic monogenetic volcano in the basaltic intraplate Newer Volcanics Province, southeast Australia. *Contributions to Mineralogy and Petrology*, *169*, 11.

Brady, J. B. (1995). Diffusion data for silicate minerals, glasses, and liquids. *Mineral Physics and Crystallography: A Handbook of Physical Constants*, *2*, 269–290.

Brenna, M. (2012). *Geological evolution and magmatic models for spatially and temporally variable modes of distributed volcanism, Jeju Island, Republic of Korea*, Institute of Agriculture and Environment. PhD Thesis, Massey University, Palmerston North, p. 229.

Brenna, M., Cronin, S. J., Németh, K., Smith, I. E. M., & Sohn, Y. K. (2011). The influence of magma plumbing complexity on monogenetic eruptions, Jeju Island, Korea. *Terra Nova*, *23*, 70–75.

Brenna, M., Cronin, S. J., Smith, I. E., Tollan, P. M., Scott, J. M., Prior, D. J., et al. (2018). Olivine xenocryst diffusion reveals rapid monogenetic basaltic magma ascent following complex storage at Pupuke Maar, Auckland Volcanic Field, New Zealand. *Earth and Planetary Science Letters*, *499*, 13–22.

Brenna, M., Cronin, S. J., Smith, I. E. M., Maas, R., & Sohn, Y. K. (2012a). How small-volume basaltic magmatic systems develop: A case study from the Jeju Island Volcanic Field, Korea. *Journal of Petrology*, *53*, 985–1018.

Brenna, M., Cronin, S. J., Smith, I. E. M., Sohn, Y. K., & Maas, R. (2012b). Spatio-temporal evolution of a dispersed magmatic system and its implications for volcano growth, Jeju Island Volcanic Field, Korea. *Lithos*, *148*, 337–352.

Brenna, M., Cronin, S. J., Smith, I. E. M., Sohn, Y. K., Németh, K. (2010). Mechanisms driving polymagmatic activity at a monogenetic volcano, Udo, Jeju Island, South Korea. *Contributions to Mineralogy and Petrology*, *160*, 931–950.

Brenna, M., Németh, K., Cronin, S. J., Sohn, Y. K., Smith, I. E., & Wijbrans, J. (2015). Co-located monogenetic eruptions~200 kyr apart driven by tapping vertically separated mantle source regions, Chagwido, Jeju Island, Republic of Korea. *Bulletin of Volcanology*, *77*, 43.

Brenna, M., Pontesilli, A., Mollo, S., Masotta, M., Cronin, S. J., Smith, I. E., et al. (2019). Intra-eruptive trachyte-phonolite transition: Natural evidence and experimental constraints on the role of crystal mushes. *American Mineralogist*, *104*, 1750–1764.

Brey, G. P., Bulatov, V. K., & Girnis, A. V. (2009). Influence of water and fluorine on melting of carbonated peridotite at 6 and 10 GPa. *Lithos*, *112*, 249–259.

Briggs, R. M., & McDonough, W. F. (1990). Contemporaneous convergent margin and intraplate magmatism, North Island, New Zealand. *Journal of Petrology*, *31*, 813–851.

Bultitude, R. J., & Green, D. H. (1971). Experimental study of crystal-liquid relationships at high pressure in olivine nephelinite and basanite compositions. *Journal of Petrology*, *12*, 121–147.

Burgisser, A., Alletti, M., & Scaillet, B. (2015). Simulating the behavior of volatiles belonging to the C–O–H–S system in silicate melts under magmatic conditions with the software D-Compress. *Computers & Geosciences*, *79*, 1–14.

Camp, V. E., Hooper, P. R., Roobol, M. J., & White, D. L. (1987). The Madinah eruption, Saudi Arabia: Magma mixing and simultaneous extrusion of three basaltic chemical types. *Bulletin of Volcanology*, *49*, 489–508.

Carrigan, C. R., Schubert, G., & Eichelberger, J. C. (1992). Thermal and dynamical regimes of single-and two-phase magmatic flow in dikes. *Journal of Geophysical Research: Solid Earth*, *97*, 17377–17392.

Cawthorn, R. G. (1975). Degrees of melting in mantle diapirs and the origin of ultrabasic liquids. *Earth and Planetary Science Letters*, *27*, 113–120.

Cervantes, P., & Wallace, P. J. (2003). Role of H_2O in subduction-zone magmatism: New insights from melt inclusions in high-Mg basalts from central Mexico. *Geology*, *31*, 235–238.

Chen, Y., Zhang, Y., Graham, D., Su, S., & Deng, J. (2007). Geochemistry of Cenozoic basalts and mantle xenoliths in Northeast China. *Lithos*, *96*, 108–126.

Choi, S. H., Kwon, S. T., Mukasa, S. B., & Sagong, H. (2005). Sr-Nd-Pb isotope and trace element systematics of mantle xenoliths from Late Cenozoic alkaline lavas, South Korea. *Chemical Geology*, *221*, 40–64.

Clague, D. A., & Frey, F. A. (1982). Petrology and trace element geochemistry of the Honolulu Volcanics, Oahu: Implications for the oceanic mantle below Hawaii. *Journal of Petrology*, *23*, 447–504.

Cohen, A. S., & O'Nions, R. K. (1993). Melting rates beneath Hawaii: Evidence from uranium series isotopes in recent lavas. *Earth and Planetary Science Letters*, *120*, 169–175.

Coltorti, M., Beccaluva, L., Bonadiman, C., Faccini, B., Ntaflos, T., & Siena, F. (2004). Amphibole genesis via metasomatic reaction with clinopyroxene in mantle xenoliths from Victoria Land, Antarctica. *Lithos*, *75*, 115–139.

Condamine, P., & Médard, E. (2014). Experimental melting of phlogopite-bearing mantle at 1 GPa: Implications for potassic magmatism. *Earth and Planetary Science Letters*, *397*, 80–92.

Condit, C. D., & Connor, C. B. (1996). Recurrence rates of volcanism in basaltic volcanic fields: An example from the Springerville volcanic field, Arizona. *Geological Society of America Bulletin*, *108*, 1225–1241.

Conrad, C. P., Bianco, T. A., Smith, E. I., & Wessel, P. (2011). Patterns of intraplate volcanism controlled by asthenospheric shear. *Nature Geoscience*, *4*, 317.

Coote, A., & Shane, P. (2018). Open-system magmatic behaviour beneath monogenetic volcanoes revealed by the geochemistry, texture and thermobarometry of clinopyroxene, Kaikohe-Bay of Islands volcanic field (New Zealand). *Journal of Volcanology and Geothermal Research*, *368*, 51–62.

Coote, A., Shane, P., Stirling, C., & Reid, M. (2018). The origin of plagioclase phenocrysts in basalts from continental monogenetic volcanoes of the Kaikohe-Bay of Islands field, New Zealand: Implications for magmatic assembly and ascent. *Contributions to Mineralogy and Petrology*, *173*, 14.

Costa, F., Dohmen, R., & Chakraborty, S. (2008). Time scales of magmatic processes from modeling the zoning patterns of crystals. *Reviews in Mineralogy and Geochemistry*, *69*, 545–594.

Costa, F., & Morgan, D. (2011). Time constraints from chemical equilibration in magmatic crystals. In A. Dosseto, S. P. Turner, J. A. Van Orman (Eds.), *Timescales of magmatic processes* (pp. 125–159). Wiley-Blackwell.

Crossingham, T., Ubide, T., Vasconcelos, P., & Mallmann, G. (2018). Parallel plumbing systems feeding a pair of coeval volcanoes in eastern Australia. *Journal of Petrology*, *59*, 1035–1066.

D'oriano, C., Bertagnini, A., Cioni, R., & Pompilio, M. (2014). Identifying recycled ash in basaltic eruptions. *Scientific Reports*, *4*, 5851.

Dalton, H. B., Scott, J. M., Liu, J., Waight, T. E., Pearson, D. G., Brenna, M., et al. (2017). Diffusion-zoned pyroxenes in an isotopically heterogeneous mantle lithosphere beneath the Dunedin Volcanic Group, New Zealand, and their implications for intraplate alkaline magma sources. *Lithosphere*, *9*, 463–475.

Dasgupta, R., & Hirschmann, M. M. (2006). Melting in the Earth's deep upper mantle caused by carbon dioxide. *Nature*, *440*, 659.

Dasgupta, R., Hirschmann, M. M., & Smith, N. D. (2007). Partial melting experiments of peridotite+ CO_2 at 3 GPa and genesis of alkalic ocean island basalts. *Journal of Petrology*, *48*, 2093–2124.

Dasgupta, R., Hirschmann, M. M., & Withers, A. C. (2004). Deep global cycling of carbon constrained by the solidus of anhydrous, carbonated eclogite under upper mantle conditions. *Earth and Planetary Science Letters*, *227*, 73–85.

Davidson, J., Morgan, D., Charlier, B., Harlou, R., & Hora, J. (2007). Microsampling and isotopic analysis of igneous rocks: Implications for the study of magmatic systems. *Annual Review of Earth and Planetary Sciences*, *35*, 273–311.

Davies, D. R., & Rawlinson, N. (2014). On the origin of recent intraplate volcanism in Australia. *Geology*, *42*, 1031–1034.

Davies, J., & Bunge, H.-P. (2006). Are splash plumes the origin of minor hotspots? *Geology*, *34*, 349–352.

de Maisonneuve, C. B., Costa, F., Huber, C., Vonlanthen, P., Bachmann, O., & Dungan, M. A. (2016). How do olivines record magmatic events? Insights from major and trace element zoning. *Contributions to Mineralogy and Petrology*, *171*, 56.

Demidjuk, Z., Turner, S., Sandiford, M., George, R., Foden, J., & Etheridge, M. (2007). U-series isotope and geodynamic constraints on mantle melting processes beneath the Newer

Volcanic Province in South Australia. *Earth and Planetary Science Letters*, *261*, 517–533.

Demouchy, S., Jacobsen, S. D., Gaillard, F., & Stern, C. R. (2006). Rapid magma ascent recorded by water diffusion profiles in mantle olivine. *Geology*, *34*, 429–432.

Dixon, J. E. (1997). Degassing of alkalic basalts. *American Mineralogist*, *82*, 368–378.

Dixon, J. E., & Stolper, E. M. (1995). An experimental study of water and carbon dioxide solubilities in mid-ocean ridge basaltic liquids. Part II: Applications to degassing. *Journal of Petrology*, *36*, 1633–1646.

Dobosi, G., Schultz-Güttler, R., Kurat, G., & Kracher, A. (1991). Pyroxene chemistry and evolution of alkali basaltic rocks from Burgenland and Styria, Austria. *Mineralogy and Petrology*, *43*, 275–292.

Duan, X. (2014). A general model for predicting the solubility behavior of H_2O–CO_2 fluids in silicate melts over a wide range of pressure, temperature and compositions. *Geochimica et Cosmochimica Acta*, *125*, 582–609.

Duan, Z., & Zhang, Z. (2006). Equation of state of the H_2O, CO_2, and H_2O–CO_2 systems up to 10 GPa and 2573.15 K: Molecular dynamics simulations with ab initio potential surface. *Geochimica et Cosmochimica Acta*, *70*, 2311–2324.

Duda, A., & Schmincke, H.-U. (1985). Polybaric differentiation of alkali basaltic magmas: Evidence from green-core clinopyroxenes (Eifel, FRG). *Contributions to Mineralogy and Petrology*, *91*, 340–353.

Elliott, T., Plank, T., Zindler, A., White, W., & Bourdon, B. (1997). Element transport from slab to volcanic front at the Mariana arc. *Journal of Geophysical Research: Solid Earth*, *102*, 14991–15019.

Feng, M., & Whitford-Stark, J. (1986). The 1719–1721 eruptions of potassium-rich lavas at Wudalianchi, China. *Journal of Volcanology and Geothermal Research*, *30*, 131–148.

Ferlito, C., & Lanzafame, G. (2010). The role of supercritical fluids in the potassium enrichment of magmas at Mount Etna volcano (Italy). *Lithos*, *119*, 642–650.

Ferrari, L., Petrone, C. M., & Francalanci, L. (2001). Generation of oceanic-island basalt-type volcanism in the western Trans-Mexican volcanic belt by slab rollback, asthenosphere infiltration, and variable flux melting. *Geology*, *29*, 507–510.

Floyd, P. (1991). *Oceanic islands and seamounts, Oceanic Basalts* (pp. 174–218). Springer.

Foley, S. (1991). High-pressure stability of the fluor- and hydroxy-endmembers of pargasite and K-richterite. *Geochimica et Cosmochimica Acta*, *55*, 2689–2694.

Foulger, G. R., & Jurdy, D. M. (2007). *Plates, plumes, and planetary processes*. Geological Society of America.

Foulger, G. R., Natland, J. H., Presnall, D. C., & Anderson, D. L. (2005). *Plates, plumes, and paradigms*. Geological Society of America.

Francis, D., & Ludden, J. (1995). The signature of amphibole in mafic alkaline lavas, a study in the northern Canadian Cordillera. *Journal of Petrology*, *36*, 1171–1191.

Giacomoni, P., Ferlito, C., Coltorti, M., Bonadiman, C., & Lanzafame, G. (2014). Plagioclase as archive of magma ascent dynamics on "open conduit" volcanoes: The 2001–2006 eruptive period at Mt. Etna. *Earth-Science Reviews*, *138*, 371–393.

Girona, T., & Costa, F. (2013). DIPRA: A user-friendly program to model multi-element diffusion in olivine with applications to timescales of magmatic processes. *Geochemistry, Geophysics, Geosystems*, *14*, 422–431.

Godard, M., Bodinier, J.-L., & Vasseur, G. (1995). Effects of mineralogical reactions on trace element redistributions in mantle rocks during percolation processes: A chromatographic approach. *Earth and Planetary Science Letters*, *133*, 449–461.

Graettinger, A., Valentine, G., & Sonder, I. (2016). Recycling in debris-filled volcanic vents. *Geology*, *44*, 811–814.

Green, D., & Ringwood, A. (1967). The genesis of basaltic magmas. *Contributions to Mineralogy and Petrology*, *15*, 103–190.

Green, D. H. (1973). Experimental melting studies of a model upper mantle composition at high pressure under water-saturated and water undersaturated conditions. *Earth and Planetary Science Letters*, *19*, 37–53.

Green, D. H. (2015). Experimental petrology of peridotites, including effects of water and carbon on melting in the Earth's upper mantle. *Physics and Chemistry of Minerals*, *42*, 95–122.

Harangi, S. (2001). Neogene magmatism in the Alpine-Pannonian Transition Zone-a model for melt generation in a complex geodynamic setting. *Acta Vulcanologica*, *13*, 25–39.

Harangi, S., Jankovics, M. É., Sági, T., Kiss, B., Lukács, R., & Soós, I. (2015). Origin and geodynamic relationships of the Late Miocene to Quaternary alkaline basalt volcanism in the Pannonian basin, eastern–central Europe. *International Journal of Earth Sciences (Geologische Rundschau)*, *104*, 2007–2032.

Harangi, S., Sági, T., Seghedi, I., & Ntaflos, T. (2013). Origin of basaltic magmas of Perşani volcanic field, Romania: A combined whole rock and mineral scale investigation. *Lithos*, *180*, 43–57.

Harangi, S., Vaselli, O., Tonarini, S., Szabó, C., Harangi, R., & Coradossi, N. (1995). Petrogenesis of Neogene extension-related alkaline volcanic rocks of the Little Hungarian Plain volcanic field (Western Hungary). *Acta Vulcanologica*, *7*, 173–188.

Harte, B., Hunter, R., & Kinny, P. (1993). Melt geometry, movement and crystallization, in relation to mantle dykes, veins and metasomatism. *Philosophical Transactions of the Royal Society of London. Series A: Physical and Engineering Sciences*, *342*, 1–21.

Hawkesworth, C., Gallagher, K., Hergt, J., & McDermott, F. (1994). Destructive plate margin magmatism: Geochemistry and melt generation. *Lithos*, *33*, 169–188.

Herzberg, C. (2010). Identification of source lithology in the Hawaiian and Canary Islands: Implications for origins. *Journal of Petrology*, *52*, 113–146.

Hidas, K., Guzmics, T., Szabó, C., Kovács, I., Bodnar, R. J., Zajacz, Z., et al. (2010). Coexisting silicate melt inclusions and H_2O-bearing, CO_2-rich fluid inclusions in mantle peridotite xenoliths from the Carpathian–Pannonian region (central Hungary). *Chemical Geology*, *274*, 1–18.

Hirano, N., Takahashi, E., Yamamoto, J., Abe, N., Ingle, S. P., Kaneoka, I., et al. (2006). Volcanism in response to plate flexure. *Science*, *313*, 1426–1428.

Hirschmann, M. M. (2000). Mantle solidus: Experimental constraints and the effects of peridotite composition. *Geochemistry, Geophysics, Geosystems*, *1*.

Hoernle, K., White, J. D. L., van den Bogaard, P., Hauff, F., Coombs, D. S., Werner, R., et al. (2006). Cenozoic intraplate volcanism on New Zealand: Upwelling induced by lithospheric removal. *Earth and Planetary Science Letters*, *248*, 350–367.

Holloway, J. R., & Blank, J. G. (1994). Application of experimental results to COH species in natural melts. *Reviews in Mineralogy*, *30*, 187–230.

Homrighausen, S., Hoernle, K., Hauff, F., Geldmacher, J., Wartho, J.-A., van den Bogaard, P., & Garbe-Schönberg, D. (2018). Global distribution of the HIMU end member: Formation through Archean plume-lid tectonics. *Earth-Science Reviews*, *182*, 85–101.

Hopkins, J. L., Millet, M.-A., Timm, C., Wilson, C. J., Leonard, G. S., Palin, J. M., & Neil, H. (2015). Tools and techniques for developing tephra stratigraphies in lake cores: A case study from the basaltic Auckland Volcanic Field, New Zealand. *Quaternary Science Reviews*, *123*, 58–75.

Hopkins, J. L., Wilson, C. J. N., Millet, M.-A., Leonard, G. S., Timm, C., McGee, L. E., et al. (2017). Multi-criteria correlation of tephra deposits to source centres applied in the Auckland Volcanic Field, New Zealand. *Bulletin of Volcanology*, *79*, 55.

Horspool, N., Savage, M., & Bannister, S. (2006). Implications for intraplate volcanism and back-arc deformation in northwestern New Zealand, from joint inversion of receiver functions and surface waves. *Geophysical Journal International*, *166*, 1466–1483.

Houghton, B. F., & Smith, R. T. (1993). Recycling of magmatic clasts during explosive eruptions: Estimating the true juvenile content of phreatomagmatic volcanic deposits. *Bulletin of Volcanology*, *55*, 414–420.

Iacono-Marziano, G., Morizet, Y., Le Trong, E., & Gaillard, F. (2012). New experimental data and semi-empirical parameterization of H_2O–CO_2 solubility in mafic melts. *Geochimica et Cosmochimica Acta*, *97*, 1–23.

Irving, A. J., & Green, D. H. (2008). Phase relationships of hydrous alkalic magmas at high pressures: Production of nepheline hawaiitic to mugearitic liquids by amphibole-dominated fractional crystallization within the lithospheric mantle. *Journal of Petrology*, *49*, 741–756.

Irving, A. J., & Price, R. C. (1981). Geochemistry and evolution of Iherzolite-bearing phonolitic lavas from Nigeria, Australia, East Germany and New Zealand. *Geochimica et Cosmochimica Acta*, *45*, 1309–1320.

Jakobsson, S., & Holloway, J. R. (1986). Crystal—Liquid experiments in the presence of a COH fluid buffered by graphite+ iron+ wustite: Experimental method and near-liquidus relations in basanite. *Journal of Volcanology and Geothermal Research*, *29*, 265–291.

Jankovics, M.É., Dobosi, G., Embey-Isztin, A., Kiss, B., Sági, T., Harangi, S., & Ntaflos, T. (2013). Origin and ascent history of unusually crystal-rich alkaline basaltic magmas from the western Pannonian Basin. *Bulletin of Volcanology*, *75*, 1–23.

Jankovics, M. É., Harangi, S., Kiss, B., & Ntaflos, T. (2012). Open-system evolution of the Füzes-tó alkaline basaltic magma, western Pannonian Basin: Constraints from mineral textures and compositions. *Lithos*, *140*, 25–37.

Jankovics, M. É., Harangi, S., Németh, K., Kiss, B., & Ntaflos, T. (2015). A complex magmatic system beneath the Kissomlyó monogenetic volcano (western Pannonian Basin): Evidence from mineral textures, zoning and chemistry. *Journal of Volcanology and Geothermal Research*, *301*, 38–55.

Jankovics, M. É., Sági, T., Astbury, R. L., Petrelli, M., Kiss, B., Ubide, T., et al. (2019). Olivine major and trace element compositions coupled with spinel chemistry to unravel the magmatic systems feeding monogenetic basaltic volcanoes. *Journal of Volcanology and Geothermal Research*, *369*, 203–223.

Jankovics, M. É., Taracsák, Z., Dobosi, G., Embey-Isztin, A., Batki, A., Harangi, S., & Hauzenberger, C. A. (2016). Clinopyroxene with diverse origins in alkaline basalts from the western Pannonian Basin: Implications from trace element characteristics. *Lithos*, *262*, 120–134.

Kahl, M., Chakraborty, S., Costa, F., & Pompilio, M. (2011). Dynamic plumbing system beneath volcanoes revealed by kinetic modeling, and the connection to monitoring data: An example from Mt. Etna. *Earth and Planetary Science Letters*, *308*, 11–22.

Kahl, M., Chakraborty, S., Pompilio, M., & Costa, F. (2015). Constraints on the nature and evolution of the magma plumbing system of Mt. Etna volcano (1991–2008) from a combined thermodynamic and kinetic modelling of the compositional record of minerals. *Journal of Petrology*, *56*, 2025–2068.

Kamenetsky, V., & Clocchiatti, R. (1996). Primitive magmatism of Mt. Etna: Insights from mineralogy and melt inclusions. *Earth and Planetary Science Letters*, *142*, 553–572.

Katz, R.F., Spiegelman, M., Holtzman, B., 2006. The dynamics of melt and shear localization in partially molten aggregates. *Nature 442*, 676–679.

Kereszturi, G., Németh, K., Cronin, S. J., Agustín-Flores, J., Smith, I. E. M., & Lindsay, J. (2013). A model for calculating eruptive volumes for monogenetic volcanoes — Implication for the Quaternary Auckland Volcanic Field, New Zealand. *Journal of Volcanology and Geothermal Research*, *266*, 16–33.

Kessel, R., Schmidt, M. W., Ulmer, P., & Pettke, T. (2005). Trace element signature of subduction-zone fluids, melts and supercritical liquids at 120–180 km depth. *Nature*, *437*, 724.

Kienle, J., Kyle, P. R., Self, S., Motyka, R. J., & Lorenz, V. (1980). Ukinrek Maars, Alaska, I. April 1977 eruption sequence, petrology and tectonic setting. *Journal of Volcanology and Geothermal Research*, *7*, 11–37.

Kim, J.-I., Choi, S. H., Koh, G. W., Park, J. B., & Ryu, J.-S. (2019). Petrogenesis and mantle source characteristics of volcanic rocks on Jeju Island, South Korea. *Lithos*, *326*, 476–490.

Kimura, J.-I., Sakuyama, T., Miyazaki, T., Vaglarov, B. S., Fukao, Y., & Stern, R. J. (2018). Plume-stagnant slab-lithosphere interactions: Origin of the late Cenozoic intra-plate basalts on the East Eurasia margin. *Lithos*, *300*, 227–249.

Kogiso, T., & Hirschmann, M. M. (2006). Partial melting experiments of bimineralic eclogite and the role of recycled mafic oceanic crust in the genesis of ocean island basalts. *Earth and Planetary Science Letters*, *249*, 188–199.

Langmuir, C. H., Klein, E. M., & Plank, T. (1992). Petrological systematics of mid-ocean ridge basalts: Constraints on melt generation beneath ocean ridges. *Mantle Flow and Melt Generation at Mid-Ocean Ridges*, *71*, 183–280.

Laporte, D., Lambart, S., Schiano, P., & Ottolini, L. (2014). Experimental derivation of nepheline syenite and phonolite liquids by partial melting of upper mantle peridotites. *Earth and Planetary Science Letters*, *404*, 319–331.

Larrea, P., Salinas, S., Widom, E., Siebe, C., & Abbitt, R. J. (2017). Compositional and volumetric development of a monogenetic lava flow field: The historical case of Paricutin (Michoacan, Mexico). *Journal of Volcanology and Geothermal Research*, *348*, 36–48.

Le Maitre, R. W., Streckeisen, A., Zanettin, B., Le Bas, M., Bonin, B., & Bateman, P. (2005). *Igneous rocks: A classification and glossary of terms: Recommendations of the International Union of Geological Sciences Subcommission on the Systematics of Igneous Rocks*. Cambridge University Press, Cambridge (UK).

Lee, C.-T. A., & Chin, E. J. (2014). Calculating melting temperatures and pressures of peridotite protoliths: Implications for the origin of cratonic mantle. *Earth and Planetary Science Letters*, *403*, 273–286.

Leonard, G. S., Calvert, A. T., Hopkins, J. L., Wilson, C. J., Smid, E. R., Lindsay, J. M., & Champion, D. E. (2017). High-precision 40Ar/39Ar dating of Quaternary basalts from Auckland Volcanic Field, New Zealand, with implications for eruption rates and paleomagnetic correlations. *Journal of Volcanology and Geothermal Research*, *343*, 60–74.

Lesne, P., Kohn, S. C., Blundy, J., Witham, F., Botcharnikov, R. E., & Behrens, H. (2011). Experimental simulation of closed-system degassing in the system basalt–H_2O–CO_2–S–Cl. *Journal of Petrology*, *52*, 1737–1762.

Liu, J.-Q., Ren, Z.-Y., Nichols, A. R., Song, M.-S., Qian, S.-P., Zhang, Y., & Zhao, P.-P. (2015). Petrogenesis of Late Cenozoic basalts from North Hainan Island: Constraints from melt inclusions and their host olivines. *Geochimica et Cosmochimica Acta*, *152*, 89–121.

Loges, A., Schultze, D., Klügel, A., & Lucassen, F. (2019). Phonolitic melt production by carbonatite Mantle metasomatism: Evidence from Eger Graben xenoliths. *Contributions to Mineralogy and Petrology*, *174*, 93.

Lustrino, M. (2005). How the delamination and detachment of lower crust can influence basaltic magmatism. *Earth-Science Reviews*, *72*, 21–38.

Maclennan, J. (2017). Bubble formation and decrepitation control the CO_2 content of olivine-hosted melt inclusions. *Geochemistry, Geophysics, Geosystems*, *18*, 597–616.

Mahony, S. H., Wallace, L. M., Miyoshi, M., Villamor, P., Sparks, R. S. J., & Hasenaka, T. (2011). Volcano-tectonic interactions during rapid plate-boundary evolution in the Kyushu region, SW Japan. *Geological Society of America Bulletin*, *123*, 2201–2223.

Mallik, A., & Dasgupta, R., 2012. Reaction between MORB-eclogite derived melts and fertile peridotite and generation of ocean island basalts. *Earth and Planetary Science Letters*, *329*, 97–108.

Manikyamba, C., & Kerrich, R. (2011). Geochemistry of alkaline basalts and associated high-Mg basalts from the 2.7Ga Penakacherla Terrane, Dharwar craton, India: An Archean depleted mantle-OIB array. *Precambrian Research*, *188*, 104–122.

Márquez, A., Oyarzun, R., Doblas, M., & Verma, S. P. (1999). Alkalic (ocean-island basalt type) and calc-alkalic volcanism in the Mexican volcanic belt: A case for plume-related magmatism and propagating rifting at an active margin? *Geology*, *27*, 51–54.

Mashima, H. (2009). A melting anomaly in Northwest Kyushu, Southwest Japan: A consequence of the tectonic evolution of NW Kyushu and the origin of a pseudo hot spot in a convergent zone. *Journal of Volcanology and Geothermal Research*, *186*, 195–209.

Masotta, M., Pontesilli, A., Mollo, S., Armienti, P., Ubide, T., Nazzari, M., & Scarlato, P. (2020). The role of undercooling during clinopyroxene growth in trachybasaltic magmas: Insights on magma decompression and cooling at Mt. Etna volcano. *Geochimica et Cosmochimica Acta*, *268*, 258–276.

Mayer, B., Jung, S., Romer, R., Pfänder, J., Klügel, A., Pack, A., & Gröner, E. (2014). Amphibole in alkaline basalts from intraplate settings: Implications for the petrogenesis of alkaline lavas from the metasomatised lithospheric mantle. *Contributions to Mineralogy and Petrology*, *167*, 989.

McDonald, G. W., Smith, N. J., Kim, J.-h., Cronin, S. J., & Proctor, J. N. (2017). The spatial and temporal 'cost' of volcanic eruptions: Assessing economic impact, business inoperability, and spatial distribution of risk in the Auckland region, New Zealand. *Bulletin of Volcanology*, *79*, 48.

McGee, L. E., Beier, C., Smith, I. E. M., & Turner, S. P. (2011). Dynamics of melting beneath a small-scale basaltic system: A U-Th-Ra study from Rangitoto volcano, Auckland volcanic field, New Zealand. *Contributions to Mineralogy and Petrology*, *162*, 547–563.

McGee, L. E., Millet, M.-A., Smith, I. E. M., Németh, K., & Lindsay, J. M. (2012). The inception and progression of melting in a monogenetic eruption: Motukorea Volcano, the Auckland Volcanic Field, New Zealand. *Lithos*, *155*, 360–374.

McGee, L. E., & Smith, I. E. (2016). Interpreting chemical compositions of small scale basaltic systems: A review. *Journal of Volcanology and Geothermal Research*, *325*, 45–60.

McGee, L. E., Smith, I. E. M., Millet, M.-A., Handley, H. K., & Lindsay, J. M. (2013). Asthenospheric control of melting processes in a monogenetic basaltic system: A case study of the Auckland Volcanic Field, New Zealand. *Journal of Petrology*, *54*, 2125–2153.

Melluso, L., Tucker, R., Cucciniello, C., le Roex, A., Morra, V., Zanetti, A., & Rakotoson, R. (2018). The magmatic evolution and genesis of the Quaternary basanite-trachyphonolite suite of Itasy (Madagascar) as inferred by geochemistry, Sr-Nd-Pb isotopes and trace element distribution in coexisting phases. *Lithos*, *310*, 50–64.

Menzies, M., & Hawkesworth, C. (1986). *Mantle metasomatism*. Academic Press Inc. (London) Ltd., London (UK).

Menzies, M., & Murthy, V. R. (1980). Mantle metasomatism as a precursor to the genesis of alkaline magmas-isotopic evidence. *American Journal of Science*, *280*, 622–638.

Menzies, M. A., Kyle, P. R., Jones, M., & Ingram, G. (1991). Enriched and depleted source components for tholeiitic and alkaline lavas from Zuni-Bandera, New Mexico: Inferences about intraplate processes and stratified lithosphere. *Journal of Geophysical Research: Solid Earth*, *96*, 13645–13671.

Merrill, R., & Wyllie, P. (1975). Kaersutite and kaersutite eclogite from Kakanui, New Zealand—water-excess and water-deficient melting to 30 kilobars. *Geological Society of America Bulletin*, *86*, 555–570.

Métrich, N., & Wallace, P. J. (2008). Volatile abundances in basaltic magmas and their degassing paths tracked by melt inclusions. *Reviews in Mineralogy and Geochemistry*, *69*, 363–402.

Mollo, S., Blundy, J., Scarlato, P., De Cristofaro, S. P., Tecchiato, V., Di Stefano, F., et al. (2018). An integrated P-T-H 2 O-lattice strain model to quantify the role of clinopyroxene fractionation on REE+ Y and HFSE patterns of mafic alkaline magmas: Application to eruptions at Mt. Etna. *Earth-Science Reviews*, *185*, 32–56.

Mollo, S., Del Gaudio, P., Ventura, G., Iezzi, G., & Scarlato, P. (2010). Dependence of clinopyroxene composition on cooling rate in basaltic magmas: Implications for thermobarometry. *Lithos*, *118*, 302–312.

Mollo, S., Giacomoni, P., Coltorti, M., Ferlito, C., Iezzi, G., & Scarlato, P. (2015). Reconstruction of magmatic variables governing recent Etnean eruptions: Constraints from mineral chemistry and P–T–fO_2–H_2O modeling. *Lithos*, *212*, 311–320.

Mollo, S., Putirka, K., Iezzi, G., & Scarlato, P. (2013). The control of cooling rate on titanomagnetite composition: Implications for a geospeedometry model applicable to alkaline rocks from Mt. Etna volcano. *Contributions to Mineralogy and Petrology*, *165*, 457–475.

Moore, G. (2008). Interpreting H_2O and CO_2 contents in melt inclusions: Constraints from solubility experiments and modeling. *Reviews in Mineralogy and Geochemistry*, *69*, 333–362.

Morgan, W. J. (1971). Convection plumes in the lower mantle. *Nature*, *230*, 42–43.

Moufti, M., Moghazi, A., & Ali, K. (2012). Geochemistry and Sr–Nd–Pb isotopic composition of the Harrat Al-Madinah Volcanic Field, Saudi Arabia. *Gondwana Research*, *21*, 670–689.

Namur, O., Charlier, B., Toplis, M. J., & Vander Auwera, J. (2012). Prediction of plagioclase-melt equilibria in anhydrous silicate melts at 1-atm. *Contributions to Mineralogy and Petrology*, *163*, 133–150.

Neave, D. A., & Putirka, K. D. (2017). A new clinopyroxene-liquid barometer, and implications for magma storage pressures under Icelandic rift zones. *American Mineralogist*, *102*, 777–794.

Needham, A. J., Lindsay, J. M., Smith, I. E. M., Augustinus, P., & Shane, P. A. (2011). Sequential eruption of alkaline and sub-alkaline magmas from a small monogenetic volcano in the Auckland Volcanic Field, New Zealand. *Journal of Volcanology and Geothermal Research*, *201*, 126–142.

Newman, S., & Lowenstern, J. B. (2002). VolatileCalc: A silicate melt–H_2O–CO_2 solution model written in Visual Basic for excel. *Computers & Geosciences*, *28*, 597–604.

O'Reilly, S. Y., & Griffin, W. (2011). Rates of magma ascent: Constraints from mantle-derived xenoliths. In A. Dosseto, S. Turner, J. van Orman(Eds.), *Timescales of Magmatic Processes: From Core to Atmosphere* (pp. 116–124). Blackwell Publishing Ltd., Chichester (UK).

Oeser, M., Dohmen, R., Horn, I., Schuth, S., & Weyer, S. (2015). Processes and time scales of magmatic evolution as revealed by Fe–Mg chemical and isotopic zoning in natural olivines. *Geochimica et Cosmochimica Acta*, *154*, 130–150.

Oxburgh, E. R., & Turcotte, D. (1968). Mid-ocean ridges and geotherm distribution during mantle convection. *Journal of Geophysical Research*, *73*, 2643–2661.

Papale, P. (1999). Modeling of the solubility of a two-component H_2O+ CO_2 fluid in silicate liquids. *American Mineralogist*, *84*, 477–492.

Papale, P., Moretti, R., & Barbato, D. (2006). The compositional dependence of the saturation surface of H_2O+ CO_2 fluids in silicate melts. *Chemical Geology*, *229*, 78–95.

Paulick, H., & Franz, G. (1997). The color of pumice: Case study on a trachytic fall deposit, Meidob volcanic field, Sudan. *Bulletin of Volcanology*, *59*, 171–185.

Pearce, J. A., & Peate, D. W. (1995). Tectonic implications of the composition of volcanic arc magmas. *Annual Review of Earth and Planetary Sciences*, *23*, 251–285.

Pearson, D., Canil, D., & Shirey, S. (2003). Mantle samples included in volcanic rocks: Xenoliths and diamonds. *Treatise on Geochemistry*, *2*, 568.

Perinelli, C., Mollo, S., Gaeta, M., De Cristofaro, S., Palladino, D., & Scarlato, P. (2018). Impulsive supply of volatile-rich magmas in the shallow plumbing system of Mt. Etna volcano. *Minerals*, *8*, 482.

Perinelli, C., Mollo, S., Gaeta, M., De Cristofaro, S. P., Palladino, D. M., Armienti, P., et al. (2016). An improved clinopyroxene-based hygrometer for Etnean magmas and implications for eruption triggering mechanisms. *American Mineralogist*, *101*, 2774–2777.

Pertermann, M., & Hirschmann, M. M. (2003). Partial melting experiments on a MORB-like pyroxenite between 2 and 3 GPa: Constraints on the presence of pyroxenite in basalt source regions from solidus location and melting rate. *Journal of Geophysical Research: Solid Earth*, *108*.

Peters, T. J., Menzies, M., Thirlwall, M., & Kyle, P. R. (2008). Zuni–Bandera volcanism, Rio Grande, USA — Melt formation in garnet- and spinel-facies mantle straddling the asthenosphere–lithosphere boundary. *Lithos*, *102*, 295–315.

Pilet, S. (2015). Generation of low-silica alkaline lavas: Petrological constraints, models, and thermal implications. *Geological Society of America Special Papers*, *514*, SPE514–517.

Pilet, S., Baker, M. B., & Stolper, E. M. (2008). Metasomatized lithosphere and the origin of alkaline lavas. *Science*, *320*, 916–919.

Pilet, S., Hernandez, J., Sylvester, P., & Poujol, M. (2005). The metasomatic alternative for ocean island basalt chemical heterogeneity. *Earth and Planetary Science Letters*, *236*, 148–166.

Putirka, K. (1999). Clinopyroxene+ liquid equilibria to 100 kbar and 2450 K. *Contributions to Mineralogy and Petrology*, *135*, 151–163.

Putirka, K. (2005). Igneous thermometers and barometers based on plagioclase + liquid equilibria: Tests of some existing models and new calibrations. *American Mineralogist*, *90*, 336–346.

Putirka, K. (2016). Amphibole thermometers and barometers for igneous systems and some implications for eruption mechanisms of felsic magmas at arc volcanoes. *American Mineralogist*, *101*, 841–858.

Putirka, K., & Condit, C. D. (2003). Cross section of a magma conduit system at the margin of the Colorado Plateau. *Geology*, *31*, 701–704.

Putirka, K. D. (2008). Thermometers and barometers for volcanic systems. *Reviews in Mineralogy & Geochemistry*, *69*, 61–120.

Ray, A., Hatui, K., Paul, D. K., Sen, G., Biswas, S., & Das, B. (2016). Mantle xenolith-xenocryst-bearing monogenetic alkali basaltic lava field from Kutch Basin, Gujarat, Western India: Estimation of magma ascent rate. *Journal of Volcanology and Geothermal Research*, *312*, 40–52.

Re, G., Palin, J. M., White, J. D. L., & Parolari, M. (2017). Unravelling the magmatic system beneath a monogenetic volcanic complex (Jagged Rocks Complex, Hopi Buttes, AZ, USA). *Contributions to Mineralogy and Petrology*, *172*, 94.

Reiners, P. W. (2002). Temporal-compositional trends in intraplate basalt eruptions: Implications for mantle heterogeneity and melting processes. *Geochemistry, Geophysics, Geosystems (G^3)*, 3.

Ridolfi, F., & Renzulli, A. (2012). Calcic amphiboles in calc-alkaline and alkaline magmas: Thermobarometric and chemometric empirical equations valid up to 1,130° C and 2.2 GPa. *Contributions to Mineralogy and Petrology*, *163*, 877–895.

Ritter, J. R. R., Jordan, M., Christensen, U. R., & Achauer, U. (2001). A mantle plume below the Eifel volcanic fields, Germany. *Earth and Planetary Science Letters*, *186*, 7–14.

Robinson, J. A. C., Wood, B. J., & Blundy, J. D. (1998). The beginning of melting of fertile and depleted peridotite at 1.5 GPa. *Earth and Planetary Science Letters*, *155*, 97–111.

Rooney, T. O., Nelson, W. R., Dosso, L., Furman, T., & Hanan, B. (2014). The role of continental lithosphere metasomes in the production of HIMU-like magmatism on the northeast African and Arabian plates. *Geology*, *42*, 419–422.

Rosenbaum, G., Sandiford, M., Caulfield, J., & Garrison, J. M. (2018). A trapdoor mechanism for slab tearing and melt generation in the northern Andes. *Geology*, *47*, 23–26.

Rowe, M. C., Lassiter, J. C., & Goff, K. (2015). Basalt volatile fluctuations during continental rifting: An example from the Rio Grande Rift, USA. *Geochemistry, Geophysics, Geosystems*, *16*, 1254–1273.

Rowe, M. C., Peate, D. W., & Newbrough, A. (2011). Compositional and thermal evolution of olivine-hosted melt inclusions in small-volume basaltic eruptions: A "simple" example from Dotsero Volcano, NW Colorado. *Contributions to Mineralogy and Petrology*, *161*, 197–211.

Rubin, A.M. (1995). Propagation of magma-filled cracks. *Annual Review of Earth and Planetary Sciences*, *23*, 287–336.

Sakuyama, T., Ozawa, K., Sumino, H., & Nagao, K. (2009). Progressive melt extraction from upwelling mantle constrained by the Kita-Matsuura basalts in NW Kyushu, SW Japan. *Journal of Petrology*, *50*, 725–779.

Scarlato, P., Mollo, S., Blundy, J., Iezzi, G., & Tiepolo, M. (2014). The role of natural solidification paths on REE partitioning between clinopyroxene and melt. *Bulletin of Volcanology*, *76*, 810.

Schmitt, A. K., Klitzke, M., Gerdes, A., & Schäfer, C. (2017). Zircon Hafnium–Oxygen isotope and trace element petrochronology of intraplate volcanic rocks from the Eifel (Germany) and implications for mantle versus crustal origins of zircon megacrysts. *Journal of Petrology*, *58*, 1841–1870.

Scott, J. M., Brenna, M., Crase, J. A., Waight, T. E., van der Meer, Q. H., Cooper, A. F., et al. (2016). Peridotitic lithosphere metasomatized by volatile-bearing melts, and its association with intraplate alkaline HIMU-like magmatism. *Journal of Petrology*, *57*, 2053–2078.

Segerstrom, K. (1966). Paricutin, 1965–aftermath of eruption. *Geological Survey Professional Paper*, *550*, 93.

Shane, P., & Coote, A. (2018). Thermobarometry of Whangarei volcanic field lavas, New Zealand: Constraints on plumbing systems of small monogenetic basalt volcanoes. *Journal of Volcanology and Geothermal Research*, *354*, 130–139.

Shane, P., & Smith, I. (2000). Geochemical fingerprinting of basaltic tephra deposits in the Auckland Volcanic Field. *New Zealand Journal of Geology and Geophysics*, *43*, 569–577.

Shea, T., Lynn, K. J., & Garcia, M. O. (2015). Cracking the olivine zoning code: Distinguishing between crystal growth and diffusion. *Geology*, *43*, 935–938.

Shimizu, K., Saal, A. E., Myers, C. E., Nagle, A. N., Hauri, E. H., Forsyth, D. W., et al. (2016). Two-component mantle melting-mixing model for the generation of mid-ocean ridge basalts: Implications for the volatile content of the Pacific upper mantle. *Geochimica et Cosmochimica Acta*, *176*, 44–80.

Siebel, W., Schmitt, A. K., Danišík, M., Chen, F., Meier, S., Weiß, S., & Eroğlu, S. (2009). Prolonged mantle residence of zircon xenocrysts from the western Eger rift. *Nature Geoscience*, *2*, 886.

Smith, I., & Németh, K. (2017). Source to surface model of monogenetic volcanism: A critical review. *Geological Society, London, Special Publications*, *446*, 1–28.

Smith, I. E. M., Blake, S., Wilson, C. J. N., & Houghton, B. F. (2008). Deep-seated fractionation during the rise of a small-volume basalt magma batch: Crater Hill, Auckland, New Zealand. *Contributions to Mineralogy and Petrology*, *155*, 511–527.

Smith, I. E. M., Okada, T., Itaya, T., & Black, P. M. (1993). Age relationship and tectonic implications of the Cenozoic basaltic volcanism in Northland, New Zealand. *New Zealand Journal of Geology and Geophysics*, *36*, 385–393.

Sohn, C., & Sohn, Y. K. (2019). Volcaniclastic tide-modulated tempestite in a coastal tuff ring, Jeju Island, Korea. *Scientific Reports*, *9*, 3561.

Sohn, Y. K., Cronin, S. J., Brenna, M., Smith, I. E. M., Németh, K., White, J. D. L., et al. (2012). Ilchulbong tuff cone, Jeju Island, Korea, revisited: A compound monogenetic volcano involving multiple magma pulses, shifting vents, and discrete eruptive phases. *Geological Society of America Bulletin*, *124*, 259–274.

Späth, A., Le Roex, A. P., & Opiyo-Akech, N. (2001). Plume–lithosphere interaction and the origin of continental rift-related alkaline volcanism—the Chyulu Hills Volcanic Province, southern Kenya. *Journal of Petrology*, *42*, 765–787.

Spera, F. J. (1984). Carbon dioxide in petrogenesis III: Role of volatiles in the ascent of alkaline magma with special reference to xenolith-bearing mafic lavas. *Contributions to Mineralogy and Petrology*, *88*, 217–232.

Spilliaert, N., Allard, P., Métrich, N., & Sobolev, A. (2006). Melt inclusion record of the conditions of ascent, degassing, and extrusion of volatile-rich alkali basalt during the powerful 2002 flank eruption of Mount Etna (Italy). *Journal of Geophysical Research: Solid Earth*, *111*.

Streck, M. J. (2008). Mineral textures and zoning as evidence for open system processes. *Reviews in Mineralogy and Geochemistry*, *69*, 595–622.

Strong, M., & Wolff, J. (2003). Compositional variations within scoria cones. *Geology*, *31*, 143–146.

Sun, S. S., & McDonough, W. F. (1989). Chemical and isotopic systematics of oceanic basalts: Implications for mantle composition and processes. In A. D. Saunders, M. J. Norry (Eds.), *Magmatism in the Ocean Basins* (pp. 313–345). Geological Society, London.

Taisne, B., & Tait, S. (2009). Eruption versus intrusion? Arrest of propagation of constant volume, buoyant, liquid-filled cracks in an elastic, brittle host. *Journal of Geophysical Research*, *114*, B06202.

Tatsumi, Y., Hamilton, D., & Nesbitt, R. (1986). Chemical characteristics of fluid phase released from a subducted lithosphere and origin of arc magmas: Evidence from high-pressure experiments and natural rocks. *Journal of Volcanology and Geothermal Research*, *29*, 293–309.

Timm, C., Hoernle, K., Werner, R., Hauff, F., den Bogaard, P. V., White, J., et al. (2010). Temporal and geochemical evolution of the Cenozoic intraplate volcanism of Zealandia. *Earth-Science Reviews*, *98*, 38–64.

Ubide, T., Galé, C., Arranz, E., Lago, M., & Larrea, P. (2014a). Clinopyroxene and amphibole crystal populations in a lamprophyre sill from the Catalonian Coastal Ranges (NE Spain): A record of magma history and a window to mineral-melt partitioning. *Lithos*, *184*, 225–242.

Ubide, T., Galé, C., Larrea, P., Arranz, E., & Lago, M. (2014b). Antecrysts and their effect on rock compositions: The Cretaceous lamprophyre suite in the Catalonian Coastal Ranges (NE Spain). *Lithos*, *206*, 214–233.

Ubide, T., & Kamber, B. S. (2018). Volcanic crystals as time capsules of eruption history. *Nature communications*, *9*, 326.

Ubide, T., Mollo, S., Zhao, J.-X., Nazzari, M., & Scarlato, P. (2019). Sector-zoned clinopyroxene as a recorder of magma history, eruption triggers, and ascent rates. *Geochimica et Cosmochimica Acta*, *251*, 265–283.

Ustunisik, G., Kilinc, A., & Nielsen, R. L. (2014). New insights into the processes controlling compositional zoning in plagioclase. *Lithos*, *200*, 80–93.

Valentine, G. A., & Gregg, T. K. P. (2008). Continental basaltic volcanoes - Processes and problems. *Journal of Volcanology and Geothermal Research*, *177*, 857–873.

Valentine, G. A., & Hirano, N. (2010). Mechanisms of low-flux intraplate volcanic fields--Basin and Range (North America) and northwest Pacific Ocean. *Geology*, *38*, 55–58.

Valentine, G. A., & Perry, F. V. (2006). Decreasing magmatic footprints of individual volcanoes in a waning basaltic field. *Geophysical Research Letters*, *33*, L14305.

Valentine, G. A., & Perry, F. V. (2007). Tectonically controlled, time-predictable basaltic volcanism from a lithospheric mantle source (central Basin and Range Province, USA). *Earth and Planetary Science Letters*, *261*, 201–216.

Van Otterloo, J., Raveggi, M., Cas, R., & Maas, R.(2014). Polymagmatic activity at the monogenetic Mt Gambier Volcanic Complex in the Newer Volcanics Province, SE Australia: New insights into the occurrence of intraplate volcanic activity in Australia. *Journal of Petrology*, *55*, 1317–1351.

Vaselli, O., Downes, H., Thirlwall, M., Dobosi, G., Coradossi, N., Seghedi, I., et al. (1995). Ultramafic xenoliths in Plio-Pleistocene alkali basalts from the Eastern Transylvanian Basin: Depleted mantle enriched by vein metasomatism. *Journal of Petrology*, *36*, 23–53.

Verolino, A., White, J., & Brenna, M. (2018). Eruption dynamics at Pahvant Butte volcano, Utah, western USA: Insights from ash-sheet dispersal, grain size, and geochemical data. *Bulletin of Volcanology*, *80*, 81.

Vetere, F., Botcharnikov, R. E., Holtz, F., Behrens, H., & De Rosa, R. (2011). Solubility of H_2O and CO_2 in shoshonitic melts at 1250 C and pressures from 50 to 400 MPa: Implications for Campi Flegrei magmatic systems. *Journal of Volcanology and Geothermal Research*, *202*, 251–261.

Vetere, F., Mollo, S., Giacomoni, P., Iezzi, G., Coltorti, M., Ferlito, C., et al. (2015). Experimental constraints on the origin of pahoehoe "cicirara" lavas at Mt. Etna Volcano (Sicily, Italy). *Bulletin of Volcanology*, *77*, 44.

Villaseca, C., Dorado, O., & Orejana, D. (2019). Mineral chemistry of megacrysts and associated clinopyroxenite enclaves in the Calatrava volcanic field: Crystallization processes in mantle magma chambers. *Journal of Iberian Geology*, *45*, 401–426.

Wass, S. Y., & Roge, N. (1980). Mantle metasomatism—precursor to continental alkaline volcanism. *Geochimica et Cosmochimica Acta*, *44*, 1811–1823.

Waters, L. E., & Lange, R. A., 2015. An updated calibration of the plagioclase-liquid hygrometer-thermometer applicable to basalts through rhyolites. *American Mineralogist*, *100*, 2172–2184.

Weiss, Y., Class, C., Goldstein, S. L., & Hanyu, T. (2016). Key new pieces of the HIMU puzzle from olivines and diamond inclusions. *Nature*, *537*, 666.

Williams, R. W., & Gill, J. B. (1989). Effects of partial melting on the uranium decay series. *Geochimica et Cosmochimica Acta*, *53*, 1607–1619.

Wilson, J. T. (1963). A possible origin of the Hawaiian Islands. *Canadian Journal of Physics*, *41*, 863–870.

Witham, F., Blundy, J., Kohn, S. C., Lesne, P., Dixon, J., Churakov, S. V., & Botcharnikov, R. (2012). SolEx: A model for mixed COHSCl-volatile solubilities and exsolved gas compositions in basalt. *Computers & Geosciences*, *45*, 87–97.

Wood, D. A. (1979). A variably veined suboceanic upper mantle—genetic significance for mid-ocean ridge basalts from geochemical evidence. *Geology*, *7*, 499–503.

Wörner, G., & Schmincke, H.-U. (1984). Petrogenesis of the zoned Laacher See tephra. *Journal of Petrology*, *25*, 836–851.

Wyllie, P. J. (1995). Experimental petrology of upper mantle materials, processes and products. *Journal of Geodynamics*, *20*, 429–468.

Xu, Y.-G. (2014). Recycled oceanic crust in the source of 90–40Ma basalts in North and Northeast China: Evidence, provenance and significance. *Geochimica et Cosmochimica Acta*, *143*, 49–67.

Yamamoto, T., Soya, T., Suto, S., Uto, K., Takada, A., Sakaguchi, K., & Ono, K. (1991). The 1989 submarine eruption off eastern Izu Peninsula, Japan: Ejecta and eruption mechanisms. *Bulletin of Volcanology*, *53*, 301–308.

Zeng, G., Chen, L.-H., Xu, X.-S., Jiang, S.-Y., Hofmann, A. W. (2010). Carbonated mantle sources for Cenozoic intra-plate alkaline basalts in Shandong, North China. *Chemical Geology*, *273*, 35–45.

Zou, H., Fan, Q., & Yao, Y. (2008). U-Th systematics of dispersed young volcanoes in NE China: Asthenosphere upwelling caused by piling up and upward thickening of stagnant Pacific slab. *Chemical Geology*, *255*, 134–142.

Part II

Experimental and Numerical Constraints on Magmatic Processes

5

Magma Differentiation and Contamination: Constraints From Experimental and Field Evidences

Antonio Castro[1], Carmen Rodríguez[2,3], Juan Díaz-Alvarado[2], Carlos Fernández[2], and Olga García-Moreno[4]

ABSTRACT

Differentiation and contamination of silicic magmas are common phenomena characterizing the granite batholiths and large igneous provinces that build up most of the continental crust. Although they can be identified by means of geochemical relations of igneous rocks exposed in the continents, the mechanisms allowing magmas to undergo the necessary crystal–liquid separation and digestion of country rocks for differentiation and contamination are poorly constrained. In this chapter, we show two independent approaches that are essential to understand fractionation and contamination of magmas. These are (a) the study and interpretation of field relations in exposed deep sections of batholiths and (b) the results of laboratory experiments carried out at middle–upper crust pressure. Experiments support that fractionation is intrinsic to crystallization of water-bearing magmas in thermal boundary layers created at the sidewalls of ascent conduits and walls of magma chambers. Gravitational collapse and fluid migration are processes identified in experimental capsules. Similarly, reaction experiments in mixed capsules support reactive bulk assimilation as a plausible mechanism that is compatible with field and petrographic observations in contaminated granitic rocks.

5.1. INTRODUCTION

Magmatic fractionation (closed system) and contamination (open system) are common processes involved in the overall differentiation of igneous rocks in the continental crust (Bowen, 1928). The two processes can act jointly in magma chambers and conduits. Many silicic ($SiO_2 > 53$ wt%) igneous rocks, in particular those formed in active continental margins, can be modeled geochemically as resulting from a combination of assimilation and fractional crystallization (AFC) (Bohrson & Spera, 2001; DePaolo, 1981). However, the relative contribution of each process and the mechanisms of operation in magmas remain unconstrained.

Many igneous rocks appearing in the continental crust, and particularly those richer in SiO_2, contain isotopic signatures indicating contamination with older crustal rocks (Allègre & Ben Othman, 1980; Hawkesworth & Kemp, 2006; Kemp et al., 2007; McCulloch & Wasserburg, 1978). Contamination may be acquired either during ascent and emplacement in the crust, or may be inherited from an already crustal-contaminated source. Trace elements and isotopic ratios, which are regularly used to make AFC modeling, are unable to discern between the two processes. Fortunately, the major element compositions of melts are dependent on the composition of the solid saturation assemblage, which is in turn imposed by intensive variables in a given system,

---

[1] *Instituto Andaluz de Ciencias de la Tierra, Consejo Superior de Investigaciones, Científicas–Universidad de Granada, Granada, Spain*

[2] *Departamento de Ciencias de la Tierra, Universidad de Huelva, Huelva, Spain*

[3] *Geosciences Barcelona (formerly ICTJA), Consejo Superior de Investigaciones Científicas, Barcelona, Spain*

[4] *Departamento de Geología, Universidad de Oviedo, Oviedo, Spain*

Crustal Magmatic System Evolution: Anatomy, Architecture, and Physico-Chemical Processes, Geophysical Monograph 264, First Edition.
Edited by Matteo Masotta, Christoph Beier, and Silvio Mollo.

DOI: 10.1002/9781119564485.ch5

in such a way that the composition of melts in closed systems will follow cotectic lines that can be determined by means of phase equilibrium experiments and thermodynamic modeling. Comparisons between rocks and experimental liquids may help to distinguish open from closed magmatic systems. It is expected that open-system processes may introduce characteristic departures in the composition of rocks from that of cotectic liquids. In a theoretical case, rocks belonging to a magma fractionation series will represent liquids extracted at any time in the course of crystallization. These are the so-called *liquid lines of descent* (LLD) (Bowen, 1928). However, in practice, rock series may depart from the ideal composition of LLDs, even if the system is closed. The reason is that the extracted liquid fraction may carry magmatic crystals in suspension from a magma chamber or may drag crystals from the consolidated parts of the chamber or conduits on the way up. These are self-contaminated liquids (Figure 5.1). Similarly, the crystal-rich residue left after a partial extraction of melt becomes a new magma system that neatly departs form the cotectic. This is a very common case in granitic rocks, in which a residual liquid escaped in the course of crystallization. These are called *disguised cumulates* (Lee & Morton, 2015), as a cumulate texture is not recognized, whereas an off-cotectic composition is identified. Magmatic differentiation by crystal fractionation is possible if either a liquid fraction is removed from the crystallizing magma or a fraction of crystals is separated away from the magma. Both processes differ significantly from each other and can operate under different circumstances. The virtual absence of monomineralic layering in silica-rich calc-alkaline systems indicates that crystal settling is not a dominant mechanism.

Understanding how crystals and liquids are separated in crustal magmas requires paying special attention to the physical and chemical features of crystallizing magmas. Most crustal magmas are characterized by high silica content. The implication is that the viscosity is much higher than that of basaltic magmas, making crystal–liquid separation difficult to achieve (Glazner, 2014). However, many lines of evidence, mostly supplied by geological and geochemical relations, point to an effective fractionation in nearly closed magma systems. A solution to this paradox has been addressed by several approaches, including numerical modeling (Bachmann & Bergantz, 2004; Bachmann & Huber, 2016; Burgisser & Bergantz, 2011; Gelman et al., 2014), analog experiments (Michioka & Sumita, 2005; Shibano et al., 2012, 2013), and experiments with silicate melts at high pressure and high temperature (Masotta et al. [2012]; Huang et al. [2009]; Rodríguez & Castro [2017]). Magma

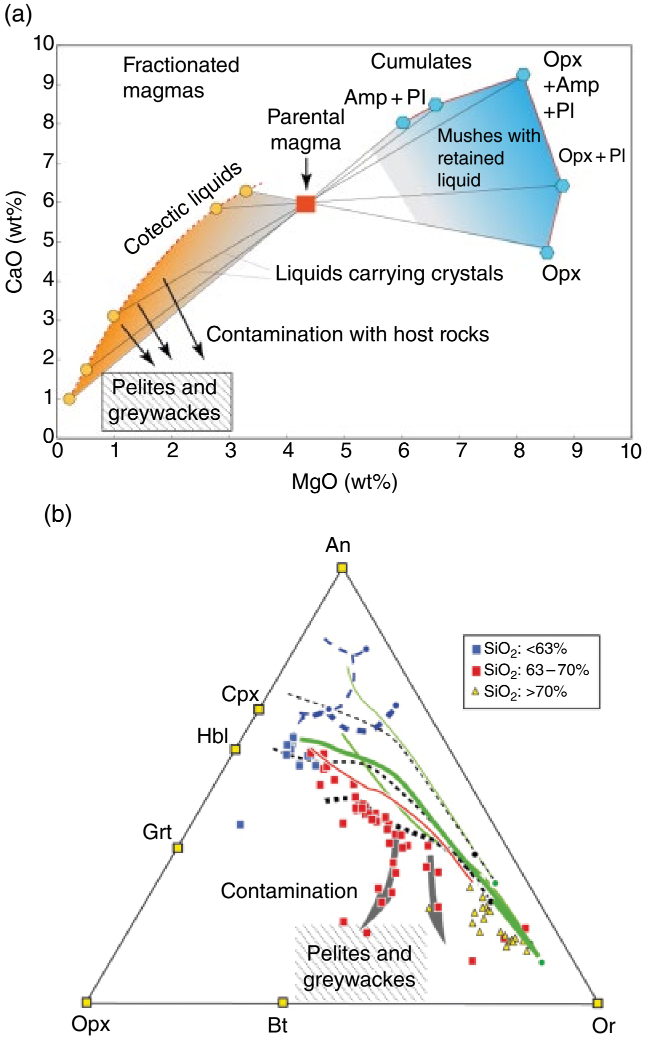

Figure 5.1 Geochemical variation plots, taken as proxies of phase diagrams, depicting possible arrays of fractionation and contamination in calc-alkaline magma systems. (a) The CaO–MgO diagram showing the curved array of experimental cotectic liquids (orange dots) and their corresponding solid assemblages (blue hexagons) formed in equilibrium at 3 kbar from an andesitic parental magma (Castro, 2013). The orange field below the cotectic line represents the area of magmas that carry crystals from the cumulate. The blue area represents the field crystal mushes that retain a liquid fraction after extraction. Many rocks in batholiths appear in the two areas, indicating that fractionation is not perfect. Also shown are the lines of contamination with metasedimentary rocks in the case of open systems. (b) Projected space in the diagram Opx–An–Or showing cotectic lines from experimental liquids under various conditions of pressure and water content. Rocks of the Gredos batholith in Central Spain are shown as an example. These appear in part in the array of fractionation and in part in that of assimilation (Modified from Castro, 2013). Source: Modified from Castro (2013).

crystallization in a thermal boundary layer (TBL), created, for instance, at the walls of magma chambers and conduits (Rodríguez & Castro, 2017), is the most plausible mechanism that contributes to separation of liquids from crystals within a solidification front (Marsh, 2002).

Because assimilation is usually considered an energy-consuming process, its role in accounting for significant differentiation of igneous rocks has been questioned (Bowen, 1922; Glazner, 2007; Thompson et al., 2002). Energy balance is applied in terms of xenolith melting and, thus, assimilation is considered as a particular case of magma mixing (Thompson et al., 2002) between melts from the xenoliths and the intruding magma. Also limiting is the assumed low temperature for the country rocks to be assimilated (Glazner, 2007). However, the reach of assimilation, far from being a self-limiting process, can be enlarged in cases of hot country rocks and repeated intrusions of magma (Glazner, 2007). In addition, country-rock xenoliths can be disaggregated mechanically by inducing melting at low melt fractions, contributing to the so-called *reactive bulk assimilation* (Beard et al., 2005) in which energy consumption is minimized. The observation of contaminated rocks over kilometric extensions of plutonic intrusions from the Variscan Gredos batholith in Central Spain, which were emplaced in repeated layers into migmatitic metasediments (Díaz-Alvarado et al., 2011), points to country-rock assimilation as an efficient mechanism that contributes to differentiation of magmas in the continental crust. These areas provide relevant field relations that may help one understand the intricacies of assimilation. A summary of these relations is shown in this chapter.

In regard to the mechanisms of assimilation, essential questions are: What are the details of the process of assimilation? How do exotic elements incorporate to the magmas? What is the scope of assimilation in nature? Answering these questions require a knowledge of the process. Although some geochemical features may be indicative of magmatic assimilation, the study of field relations between igneous intrusions and country rocks in deep-seated plutons is essential to reveal the mechanisms of magma–host interactions. Even in field-based examples, the intricacies of the processes of magma–host interaction leading to contamination are poorly constrained. Experiments are useful to set limits to possible processes involving chemical equilibrium and disequilibrium. Integration of petrological phase equilibrium relations and field-based studies are essential to distinguish between competing processes. Furthermore, the identification of paleotectonic environments through the geochemistry of magmas requires a wholly understanding of petrogenetic processes, contamination being a very common one and, at the same time, the most difficult to reveal. At this purpose, we present new field descriptions from the Gredos batholith (Central Spain) that are interpreted in the light of evidences from relevant laboratory experiments on magma differentiation and crustal contamination.

5.2. GEOLOGICAL AND GEOCHEMICAL INFERENCES ON FRACTIONATION

On the basis of geochemical studies, granites of the Cordilleran batholiths are linked to fractionation from an intermediate magma precursor of andesitic to basaltic andesitic composition, for example, Sierra Nevada batholith (Lee et al., 2006) and Patagonian batholith (Castro et al., 2020; Castro et al., 2011; Pankhurst et al., 1999). Experimental phase equilibria (Castro, 2019, and references herein) also point to a similar path adopting an intermediate precursor as the parental magma to batholiths. Even in intracontinental calc-alkaline batholiths (e.g., Caledonian Newer granites and Variscan batholiths of Iberia), whose origin points to fluid-assisted melting of the lower crust (secondary I-type granites; Castro, 2019), a fractionation trend from tonalites and quartz-diorites to granodiorites and granites is observed. Curved patterns in Harker diagrams are characteristic of cotectic variations and, hence, of liquid fractionation from one or various parental magmas. By contrast, rectilinear patterns are considered as indicative of magma mixing or contamination, as they result from a mechanical mixing between two systems, namely magma–host or magma–magma. However, mixing of fractionated liquids with their cognate crystals may also produce rectilinear patterns while the system is closed to external contaminants (Bea et al., 2005). Figure 5.1a shows internal mixing relations between liquid and crystals in the MgO–CaO diagram, which can be taken as a proxy of cotectic variations in an ample variety of mafic and intermediate systems, including the calc-alkaline series. The two components, MgO and CaO, are preferentially partitioned into the solid saturating assemblage, which is dominated by Pl+Cpx or Pl–Amp (mineral abbreviations after Whitney & Evans [2010]) along a wide temperature interval from near-liquidus to near-solidus conditions. Commonly, rocks fractionated in closed systems within the continental crust evolve following the curved patterns dictated by the thermodynamic cotectic. However, rock series evolving in a closed system may plot outside the cotectic, as internal mixing between fractionated liquid and crystals from the cumulate is also possible (Figure 5.1a). In sum, the geochemical inferences on fractionation must be taken with care. Only curved patterns are indicative of fractionation, as they are governed by thermodynamic cotectic variations. A better way to delimitate patterns of fractionation from those of assimilation is by plotting rocks on triangular diagrams using a multicomponent space projected onto the plane Orthopyroxene–Orthoclase–Anorthite (Figure 5.1b).

In calc-alkaline plutonic systems, layered monomineralic cumulates are rare. Paradoxically, plutons are formed by rocks that display nearly cotectic variations. Thus, where are the cumulates from which fractionated liquids were extracted? The explanation is that fractionation proceeds by expulsion of liquid from a crystallizing magma, and not by separation of crystals from the magma. The resulting cumulates are hardly identified by textures or compositions. Many diorites and gabbros of the calc-alkaline plutonic associations are "disguised" cumulates (Lee & Morton, 2015). That is, they represent crystals aggregates, or mushes, that lost a residual liquid in the course of crystallization. For this reason, rocks of intermediate composition (diorites and quartz-diorites) from batholithic associations are scattered in MgO–silica and MgO–CaO diagrams. These cumulate-like diorites share the same scattered region of lower crust granulites, pointing to fractionation as an overall process responsible for the differentiation of the lower and upper continental crust (Castro, 2013).

5.3. MECHANISMS OF LIQUID-CRYSTAL SEPARATION

Although fractionation by liquid–crystal separation is a necessary process to account for geochemical (e.g., cotectic variations in closed systems) and geological (e.g., zoned plutons) observations, the mechanisms of such a physical separation remain debated. Liquid expulsion from a crystallizing aggregate is a preferred mechanism in silicic magmas, in which individual crystal separation by gravity settling is impeded by the high viscosity of melts and the low density contrast between melt and crystals (Brandeis & Jaupart, 1986). However, gravity compaction and expulsion of liquid may be encountered in the crystal-rich mush formed atop of solidification fronts. Also, the interstitial melt trapped in the mush may undergo water saturation, leading to boiling and vesiculation that may force deformation and expulsion of the liquid from a crystalline aggregate. The two processes, gravitational collapse and fluid-assisted filter pressing, are analyzed here.

5.3.1. Gravitational Collapse and Compaction

In spite of the scarce theoretical support to an efficient process of crystal–liquid separation that makes large volumes of silicic magmas available in the continental crust in short periods of time (Bachmann & Huber, 2018), it is a fact that fractionation is identified on the basis of geochemical nearly cotectic trends (Castro, 2013; Castro, 2019), continuous variations in zoned intrusions, and large volcanic eruptions of silicic (rhyolitic) magmas (Lipman, 1988). The two main approaches to understand the mechanisms of silicic magma fractionation, namely analog modeling and experiments, have failed to account for the generation of fractionated liquids in the required volumes and at the necessary rate, in a time span shorter than the cooling time in the upper crust. Mechanical interaction of falling particles (crystals) in silicic magmas can occur even at low crystal fractions, leading to a "hindered" settling processes with the implication of slow rates of melt extraction (Bachmann & Bergantz, 2004; Bachmann & Huber, 2018). An alternative mechanism is compaction of a crystal-rich matrix, which is considered to be effective in increasing the rate of melt extraction (McKenzie, 1984). Compaction is a common phenomenon in long-duration (>10 days) experimental runs. We discuss below evidences from analog materials and high-pressure–high-temperature experiments carried out in the presence of temperature gradients. These may shed light on the relative importance of gravity settling and compaction in magma chambers.

Analog Experiments and Modeling

Separation of liquid and crystals in the magma chambers was explained in the conceptual and analytical model of Marsh (1988) as due to convection beneath the *capture front*, defined as the surface separating the rigid crust and crystal mush layers (crystallinity larger than 25%) from a crystal suspension zone. According to that model, the resulting convection pattern includes crystal-laden plumes falling from the suspension zone to the deeper parts of the chamber. The analog experiments of Michioka and Sumita (2005) simulated a solidifying magma chamber by means of an experimental cell consisting of a thin particle layer (glass beads) at the top, overlying a thick liquid layer (glycerin solution or silicone oil). A limited zone, located at the interface between the particle-rich and the liquid-rich layers, became unstable, forming descending plumes, thereby presenting experimental confirmation of the convection model of Marsh (1988). The similar analog experiments of Shibano et al. (2012) extended those results to the case of a thick particle-rich layer and found that the downwelling crystal-laden plumes actually come from a dilated boundary layer located beneath a granular layer whose particles are in a jammed state. Descent of the plumes caused a cellular convection pattern within the liquid layer, which eroded the dilated boundary layer. This mechanism differs from those of compaction, Stokes settling, hindered settling, and Rayleigh–Taylor instabilities, and permits the upward migration of the liquid layer, becoming a potentially efficient process of melt transport within magma chambers. Interestingly, some of the experiments performed by Shibano et al. (2012) do not rule out the activity of permeable flow (compaction and hindered settling) as a secondary mechanism for liquid transport, particularly when the granular layer slides downward as a whole, allowing the generation of a liquid-rich layer at its top. This mechanism is akin to that described by Marsh (2002) to explain the presence of large silicic lenses in the upper part of mafic intrusions. Finally, Shibano et al. (2013) advanced in the analysis of magma chamber processes simulating roof melting by means of experimental cells filled with wax and glass beads. Those experiments, which do not preclude the effects of crystallization within the magma chamber, are able to explain the generation of rhythmic layering at the bottom of the chamber, and showed that magma ascent can be a cyclical and intermittent process.

Compaction Experiments at High Pressure–High Temperature

Crystal accumulation is commonly observed in experimental capsules in long-duration runs of several days, overcoming the limitations imposed by the small size of crystals and the expected high viscosity of silica-rich liquids. This phenomenon allows us to experimentally simulate the role of gravity compaction and expulsion of an interstitial liquid from a crystal-rich mush and to compare the results with magmatic differentiation series. In this way, geological inferences regarding, and mechanical analysis of, a possible collapse of the partially crystallized solidification front atop of magma chambers (Marsh, 2002) were confirmed experimentally by Masotta et al., (2012) and contrasted with petrological relations of mush fragments (crystal-rich enclaves) in volcanic rocks (Masotta et al., 2016). Another interesting crystallization experiment, possibly accompanied by compaction, was carried out by Huang et al. (2009) using a natural andesite (the AGV USGS standard; Flanagan, 1967) as starting material with added water, crystallizing within a thermal gradient of 600 °C. The favored interpretation was differentiation by ion migration in response to the thermal gradient (Huang et al., 2009). However, the presence of monomineralic crystal layers at the bottom of the capsule indicates that compaction was an effective mechanism of differentiation by crystal–liquid separation in that experiment. It is interesting that experiments with a dry andesite in a thermal gradient (ca. 300 °C) produced no significant differences in composition along the capsule, whereas marked differences were found in capsules with the same starting material with added water (Rodríguez & Castro, 2017). Thus, the cause of element fractionation must be found in the presence of water and not in the thermal gradient. One of the experiments reported by Rodríguez and Castro (2017) was carried out with the abovementioned AGV andesite within a 30 °C/mm gradient at 5 kbar in the classical vertical position of the piston cylinder. In this arrangement, identical to the experiment by Huang et al. (2009), the thermal gradient within the capsule acts in the same direction as gravity. This vertical experiment was carried out as a benchmark run (Run CRV2; Rodríguez & Castro [2017]) to compare with horizontally arranged runs of the same study in which the thermal gradient and gravity were orthogonal (see the next section). After comparison, fractionation was less effective compared with the horizontal runs as crystal–liquid separation is controlled by gravity compaction and not by exsolution of a strongly fractionated (rich in silica and alkalis) fluid phase within the solidification front (see below). Nevertheless, we found interesting relations in that vertical run that merit the attention here. By contrast with the other thermal gradient experiments in which temperature remains constant at the hot spot, in the run CRV2 (Rodríguez & Castro, 2017) a dynamic thermal gradient is imposed following a programmed cooling ramp of 0.6 °C/hour, representing a more realistic scenario of a cooling magma chamber or dike. A half-polished section of the vertical run CRV2 is compared with a horizontal run crystallized under identical conditions but with the gravity vector arranged orthogonal to the gradient temperature vector (Figure 5.2). It can be observed that crystals are mostly concentrated at the bottom of the capsule (Figure 5.2b) compared with the horizontal run (Figure 5.2a). Because both experiments were set at the same initial conditions and both were slowly cooled at the rate 0.6 °C/hour during 309 hours, the only explanation for the observed differences is compaction and liquid expulsion from the cumulate in the vertical run. Moreover, a thin monomineralic carapace of Amp, the *liquidus* phase of this water-rich system, is broken and collapses leaving free space near the walls, allowing interstitial liquid to escape upward (Figure 5.2e). The upper layer, containing tiny magnetite crystals, is possibly formed during intrusion of upward-moving liquid plumes. The composition of glass (quenched melt) along the capsule is fractionated. In the crystal-free zone, glasses are richer in SiO_2 and K_2O, and poorer in CaO (Figure 5.2d) compared with the original composition of the AGV andesite (Rodríguez & Castro, 2017). The constant composition of glasses in the crystal-free zone within a strong thermal

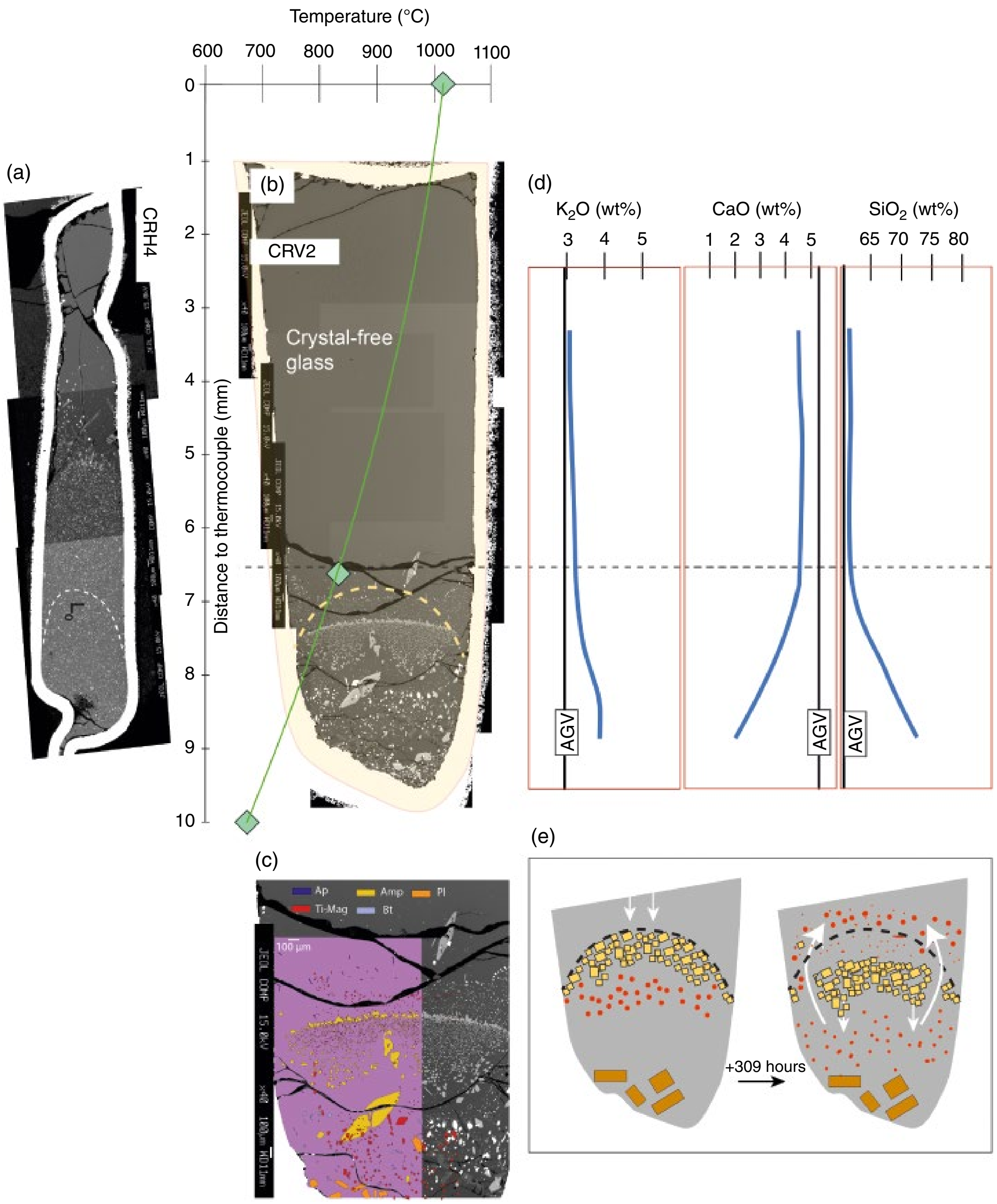

Figure 5.2 Electronic compositional images (backscattered electrons) and compositional relations of a vertically arranged experimental run simulating magma crystallization in a thermal gradient at 5 kbar. (a) Capsule section from a horizontally arranged run under the same conditions as the vertical run (b). The thermal gradient of the assembly is shown in (b) with a green curve and green diamonds from double thermocouple measurements. The dashed curves L_0 in (b) represent the liquidus temperature taken from run CRH5 (see Figure 5.4a). (c) Phase map of the bottom part of the vertical capsule. (d) Compositional profiles of glasses (quenched liquid) along the vertical capsule. (e) Interpretation of gravitational collapse of the upper carapace and liquid expulsion at the bottom of the vertical capsule. The dashed curve represents the theoretical position of the liquidus in the absence of gravity collapse. Sources: Based on Rodríguez and Castro (2017); Huang et al. (2009).

gradient of ~30 °C/mm (see the green curve in Figure 5.2b) precludes a Soret effect (Huang et al., 2009) as the cause of liquid fractionation. By contrast, these results reinforce the role of gravitational instability as an efficient mechanism to produce liquid–crystal separation. In summary, application of a dynamic thermal gradient enhances fractionation of the bulk magma system accompanied by compaction of the crystal-rich mush formed at the solidification front. Moreover, the results of other compaction experiments (Huang et al., 2009; Masotta et al., 2016) are totally comparable as they are characterized by expulsion from the mush zone (i.e., the side walls of conduits and/or magma chambers) of a fractionated liquid that mixed with the pristine liquid ahead of the front, leading to fractionation of the whole system.

5.3.2. Crystallization in a Vertical (Non-Gravitational) TBL

The mechanism of compaction and gravitational collapse of a crystal-rich mush requires that the thermal gradient that creates the solidification front be closely parallel to the gravity vector. This condition is satisfied in both the roof and bottom of magma chambers for which most mechanical models have been developed (Bachmann & Bergantz, 2004; Lake, 2013; Marsh, 2002). However, the processes of magma crystallization at the vertical walls of magma chambers and the sidewalls of ascent conduits have received less attention (Humphreys & Holness, 2010; Namur et al., 2013). The case of vertical conduits is relevant as most intermediate magmas (e.g., calc-alkaline batholiths) that feed plutons at the upper crust have traveled tens of kilometers from the source region of melt segregation at the lower crust or the upper mantle. In the case of horizontal thermal gradients, as the sidewalls of conduits, the alternative to hindered settling and gravitational collapse is liquid expulsion by *gas-driven filter pressing* (Pistone et al., 2015).

Effects of Volatile Exsolution

Rodríguez and Castro (2017) demonstrated experimentally that *gas-driven filter pressing* is a mechanism that can operate in a water-bearing magma crystallizing in a TBL in which a continuous variation in the crystal fraction or crystallinity (X_c=crystals/crystals+liquid) from all-solid ($X_c = 1$) to all-liquid ($X_c = 0$) is established. Other properties, such as magma viscosity and strength, also change across the TBL, making the walls of magma conduits and chambers places of special relevance in the generation of textural heterogeneities in magmas (Fernández & Castro, 2018). In this section, only the petrological consequences of gas expulsion and vesiculation by second boiling are explored on the basis of laboratory experiments (Rodríguez & Castro, 2017).

The principle is that any water-bearing liquid, the general case of calc-alkaline magma systems, will reach saturation by second boiling in the course of crystallization, in the same way as water is partitioned into the remaining liquid, reaching saturation at a given state of crystallinity. The value of X_c for boiling depends on the initial water content (in wt% H_2O) of the magma (W_0) and the water solubility at the pressure of crystallization $[W_s]_{(P)}$. The fraction of water-saturated liquid (X_{sl}) is given by the expression

$$X_{sl} = W_0 / [W_s]_{(P)} \tag{5.1}$$

Water solubility is strongly dependent on pressure and weakly on temperature (Burnham, 1979). A relation between pressure and solubility is obtained by second-order polynomial regression of the Burnham´s solubility curve for granite liquids (Castro, 2013):

$$W_s = -0.27P^2 + 3.54P + 0.42; \; (\text{for } P < 6 \text{ kbar}) \tag{5.2}$$

By substitution in Eq. (5.1), we get the empirical relation

$$X_{sl} = W_0 / -0.27P^2 + 3.54P + 0.42; \; (\text{for } P < 6 \text{ kbar}) \tag{5.3}$$

From this relation, it is possible to obtain the critical crystallinity ($X_{cc} = 1 - X_{sl}$), that is, the crystal fraction at which the remaining liquid reaches saturation. The value of X_{cc} depends on the pressure of crystallization and the initial water content of magmas (Figure 5.3). The effectiveness of boiling and vesiculation in promoting liquid expulsion and fractionation depends on the rheological state of the partially crystallized magma at the time of water saturation. At relatively high crystallinity ($X_{cc} > 0.7$), deformation of the rigid crust is impeded by the crystal interlocking structure of the magma. Formation of tension gashes can be formed at this state (Fernández & Castro, 2018). Many aplites and pegmatites in granite plutons are true *degassing* structures. These form dikes and irregular pods in which the contacts with the host granite are at the scale of crystals, denoting that the host was a crystal-rich magma, and not a solid rock, at the time of fracturing and fluid segregation. It can be expected that fluids expelled out via fractures (dikes) from the rigid crust of a solidification front will carry strongly fractionated components that may mix and/or dissolve into the liquid-rich area ahead of the saturation front. Such a mechanism of "fluid migration" is very efficient in granitic magmas, giving rise to zoned intrusions and fractionated cupolas atop of plutons. This principle is the basis for crystallization experiments of a water-bearing magma in a thermal gradient (see below).

Depending on the initial water content and the pressure of crystallization, the magma can reach water saturation at varied crystal contents and, thus, varied

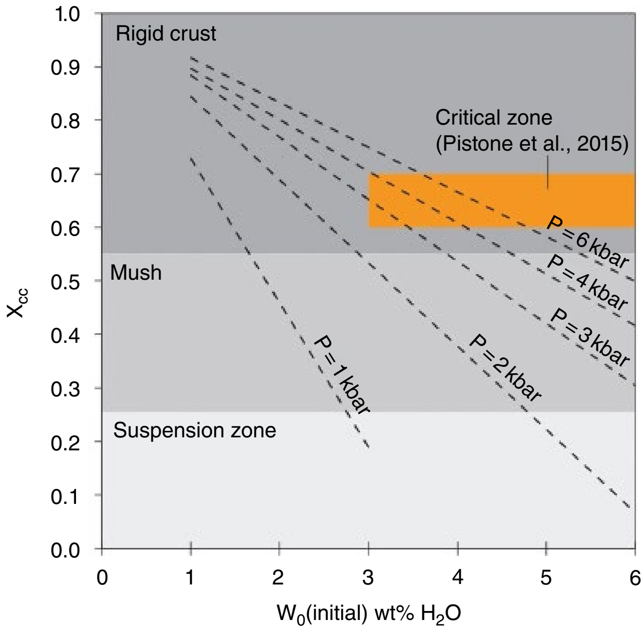

Figure 5.3 Plot of critical crystallinity ($X_{cc} = 1 - X_{sl}$) versus initial water content (W_0) of a granitic liquid using Eq. (3) at variable pressures from 3 to 6 kbar. The critical crystallinity represents the crystal fraction at which the remaining liquid reaches water saturation and boiling. The three zones of the solidification front (suspension, mush, and rigid crust) are marked using the boundaries given by (Marsh, 2002). The most favorable conditions to promote crystal–liquid separation by fluid-assisted filter pressing according to experiments (Pistone et al., 2015) are also depicted. Sources: Pistone et al. (2015); Marsh (2002).

rheological states within the saturation front can be found (Fernández & Castro, 2018; Rodríguez & Castro, 2017). The most favorable state is that of a deformable mush in which the formation of bubbles can push liquid away from the crystal framework by promoting compaction of the crystal aggregate (cf. Bachmann & Huber, 2018). In the case of the sidewalls of conduits, shear deformation of the solidification front may favor liquid expulsion by compaction of the mush. Many flow structures with high concentration of K-feldspar crystals can be explained by this mechanism. Outside the mush zone, in the suspension zone (X_c < 0.25), flow is controlled by the liquid phase as crystals are "floating" in the liquid with scarce mechanical interactions. Moreover, water saturation can only be reached in the suspension zone in anomalous cases of high initial water content and very low pressure (Figure 5.3). For a magma to reach saturation at X_c < 0.5 at the pressure of 3 kbar, the initial water content must be higher than 6 wt% H_2O.

The most favorable mechanical conditions for water saturation and vesiculation to effectively promote the expulsion of liquid from the crystalline framework are found within the rigid crust (X_{cc} > 0.55), within a critical zone of X_{cc} from 0.6 to 0.7, for magmas with initial water content W_0 > 3 wt% (Pistone et al., 2015). These critical conditions can be encountered within a wide range of pressure from 3 to 6 kbar (Figure 5.3). For shallower conditions (P < 2 kbar), low initial water content (W_0<3 wt%) is required to get X_{cc} within the critical zone of rigid crust of a solidification front. In sum, the rheological state of the magma must be deformable at the time of melt water saturation to promote liquid expulsion. At values of X_{cc} > 0.7, the rigid crust can experience hydraulic fracturing and segregation of a water-saturated melt.

Magma Splitting in a TBL: An Experimental Finding with Implications

The sidewalls of magma ascent conduits represent large transient interfaces along which magma loses heat to the surrounding host with the consequent generation of TBLs along several tens of kilometers from the region of magma segregation to the final level of emplacement. It is inferred that these large TBL structures play an important role in magma differentiation during ascent, particularly in the case of water-bearing magmas, as water saturation will be encountered within the TBL. All phenomena referred to in the previous section can operate along the conduits. The main inference for differentiation in TBL at the conduits comes from the presence of autoliths in granite (sensu lato) plutons. It has been demonstrated that most mafic microgranular enclaves characterizing calc-alkaline batholiths are true autoliths and not fragments from synplutonic dikes (Paterson et al., 2016; Žák & Paterson, 2010). Autoliths represent eroded fragments from different parts of the TBL (chilled margins) of conduits. All textural observations in autoliths, such as the fine-grain size, the presence of resorbed crystals of plagioclase, the presence of double enclaves, together with the observed geochemical and isotopic features (Rodríguez & Castro, 2019), support such an interpretation. A mechanical analysis of the rheology of conduits at the TBL accounts satisfactorily for the observed field relations, shape, and size of autoliths (Fernández & Castro, 2018).

Rodríguez and Castro (2017) carried out experiments to simulate the crystallization of a water-bearing magma in a vertical TBL representing the sidewalls of conduits. The results constituted a significant finding: The liquid ahead of the solidification front is fractionated only if water is present as an initially dissolved phase in the magma (Rodríguez & Castro, 2017). Under identical conditions, runs with dry compositions produced no differentiation effect on the liquid phase. The other interesting result is the sharp boundary between the crystalline zone (the solidification front) and the liquid. The consequence is that a water-bearing magma splits into two systems with a compositional jump. One system is a differentiated

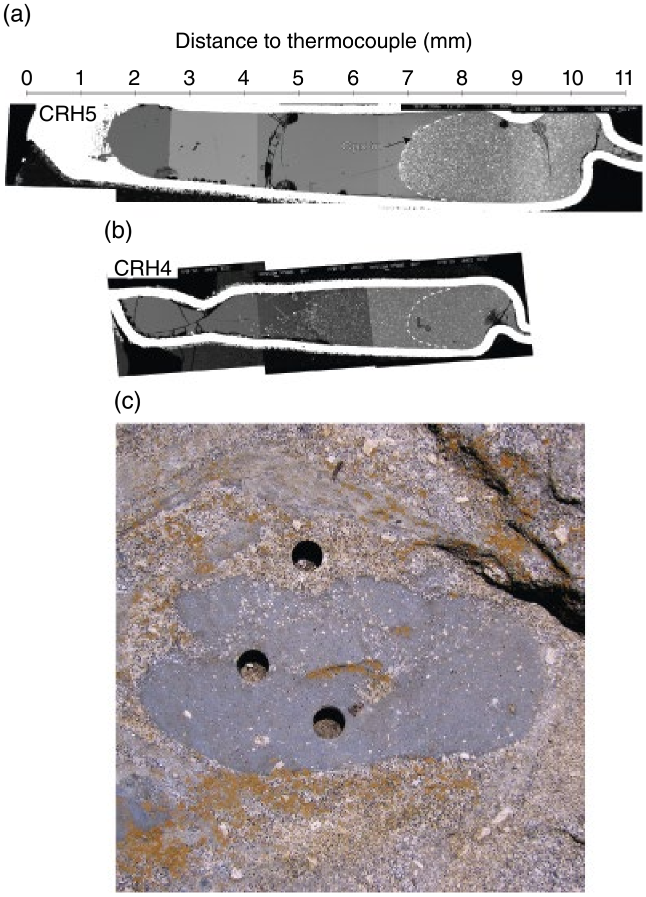

Figure 5.4 Mosaics of backscattered electron images from two polished sections of runs CRH5 (a) and CRH4 (b) with the AGV andesite (Rodríguez & Castro, 2018) using the thermal gradient imposed by the experimental assemblage. The initial conditions are P = 5 kbar and T = 1200 °C at a distance of 0–3 mm from the thermocouple. CRH5 was quenched after 315 hours under the initial conditions. The liquidus (Cpx) is set approximately at 980 °C. In CRH4, T was dropped at the rate of 0.6 °C/hour over 308 hr (until the thermocouple reached 1016 °C). The composition of glass (quenched liquid) at 2 mm of the thermocouple is more fractionated (richer in K_2O and SiO_2 and poorer in CaO and MgO) in CRH4 compared with CRH5, in which no gradient was applied. (c) Field photographs of partially dismembered autoliths from the Gredos batholith in Puente del Congosto (Central Spain). Source: Rodríguez and Castro (2018).

liquid, and the other is a crystal-rich mush (Figure 5.4). The latter is comparable to natural autoliths (Rodríguez & Castro, 2019).

In sum, differentiation in a TBL is interpreted as the result of liquid expulsion from the solidification front in the course of crystallization and water saturation. The liquid ahead of the solidification front is modified by two combined phenomena, namely the expulsion of a water-saturated liquid and the arrival of fluids released by boiling and vesiculation. Because the system under study is a high-silica andesite (the AGV standard), the residual water-saturated liquid has the minimum composition of the granite system. This residual melt will be mixed with the pristine liquid ahead of the TBL, leading to its fractionation. The change in the composition of the system has been modeled by using the general equation for *in situ crystallization* (Langmuir, 1989):

$$C_M = C_0 \, F^{(f_A(E-1)/(f_A-1)} \tag{5.4}$$

where C_0 is the initial magma composition (in this case the standard AGV andesite), F is the fraction of melt (liquid / liquid + crystals), f_A is the fraction of liquid returned to the magma from the solidification front, and E is the partitioning coefficient, in this case taken as the ratio of the composition of the saturated liquid in the element of reference (C_{SL}) to the composition of magma in the same element of reference (C_M). The composition at any distance from the wall, after separation of the cumulate, requires integration over discrete increments of magma crystallization in which, F, E, and f_A must be recalculated for every increment (Δ) of magma crystallization. We have introduced a restriction in the equation to calculate the amount of solid fraction at which the intercumulus liquid is expulsed from the crystal-rich mush. That solid fraction (1-F), or cumulate, at every discrete increment (Δ) is determined by the fraction of saturated liquid (X_{sl}), which is dictated by the ratio of the water content of magma (W_0) to the water content at saturation (Eq. 5.1). An iterative calculation at fixed increments of a unit volume of magma allows us to know the composition of the modified liquid ahead of the solidification front and, by simple mass balance, the composition of the solid residue. A plot of the silica content of the modified liquid versus the fraction of the remaining magma is shown in Figure 5.5 for three values of the initial water content (W_0) of 2, 3, and 5 wt% H_2O and at a pressure of 5 kbar. Because water saturation is key in determining the fraction of saturated liquid that is available to modify the pristine liquid, it is clear that the effect of fractionation is higher for systems containing the higher initial content of water (W_0). For values of $W_0 = 5$, the modified liquid reaches minimum silica values (SiO_2>63 wt%) of granitic rocks when only 20% of the whole magma is crystalized. However, magma with initial water content $W_0 = 3$ must crystallize about 50% of its initial volume to produce a fractionated liquid with $SiO_2 > 63$ wt%. Interestingly, the composition of cumulates remains almost constant compared with the continuous changing compositions of liquids. In nature, cumulates are represented by the fine-grained microgranular enclaves interpreted as autoliths, whose composition is very uniform within a particular pluton. Also, note that the most fractionated magma ($W_0 = 5$) yields the most mafic (less silicic) cumulates.

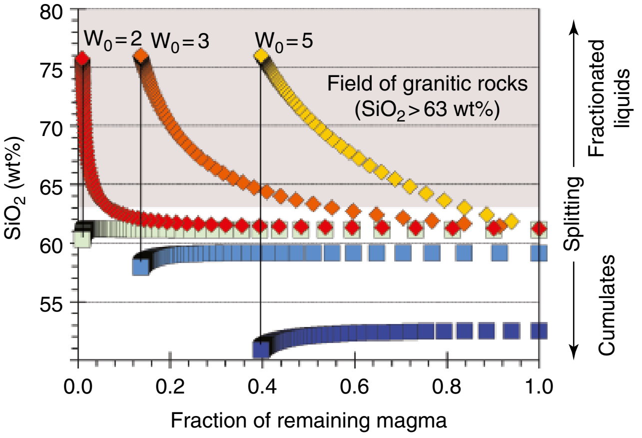

Figure 5.5 Variation in the silica content of liquids (in a unit magma chamber) that are modified by influx of residual water-saturated liquid coming from the solidification front (thermal boundary layer) at the sidewalls. Liquid curves are calculated with Langmuir's equation (Langmuir, 1989) for in situ crystallization (see text for further explanations). Source: Based on Langmuir (1989).

5.4. MAGMA CONTAMINATION BY COUNTRY-ROCK ASSIMILATION

Contamination can be seen as an open-system mechanism of magma differentiation in the crust as in the most general case contaminants are richer in evolved components, such as alkali elements and silica, than the pristine magmas. Contamination may proceed in two ways that are not exclusive each other: (a) Assimilation of country rocks and (b) contamination by fluids derived from the host. Although contamination can be traced by means of isotopic ratios, source contamination can be difficult to distinguish from crustal-related processes. Fluids released by prograde metamorphic reactions in the thermal aureoles of plutons may expectedly contaminate the intruding magmas. However, this process is rarely identified in plutonic intrusions. Assimilation is the most documented process in crustal intrusions. Partial or total digestion of country rocks by the intruding magma is intrinsic to assimilation as an efficient mechanism that contributes to the contamination of magmas in the continental crust.

Although contamination by country-rock assimilation can be identified in geochemical diagrams, the intricacies of the process can be varied. The study of field relations in plutons is essential to constrain possible mechanisms. Experimental studies on magma–rock interactions are also relevant to test reactions and mineralogical implications and to assess the feasibility of assimilation on a regional scale. The two methods, field relations and experiments, are explored here on the basis of recently developed studies.

5.4.1. Field Relations Supporting Assimilation and Magma Contamination

Contamination of magmas with their host rocks can be identified easily by means of geochemical and isotopic relations. Paradoxically, although intermediate and silicic magmas have traveled long distances through the crust until their final storage in magma chambers or plutons and volcanic eruptions, not all silicic rocks are contaminated to the same extent, and many of them maintain their pristine composition. There will be scenarios in which magma–host interactions are favored. Assimilation depends not only on the reactiveness between magma and country rocks but also on the dynamics of ascent and emplacement and the rheological behavior of the two systems. An approach to the mechanical processes leading to assimilation of country rocks, and the consequent contamination of intruding magmas, can be made on the basis of field relations in areas of intense assimilation. A summary of these relations, based on relevant exposures of hybrid granites from the Gredos batholith (Central Spain), is shown in this section.

The Gredos batholith has been revealed during the last decade as one of the most outstanding and voluminous granitic exposures (more than 300 km in length and 60 km in width) to explore the interactions between intrusive magmas and a medium- to high-grade crustal sections. The batholith is mainly composed of biotite (Bt) ± cordierite (Crd) granodiorites and monzogranites and minor amounts of basic rocks (Scarrow et al., 2009) that depict a K-rich calc-alkaline suite characteristic of I-type post-collisional batholiths (Castro, 2019), emplaced during the late D2 and D3 Variscan phases (320–290 Ma) (Díaz-Alvarado et al., 2013; Díaz-Alvarado et al., 2011). Detailed studies of the central area of the batholith have evidenced a laminar structure formed by mostly migmatitic host rocks and intrusive layers. The conspicuous magmatic fabrics (foliations, lineations, folds, and shear zones) are continued through the migmatitic structure of the host rocks, which involve the synkinematic and sequential emplacement of intrusive magmas assisted by crustal-scale extensional shear zones, as have been revealed by structural and U–Pb geochronological studies (Díaz-Alvarado et al., 2013; Díaz-Alvarado et al., 2012). These characteristics of the emplacement process reinforced the long-lasting and close interaction between magmas and partially melted host rocks that promoted the intense mingling and, finally, the chemical hybridization between both systems.

Geochemical, field, and experimental evidences have shown that the hybridization between an intrusive magma and its host rock is an effective mechanism of magma diversification during its ascent and emplacement (Beard et al., 2005; Díaz-Alvarado et al., 2011; Erdmann et al., 2007). The high diffusivity of some elements (e.g., the alkali elements) may favor the crystallization in the magma of particular phases, such as Kfs, in areas far from the external contacts of the pluton with the host rocks (Díaz-Alvarado, 2017; London et al., 2012). However, Al-rich phases present in calc-alkaline granodiorites, such as Crd and Grt, are diagnostic of assimilation processes and only appear in reactive domains where metasedimentary xenoliths were consumed, or at least they lost their integrity (Figure 5.6). In those cases, the original mineralogy of the xenoliths has been in part consumed by peritectic melting reactions to yield residual and peritectic minerals plus a granite melt, and in part is dispersed and camouflaged within the host magma. The only mineral species that can be considered exotic, in the sense that they are not present in the pristine magma, are the peritectic phases cordierite or garnet. The amount of assimilated material in hybrid granites can be estimated by mass balance using the fraction of Crd (Díaz-Alvarado et al., 2011; Erdmann et al., 2007).

The main conditioning factor for this process is the effectiveness of the heterogeneous interaction process between the partially crystallized magma and the partially molten metasedimentary host rocks. The rheological characteristics of both systems tend to converge during the emplacement process, that is, while the migmatitic system increases its melt percentage and the magma continues its crystallization process (e.g., [Vigneresse et al., 1996]). The driving forces of the emplacement process, including the stress state and the tectonic evolution of the crust, trigger the joint flow and deformation of the two systems, which yields a number of heterogeneous structures at all the scales (e.g., Paterson et al., 2018; Paterson et al., 1998) that are evidenced by the observed field relations (Figure 5.7). Those structures can be ascribed to the following mechanisms of mechanical interaction between intruding magma and host rock: (a) viscous folding, (b) host-rock dragging, and (c) migmatitic tearing apart. These structures can be ascribed to the following mechanisms of mechanical interaction between the intruding magma and the host rock: (a) viscous folding (Figure 5.7a–d), (b) host-rock dragging (Figure 5.7e), and (3) migmatitic tearing apart (Figure 5.7f).

Viscous Folding and Shearing

Complex fold geometries and distinct types of brittle and ductile shear zones are the most common structural features in migmatitic terrains (e.g., Hopgood, 1999). In the case of a migmatitic crust intruded by a partially crystallized magma whose viscosities converge during the evolution of both systems, the development of ductile deformation structures such as folds and shears considerably increases the contact surface between both systems and the isolation of host-rock fragments within the

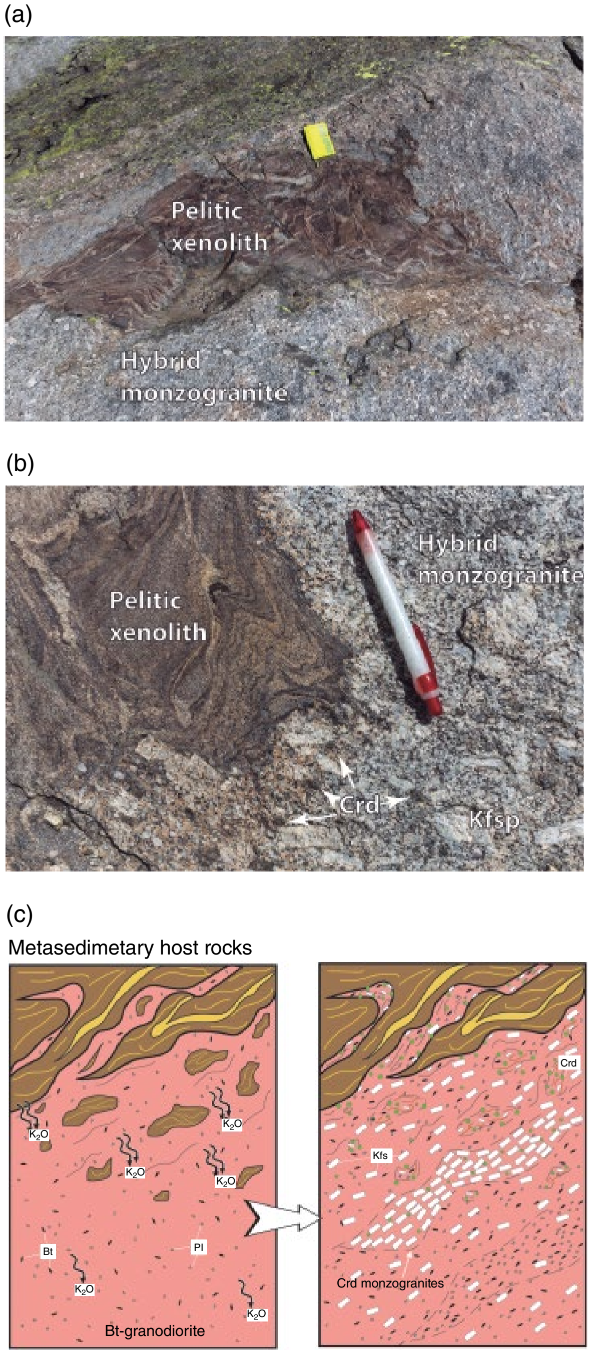

Figure 5.6 Field relations of partially digested pelitic xenoliths enclosed in calc-alkaline monzogranites and granodiorites of the Gredos batholith (Central Spain). (a) Large xenolith of partially molten (migmatite) metasediments showing irregular contacts. (b) Detail of another xenolith showing the concentration of large Crd crystals (dark dots) around the contacts. (c) Sketch in two stages showing the possible digestion of xenoliths by peritectic melting reaction and the formation of Crd (green dots) and Kfs that appear finally disseminated in the contaminated zones. The arrival of K at the pristine granodiorite shifts the composition of the final contaminated magma to monzogranite. Source: J. Díaz–Alvarado.

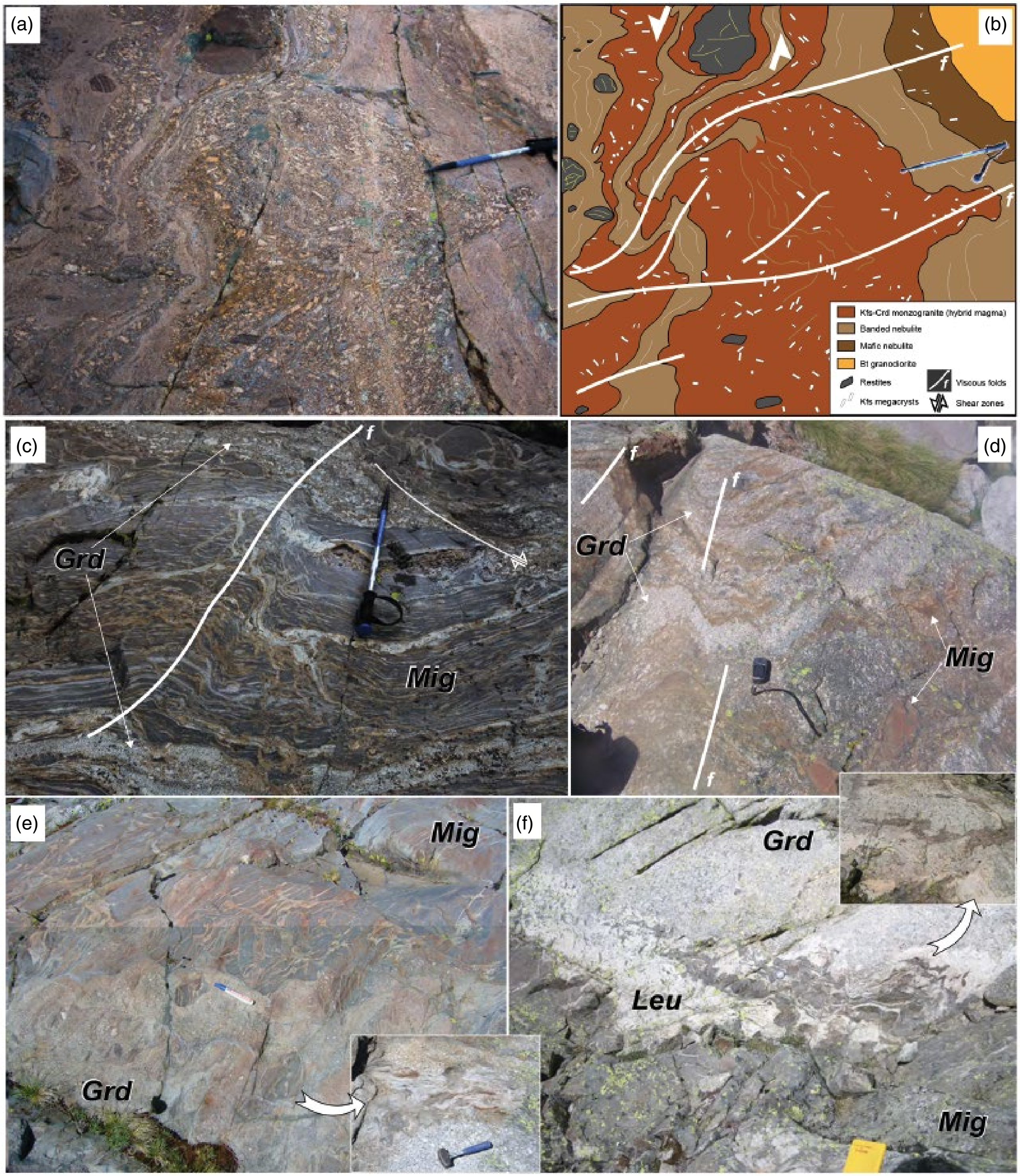

Figure 5.7 Field examples (Gredos massif, Spain) of heterogeneous structures resulting from the interaction processes between a partially crystallized magma and a partially molten metasedimentary host rock. (a) to (d) are cases illustrating mechanisms of viscous folding and shearing. (a) and (b) Field photograph and interpretative sketch of complexly interleaved and folded sheets of migmatites, intrusive Bt granodiorite, and hybrid Kfs–Crd monzogranite. (c) and (d) Coeval folding (*f* is the axial trace) of metatexite and granodiorite intrusive sheets. Shear zones are also seen affecting the system. (e) Sharp contact between the intrusive granodiorite (lower half of the photograph) and the migmatitic host rock (upper half) showing xenolithic fragments dragged by the intruding magma from its host rock. Inset depicts the final result of this process, with disaggregation of the metasedimentary xenoliths (melt + restitic and peritectic phases) within the granodiorite magma. (f) Tearing apart of migmatite mesosome from an intruding wedge of granodiorite magma promoted by the formation of a three-dimensional network of interconnected leucosome veins. Inset shows the individualization and disruption of sheets of mesosome and melanosome into the intruding magma. Grd: Intrusive granodiorite. Mig: Migmatite. Leu: Leucosome. Sources: Gogoi and Saikia (2018); Biot (1961); Chapple (1968); Johnson and Fletcher (1994); Ramberg (1961).

intrusive magma (Figure 5.7a,b). This process has been shown to be a necessary condition for the complete hybridization that results in contaminated magma (Gogoi & Saikia, 2018). Assimilation through reaction of host-rock fragments implies the successive injection of low-crystal-fraction magma batches, simultaneous development of assorted structures under a viscous but evolutionary regime, melting reactions, and chemical diffusion. Therefore, deformation of the complex composite system may be achieved through the mechanism of viscous folding, which implies a viscosity contrast between magma and host-rock bodies (Figure 5.7c,d) (e.g., Biot, 1961; Chapple, 1968; Johnson & Fletcher, 1994; Ramberg, 1961). A viscosity switch is expected along the interaction process, such that the less viscous unit at the very beginning of the interaction process (i.e., the intruding magma) becomes the more viscous one as it crystallizes, generating a very complex and heterogeneous set of folding structures. This is evidenced by the complex arrangement of Kfs megacryst fabrics that results first from the flow and interaction of crystals in a fluid flow and the subsequent orientation of the same rigid particles according to the contacts and the stress regime in a highly crystallized magma (Figures 5.7a,b).

5.4.2. Experiments on Contamination

One of the most outstanding criteria for identifying a process of assimilation is the presence of the peritectic phase Crd and/or Grt, which is formed by fluid-absent (dehydration) partial melting of pelitic metasediments, in a non-anatectic granodiorite or monzogranite. A proof that Crd is not in equilibrium is that such Ca-rich granite magma composition is supplied by experiments with Crd-bearing monzogranites, as these failed to reproduce the Crd-bearing assemblage observed in nature (García-Moreno et al., 2017). These experiments were performed using a synthetic glass with the composition of a Crd-bearing peraluminous monzogranite of the Iberian Massif. This is the Cabeza de Araya granite, whose composition is taken as representative of the so-called “mixed granites” (Capdevila et al., 1973), characterized by sharing features of typical anatectic granites (S-type) and Bt-granodiorites (I-type). Crd-bearing monzogranites appear in the Variscan belt of Iberia as isolated intrusions or as large irregular domains inside calc-alkaline granodiorite batholiths. The origin of these “atypical” granitic series has attracted much attention from petrologists over decades. We contend on the basis of geochemical, geological, and experimental grounds that they are the products of crustal contamination by pelitic and semipelitic host rocks. In the case of the Cabeza de Araya intrusion (Corretgé, 1971), the Crd-bearing monzogranites are located at the margins of the pluton. These represent the less evolved rocks that gradually transition into the central parts composed of two-mica granites and aplitic leucogranites. The emplacement age of the Cabeza de Araya granites obtained by SHRIMP lies between 308 ± 1.5 Ma and 305 ± 2 Ma for the different facies that make up the batholith (Rubio-Ordóñez et al., 2016).

Large prismatic crystals (1 to 4 cm) of Crd are the most distinguishing feature of these “mixed” granites. The presence of Crd in this kind of granite has been interpreted as the result of a peritectic reaction in the local domain of the xenoliths after wall-rock assimilation (García-Moreno et al., 2017). Interestingly, the outer zone of the pluton, in contact with the pelitic metasedimentary host, is richer in Crd. The abundance of mafic microgranular enclaves (autoliths) and xenoliths is also greater in the margin zones compared to the inner parts. The inferences from field relations were tested with varied experimental designs using that and similar compositions.

Experimental approaches to test contamination processes are rooted in field and geochemical relationships in large composite batholiths, which point to physical and chemical interactions between the intruding magmas and its host rocks during ascent and emplacement (e.g., Beard et al., 2005; Díaz-Alvarado et al., 2011; Erdmann et al., 2007; London et al., 2012). Different experimental procedures and strategies have led to relevant conclusions about diffusion and reactions between both subsystems.

Selective Assimilation Experiments

Experimental simulations in granodioritic and monzogranitic systems have shown that Crd or Grt do not precipitate during crystallization sequences, even when synthetic starting materials representing the whole composition of Crd- or Grt-bearing granitic rocks are used (Díaz-Alvarado, 2017; García-Moreno et al., 2017). The addition of aluminous phases to experimental capsules simulates the usual presence of And-, Sill- or/and Crd-rich restites in the migmatitic contact zones of intrusive bodies (Acosta-Vigil et al., 2002; Díaz-Alvarado et al., 2011). Local domains are observed around xenocrysts in doped experiments, resembling reactive zones of high Al activity in melts around crystals or along layered contacts (Acosta-Vigil et al., 2002; Díaz-Alvarado et al., 2011; García-Moreno et al., 2017), but far from the conditions expected for the massive crystallization of large euhedral diagnostic phases such as Kfs and Grt or Crd. The dissolution of exotic phases is governed by the mineral reaction rates and diffusion through the melt, besides other conditions such as H_2O content and convection (Acosta-Vigil et al., 2002, 2006). Nevertheless, the abovementioned experiments show the resilience of exotic xenocrysts in the intrusive magmas and the presence of local reactive domains.

Layered Experiments

Reaction at the interface between metasedimentary rocks and granitic melt (granodioritic or haplogranitic depending on the experimental study) indicate that homogenization took place for particular components such as K, Na, and H_2O between partial melts at both sides of the interface (Díaz-Alvarado, 2017; Erdmann et al., 2007; London et al., 2012). The melt percentage increases in the pelitic system as it shifts to a more haplogranitic composition (Erdmann, London op cit.). Two-layer experiments represent static situations, being the crystallization of diagnostic phases restricted to a narrow zone close to contact (Erdmann et al., 2007; London et al., 2012). However, the application of these results to the dynamic scenario of an ascent conduit, in which the narrow zone of contaminated magma is continuously removed by flow. Contamination can be effective for large volumes of magma feeding an upper reservoir or pluton. Contaminated granites can occupy large areas of zoned plutons. The process can stop with time as the later magma pulses use the core of conduits and prevent contamination. This, combined with increasing fractionation in conduits by crystallization in a TBL (see above), can plausibly explain many zoned plutons in which the most contaminated and most mafic granites are disposed of at the outer rims, and the less contaminated and more felsic types are disposed of at the core.

Bulk-Assimilation Experiments

Bulk assimilation (Beard et al., 2005) has been reproduced experimentally by introduction of pelitic fragments into a granodiorite powder (Figure 5.8) (Díaz-Alvarado et al., 2011), with significant implications for the linkage of this assimilation mechanism with the geochemical and mineralogical changes observed in large batholiths (Díaz-Alvarado et al., 2011; Saito et al., 2007). Partially

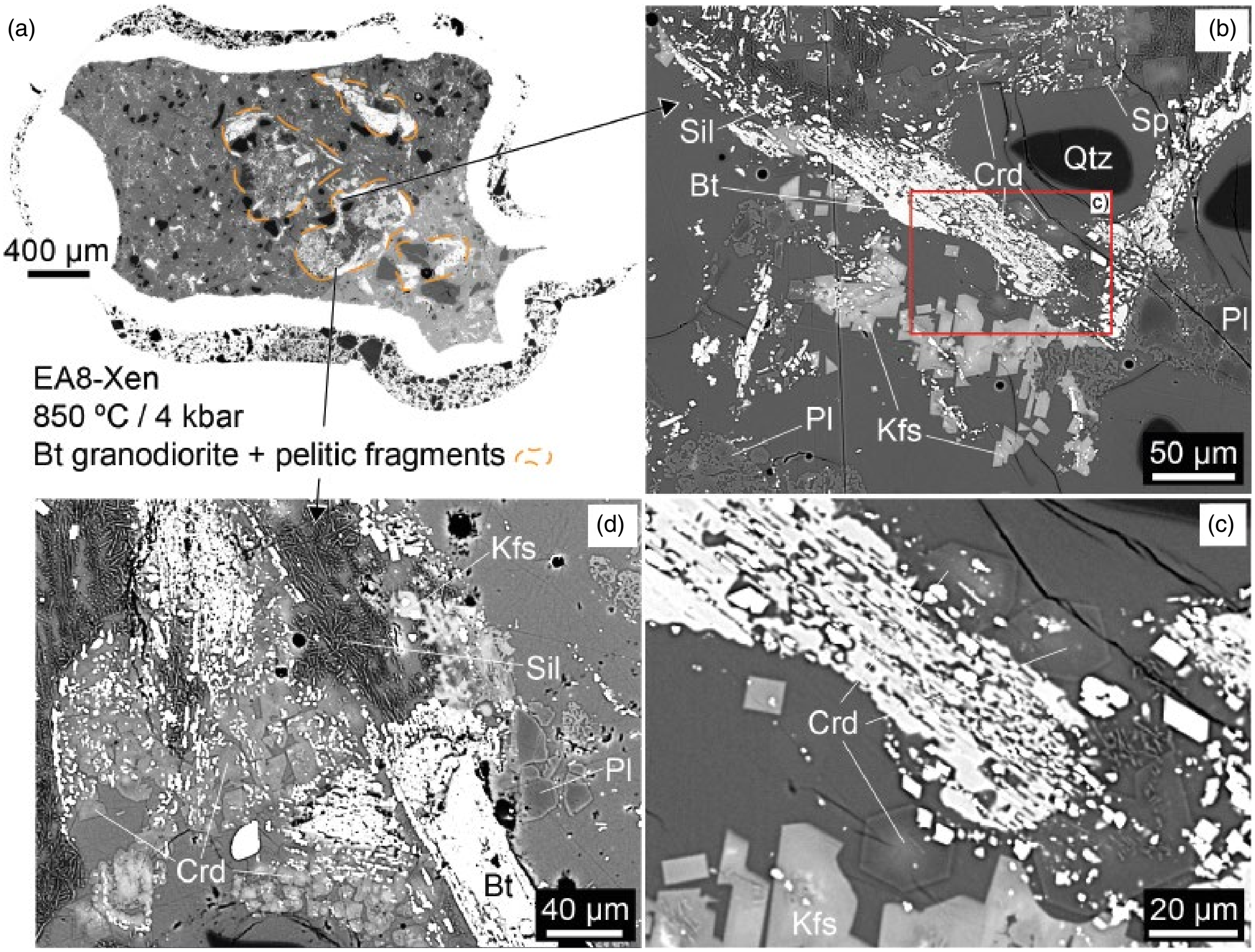

Figure 5.8 Electronic compositional images (backscattered electrons) of experimental run products simulating reaction between a pelitic xenolith and a granodiorite liquid, after Díaz–Alvarado et al. (2011). (a) Section of the whole capsule showing the remnants of partially molten and dismembered xenoliths. (b), (c), and (d) Details of the same run product showing the formation of euhedral Crd and Kfs as peritectic phases. Source: J. Díaz–Alvarado.

disintegrated xenoliths are still recognizable in the experimental runs (Figure 5.8). Partial melts inside and far from the xenolith domain still have important compositional differences (Al, Mg#) except for the alkalis, expelled from the xenoliths toward the granodioritic host, with the consequent enrichment in K and the early crystallization of Kfs, denoting a sort of mixing between the granodioritic and the xenolith-derived melts (e.g., Díaz-Alvarado, 2017; Masotta et al., 2018). As in the layered experiments, euhedral Crd and Kfs are crystallized along the reactive xenolith area (Díaz-Alvarado et al., 2011). A dynamic scenario, as mentioned above, may contribute to disaggregation of xenoliths, leading to total digestion and dissemination of minerals within the intruding granite. Xenocrystic Pl, Bt, or Qz are camouflaged in the contaminated magma, the euhedral Crd (Figure 5.8) remaining the only diagnostic mineral of the bulk assimilation, as described in natural examples (Figure 5.6). However, a rapid segregation of interstitial melts in the crustal xenoliths may inhibit mineral–melt equilibrium and prompt the zonation of residual minerals (Masotta et al., 2018).

Although a significant percentage of the assimilated material gained by the contaminated magma is unrecognizable, it is possible to assess the extent of assimilation by measuring the abundance of Crd in the contaminated granites (Díaz-Alvarado et al., 2011). The results show that the assimilated material is approximately five times the proportion of Crd. This figure depends on the amount of pelitic components (Al, Fe, Mg) of the contaminant; the more pelitic components there are, the less is the fraction of contaminant in the final hybrid rock. Mass balance calculations and other approximations through Sr–Nd isotopic ratios agree with these results (Clarke et al., 2004; Díaz-Alvarado et al., 2011; Erdmann et al., 2007; Fowler et al., 2001; Ugidos & Recio, 1993).

Batholithic examples, such as the Gredos batholith (Iberian Massif), show that hybrid magmas may contain between 50% and 10% of assimilated material, depending on the proximity to the metasedimentary host, which fits well with the volume of Crd and Kfs estimated in the contaminated rocks (Díaz-Alvarado et al., 2011). The layered structure of the batholith and the coherent and tectonically induced viscous deformation of intrusive magmas and migmatitic host rocks favored the increase in contact surfaces between both subsystems, which has been proved essential for the efficacy of bulk assimilation. Besides, the sequential character of the emplacement process involves a long-lasting high-grade area in the host crust. The similar crystallization ages obtained from intrusive magmas and anatectic leucogranites (Díaz-Alvarado et al., 2013) formed and locally segregated in the migmatitic host rocks imply that both the intrusive magmas and partially melted metasediments sustain a similar, albeit changing, rheologic state during their heterogeneous and intense interaction, triggering the geochemical and mineralogical changes that are characteristic of the assimilation process and similar to the experimentally proved conditions that favor magma mixing (Laumonier et al., 2014a, b).

5.5. CONCLUDING REMARKS

Differentiation and contamination are common processes in continental environments. To a large extent, the fractionated character of the continental crust with respect to the underlying mantle is, overall, the result of a protracted process of combined differentiation and contamination. The latter is particularly relevant if the available contaminants are terrigenous metasediments, as these represent substantial geochemical fractionation imposed by surface weathering. In most cases, isotopic relations are good indicators to distinguish between fractionation (closed systems) and contamination (open systems). However, understanding the mechanisms that cause magmas to fractionate and/or to assimilate portions of country rocks requires a deep knowledge of complex magma systems. Two approaches, experimental and geological, have been used in this chapter to address the problem.

Field evidences from the Gredos batholith (Central Spain) support the hypothesis that assimilation of pelitic metasediments caused the formation of Crd in local domains of the intrusive granodiorite (calc-alkaline) magmas. Partial digestion of pelitic migmatites is common at the contacts, where Crd formed by peritectic melting reactions in the pelites in the course of xenolith disaggregation. These reactions are confirmed by means of laboratory experiments using magma–pelite heterogeneous systems under conditions of granodiorite emplacement of 850 °C and 4 kbar. Experiments reported that Crd is not reproduced otherwise by crystallization of a glass with the composition of a Crd-bearing monzogranite. These results reinforce the idea that Crd in non-anatectic monzogranites and granodiorites is in equilibrium within the local subsystem created by assimilation of country-rock xenoliths. The existence of a thick (>5 km) sequence of Neoproterozoic pelites and greywackes, as the regional host of Variscan batholiths, is the reason for the conspicuous presence of Crd in varied types of granites, from tonalites to monzogranites. For the same reason, anatectic leucogranites with primordial (peritectic) Crd are abundant in Iberia. Granites emplaced into older igneous, either volcanic or plutonic, host rocks are less prone to undergo contamination. This is the general case of the Cordilleran granite batholiths. In sum, the reactiveness of the host is a fundamental factor determining the feasibility of assimilation and contamination. Pelites are the most reactive systems, and the formation of Crd in non-anatectic granites is diagnostic in such cases.

In regard to differentiation, our experiments in a thermal gradient or TBL are conclusive about the role of dissolved water in the magma in the separation of crystal and liquid, a necessary process to account for the origin of rock series that are linked to a parental magma by fractionation. Experiments with a natural andesite in horizontal capsules, which are not affected by gravitational processes, produce an interesting phenomenon called *splitting* that may help to understand geological and geochemical observations. Basically, a water-bearing magma crystallizing in a TBL is broken into two subsystems with a sharp boundary between them. One subsystem is formed by a crystal-rich aggregate, whose composition resembles the fine-grained microgranular enclaves that commonly appear in calc-alkaline batholiths, and the other subsystem is a fractionated liquid. The latter has a composition that resembles that of the calc-alkaline granodiorites and granites. As enclaves are mostly autoliths, they represent magma fragments with high crystal content that are dragged from the walls of ascent conduits. In this sense, we contend that conduits may have a primordial role in producing magmatic differentiation in the crust. We found that a plausible cause for liquid expulsion from the partially crystallized mush at the TBL is boiling and vesiculation, as water saturation is necessarily encountered at any point of the solidification front generated in a TBL. Vertical experiments, in which the thermal gradient and gravity acceleration vector are parallel, reveal that crystal settling can be impeded by solid particle interactions, but that gravitational collapse of magma mushes from the top of the solidification front is possible.

ACKNOWLEDGMENTS

This work is supported by the State Agency for Research (AEI) (Project: PGC2018–096534–B–I00). C.R. is grateful for her postdoctoral contract from the University of Huelva (Grant: Estrategia de Politíca Científica UHU 2016/2017).

REFERENCES

Acosta-Vigil, A., London, D., Dewers, T. A., & Morgan, G. B. VI (2002). Dissolution of corundum and andalusite in H_2O-saturated haplogranitic melts at 800 °C and 200 MPa: Constraints on diffusivities and the generation of peraluminous melts. *Journal of Petrology*, *43*, 1885–1908.

Acosta-Vigil, A., London, D., Morgan, G. B. VI, & Dewers, T. A. (2006). Dissolution of quartz, albite, and orthoclase in H_2O-saturated haplogranitic melt at 800 °C and 200 MPa: diffusive transport properties of granitic melts at crustal anatectic conditions. *Journal of Petrology*, *47*, 231–254.

Allègre, C. J., & Ben Othman, D. (1980). Nd-Sr isotopic relationship in granitoid rocks and continental crust development: a chemical approach to orogenesis. *Nature*, *286*, 335–341.

Bachmann, O., & Bergantz, G. W. (2004). On the origin of crystal-poor rhyolites: Extracted from batholitic crystal mushes. *Journal of Petrology*, *45*, 1565–1582.

Bachmann, O., & Huber, C. (2016). Silicic magma reservoirs in the Earth's crust, *American Mineralogist*, *101*(11), 2377–2404. doi:10.2138/am-2016-5675.

Bachmann, O., & Huber, C. (2018). The inner workings of crustal distillation columns; the physical mechanisms and rates controlling phase separation in silicic magma reservoirs. *Journal of Petrology*, *60*(1), 3–18. doi:10.1093/petrology/egy103.

Bea, F., Fershtater, G. B., Montero, P., Smirnov, V. N., & Molina, J. F. (2005). Deformation-driven differentiation of granitic magma: The Stepninsk pluton of the Uralides, Russia, *Lithos*, *81*(1–4), 209–233.

Beard, J. S., Ragland, P. C., & Crawford, M. L. (2005). Reactive bulk assimilation: A model for crust-mantle mixing in silicic magmas. *Geology*, *33*(8), 681–684.

Biot, M. A. (1961). Theory of folding of stratified viscoelastic media and its implications in tectonics and orogenesis. *GSA Bulletin*, *72*(11), 1595–1620. doi:10.1130/0016-7606(1961)72(1595:tofosv).0.co;2.

Bohrson, W. A., & Spera, F. J. (2001), Energy-constrained open-system magmatic processes II: Application of energy-constrained assimilation–fractional crystallization (EC-AFC) model to magmatic systems. *Journal of Petrology*, *42*(5), 1019–1041. doi:10.1093/petrology/42.5.1019.

Bowen, N. L. (1922). The behaviour of inclusions in igneous magmas. *Journal of Geology*, *30*, 513–570.

Bowen, N. L. (1928). *The evolution of igneous rocks*. Princeton, New Jersey USA.

Brandeis, G., & Jaupart, C. (1986). On the interaction between convection and crystallization in cooling magma chambers, *Earth and Planetary Science Letters*, *77*, 345–361.

Burgisser, A., & Bergantz, G. W. (2011). A rapid mechanism to remobilize and homogenize highly crystalline magma bodies. *Nature*, *471*, 212–217.

Burnham, C. W. (1979). The importance of volatile constituents. In H. S. J. Yoder (Ed.), *The evolution of the igneous rocks* (pp. 439–482). Princeton University Press, Princeton.

Capdevila, R., Corretgé, L. G., & Floor, P. (1973). Les granitoides varisquies de la Mesete Iberique. *Bulletin de la Société Géologique de France*, *7-15*, 209–228.

Castro, A. (2013). Tonalite-granodiorite suites as cotectic systems: A review of experimental studies with applications to granitoid petrogenesis. *Earth-Science Reviews*, *124*, 68–95. doi:10.1016/j.earscirev.2013.05.006.

Castro, A. (2019). The dual origin of I-type granites: the contribution from experiments. *Geological Society, London, Special Publications*, *491*, SP491-2018–2110. doi:10.1144/SP491-2018-110.

Castro, A., Rodríguez, C., Fernández, C., Pereira, M. F., & Aragón, E. (2020). Secular variations of magma source compositions in the North Patagonian batholith from Jurassic to Tertiary. Is mélange melting involved? Geosphere *(in press)*.

Castro, A., Moreno-Ventas, I., Fernández, C., Vujovich, G., Gallastegui, G., Heredia, N., et al. (2011). Petrology and SHRIMP U-Pb zircon geochronology of Cordilleran granitoids of the Bariloche area, Argentina. *Journal of South American Earth Sciences.* doi:10.1016/j.jsames.2011.03.011.

Chapple, W. M. (1968). A mathematical theory of finite–amplitude rock–folding. *GSA Bulletin*, *79*(1), 47–68. doi:10.1130/0016-7606(1968)79(47:AMTOFR).0.CO;2.

Clarke, D. B., MacDonald, M. A., & Erdmann, S. (2004). Chemical variation in Al_2O_3-CaO-Na_2O-K_2O space: Controls on the peraluminosity of the South Mountain Batholith. *Canadian Journal of Earth Sciences*, *41*(7), 785–798.

Corretgé, L. G. (1971). Estudio petrológico del batolito de Cabeza de Araya (Cáceres). *Tesis Doctoral Univ. de Salamanca. P453*.

DePaolo, D. J. (1981). Trace element and isotopic effects of combined wallrock assimilation and fractional crystallization. *Earth and Planetary Science Letters*, *53*(2), 189–202. doi:10.1016/0012-821X(81)90153-9.

Díaz-Alvarado, J., Fernández, C., Castro, A., & Moreno-Ventas, I. (2013). SHRIMP U–Pb zircon geochronology and thermal modeling of multilayer granitoid intrusions: Implications for the building and thermal evolution of the Central System batholith, Iberian Massif, Spain. *Lithos*, *175–176*(0), 104–123. doi:http://dx.doi.org/10.1016/j.lithos.2013.05.006.

Díaz-Alvarado, J. (2017). Experimental early crystallization of K-feldspar in granitic systems. Implications on the origin of magmatic fabrics in granitic rocks. *Gologica Acta*, *15*, 261–281.

Díaz-Alvarado, J., Castro, A., Fernández, C., & Moreno-Ventas, I. (2011). Assessing bulk assimilation in cordierite-bearing granitoids from the central system batholith, Spain; experimental, geochemical and geochronological constraints, *Journal of Petrology*, *52*(2), 223–256. doi:10.1093/petrology/egq078.

Díaz-Alvarado, J., Fernández, C., Díaz-Azpiroz, M., Castro, A., & Moreno-Ventas, I. (2012). Fabric evidence for granodiorite emplacement with extensional shear zones in the Variscan Gredos massif (Spanish Central System). *Journal of Structural Geology*, *42*, 74–90. doi:https://doi.org/10.1016/j.jsg.2012.06.012.

Erdmann, S., London, D., Morgan Vi, G. B., & Clarke, D. B. (2007). The contamination of granitic magma by metasedimentary country-rock material: An experimental study, *Canadian Mineralogist*, *45*(1), 43–61.

Fernández, C., & Castro, A. (2018). Mechanical and structural consequences of magma differentiation at ascent conduits: A possible origin for some mafic microgranular enclaves in granites, *Lithos*, *320–321*, 49–61. doi:10.1016/j.lithos.2018.09.004.

Flanagan, F. J. (1967). U.S. Geological Survey silicate rock standards. *Geochimica et Cosmochimica Acta*, *31*, 289–308.

Fowler, M. B., Henney, P. J., Darbyshire, D. P. F., & Greenwood, P. B. (2001). Petrogenesis of high Ba-Sr granites: The Rogart pluton, Sutherland. *Journal of the Geological Society*, *158*(3), 521–534.

García-Moreno, O., Corretgé, L. G., Holtz, F., García-Arias, M., & Rodríguez, C. (2017). Phase relations in the Cabeza de Araya cordierite monzogranite, Iberian Massif: Implications for the formation of cordierite in a crystal mush, *Geologica Acta*, *15*(4), 337–359, doi: 10.1344/GeologicaActa2017.15.4.6.

Gelman, S. E., Deering, C. D., Bachmann, O., Huber, C., & Gutiérrez, F. J. (2014). Identifying the crystal graveyards remaining after large silicic eruptions, *Earth and Planetary Science Letters*, *403*, 299–306, doi:http://dx.doi.org/10.1016/j.epsl.2014.07.005.

Glazner, A. F. (2007). Thermal limitations on incorporation of wall rock into magma, *Geology*, *35*(4), 319–322. doi:10.1130/G23134A.1.

Glazner, A. F. (2014). Magmatic life at low Reynolds number. *Geology*, *42*(11), 935–938. doi:10.1130/g36078.1.

Gogoi, B., & A. Saikia (2018). Role of viscous folding in magma mixing, *Chemical Geology*, *501*, 26–34. doi:https://doi.org/10.1016/j.chemgeo.2018.09.035.

Hawkesworth, C. J., & Kemp, A. I. S. (2006). The differentiation and rates of generation of the continental crust, *Chemical Geology*, *226*(3–4), 134–143.

Hopgood, A. M. (1999). *Determination of Structural Successions in Migmatites and Gneisses* (364 pp.). Springer Science.

Huang, F., Lundstrom, C. C., Glessner, J., Ianno, A., Boudreau, A., Li, J., et al. (2009). Chemical and isotopic fractionation of wet andesite in a temperature gradient: Experiments and models suggesting a new mechanism of magma differentiation, *Geochimica et Cosmochimica Acta*, *73*(3), 729–749.

Humphreys, M. C. S., & Holness, M. B. (2010). Melt-rich segregations in the Skaergaard Marginal Border Series: Tearing of a vertical silicate mush, *Lithos*, *119*(3-4), 181–192. doi:10.1016/j.lithos.2010.06.006.

Johnson, A. M., & R. C. Fletcher (1994), *Folding of Viscous Layers*. Columbia University Press, New York.

Kemp, A. I. S., Hawkesworth, C. J., Foster, G. L., Paterson, B. A., Woodhead, J. D., Hergt, J. M., et al. (2007). Magmatic and crustal differentiation history of granitic rocks from Hf-O isotopes in zircon, *Science*, *315*(5814), 980–983.

Lake, E. T. (2013). Crystallization and saturation front propagation in silicic magma chambers, *Earth and Planetary Science Letters*, *383*(0), 182–193, doi:http://dx.doi.org/10.1016/j.epsl.2013.09.039.

Langmuir, C. H. (1989), Geochemical consequences of In situ crystallization, *Nature*, *340*, 199–205.

Laumonier, M., Scaillet, B., Pichavant, M., Champallier, R., Andujar, J., & Arbaret, L. (2014a). On the conditions of magma mixing and its bearing on andesite production in the crust. *Nature Communications*, *5*, 5607.

Laumonier, M., Scaillet, B., Arbaret, L., & R. Champallier (2014b), Experimental simulation of magma mixing at high pressure. *Lithos*, *196*, 281–300.

Lee, C. T. A., Cheng, X., & Horodyskyj, U. (2006). The development and refinement of continental arcs by primary basaltic magmatism, garnet pyroxenite accumulation, basaltic recharge and delamination: Insights from the Sierra Nevada, California, *Contributions to Mineralogy and Petrology*, *151*(2), 222–242.

Lee, C. T. A., & Morton, D. M. (2015), High silica granites: Terminal porosity and crystal settling in shallow magma chambers. *Earth and Planetary Science Letters*, *409*, 23–31.

Lipman, P. W. (1988). Evolution of silicic magma in the upper crust: the mid-Tertiary Latir volcanic field and its cogenetic granitic batholith, northern New Mexico, USA, *Transactions of the Royal Society of Edinburgh, Earth Sciences*, *79*, 265–288.

London, D., Morgan, G. B., & Acosta-Vigil, A. (2012), Experimental simulations of anatexis and assimilation involving metapelite and granitic melt, *Lithos*, *153*, 292–307, doi:https://doi.org/10.1016/j.lithos.2012.04.006.

Marsh, B. D. (1988). Crystal capture, sorting, and retention in convecting magma, *Geological Society of America Bulletin*, *100*, 1720–1737.

Marsh, B. D. (2002). On bimodal differentiation by solidification front instability in basaltic magmas, part 1: Basic mechanics. *Geochimica et Cosmochimica Acta*, *66*, 2211–2229.

Masotta, M., Freda, C., & Gaeta, M. (2012). Origin of crystal-poor, differentiated magmas: Insights from thermal gradient experiments, *Contributions to Mineralogy and Petrology*, *163*(1), 49–65. doi:10.1007/s00410-011-0658-8.

Masotta, M., Mollo, S., Gaeta, M., & Freda, C. (2016), Melt extraction in mush zones: The case of crystal-rich enclaves at the Sabatini Volcanic District (central Italy), *Lithos*, *248–251*, 288–292. doi:http://dx.doi.org/10.1016/j.lithos.2016.01.030.

McCulloch, M. T., & Wasserburg, G. J. (1978). Sm-Nd and Rb-Sr chronology of continental crust formation. *Science*, *200*, 1003–1011.

McKenzie, D. (1984). The generation and compaction of partially molten rock. *Journal of Petrology*, *25*(3), 713–765, doi:10.1093/petrology/25.3.713.

Michioka, H., & Sumita, I. (2005). Rayleigh-Taylor instability of a particle packed viscous fluid: Implications for a solidifying magma, *Geophysical Research Letters*, *32*, L03309. doi:10.1029/2004GL021827.

Namur, O., M. C. S. Humphreys, & M. B. Holness (2013), Lateral Reactive Infiltration in a Vertical Gabbroic Crystal Mush, Skaergaard Intrusion, East Greenland, *Journal of Petrology*, *54*(5), 985–1016, doi:10.1093/petrology/egt003.

Pankhurst, R. J., Weaver, S. D., Herve, F., & Larrondo, P. (1999). Mesozoic-Cenozoic evolution of the North Patagonian Batholith in Aysen, southern Chile, *Journal of the Geological Society*, *156*(4), 673–694.

Paterson, S. R., Ardill, K., Vernon, R., & Žák, J. (2018). A review of mesoscopic magmatic structures and their potential for evaluating the hypersolidus evolution of intrusive complexes. *Journal of Structural Geology*, *125*, 134–147. doi:https://doi.org/10.1016/j.jsg.2018.04.022.

Paterson, S., V. Memeti, R. Mundil, & J. Žák (2016), Repeated, multiscale, magmatic erosion and recycling in an upper-crustal pluton: Implications for magma chamber dynamics and magma volume estimates, *American Mineralogist*, *101*(10), 2176–2198, doi:10.2138/am-2016-5576.

Paterson, S. R., Fowler, T. K., Schmidt, K. L., Yoshinobu, A. S., Yuan, E. S., & Miller, R. B. (1998). Interpreting magmatic fabric patterns in plutons, *Lithos*, *44*(1), 53–82, doi:https://doi.org/10.1016/S0024-4937(98)00022-X.

Pistone, M., Arzilli, F., Dobson, K. J., Cordonnier, B., Reusser, E., Ulmer, P., et al. (2015). Gas-driven filter pressing in magmas: Insights into in-situ melt segregation from crystal mushes, *Geology*, *43*(8), 699–702, doi:10.1130/G36766.1.

Ramberg, H. (1961), Contact strain and folding instability of a multilayered body under compression. *Geologische Rundshau* *51*, 405–439.

Rodríguez, C., & Castro, A. (2017). Silicic magma differentiation in ascent conduits. Experimental constraints, *Lithos*, *272–273*, 261–277, doi:http://dx.doi.org/10.1016/j.lithos.2016.12.017.

Rodríguez, C., & Castro, A. (2019), Origins of mafic microgranular enclaves and enclave swarms in granites: Field and geochemical relations, *Geological Society of America Bulletin*, *131*(3/4), 635–660. doi:https://doi.org/10.1130/B32028.1.

Rubio-Ordóñez, A., García-Moreno, O., Montero, P., & Bea, F. (2016). Nuevas aportaciones a la datación cronológica de los granitos de Cabeza de Araya, (Cáceres). *Geotemas*, *16*(2), 43–46.

Saito, S., Arima, M., & Nakajima, T. (2007). Hybridization of a shallow 'I-type' granitoid pluton and its host migmatite by magma-chamber wall collapse: The Tokuwa pluton, Central Japan, *Journal of Petrology*, *48*(1), 79–111.

Scarrow, J. H., Molina, J. F., Bea, F., & Montero, P. (2009). Within-plate calc-alkaline rocks: Insights from alkaline mafic magma–peraluminous crustal melt hybrid appinites of the Central Iberian Variscan continental collision. *Lithos*, *110*, 50–64.

Shibano, Y., Namiki, A., & Sumita, I. (2012), Experiments on upward migration of a liquid layer in a granular medium: Implications for a crystalline magma chamber, *Geochemistry, Geophysics, Geosystems*, *13*, Q03007. doi:10.1029/2011GC003994.

Shibano, Y., Sumita, I., & Namiki, A. (2013), A laboratory model for melting erosion of a magma chamber roof and the generation of a rhythmic layering. *Journal of Geophysical Research: Solid Earth*, *118*, 4101–4116. doi:10.1002/jgrb.50295.

Thompson, A. B., Matile, L., & Ulmer, P. (2002). Some thermal constraints on crustal assimilation during fractionation of hydrous, mantle-derived magmas with examples from Central Alpine Batholiths. *Journal of Petrology*, *43*(3), 403–422.

Ugidos, J. M., & Recio, C. (1993). Origin of cordierite-bearing granites by assimilation in the Central Iberian Massif (CIM), Spain. *Chemical Geology*, *103*(1–4), 27–43.

Vigneresse, J. L., Barbey, P., & Cuney, M. (1996). Rheological transitions during partial melting and crystallization with application to felsic magma segregation and transfer. *Journal of Petrology*, *37*, 1579–1600.

Whitney, D. L., & Evans, B. W. (2010), Abbreviations for names of rock-forming minerals. *American Mineralogist*, *95*(1), 185–187. doi:10.2138/am.2010.3371.

Žák, J., & Paterson, S. R. (2010). Magmatic erosion of the solidification front during reintrusion: The eastern margin of the Tuolumne batholith, Sierra Nevada, California. *International Journal of Earth Sciences*, *99*(4), 801–812. doi:10.1007/s00531-009-0423-7.

6

Crystal and Volatile Controls on the Mixing and Mingling of Magmas

Paul A. Jarvis[1], Mattia Pistone[2,3], Alexia Secretan[2], Jon D. Blundy[4], Katharine V. Cashman[4], Heidy M. Mader[4], and Lukas P. Baumgartner[2]

ABSTRACT

The mixing and mingling of magmas of different compositions are important geological processes. They produce various distinctive textures and geochemical signals in both plutonic and volcanic rocks and have implications for eruption triggering. Both processes are widely studied, with prior work focusing on field and textural observations, geochemical analysis of samples, theoretical and numerical modeling, and experiments. However, despite the vast amount of existing literature, there remain numerous unresolved questions. In particular, how does the presence of crystals and exsolved volatiles control the dynamics of mixing and mingling? Furthermore, to what extent can this dependence be parameterized through the effect of crystallinity and vesicularity on bulk magma properties such as viscosity and density? In this contribution, we review the state of the art for models of mixing and mingling processes and how they have been informed by field, analytical, experimental, and numerical investigations. We then show how analytical observations of mixed and mingled lavas from four volcanoes (Chaos Crags, Lassen Peak, Mt. Unzen, and Soufrière Hills) have been used to infer a conceptual model for mixing and mingling dynamics in magma storage regions. Finally, we review recent advances in incorporating multi-phase effects in numerical modeling of mixing and mingling, and highlight the challenges associated with bringing together empirical conceptual models and theoretically based numerical simulations.

6.1. INTRODUCTION: MAGMA MIXING AND MINGLING AND VOLCANIC PLUMBING SYSTEMS

It is now widely accepted that magmas of different compositions can mix and mingle together (Blake et al., 1965; Eichelberger, 1980; Morgavi et al., 2019; Perugini & Poli, 2012; Snyder, 1997; Sparks & Marshall, 1986, Wiebe, 1987; Wilcox, 1999). Textural consequences of mingling have long been observed (Judd, 1893; Phillips, 1880), although the earliest observations were not necessarily interpreted correctly (Wilcox, 1999), with heterogeneities interpreted as originating from metasomatism (Fenner, 1926) or solid-state diffusion (Nockolds, 1933). Advancements in geochemical analysis combined with an understanding of phase equilibria led to acknowledgment of mixing and mingling as key processes, alongside crystal fractionation, in producing the compositional diversity of igneous rocks (Vogel et al., 2008). In addition, interaction between magmas became recognized as a potential trigger for volcanic eruptions (Sparks et al., 1977). Evidently, understanding mixing and mingling processes is crucial for deciphering the evolution of igneous rocks and the eruptive dynamics of volcanoes.

---

[1] *Department of Earth Sciences, University of Geneva, Geneva, Switzerland*

[2] *Institute of Earth Sciences, University of Lausanne, Lausanne, Switzerland*

[3] *Department of Geology, University of Georgia, Athens Georgia, USA*

[4] *School of Earth Sciences, University of Bristol, Bristol, United Kingdom*

Crustal Magmatic System Evolution: Anatomy, Architecture, and Physico-Chemical Processes, Geophysical Monograph 264, First Edition.
Edited by Matteo Masotta, Christoph Beier, and Silvio Mollo.

DOI: 10.1002/9781119564485.ch6

Previous work has sometimes been flexible with regard to precise definitions of the terms "mixing" and "mingling." We here define mixing to be chemical interaction between two magmas that produces a composition intermediate between the original end-members (Bunsen, 1851). Chemical mixing proceeds by chemical diffusion (Lesher, 1994; Watson, 1982) and, if allowed to complete, leads to hybridization and homogeneous products (Humphreys et al., 2010). By contrast, mingling is the physical interaction of the two magmas, such as through convective stirring (e.g., Oldenburg et al., 1989) or chaotic advection (e.g., Morgavi et al., 2013; Perugini & Poli, 2004), and creates compositional heterogeneities. Mixing and mingling often occur together, with mixing acting to "smooth out" the compositional heterogeneities produced by mingling. However, mixing and mingling can be inhibited by large contrasts in magma viscosity (Frost & Mahood, 1987; Sato & Sato, 2009; Sparks & Marshall, 1986) and density (Blake & Fink, 1987; Grasset & Albarade, 1994; Koyaguchi & Blake, 1989). If homogenization is sufficiently slow, then cooling and/or degassing of the system can lead to crystallization and preservation of a variety of textural and chemical signatures (D'Lemos, 1987; Morgavi et al., 2016) reflecting the temperatures, compositions, crystallinities, and relative proportions of the initial magmas (Bacon, 1986; Eichelberger, 1980; Sparks & Marshall, 1986).

Mixing and mingling models typically assume injection of a hotter, mafic magma into a cooler, more felsic host (Campbell & Turner, 1989; Clynne, 1999). This can be followed by later intrusion (or back-injection) of veins and pipes of remobilized felsic material into the mafic component (Elwell et al., 1960, 1962; Wiebe, 1992, 1994; 1996; Wiebe & Collins, 1998; Wiebe et al., 2002; Wiebe & Hawkins, 2015). Such injections have been modeled experimentally (Campbell & Turner, 1986; Huppert et al., 1984, 1986; Snyder & Tait, 1995; Perugini & Poli, 2005), theoretically (Sparks & Marshall, 1986) and numerically (Andrews & Manga, 2014; Montagna et al., 2015). Furthermore, heat and volatile transfer from the mafic to the felsic end-member induces physico-chemical responses in both magmas. The mafic component undergoes crystallization and degassing due to undercooling (Cashman & Blundy, 2000; Coombs et al., 2002; Eichelberger, 1980; Petrelli et al., 2018), leading to an increase in bulk viscosity (Caricchi et al., 2007; Mader et al., 2013) and potentially a decrease in density (if bubbles of the exsolved gas phase remain trapped), whereas the felsic magma partially melts due to super-heating (Pistone et al., 2017). This can create a temporal window where the bulk viscosities of the two magmas become closer, thereby facilitating mingling and mixing before continued crystallization of the mafic magma increases its viscosity. Another scenario is mixing and mingling between partially molten silicic rocks and a hot, rhyolitic injection (Bindeman & Simakin, 2014), which is important for the formation of large, eruptible magma bodies containing crystals mixed from different portions of the same magma storage system (antecrysts; Bindeman & Melnik, 2016; Francalanci et al., 2011; Ubide et al., 2014a; Seitz et al., 2018; Stelten et al., 2015). In all cases, the physico-chemical changes and their associated timescales govern the style of mixing, the resultant textures, and the eruptive potential.

6.1.1. Chemical Mixing

Chemical mixing occurs through the diffusion of different components along spatial gradients in chemical potential (Adkins, 1983) to create homogeneous products. If all components have equal diffusivities, the mixing of two chemically distinct magmas gives rise to linear trends on Harker-type variation diagrams (Harker, 1909) that can be used to constrain the end-member compositions. Nonlinear mixing trends produced by variable diffusivities among melt components, including trace elements (Nakamura & Kushiro, 1998; Perugini et al., 2008; Perugini et al., 2013), are also common and have been identified in various localities (Reid et al., 1983; Bacon, 1986; Bacon & Metz, 1984; Bateman, 1995; Cantagrel et al., 1984; Choe & Jwa, 2004; Coombs et al., 2000; Gourgaud & Maury, 1984; Janoušek et al., 2004; Kim et al., 2014; Kumar & Rino, 2006; Perugini et al., 2003; Prelević et al., 2004; Troll & Schmicke, 2002; Ruprecht et al., 2012; Weidendorfer et al., 2014). Further complexity arises from uphill diffusion in some species (e.g., Sr, Nd, Al), because diffusion is governed by gradients in chemical potential rather than concentration, and the temporal dependence of diffusivities in mixing events caused by changes in temperature and bulk composition (Bindeman & Davis, 1999; Lesher, 1994).

Evidence of mixing is preserved primarily at the microscale because the relatively slow rate of diffusion alone (Acosta-Vigil et al., 2012; Morgan et al., 2008) cannot redistribute chemical components over large spatial scales (Bindeman & Davis, 1999). Crystals, in particular, can preserve chemical records of changing storage conditions that can be associated with mixing. For instance, resorption zones and reverse zoning in plagioclase might indicate changes to more mafic melt compositions, possibly due to multiple mixing events (Hibbard, 1981; Lipman et al., 1997; Tsuchiyama, 1985). The mixing history can be determined by combining these observations with methodologies such as major-element (Rossi et al., 2019), trace-element (Humphreys et al., 2009), and isotopic analyses (Davidson et al., 2007), along with measurements from the bulk rock or other minerals. This can include timescales of mixing (Chamberlain et al., 2014;

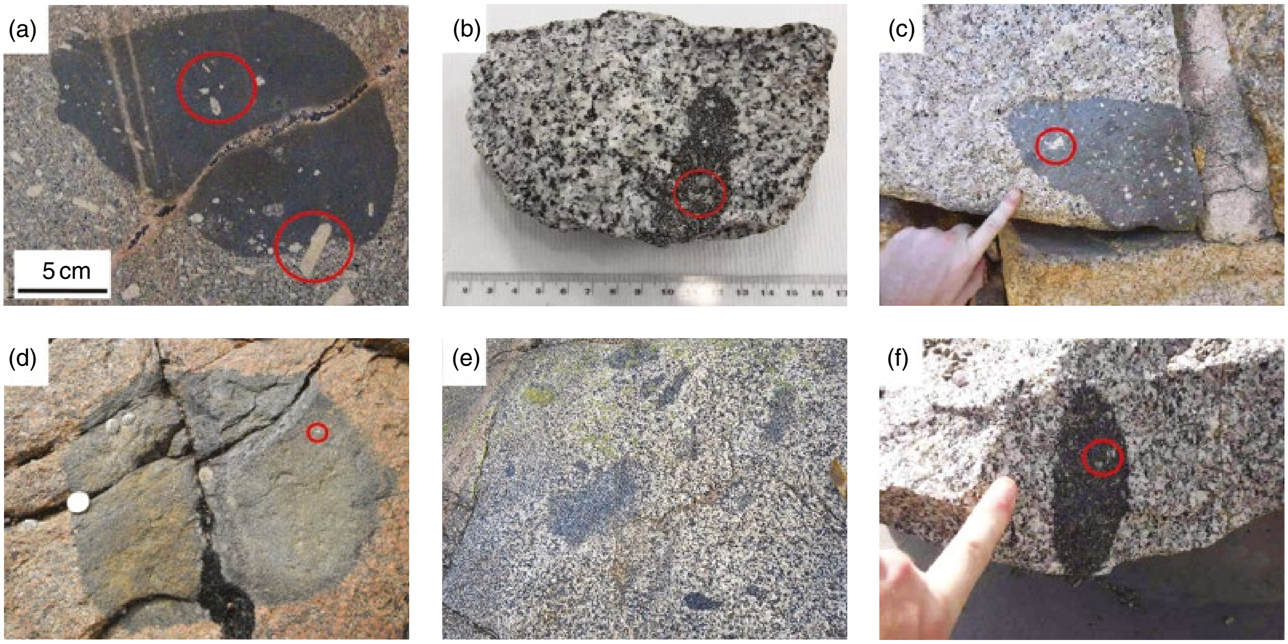

Figure 6.1 Examples of mafic enclaves. All are generally finer-grained than their hosts but contain occasional large crystals (circled in red), which are xenocrysts mechanically transferred from the host. (a) Large (≈18 cm) fine-grained enclave hosted in alkali feldspar granite from Blackenstone Quarry, Dartmoor, England. (b) High-aspect-ratio enclave from the Adamello Massif, Italy. (c) Mafic enclave in granite of stone wall at Hiroshima Castle, Japan. (d) Mafic enclave within the Cobo Granite, Guernsey. (e) Numerous enclaves in an outcrop of the Northern Igneous Complex, Guernsey. The outcrop shown is about 1 m^2. (f) Mafic enclave in a granite statue in Alexander Garden, Moscow.

Rossi et al., 2019) and ascent (Humphreys et al., 2010), temperatures and pressures of mixing (Samaniego et al., 2011), and the relative contribution of processes such as fractional crystallization (Foley et al., 2012; Ruprecht et al., 2012; Scott et al., 2013).

6.1.2. Physical Mingling

Mingling results from fluid flow, either directly due to shear between two magmas during injection, or as a consequence of buoyancy-driven convection. Although mingling cannot occur in the complete absence of mixing, if convection timescales are shorter than diffusive timescales, mingling dominates the interaction and produces heterogeneities that are preserved as mingling textures if the magma cools and consolidates before homogenization is complete. Examples include composite dikes and sills (Wiebe, 1973), intermingled layered intrusions of alternating composition (Wiebe, 1996; Wiebe, 1998), banded pumice (Clynne, 1999), and mafic enclaves (Eichelberger, 1980). Enclaves are perhaps the most widely reported mingling texture and are widespread in both plutonic (Baxter & Feeley, 2002; Blundy & Sparks, 1992; D'Lemos, 1986, 1996; Topley et al., 1990; Williams & Tobisch, 1994) and volcanic (Bacon, 1986; Browne et al., 2006a,b; Fomin & Plechov, 2012; Martin et al., 2006; Perugini et al., 2007) settings. Enclaves are produced by disaggregation of intrusions into host magmas (Andrews & Manga, 2014; Caricchi et al., 2012; Eichelberger, 1980; Hodge et al., 2012; Hodge & Jellinek, 2012; Perugini & Poli, 2005; Tepley et al., 1999; Thomas, et al., 1993; Vetere et al., 2015); Figure 6.1 illustrates the sizes, shapes, and crystallinities that can result. Enclaves often contain crystals mechanically transferred from the surrounding host magma (xenocrysts), which can be interrogated to infer conditions (e.g., temperature, crystallinity, melt, or bulk rock composition) at the time of mixing (Borisova et al., 2014; Cantagrel et al., 1984; Coombs et al., 2000; Humphreys et al., 2009; Reid et al., 1983; Ubide et al., 2014b; Wiebe, 1992).

The multi-phase nature of magma is important for mingling dynamics. Experiments have demonstrated that the presence of phenocrysts can enhance mixing (Kouchi & Sunagawa, 1983, 1985), although a crystal framework can also inhibit efficient mingling (Laumonier et al., 2014, 2015). Crystallization-induced degassing (Cashman & Blundy, 2000) of the mafic end-member due to heat and water loss to the felsic component (Pistone et al.,

2017) causes the exsolution of buoyant volatile phases that can enhance mingling (Eichelberger, 1980; Wiesmaier et al., 2015). There is also growing recognition that magma storage systems are dominated by mushy regions with melt concentrated in isolated, possibly transient, lenses (Bachmann & Huber, 2016; Cashman et al., 2017; Hildreth, 1981, 2004; Sparks et al., 2019). Despite this, many studies continue to model mingling as taking place between two crystal-free fluids in a vat (Montagna et al., 2015). Such a picture is hard to reconcile with evidence from petrological analysis (Cooper, 2017; Druitt et al., 2012; Turner & Costa, 2007) and the lack of geophysical evidence for large extended bodies of melt (Farrell et al., 2014; Miller & Smith, 1999; Pritchard et al., 2018; Sinton & Detrick, 1992). It is therefore clear that the presence of crystals and volatiles, and their effect on magma rheology (Caricchi et al., 2007; Mader et al., 2013; Mueller et al., 2010; Pistone et al., 2012), must be accounted for when modeling mingling (Andrews & Manga, 2014; Hodge et al., 2012; Laumonier et al., 2014).

6.2. CONTROLS ON MAGMA MINGLING: OBSERVATIONS, EXPERIMENTS, AND NUMERICAL MODELS

6.2.1. Field Observations

Mingling textures preserved in the field record the varying extents to which magma mingling can occur. At one extreme, mafic sheets in granite plutons (Bishop & French, 1982; Topley et al., 1990; Wiebe, 1992, 1996) provide an example of individual intrusions that remain intact following injection. Multiple injected sheets can create layered intrusions that remain hot for an extended period of time, although such layers could also result from porosity waves within a mush (Jackson & Cheadle, 1998; Solano et al., 2012). When buoyant (silicic and volatile-rich) layers underlie mafic sheets, irregular protrusions or pipes of felsic magma are generated by gravitational instabilities and can penetrate the overlying mafic sheets (Figure 6.2; Caroff et al., 2011; d'Ars &

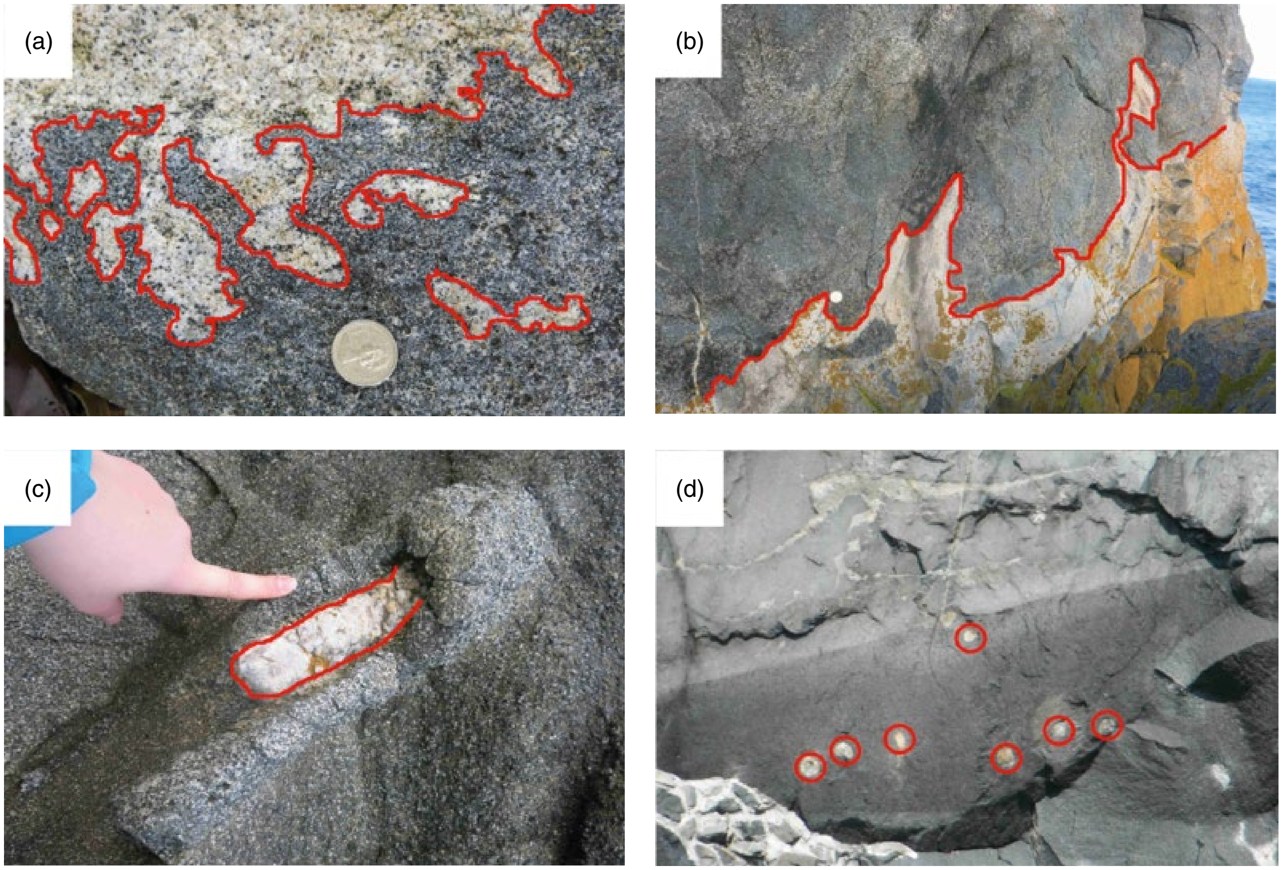

Figure 6.2 Examples of mingling textures from layered intrusions of the Northern Igneous Complex, Guernsey. Noted textures are outlined in red. (a) Loose block showing intimate mingling between a felsic and a mafic magma. (b) Diapir-like structures of felsic material rising into a mafic layer. (c) Pipe of felsic material penetrating a mafic layer. (d) Cross section through pipes similar to that seen in (c).

Davy, 1991; Elwell et al., 1960, 1962; Snyder & Tait, 1995). By contrast, examples of intimate mingling include compositionally banded pumice (Andrews & Manga, 2014; Clynne, 1999), which might have hybridized fully had eruption not interrupted the mixing process. Enclaves represent an intermediate outcome between layered intrusions and banded/hybridized products and are the preserved fragments of a disaggregated mafic intrusion into a more felsic body. Some, but not all, show fine-grained quenched margins and coarse, vesicular cores suggesting slower cooling toward the center of the enclave (Bacon, 1986; Bacon & Metz, 1984; Blundy & Sparks, 1992; Browne et al., 2006a; Eichelberger, 1980).

In mingled rocks, it is common to find crystals derived from one mixing end-member residing in the other (Figure 6.3). Such xenocrysts have been found in composite dikes (Judd, 1893; King, 1964, Litvinovsky et al., 2012; Prelević et al., 2004; Ubide et al., 2014b), mafic sheets (Bishop & French, 1982; Topley et al., 1990; Wiebe, 1992; Wiebe & Collins, 1998), and basaltic lava flows (Diller, 1891; Hiess et al., 2007; Iddings, 1890), but are most commonly described in mafic enclaves hosted in both volcanic (Bacon 1986; Bacon & Metz, 1984; Borisova et al., 2014; Browne et al., 2006a; Coombs et al., 2000; Fenner, 1926; Humphreys et al., 2009; Leonard et al., 2002; Martin et al., 2006; Murphy et al., 2000; Ruprecht et al., 2012; Stimac & Pearce, 1992) and plutonic (Akal & Helvaci, 1999; Bateman, 1995; Baxter & Feeley, 2002; Blundy & Sparks, 1992; Choe & Jwa, 2004; D'Lemos, 1986, 1996; Frost & Mahood, 1987; Janoušek et al., 2004; Kim et al., 2002; Kim et al., 2014; Kumar & Rino, 2006; Larsen & Smith, 1990; Pin et al., 1990; Reid et al., 1983; Şahin, 2008; Silva et al., 2000; Vernon, 1990; Wada et al., 2004; Wiebe, 1994; Wiebe et al., 1997; Xiong et al., 2012) rocks. Textures within these minerals, such as reaction rims on olivine xenocrysts in andesites, can be used to estimate magma ascent timescales (Dirksen et al., 2014; Matthews et al., 1992, 1994; Reagan et al., 1987; Zhang et al., 2015). Transfer of different minerals can also influence the mixing signature on Harker diagrams (Ubide et al., 2014b). Crystal transfer is likely to be accompanied by entrainment of its original melt (Cantagrel et al., 1984; Coombs et al., 2000; Gourgaud & Maury, 1984; Perugini & Poli, 2012; Ubide et al., 2014b; Wright et al., 2011). However, direct observation of entrained melt is rare in natural volcanic examples (Wright et al., 2011) and is not evident in plutons where melts hybridize and crystallize. One example (Figure 6.3b) shows an olivine xenocryst in an andesitic scoria cone (White Island, New Zealand), where the crystal is surrounded by a film of basaltic glass (light gray) that is clearly distinct from the bulk of the scoria (dark gray) and is the original melt from which the olivine crystallized. Such entrainment provides a mechanism by which the crystal's original magma can "dilute" the intrusion (Perugini & Poli, 2012; Ubide et al., 2014b) and enhance mingling. However, outstanding questions concerning the role of crystal shape on entrainment remain.

In addition to xenocryst capture, evidence for crystal transfer from the enclave back to the host is provided by disequilibrium phenocryst textures indicative of interaction with a more mafic magma (Cantagrel et al., 1984; Clynne, 1999; Coombs et al., 2000; Humphreys et al., 2009; Nakada & Motomura, 1999; Ruprecht & Wörner, 2007; Ruprecht et al., 2012; Stimac & Pearce, 1992; Tepley et al., 1999; Troll & Schmincke, 2002). This can occur through disaggregation of xenocrystic enclaves that disperse their load into the host (Fomin & Plechov, 2012; Humphreys et al., 2009; Tepley et al., 1999).

6.2.2. Analogue Experiments

Early analogue experiments used non-magmatic fluids and particles to model magma mingling by injecting one viscous fluid into another (Campbell & Turner, 1986; Huppert et al., 1984, 1986). These studies considered magmas as pure melts and demonstrated that large viscosity contrasts prohibit efficient mingling. Field observations that some mafic magmas became vesiculated in response to undercooling by the host magma (Bacon, 1986; Bacon & Metz, 1984; Eichelberger, 1980) motivated experiments focused on bubble transfer from one viscous layer into another, and demonstrated that the rise of bubble plumes could cause mingling (Phillips & Woods, 2001, 2002; Thomas et al., 1993). Recent experiments have examined the effect of crystals on intrusion breakup. For example, Hodge et al. (2012) injected a particle-rich corn syrup (high density and viscosity) into a large, horizontally-sheared body of particle-free corn syrup (low density and viscosity) to model the injection of cooling (partially crystallized) mafic magma into a convecting magma chamber. They found that low particle concentrations caused the injection to fragment and form "enclaves," whereas at high particle concentrations it remained intact and formed a coherent layer. These experiments further suggest that in the presence of a yield stress in the injected magma, the greater the bulk viscosity contrast the smaller the length scale of intrusion fragmentation, thus enhancing homogeneity at the macroscopic scale (Hodge & Jellinek, 2020). Although no analogue experiments have considered liquid injection into variably crystalline suspensions, experiments with gas injection into particle-liquid suspensions show a strong control of particle concentration and injection style, with a threshold between ductile and brittle behavior at random close packing (Oppenheimer et al., 2015; Spina et al., 2016).

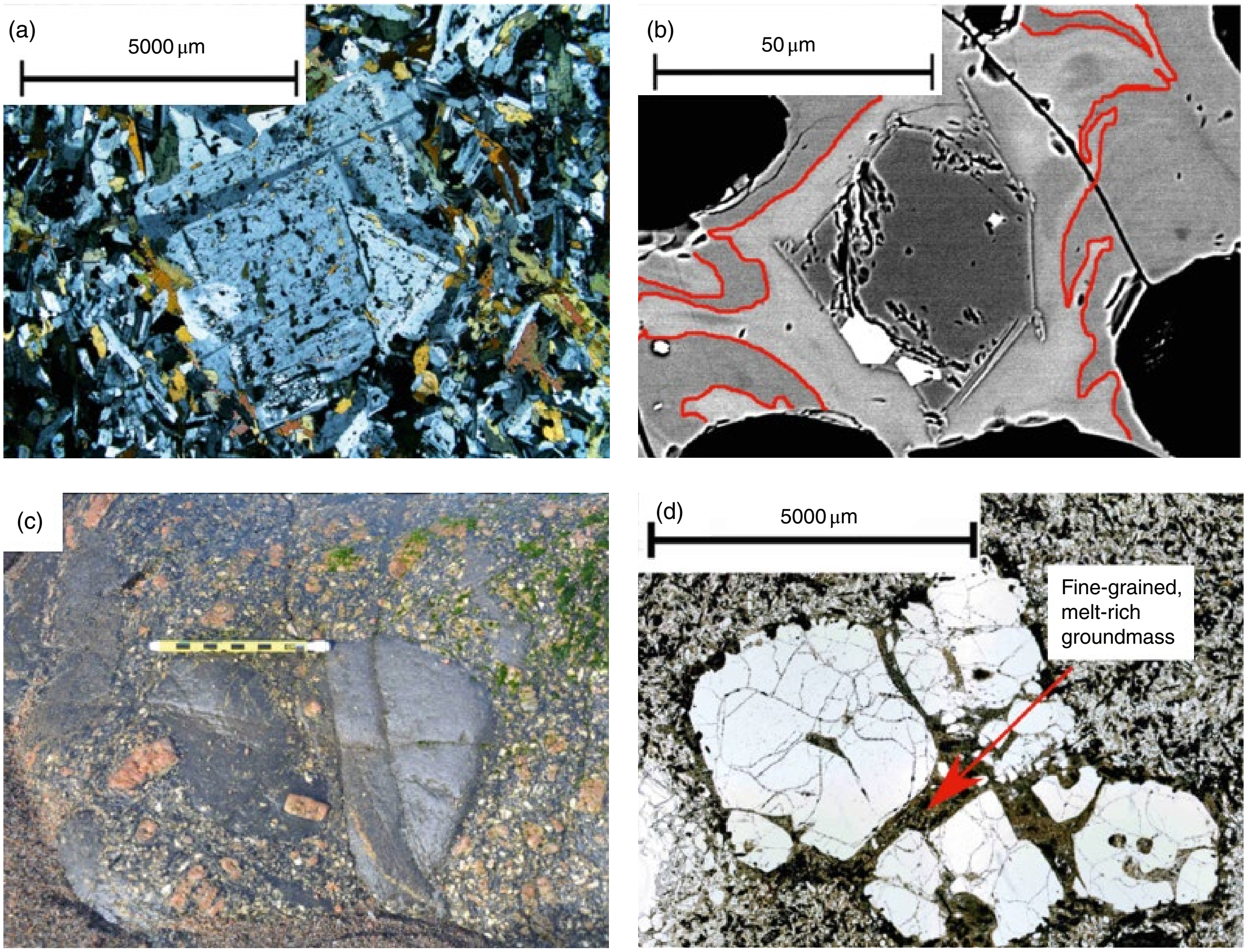

Figure 6.3 Examples of magmatic xenocrysts. (a) Plagioclase xenocryst in a mafic enclave from the Adamello Massif, Italy, showing a sieved core with many inclusions of hornblende. (b) Backscatter electron (BSE) image of an olivine xenocryst in an andesitic scoria sample from White Island volcano, New Zealand. The crystal is surrounded by an irregular film of basaltic glass (bounded by red contour). Source: Image courtesy of Geoff Kilgour. (c) Alkali feldspar xenocrysts, up to 3 cm, within mafic rocks on Shetland, Scotland. The relation of the mafic rocks to the felsic rocks from which the feldspars originated is unknown because the contact is in the subsurface. Source: Image courtesy of Amy Gilmer. (d) A cluster of rounded and highly fractured quartz xenocrysts in the Cardones ignimbrite, Chile (van Zalinge et al., 2016). The surrounding groundmass is much finer-grained and melt-rich than the rest of the material. The cluster has a rim of opaque crystals.

6.2.3. High-Temperature and/or High-Pressure Experiments

Investigations of magma interactions in high-temperature and/or high-pressure experiments can be broadly divided into two categories. Static experiments consider the juxtaposition of heated magmas and study mixing resulting from the diffusion of different melt components (Carroll & Wyllie, 1989; Van der Laan & Wyllie, 1993; Watson & Jurewicz, 1984; Wyllie et al., 1989). Fluid motion can still occur in these static experiments, as variable diffusion rates between elements can create density gradients that drive compositional convection (Bindeman & Davis, 1999). Additionally, because water diffuses much more rapidly than other components (Ni & Zhang, 2008), transfer of water from hydrous mafic magmas to silicic bodies lowers the liquidus temperature of the latter, leading to undercooling and the production of quenched margins in the mafic member, even without a temperature contrast (Pistone et al., 2016a). Bubbles that exsolve in a lower, mafic layer can also rise buoyantly into the upper layer, entraining a filament of mafic melt behind them (Wiesmaier et al., 2015). Such bubble-induced mingling can be highly efficient and has also been documented in natural samples (Wiesmaier et al., 2015). It has been proposed that a similar style of mingling can occur through crystal settling (Jarvis et al., 2019; Renggli et al., 2016).

Dynamic experiments apply shear across the interface between two magmas and reproduce mingling behavior. The shear can be applied in various ways, with a rotating parallel plate geometry (Kouchi & Sungawa, 1982, 1985; Laumonier et al., 2014, 2015), a Taylor–Couette configuration (De Campos et al., 2004, 2008; Perugini et al., 2008; Zimanowski et al., 2004), a Journal Bearing System (De Campos et al., 2011; Perugini et al., 2012), or by using a centrifuge (Perugini et al., 2015). These experiments have produced a variety of textures from homogenous mixed zones to banding. When pure melts are used, the combination of diffusional fractionation and chaotic advection can produce phenomena such as double-diffusive convection (De Campos et al., 2008) and reproduce nonlinear mixing trends for various major and trace elements (De Campos et al., 2011; Perugini et al., 2008). Experimental results also suggest new quantities to describe the completeness of mixing, such as the concentration variance (Perugini et al., 2012) and the Shannon entropy (Perugini et al., 2015). Where crystals are considered, the presence of phenocrysts can enhance mingling by creating local velocity gradients and disturbing the melt interface (De Campos et al., 2004; Kouchi & Sunagawa, 1982, 1985;). In contrast, other studies (Laumonier et al., 2014, 2015) have shown that the presence of a crystal framework in the mafic member prevents mingling, whereas the presence of water can enhance mingling by lowering the liquidus temperature, and thus the crystallinity, of the magma (Laumonier et al., 2015).

6.2.4. Numerical Models

Sparks and Marshall (1986) developed the first simple model to describe viscosity changes caused by thermal equilibration of a hot mafic magma and a cooler silicic magma, and the resulting (limited) time window in which mingling/mixing can occur. More sophisticated models have simulated mingling between melts driven by double-diffusive convection (Oldenburg et al., 1989), compositional melting (Cardoso & Woods, 1996; Kerr, 1994), and the Rayleigh–Taylor instability (Semenov & Polyansky, 2017). Another group of studies has used single-phase models to simulate elemental diffusion and advection in a chaotic flow field (Perugini & Poli, 2004; Petrelli et al., 2006). These models reproduce naturally observed geochemical mixing relationships, including linear-mixing trends between elements with similar diffusion coefficients and large degrees of scatter when diffusion coefficients differ (Nakamura & Kushiro, 1998; Perugini & Poli, 2004). Interestingly, the simulations produce both regular and chaotic regions, which are unmixed and well mixed, respectively, and have been interpreted to correspond to enclaves and host rock (Petrelli et al., 2006). This framework has been extended to account for a solid crystal phase (Petrelli et al., 2016) by including a Hershel-Buckley shape-dependent rheology (Mader et al., 2013) and a parameterization of the relationship between temperature and crystallinity (Nandedekar et al., 2014). This body of work has demonstrated that chaotic advection can speed up homogenization.

Models of mixing and mingling that consider two-phase magmas containing either solid crystals or exsolved volatiles often assume coupling between the phases. In this way, the solid or volatile phase can be represented as a continuous scalar field, and the resultant effect on rheology is accounted for through a constitutive relationship. For example, Thomas and Tait (1997) used such a framework to show that volatile exsolution in an underplating mafic magma could create a foam at the interface with an overlying silicic magma. Depending on the exsolved gas volume fraction and melt viscosity ratio, mixing and mingling could then proceed through foam destabilization, enclave formation, or a total overturn of the system. Folch and Martí (1998) showed analytically that such exsolution could lead to overpressures capable of causing volcanic eruptions. Recent finite-element models show that injection of a volatile-rich mafic magma into a silicic host can cause intimate mingling when viscosities and viscosity contrasts are low (Montagna et al., 2015; Morgavi et al., 2019). The combination of reduced density in the chamber and the compressibility of volatiles can (non-intuitively) lead to depressurization in the chamber (Papale et al., 2017), which is important for interpretation of ground deformation signals (McCormick Kilbride et al., 2016).

The effect of crystals on mixing and mingling has also been modeled by treating the crystals as a continuous scalar field. Examples include simulations of mixing across a vertical interface between a crystal suspension (30% volume fraction) and a lighter, crystal-free magma (Bergantz, 2000), and injection of a mafic magma into a silicic host with associated melting and crystallization (Schubert et al., 2013). The role of crystal frameworks in both the intruding and host magma is addressed by Andrews and Manga (2014), who model the role of thermal convection in the host, and associated shear stress on the intruding dike. If convection occurs while the dike is still ductile, then mingling will produce banding. Otherwise, the dike will fracture to form enclaves. Woods and Stock (2019) have also coupled thermodynamic and fluid modeling to simulate injection, melting, and crystallization in a sill-like geometry.

Finally, isothermal computational fluid dynamic simulations have been used to examine the case of aphyric magma injecting into a basaltic mush. For sufficiently slow injection rates, the new melt percolates through the porous mush framework, whereas for faster injections, fault-like surfaces delimit a "mixing bowl" within which the crystals fluidize and energetic mixing takes place (Bergantz et al., 2015, 2017; Carrara et al., 2020; McIntire et al., 2019; Schleicher & Bergantz, 2017; Schleicher et al., 2016). By explicitly modeling the particles with a Lagrangian scheme, it is possible to account for particle-scale effects, including lubrication forces (Carrara et al., 2019), that are neglected when using constitutive relations from suspension rheology. These simulations suggest that mushes with ≤60% crystals can be mobilized by injection, but neglect welded crystals or recrystallization of crystal contacts. Furthermore, geophysical observations suggest that mushes spend the majority of their lifetimes with much higher crystallinities (80%–90%; Farrell et al., 2014; Pritchard et al., 2018; Sinton & Detrick, 1992). Despite these limitations, recent simulations using the model have shown that the contrast between the intruding and resident melt densities, rather than bulk densities, controls the morphology of intrusion (Carrara et al., 2020).

6.3. PETROLOGIC CONSTRAINTS ON MINGLING CONDITIONS: PETROGRAPHIC INTERPRETATIONS

Here, through the use of examples, we show how the texture and chemistry of enclaves and xenocrysts have been interrogated to interpret information on mixing and mingling processes. Although many studies have examined mixed and mingled rocks from both plutonic and volcanic realms, here we review work on examples from four volcanoes (Chaos Crags and Lassen Peak, both United States; Mt. Unzen, Japan; and Soufrière Hills, Montserrat) which have erupted intermediate composition lavas containing mafic enclaves (Figure 6.4). We use common features, as recorded in the literature and augmented by an additional sample of Mt. Unzen lava from the 1792 dome collapse deposit, to develop a conceptual model that describes how volatile and crystal contents control mixing and mingling in magma storage regions. We analyze the latter using backscatter electron images (BSE) obtained using both a Hitachi S-3500N (University of Bristol) and a TESCAN Mira II (University of Lausanne) scanning electron microscope (SEM). Plagioclase compositions were measured on a Cameca SX100 (University of Bristol) with an accelerating voltage of 20 kV, emission current of 10 nA, and a spot size of 3 μm.

6.3.1. Volcanic Systems

Chaos Crags

Chaos Crags comprises a series of enclave-bearing rhyodacite lava domes that erupted between 1125 and 1060 years ago (Clynne, 1990). The host lavas are crystal-rich, containing phenocrysts of plagioclase, hornblende, biotite, and quartz, whereas the enclaves are basaltic andesite to andesite with occasional olivine, clinopyroxene, and plagioclase phenocrysts in a groundmass of amphibole and plagioclase microphenocrysts (Heiken & Eichelberger, 1980). Many, but not all, enclaves have fine-grained and crenulated margins, and all contain resorbed phenocrysts captured from the host (Figure 6.4a). Some phenocrysts in the host also show resorption textures (Tepley et al., 1999).

Lassen Peak

Lassen Peak erupted in 1915, producing a dacite dome and lava flow followed by a sub-Plinian eruption that deposited two types of pumice: homogeneous dacite and banded dacite/andesite. The dome and flow are porphyritic with phenocrysts of plagioclase, biotite, hornblende, and quartz in a glassy, vesicular groundmass containing microphenocrysts of plagioclase, pyroxenes, and Fe-Ti oxides. The dacite dome and lava flow also contain xenocryst-bearing andesitic enclaves with equigranular texture and a lack of crenulated margins (Figure 6.4b; Clynne, 1999). The enclaves have olivine phenocrysts (which occasionally appear as xenocrysts in the host) with plagioclase and pyroxene microphenocrysts.

Mt. Unzen

Mt. Unzen has erupted lavas and domes since 300–200 ka (Hoshizumi et al., 1999), most recently during the 1991–1995 eruption. With the exception of an andesitic lava flow from 1663, Mt. Unzen lavas are consistently dacitic, containing basaltic to andesitic enclaves (Hoshizumi et al., 1999; Browne et al., 2006a). Dacite erupted in the 1991–1995 eruption is porphyritic with about 20% phenocrysts of plagioclase, hornblende, biotite, and quartz, with plagioclase, pargasite, pyroxenes, apatite, and Fe-Ti oxides occurring as microlites in a highly crystalline groundmass (Cordonnier et al., 2009; Hornby et al., 2015; Nakada & Fuji, 1993; Nakada et al., 1999; Nakada & Motomura, 1999; Venezky & Rutherford, 1999). Two types of enclaves are observed: porphyritic and equigranular. Porphyritic enclaves contain large crystals of plagioclase, hornblende, and rare quartz within a finer groundmass of plagioclase and hornblende microphenocrysts, minor amounts of clinopyroxene and olivine, and interstitial glass (Figure 6.4c). The overall crystallinity is 70%–90%. Equigranular enclaves contain equant microphenocrysts of plagioclase with smaller quantities of hornblende and orthopyroxene (Browne et al., 2006a).

Soufrière Hills

The 1995–2010 Soufrière Hills eruption produced a series of andesitic lava domes containing enclaves of basaltic to basaltic-andesitic composition (Plail et al., 2014;

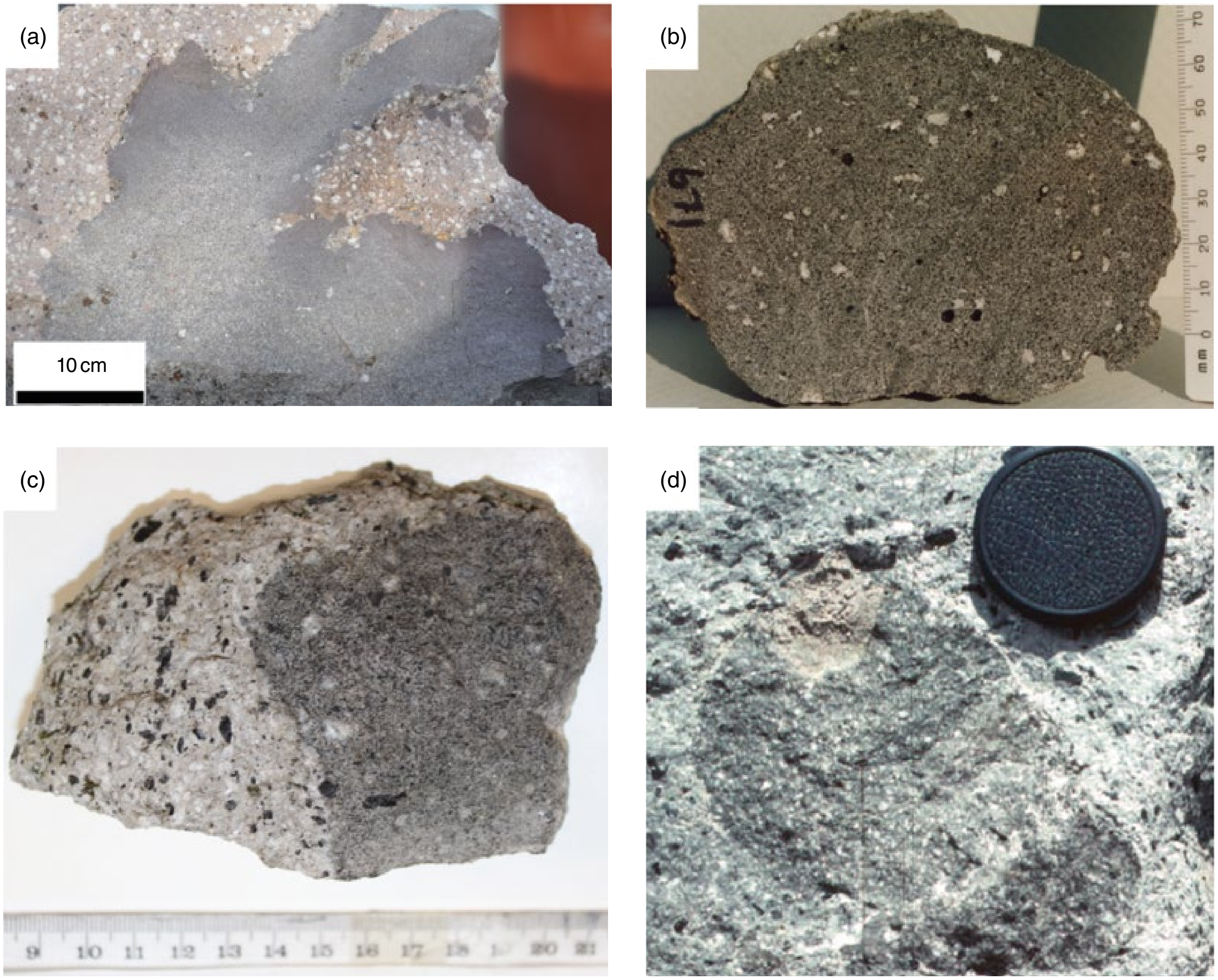

Figure 6.4 Examples of enclaves from four volcanic systems. (a) Mafic enclave, with fine-grained, crenulate margin and numerous xenocrysts, from Chaos Crags. Source: Image courtesy of Michael Clynne. (b) Andesitic enclave from 1915 eruption of Lassen Peak, showing an equigranular texture and numerous partially reacted xenocrysts. Source: Reproduced with permission from Clynne (1999). (c) Basaltic enclave in an andesitic lava flow from the 1792 dome collapse at Mt. Unzen, Japan, at about 4 ka. There is no evidence for a fine-grained margin in the enclave. Sample collected by Julie Oppenheimer, Karen Strehlow and Emma Liu. (d) Mafic enclave from 1995–2010 eruption of Soufrière Hills volcano. Source: Image courtesy of Steve Sparks.

Wadge et al., 2014). The andesite contains approximately 40% phenocrysts (plagioclase, hornblende, orthopyroxene, Fe-Ti oxides, and minor quartz) in a much finer-grained groundmass with up to 25% glass (Edmonds et al., 2016; Humphreys et al., 2009; Murphy et al. 2000). The enclaves have a diktytaxitic groundmass of plagioclase, pyroxenes, amphibole, and Fe-Ti oxides with larger xenocrysts inherited from the andesite (Figure 6.4d). Some enclaves have crenulated and fine-grained margins, whereas others are more equigranular and of a less mafic composition (Murphy et al., 2000; Plail et al., 2014, 2018).

6.3.2. Phenocryst, Xenocryst, and Groundmass Textures and Chemistries

Enclave Groundmass Textures

The enclaves from all four volcanoes show both similar and contrasting textural features. At Chaos Crags, most enclaves have fine-grained and crenulate margins (Figure 6.4a; Tepley et al., 1999), although those erupted in later domes are more angular and lack fine-grained margins. Enclaves in Lassen Peak samples are subrounded to subangular with an equigranular texture (Figure 6.4b; Clynne, 1999). Many enclaves from the 1991–1995 eruption at Mt. Unzen have crenulate and fine-grained margins (Browne et al., 2006a), although some have angular edges and a uniform crystal size (Figure 6.4c; Fomin & Plechov, 2012). Similar features are observed at Soufrière Hills, with many inclusions being ellipsoidal (Figure 6.4d) and some angular; most, but not all, have fine-grained, crenulate margins (Murphy et al., 2000). Both the size and volume fraction of enclaves increased during the eruption (Barclay et al., 2010; Plail et al., 2014, 2018).

In all localities, fine-grained margins and crenulate contacts are attributed to undercooling of the mafic magma due to juxtaposition against the much cooler felsic host (Eichelberger, 1980) and associated rapid crystallization of the mafic melt near the contact with the felsic host. These crystalline rims have a greater rigidity than the lower-crystallinity enclave interiors so that as the enclave continues to cool and contract, the rims deform to a crenulate shape that preserves the original surface area (Blundy & Sparks, 1992). Enclaves not exhibiting such quench textures are also found at all localities.

Plagioclase

The composition and texture of plagioclase crystals are extremely good recorders of magmatic processes because (a) their stability field in pressure-temperature-composition (P-T-X) space is very large in volcanic systems, and (b) compositional zoning modulated by changes in the P-T-X space is well preserved due to the relatively slow diffusion in the coupled substitution between Na-Si and Ca-Al (Berlo et al., 2007; Grove et al., 1984; Morse, 1984).

Texturally, plagioclase phenocrysts in the host lavas at all four localities comprise a population of unreacted, oscillatory zoned crystals with a smaller amount of reacted crystals that have sieved cores and/or resorption rims (Figure 6.5a; Browne et al., 2006b; Clynne 1999; Murphy et al., 2000; Tepley et al., 1999). Associated enclaves contain plagioclase xenocrysts incorporated from the host with sieved-texture resorption zones that consist of patchy anorthite-rich plagioclase and inclusions of glass (quenched melt). These reacted zones can penetrate to the cores of smaller crystals (Figures 6.5b,c), but in larger xenocrysts appear as a resorption mantle surrounding a preserved oscillatory zoned core (Figure 6.5d). All xenocrysts are surrounded by a clean rim that is of the same composition as the plagioclase microphenocrysts in the enclave groundmass.

The relationship between the anorthite (An) and FeO content of plagioclase crystals can also provide insight into magma mixing and mingling. Plagioclase crystals erupted from Soufrière Hills volcano between 2001 and 2007 show a shallow, linear trend between FeO and An contents in oscillatory zoned regions of plagioclase phenocrysts in the host (Humphreys et al., 2009); sieved zones in the same phenocrysts form a curved trend at higher FeO (Figure 6.6d). In enclave-hosted xenocrysts, oscillatory zoned cores plot on the same linear trend as oscillatory zoned phenocrysts, whereas the clean rims overlap with the curved trend of the phenocryst sieved zones (Figure 6.6f). The same curved trend is found for enclave microphenocrysts (Figure 6.6e; Humphreys et al., 2009). We observe similar characteristics in our sample of Mt. Unzen dome lava (Figures 6.6a–c).

Quartz

Quartz crystals in mingled lavas can also show distinctive features. Host phenocrysts are rounded and embayed (Figure 6.7a; Browne et al., 2006a; Christopher et al., 2014; Clynne, 1999; Murphy et al., 2000; Tepley et al., 1999) and can also be fractured (Clynne, 1999). In the enclaves, quartz xenocrysts are surrounded by reaction rims of clinopyroxene and hornblende microphenocrysts and glass (Figure 6.7b; Browne et al., 2006a; Clynne, 1999; Murphy et al., 2000; Tepley et al., 1999).

6.3.3. Interpretation of Textures and Chemistries

The common textural and chemical features of these volcanic systems suggest commonalities in the mixing and mingling processes. First, because enclaves from all volcanoes contain xenocrysts that originated in the host magmas, the mafic component must have been sufficiently ductile to incorporate these crystals during mixing. Plagioclase xenocrysts contain rounded, patchy zones with a sieved texture showing that both partial and simple dissolution occurred (Cashman & Blundy, 2013; Nakamura & Shimakita, 1998; Tsuchiyama, 1985), suggesting that the enclave magmas were undersaturated in plagioclase at the time of incorporation. Because up to 70% of the enclave groundmass consists of plagioclase microphenocrysts, this implies the mafic magmas were crystal-poor at the time of xenocryst incorporation.

Compositional variations of FeO and An in the plagioclase crystals provide further information on the relative compositions of the host and enclave melt at Soufrière Hills (Humphreys et al., 2009) and Mt. Unzen (Figure 6.6). Most analyses from host phenocrysts show a shallow, increasing linear trend between An and FeO content (Figures 6.6a,d); the few points with FeO enrichment correspond to resorbed zones. Unresorbed cores of xenocrysts have similar compositions, suggesting that both crystal core populations derive from the same host dacite magma. Enclave microphenocrysts, however, show greater FeO enrichment (Figures 6.6b,e) and overlap with xenocryst rim compositions. Similar results are reported for plagioclase in andesite lavas erupted from El Misti, Peru, which underwent resorption in response to mafic recharge (Ruprecht & Wörner, 2007). At Mt. Unzen,

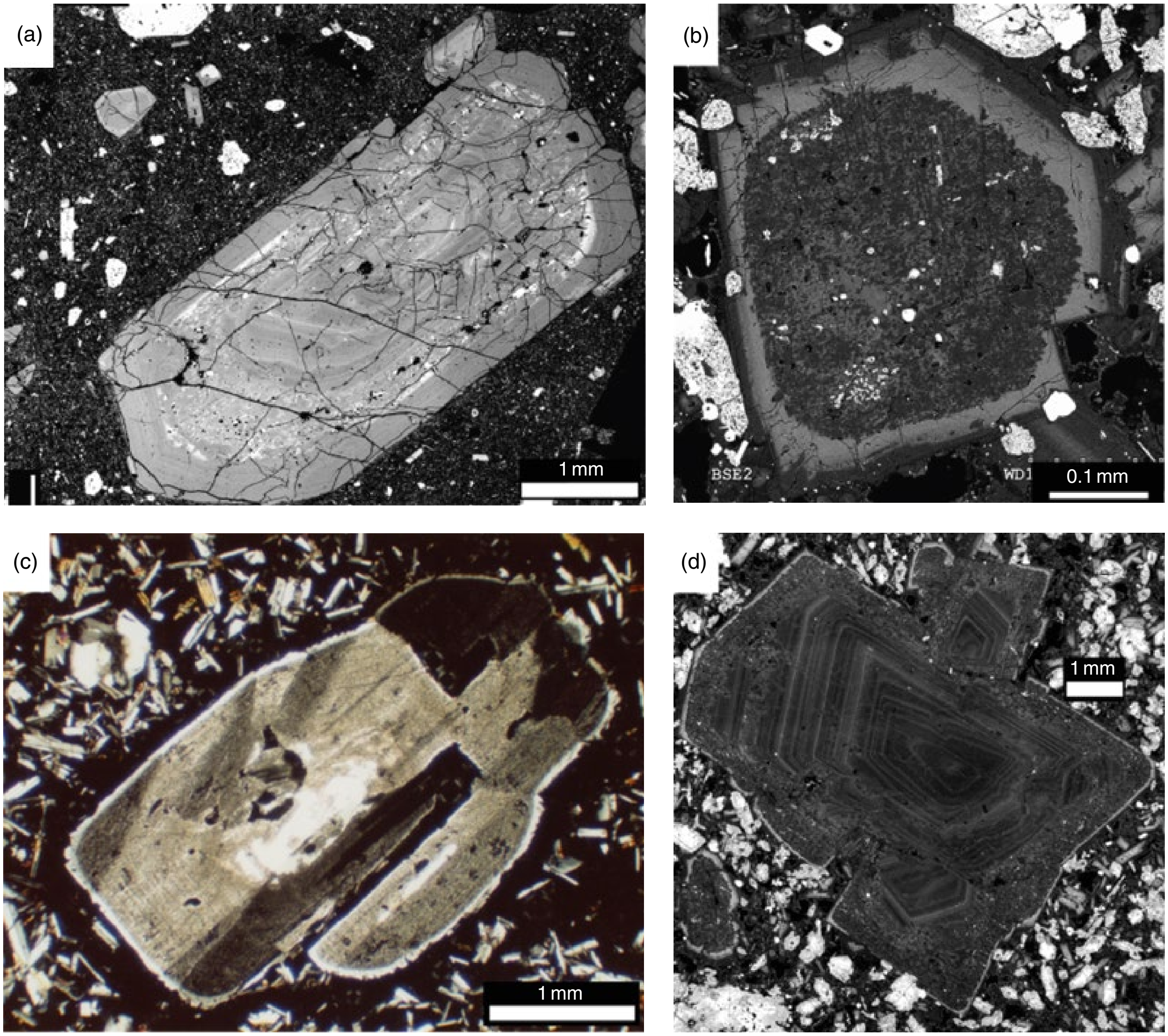

Figure 6.5 BSE and optical images of plagioclase phenocrysts and xenocrysts from Mt. Unzen (a, b, d) and Lassen Peak (c). (a) Host-rock plagioclase phenocryst with a wide heterogeneous zone and many mineral and glass inclusions. (b) Plagioclase xenocryst in an enclave with a sieved core. (c) Heavily reacted plagioclase xenocryst with a clear overgrowth rim within an andesitic enclave. Source: Reproduced with permission from Clynne (1999). (d) Plagioclase xenocryst in a mafic enclave with an oscillatory zoned core surrounded by a patchily zoned and inclusion-rich mantle bounded by a normally zoned rim.

enclave microphenocryst and xenocryst rims show a strong positive correlation for the whole An range, whereas these phases at Soufrière Hills show a negative correlation for An > 75 mol% (Figure 6.6). This difference is attributed to the absence of Fe-Ti oxide as an early crystallizing phase in the Soufrière Hills mafic end-member, which would cause FeO to increase in the residual melt as other phases precipitated until the point of oxide saturation (Humphreys et al., 2009). The lack of this inflection in the Mt. Unzen sample suggests that Fe-Ti oxides were present in the mafic magma prior to mixing, as suggested for the 1991–1995 eruption (Botcharnikov et al., 2008; Holtz et al., 2005).

Whereas the observed enrichment in FeO in enclave microphenocrysts, sieved zones in phenocrysts and xenocrysts, and xenocryst rims is likely due to crystallization from a more mafic melt, it is also possible that growth of these regions may be sufficiently fast for kinetic effects to play a role; if growth is faster than diffusion of FeO in the melt, then an FeO-rich boundary layer may develop around the crystals (Bacon, 1989; Bottinga et al., 1966; Mollo et al., 2011) that could also explain the

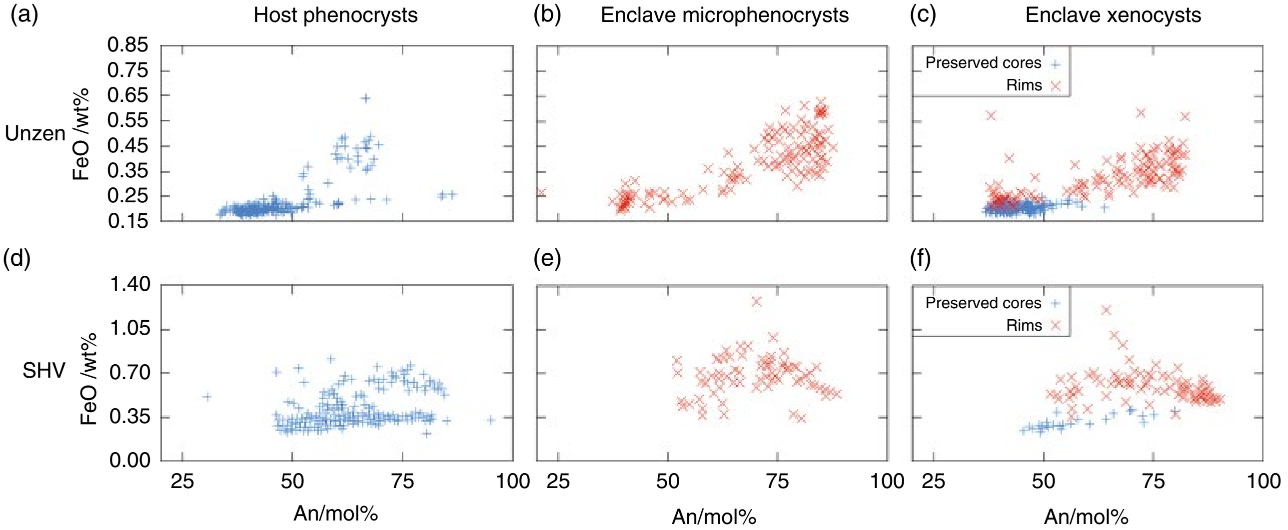

Figure 6.6 Plots of FeO versus An from transects across plagioclase for (a,d) host phenocrysts, (b,e) enclave microphenocrysts, and (c,f) xenocrysts in enclaves. Data shown for Mt. Unzen sample in Figure 6.4c and for rocks from Soufrière Hills (Humphreys et al., 2009). (a,d) Most host phenocrysts lie on a shallow, linear trend with a slight positive correlation in the range An = 33–88 mol% for Mt. Unzen and An = 45– 80 mol% for Soufrière Hills. Some analyses show much greater FeO enrichment and correspond to resorbed zones. (b,e) Enclave microphenocrysts show FeO enrichment compared to host phenocrysts, up to 0.65 wt% for Mt. Unzen and 1.3 wt% for Soufrière Hills. (c,f) The preserved cores of xenocrysts plot on the same shallow trend as host phenocrysts, whereas rim compositions overlap with enclave microphenocryst compositions. Source: Based on Humphreys et al. (2009).

enrichment. However, such a process would generate a negative correlation between FeO and An (Neill et al., 2015), not the positive correlation observed at Unzen and Soufrière Hills.

The contrasting textures of quartz in the host and enclaves also provide insight into the mingling/mixing process. Rounding of quartz xenocrysts, together with glass-filled embayments, suggests dissolution of quartz in the host. Conversely, quartz reaction rims comprising hornblende microphenocrysts, glass, and vesicles in the enclaves (Figures 6.3d, 6.7b) suggest that the dissolution-induced increase in the silica content (and H_2O solubility) of the surrounding melt caused diffusion of H_2O toward the quartz (Pistone et al., 2016a).

Whereas the presence of resorbed xenocrysts in enclaves suggests that there was time for crystals to be incorporated, and to react, before the enclave started to crystallize, the presence of fine-grained rims on some enclaves (Barclay et al., 2010; Browne et al, 2006a; Murphy et al., 2000; Plail et al., 2014; Tepley et al., 1999) implies rapid cooling and crystallization (chilling) of the mafic magma against the cooler silicic host (Bacon, 1986). Xenocrysts must therefore have been incorporated prior to the formation of the chilled margin, providing a limited temporal window for crystal transfer. A comparison of the thickness of xenocryst resorption zones at Mt. Unzen (Browne et al. 2006a) with those produced experimentally (Nakamura & Shimakita, 1998; Tsuchiyama & Takahasi, 1983; Tshuchiyama, 1985) suggests resorption on a timescale of days; this contrasts with thermal modeling (Carslaw & Jaeger, 1959) suggesting that enclaves should thermally equilibrate on a timescale of hours. Again, this requires incorporation of xenocrysts prior to intrusion disaggregation and enclave formation (Browne et al., 2006a). As all the considered volcanic lavas contain similarly resorbed plagioclase xenocrysts within enclaves of comparable sizes, it seems likely that this temporal constraint on the sequence of crystal transfer prior to enclave formation is generally true for the systems presented here.

Importantly, all locations also contain enclaves with unquenched margins (Plail et al., 2014; Tepley et al., 1999) and equigranular textures (Browne et al., 2006a; Heiken & Eichelberger, 1980). Equigranular enclaves at Mt. Unzen have been interpreted as originating from disaggregation of the interior of the intruding magma, which cooled more slowly than the intrusion margin where porphyritic enclaves (xenocrysts-bearing, chilled margin) formed. Similarly, at Soufrière Hills, the quenched enclaves may form from an injected plume of mafic magma, whereas unquenched and more hybridized enclaves form from disturbance of a hybrid layer at the felsic–mafic interface (Plail et al., 2014). Angular enclaves

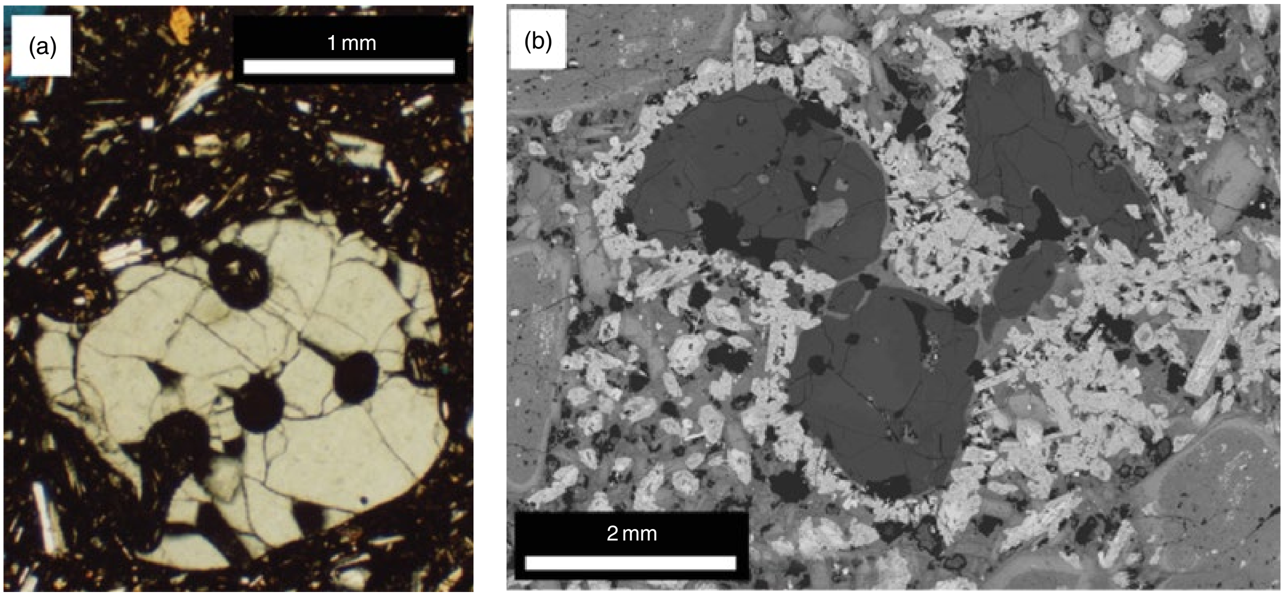

Figure 6.7 (a) Image of a quartz phenocryst in the dacitic lava dome from the 1915 Lassen Peak eruption. It appears unreacted but has rounded edges and embayments. Source: Image courtesy of Michael Clynne. (b) BSE image of a cluster of quartz xenocrysts in an enclave from the 1991–1995 Mt. Unzen eruption. They are rounded and surrounded by an extended region of hornblende microphenocrysts (very bright), glass (light gray) and vesicles (black).

with unquenched margins may record the break-up of larger enclaves (Clynne, 1999; Fomin & Plechov, 2012; Murphy et al, 2000; Plail et al., 2014), which can return resorbed host-derived crystals to the host; this explains the presence of resorption zones in crystals in the host lavas (Figure 6.5b), and chemical signatures (Figure 6.6a) of crystallization from mafic magma. Further support for enclave fragmentation comes from microlites that are chemically indistinguishable from enclave phases at Soufrière Hills (Humphreys et al., 2009). A possible method to determine whether equigranular enclaves form from a hybrid layer or disaggregation of larger enclaves is to examine the mineralogy of the crystals in the enclave. The two different mechanisms will produce different degrees of undercooling within the enclave magma, which, in the hybrid-layer model, will depend on the relative proportions of the end-member magmas, and thus can produce different crystal assemblages/textures (Humphreys et al., 2006).

6.3.4. Conceptual Model of Magma Mixing and Mingling

The common features of the eruptive products described above suggest common aspects of mixing and mingling. Xenocrystic mafic enclaves with chilled margins, in particular, require that magma injection be accompanied by crystal incorporation from the host magma, as also suggested by a comparison of thermal timescales with the times needed to generate the observed thicknesses of resorption zones (Browne et al., 2006a). These constraints on the sequence of mixing processes have led to a similar conceptual model of mixing and mingling (Figure 6.8; Browne et al., 2006a; Clynne, 1999; Murphy et al., 2000; Plail et al., 2014; Tepley et al., 1999) in which the mafic magma is injected as a fountain (Clynne, 1999) or collapsing plume (Plail et al., 2014) before ponding at the base of the silicic host (Figure 6.8a). Shear caused by the injection disrupts the interface between the two magmas, leading to the formation of blobs of hybridized magma with incorporated host crystals that then rapidly chill against the silicic host, preventing further hybridization (Plail et al, 2014; Tepley et al., 1999). Heating of the host, in turn, causes partial melting, reducing the crystallinity and causing convective motions that disperse the enclaves. Meanwhile, at the mafic–silicic contact, a hybrid interface layer forms (Figure 6.8b). As this layer crystallizes, second boiling drives fluid saturation; exsolved buoyant fluids produce a low-density, gravitationally unstable, interface layer that breaks up to form further enclaves (Figure 6.8c; Browne et al., 2006a; Clynne, 1999). As cooling propagates downward through the mafic body, enclaves can come from deeper portions resulting in more equigranular enclaves that lack chilled margins or xenocrysts (Brown et al., 2006a; Plail et al., 2014).

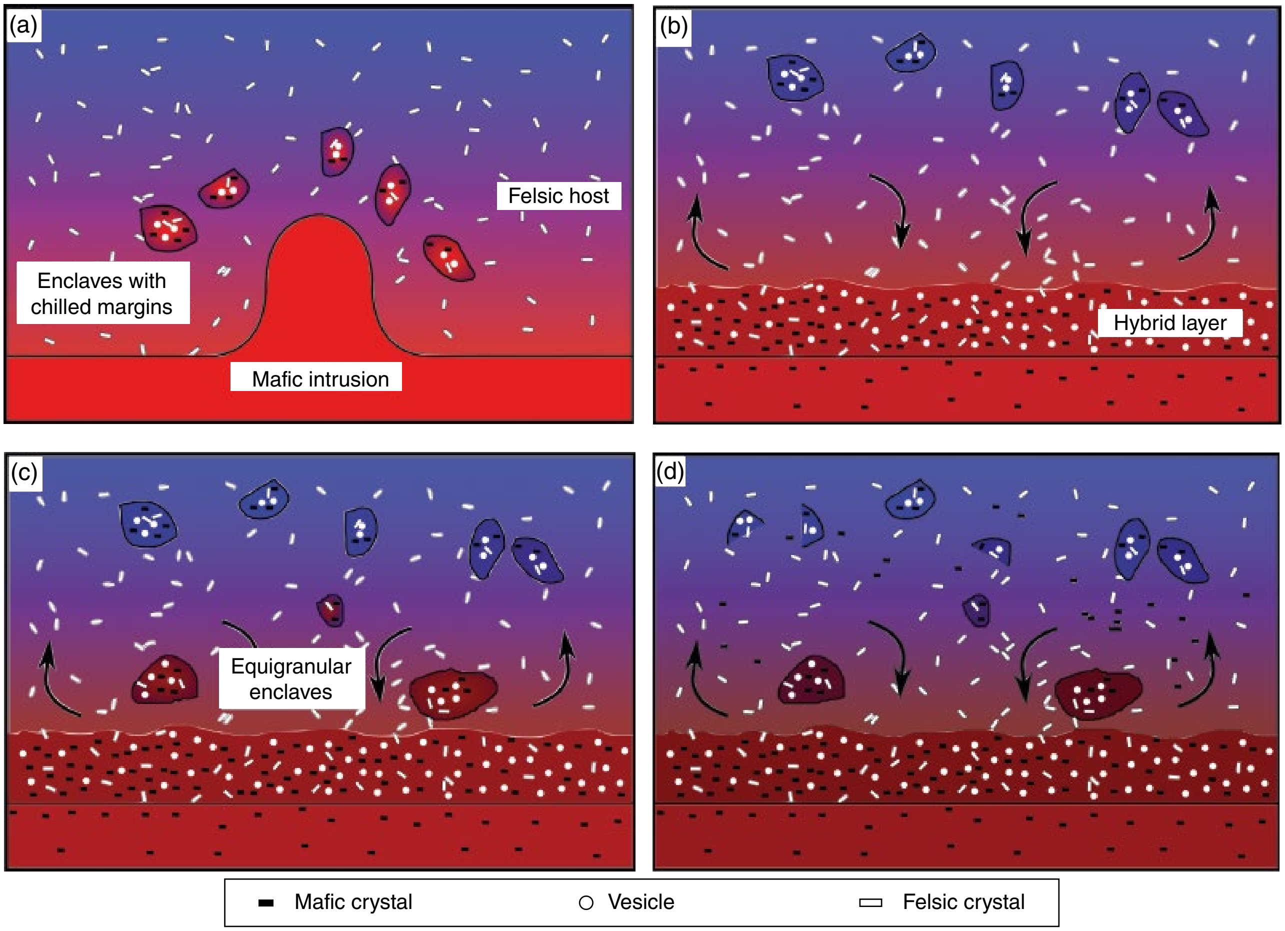

Figure 6.8 Conceptual model of the different stages of magma mixing and mingling following injection of a mafic magma into a partially crystallized silicic host. The processes shown follow similar diagrams from Clynne (1999), Tepley et al. (1999), Browne et al. (2006a), and Plail et al. (2014). (a) Mafic magma is injected into a partially crystallized host. Injected magma is initially denser and so ponds beneath the silicic host, although the momentum of the injection may produce a collapsing fountain. (b) Disaggregation of the collapsing fountain produces quenched enclaves with chilled margins. These enclaves contain xenocrysts captured from the host, which became entrained during the injection. Heat transfer from the mafic to the silicic magma produces partial melting of the silicic member, reducing the crystallinity and creating convective motions that disperse the enclaves. In addition, a hybrid layer forms at the interface between the mafic and silicic magmas. Crystallization in this layer leads to exsolution of volatile phases. (c) The presence of exsolved volatiles in the interface layer leads to a reduction in density, and the hybrid layer destabilizes due to a Rayleigh–Taylor instability. This leads to the formation of enclaves without chilled margins that are dispersed within the silicic host. (d) Continued convective motions in the host lead to brittle disaggregation of enclaves, creating angular enclave fragments and dispersing mafic groundmass and resorbed host crystals into the host. Sources: Clynne (1999); Tepley et al. (1999); Browne et al. (2006a,b); Plail et al. (2014).

Enclaves, once formed, can disaggregate. Disaggregation is shown by the presence of broken enclaves (Clynne, 1999; Fomin & Plechov, 2012; Tepley et al., 1999), host phenocrysts with resorption zones and Fe enrichment caused by previous engulfment in mafic magma (Browne et al., 2006b; Clynne, 1999; Humphreys et al., 2009; Tepley et al., 1999), and small clusters of enclave-derived microlite material within the host lavas (Humphreys et al., 2009). Disaggregation allows for subsequent mixing of a type precluded during initial enclave formation, but the timing of disaggregation is poorly constrained. It could occur during high-shear conditions in the conduit (Humphreys et al., 2009); alternatively, disaggregation may be part of a continuous cycle of injection, enclave formation, and fragmentation (Figure 6.8d) that gives rise to a continuously convecting magma storage region, which is sometimes sampled during a volcanic eruption (Browne et al., 2006a). Regardless, the dispersion of mafic groundmass into the host has implications for interpreting end-member compositions from petrologic studies (Humphreys et al., 2009; Martel et al., 2006). Importantly, neglecting such transfer can lead to an underestimate of the initial silica content of the felsic member.

6.4. QUANTITATIVE MODELING OF CRYSTAL AND VOLATILE CONTROLS ON MIXING AND MINGLING

Many conceptual models of magma mixing (e.g., Figure 6.8) have been produced based on petrologic evidence. However, quantitative models of magma mixing are limited. As described in Section 6.2.4, Sparks and Marshall (1986) first developed a simple model describing how thermal equilibration of a juxtaposed mafic and silicic magma led to rapid viscosity changes that inhibited mixing after a short time. Since then, models developed to account for the role of either crystals or exsolved volatiles have produced significant insights into mingling and mixing dynamics, but have failed to incorporate petrological data within quantitative frameworks. Here, we examine three models: Andrews and Manga (2014), who use continuum modeling and suspension rheology to model mingling resulting from dike injection into a silicic host; Bergantz et al. (2015), who model the injection of melt into a basaltic mush, resolving both fluid and granular behavior; and Montagna et al. (2015), who simulate the effect of exsolved volatiles on mafic injection. We compare the model assumptions and results, as well as their implications for interpreting petrological data.

6.4.1. The Model of Andrews and Manga (2014)

The model considers the instantaneous injection of a mafic dike into a silicic host, with a prescribed initial composition and temperature, and numerically solves the 1D heat equation. Changes in the crystallinity and bulk viscosity of magmas with time are calculated using MELTS simulations (Asimow & Ghiorso, 1998; Ghiorso & Sack, 1995) and viscosity models for melt (Giordano et al., 2008) and crystal-bearing suspensions (Einstein, 1906; Roscoe, 1952). If the viscosity of the host immediately juxtaposed with the dike decreases sufficiently, then the host starts to convect (as determined by a Rayleigh number criterion), which exerts a shear stress on the dike. If this shear stress exceeds the yield stress of the dike (which depends on its crystal content), the dike deforms in a ductile fashion and the model predicts banded products. Alternatively, if the yield stress exceeds the shear stress, then the dike fractures in a brittle fashion and enclaves form.

In this model context, the principal control on mingling dynamics is the development of crystal frameworks within the dike. Dike crystallization, in turn, is controlled by composition and temperature contrasts. For example, injection of hot, large, and wet dikes causes the silicic host to convect before a crystal framework forms in the dike. The resultant shear causes ductile disruption of the dike and intimate mingling of the two magmas, producing banding and, with time, homogenization. Small and dry dikes, by contrast, experience extensive crystallization before the host starts to convect and thus fracture to form enclaves. The precise initial conditions (temperature, dike size, and water content) that determine mingling style are sensitive to the parameterizations used (e.g., critical Rayleigh number for convection), but the qualitative results are useful.

The principal limitation of the model of Andrews and Manga (2014) is that it assumes an instantaneous injection of the mafic dike and therefore neglects any mixing/mingling that occurs during injection itself. Instead, the dike is disrupted only by shear due to convection in the host. Indeed, the relative importance of shear due to injection versus shear due to convection remains a considerable unknown. The assumption that brittle fragmentation of the dike produces enclaves is supported by three-dimensional tomographic observations of enclaves from Chaos Crags, which have crystal frameworks that are lacking in banded pumices from Lassen Peak (Andrews & Manga, 2014). The inference is that these crystal frameworks created a yield stress such that the enclaves formed by solid-like fracturing and banded pumice by ductile deformation. However, this is in direct contradiction with the conceptual model presented above (Figure 6.8), which is based on field and petrographic observations that suggest enclaves form from fluid-like deformation of the mafic magma. This contradiction highlights the extent to which conditions of enclave formation are unknown.

6.4.2. The Model of Bergantz et al. (2015)

The discrete-element model, which resolves both fluid and granular physics, considers the injection of a crystal-free magma into the base of a crystal mush at random loose packing (approximately 60% crystallinity). The response of the mush is governed by stress chains formed by crystal–crystal contacts. For sufficiently slow injections, the new melt permeates through the mush, which behaves as a porous medium. Once the injection speed is large enough to disrupt the stress chains, however, part of the mush can become fluidized to form a mixing cavity, which is an isolated region where the host melt, crystals, and new melt undergo overturning. The new melt then escapes from the cavity through porous flow into the rest of the mush. For still faster flow speeds, the stress chains orientate to create two fault-like surfaces at angles of about 60° to the horizontal that bound a fluidized region of the mush, within which extensive circulation occurs. Recently, this model has been extended to investigate the effect of a density contrast between the intruding and resident melts on the style of mingling (Carrara et al., 2020), showing that the intrusion geometry is controlled to first order by the contrast between the melt densities rather than by the bulk densities.

Although this model captures granular and fluid dynamics on the crystal scale and demonstrates the impact of varying the injection velocity, there are numerous outstanding questions. First, varying the crystallinity of the mush has not been addressed and will presumably affect the values of the injection velocity at which transitions between mingling styles occur. Furthermore, temporal and spatial variations in temperature (due to heat transfer or latent heat release), and therefore in viscosity and crystallinity, have not been considered. Cooling and crystallization of the new melt should control the dynamics of the system, as will associated latent heat release. Finally, the geometry of the modeled magma reservoir (laterally homogenous layers) will affect the specifics of the mixing process, such as the orientation of the bounding faults, and it is not yet clear if the model scales to natural systems.

6.4.3. The Model of Montagna et al. (2015)

The two-dimensional finite-element model considers two vertically separated magma chambers that are superliquidus and connected by a narrow conduit. The upper chamber initially contains a felsic phonolite, and the lower chamber and conduit are filled with a mafic shoshonite, compositions chosen to represent eruptions from Campi Flegrei. H_2O and CO_2 exsolve as functions of temperature and pressure (Papale et al., 2006), whereas the transport of exsolved volatiles is modeled as a continuum scalar field satisfying a transport equation. Bubbles are assumed to be sufficiently small that they are undeformable, and an empirical law is used to parameterize their effect on bulk viscosity (Ishii & Zuber, 1979). The shoshonite initially contains exsolved volatiles and so is lighter than the phonolite, creating an unstable density interface at the inlet to the upper chamber.

Upon initiation, a Rayleigh–Taylor instability develops at the inlet to the upper chamber, and a plume of light material rises into the chamber while the conduit is filled with a mixed, hybrid magma. Intimate mingling within the chamber is reminiscent of that created by chaotic advection (Perugini & Poli, 2004). The magma entering the upper chamber is a partial hybrid, and the pure parent shoshonite never enters the upper conduit. Intensive mingling occurs on a timescale of hours, promoted by a large initial density contrast and horizontally elongated chambers. Importantly, the reduction in density of the upper chamber can cause depressurization, which has implications for interpreting ground deformation signals (Papale et al., 2017).

Although an obvious limitation of the model is the two-dimensional domain, it seems reasonable that the results can be extrapolated to three-dimensional systems. A greater limitation is the restricted range of compositions and temperatures for which the model is valid. The end-member compositions are similar and superliquidus, so that both the absolute bulk viscosities (<3500 Pa s) and their contrast (factor of 7) are relatively low. This allows rapid mingling and entirely ignores the effect of crystals on the flow dynamics.

6.4.4. Comparison and Common Limitations

Both Andrews and Manga (2014) and Bergantz et al. (2015) focused on the effect of crystals, but a key difference in the two models is the initial condition. Andrews and Manga (2014) assume the instantaneous injection of a dike into an initial rheologically locked host, whereas Bergantz et al. (2015) simulate the flow of new melt into a melt-crystal mixture; they show that new melt flows permeably through a rheologically locked mush. The conditions that spatially constrain a mafic injection (e.g., as a dike) have not been defined. The two models also simulate the role of crystals differently. Andrews and Manga (2014) calculate the crystallinity of a magma at a given temperature and assume the presence of a crystal framework (and yield stress) above a threshold value. Bergantz et al. (2015) allow the crystals to form force chains through which stresses are transmitted (Bergantz et al., 2017), but they consider the system to be isothermal such that no crystallization occurs, a key feature of Andrews and Manga (2014).

Both models are limited in addressing the role of volatiles. Diffusion of volatiles from the mafic to felsic member can strongly influence the crystal composition and textures of the silicic member (Pistone et al., 2016a), whereas exsolution of volatiles leads to a reduction in bulk density that can drive convective motions in the mixing dynamics (Eichelberger, 1980; Montagna et al., 2015; Phillips & Woods, 2001, 2002; Thomas et al., 1993; Wiesmaier et al., 2015). The presence of exsolved volatiles also affects the magma rheology and requires the use of three-phase rheological models (Mader at al., 2013; Pistone et al., 2016b). One strategy is to treat the exsolved phase as a continuum scalar field and use a suspension model for bulk rheology (Montagna et al., 2015). However, as has been shown for solid phases (Carrara et al., 2019), small-scale effects can be overlooked by this approach, and explicit modeling of such phases may be needed to accurately constrain mixing/mingling processes.

Additional complications arise in the number of parameters required for a given model. For example, the Andrews and Manga (2014) model requires values for a maximum crystal packing fraction and a critical Rayleigh number for convection in the host. Constraining these parameters will require extensive experimental efforts involving both high-temperature/high-pressure and analogue experiments.

6.5. CONCLUSIONS AND OUTLOOK FOR FUTURE RESEARCH

We have reviewed progress in understanding magma mixing and mingling, focusing on volatile and crystal controls on mingling processes. Although field and petrologic observations of mixed and mingled products are numerous, models of these processes do not yet include the full range of observed complexities. In particular, conceptual models derived from observations (Browne et al., 2006a; Clynne, 1999; Plail et al., 2014; Tepley et al., 1999;) suggest very different dynamics to those from numerical models (Andrews & Manga, 2014; Bergantz et al., 2015; Montagna et al., 2015). To resolve this discrepancy, several key questions need to be addressed:

1. How do mixing and mingling occur within the framework of crystal mushes, and how does the volume fraction of crystals control the interaction dynamics?
2. How do volatiles, both exsolved and dissolved, affect mixing and mingling? What is the relative importance of chemical quenching (due to volatile diffusion) versus thermal quenching (due to heat diffusion)?
3. How much mingling/mixing takes place during intrusion of the mafic magma compared to that driven by later processes such as convection in the host or the buoyant rise of vesicular mafic/hybrid magma?
4. How does latent heat, released from crystallization of the mafic component and absorbed by melting of the felsic component, affect the mixing and mingling process? Latent heat release may have a strong local effect in a dynamic system but is not evaluated, for example, in isothermal experiments.
5. To what extent are mafic injections spatially limited, for example, dikes, and under what conditions might they affect the entire intrusion?
6. If magma storage regions undergo repeated replenishments with occasional eruptions, what factors determine if a particular injection leads to an eruption?

Only by combining field and analytical observations with experimental (analogue and natural materials) and numerical modeling can we start to address these challenges.

ACKNOWLEDGMENTS

PAJ was supported by the National Environmental Research Council (grant number NE/K500823/1) and thanks Alison Rust, Steve Tait, and Julie Oppenheimer for valuable discussions. The authors acknowledge Stuart Kearns, Ben Buse (University of Bristol), Pierre Vonlanthen, and Martin Robyr (University of Lausanne) for their support during SEM and EPMA analyses. MP acknowledges funds from the Ambizione Fellowship (PZ00P2_168166) sponsored by the Swiss National Science Foundation, which supported the bachelor's thesis of AS. KVC acknowledges funding from the AXA Research Fund and a Wolfson Merit Award from the Royal Society.

REFERENCES

Acosta-Vigil, A., London, D., & Morgan, G. B., VI (2012). Chemical diffusion of major components in granitic liquids: Implications for the rates of homogenization of crustal melts. *Lithos*, *153*, 308–323. https://doi.org/10.1016/j.lithos.2012.06.017

Adkins, P. (1983). *Equilibrium Thermodynamics*. Cambridge: Cambridge University Press.

Andrews, B. J., & Manga, M. (2014). Thermal and rheological controls on the formation of mafic enclaves or banded pumice. *Contributions to Mineralogy and Petrology*, *167*, 961. https://doi.org/10.1007/s00410-013-0961-7

Akal, C., & Helvaci, C. (1999). Mafic microgranular enclaves in the Kozak Granodiorite, Western Anatolia. *Turkish Journal of Earth Sciences*, *8*, 1–17.

Asimow, P. D., & Ghiorso, M. S. (1998). Algorithmic modifications extending MELTS to calculate subsolidus phase relations. *American Mineralogist*, *83*(9-10), 1127–1132. https://doi.org/10.2138/am-1998-9-1022

Bachmann, O., & Huber, C. (2016). Silicic Magma reservoirs in the Earth's Crust. *American Mineralogist*, *101*, 2377–2404. http://dx.doi.org/10.2138/am-2016-5675

Bacon, C. (1986). Magmatic inclusions in silicic and intermediate volcanic rocks. *Journal of Geophysical Research*, *91*(B6), 6091–6112. https://doi.org/10.1029/JB091iB06p06091

Bacon, C. R. (1989). Crystallization of accessory phases in magmas by local saturation adjacent to phenocrysts. *Geochimica et Cosmochimica Acta*, *53*(5), 1055–1066. https://doi.org/10.1016/0016-7037(89)90210-X

Bacon, C. R., & Metz, J. (1984). Magmatic inclusions in rhyolites, contaminated basalts, and compositional zonation beneath the Coso volcanic field. *Contributions to Mineralogy and Petrology*, *85*, 346–365. https://doi.org/10.1007/BF01150292

Barclay, J., Herd, R. A., Edwards, B. R., Christopher, T., Kiddle, E. J., Plail, M., & Donovan, A. (2010). Caught in the act: Implications for the increasing abundance of mafic enclaves during the recent eruptive episodes of the Soufrière Hills Volcano, Montserrat. *Geophysical Research Letters*, *37*, L00E09. https://doi.org/10.1029/2010GL042509

Bateman, R. (1995). The interplay between crystallisation, replenishment and hybridization in large felsic magma chambers. *Earth-Science Reviews*, *39*(1–2), 91–106. https://doi.org/10.1016/0012-8252(95)00003-S

Baxter, S., & Feely, M. (2002). Magma mixing and mingling textures in granitoids: examples from the Galway Granite, Connemara, Ireland. *Mineralogy and Petrology*, *76*(1–2), 63–74. https://doi.org/10.1007/s007100200032

Bergantz, G. W. (2000). On the dynamics of magma mixing by reintrusion: Implications for pluton assembly processes. *Journal of Structural Geology*, *22*, 1297–1309. https://doi.org/10.1016/S0191-8141(00)00053-5

Bergantz, G. W., Schleicher, J. M., & Burgisser, A. (2015). Open system dynamics and mixing in magma mushes. *Nature Geoscience*, *8*, 793–797. https://doi.org/10.1038/ngeo2534

Bergantz, G. W., Schleicher, & J. M., Burgisser, A. (2017), On the kinematics and dynamics of crystal-rich systems, *Journal of Geophysical Research Solid Earth, v. 122*, doi:10.1002/2017JB014218

Berlo, K., Blundy, J., Turner, S., & Hawkesworth, C. (2007). Textural and chemical variations in plagioclase phenocrysts from the 1980 eruptions of Mount St. Helens, USA. *Contributions to Mineralogy and Petrology*, *154*(3), 291–308. https://doi.org/10.1007/s00410-007-0194-8

Bindeman, I. N., & Davis A. M. (1999). Convection and redistribution of alkalis and trace elements during the mingling of basaltic and rhyolitic melts. *Petrology*, *7*(1), 91–101.

Bindeman, I. N., & Melnik, O. E. (2016). Zircon survival, rebirth and recycling during crustal melting, magma crystallization, and mixing based on numerical modelling. *Journal of Petrology*, *57*(3), 437–460. https://doi.org/10.1093/petrology/egw013

Bindeman, I. N., & Simakin, A. G. (2014). Rhyolites – Hard to produce, but easy to recycle and sequester: Integrating microgeochemical observations and numerical models. *Geosphere*, *10*(5), 930–957. https://doi.org/10.1130/GES00969.1

Bishop, A. C., & French, W. J. (1982). Nature and origin of meladiorite layers in northern Guernsey, Channel Islands. *Mineralogical Magazine*, *46*(340), 301–321. https://doi.org/10.1180/minmag.1982.046.340.03

Blake, D. H., Elwell, R. W. D., Gibson, I. L., Skelhorn, R. R., & Walker, G. P. L. (1965). Some relationships resulting from the intimate association of acid and basic magmas. *Quarterly Journal of the Geological Society*, *121*(1-4),31–49.

Blake, S., & Fink J. H. (1987). The dynamics of magma withdrawal from a density stratified dyke. *Earth and Planetary Science Letters*, *85*(4), 516–524. https://doi.org/10.1016/0012-821X(87)90145-2

Blundy, J. D., & Sparks, R. S. J. (1992). Petrogenesis of mafic inclusions in granitoids of the Adamello Massif, Italy. *Journal of. Petrology*, *33*(5), 1039–1104. https://doi.org/10.1093/petrology/33.5.1039

Borisova, A. Y., Toutain, J., Dubessy, J., Pallister, J., Zwick, A., & Salvi, S. (2014). H_2O-CO_2-S fluid triggering the 1991 Mount Pinatubo climactic eruption (Philippines). *Bulletin of Volcanology*, *76*, 800. https://doi.org/10.1007/s00445-014-0800-3

Botcharnikov, R. E., Holtz, F., Almeev, R. R., Sato, H., & Behrens, H. (2008). Storage conditions and evolution of andesitic magma prior to the 1991-1995 eruption of Unzen volcano: Constraints from natural sample and phase equilibria experiments. *Journal of Volcanology and Geothermal Research*, *175*(1–2), 168–180. https://doi.org/10.1016/j.jvolgeores.2008.03.026

Bottinga, Y., Kudo, A., & Weill, D. (1966). Some observations on oscillatory zoning and crystallisation of magmatic plagioclase. *American Mineralogist*, *51*(5–6), 792–806.

Browne, B. L., Eichelberger, J. C., Patino, L. C., Vogel, T. A., Dehn, J., Uto, K., & Hoshizumi, H. (2006a). Generation of Porphyritic and equigranular mafic enclaves during magma recharge events at Unzen Volcano, Japan. *Journal of Petrology*, *47*(2), 301–328. https://doi.org/10.1093/petrology/egi076

Browne, B. L., Eichelberger, J. C., Patino, L. C., Vogel, T. A., Dehn, J., Uto, K., & Hoshizumi, H. (2006b). Magma mingling as indicated by texture and Sr/Ba ratios of plagioclase phenocrysts from Unzen volcano, SW Japan. *Journal of Volcanology and Geothermal Research*, *154*(1–2), 103–116. https://doi.org/10.1016/j.jvolgeores.2005.09.022

Bunsen, R. W. (1851). Über die Processe des vulkanischen Gesteinsbildungen Islands. *Annalen der Physik und Chemie* (*Dritte Reihe*), *83*, 197–272.

Campbell, I. H., & Turner, J. S. (1986). The influence of viscosity on fountains in Magma chambers. *Journal of. Petrology*, *27*(1), 1–30. https://doi.org/10.1093/petrology/27.1.1

Campbell, I. H., & Turner, J. S. (1989). Fountains in Magma chambers. *Journal of Petrology*, *30*(4), 885–923. https://doi.org/10.1093/petrology/30.4.885

Cantagrel, J., Didier, J., & Gourgaud, A. (1984). Magma mixing: Origin of intermediate rocks and enclaves from volcanism to plutonism. *Physics of the Earth and Planetary Interiors*, *35*(1–3), 63–76. https://doi.org/10.1016/0031-9201(84)90034-7

Cardoso, S. S. S., & Woods. A. W. (1996). Interfacial turbulent mixing in stratified magma reservoirs. *Journal of Volcanology and Geothermal Research*, *73*(3–4), 157–175. https://doi.org/10.1016/0377-0273(96)00028-5.

Caricchi, L., Burlini, L., Ulmer, P., Gerya, T., Vassalli, M., & Papale, P. (2007). Non-Newtonian rheology of crystal-bearing magmas and implications for magma ascent dynamics. *Earth and Planetary Science Letters*, *264*(3–4), 402–419. https://doi.org/10.1016/j.epsl.2007.09.032

Caricchi, L., Annen, C., Rust, A., & Blundy, J. (2012). Insights into the mechanisms and timescales of pluton assembly from deformation patterns of mafic enclaves. *Journal of Geophysical Research*, *117, B11206*. https://doi.org/10.1029/2012JB009325

Caroff, M., Coint, N., Hallot, E., Hamelin, C., Peucat, J. & Charreteur, G. (2011). The mafic-silicic layered intrusions of Saint-Jean du Doigt (France) and North Guernsey (Channel Islands), Armorican Massif: Gabbro-diorite layering and mafic cumulate-pegmatoid association. *Lithos*, *125*(1–2), 675–692. https://doi.org/10.1016/j.lithos.2011.03.019

Carrara, A., Burgisser, A., & Bergantz, G. W. (2019). Lubrication effects on magmatic mush dynamics. *Journal of Volcanology and Geothermal Research*, *380*, 19–30. https://doi.org/10.1016/j.jvolgeores.2019.05.008

Carrara, A., Burgisser, A. & Bergantz, G. W. (2020). The architecture of intrusions in magmatic mush. *Earth and Planetary*

Science Letters, *549*, 116539. https://doi.org/10.1016/j.epsl.2020.116539

Carroll, M. R., & Wyllie, P. J. (1989). Granite melt convecting in an experimental micro-magma chamber at 1050 °C, 15 kbar. *European Journal of Mineralogy*, *1*(2), 249–260. DOI: 10.1127/ejm/1/2/0249

Carslaw, H. S., & Jaeger, J. C. (1959). *Conduction of Heat in Solids*. Oxford: Clarendon Press.

Cashman, K., & Blundy, J. (2000). Degassing and crystallization of ascending andesite and dacite. *Philosophical Transactions of the Royal Society A*, *358*(1770), 1487–1513. https://doi.org/10.1098/rsta.2000.0600

Cashman, K., & Blundy, J. (2013). Petrological cannibalism: The chemical and textural consequences of incremental magma body growth. *Contributions to Mineralogy and Petrology*, *166*(3), 703–729. https://doi.org/10.1007/s00410-013-0895-0

Cashman, K. V., Sparks, R. S. J., & Blundy, J. B. (2017). Vertically extensive and unstable magmatic systems: A unified view of igneous processes. *Science*, *355*(6331), eeag3055. DOI: 10.1126/science.aag3055

Chamberlain, K. J., Morgan, D. J., & Wilson, C. J. N. (2014). Timescales of mixing and mobilisation in the Bishop Tuff magma body: Perspectives from diffusion chronometry. *Contributions to Mineralogy and Petrology*, *168*, 1034. https://doi.org/10.1007/s00410-014-1034-2

Choe, W., & Jwa, Y. (2004). Petrological and geochemical evidences for magma mixing in the Palgongsan Pluton. *Geosciences Journal*, *8*, 343–354. https://doi.org/10.1007/BF02910470

Christopher, T. E., Humphreys, M. C. S., Barclay, J., Genereau, K., De Angelis, S. M. H., Plail, M., & Donovan, A. (2014). Petrological and geochemical variation during the Soufrière Hills eruption, 1995 to 2010. *Geological Society London Memoirs*, *39*, 317–342. https://doi.org/10.1144/M39.17

Clynne, M. A. (1990). Stratigraphic, lithogic and major element geochemical constrains on magmatic evolution at Lassen Volcanic Center, California. *Journal of Geophysical Research*, *95*(B12), 19651–19669. https://doi.org/10.1029/JB095iB12p19651

Clynne, M. A. (1999). A complex magma mixing origin for rocks erupted in 1915, Lassen Peak, California. *Journal of Petrology*, *40*(1), 105–132. https://doi.org/10.1093/petroj/40.1.105

Coombs, M. L., Eichelberger, J. C., & Rutherford, M. J. (2000). Magma storage and mixing conditions for the 1953-1974 eruptions of Southwest Trident volcano, Katmai National Park, Alaska. *Contributions to Mineralogy and Petrology*, *140*(1), 99–118. https://doi.org/10.1007/s004100000166

Coombs, M. L., Eichelberger, J. C., & Rutherford, M. J. (2002). Experimental and textural constraints on mafic enclave formation in volcanic rocks. *Journal of Volcanology and Geothermal Research*, *119*(*1–4*), 125–144. https://doi.org/10.1016/S0377-0273(02)00309-8

Cooper, K. M. (2017). What does a magma reservoir look like? The "Crystal's-Eye" view. *Elements*, *13*(1), 23–29. https://doi.org/10.2113/gselements.13.1.23

Cordonnier, B., Hess, K.-U., Lavallée, Y., & Dingwell, D. B. (2009). Rheological properties of dome lavas: Case study of Unzen volcano. *Earth and Planetary Science Letters*, *279*(3–4), 263– 272, doi:10.1016/j.epsl.2009.01.014.

d'Ars, J. B., & Davy, P. (1991). Gravity instabilities in magma chambers: Rheological modelling. *Earth and Planetary Science Letters*, *105*(1–3), 319–329. https://doi.org/10.1016/0012-821X(91)90140-D

Davidson, J. P., Morgan, D. J., Charlier, B. L. A., Harlou, R., & Hora, J. M. (2007). Microsampling and isotopic analysis of igneous rocks: Implications for the study of magmatic systems. *Annual Review of Earth and Planetary Sciences*, *35*, 273–311. https://doi.org/10.1146/annurev.earth.35.031306.140211

De Campos, C. P., Dingwell, D. B., & Fehr, K. T. (2004). Decoupled convection cells from mixing experiments with alkaline melts from Phlegrean Fields. *Chemical Geology*, *213*, 227–251. https://doi.org/10.1016/j.chemgeo.2004.08.045

De Campos, C. P., Dingwell, D. B., Perugini, D., Civetta, L., & Fehr, T. K. (2008). Heterogeneities in magma chambers: Insights from the behaviour of major and minor elements during mixing experiments with natural alkaline melts. *Chemical Geology*, *256*, 131–145. https://doi.org/10.1016/j.chemgeo.2008.06.034

De Campos, C. P., Perugini, D., Ertel-Ingrisch, W., Dingwell, D. B., & Poli, G. (2011). Enhancement of magma mixing efficiency by chaotic dynamics: An experimental study. *Contributions to Mineralogy and Petrology*, *161*, 863–881. https://doi.org/10.1007/s00410-010-0569-0

Diller, J. S. (1891). A late volcanic eruption in northern California and its peculiar lava. *Bulletin of the U.S. Geological Survey*, 79.

Dirksen, O., Humphreys, M. C. S., Pletchov, P., Melnik, O., Demyanchuk, Y. Sparks, R. S. J., & Mahony, S. (2006). The 2001-2004 dome-forming eruption of Shiveluch volcano, Kamchatka: Observation, petrological investigation and numerical modelling. *Journal of Volcanology and Geothermal Research*, *155*(3–4), 201–226. https://doi.org/10.1016/j.jvolgeores.2006.03.029

D'Lemos, R. S. (1986). Interaction between co-existing magmas: Field evidence from the Cobo Granite and the Bordeaux Diorite Complex, north-west Guernsey, Channel Islands. *Proceedings of the Ussher*, *6*, 323–329.

D'Lemos, R. S. (1987). *Relationships between the Cobo Granite and the Bordeaux Diorite Complex, Guernsey*. (Doctoral dissertation). Retrieved from EThOS(https://ethos.bl.uk/OrderDetails.do?uin=uk.bl.ethos.304090) Oxford: Oxford Brookes University.

D'Lemos, R. S. (1996). Mixing between granitic and dioritic crystal mushes, Guernsey, Channel Islands, UK. *Lithos*, *38*(3–4), 233–257. https://doi.org/10.1016/0024-4937(96)00007-2

Druitt, T. H., Costa, F., Deloule, E., Dungan, M., & Scaillet, B. (2012). Decadal to monthly timescales of magma transfer and reservoir growth at a caldera volcano. *Nature*, *482*, 77–80. https://doi.org/10.1038/nature10706

Edmonds, M., Kohn, S. C., Hauri, E. H., Humphreys, M. C. S., & Cassidy, M. (2016). Extensive, water-rich magma reservoir beneath southern Montserrat. *Lithos*, *252–253*, 216–233. https://doi.org/10.1016/j.lithos.2016.02.026

Eichelberger, J. C. (1980). Vesiculation of mafic magma during the replenishment of silicic magma reservoirs. *Nature*, *288*, 446–450. https://doi.org/10.1038/288446a0

Einstein, A. (1906). Eine neue Bestimmung der Molekuldimensionen. *Annals of Physics*, *324*(2), 289–306. https://doi.org/10.1002/andp.19063240204

Elwell, R. W. D., Skelhorn, R. R., & Drysdall, A. R. (1960). Inclined dioritic pipes in the diorites of Guernsey. *Geological Magazine*, *97*(2), 89–105. https://doi.org/10.1017/S0016756800061215

Elwell, R. W. D., Skelhorn, R. R., & Drysdall, A. R. (1962). Net-veining in the diorite of northeast Guernsey, Channel Islands. *Journal of Geology*, *70*(2), 215–226. https://doi.org/10.1086/626810

Farrell, J., Smith, R. B., Husen, S., & Diehl, T. (2014). Tomography from 26 years of seismicity revealing that the spatial extent of the Yellowstone crustal magma reservoir extends well beyond the Yellowstone caldera. *Geophysical Research Letters*, *41*(9), 3068–3073. https://doi.org/10.1002/2014GL059588

Fenner, C. N. (1926). The Katmai magmatic province. *Journal of Geology*, *34*(7 Part 2), 673–772. https://doi.org/10.1086/623350

Folch, A., & Martí, J. (1998). The generation of overpressure in felsic magma chambers by replenishment. *Earth and Planetary Science Letters*, *163*, 301–314. https://doi.org/10.1016/S0012-821X(98)00196-4

Foley, F. V., Pearson, N. J., Rushmer, T., Turner, S., & Adam, J. (2012). Magmatic evolution and magma mixing of Quaternary Adakites at Solander and Little Solander islands, New Zealand. *Journal of Petrology*, *54*(4), 703–744. https://doi.org/10.1093/petrology/egs082

Fomin, S., & Plechov, P. Y. (2012). Exchange between Mafic Enclaves and Host Magma: Case of 1991-1995 Mount Unzen Eruption. *Journal of Earth Science and Engineering*, *2*, 631–635.

Francalanci, L., Avanzinelli, R., Nardini, I., Tiepolo, M., Davidson, J. P., & Vannucci, R. (2011). Crystal recycling in the steady-state system of the active Stromboli volcano: A 2.5 ka story inferred from in situ Sr-isotope and trace element data. *Contributions to Mineralogy and Petrology*, *163*, 109–131. https://doi.org/10.1007/s00410-011-0661-0

Frost, T. P., & Mahood, G. A. (1987). Field, chemical and physical constraints on mafic-felsic interaction in the Lamarck Granodiorite, Sierra Nevada, California. *Geological Society of America Bulletin*, *99*(2), 272–291. https://doi.org/10.1130/0016-7606(1987)99%3C272:FCAPCO%3E2.0.CO;2

Ghiorso, M. S., & Sack, R. O. (1995). Chemical mass transfer in magmatic processes IV. A revised and internally consistent thermodynamic model for the interpolation and extrapolation of liquid-solid equilibria in magmatic systems at elevated temperatures and pressures. *Contributions to Mineralogy and Petrology*, *119*, 197–212. https://doi.org/10.1007/BF00307281

Giordano, D., Russel, J. K., & Dingwell, D. B. (2008). Viscosity of magmatic liquids: A model. *Earth and Planetary Science Letters*, *271*, 123–134. https://doi.org/10.1016/j.epsl.2008.03.038

Gourgaud, A., & Maury, R. C. (1984). Magma mixing in Alkaline Series: An Example from Sancy Volcano (More-Dore, Massif Central, France). *Bulletin of Volcanology*, *47*(4), 827–848. https://doi.org/10.1007/BF01952346

Grasset, O., & Albarède, F. (1994). Hybridization of mingling magmas with different densities. *Earth and Planetary Science Letters*, *121*(3–4), 327–332. https://doi.org/10.1016/0012-821X(94)90075-2

Grove, T. L., Baker, M. B., & Kinzler, R. J. (1984). Coupled CaAl-NaSi diffusion in plagioclase feldspar: Experiments and applications to cooling rate speedometry. *Geochimica et Cosmochimica Acta*, *48*(10), 3785–3793. https://doi.org/10.1016/0016-7037(84)90391-0

Harker, A. (1909). *The Natural History of Igneous Rocks*. Cambridge: Cambridge University Press.

Heiken, G., & Eichelberger, J. C. (1980). Eruptions at Chaos Crags, Lassen Volcanic National Park, California. *Journal of Volcanology and Geothermal Research*, *7*(3–4), 443–481. https://doi.org/10.1016/0377-0273(80)90042-6

Hibbard, M. J. (1981). The magma mixing origin of mantled feldspars. *Contributions to Mineralogy and Petrology*, *76*(2), 158–170. https://doi.org/10.1007/BF00371956

Hiess, J., Cole, J. W., & Spinks, K. D. (2007). Influence of the crust and crustal structure on the location and composition of high-alumina basalts of the Taupo Volcanic Zone, New Zealand. *New Zealand Journal of Geology and Geophysics*, *50*(4), 327–342. https://doi.org/10.1080/00288300709509840

Hildreth, W. (1981). Gradients in silicic magma chambers: Implications for lithospheric magmatism. *Journal of Geophysical Research*, *86*, 10153–10192. https://doi.org/10.1029/JB086iB11p10153

Hildreth, W. (2004). Volcanological perspectives on Long Valley, Monmouth Mountain, and Mono Craters: Several contiguous but discrete systems. *Journal of Volcanology and Geothermal Research*, *136*(3–4), 169–198. https://doi.org/10.1016/j.jvolgeores.2004.05.019

Hodge, K. F., Carazzo, G., & Jellinek, A. M. (2012). Experimental constraints on the deformation and breakup of injected magma. *Earth and Planetary Science Letters*, *325–326*, 52–62. https://doi.org/10.1016/j.epsl.2012.01.031

Hodge, K. F., & Jellinek, A. M. (2012). Linking enclave formation to magma rheology. *Journal of Geophysical Research*, *117*(B10), 208. https://doi.org/10.1029/2012JB009393

Hodge, K. F. & Jellinek, A., M. (2020). The Influence of Magma Mixing on the Composition of Andesite Magmas and Silicic Eruption Style. *Geophysical Research Letters*, *47*(13), e2020GL087439. https://doi.org/10.1029/2020GL087439

Holtz, F., Sato, H., Lewis, J., Behrens, H., & Nakada, S. (2005). Experimental Petrology of the 1991-1995 Unzen Dacite, Japan. Part I: Phase relations, Phase Composition and Pre-eruptive Conditions. *Journal of Petrology*, *46*(2), 319–337. https://doi.org/10.1093/petrology/egh077

Hornby, A. J., Kendrick, J. E., Lamb, O. D., Hirose, T., De Angelis, S., von Aulock, F. W., et al. (2015). Spine growth and seismogenic faulting at Mt. Unzen, Japan. *Journal of Geophysical Research: Solid Earth*, *120*, 4034– 4054. doi: 10.1002/2014JB011660.

Hoshizumi, H., Uto, K., & Watanabe, K. (1999). Geology and eruptive history of Unzen volcano, Shimbara Peninsula, Kyushu, SW Japan. *Journal of Volcanology and Geothermal Research.*, *89*(1-4), 81–94. https://doi.org/10.1016/S0377-0273(98)00125-5

Humphreys, M. C. S., Blundy, J. D., & Sparks, R. S. J. (2006). Magma evolution and open-system processes at Shiveluch Volcano: Insights from phenocryst zoning. *Journal of*

Petrology, *47*(12), 2303–2334. https://doi.org/10.1093/petrology/egl045

Humphreys, M. C. S., Christopher, T., & Hards, V. (2009). Microlite transfer by disaggregation of mafic inclusions following magma mixing at Soufrière Hills volcano, Montserrat. *Contributions to Mineralogy and Petrology*, *157*(5), 609–624. https://doi.org/10.1007/s00410-008-0356-3

Humphreys, M. C. S., Edmonds, M., Christopher, T., & Hards, V. (2010). Magma hybridisation and diffusive exchange recorded in heterogeneous glasses from Soufrière Hills Volcano, Montserrat. *Geophysical Research Letters*, *37*(19). https://doi.org/10.1029/2009GL041926

Huppert, H. E., Sparks, R. S. J. S., & Turner, J. S. (1984). Some effects of viscosity on the dynamics of replenished magma chambers. *Journal of Geophysical Research*, *89*(B8), 6857–6877. https://doi.org/10.1029/JB089iB08p06857

Huppert, H. E., Sparks, R. S. J., Whitehead, J. A., & Hallworth, M. A. (1986). Replenishment of magma chambers by light inputs. *Journal of Geophysical Research*, *91*(B6), 6113–6122. https://doi.org/10.1029/JB091iB06p06113

Iddings, J. P. (1890). A group of volcanic rocks from the Tewan Mountains, New Mexico, and on the occurrence of primary quartz in certain basalts. *Bulletin of the U.S. Geological Survey*, 66.

Ishii, M., & Zuber, N. (1979). Drag coefficient and relative velocity in bubbly, droplet or particulate flows. *AiChE Journal*, *25*(5), 843–855. https://doi.org/10.1002/aic.690250513

Jackson, M. D., & Cheadle, M. J. (1998). A continuum model for the transport of heat, mass and momentum in a deformable, multicomponent mush, undergoing solid-liquid phase change. *International Journal of Heat and Mass Transfer*, *41*(8-9), 1035–1048. https://doi.org/10.1016/S0017-9310(97)00197-X

Janoušek, C., Braithwaite, C. J. R., Bowes, D. R., & Gerdes, A. (2004). Magma-mixing in the genesis of Hercynian calc-alkaline granitoids: An integrated petrographic and geochemical study of the Sázava intrusion, Central Bohemian Pluton, Czech Republic. *Lithos*, *78*(1-2), 67–99. https://doi.org/10.1016/j.lithos.2004.04.046

Jarvis, P. A., Mader, H. M., Huppert, H. E., Cashman, K. V., & Blundy, J. D. (2019). Experiments on the low-Reynolds number settling of a sphere through a fluid interface. *Physical Review Fluids*, *4*, 024003. https://doi.org/10.1103/PhysRevFluids.4.024003

Judd, J. W. (1893). On composite dykes in Arran. *Quarterly journal of the Geological Society of London*, *49*, 536–565. https://doi.org/10.1144/GSL.JGS.1893.049.01-04.63

Kerr, R. C. (1994). Melting driven by vigorous compositional convection. *Journal of Fluid Mechanics*, *280*, 255–285. https://doi.org/10.1017/S0022112094002922

Kim, J., Shin, K., & Lee, J. D. (2002). Petrographical study on the Yucheon granite and its enclaves. *Geosciences Journal*, *6*, 289–302. https://doi.org/10.1007/BF03020614

Kim, J., Son, M., Hwang, B., Shin, K., Cho, H., & Sohn, Y. K. (2014). Double injection events of mafic magmas into supersolidus Yucheon granites to produce two types of mafic enclaves in the Cretaceous Gyeongsang Basin, SE Korea. *Mineralogy and Petrology*, *108*(2), 207–229. https://doi.org/10.1007/s00710-013-0296-0

King, B. C. (1964). The nature of basic igneous rocks and their relations with associated acid rocks. Part IV. *Science Progress*, *52*(206), 282–292.

Koyaguchi, T., & Blake, S. (1989). The dynamics of magma mixing in a rising magma batch. *Bulletin of Volcanology*, *52*(2), 127–137. https://doi.org/10.1007/BF00301552

Kouchi, A., & Sunagawa, I. (1983). Mixing basaltic and dacitic magmas by forced convection. *Nature*, *304*, 527–528. https://doi.org/10.1038/304527a0

Kouchi, A., & Sunagawa, I. (1985). A model for mixing basaltic and dacitic magmas as deduced from experimental data. *Contributions to Mineralogy and Petrology*, *89*(1), 17–23. https://doi.org/10.1007/BF01177586

Kumar, S., & Rino, V. (2006). Mineralogy and geochemistry of microgranular enclaves in Paleoproterozoic Malanjkhand granitoids, central India: Evidences of magma mixing, mingling and chemical equilibration. *Contributions to Mineralogy and Petrology*, *152*, 591–609. https://doi.org/10.1007/s00410-006-0122-3

Larsen, L. L., & Smith, E. I. (1990). Mafic enclaves in the Wilson Ridge Pluton, Northwestern Arizona: Implications for the generation of a Calc-Alkaline Intermediate Pluton in an extensional environment. *Journal of Geophysical Research*, *95*(B11), 17693–17716. https://doi.org/10.1029/JB095iB11p17693

Laumonier, M., Scaillet, B., Arbaret, L., & Champallier, R. (2014). Experimental simulation of magma mixing at high pressure. *Lithos*, *196–197*, 281–300. https://doi.org/10.1016/j.lithos.2014.02.016

Laumonier, M., Scaillet, B., Arbaret, L., Andújar, J., & Champallier, R. (2015). Experimental mixing of hydrous magmas. *Chemical Geology*, *418*, 158–170. https://doi.org/10.1016/j.chemgeo.2015.10.031

Leonard, G. S., Cole, J. W., Nairn, I. A., & Self, S. (2002). Basalt triggering of the c. AD 1305 Kaharoa rhyolite eruption, Tarawere Volcanic Complex, New Zealand. *Journal of Volcanology and Geothermal Research*, *115*(3-4), 461–486. https://doi.org/10.1016/S0377-0273(01)00326-2

Lesher, C. E. (1994) Kinetics of Sr and Nd exchange in silicate liquids: Theory, experiments, and applications to uphill diffusion, isotopic equilibration, and irreversible mixing of magmas. *Journal of Geophysical Research*, *99*(B5), 9585–9604. https://doi.org/10.1029/94JB00469

Lipman, P., Dungan, M., & Bachmann, O. (1997). Comagmatic granophyre granite in the Fish Canyon Tuff, Colorado: Implications for magma-chamber processes during a large ash-flow eruption. *Geology*, *25*(10), 915–918. https://doi.org/10.1130/0091-7613(1997)025%3C0915:CGGITF%3E2.3.CO;2

Litvinovsky, B. A., Zanvilevich, A. N., & Katzir, Y. (2012). Formation of composite dykes by contact remelting and magma mingling: The Shaluta pluton, Transbaikalia (Russia). *Journal of Asian Earth Sciences*, *60*, 18–30. https://doi.org/10.1016/j.jseaes.2012.07.018

Mader, H. M., Llewellin, E. W., & Mueller, S. P. (2013). The rheology of two phase magmas: A review and analysis. *Journal of Volcanology and Geothermal Research*, *257*, 135–158. https://doi.org/10.1016/j.jvolgeores.2013.02.014

Martel, C., Ali, R. A., Poussineau, S., Gourgaud, A., & Pichavant, M. (2006). Basalt-inherited microlites in silicic magmas: Evidence for Mount Pelée (Martinique, French West Indies), *Geology*, *34*, 905–908. https://doi.org/10.1130/G22672A.1

Martin, V. M, Pyle, D. M., & Holness, M. B. (2006). The role of crystal frameworks in the preservation of enclaves during magma mixing. *Earth and Planetary Science Letters*, *248*(3–4), 787–799. https://doi.org/10.1016/j.epsl.2006.06.030

Matthews, S. J., Jones, A. P., & Bristow, C. S. (1992). A simple magma-mixing model for sulphur behaviour in calc-alkaline volcanic rocks: Mineralogical evidence from Mount Pinatubo 1991 eruption. *Journal of the Geological Society*, *149*, 863–866. https://doi.org/10.1144/gsjgs.149.6.0863

Matthews, S. J., Jones, A. P., & Gardeweg, M. C. (1994). Lascar Volcano, Northern Chile; Evidence for steady-state disequilibrium. *Journal of Petrology*, *35*(2), 401–432. https://doi.org/10.1093/petrology/35.2.401

McCormick Kilbride, B., Biggs, J., & Edmonds, M. (2016). Observing eruptions of gas-rich compressible magmas from space. *Nature Communications*, *7*, 13744. https://doi.org/10.1038/ncomms13744

McIntire, M. Z., Bergantz, G. W., & Schleicher, J. M. (2019), On the hydrodynamics of crystal clustering, *Philosophical Transactions of the Royal Society A*, *377*(2139), 20180015. https://doi.org/10.1098/rsta.2018.0015

Miller, D. S., & Smith, R. B. (1999). P and S velocity structure of the Yellowstone volcanic field from local earthquake and controlled source tomography. *Journal of Geophysical Research*, *104*(B7), 15105–15121. https://doi.org/10.1029/1998JB900095

Mollo, S., Putirka, K., Iezzi, G., Del Gaudio, P., & Scarlato, P. (2011). Plagiocalse-melt (dis)equilibrium due to cooling dynamics: Implications for thermometry, barometry and hygrometry, *Lithos*, *125*, 221–235. https://doi.org/10.1016/j.lithos.2011.02.008

Montagna, C. P., Papale, P., & Longo, A. (2015). Timescales of mingling in shallow magmatic reservoirs. *Geol. Soc. Spec. Pub.*, *422*, 131–140. https://doi.org/10.1144/SP422.6

Morgan, G. B., Acosta-Vigil, A., & London, D. (2008) Diffusive equilibration between hydrous metaluminous-peraluminous haplogranite liquid couples at 200 MPa (H_2O) and alkali transport in granitic liquids. *Contributions to Mineralogy and Petrology*, *155*(2), 257–269. https://doi.org/10.1007/s00410-007-0242-4

Morgavi, D., Arienzo, I., Montagna, C., Perugini, D., & Dingwell, D. B. (2019). Magma mixing: History and dynamics of an eruption trigger. In *Volcanic Unrest* (123–137). Springer, Cham.

Morgavi, D., Arzilli, F., Pritchard, C., Perugini, D., Mancini, L., Larson, P., & Dingwell, D. B. (2016). The Grizzy Lake complex (Yellowstone Volcano, USA): Mixing between basalt and rhyolite unravelled by microanalysis and X-ray microtomography. *Lithos*, *260*, 457–474. https://doi.org/10.1016/j.lithos.2016.03.026

Morgavi, D., Perugini, D., De Campos, C. P., Ertl-Ingrisch, W., Lavalée, Y., Morgan, L. & Dingwell, D. B. (2013). Interactions between rhyolitic and basaltic melts unraveled by chaotic mixing experiments. *Chemical Geology*, (*346*), 199–212. https://doi.org/10.1016/j.chemgeo.2012.10.003

Morse, S. A. (1984). Cation diffusion in Plagioclase Feldspar. *Science*, *225*(4661), 504–505. DOI: 10.1126/science.225.4661.504

Mueller, S., Llewellin, E. W., & Mader, H. M. (2009). The rheology of suspensions of solid particles. *Proceedings of the Royal Society of London*, *466*(2116), 1201–1228. https://doi.org/10.1098/rspa.2009.0445

Murphy, M. D., Sparks, R. S. J., Barclay, J., Carroll, M. R., & Brewer, T. S. (2000). Remobilisation of Andesite Magma by Intrusion of Mafic Magma at the Soufrière Hills Volcano, Montserrat, West Indies. *Journal of Petrology*, *41*(1), 21–42. https://doi.org/10.1093/petrology/41.1.21

Nakada, S., & Fujii, T. (1993). Preliminary report on the activity at Unzen Volcano (Japan), November 1990–November 1991: Dacite lava domes and pyroclastic flows. *Journal of Volcanology and Geothermal Research*, *54*(3-4), 319–333. https://doi.org/10.1016/0377-0273(93)90070-8

Nakada, S., & Motomura, Y. (1999). Petrology of the 1991–1995 eruption at Unzen: Effusion pulsation and groundmass crystallization. *Journal of Volcanology and Geothermal Research*, *89*(1-4), 173–196. https://doi.org/10.1016/S0377-0273(98)00131-0

Nakada, S., Shimizu, H., & Ohta, K. (1999). Overview of the 1991-1995 eruption at Unzen Volcano. *Journal of Volcanology and Geothermal Research*, *89*(1-4), 1–22. https://doi.org/10.1016/S0377-0273(98)00118-8

Nakamura, E. &. Kushiro, I. (1998). Trace element diffusion in jadeite and diopside melts at high pressures and its geological implication. *Geochimica et Cosmochimica Acta*, *62*(18), 3151–3160. https://doi.org/10.1016/S0016-7037(98)00223-3

Nakamura, M., & Shimakita, S. (1998). Dissolution origin and syn-entrapment compositional change of melt inclusions in plagioclase. *Earth and Planetary Science Letters*, *161*(1-4), 119–133. https://doi.org/10.1016/S0012-821X(98)00144-7

Nandedekar, R. H., Ulmer, P., & Müntener, O. (2014). Fractional crystallisation of primitive, hydrous arc magmas: An experimental study at 0.7 GPa. *Contributions to Mineralogy and Petrology*, *167*, 1015. https://doi.org/10.1007/s00410-014-1015-5

Neill, O. K., Larsen, J. F., Izbekov, P. E., & Nye, C. J. (2015). Pre-eruptive magma mixing and crystal transfer revealed by phenocryst and microlite compositions in basaltic andesite from the 2008 eruption of Kasatochi Island volcano. *American Mineralogist*, *100*(4), 722–737. https://doi.org/10.2138/am-2015-4967

Ni, H., & Zhang, Y. (2008). H_2O diffusion models in rhyolite melt with new pressure data. *Chemical Geology*, *250*(1-4), 68–78. https://doi.org/10.1016/j.chemgeo.2008.02.011

Nockolds, S. R. (1933). Some theoretical aspects of contamination in acid magmas. *Journal of Geology*, *41*(6), 561–589. https://doi.org/10.1086/624072

Oldenburg, C. M., Spera, F. J., Yuen, D. A., & Sewell, G. (1989). Dynamic mixing in magma bodies: Theory, simulations and implications. *Journal of Geophysical Research*, *94*(B7), 9215–9236. https://doi.org/10.1029/JB094iB07p09215

Oppenheimer, J., Rust, A. C., Cashman, K. V., & Sandnes, B. (2015). Gas migration regimes and outgassing in particle-rich suspensions. *Frontiers in Physics*, *3*, 60. https://doi.org/10.3389/fphy.2015.00060

Papale, P., Montagna, C. P., & Longo, A. (2017). Pressure evolution in shallow magma chambers upon buoyancy driven replenishment. *Geochemistry, Geophysics, Geosystems*, *18*, 1214–1224. https://doi.org/10.1002/2016GC006731

Papale, P., Moretti, R., & Barbato, D. (2006). The compositional dependence of the saturation surface of $H_2O + CO_2$ fluids in a silicate melt. *Chemical Geology*, *229*(1-3), 78–95. https://doi.org/10.1016/j.chemgeo.2006.01.013

Perugini, D., De Campos, C. P., Dingwell, D. P., & Dorfman, A. (2013). Relaxation of concentration variance: A new tool to measure chemical element variability during mixing of magmas. *Chemical Geology*, *335*, 8–23. https://doi.org/10.1016/j.chemgeo.2012.10.050

Perugini, D., De Campos, C. P., Dingwell, D. B., Petrelli, M., & Poli, G. (2008). Trace element mobility during magma mixing: Preliminary experimental results. *Chemical Geology*, *256*(3-4), 146–157. https://doi.org/10.1016/j.chemgeo.2008.06.032

Perugini, D., De Campos, C. P., Ertel-Ingrisch, W., & Dingwell, D. B. (2012). The space and time complexity of mixing silicate melts: Implications for igneous petrology. *Lithos*, *155*, 326–340. https://doi.org/10.1016/j.lithos.2012.09.010

Perugini, D., De Campos, C. P., Petrelli, M., Morgavi, D., Vetere, F. P., & Dingwell, D. B. (2015). Quantifying magma mixing with the Shannon entropy: Application to simulations and experiments. *Lithos*, *236-237*, 299–310. https://doi.org/10.1016/j.lithos.2015.09.008

Perugini, D., & Poli, G. (2004). Analysis and numerical simulation of chaotic advection and chemical diffusion during magma mixing: Petrological implications. *Lithos*, *78*(1–2), 43–66. https://doi.org/10.1016/j.lithos.2004.04.039

Perugini, D., & Poli, G. (2005). Viscous fingering during replenishment of felsic magma chambers by continuous inputs of mafic magmas: Field evidence and fluid mechanics experiments. *Geology*, *33*(1), 5–8. https://doi.org/10.1130/G21075.1

Perugini, D., & Poli, G. (2012). The mixing of magmas in plutonic and volcanic environments: Analogies and differences. *Lithos*, *153*, 261–277. https://doi.org/10.1016/j.lithos.2012.02.002

Perugini, D., Poli, G., Christofides, G., & Eleftheriadis, G. (2003). Magma mixing in the Sithonia Plutonic Complex, Greece: Evidence from mafic microgranular enclaves. *Mineralogy and Petrology*, *78*(3–4), 173–200. https://doi.org/10.1007/s00710-002-0225-0

Perugini, D., Valentini, L., & Poli, G. (2007). Insights into magma chamber processes from the analysis of size distributions of enclaves in lava flows: A case study from Vulcano Island (Southern Italy). *Journal of Volcanology and Geothermal Research*, *166*(3-4), 193–203. https://doi.org/10.1016/j.jvolgeores.2007.07.017

Petrelli, M., El Omari, K., Le Guer, Y., & Perugini, D. (2016). Effects of chaotic advection on the timescales of cooling and crystallization of magma bodies at mid crustal levels. *Geochemistry, Geophysics, Geosystems*, *17*, 425–441. https://doi.org/10.1002/2015GC006109

Petrelli, M., El Omari, K., Spina, L., Le Guer, Y., La Spina, G., & Perugini, D. (2018). Timescales of water accumulation in magmas and implications for short warning times of explosive eruptions. *Nature Communications*, *9*(1), 1–14. https://doi.org/10.1038/s41467-018-02987-6

Petrelli, M., Perugini, D., & Poli, G. (2006). Timescales of hybridisation of magmatic enclaves in regular and chaotic flow fields: Petrologic and volcanologic implications. *Bulletin of Volcanology*, *68*, 285–293. https://doi.org/10.1007/s00445-005-0007-8

Phillips, J. A. (1880). On concretionary patches and fragments of other rocks contained in granite. *Quarterly Journal of the Geological Society of London*, *36*, 1–22. https://doi.org/10.1144/GSL.JGS.1880.036.01-04.03

Phillips, J. C., & Woods A. W. (2001). Bubble plumes generated during recharge of basaltic magma reservoirs. *Earth and Planetary Science Letters*, *186*(2), 297–309. https://doi.org/10.1016/S0012-821X(01)00221-7

Phillips, J. C., & Woods, A. W. (2002). Suppression of large-scale magma mixing by melt-volatile separation. *Earth and Planetary Science Letters*, *204*, 47–60. https://doi.org/10.1016/S0012-821X(02)00978-0

Pin, C., Binon, M., Belin, J. M., Barbarin, B., & Clemens, J. D. (1990). Origin of microgranular enclaves in granitoids: Equivocal Sr-Nd Evidence from Hercynian Rocks in the Massif Central (France). *Journal of Geophysical Research*, *95*(B11), 17821–17828. https://doi.org/10.1029/JB095iB11p17821

Pistone, M., Caricchi, L., Ulmer, P., Burlini, L., Ardia, P., Reusser, E., et al. (2012). Deformation experiments of bubble and crystal-bearing magmas: Rheological and microstructural analysis. *Journal of Geophysical Research*, *117*(B5). https://doi.org/10.1029/2011JB008986

Pistone, M., Blundy, J. D., Brooker, R. A., & EIMF (2016a). Textural and chemical consequences of interaction between hydrous and felsic magmas: An experimental study. *Contributions to Mineralogy and Petrology*, *171*(1), 8. https://doi.org/10.1007/s00410-015-1218-4

Pistone, M., Cordonnier, B., Ulmer, P., & Caricchi, L. (2016b). Rheological flow laws for multiphase magmas: An empirical approach. *Journal of Volcanology and Geothermal Research*, *321*, 158–170, https://doi.org/10.1016/j.jvolgeores.2016.04.029

Pistone, M., Blundy, J., & Brooker, R. A. (2017). Water transfer during magma mixing events: Insights into crystal mush rejuvenation and melt extraction processes. *American Mineralogist*, *102*(4), 766–776. https://doi.org/10.2138/am-2017-5793

Plail, M., Barclay, J., Humphreys, M. C. S., Edmonds, M., Herd, R. A., & Christopher, T. E. (2014). Characterization of mafic enclaves in the erupted products of Soufrière Hills Volcano, Montserrat, 2009 to 2010. *Geological Society London Memoirs*, *39*, 343–360. https://doi.org/10.1144/M39.18

Plail, M., Edmonds, E., Woods, A. W., Barclay, J., Humphreys, M. C. S., Herd, R. A., & Christopher, T. (2018). Mafic enclaves record syn-eruptive basalt intrusion and mixing. *Earth and Planetary Science Letters*, *484*, 30–40. https://doi.org/10.1016/j.epsl.2017.11.033

Prelević, D., Foley, S. F., Cvetković, V., & Romer, R. L. (2004). Origin of minette by mixing of lamproite and dacite magmas in Veliki Majdan, Serbia. *Journal of Petrology*, *45*(4), 759–792. https://doi.org/10.1093/petrology/egg109

Pritchard, M. E., de Silva, S. L., Michelfelder, G., Zandt, G., McNutt, S. R., Gottsmann, J., et al. (2018). Synthesis: PLUTONS: Investigating the relationship between pluton growth and volcanism in the Central Andes. *Geosphere*, *14*(3), 954–982. https://doi.org/10.1130/GES01578.1

Reagan, M. K., Gill, J. B., Malavassi, E., & Garcia, M. O. (1987). Changes in magma composition at Arenal volcano, Costa Rica, 1968-1985: Real-time monitoring of open-system differentiation. *Bulletin of Volcanology*, *49*, 415–434. https://doi.org/10.1007/BF01046634

Reid, J. B., Evans, O., & Fates, D. G. (1983). Magma mixing in granitic rocks of the central Sierra Nevada, California. *Earth and Planetary Science Letters*, *66*, 243–261. https://doi.org/10.1016/0012-821X(83)90139-5

Renggli, C. J., Wiesmaier, S., De Campos, C. P., Hess, K., & Dingwell, D. B. (2016). Magma mixing induced by particle settling., *171*, 96. https://doi.org/10.1007/s00410-016-1305-1

Roscoe, R. (1952). The viscosity of suspensions of rigid spheres. *British Journal of Applied Physics*, *3*(8), 267–269. https://doi.org/10.1088/0508-3443/3/8/306

Rossi, S., Petrelli, M., Morgavi, D., Vetere, F. P., Almeev, R. R., Astbury, R. L., & Perugini, D. (2019). Role of magma mixing in the pre-eruptive dynamics of the Aeolian Islands volcanoes (Southern Tyrrhenian Sea, Italy). *Lithos*, *324–325*, 165–179. https://doi.org/10.1016/j.lithos.2018.11.004

Ruprecht, P., & Wörner, G. (2007). Variable regimes in magma systems documented in plagioclase zoning patterns: El Misti stratovolcano and Andahua monogenetic cones. *Journal of Volcanology and Geothermal Research*, *165*(3–4), 142–162. https://doi.org/10.1016/j.jvolgeores.2007.06.002

Ruprecht, P., Bergantz, G. W., Cooper, K. M., & Hildreth, W. (2012). The crustal magma storage system of Volcán Quizapu, Chile, and the effects of magma mixing on magma diversity. *Journal of Petrology*, *53*(4), 801–840. https://doi.org/10.1093/petrology/egs002

Şahin, S. Y. (2008). Geochemistry of mafic microgranular enclaves in the Tamdere Quartz Monzonite, south of Dereli/Giresum, Eastern Pontides, Turkey. *Chemie der Erde-geochemistry*, *68*(1), 81–92. https://doi.org/10.1016/j.chemer.2005.05.002

Samaniego, P., Le Pennec, J., Robin, C., & Hidalgo, S. (2011). Petrological analysis of the pre-eruptive magmatic process prior to the 2006 explosive eruptions at Tungurahua volcano (Ecuador). *Journal of Volcanology and Geothermal Research*, *199*(1–2), 69–84. https://doi.org/10.1016/j.jvolgeores.2010.10.010

Sato, E., & Sato, H. (2009). Study of effect of magma pocket on mixing of two magmas with different viscosities and densities by analogue experiments. *Journal of Volcanology and Geothermal Research 181*(1-2), 115–123. https://doi.org/10.1016/j.jvolgeores.2009.01.005

Schleicher, J. M., Bergantz, G. W., Breidenthal, R. E., & Burgisser, A. (2016). Time scales of crystal mixing in magma mushes. *Geophysical Research Letters*, *43*(4), 1543–1550. https://doi.org/10.1002/2015GL067372

Schleicher, J. M., & Bergantz, G. W. (2017). The mechanics and temporal evolution of an open system magmatic intrusion into a crystal-rich magma. *Journal of Petrology*, *58*(6), 1059–1072. https://doi.org/10.1093/petrology/egx045

Schubert, M., Driesner, T., Gerya, T. G., & Ulmer, P. (2013). Mafic injection as a trigger for felsic magmatism: A numerical study. *Geochemistry, Geophysics, Geosystems*, *14*(6), 1910–1928. https://doi.org/10.1002/ggge.20124

Scott, J. A. J., Pyle, D., M., Mather, T. A., & Rose, W. I. (2013). Geochemistry and evolution of the Santiaguito volcanic dome complex, Guatemala. *Journal of Volcanology and Geothermal Research*, *252*, 92–107. https://doi.org/10.1016/j.jvolgeores.2012.11.011

Seitz, S., Putlitz, B., Baumgartner, L. P., & Bouvier, A. (2018). The role of crustal melting in the formation of rhyolites: Constraints from SIMS oxygen isotope data (Chon Aike Province, Patagonia, Argentina). *American Mineralogist*, *103*(12), 2011–2027. https://doi.org/10.2138/am-2018-6520

Semenov, A. N., & Polyansky, O. P. (2017). Numerical modelling of the mechanisms of magma mingling and mixing: A case study of the formation of complex intrusions. *Russian Geology and Geophysics*, *58*(11), 1317–1332. https://doi.org/10.1016/j.rgg.2017.11.001

Silva, M. M. V. G., Neiva, A. M. R., & Whitehouse, M. J. (2000). Geochemistry of enclaves and host granites from the Nelas area, central Portugal. *Lithos*, *50*(1–3), 153–170. https://doi.org/10.1016/S0024-4937(99)00053-5

Sinton, J. M., & Detrick, R. S. (1992). Mid Ocean Ridge magma chambers. *Journal of Geophysical Research*, *97*(B1), 197–216. https://doi.org/10.1029/91JB02508

Snyder, D. (1997). The mixing and mingling of magmas. *Endeavour*, *21*(1), 19–22. https://doi.org/10.1016/S0160-9327(96)10032-6

Snyder, D., & Tait, S. (1995). Replenishment of magma chambers: A comparison of fluid mechanic experiments with field relations. *Contributions to Mineralogy and Petrology*, *122*(3), 230–240. https://doi.org/10.1007/s004100050123

Solano, J. M. S., Jackson, M. D., Sparks, R. S. J. Blundy, J. D., & Annen, C. (2012). Melt Segregation in deep crustal hot zones: A mechanism for chemical differentiation, crustal assimilation and the formation of evolved magmas. *Journal of Petrology*, *53*(10), 1999–2026. https://doi.org/10.1093/petrology/egs041

Sparks, R. S. J., Annen, C., Blundy, J. D., Cashman, K. V., Rust, A. C., & Jackson, M. D. (2019). Formation and dynamics of magma reservoirs. *Philosophical Transactions of the Royal Society*, *377*(2139), 20180019. https://doi.org/10.1098/rsta.2018.0019

Sparks, R. S. J., & Marshall, L. A. (1986). Thermal and mechanical constraints on mixing between mafic and silicic magmas. *Journal of Volcanology and Geothermal Research*, *29*(1–4), 99–124. https://doi.org/10.1016/0377-0273(86)90041-7

Sparks, R. S. J., Sigurdsson, H., & Wilson, L. (1977). Magma mixing: A mechanism for triggering acid explosive eruptions. *Nature*, *267*, 315–318. https://doi.org/10.1038/267315a0

Spina, L., Cimarelli, C., Scheu, B., Di Genova, D., & Dingwell, D. B. (2016). On the slow decompressive response of volatile- and crystal-bearing magmas: An analogue experimental investigation. *Earth and Planetary Science Letters*, *433*, 44–53. https://doi.org/10.1016/j.epsl.2015.10.029

Stelten, M. E., Cooper, K. M., Vazquez, J. A., Calvert, A. T., & Glessner, J. J. G. (2015). Mechanisms and timescales of generating eruptible magmas at Yellowstone Caldera from zircon and sanidine geochronology and geochemistry. *Journal of Petrology*, *56*(8), 1607–1642. https://doi.org/10.1093/petrology/egv047

Stimac, J. A., & Pearce, T. H. (1992). Textural evidence of mafic-felsic magma interaction in dacite lavas, Clear Lake, California. *American Mineralogist*, *77*(7-8).

Tepley, F. J., Davidson, J. P., & Clynne, M. A. (1999). Magmatic interactions as recorded in Plagioclase Phenocrysts of Chaos Crags, Lassen Volcanic Centre, California. *Journal of Petrology*, *40*(5), 787–809. https://doi.org/10.1093/petroj/40.5.787

Thomas, N., & Tait, S. (1997). The dimensions of magmatic inclusions as a constraint on the physical mechanism of mixing. *Journal of Volcanology and Geothermal Research*, *75*, 167–178. https://doi.org/10.1016/S0377-0273(96)00034-0

Thomas, N., Tait, S., & Koyaguchi, T. (1993). Mixing of stratified liquids by the motion of gas bubbles: Application to magma mixing. *Earth and Planetary Science Letters*, *115*(1-4), 161–175. https://doi.org/10.1016/0012-821X(93)90220-4

Topley, C. G., Brown, M., D'Lemos, R. S., Power, G. M., & Roach, R. A. (1990). The northern igneous complex of Guernsey, Channel Islands. *Geological Society Special Publication*, *51*, 245–259. https://doi.org/10.1144/GSL.SP.1990.051.01.15

Troll, V. R., & Schmicke, H. (2002). Magma mixing and crustal recycling recorded in ternary feldspar from compositionally zoned peralkaline ignimbrite 'A', Gran Canaria, Canary Islands. *Journal of Petrology*, *43*(2), 243–270. https://doi.org/10.1093/petrology/43.2.243

Tsuchiyama, A. (1985). Dissolution kinetics of plagioclase in the melt of the system diopside-albite-anorthite, and the origin of dusty plagioclase in andesites. *Contributions to Mineralogy and Petrology*, *89*(1), 1–16. https://doi.org/10.1007/BF01177585

Tsuchiyama, A., & Takahashi, E. (1983). Melting kinetics of a plagioclase feldspar. *Contributions to Mineralogy and Petrology*, *84*(4), 345–354. https://doi.org/10.1007/BF01160286

Turner, S., & Costa, F. (2007). Measuring timescales of magmatic evolution. *Elements*, *3*(4), 267–272. https://doi.org/10.2113/gselements.3.4.267

Ubide, T., Galé, C., Larrea, P., Arranz, E., & Lago, M. (2014a). Antecrysts and their effect on rock compositions: The Cretaceous lamprophyre suite in the Catalonian Coastal Ranges (NE Spain). *Lithos*, *206–207*, 214–233. https://doi.org/10.1016/j.lithos.2014.07.029

Ubide, T., Galé, C., Larrea, P., Arranz, E., Lago, M., & Tierz, P. (2014b). The relevance of crystal transfer to magma mixing: A Case study in composite dykes from the central Pyrenees. *Journal of Petrology*, *55*(8), 1535–1559. https://doi.org/10.1093/petrology/egu033

Van der Laan, S. R., & Wyllie, P. J. (1993). Experimental Interaction of Granitic and Basaltic Magmas and Implications for Mafic Enclaves. *Journal of Petrology*, *34*(3), 491–517. https://doi.org/10.1093/petrology/34.3.491

Van Zalinge, M. E., Sparks, R. S. J., Cooper, F. J., & Condon, D. J. (2016). Early Miocene large-volume ignimbrites of the Oxaya Formation, Central Andes. *Journal of the Geological Society*, *173*(5), 716–733. https://doi.org/10.1144/jgs2015-123

Venezky, D. Y., & Rutherford, M. J. (1999). Petrology and Fe-Ti oxide reequilibration of the 1991 Mount Unzen mixed magma. *Journal of Volcanology and Geothermal Research*, *89*(1–4), 213–230. https://doi.org/10.1016/S0377-0273(98)00133-4

Vernon, R. H. (1990). Crystallization and hybridism in microgranitoid enclave magmas: Microstructural evidence. *Journal of Geophysical Research*, *95*(B11), 17849–17859. https://doi.org/10.1029/JB095iB11p17849

Vetere, F., Petrelli, M., Morgavi, D., & Perugini, D. (2015). Dynamics and time evolution of a shallow plumbing system: The 1739 and 1888-90 eruptions, Vulcano Island, Italy. *Journal of Volcanology and Geothermal Research*, *306*, 74–82. https://doi.org/10.1016/j.jvolgeores.2015.09.024

Vogel, T. A., Hidalgo, P. J., Patino, L., Tefend, K. S., & Ehrlich, R. (2008), Evaluation of magma mixing and fractional crystallization using whole-rock chemical analyses: Polytopic vector analyses, *Geochemistry, Geophysics*, *Geosystems*, *9*(4), Q04020. https://doi.org/10.1029/2007GC001790

Wada, H., Harayama, S., & Yamaguchi, Y. (2004). Mafic enclaves densely concentrated in the upper part of a vertically zoned felsic magma chamber: The Kurobegawa granitic pluton, Hida Mountain Range, central Japan. *Geological Society of America Bulletin*, *116*(7-8), 788–801. https://doi.org/10.1130/B25287.1

Wadge, G., Voight, B., Sparks, R. S. J., Cole, P. D., Loughlin, S. C. & Robertson, R. E. A. (2014). An overview of the eruption of Soufrière Hills Volcano, Montserrat from 2000 to 2010. *Geological Society London Memoirs*, *39*, 1–40. https://doi.org/10.1144/M39.1

Watson, E. B. (1982) Basaltic contamination by continental crust: Some experiments and models. *Contributions to Mineralogy and Petrology*, *80*(1), 73–87. https://doi.org/10.1007/BF00376736

Watson, E. B., & Jurewicz, S. R. (1984). Behavior of alkalis during diffusive interaction of grantic xenoliths with basaltic magma. *Journal of Geology*, *92*(2), 121–131. https://doi.org/10.1086/628843

Weidendorfer, D., Mattsson, H. B., & Ulmer, P. (2014). Dynamics of magma mixing in partially crystallized magma chambers: Textural and petrological constraints from the basal complex of the Austurhorn intrusion (SE Iceland). *Journal of Petrology*, *55*(9), 1865–1903. https://doi.org/10.1093/petrology/egu044

Wiebe, R. A. (1973). Relations between coexisting basaltic and granitic magmas in a composite dike. *American Journal of Science*, *273*, 130–151.

Wiebe, R. A. (1987). Rupture and inflation of a basic magma chamber by silicic liquid. *Nature*, *326*, 69–71. https://doi.org/10.1038/326069a0

Wiebe, R. A. (1992). The pleasant bay layered Gabbro-Diorite, coastal Maine: Ponding and crystallization of basaltic injections into a silicic magma chamber. *Journal of Petrology*, *34*(3), 461–489. https://doi.org/10.1093/petrology/34.3.461

Wiebe, R. A. (1994). Silicic magma chambers as traps for Basaltic magmas: The Cadillac Mountain Intrusive Complex, Mount Desert Island, Maine. *Journal of Geology*, *102*(4), 423–437. https://doi.org/10.1086/629684

Wiebe, R. A. (1996). Mafic-silicic layered intrusions: The role of basaltic injections on magmatic processes and the evolution of silicic magma chambers. *Transactions of the Royal Society of Edinburgh: Earth Sciences*, *87*(1-2), 233–242. https://doi.org/10.1017/S0263593300006647

Wiebe, R. A., & Collins, W. J. (1998). Depositional features and stratigraphic sections on granitic plutons: Implications for the emplacement and crystallization of granitic magma. *Journal of Structural Geology.*, *20*(9-10), 1273–1289. https://doi.org/10.1016/S0191-8141(98)00059-5

Wiebe, R. A., Blair, K. D., Hawkins, D. P., & Sabine, C. P. (2002). Mafic injections, in situ hybridization, and crystal accumulation in the Pyramid Peak granite, California. *GSA Bulletin*, *114*(7), 909–920. https://doi.org/10.1130/0016-7606(2002)114%3C0909:MIISHA%3E2.0.CO;2

Wiebe, R. A., & Hawkins, D. P. (2015). Growth and impact of a mafic-silicic layered intrusion in the Vinalhaven intrusive complex, Maine. *Journal of Petrology*, *56*(2), 273–298. https://doi.org/10.1093/petrology/egu078

Wiebe, R. A., Smith, D., Sturm, M., King, E. M., & Seckler, M. S. (1997). Enclaves in the Cadillac Mountain Granite (coastal Maine): Samples of hybrid magma from the base of the chamber. *Journal of Petrology*, *38*(3), 393–423. https://doi.org/10.1093/petroj/38.3.393

Wiesmaier, S., Morgavi, D., Renggli, C. J., Perugini, D., De Campos, C. P., Hess, K. U., et al. (2015). Magma mixing enhanced by bubble segregation. *Solid Earth*, *6*, 1007–1023. https://doi.org/10.5194/se-6-1007-2015

Wilcox, R. (1999). The idea of magma mixing: History of a struggle for acceptance. *Journal of Geology*, *107*(4), 421–432. https://doi.org/10.1086/314357

Williams, Q., & Tobisch, O. T. (1994). Microgranitic enclave shapes and magmatic strain histories: Constraints from drop deformation theory. *Journal of Geophysical Research*, *99*(B12), 24359–24368. https://doi.org/10.1029/94JB01940

Woods, A. W., & Stock, M. J. (2019). Some fluid mechanical constraints on crystallization and recharge within sills. *Philosophical Transactions of the Royal Society A*, *377*, 20180007. http://dx.doi.org/10.1098/rsta.2018.0007

Wright, H. M. N., Folkes, C. B., Cas, R. A. F., & Cashman, K. V. (2011). Heterogeneous pumice populations in the 2.08-Ma Cerro Galán Ignimbrite: Implications for magma recharge and ascent preceding a large volume silicic eruption. *Bulletin of Volcanology*, *73*(10), 1513–1533. https://doi.org/10.1007/s00445-011-0525-5

Wyllie, P. J., Carroll, M. R., Johnston, A. D., Rutter, M. J., Sekine, T., & Van der Laan, R. (1989). Interactions among magmas and rocks in subduction zone regions: Experimental studies from slab to mantle to crust. *European Journal of Mineralogy*, *1*(2), 165–179.

Xiong, F., Ma, C., Zhang, J., & Liu, B. (2012). The origin of mafic microgranular enclaves and their host granodiorites from East Kunlun, Northern Qinghai-Tibet Plateau: Implications for magma mixing during subduction of Paleo-Tethyan lithosphere. *Mineralogy and Petrology*, *104*(3–4), 211–224. https://doi.org/10.1007/s00710-011-0187-1

Zimanowski, B., Büttner, R., & Koopman, A. (2004). Experiments on magma mixing. *Geophysical Research Letters*, *31*, L09612. https://doi.org/10.1029/2004GL019687

Zhang, J., Davidson, J. P., Humphreys, M. C. S., Macpherson, C. G., & Neill, I. (2015). Magmatic enclaves and andesite lavas from Mt. Lamington, Papua New Guinea: Implications for recycling of earlier-fractionated minerals through magma recharge. *Journal of Petrology*, *56*(11), 2223– 2256. https://doi.org/10.1093/petrology/egv071

7

From Binary Mixing to Magma Chamber Simulator: Geochemical Modeling of Assimilation in Magmatic Systems

Jussi S. Heinonen[1], Kieran A. Iles[1,2], Aku Heinonen[1], Riikka Fred[1], Ville J. Virtanen[1], Wendy A. Bohrson[3,4], and Frank J. Spera[5]

ABSTRACT

The interactions of magmas with their surroundings are important in the evolution of igneous systems and the crust. In this chapter, we conceptually distinguish assimilation from other modes of magmatic interaction and discuss a range of geochemical assimilation models. We define assimilation in its simplest form as an end-member mode of magmatic interaction in which an initial state (t_0) that includes a system of melt and solid wall rock evolves to a later state (t_n) where the two entities have been homogenized. In complex natural systems, assimilation can refer more broadly to a process where a mass of magma wholly or partially homogenizes with materials derived from wall rock that initially behaves as a solid. The first geochemical models of assimilation used binary mixing equations and then evolved to take account mass balance and fractional crystallization. Most recent tools, such as the Magma Chamber Simulator, treat open systems thermodynamically in order to simulate geochemical changes in crystallizing magma and partially melting wall rock. Such thermodynamic considerations are a prerequisite for understanding the consequences of assimilation. The geochemical signatures of magmatic systems—although dominated for some elements (particularly major elements) by crystallization processes—may be considerably influenced by simultaneous assimilation of partial melts of compositionally distinct wall rock.

7.1. INTRODUCTION

Before Bowen (1915a, 1915b, 1915c, 1928) demonstrated the significance of fractional crystallization, assimilation of country (wall) rocks and mixing of magmas (Bunsen, 1851) were considered the primary means leading to the diversity of magma compositions and hence igneous rocks (e.g., Daly, 1905, 1910; Fenner, 1926; see McBirney, 1979). During Bowen's time, there were few petrologists able to utilize experimental methods, and thermodynamic properties of silicate phases were too poorly constrained to quantitatively investigate the physico-chemical consequences of assimilation. The initial assessment of the assimilation hypothesis was largely based on rudimentary major element data and field observations (e.g., often diffuse or stoped contact zones at the intrusion–wall-rock interface). Bowen's initial findings, its ripples over the decades, and the accumulation of evidence from experimental petrology have shown that formation of large amounts of country rock melt is limited by the enthalpy available from the magma

---

[1] *Department of Geosciences and Geography, University of Helsinki, Helsinki, Finland*

[2] *Finnish Museum of Natural History, University of Helsinki, Helsinki, Finland*

[3] *Department of Geological Sciences, Central Washington University, Ellensburg, Washington, USA*

[4] *Geology and Geological Engineering Department, Colorado School of Mines, Golden, Colorado, USA*

[5] *Department of Earth Science and Earth Research Institute, University of California Santa Barbara, Santa Barbara, California, USA*

Crustal Magmatic System Evolution: Anatomy, Architecture, and Physico-Chemical Processes, Geophysical Monograph 264, First Edition.
Edited by Matteo Masotta, Christoph Beier, and Silvio Mollo.

DOI: 10.1002/9781119564485.ch7

(e.g., Bowen, 1928; McBirney, 1979; Nicholls & Stout, 1982; Pushkar et al., 1971; Reiners et al., 1995; Sparks, 1986; Taylor, 1980; Wilcox, 1954). Furthermore, the heat required to melt wall rock cannot come from the sensible heat of the magma alone, but also requires a substantial amount of heat released by its crystallization (i.e., latent heat of crystallization).

Regardless of crystallization being recognized as the single most effective process in modifying major element compositions of magmas (Bowen, 1928), simultaneous assimilation is possible and has been described in many geological environments. Assimilation of compositionally distinct country rocks has been shown to have a considerable effect on the trace element and isotopic compositions of crystallizing magmas (e.g., Bohrson & Spera, 2001; Carter et al., 1978; Hansen & Nielsen, 1999; Heinonen et al., 2016; Huppert et al., 1985; Taylor, 1980; Tegner et al., 1999). Identifying mantle sources of basalts in different environments relies heavily on constraining the effects of crustal assimilation (e.g., Borisova et al., 2017; Carlson, 1991; Jung et al., 2011;Lightfoot et al., 1993; Ramos & Reid, 2005). Assimilation may also be important in formation of economically valuable mineralizations: for example, in some magmatic Ni-Cu-PGE sulfide deposits, a large portion of S is thought to be derived from assimilated sedimentary country rocks (e.g., Hayes et al., 2015; Iacono-Marziano et al., 2017; Mariga et al., 2006; Samalens et al., 2017; Thakurta et al., 2008). In addition, assimilation processes influence the eruptive behavior of many volcanic systems, especially by increasing the volatile budgets of magmas (e.g., Borisova et al., 2013; Gardner et al., 2013; Handley et al., 2018).

Before venturing further, we seek to clarify what the term *assimilation* means with respect to magmatic systems. How does "assimilation" differ from "mixing"? Some of the earliest chemical models of assimilation actually used a simple binary mixing equation. Geoscientists have subsequently had difficulties agreeing on a consistent lexicon for assimilation phenomena. For example, in the first edition of the *Glossary of Geology* (Gary et al., 1972; p. 42), assimilation is described as "the process of incorporating solid or fluid foreign material, i.e., wall rock, into magma. The term implies no specific mechanisms or results. Such a magma, or the rock it produces, may be called *hybrid* or *anomalous*." More than 30 years later, in the fifth edition (Neuendorf et al., 2005; p. 40), the description had evolved to "the incorporation and digestion of xenoliths and their chemical constituents into a body of magma. Such a magma, or the rock it produces, may be called *hybrid* or *contaminated*." These murky definitions create confusion, and consequently, the first part of this contribution concentrates on distinguishing end-member modes of magmatic interaction: hybridization (complete chemical mixing of two melts) versus mingling (the mixed melts stay separated chemically) versus assimilation (complete chemical mixing of a melt and its initially solid wall rock) versus stoping (the melt and wall-rock blocks stay separated chemically). The outcomes of these pure end-member modes can all be considered mixtures—either homogeneous (mixing and assimilation) or heterogeneous (mingling and stoping). We accomplish the division by constraining the initial (t_0) and later (t_n) states of the system for each end-member interaction mode. By establishing this framework, intermediate forms of interaction that are of geological interest can be placed in relation to these end-member modes and the mathematical models that describe them.

The second part of this chapter reviews the development of geochemical modeling of assimilation: how models evolved from a binary mixing equation (e.g., Bell & Powell, 1969; Faure et al., 1974; Vollmer, 1976) through more complicated but still purely chemical models, such as the widely used assimilation fractional crystallization (AFC) model of DePaolo (1981; hereinafter referred to as $\mathrm{AFC_{DP}}$; see also Allégre & Minster, 1978; O'Hara, 1977; Taylor, 1980), toward energy-constrained AFC (EC-AFC) models that take into account the heat budget of the system (Bohrson & Spera, 2001, 2003, 2007; Spera & Bohrson, 2001, 2002, 2004). The energy-constrained approach has most recently culminated in the development of the Magma Chamber Simulator (MCS; Bohrson et al., 2014, 2020; Heinonen et al., 2020) that also considers phase equilibria. Here, we provide a comprehensive historical overview of the concepts associated with the modeling of assimilation. We review the usefulness of the different geochemical models of assimilation in magmatic systems and provide an example of MCS applied to a natural system (continental flood basalts).

7.2. THE END-MEMBER MODES OF MAGMATIC INTERACTION

7.2.1. Defining Homogeneity in Mixtures

In order to understand the concept of assimilation, we first have to define a few basic concepts related to mixtures. That is, a terminological demarcation has to be made between homogeneous and heterogeneous mixtures, which can be defined either purely compositionally or relative to their phase states. In this study, we define homogeneity in mixtures in terms of their compositional characteristics. Chemical heterogeneity is also often intrinsically linked to phase heterogeneity in multicomponent magmatic environments.

An even more important demarcation between homogeneous and heterogeneous mixtures is the issue of sampling scale. The size of samples or "sample resolution" may dictate whether a system is considered homogeneous or heterogeneous as all materials composed of multiple substances can be defined as compositionally heterogeneous if the sample resolution is adequately small. For the purpose of describing homogeneity in magmatic environments, we focus our treatment on spatial scales greater than typical magmatic diffusive scales that are on the order of millimeters to centimeters (see Spera et al., 2016). At such scales, the composition of a homogeneous mixture at any location corresponds to its average composition. This definition applies to the end-member modes of magmatic interaction discussed in section 7.2.4.

7.2.2. Terminology of Mixing in Magmatic Systems

Although mixing, hybridization, and mingling are key concepts related to the compositional evolution of magmas in almost all geotectonic environments, the terms are often used ambiguously and rather loosely in the petrological literature. It is important to be precise about which subsystems are being handled, what the controlling processes are, and what types of compositional changes are imposed on those subsystems. In some studies of magmatic systems, complete chemical mixing of two end-members resulting in a homogeneous mixture has been called hybridization or complete hybridization (e.g., Sparks & Marshall, 1986; Spera et al., 2016). In others—like those that describe different magmatic interactions in the field—chemical mixing has simply been called mixing to distinguish it from solely physical mixing, that is, mingling (Figures 7.1a,b; see section 7.2.4; e.g., Metcalf et al., 1995; Clemens & Stevens, 2016). To add to the confusion, some studies consider mingling as a type of hybridization (e.g., Asrat et al., 2003; Burda et al., 2011).

In the petrological literature, Oldenburg et al. (1989) first proposed quantitative metrics to describe mixing in convectively driven magma bodies. Later studies by Petrelli et al. (2006, 2011) and Spera et al. (2016) showed how various metrics could be used to study interactions of two distinct melts. Following Spera et al. (2016), we consider melt mixing to be the umbrella term that encompasses the spectrum between the following end-member processes: (a) hybridization (formation of a single homogeneous melt by the chemical mixing of two end-member melts) and (b) physical mixing (mingling) without chemical mixing. Therefore, mixing involves interaction of two melts in the recommended approach; the end result can be hybridization, mingling, or something in between (see section 7.2.4).

7.2.3. Mixing Versus Assimilation

Our division between magma mixing and assimilation processes is related to the degree of solidity—or melting—of the other entity taking part in the magmatic interaction process. Practical difficulties of strict definitions of mixing in magmatic systems (hybridization or mingling) and assimilation arise from the gradational character of these processes in nature. To illustrate the gradational nature, a melt (entity A in Figure 7.2a) intruding a hypothetical magmatic environment with spatial variations between completely solid and completely molten material (entity B in Figure 7.2a) is considered. The distribution of liquid and crystals gradually varies upward through the system from a completely solid lowermost part to a completely liquid uppermost part. Such an environment describes, for example, magmas in which varying degrees of crystallization and crystal accumulation have taken place or partially molten migmatite complexes deep in the crust. If another genetically unrelated (ruling out a replenishment/recharge scenario of syngenetic magmas) and compositionally distinct melt (entity A in Figure 7.2a) were to intrude this system, penetrating all layers, a broad array of different kinds of interaction scenarios would ensue. Within square 1 in Figure 7.2a, where the intruding melt is in contact with 100% liquid material, a hybridization or mingling process is possible (see Figures 7.1a,b). Within square 2 in Figure 7.2a, where the melt is in contact with 100% solid material (i.e., wall rock), a "classical" case of assimilation (see Figure 7.1c) or, if there were no chemical exchange, stoping (see Figure 7.1d) would take place. Everything in-between these extremes describes the spectrum of interactions between liquids and solids (and, potentially, fluids) that could take place between entities A and B in Figure 7.2a in nature. The overarching processes, the end-member modes of magmatic interaction (cases 1A–D in Figure 7.2b), are defined and discussed in the following section.

7.2.4. Defining the End-Member Modes of Magmatic Interaction

The Intrinsic Parameters

In order to conceptually distinguish hybridization, mingling, and assimilation as end-member modes of magmatic interaction, we focus our investigation on the initial (t_0) and later (t_n) states of the system (Figures 7.2 and 7.3). The "later state" should not be confused with

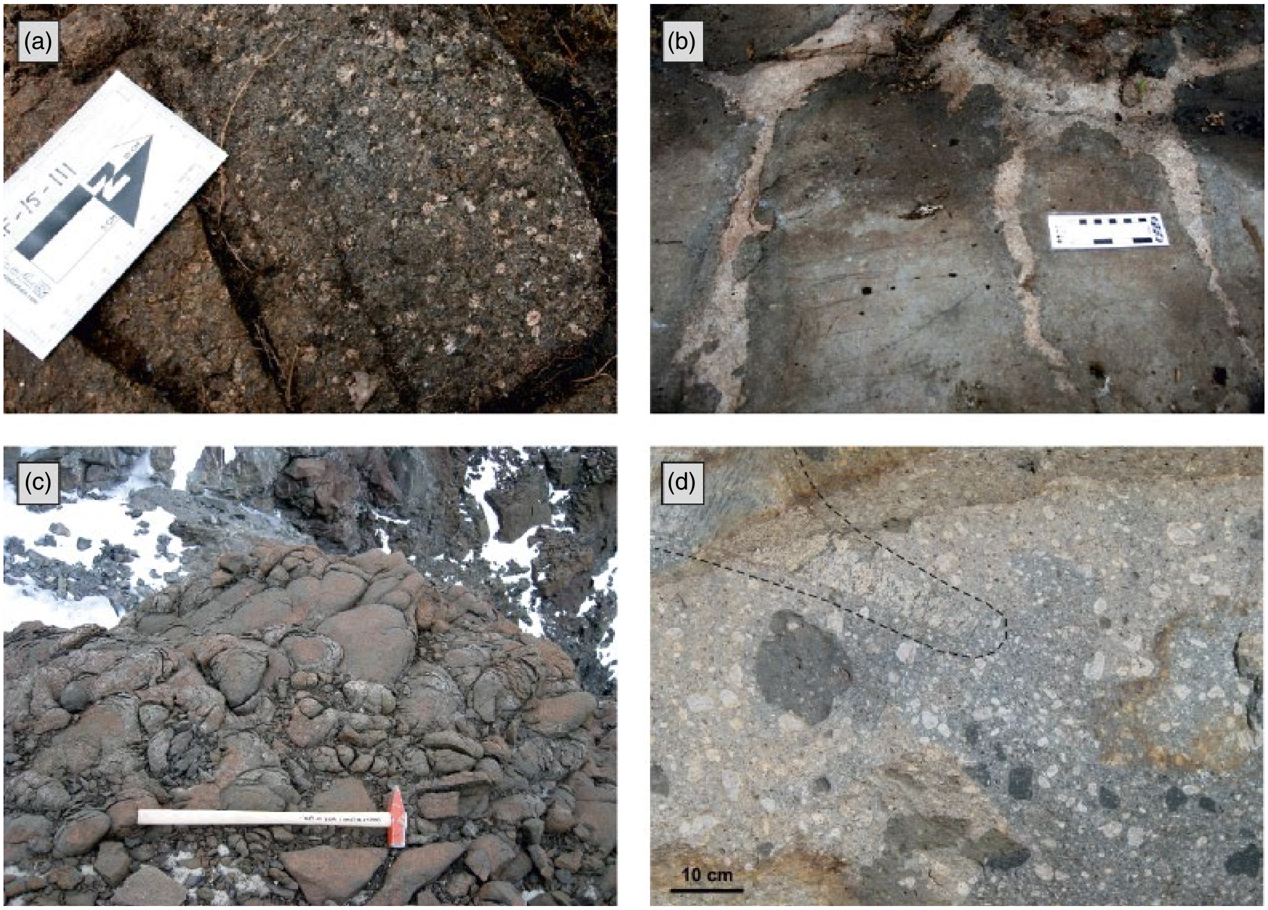

Figure 7.1 Textures and structures of rocks that illustrate a range of magmatic interaction processes. (a) A natural example of a product (quartz monzodiorite) of magmatic interaction dominated by hybridization from the Proterozoic Ahvenisto complex in SE Finland. The composition of the dark groundmass is a mixture of monzodioritic and granitic end-member melts, and the pink alkali feldspar crystals are "inherited" from the granitic magma that was already partially crystallized at the time of interaction. The length of the arrow is 10 cm. (b) A natural example of mingling of two magmas, one with monzodioritic (dark pillows) and the other with granitic (pink veins) composition, also from the Ahvenisto complex. The length of the scale bar is 10 cm. Compositional evolution of the mafic end-member magma and the style and the timing of intrusion most likely dominated the interaction process in (a) and (b); for more details, see Fred et al. (2019). (c) An outcrop of continental flood basalt flow from the Antarctic extension of the ~180 Ma Karoo large igneous province. Some of the basalt types show trace element and isotopic evidence of up to 15 wt.% of assimilation of Archean crust (Heinonen et al., 2016), but in the field, the rocks are homogeneous and do not show relict features (e.g., xenoliths or xenocrysts) of the interaction with the wall rock. The length of the hammer is ~50 cm. (d) Evidence for different types of magmatic interactions in a single outcrop of a granitic rock of the 17–15 Ma Spirit Mountain batholith, southern Nevada (Walker et al., 2007). More mafic magma mingled with the more felsic magma and formed the dark pillows. A xenolith composed of gneissic country rock (surrounded with a dashed line in the upper-left corner of the image) has been engulfed by the magma.

the final or equilibrium state, as the system may evolve from a physically separated (mingled) magma-magma system to a chemically mixed uniform magma, if thermal equilibration of the two magmas is attained (see Figures 7.1a,b) and reactive processes (Farner et al., 2014) do not restrict mixing. Rather, the later state is a "snapshot" of the system after an arbitrary degree of interaction has occurred. Depending on the rate of cooling and other physico-chemical factors, the "final" completely crystallized products (i.e., rocks) of the different processes may preserve traces of one or several t_n states of the system (Figure 7.1), but the majority of these infinite states get overprinted during polybaric ascent, cooling, and crystallization.

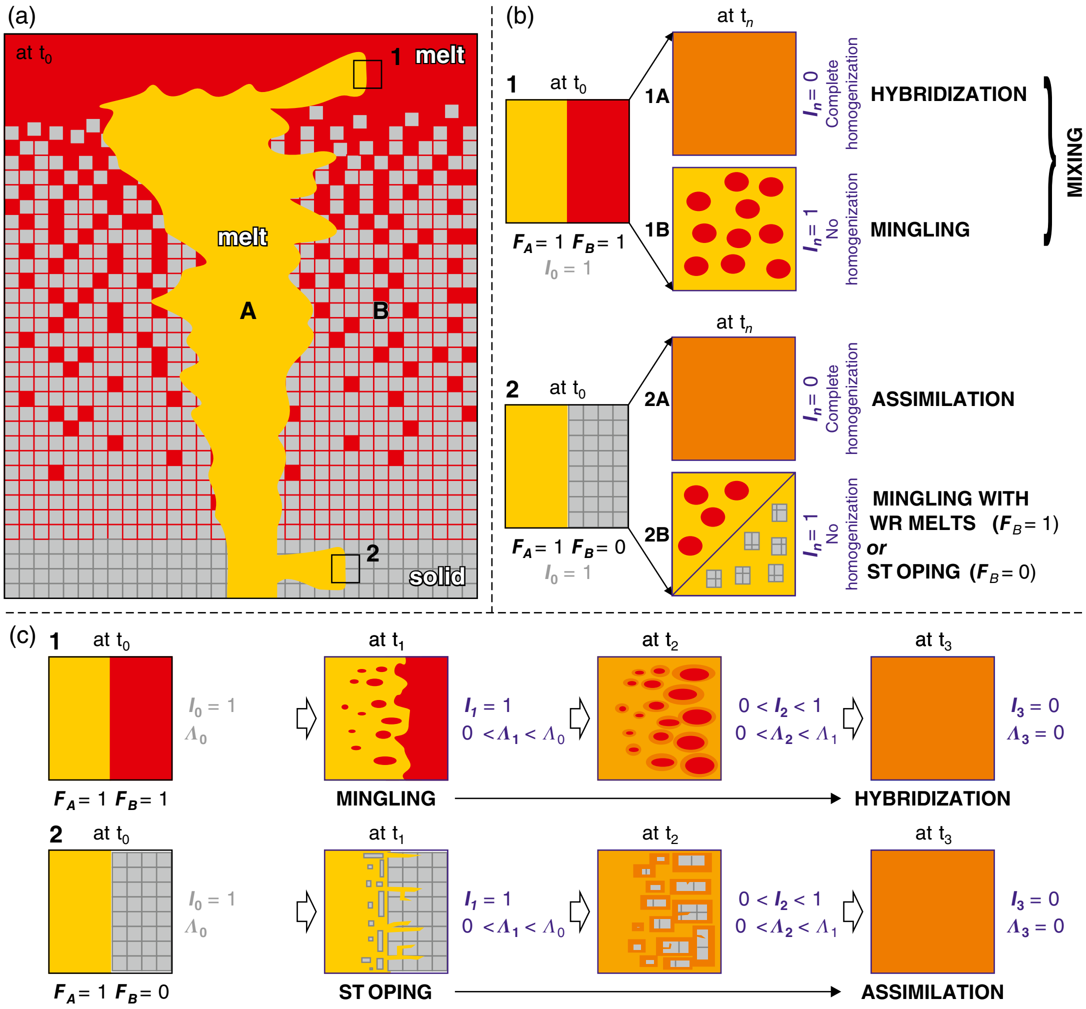

Figure 7.2 (a) A schematic and simplified model illustrating a melt (A; in yellow) intruding a genetically unrelated environment (B) composed of solid (i.e., wall rock) at the bottom (in gray), melt at the top (in red), and a mixture of solid and melt in between. After t_0, the intruding melt is not thoroughly homogenized, and thus the squares can subsequently be considered as separate systems. (b) The squares demonstrate the definitions of the end-member modes of magmatic interaction according to squares 1 and 2 in (a): t_0 and t_n mark the initial and later states of the system, respectively, *F* refers to the melt fraction, and *I* stands for the intensity of segregation of the system at the observed scale. Comparison to (a) reveals the gradation of mixing processes to assimilation/stoping. (c) The squares demonstrate the temporal evolution and gradation from mingling to hybridization (upper set of squares) and from stoping to assimilation (lower set of squares) with the help of linear scale of segregation (Λ). Other parameters are as in (b). Note that the process definitions in (b) and (c) do not allow crystallization, fluid separation, newly formed immiscible liquids, or compositionally heterogeneous wall rock (the latter in the case of stoping). For more details, see section 7.2.

At t_0, the system consists of a melt body (entity A) that intrudes into surroundings composed of vertically varying amounts of liquid and solid rock material (entity B) as described in the previous section (Figure 7.2). Three important measures are utilized in the following discussion: melt fraction (*F*), linear scale of segregation (Λ), and the intensity of segregation (*I*). *F* is simply the fraction of melt in A or B and has a value of $0 \le F \le 1$. The segregation parameters, which measure spatial patterns of heterogeneity, were developed for chemical reactor analysis by Danckwerts (1952, 1953) and introduced to geology by Oldenburg et al. (1989). Λ is defined as

$$\Lambda = \int_0^{r^*} R(r)\,dr \tag{7.1}$$

where

$$R(r)=\frac{\overline{\left(X_1-\bar{X}\right)\times\left(X_2-\bar{X}\right)}}{\overline{\left(X_i-\bar{X}\right)^2}} \tag{7.2}$$

The correlation function R is based upon the deviations of a compositional variable (X; e.g., oxide or trace element concentration) from the mean composition ($\bar{X}$); the subscript i denotes any point in the mixing domain, and the subscripts 1 and 2 denote two points separated by distance r. The correlation function is then integrated over all values of r between 0 and r^*, which denotes the distance at which a perfect random correlation exists. In short, Λ quantifies the mixing state of the system in terms of the "clumpiness" of heterogeneities, is dependent on the size and shape of the heterogeneities, and is initially equal to the maximal linear scale depending on the premixing configuration. If stirring of the mixture continues to infinity and the clumps break down progressively until they become vanishingly small, Λ evolves toward zero (Figure 7.2c).

In contrast to Λ, I is a purely scalar measure of homogeneity and is completely independent of the shape, spatial distribution, or relative amounts of the possible heterogeneities. I is defined as

$$I=\frac{\overline{\left(X_i-\bar{X}\right)^2}}{\left(\left(\bar{X}-X_A\right)\times\left(X_B-\bar{X}\right)\right)} \tag{7.3}$$

where X_A and X_B denote the compositions of the pure end-members A and B. I thus records the compositional variance of the system divided by the variance before mixing and can have values $0 \leq I \leq 1$ (assuming neither precipitation nor exsolution occurs concurrently with mixing). In the coalescence of two compositionally distinct entities, for $I = 1$, entity A stays completely separated from entity B, and the mixture is fully heterogeneous at a relevant scale. By contrast, for $I = 0$, entities A and B have formed a compositionally homogeneous mixture, and no discernible heterogeneities or "clumps" of either A or B exist at the given scale. For more detailed explanations of Λ and I in relation to geological processes, the reader is referred to Oldenburg et al. (1989), Todesco and Spera (1992), and Spera et al. (2016).

End-Member Modes of Magmatic Interaction

To define the end-member modes of magmatic interaction, we first consider a system that is composed of two compositionally distinct homogeneous melts or a compositionally distinct homogeneous melt and a solid (squares 1 and 2 in Figure 7.2a). At t_0, melt–melt interaction can be separated from melt–solid interaction on the basis of the present melt fraction (F). In the end-member modes hybridization (case 1A in Figure 7.2b) and mingling (case 1B), both F_A and F_B are 1 at t_0, but for hybridization $I = 0$ and for mingling $I = 1$ at t_n. In the end-member mode of assimilation (case 2A), F_A is 1, but F_B is 0 at t_0 and $I = 0$ at t_n, denoting complete "assimilation" of a given portion of wall rock by the melt. Also, for $F_A = 1$ and $F_B = 0$ at t_0, mingling with wall-rock melts ($I = 1$ and $F_B = 1$ at t_n) or stoping ($I = 1$ and $F_B = 0$ at t_n) can also be defined (case 2B). Almost any variations between the end-member modes are possible, that is, at t_0, $0 \leq F_A < 1$ and $0 \leq F_B \leq 1$ and at t_n, $0 \leq I \leq 1$ (Figure 7.2), and the resulting exchange of different elements and their isotopes between the initial end-members is governed by mass balance (in the absence of kinetic considerations). In utilizing Λ, it is possible to examine the temporal relationships of the end-member processes. At an early stage of magmatic interaction (at t_1 in Fig 2c), the melts or the melt and the solid may be fully separated, but as the time progresses, complete homogenization of the system may take place (at t_3 in Fig 2c).

There are obvious limitations to the applicability of Λ and I in describing magmatic interaction in nature: simultaneous crystallization, fluid separation, or newly formed immiscible liquids are not included in the definitions above. For example, $I = 0$ at t_n does not allow for any additional compositional heterogeneity to have emerged within the system in cases 1A and 2A at the given scale. Because I is a scalar variable, it could be defined only for the liquid(s), but this approach is also hampered by crystallization causing compositional change within the residual melt(s), potentially resulting in X_i values not within the range X_A–X_B in any of the cases at t_n (and I for the liquid, thus giving values outside of the range 0–1). Given that mixing and assimilation are almost always accompanied by crystallization (see Figure 7.3; for special cases of mixing causing cessation of crystallization in binary eutectic systems, see Spera et al., 2016), melt A would generally have to be superheated in the pure 1A or 2A cases to prevent crystallization. Clearly, these four cases represent highly idealized examples that could be viewed as extreme end-member approximations of natural processes. Nevertheless, they provide a framework for describing magmatic interactions that are relevant for modeling (Figure 7.3) and have taken place in natural igneous systems (Figure 7.1).

A potentially useful way to make the distinction for processes that are somewhere between the presented end-members would be to utilize the critical melt fraction (F_c) for the entity B at t_0 (Figure 7.2). Above this composition- and condition-dependent critical melt fraction (see, e.g., Arzi, 1978; van der Molen & Paterson, 1979), the crystalline framework that holds the rock together collapses, and the rock behaves more as a liquid that

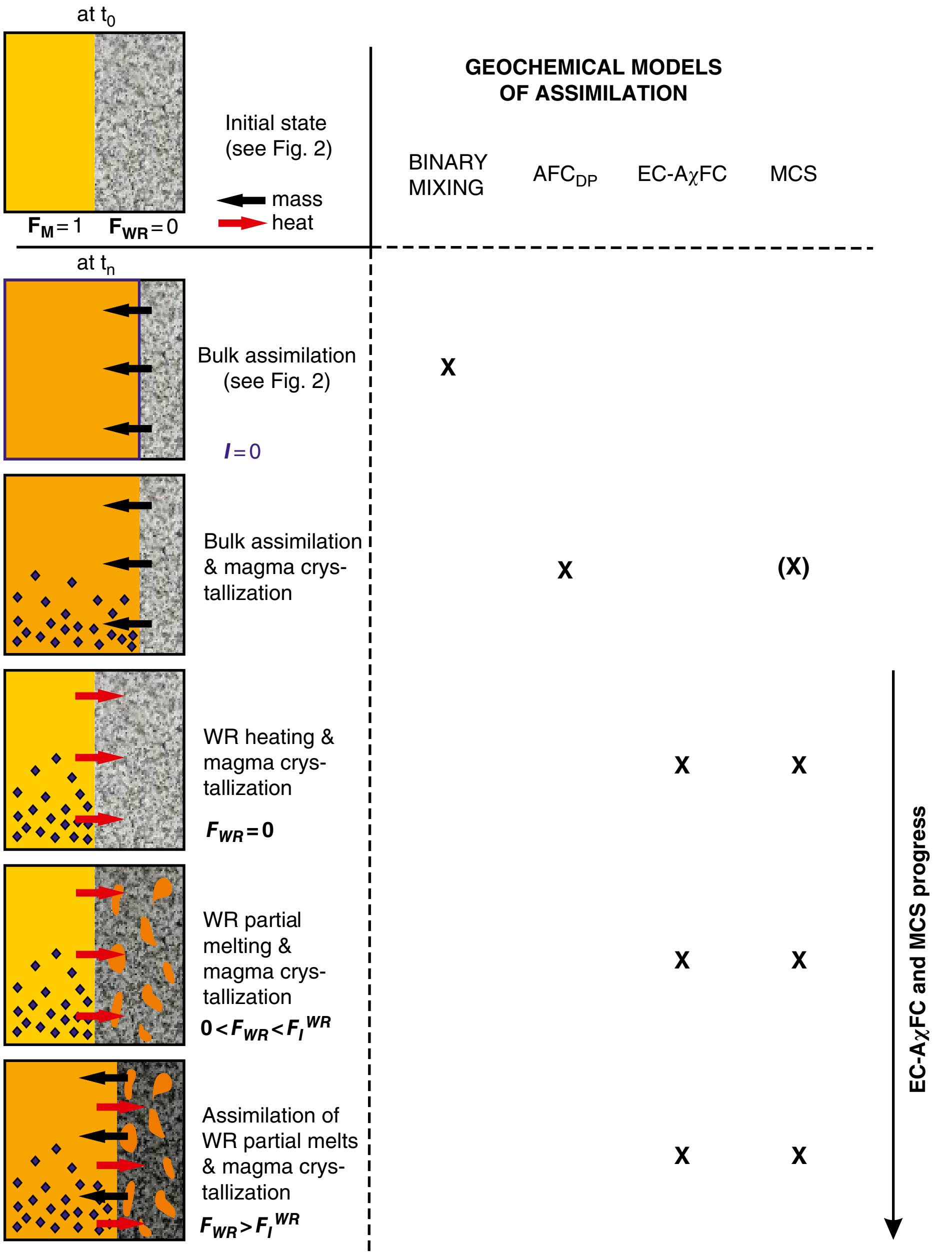

Figure 7.3 Schematic models illustrating processes at t_n resulting from an initial state of a melt and a solid wall rock at t_0 (see Figure 7.2). The compatibility of the processes to the geochemical models of assimilation discussed in this paper is marked with an X. The X in parentheses highlights the case in which assimilation is modeled in MCS as bulk assimilation of a stoped wall-rock block input as a "recharge magma" (see section 7.3.4). The higher the initial magma T (and the initial wall-rock T) relative to wall-rock solidus T, the farther the EC-AχFC and MCS models proceed. F_l^{WR} is the melt percolation threshold of the wall rock; for other variables, see section 7.2.4 and Figure 7.2.

contains suspended crystals (i.e., $F_c \le F_B \le 1$: subsequent interaction with A could be called magma mixing) than as a solid, which is the case when F_c is below the critical value (i.e., $0 \le F_B \le F_c$: subsequent interaction with A could be called assimilation or stoping). On the other hand, the initial state of the entities may be difficult to define in many natural cases. Any interaction evidenced by rocks or included in modeling can nevertheless be called a combination of the relevant end-member modes or on the basis of the mode suspected to dominate the interaction on the basis of petrological and/or geochemical evidence (see Figures 7.1 and 7.2). For example, although the EC-AFC model mostly considers assimilation of wall-rock partial melts instead of bulk assimilation of the wall rock (Figure 7.3; see sections 7.3.3 and 7.3.4), the governing mode of magmatic interaction still most closely corresponds to the end-member process 2A in Figure 7.2. For determining I in such a case, X_B in equation (7.3) should represent the wall-rock partial melt composition just before the interaction takes place. As another example of a reasonable flexibility of the naming convention, terms like "mixing with fluids" or "assimilation of fluids" can also be used, if entity B largely consists of fluid(s).

The dynamic and thermodynamic constraints for pure hybridization and mingling processes as defined here are discussed in detail in Spera et al. (2016; see also Spera & Bohrson, 2018) and will not be considered further. Rather, the following discussion will concentrate on geochemical (± thermodynamical) modeling of assimilation (± crystallization). Finally, we would like to emphasize that in any of the defined processes, it is important to recognize that the final composition of the resulting mixture is governed by the mass balance of individual elements in the interacting entities. Therefore, it should always be specified with respect to what element (or other feature) the impact of a particular magmatic interaction process is defined.

7.3. OVERVIEW OF GEOCHEMICAL MODELS OF ASSIMILATION

Several studies have discussed the geochemical modeling of assimilation either in purely chemical terms (mass balance of different elements) or by including some considerations of the effects of thermodynamics or other constraints (energy balance of the system) on the process. Here, we concentrate on three widely used models (binary mixing, AFC_{DP}, and EC-AχFC) and the most recent and the most comprehensive model, which is MCS. The models are reviewed on the basis of the most influential properties in Table 7.1 and in Figure 7.3. The outcomes of the different models for a representative assimilation case are presented and compared in section 7.3.5.

Table 7.1 A Review of Geochemical Models of Assimilation

Model[a]	Components/ subsystems	Progress variable	Input constraints	Geochemical output	Improvement relative to the previous model
Binary mixing	Two compositional end-members	End-member fraction	Composition	Major and trace elements, isotopes	–
AFC_{DP}	Magma body, cumulate reservoir, and bulk wall rock	Residual melt fraction of magma	Composition, rate of assimilation relative to rate of crystallization, partition coefficients for trace elements in magma	Trace elements and radiogenic and O isotopes	Recognizes clear link between crystallization and assimilation
EC-AχFC	Magma body, cumulate reservoir, and wall rock	Resident magma temperature	Initial thermal constraints, specific heat, enthalpy of fusion/crystallization, composition, and partition coefficients for trace elements in magma and wall rock; proportion of wall-rock melt entering the magma	Trace elements and radiogenic and O isotopes	Accounts for bulk thermodynamics of the system and progressive partial melting of the wall rock
MCS	Magma body, cumulate reservoir, and wall rock	Resident magma temperature	Pressure of the system (isobaric); initial thermal constraints, composition, and phase-specific trace element partition coefficients for magma and wall rock; melt percolation threshold for wall rock	Major and trace elements, phase equilibria, and radiogenic and O isotopes	Calculates thermal properties using MELTS engine; includes major elements and phase equilibria that are calculated for the magma and wall rock each temperature step; phase-specific trace element partition coefficients

[a] See more detailed discussion in section 7.3. Note that the recharge option is not included in this comparison but is available in some models.

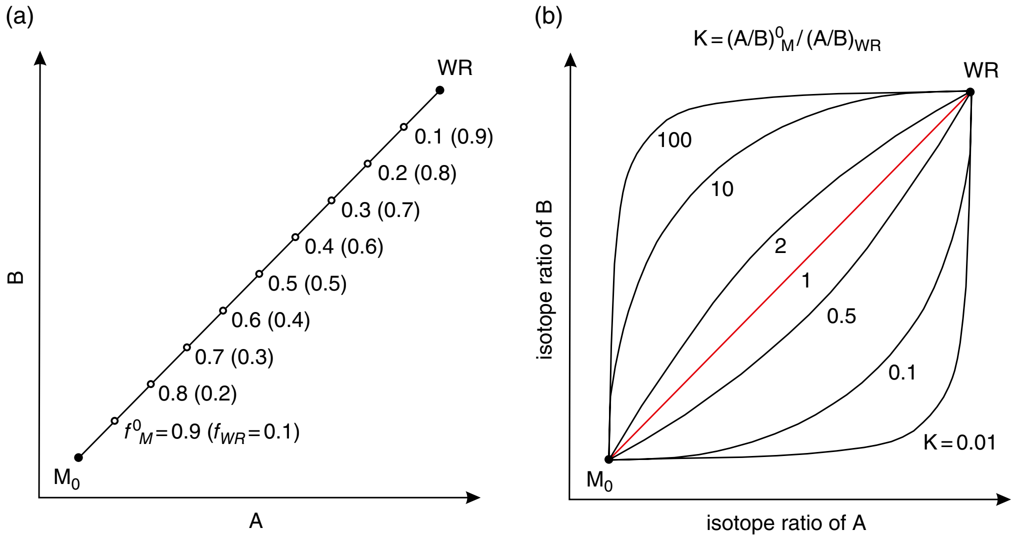

Figure 7.4 Magma–wall-rock binary mixing models in an element A versus element B concentration plot (a) and in a plot of their respective isotopic ratios (b). f_M^0 and f_{WR} are only given in (a). In (b), the different curves indicate different ratios of element A versus element B concentrations in the magma and the wall rock (note the definition for K).

7.3.1. In Bunsen's Footsteps: Simple Binary Mixing Model

The concept of mixing in igneous petrology was first discussed by Bunsen (1851), who suggested that the major element compositions of certain volcanic rocks in Iceland result from hybridization of varying proportions of the most primitive and the most evolved lavas (see also Langmuir et al., 1978; Wilcox, 1999). Bunsen hypothesized that two end-member magmas, basaltic and rhyolitic, are present as separate layers below Iceland and mix during ascent (see case 1A in Figure 7.2b). The same idea of binary mixing of two compositional end-members was also adopted for geochemical modeling of assimilation (e.g., Bell & Powell, 1969; Faure et al., 1974; Vollmer, 1976; see case 2A in Figure 7.2b), regardless of the early realizations that substantial energy is required to heat and assimilate wall rock (e.g., Bowen, 1928; Wilcox, 1954). Binary mixing of end-members (here melt and wall rock) can be chemically quantified as

$$X_M = f_M^0 X_M^0 + \left(1 - f_M^0\right) X_{WR} \qquad (7.4)$$

where X_M is the concentration of an element in the homogenized melt, X_M^0 and X_{WR} are the respective concentrations of the element in the parental melt and wall rock, and f_M^0 is the fraction of parental melt in the mixture. For the isotopic composition of the element in the mixture (ε_M), the isotopic composition of the parental melt (ε_M^0) and wall rock (ε_{WR}) are needed, and the respective equation can be formulated as

$$\varepsilon_M = f_M^0\left(\frac{X_M^0}{X_M}\right)\varepsilon_M^0 + \left(1 - f_M^0\right)\left(\frac{X_{WR}}{X_M}\right)\varepsilon_{WR} \qquad (7.5)$$

In element versus element diagrams, binary mixing models are straight lines, but in ratio versus element or ratio versus ratio diagrams, they are hyperbolae, unless the end-members have uniform elemental ratios (i.e., K = 1 in Figure 7.4). If the element and isotopic compositions of the end-members are known, the mixing ratio of the end-members can be determined by the position of the mixture composition on the mixing line/curve (Figure 7.4a). Equations 7.4 and 7.5 are compatible with the pure end-member case of assimilation (2A) in Figure 7.2b (see also Figure 7.3). Because assimilation is almost always accompanied by crystal fractionation in nature (section 7.2.4.2), utilization of more complex equations and input is required for the modeling.

7.3.2. Assimilation Coupled With Fractional Crystallization: AFC$_{DP}$

The simultaneous compositional effects of assimilation and fractional crystallization are taken into account in the AFC$_{DP}$ equation (DePaolo, 1981) (Figure 7.5; for earlier approaches, see Allégre & Minster, 1978; O'Hara, 1977; Taylor, 1980):

$$X_M = X_M^0\left[F^{-z} + \left(\frac{\mathrm{r}}{\mathrm{r}-1}\right)\left(\frac{X_{WR}}{zX_M^0}\right)\left(1 - F^{-z}\right)\right] \qquad (7.6)$$

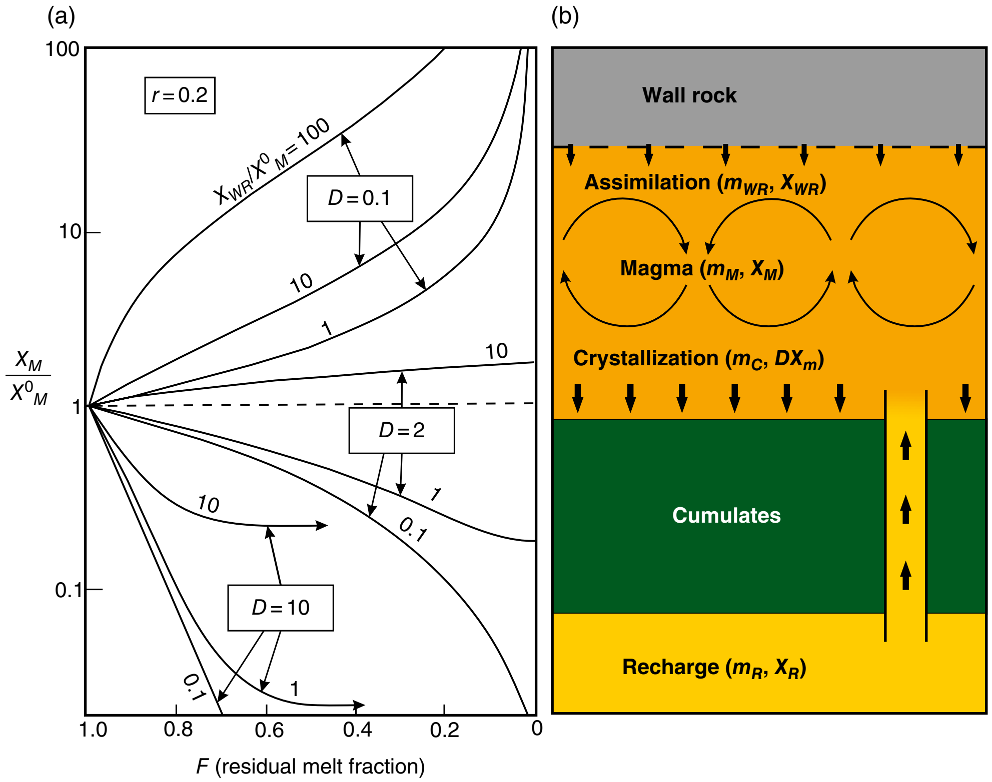

Figure 7.5 (a) A diagram showing the evolution of X_M/X^0_M in AFC$_{DP}$ models with constant r (0.2) but with different values of bulk solid-melt partition coefficient for the magma (D = 0.1, 2, and 10) and X_{WR}/X^0_M (0.1, 1, 10, and 100; the latter only for the model with D = 0.1). Modified after DePaolo (1981). (b) A graphical illustration of the RAFC$_{DP}$ model displaying the relations of the different reservoirs. The circular arrows indicate that the resident melt is constantly homogenized by convection. The thick arrows are mass flow vectors between reservoirs.

where X_M is the concentration of a trace element in the contaminated crystallizing resident melt, X^0_M and X_{WR} are the respective concentrations of the trace element in the parental melt and wall rock, F is the residual melt fraction relative to the parental melt, r is the rate of assimilation (mass/unit time; r ≠ 1) divided by the rate of crystallization (mass/unit time) within an F step, and $z = (r + D - 1)/(r - 1)$, where D is the bulk partition coefficient for the trace element in the magma. The progress variable in the AFC$_{DP}$ equation is F (Figure 7.5a).

For the isotopic composition of the trace element in the resident melt (ε_M), the isotopic composition of the parental melt (ε^0_M) and wall rock (ε_{WR}) are needed, and the respective equation can be formulated as

$$\varepsilon_M = \left(\varepsilon_{WR} - \varepsilon^0_M\right)\left[1-\left(\frac{X^0_M}{X_M}\right)F^{-z}\right] + \varepsilon_{WR} \qquad (7.7)$$

The AFC$_{DP}$ equation was later extended to include simultaneous melt recharge (i.e., replenishment; RAFC$_{DP}$; DePaolo, 1985). The compositional effects of continuous addition of recharge melt into the AFC system (Figure 7.5b) are incorporated into the equation based on the formulation of O'Hara (1977). If desired, periodic recharge pulses may be accomplished by running the simple AFC$_{DP}$ model until a given F, and then treating a recharge event as a simple hybridization process between the resident melt and the recharge melt. The resulting completely hybridized melt would then be modeled using equation (7.6) again until the next recharge event.

It is important to point out that equations (7.6) and (7.7) are only applicable to trace elements and their isotopes (O isotopes can be modeled with some generalized assumptions; see DePaolo, 1981), and major elements need to be modeled separately. Constraining appropriate D values nevertheless requires some knowledge of the fractionating phase assemblage, which is generally based on either petrography and/or major element modeling. AFC$_{DP}$ models generally assume a uniform D value for the modeled trace element regardless of likely changes in the fractionating phase assemblage during crystallization of the modeled system. This approach might be justified in the case of highly incompatible elements (such as Rb or Ba), but in the case of more compatible elements, especially those that are compatible in certain commonly crystallizing minerals (such as Sr in anorthitic plagioclase in silicate systems; see section 7.3.5), uniform D values should be used with caution, especially in models with low F.

Two of the major limitations of the AFC_{DP} equation are that the ratio of mass flow into and out of the magma body is constant across all F values and that the wall rock is treated as a bulk subsystem. The r value (the ratio of the "rates" at which wall rock is assimilated by the magma and crystals are fractionated from it) is, in fact, simply a mass ratio of assimilation relative to crystallization. Three situations can arise: (a) for $r < 1$, more mass is crystallized than assimilated, so the magma evolves toward a solid state [$1 \geq F > 0$ for equation (7.6)]; (b) for $r = 1$, the melt mass is in a steady state and equation (7.6) does not give a result (crystallization is exactly balanced by assimilation, that is, $F = 1$, which corresponds to zone refining; see DePaolo, 1981); and (c) for $r > 1$, the melt grows continuously because a greater mass of wall rock (liquid) is assimilated than of crystals fractionated [$F \geq 1$ for equation (7.6)]. The latter two situations are rarely utilized, would not be thermodynamically sustainable in the long run, and are thus not considered in the following comparisons between the models.

The most obvious example of changing mass flow ratio is when the wall-rock temperature is below the solidus, and latent heat of crystallization is required to provide sufficient heat to trigger wall-rock melting and mass flow into the magma chamber. Unlike the magma, in which progressive crystallization takes place, the effects of progressive partial melting are not taken into account in the AFC_{DP} equation, but wall rock is incorporated into the melt at a constant composition. Such an approach contrasts the excellent field documentation of partial melting processes at the contacts of intrusive rocks (e.g., Benkó et al., 2015; Hersum et al., 2007;Johnson et al., 2003) and is thermodynamically unlikely, which underlines the relevance of EC-AFC modeling tools. Some studies have attempted to overcome this issue by using partially molten wall rock as the assimilant in AFC_{DP} models (e.g., Brandon, 1989; Hansen & Nielsen, 1999; Tegner et al., 1999); such models are likely to be more realistic, although they do not overcome the issue of assimilant having a constant composition throughout the model.

7.3.3. Integration of Thermodynamic Constraints Into Modeling Assimilation: EC-AχFC

In order to provide more realistic estimations of the compositional effects of not only crystallization of the magma but also partial melting of the wall rock, and variations in mass flows between the reservoirs during the AFC process, the net heat budget between the reservoirs must be conserved. Applying this constraint in turn requires knowledge of the specific heat capacities of the magma and the assimilant and the crystallization and fusion enthalpies (latent heats of crystallization/melting) of relevant magma and wall-rock phases. These can be determined on the basis of experimentally defined thermodynamic data or by using a thermodynamic modeling software, such as MELTS (Ghiorso & Sack, 1995; Gualda et al., 2012), which is based on such data.

Following this approach, Spera and Bohrson (2001; see also Bohrson & Spera, 2001) introduced the first EC-AFC computational model. In this model, the magma body and wall rock are treated as thermally and compositionally homogeneous subsystems separated by diathermal and semipermeable borders to enable heat and mass flow, respectively (Figure 7.6). The subsystems comprise a composite system that has adiabatic and closed borders (i.e., heat or matter transfer is not permitted) to ensure heat and mass conservation in the system. Later enhanced versions of the model include magma recharge (R) (+ formation of enclaves), eruption, constraining the fraction of anatectic wall-rock melt delivered to the magma body (χ), and output on solids and anatectic melt (Bohrson & Spera, 2007; Spera & Bohrson, 2002, 2004). Regardless of the possibility of including several subsystems, the resident melt that can be replenished and contaminated by wall rock in EC-AFC models is always considered to be a homogeneous mixture (see section 7.2.1). Because this study focuses on modeling assimilation, we concentrate on the input and the general progression of the latest energy-constrained version (EC-RAχFC; Bohrson & Spera, 2007), but without the recharge option—for more detailed descriptions of it and the different versions available, the reader is referred to the aforementioned publications.

The development of assimilation models that are closer to the natural process requires more thorough compositional and thermal input from the user. The input in EC-AχFC is divided into physical (equilibration) and compositional (path-dependent) parameters. The thermal input consists of liquidus temperatures, initial temperatures, and specific heats of the magma and the wall rock, solidus of the composite system, and the bulk heat of crystallization for the magma and the bulk heat of fusion for the wall rock. The user can also alter melting/crystallization productivity functions and the magma temperature decrement, although default values are provided, and χ is predefined. The first stage of input is followed by a thermal simulation, after which the user can select an appropriate equilibration temperature at which equilibrium between the resident magma and the wall rock is attained. Lowering the equilibration temperature corresponds to a larger mass of the input wall rock being involved in the simulation. For a standard case, the compositional input consists of concentrations of up to

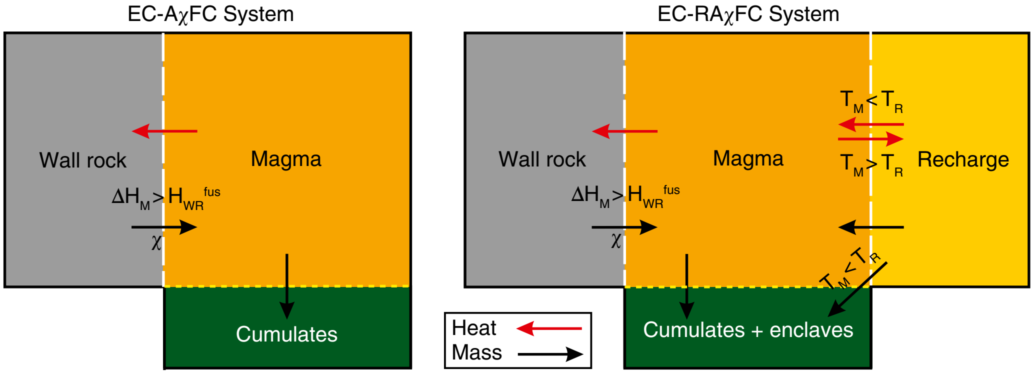

Figure 7.6 A schematic illustration of the thermodynamic systems (resident melt, cumulates ± enclaves, wall rock, and recharge) in the latest formulations of EC-AχFC and EC-RAχFC systems (Bohrson and Spera, 2007). The thick black line surrounding the entire composite system is an adiabatic and closed boundary, which restricts heat or mass flow. The yellow dotted lines represent adiabatic and semipermeable boundaries, through which only mass flow is permitted, and the white dashed lines represent diathermal and semipermeable boundaries, which allow both heat and mass flow. The arrows show possible directions for the heat and mass flows, and special conditions for certain arrows are indicated. The abbreviations are as follows: ΔH_M = sensible + latent heat released by magma, H_{WR}^{fus} = wall-rock heat of fusion, T_M = magma temperature, and T_R = recharge magma temperature, χ: fraction of anatectic wall-rock melt delivered to the magma body.

six trace elements, up to three isotopic compositions, and partition coefficients for these elements in the magma and in the wall rock. The partition coefficients can be temperature-dependent. In addition, oxygen isotopes are modeled by constraining O contents and isotopic compositions of the magma and the wall rock, but assuming no isotope partitioning during melting or crystallization.

In the EC-AFC system, the progress variable is the resident magma temperature that evolves toward the user-defined equilibration temperature. The thermal equilibrium is driven by the enthalpy (sensible and latent heat) of the composite system. The bulk latent heat of crystallization is approximated as a weighted average of the bulk enthalpy of crystallization at each step. The crystallized mass is transferred into the cumulate subsystem, which has an adiabatic and semipermeable boundary (Figure 7.6). The heat flows and distributes equally to the entire mass of the wall rock, raising its temperature until its solidus is reached. After that, the latent heat of fusion of the wall rock must be surpassed in order to trigger wall-rock partial melting, which is modeled as fractional melting. The fraction of the wall-rock melt defined by χ is extracted from the wall rock and homogenized into the resident melt. Each wall-rock melt batch added to the magma reservoir compositionally and thermally equilibrates with the resident melt instantaneously, and the composition of the residual wall rock is modified accordingly. The model proceeds accordingly in user-defined temperature steps until thermal equilibrium between the magma and wall rock is reached, upon which the run concludes.

The output of a EC-AχFC model run using the latest version (Bohrson & Spera, 2007) lists the thermal evolution of the resident magma and the wall rock; relative masses of the resident melt, cumulates, and generated and assimilated anatectic wall-rock melt; melt productivity of the magma; and the trace element (± isotopic) composition of the resident melt. Additional output lists the trace element compositions of the anatectic wall-rock melt and the magma cumulates. Isotope values for cumulates or the wall-rock anatectic melt are identical to those of the resident melt at each step and the wall rock, respectively.

Even though EC-AFC models include heat budget and partial melting of the wall rock in the trace element and isotope calculations, the phase changes governing the available latent heat are simplified, and a detailed picture of phase equilibria and energy conservation is not provided. In nature, the crystallizing and melting phase assemblages change, which lead to variations in heat production due to cooling and crystallization and, consequently, in the available energy for heating and partial melting of wall rock. Most significantly, phase changes may have profound effects on partition coefficients and hence on the trace element and isotope mass exchange between the subsystems. The addition of rigorous phase equilibria calculations instead of the approximate form utilized in the EC-AFC model provides a more accurate characterization of open system magmatic evolution. This limitation of EC-AFC led to the development of the MCS model.

7.3.4. Phase Equilibria of Assimilation: MCS

The development of computational tools based on the thermodynamic properties of geologic materials to model phase equilibria in fully or partially melted silicate systems (e.g., Ariskin et al., 1993; Carmichael et al., 1977; Ghiorso, 1985; Ghiorso & Sack, 1995; Gualda et al., 2012) has been one of the most significant advances in igneous petrology of recent decades. Although the MELTS software includes a rudimentary bulk assimilation function (Ghiorso & Kelemen, 1987; Ghiorso & Sack, 1995; see also Reiners et al., 1995), the treatment of the wall rock using a composite open system approach similar to that for the parental magma had been lacking before the introduction of MCS (Bohrson et al., 2014, 2020; Heinonen et al., 2020).

Using a selected MELTS engine (currently pMELTS or rhyolite-MELTS versions 1.0.x, 1.1.x, or 1.2.x; Ghiorso & Gualda, 2015; Ghiorso & Sack, 1995; Ghiorso et al., 2002; Gualda et al., 2012), MCS models the phase equilibria and major element evolution of a composite system composed of subsystems that are crystallizing magma body, wall rock, and up to five recharge magmas. MCS utilizes the same thermodynamic system definitions as EC-RAχFC (Figure 7.6) with the exception of excluding enclave formation associated with recharge events. The incremental portions of wall-rock partial melt exceeding the set percolation threshold (i.e., the critical melt fraction for melt extraction to be possible) and recharge magmas are always completely equilibrated with the resident melt. If using the MELTS engines 1.1.x or 1.2.x, MCS also models the evolution of a possible fluid phase (consisting of H_2O and/or CO_2) in the subsystems. MCS is continuously being developed, and the reader should refer to http://mcs.geol.ucsb.edu/, where updates are announced and the latest public version is available for users.

As in the case of EC-AFC, we focus on modeling of assimilation without recharge in MCS in the following discussion. Input for MCS is a single Microsoft Excel worksheet that the software reads before commencing a run. The input consists of system variables (e.g., wall-rock percolation threshold, excluded MELTS phases, pressure, and oxygen fugacity) and initial thermal and compositional parameters for the parental magma, wall rock (if included), and recharge magma (if any). The models are always isobaric, and the mass of the initial resident magma is 100 non-dimensional units. Note that, due to lack of thermodynamic data, modeling of systems including carbonatitic magmas or carbonate wall rock may halt the engine. In addition, the MELTS engine may not find feasible solutions for highly hydrous systems that show evidence of significant fractionation of, for example, biotite or hornblende.

As in EC-AFC models, the resident magma temperature is the progress variable in MCS; the user defines a temperature decrement that tracks cooling and crystallization of the magma body. During an MCS-AFC run, the initial temperature of the resident magma begins to decrease in user-defined steps. During each step, both the amount of heat (sensible + latent heats) that homogeneously distributes into the wall rock and the equilibrium phase assemblages for the resident magma (i.e., major element compositions of stable melt + solids ± fluid phases) are calculated. The fractional crystallization of the resident magma is modeled in these steps within which crystallization takes place in equilibrium with the melt as in the stand-alone MELTS platform; larger temperature steps more closely approximate equilibrium crystallization. For each temperature decrement, the equilibrium solids fractionate into a cumulate solid reservoir that remains chemically but not thermally isolated from the melt in the magma subsystem. Separation of a possible fluid phase is treated similarly to crystallization. The model proceeds as magma cools via the user-defined temperature decrement. If enough heat is transferred, the wall-rock partial melting begins, after which the equilibrium phase assemblages and their major element compositions are also defined for the wall rock. Unlike in the EC-AχFC model, the wall-rock melt forms via equilibrium melting rather than via fractional melting.

After assimilation begins, the amount of wall-rock partial melt that is transferred into the magma chamber is the portion that exceeds the wall-rock percolation threshold value. This wall-rock partial melt batch is thermally equilibrated and chemically homogenized with the resident melt, and the next magma temperature decrement and crystallization step is performed on the resulting homogenized melt composition. The continuous extraction of wall-rock partial melt results in a change in residual bulk composition and hence phase equilibria in the remaining wall rock, which becomes more mafic and refractory. The MCS model continues until the resident magma and the wall rock reach thermal equilibrium or a pre-constrained resident magma temperature or residual melt mass is achieved. MCS can also model bulk AFC by introducing a stoped wall-rock block that may be composed of variable proportions of solid phases, melt, and fluid. Computationally, this process utilizes the recharge function of MCS because assimilation of a stoped block can be treated with the same thermodynamic and mathematical approach. The bulk stoped block is homogenized with the resident melt, and the resulting contaminated magma reflects the thermodynamic consequences.

The MCS output includes the phase equilibria, major element compositions of the subsystem melts and all stable solid and fluid phases at each step, and various thermal and mass parameters of the system and subsystems. Calculations of the evolution of up to 48 trace elements and 8 isotope ratios ($^{87}Sr/^{86}Sr$, $^{143}Nd/^{144}Nd$, $^{176}Hf/^{177}Hf$, $^{206}Pb/^{204}Pb$, $^{207}Pb/^{204}Pb$, $^{208}Pb/^{204}Pb$, $^{187}Os/^{188}Os$, and $\delta^{18}O$) in the resident melt, solids, and fluids can be performed.

These calculations are based on equations AIV-2–4 of Spera et al. (2007) and utilize phase-specific user-input partition coefficients.

7.3.5. Comparison of the Different Assimilation Models

The differences between the aforementioned models are illustrated for a representative case of a basaltic melt derived from a depleted mantle source assimilating average continental crust (compositions in Table 7.2). The other model parameters are listed in Table 7.3, except for the extensive set of partition coefficients used for the MCS models that are listed separately in Table 7.4. The model results are illustrated in Figures 7.7–7.9. Note that the AFC_{DP} and EC-AχFC models only include trace elements. EC-AχFC thermal parameters represent the standard upper crustal case of Bohrson and Spera (2001), which have been widely used in the literature (e.g., Cucciniello et al., 2010; Günther et al., 2018; Jennings et al., 2017; Jourdan et al., 2007). In the MCS model, the amount of wall rock involved is half the amount of parental magma. The input and output of the MCS model presented here can be downloaded from the MCS website at http://mcs.geol.ucsb.edu/.

Table 7.2 Composition End-members Used in the Assimilation Models

	Parental melt[a]	Wall rock[b]
Majors		
SiO_2 (wt.%)	50.37	66.28
TiO_2	1.77	0.63
Al_2O_3	14.07	15.26
Fe_2O_3	1.79	0.84
FeO	8.98	4.24
MnO	0.18	0.10
MgO	7.97	2.45
CaO	12.33	3.55
Na_2O	2.16	3.23
K_2O	0.23	2.77
P_2O_5	0.15	0.15
H_2O	–	0.50
Traces		
Ni (ppm)	154	47
Rb	2.4	84
Sr	226	320
Nd	10.53	27
Isotopes		
$^{87}Sr/^{86}Sr$	0.702819	0.716
$^{143}Nd/^{144}Nd$	0.513074	0.51178

[a] Volatile-free parental melt composition after a depleted continental flood basalt dike sample P27-AVL (Luttinen & Furnes, 2000), except for the isotopic composition that represents the mean modern MORB (Gale et al., 2013). FeO versus Fe_2O_3 calculated from FeO^{tot} at QFM at 2 kbar with rhyolite-MELTS 1.2.0 (Gualda et al., 2012; Ghiorso & Gualda, 2015).

[b] Wall-rock composition after average upper continental crust of Rudnick and Gao (2003), except for the addition of 0.5 wt.% of water and the isotopic composition that is the estimation of the average composition of modern river waters globally (Goldstein & Jacobsen, 1988). FeO versus Fe_2O_3 calculated in the same way as for the parental melt.

As mentioned previously, the binary mixing model results in straight lines in x-y diagrams between the end-members (Figures 7.4a and 7.7a–c), except if distinct elemental and isotopic ratios are involved (Figures 7.4b and 7.7d). In comparison, the inclusion of fractional crystallization in the AFC_{DP} model is illustrated by the trend not pointing toward the wall-rock composition. Simultaneously with assimilation of the wall-rock bulk composition, crystallization depletes the melt of compatible elements and enriches it in incompatible elements. Changes in the Sr isotope composition relative to changes in the Nd isotope composition are more dramatic for the AFC_{DP} model compared to the binary mixing model because Sr is more compatible than Nd in the solids in the crystallizing resident magma (Figure 7.7d); when Sr is efficiently depleted from the resident melt, wall-rock control on its isotopic composition increases. Nevertheless, both bulk mixing and AFC_{DP} models commonly use bulk country rock composition as the contaminant, which has significant but often overlooked compositional effects: incompatible trace elements get rather subtly enriched in the resident melt relative to the degree of assimilation (Figure 7.7c). This is exemplified in studies on mafic systems, for which thermodynamically unfeasible amounts (several tens of wt.% relative to mass of the parental magma) of assimilation are implied by such models to explain the most contaminated trace element and radiogenic isotope compositions (e.g., Carlson et al., 1981; Goodrich & Patchett, 1991; Larsen & Pedersen, 2009; Molzahn et al., 1996).

In comparison to AFC_{DP}, EC-AχFC includes thermal parameters and partition coefficients for the partial melting of the wall rock. In the standard upper crustal case of Bohrson and Spera (2001), the wall rock is heated from its initial temperature (300 °C) all the way to its solidus (900 °C), which requires a significant release of latent heat via crystallization of the magma. Because of this, the start of assimilation is delayed until after about 70 wt.% of crystallization (Figure 7.8b). After assimilation begins, the earliest wall-rock partial melts, which are modeled by fractional melting in EC-AχFC, are loaded with incompatible elements, which results in considerable enrichment in their concentrations in the resident melt (e.g., Rb in Figure 7.7c). The extracted partial melts

Table 7.3 Physical and Thermal Parameters for the AFC$_{DP}$, EC-AχFC, and MCS Models and the Bulk Partition Coefficients for the AFC$_{DP}$ and EC-AFC Models

AFC$_{DP}$[a]		EC-AχFC[b]		MCS[c]	
r	0.5	Magma liquidus T (°C)	1280	Rhyolite-MELTS engine	1.2.0
Magma solid-melt D's		Magma initial T (°C)	1280	F_l^{WR} (FmZero)	0.1
D(Ni)^M	5	Wall-rock liquidus T (°C)	1000	Pressure (bars)	2000
D(Rb)^M	0.05	Wall-rock initial T (°C)	300	Magma initial T (°C)	1225
D(Sr)^M	1	Solidus T (°C)	900	Magma T decrement (°C)	5
D(Nd)^M	0.2	Specific heat of magma (J/kg·K)	1484	Wall-rock find solidus: end T (°C)	680
		Specific heat of wall rock (J/kg·K)	1370	Wall-rock find solidus: T decr. (°C)	5
		H of crystallization of magma (J/kg)	396000	Wall-rock find solidus: start T (°C)	950
		H of melting of wall rock (J/kg)	270000	Wall-rock mass (Magma = 100)	50
		χ	0.9	Wall-rock initial T (°C)	300
		Equilibration T (°C)	980		
				Phase-specific K$_D$'s given in Table 7.4	
		Magma solid-melt D's			
		D(Ni)^M	5		
		D(Rb)^M	0.05		
		D(Sr)^M	1		
		D(Nd)^M	0.2		
		Wall-rock solid-melt D's			
		D(Ni)^{WR}	2		
		D(Rb)^{WR}	0.03		
		D(Sr)^{WR}	6		
		D(Nd)^{WR}	0.3		

[a] *D* values represent average values of the MCS model (Table 7.4)

[b] Thermal parameters represent the standard upper crustal case of Bohrson and Spera (2001), *D* values represent average values of the MCS model (Table 7.4), and the model has been run using nonlinear logistical melting functions.

[c] Thermal parameters defined at 2 kbar with rhyolite-MELTS 1.2.0. (Gualda et al., 2012; Ghiorso & Gualda, 2015). Note that F_l^{WR} corresponds to 1−χ in EC-AχFC. See Bohrson et al. (2020) and MCS website (http://mcs.geol.ucsb.edu/) for details regarding the input.

Table 7.4 Phase-Specific Partition Coefficients for the MCS Models

	Magma solid-melt K$_D$'s[a]				Wall-rock solid-melt K$_D$'s[a]			
	K$_D$(Ni)^M	K$_D$(Rb)^M	K$_D$(Sr)^M	K$_D$(Nd)^M	K$_D$(Ni)^{WR}	K$_D$(Rb)^{WR}	K$_D$(Sr)^{WR}	K$_D$(Nd)^{WR}
Alkali feldspar[c]	—	—	—	—	0.5	0.4	5	0.02
Biotite	—	—	—	—	15	3	0.5	1
Clinopyroxene[b]	3	0.01	0.1	0.2	—	—	—	—
Orthopyroxene	—	—	—	—	10	0.01	0.01	1
Plagioclase[c]	0.1	0.1	3	0.1	0.5	0.02	10	0.2
Quartz	—	—	—	—	0	0	0	0
Rhm-oxide	30	0.1	0.1	0.1	5	0.04	0.1	1
Spinel	30	0.1	0.1	0.1	5	0.04	0.1	1

[a] Compiled on the basis of the EarthRef database (https://earthref.org/KDD/).

[b] MELTS identifies two distinct clinopyroxene phases in the magma in the model, but they are treated equally in the trace element model.

[c] Plagioclase and alkali feldspar are respectively denoted "feldspar {1}" and "feldspar {2}" in the model output.

progressively deplete the residual wall rock of incompatible elements as assimilation proceeds. For this reason, resident melt with higher degrees of assimilation may actually show relatively lower concentrations of such elements than earlier less contaminated resident melt. This is the case for Rb here: enrichment in the resident melt caused by fractional crystallization cannot compete with dilution caused by progressive assimilation of now Rb-depleted wall-rock partial melts (Figure 7.7c). In contrast, an element that is compatible in wall rock (e.g., Sr in

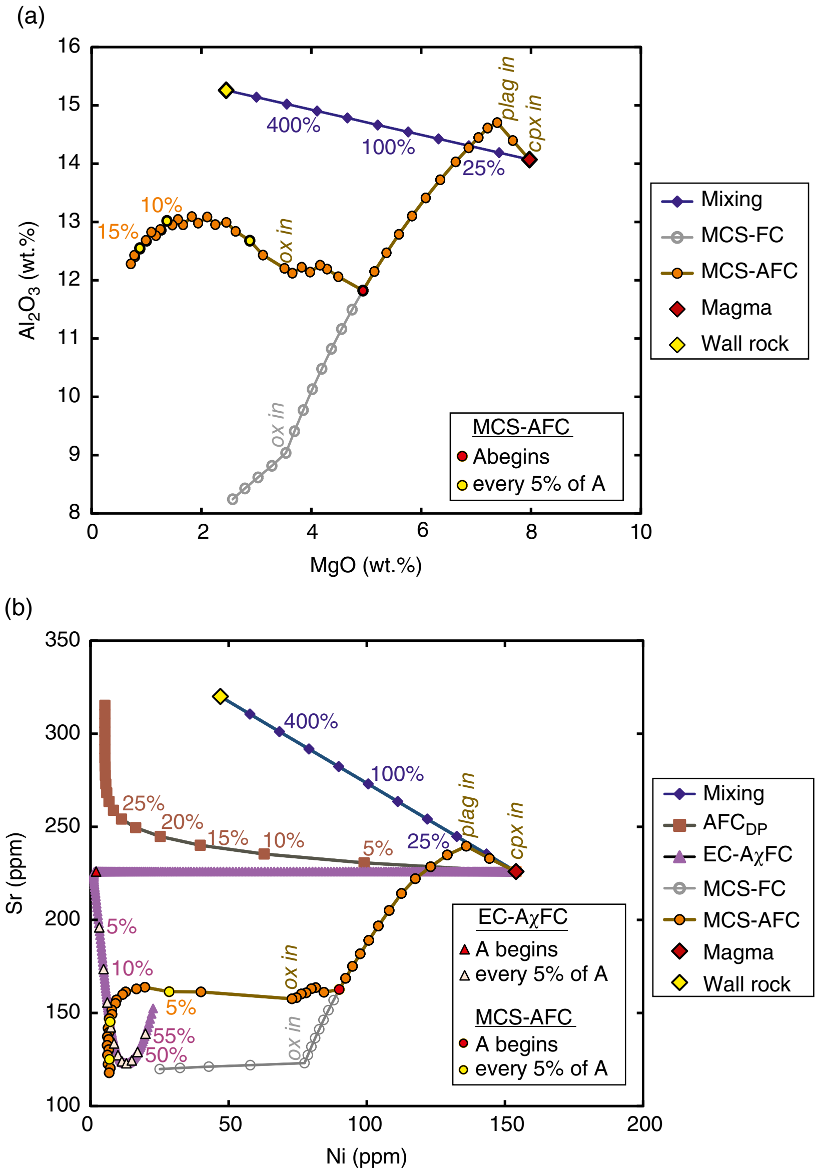

Figure 7.7 Outcomes of the resident melt composition of the binary mixing, AFC_{DP}, EC-AχFC, and MCS models (Tables 7.2–7.4) shown in MgO versus Al_2O_3 (a), Ni versus Sr (b), Ni versus Rb (c), and $^{87}Sr/^{86}Sr$ versus $^{143}Nd/^{144}Nd$ (d) diagrams. The presented AFC_{DP} and EC-AχFC models do not include major elements and are thus not shown in (a). An MCS fractional crystallization model for the parental melt (Table 7.1) is shown for reference in (a)–(c); the amount of fractionation (~80 % relative to the mass of the parental melt) in it is similar to that of the primary MCS model with assimilation. The tick marks represent additions or decrements of model-specific progress variables as listed in Table 7.1 and all starting from the parental melt composition: For the binary mixing model, tick marks denote an increase of 0.1 in the fraction of WR in the mixture; for the AFC_{DP} model, they denote decrements of 0.05 in *F* and increments of 0.05 in the mass of added assimilant relative to the parental melt; in the case of the EC-AχFC model, they denote ~1°C temperature decrements; and for the MCS model, they denote the imposed 5 °C magma temperature decrements and the assimilation steps. Note that the mass of assimilated wall rock relative to the mass of parental melt is indicated as percentages for all models. Steps during which a new phase joins the crystallization assemblage in the resident magma are indicated for the MCS models (cpx = clinopyroxene, plag = plagioclase feldspar, ox = spinel and/or rhombohedral oxide, the latter shown for the FC and AFC_{DP} models separately), except in (d).

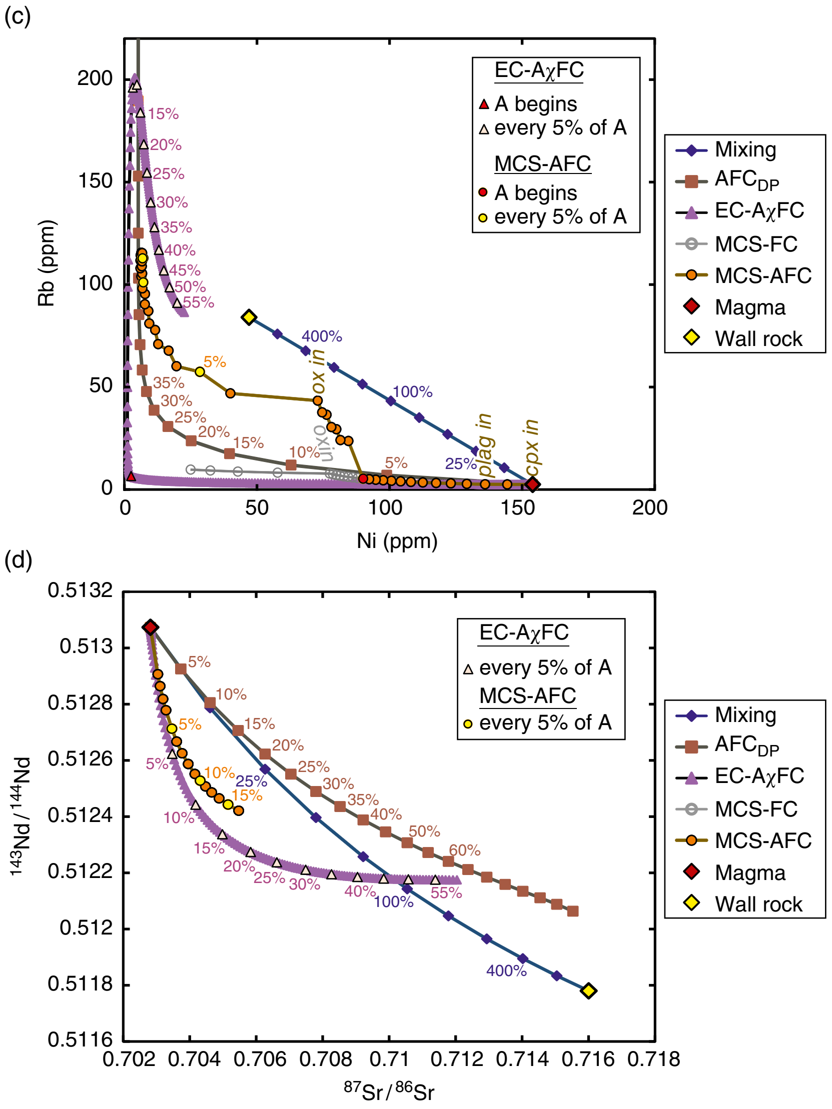

Figure 7.7 (Continued)

Figure 7.7b) shows exactly the opposite behavior. The compatibility of Sr in the wall rock also delays the effect of assimilation on the Sr isotopic composition of the resident melt (Figure 7.7d).

MCS considers the evolution of phase equilibria and major elements, trace elements, and isotopes throughout the crystallization and assimilation process (Figure 7.7). In addition, and as in EC-AχFC, it is not only possible to follow the evolution of the resident magma, but also the composition of the cumulate and the composition of the wall-rock partial melt (which forms by equilibrium melting unlike in EC-AχFC) and the residual wall rock (Figure 7.9). The output thus provides several geochemical tracers for understanding assimilation processes in various extrusive and intrusive systems. In the case of elements that show varying compatibility in stable phases (e.g., Sr and Ni; see Table 7.4), the assimilation trends may be considerably complex (Figure 7.7b). Figure 7.8 illustrates how the MCS model, which takes the changing thermodynamic properties of the resident magma and wall rock within each temperature step into account, thermally differs from the standard EC-AFC upper crustal case of Bohrson and Spera (2001). The wall rock is efficiently heated by the high amount of early crystallization in the MCS model, and the solidus of the wall rock is lower and attained earlier. Comparison with a MCS fractional crystallization model (Figures 7.7a–c) illustrates that assimilation may have notable effects, not only on incompatible element concentrations (Figure 7.7c), but also on the major element composition of the resident melt (Figure 7.7a).

The presented EC-AχFC and MCS models illustrate that considerable amounts of crystallization and heat

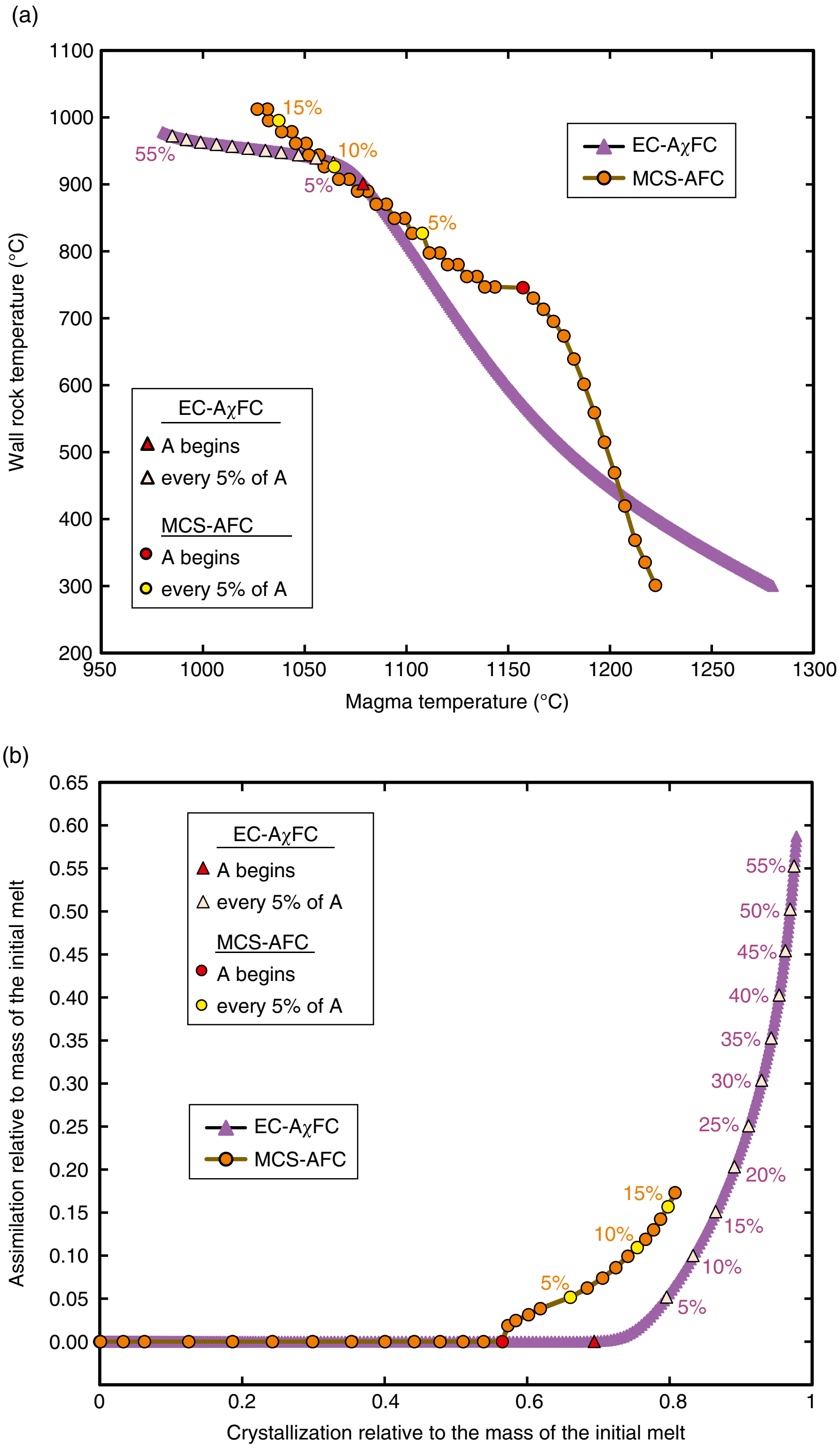

Figure 7.8 Thermodynamic comparisons of the EC-AχFC and MCS models (Tables 7.2–7.4) shown in magma temperature versus wall-rock temperature (a) and mass of cumulate versus mass of assimilated wall rock (b) diagrams. See Figure 7.7 for additional details.

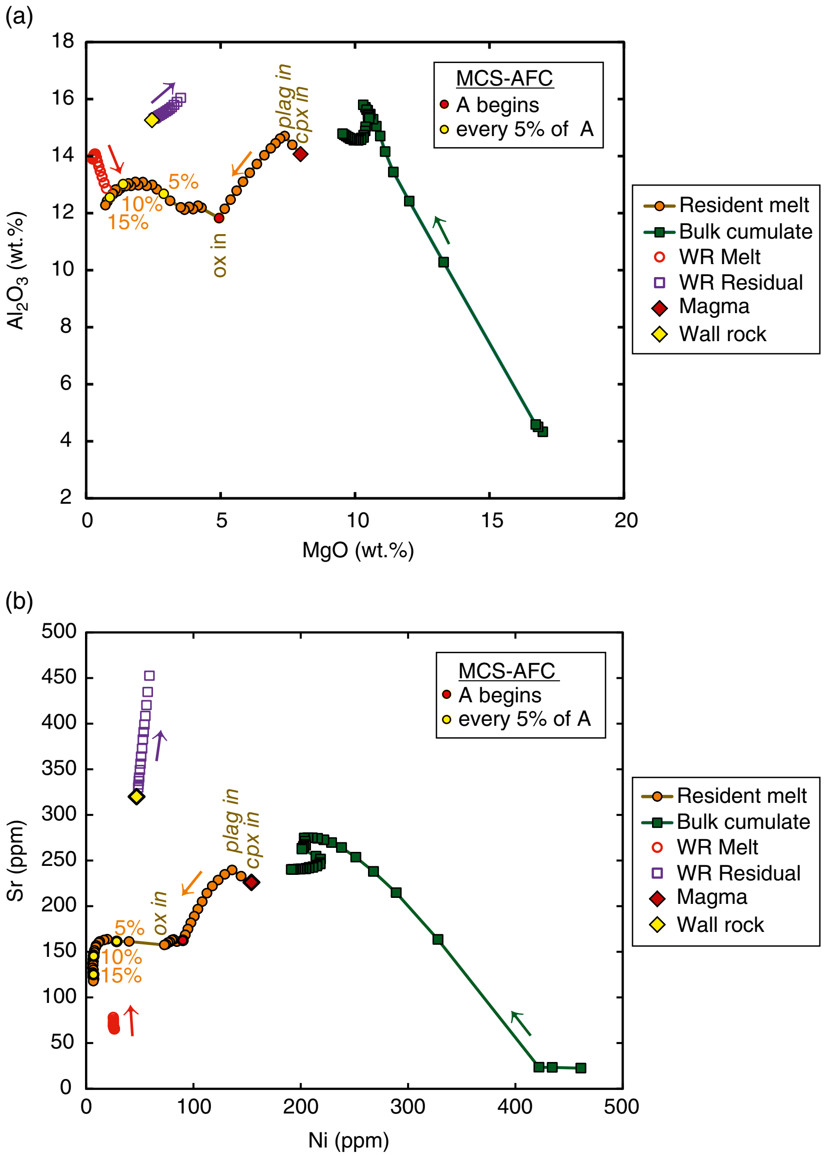

Figure 7.9 Outcomes of the resident melt, bulk cumulate, wall-rock melt, and wall-rock residual (solid + melt) compositions of the MCS-AFC model (Tables 7.2–7.4) shown in MgO versus Al_2O_3 (a) and Ni versus Sr (b) diagrams. See Figure 7.7 for additional details.

exchange between the magma and wall rock are required before assimilation begins (Figure 7.9). Movement of such magmas would obviously stall after the onset of assimilation due to their high crystal contents, unless the crystals were efficiently separated from the melt as MCS assumes. In cases where significant assimilation has obviously taken place in relatively primitive magmas, preheating of the wall rock by hydrothermal systems, previous magma pulses, or more primitive parental magma may have to be taken into consideration. Accordingly, the initial wall-rock temperature may need to be set to a higher value than would otherwise be suggested, for example, based on continental geotherms (see Heinonen et al., 2016, 2019; Moore et al., 2018). Alternatively, inclusion of a lower mass of wall rock in the model could more closely replicate the initial stages of magma emplacement, where only a thin zone of wall rock is subjected to heat exchange. The mass of wall rock to be included in MCS models in different environments is extensively discussed in Bohrson et al. (2014).

It should be noted, that whereas a standard case of wall-rock assimilation in MCS always requires partial melting, energy requirements for reactive bulk assimilation of disintegrated wall-rock blocks may be much lower (Beard et al., 2005). This may be the case in some felsic systems, where there is less heat available for complete melting reactions to take place in the wall rock. Such cases can be modeled with stoped blocks in MCS (see section 7.3.4), and the result would chemically approach the result of binary mixing. On the other hand, the strong crustal chemical overprint in many basalts lacking any macroscopic evidence of assimilation (Figure 7.1c; e.g., Carlson, 1991; Heinonen et al., 2016; Larsen & Pedersen, 2009; Lightfoot et al., 1993) testifies that (partial) melting of the wall rock and homogenization of these melts with the resident magma or complete digestion of stoped blocks must be a significant processes in their differentiation.

7.3.6. MCS Applied to a Natural System: Flood Basalts From Antarctica

Comparisons of hypothetical models presented in the previous section illustrate the differences between the discussed methods and highlight the capabilities of MCS, but it is also instructive to provide an example of MCS applied to a natural system. Fully documenting an MCS model for a natural system requires extensive background and discussion (e.g., on the feasibility of the selected input values). Thus, for illustrative purposes we provide a short overview of already published results and modeling for Antarctic flood basalts that belong to the ~180 Ma Karoo large igneous province (see also Figure 7.10). The reader is referred to the original publication (Heinonen et al., 2019) for more detailed information and for the original MCS input and output.

The lavas in question (low-ε_{Nd} CT1 magma type; Luttinen & Furnes, 2000) exhibit clear evidence of assimilation of Archean crust, such as their anomalously low ε_{Nd} (from −16 to −11 at 180 Ma; Figure 7.10d) and high Th/Nb (Heinonen et al., 2016; Luttinen & Furnes, 2000). They are characterized by typical tholeiitic low-pressure phenocryst assemblages consisting of varying amounts of plagioclase, clinopyroxene, and olivine, but some of the most primitive samples also contain orthopyroxene phenocrysts.

Before the introduction of MCS, the evolution of the parental magmas of these flood basalts was not well constrained. Although there was evidence of fractional crystallization and assimilation, it was unclear how these processes were linked and what the associated PT conditions were throughout the evolution of the magma series. MCS modeling revealed that neither FC nor AFC at constant pressure could explain the mineral, major element, trace element, and isotopic composition of the lavas (MCS-AFC model at 500 MPa shown in Figure 7.10). The crystallization of orthopyroxene required a pressure of at least 300 MPa (depth of ~10 km), but the Al_2O_3 inflection point at ~7 wt.% of MgO (i.e., beginning of plagioclase fractionation) was not produced with FC or AFC at such high pressures. The best fit was attained with a two-stage model, where the parental magmas first fractionated olivine and orthopyroxene and variably assimilated Archean wall rock at higher pressures (~300–700 MPa), and then fractionated plagioclase, clinopyroxene, and olivine at lower pressures without notable assimilation (≤100 MPa). Note that an early stage of AFC is required to explain the full range of trace element ratios (e.g., Zr/Y; Figure 7.10c) and radiogenic isotope compositions (Figure 7.10d) in the lavas. The presented model is in agreement with thermophysical considerations: assimilation is more likely in magmas either pooled in or slowly moving through deep hotter crust compared to rapid rise of magma through a shallower dike and sill network that is embedded in colder wall rock (Heinonen et al., 2019).

The presented example provides a strong case of how understanding of igneous petrology benefits from the use of thermodynamically constrained phase equilibria in modeling assimilation and crystallization processes. It could not have been modeled by binary mixing, AFC_{DP}, or EC-AχFC, but requires an internally consistent solution for phase equilibria and major element, trace element, and isotopic compositions that is provided by MCS. An additional example of MCS revealing the effect of recharge and assimilation processes in the geochemical evolution of primitive oceanic island magmas (Kerguelen) is given in Borisova et al. (2017).

7.4. SUMMARY

Assimilation, in its simplest form, can be distinguished from other end-member modes of magmatic interaction (hybridization, mingling, and stoping) by the following definition: assimilation is a process in which an initial state (t_0) that includes a system of melt and solid wall rock evolves to a later state (t_n) where the two entities have been completely homogenized into one melt at a given scale. In complex natural systems involving crystallization of the resident melt and melting of the wall rock, this definition can be broadened to describe a process where a mass of magma fully or partially homogenizes with materials derived from wall rock that initially behaves as a solid (i.e., its degree of partial melting is below the critical melt fraction).

Our comparison of geochemical assimilation models (binary mixing, AFC_{DP}, EC-AχFC, and MCS) reveals considerable differences in their outcomes using uniform parental melt and wall-rock compositions and highlights the value of MCS in understanding the thermochemical consequences of assimilation in magmatic systems. We conclude that the use of binary mixing equations in modeling assimilation without any consideration of associated

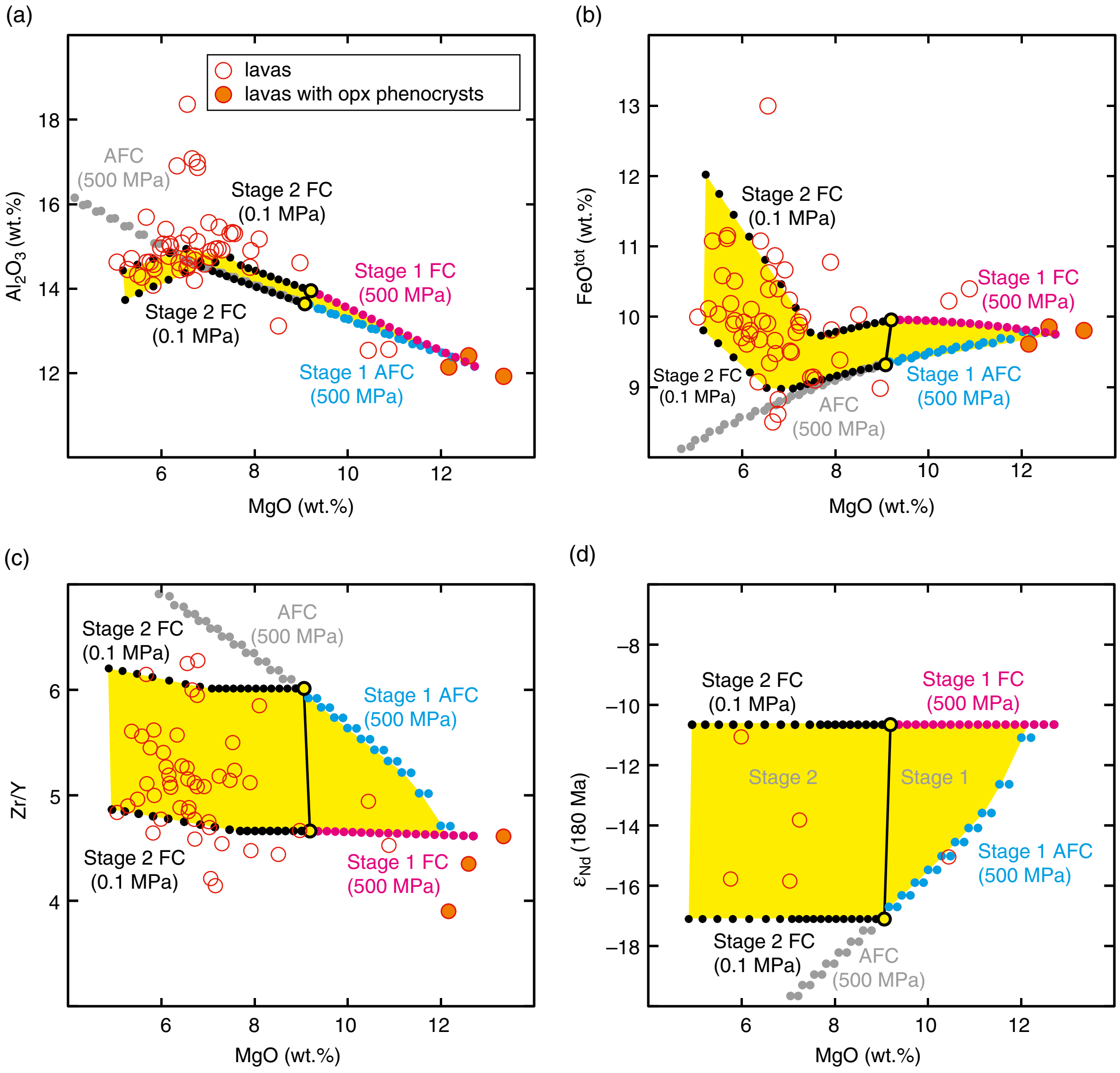

Figure 7.10 MCS modeling of Antarctic continental flood basalts (~180 Ma Karoo LIP; low-ε_{Nd} CT1 magma type of Luttinen & Furnes, 2000). Primitive lava samples with orthopyroxene phenocrysts are highlighted. Stage 1 is represented by FC and AFC at high pressures (model results at 500 MPa shown here) and is followed by FC during Stage 2 at atmospheric pressure. The yellow field encompasses all possible variations within the end-member Stage 1 + Stage 2 model scenarios. An isobaric (500 MPa) MCS-AFC model shown for reference. For more details, see section 7.3.6 and Heinonen et al. (2019).

thermodynamics should be avoided. It is very unlikely that any differentiation trend points toward the assimilant composition; therefore, an approach that attempts to define the composition of the assimilant on the basis of hypothetical mixing trends (see, e.g., Pushkar et al., 1971) is inchoate and potentially misleading. On the other end of the modeling spectrum, MCS provides insight into the phase equilibria of crystallization and assimilation. Its use should be favored over AFC_{DP} and EC-AFC models, although in the case of elements that are either highly incompatible or compatible to the resident magma (+ wall rock in the case of EC-AFC models), AFC_{DP} (at low r values) and EC-AFC trends may closely correspond to MCS trends (Figure 7.7c). Nevertheless, even in such cases, the amount of assimilation indicated by AFC_{DP} or EC-AFC models can be considerably different from that of MCS and is likely not to be as closely representative of the natural system because of the lack of complete (AFC_{DP}) or detailed (EC-AFC) thermodynamic control.

A presented example of MCS applied to a natural system manifests its capabilities by revealing a multi-stage evolution of a continental flood basalt magma system in which the magma system is best modeled by AFC and FC processes that occur at different crustal depths. Finally, we note that the influence of assimilation is always element-specific and dependent on the relative concentrations of different elements in the evolving magma and wall rock and the mass contributions of each of these to the contaminated system. Therefore, if a researcher considers assimilation important, the mass effect should always be specified with respect to what element (or other feature) this importance is defined. MCS is a modeling tool that helps to address this issue.

ACKNOWLEDGMENTS

We are grateful to the volume editors for the invitation to contribute. We are grateful to Koshi Nishimura, an anonymous reviewer, and the volume editor Christoph Beier for very valuable and balanced commentary that significantly improved the manuscript. The person responsible for the copyediting is also thanked for excellent copyediting of the chapter. This contribution has benefited from the funding by the Academy of Finland (Grant Nos. 295129 and 306962) and the Doctoral school in natural sciences, University of Helsinki. FJS acknowledges continual support from the U.S. National Science Foundation and the U.S. Department of Energy throughout the past four and a half decades.

REFERENCES

Allégre, C. J., & Minster, J. F. (1978). Quantitative models of trace element behavior in magmatic processes. *Earth and Planetary Science Letters*, *38*(1), 1–25. https://doi.org/10.1016/0012-821X(78)90123-1

Ariskin, A. A., Frenkel, M. Y., Barmina, G. S., & Nielsen, R. L. (1993). Comagmat: a Fortran program to model magma differentiation processes. *Computers & Geosciences*, *19*(8), 1155–1170. https://doi.org/10.1016/0098-3004(93)90020-6

Arzi, A. A. (1978). Critical phenomena in the rheology of partially melted rocks. *Tectonophysics*, *44*(1), 173–184. https://doi.org/10.1016/0040-1951(78)90069-0

Asrat, A., Gleizes, G., Barbey, P., & Ayalew, D. (2003). Magma emplacement and mafic–felsic magma hybridization: structural evidence from the Pan-African Negash pluton, Northern Ethiopia. *Journal of Structural Geology*, *25*(9), 1451–1469. https://doi.org/10.1016/S0191-8141(02)00182-7

Beard, J. S., Ragland, P. C., & Crawford, M. L. (2005). Reactive bulk assimilation: A model for crust-mantle mixing in silicic magmas. *Geology*, *33*(8), 681–684. https://doi.org/10.1130/G21470AR.1

Bell, K., & Powell, J. L. (1969). Strontium isotopic studies of alkalic rocks: The potassium-rich lavas of the Birunga and Toro-Ankole regions, East and Central Equatorial Africa. *Journal of Petrology*, *10*(3), 536–572. https://doi.org/10.1093/petrology/10.3.536

Benkó, Z., Mogessie, A., Molnár, F., Severson, M. J., Hauck, S. A., & Raič, S. (2015). Partial melting processes and Cu-Ni-PGE mineralization in the footwall of the South Kawishiwi Intrusion at the Spruce Road Deposit, Duluth Complex, Minnesota. *Economic Geology*, *110*(5), 1269. https://doi.org/10.2113/econgeo.110.5.1269

Bohrson, W. A., & Spera, F. J. (2001). Energy-constrained open-system magmatic processes II: Application of energy-constrained assimilation-fractional crystallization (EC-AFC) model to magmatic systems. *Journal of Petrology*, *42*(5), 1019–1041. https://doi.org/10.1093/petrology/42.5.1019

Bohrson, W. A., & Spera, F. J. (2003). Energy-constrained open-system magmatic processes IV: Geochemical, thermal and mass consequences of energy-constrained recharge, assimilation and fractional crystallization (EC-RAFC). *Geochemistry, Geophysics, Geosystems*, *4*(2), 8002. https://doi.org/10.1029/2002GC000316

Bohrson, W. A., & Spera, F. J. (2007). Energy-Constrained Recharge, Assimilation, and Fractional Crystallization (EC-RAχFC): A Visual Basic computer code for calculating trace element and isotope variations of open-system magmatic systems. *Geochemistry, Geophysics, Geosystems*, *8*(11), Q11003. https://doi.org/10.1029/2007GC001781

Bohrson, W. A., Spera, F. J., Ghiorso, M. S., Brown, G. A., Creamer, J. B., & Mayfield, A. (2014). Thermodynamic model for energy-constrained open-system evolution of crustal magma bodies undergoing simultaneous recharge, assimilation and crystallization: The Magma Chamber Simulator. *Journal of Petrology*, *55*(9), 1685–1717. https://doi.org/10.1093/petrology/egu036

Bohrson, W. A., Spera F. J., Heinonen, J. S., Brown, G. A., Scruggs, M. A., Adams, J. V., et al. (2020). Diagnosing open-system magmatic processes using the Magma Chamber Simulator (MCS): Part I – major elements and phase equilibria. *Contributions to Mineralogy and Petrology*, *175*(11), 104. https://doi.org/10.1007/s00410-020-01722-z

Borisova, A. Y., Bohrson, W. A., & Grégoire, M. (2017). Origin of primitive ocean island basalts by crustal gabbro assimilation and multiple recharge of plume-derived melts. *Geochemistry, Geophysics, Geosystems*, *18*(7), 2701–2716. https://doi.org/10.1002/2017GC006986

Borisova, A. Y., Martel, C., Gouy, S., Pratomo, I., Sumarti, S., Toutain, J., et al. (2013). Highly explosive 2010 Merapi eruption: Evidence for shallow-level crustal assimilation and hybrid fluid. *Journal of Volcanology and Geothermal Research*, *261*, 193–208. https://doi.org/10.1016/j.jvolgeores.2012.11.002

Bowen, N. L. (1915a). The later stages of the evolution of the igneous rocks. *The Journal of Geology*, *23*(S8), 1–91. https://doi.org/10.1086/622298

Bowen, N. L. (1915b). The crystallization of haplobasaltic, haplodioritic, and related magmas. *American Journal of Science*, *s4-40*(236), 161–185. https://doi.org/10.2475/ajs.s4-40.236.161

Bowen, N. L. (1915c). Crystallization-differentiation in silicate liquids. *American Journal of Science*, *s4-39*(230), 175–191. https://doi.org/10.2475/ajs.s4-39.230.175

Bowen, N. L. (1928). *The evolution of igneous rocks*. New York, United States: Dover Publications.

Brandon, A. D. (1989). Constraints on magma genesis behind the Neogene Cascade Arc: Evidence from major and trace element variation of high-alumina and tholeiitic volcanics of the Bear Creek Area. *Journal of Geophysical Research: Solid Earth*, *94*(B6), 7775–7798. https://doi.org/10.1029/JB094iB06p07775

Bunsen, R. W. (1851). Über die prozesse der vulkanischen Gesteinsbildungen Islands. *Annotations of Physical Chemistry*, *83*, 197–272.

Burda, J., Gawęda, A., & Klötzli, U. (2011). Magma hybridization in the Western Tatra Mts. granitoid intrusion (S-Poland, Western Carpathians). *Mineralogy and Petrology*, *103*(1), 19–36. https://doi.org/10.1007/s00710-011-0150-1

Carlson, R. W. (1991). Physical and chemical evidence on the cause and source characteristics of flood basalt volcanism. *Australian Journal of Earth Sciences*, *38*(5), 525–544.

Carlson, R. W., Lugmair, G. W., & Macdougall, J. D. (1981). Crustal influence in the generation of continental flood basalts. *Nature*, *289*(5794), 160−162. https://doi.org/10.1038/289160a0

Carmichael, I. S. E., Nicholls, J., Spera, F. J., Wood, B. J., Nelson, S. A., Bailey, D. K., et al. (1977). High-temperature properties of silicate liquids: Applications to the equilibration and ascent of basic magma [and discussion]. *Philosophical Transactions of the Royal Society of London. Series A: Mathematical and Physical Sciences*, *286*(1336), 373–431.

Carter, S. R., Evensen, N. M., Hamilton, P. J., & O'Nions, R. K. (1978). Neodymium and strontium isotope evidence for crustal contamination of continental volcanics. *Science*, *202*(4369), 743–747. https://doi.org/10.1126/science.202.4369.743

Clemens, J. D., & Stevens, G. (2016). Melt segregation and magma interactions during crustal melting: Breaking out of the matrix. *Earth-Science Reviews*, *160*, 333–349. https://doi.org/10.1016/j.earscirev.2016.07.012

Cucciniello, C., Langone, A., Melluso, L., Morra, V., Mahoney, J. J., Meisel, T., & Tiepolo, M. (2010). U-Pb ages, Pb-Os isotope ratios, and platinum-group element (PGE) composition of the West-Central Madagascar Flood Basalt Province. *The Journal of Geology*, *118*(5), 523–541. https://doi.org/10.1086/655012

Daly, R. A. (1905). The secondary origin of certain granites. *American Journal of Science*, *s4-20*(117), 185–216. https://doi.org/10.2475/ajs.s4-20.117.185

Daly, R. A. (1910). Origin of the alkaline rocks. *Geological Society of America Bulletin*, *21*(1), 87–118. https://doi.org/10.1130/GSAB-21-87

Danckwerts, P. V. (1952). The definition and measurement of some characteristics of mixtures. *Applied Scientific Research: Section A*, *3*(4), 279–296. https://doi.org/10.1007/BF03184936

Danckwerts, P. V. (1953). Theory of mixtures and mixing. *Research (London)*, *6*, 355–361.

DePaolo, D. J. (1981). Trace element and isotopic effects of combined wallrock assimilation and fractional crystallization. *Earth and Planetary Science Letters*, *53*(2), 189–202. https://doi.org/10.1016/0012-821x(81)90153-9

Depaolo, D. J. (1985). Isotopic studies of processes in mafic magma chambers: I. The Kiglapait intrusion, Labrador. *Journal of Petrology*, *26*(4), 925–951. https://doi.org/10.1093/petrology/26.4.925

Farner, M. J., Lee, C. A., & Putirka, K. D. (2014). Mafic–felsic magma mixing limited by reactive processes: A case study of biotite-rich rinds on mafic enclaves. *Earth and Planetary Science Letters*, *393*, 49–59. https://doi.org/10.1016/j.epsl.2014.02.040

Faure, G., Bowman, J. R., Elliot, D. H., & Jones, L. M. (1974). Strontium isotope composition and petrogenesis of the Kirkpatrick Basalt, Queen Alexandra Range, Antarctica. *Contributions to Mineralogy and Petrology*, *3*(3), 153–169. https://doi.org/10.1007/bf00383353

Fenner, C. N. (1926). The Katmai magmatic province. *The Journal of Geology*, *34*(7), 673–772.

Fred, R., Heinonen, A., & Heikkilä, P. (2019). Tracing the styles of mafic-felsic magma interaction: A case study from the Ahvenisto igneous complex, Finland. *Bulletin of the Geological Society of Finland*, *91*(1), 5–33.

Gale, A., Dalton, C. A., Langmuir, C. H., Su, Y., & Schilling, J. (2013). The mean composition of ocean ridge basalts. *Geochemistry, Geophysics, Geosystems*, *14*(3), 489–518. https://doi.org/10.1029/2012GC004334

Gardner, M. F., Troll, V. R., Gamble, J. A., Gertisser, R., Hart, G. L., Ellam, R. M., et al. (2013). Crustal differentiation processes at Krakatau volcano, Indonesia. *Journal of Petrology*, *54*(1), 149–182. https://doi.org/10.1093/petrology/egs066

Gary, M., McAfee, R., & Wolf, C. L. (Eds.). (1972). *Glossary of Geology*. Washington DC, United States: American Geological Institute.

Ghiorso, M. S. (1985). Chemical mass transfer in magmatic processes; 1, Thermodynamic relations and numerical algorithms. *Contributions to Mineralogy and Petrology*, *90*(2–3), 107–120. https://doi.org/10.1007/BF00378254

Ghiorso, M. S., & Gualda, G. A. R. (2015). An H_2O–CO_2 mixed fluid saturation model compatible with rhyolite-MELTS. *Contributions to Mineralogy and Petrology*, *169*(6), 53. https://doi.org/10.1007/s00410-015-1141-8

Ghiorso, M., & Kelemen, P. (1987). Evaluating reaction stoichiometry in magmatic systems evolving under generalized thermodynamic constraints: examples comparing isothermal and isenthalpic assimilation. In B. O. Mysen (Ed.), *Magmatic Processes: Physicochemical Principles, The Geochemical Society, Special Publication* (Vol. *1*, pp. 319–336).

Ghiorso, M. S., & Sack, R. O. (1995). Chemical mass transfer in magmatic processes IV. A revised and internally consistent thermodynamic model for the interpolation and extrapolation of liquid-solid equilibria in magmatic systems at elevated temperatures and pressures. *Contributions to Mineralogy and Petrology*, *119*(2–3), 197–212. https://doi.org/10.1007/bf00307281

Ghiorso, M. S., Hirschmann, M. M., Reiners, P. W., & Kress, V. C., III (2002). The pMELTS: A revision of MELTS for improved calculation of phase relations and major element partitioning related to partial melting of the mantle to 3 GPa. *Geochemistry, Geophysics, Geosystems*, *3*(5), 1–35. https://doi.org/10.1029/2001GC000217

Goldstein, S. J., & Jacobsen, S. B. (1988). Nd and Sr isotopic systematics of river water suspended material: implications for crustal evolution. *Earth and Planetary Science Letters*, *87*(3), 249−265. https://doi.org/10.1016/0012-821x(88)90013-1

Goodrich, C. A., & Patchett, P. J. (1991). Nd and Sr isotope chemistry of metallic iron-bearing, sediment-contaminated Tertiary volcanics from Disko Island, Greenland. *Lithos*, *27*(1), 13–27. https://doi.org/10.1016/0024-4937(91)90017-F

Gualda, G. A. R., Ghiorso, M. S., Lemons, R. V., & Carley, T. L. (2012). Rhyolite-MELTS: A modified calibration of MELTS optimized for Silica-rich, fluid-bearing magmatic systems. *Journal of Petrology*, *53*(5), 875–890. https://doi.org/10.1093/petrology/egr080

Günther, T., Haase, K. M., Klemd, R., & Teschner, C. (2018). Mantle sources and magma evolution of the Rooiberg lavas, Bushveld Large Igneous Province, South Africa. *Contributions to Mineralogy and Petrology*, *173*(6), 51. https://doi.org/10.1007/s00410-018-1477-y

Handley, H. K., Reagan, M., Gertisser, R., Preece, K., Berlo, K., McGee, L. E., et al. (2018). Timescales of magma ascent and degassing and the role of crustal assimilation at Merapi volcano (2006–2010), Indonesia: Constraints from uranium-series and radiogenic isotopic compositions. *Geochimica et Cosmochimica Acta*, *222*, 34–52. https://doi.org/10.1016/j.gca.2017.10.015

Hansen, H., & Nielsen, T. F. D. (1999). Crustal contamination in Palaeogene East Greenland flood basalts: plumbing system evolution during continental rifting. *Chemical Geology*, *157*(1–2), 89–118. https://doi.org/10.1016/S0009-2541(98)00196-X

Hayes, B., Bédard, J. H., Hryciuk, M., Wing, B., Nabelek, P., MacDonald, W. D., & Lissenberg, C. J. (2015). Sulfide Immiscibility Induced by Wall-Rock Assimilation in a Fault-Guided Basaltic Feeder System, Franklin Large Igneous Province, Victoria Island (Arctic Canada). *Economic Geology*, *110*(7), 1697–1717. https://doi.org/10.2113/econgeo.110.7.1697

Heinonen, J. S., Luttinen, A. V., & Bohrson, W. A. (2016). Enriched continental flood basalts from depleted mantle melts: modeling the lithospheric contamination of Karoo lavas from Antarctica. *Contributions to Mineralogy and Petrology*, *171*(1), 9. https://doi.org/10.1007/s00410-015-1214-8

Heinonen, J. S., Luttinen, A. V., Spera, F. J., & Bohrson, W. A. (2019). Deep open storage and shallow closed transport system for a continental flood basalt sequence revealed with Magma Chamber Simulator. *Contributions to Mineralogy and Petrology*, *174*(11), 87. https://doi.org/10.1007/s00410-019-1624-0

Heinonen, J. S., Bohrson, W. A., Spera F. J., Brown, G. A., Scruggs, M. A., & Adams, J. V. (2020). Diagnosing open-system magmatic processes using the Magma Chamber Simulator (MCS): part II – trace elements and isotopes. *Contributions to Mineralogy and Petrology*, *175*(11), 105. https://doi.org/10.1007/s00410-020-01718-9

Hersum, T. G., Marsh, B. D., & Simon, A. C. (2007). Contact partial melting of granitic country rock, melt segregation, and re-injection as dikes into Ferrar dolerite sills, McMurdo Dry Valleys, Antarctica. *Journal of Petrology*, *48*(11), 2125–2148. https://doi.org/10.1093/petrology/egm054

Huppert, H. E., Stephen, R., & Sparks, J. (1985). Cooling and contamination of mafic and ultramafic magmas during ascent through continental crust. *Earth and Planetary Science Letters*, *74*(4), 371–386. https://doi.org/10.1016/S0012-821X(85)80009-1

Iacono-Marziano, G., Ferraina, C., Gaillard, F., Di Carlo, I., & Arndt, N. T. (2017). Assimilation of sulfate and carbonaceous rocks: Experimental study, thermodynamic modeling and application to the Noril'sk-Talnakh region (Russia). *Ore Geology Reviews*, *90*, 399–413. https://doi.org/10.1016/j.oregeorev.2017.04.027

Jennings, E. S., Gibson, S. A., Maclennan, J., & Heinonen, J. S. (2017). Deep mixing of mantle melts beneath continental flood basalt provinces: Constraints from olivine-hosted melt inclusions in primitive magmas. *Geochimica et Cosmochimica Acta*, *196*, 36–57. https://doi.org/10.1016/j.gca.2016.09.015

Johnson, T. E., Gibson, R. L., Brown, M., Buick, I. S., & Cartwright, I. (2003). Partial melting of metapelitic rocks beneath the Bushveld Complex, South Africa. *Journal of Petrology*, *44*(5), 789–813. https://doi.org/10.1093/petrology/44.5.789

Jourdan, F., Bertrand, H., Schaerer, U., Blichert-Toft, J., Féraud, G., & Kampunzu, A. B. (2007). Major and trace element and Sr, Nd, Hf, and Pb isotope compositions of the Karoo large igneous province, Botswana-Zimbabwe: lithosphere vs mantle plume contribution. *Journal of Petrology*, *48*(6), 1043–1077. https://doi.org/10.1093/petrology/egm010

Jung, S., Pfänder, J. A., Brauns, M., & Maas, R. (2011). Crustal contamination and mantle source characteristics in continental intra-plate volcanic rocks: Pb, Hf and Os isotopes from central European volcanic province basalts. *Geochimica et Cosmochimica Acta*, *75*(10), 2664–2683. https://doi.org/10.1016/j.gca.2011.02.017

Langmuir, C. H., Vocke, R. D., Hanson, G. N., & Hart, S. R. (1978). A general mixing equation with applications to Icelandic basalts. *Earth and Planetary Science Letters*, *37*(3), 380–392. https://doi.org/https://doi.org/10.1016/0012-821X(78)90053-5

Larsen, L. M., & Pedersen, A. K. (2009). Petrology of the Paleocene Picrites and Flood Basalts on Disko and Nuussuaq, West Greenland. *Journal of Petrology*, *50*(9), 1667–1711. https://doi.org/10.1093/petrology/egp048

Lightfoot, P. C., Hawkesworth, C. J., Hergt, J. M., Naldrett, A. J., Gorbachev, N. S., Fedorenko, V. A., & Doherty, W. (1993). Remobilisation of the continental lithosphere by a mantle plume: major-, trace-element, and Sr-, Nd-, and Pb-isotope evidence from picritic and tholeiitic lavas of the Noril'sk District, Siberian Trap, Russia. *Contributions to Mineralogy and Petrology*, *114*(2), 171–188. https://doi.org/10.1007/BF00307754

Luttinen, A. V., & Furnes, H. (2000). Flood basalts of Vestfjella: Jurassic magmatism across an Archaean-Proterozoic lithospheric boundary in Dronning Maud Land, Antarctica. *Journal of Petrology*, *41*(8), 1271–1305. https://doi.org/10.1093/petrology/41.8.1271

Mariga, J., Ripley, E. M., & Li, C. (2006). Petrologic evolution of gneissic xenoliths in the Voisey's Bay Intrusion, Labrador, Canada: Mineralogy, reactions, partial melting, and mechanisms of mass transfer. *Geochemistry, Geophysics, Geosystems*, *7*(5), Q05013. https://doi.org/10.1029/2005GC001184

McBirney, A. R. (1979). Effects of assimilation. In H. S. Yoder (Ed.), *Evolution of the Igneous Rocks: Fiftieth Anniversary*

Perspectives (pp. 307–338). Princeton NJ, United States: Princeton University Press.

Metcalf, R. V., Smith, E. I., Walker, J. D., Reed, R. C., & Gonzales, D. A. (1995). Isotopic disequilibrium among commingled hybrid magmas: Evidence for a two-stage magma mixing-commingling process in the Mt. Perkins Pluton, Arizona. *The Journal of Geology*, *103*(5), 509–527. https://doi.org/10.1086/629773

Molzahn, M., Reisberg, L., & Wörner, G. (1996). Os, Sr, Nd, Pb, O isotope and trace element data from the Ferrar flood basalts, Antarctica: evidence for an enriched subcontinental lithospheric source. *Earth and Planetary Science Letters*, *144*(3–4), 529–545. https://doi.org/10.1016/S0012-821X(96)00178-1

Moore, N. E., Grunder, A. L., & Bohrson, W. A. (2018). The three-stage petrochemical evolution of the Steens Basalt (southeast Oregon, USA) compared to large igneous provinces and layered mafic Intrusions. *Geosphere*, *14*(6), 2505–2532. https://doi.org/10.1130/GES01665.1

Neuendorf, K. K. E., Mehl, J. P., & Jackson, J. A. (Eds.). (2005). *Glossary of Geology*, 5th Edn. Alexandria, Virginia, United States: American Geological Institute.

Nicholls, J., & Stout, M. Z. (1982). Heat effects of assimilation, crystallization, and vesiculation in magmas. *Contributions to Mineralogy and Petrology*, *81*(4), 328–339. https://doi.org/10.1007/bf00371687

O'Hara, M. J. (1977). Geochemical evolution during fractional crystallisation of a periodically refilled magma chamber. *Nature*, *266*(5602), 503–507. https://doi.org/10.1038/266503a0

Oldenburg, C. M., Spera, F. J., Yuen, D. A., & Sewell, G. (1989). Dynamic mixing in magma bodies: Theory, simulations, and implications. *Journal of Geophysical Research: Solid Earth*, *94*(B7), 9215–9236. https://doi.org/10.1029/JB094iB07p09215

Petrelli, M., Perugini, D., & Poli, G. (2006). Time-scales of hybridisation of magmatic enclaves in regular and chaotic flow fields: petrologic and volcanologic implications. *Bulletin of Volcanology*, *68*(3), 285–293. https://doi.org/10.1007/s00445-005-0007-8

Petrelli, M., Perugini, D., & Poli, G. (2011). Transition to chaos and implications for time-scales of magma hybridization during mixing processes in magma chambers. *Lithos*, *125*(1), 211–220. https://doi.org/10.1016/j.lithos.2011.02.007

Pushkar, P., McBirney, A. R., & Kudo, A. M. (1971). The isotopic composition of strontium in Central American ignimbrites. *Bulletin Volcanologique*, *35*(2), 265–294. https://doi.org/10.1007/BF02596955

Ramos, F. C., & Reid, M. R. (2005). Distinguishing melting of heterogeneous mantle sources from crustal contamination: Insights from Sr Isotopes at the Phenocryst Scale, Pisgah Crater, California. *Journal of Petrology*, *46*(5), 999–1012. https://doi.org/10.1093/petrology/egi008

Reiners, P. W., Nelson, B. K., & Ghiorso, M. S. (1995). Assimilation of felsic crust by basaltic magma: Thermal limits and extents of crustal contamination of mantle-derived magmas. *Geology*, *23*(6), 563–566. https://doi.org/10.1130/0091-7613(1995)023<0563:AOFCBB>2.3.CO;2

Rudnick, R. L., & Gao, S. (2003). Composition of the continental crust. In R. L. Rudnick (Ed.), *The Crust, Treatise on Geochemistry* (Vol. *3*, pp. 1–64). Oxford, United Kingdom: Elsevier-Pergamon. https://doi.org/10.1016/b0-08-043751-6/03016-4

Samalens, N., Barnes, S., & Sawyer, E. W. (2017). The role of black shales as a source of sulfur and semimetals in magmatic nickel-copper deposits: Example from the Partridge River Intrusion, Duluth Complex, Minnesota, USA. *Ore Geology Reviews*, *81*, 173–187. https://doi.org/10.1016/j.oregeorev.2016.09.030

Sparks, R. S. J. (1986). The role of crustal contamination in magma evolution through geological time. *Earth and Planetary Science Letters*, *78*(2), 211–223. https://doi.org/10.1016/0012-821X(86)90062-2

Sparks, R. S. J., & Marshall, L. A. (1986). Thermal and mechanical constraints on mixing between mafic and silicic magmas. *Journal of Volcanology and Geothermal Research*, *29*(1), 99–124. https://doi.org/10.1016/0377-0273(86)90041-7

Spera, F. J., & Bohrson, W. A. (2001). Energy-constrained open-system magmatic processes I: General model and energy-constrained assimilation and fractional crystallization (EC-AFC) formulation. *Journal of Petrology*, *42*(5), 999–1018. https://doi.org/10.1093/petrology/42.5.999

Spera, F. J., & Bohrson, W. A. (2002). Energy-constrained open-system magmatic processes 3. Energy-Constrained Recharge, Assimilation, and Fractional Crystallization (EC-RAFC). *Geochemistry, Geophysics, Geosystems*, *3*(12), 8001. https://doi.org/10.1029/2002GC000315

Spera, F. J., & Bohrson, W. A. (2004). Open-system magma chamber evolution: an energy-constrained geochemical model incorporating the effects of concurrent eruption, recharge, variable assimilation and fractional crystallization (EC-E′RAχFC). *Journal of Petrology*, *45*(12), 2459–2480. https://doi.org/10.1093/petrology/egh072

Spera, F. J., & Bohrson, W. A. (2018). Rejuvenation of crustal magma mush: A tale of multiply nested processes and timescales. *American Journal of Science*, *318*(1), 90–140. https://doi.org/10.2475/01.2018.05

Spera, F. J., Bohrson, W. A., Till, C. B., & Ghiorso, M. S. (2007). Partitioning of trace elements among coexisting crystals, melt, and supercritical fluid during isobaric crystallization and melting. *American Mineralogist*, *92*(11–12), 1881–1898. https://doi.org/10.2138/am.2007.2326

Spera, F. J., Schmidt, J. S., Bohrson, W. A., & Brown, G. A. (2016). Dynamics and thermodynamics of magma mixing: Insights from a simple exploratory model. *American Mineralogist*, *101*(3), 627–643. https://doi.org/10.2138/am-2016-5305

Taylor, H. P. (1980). The effects of assimilation of country rocks by magmas on $^{18}O/^{16}O$ and $^{87}Sr/^{86}Sr$ systematics in igneous rocks. *Earth and Planetary Science Letters*, *47*(2), 243–254. https://doi.org/10.1016/0012-821X(80)90040-0

Tegner, C., Robins, B., Reginiussen, H., & Grundvig, S. (1999). Assimilation of crustal xenoliths in a basaltic magma chamber: Sr and Nd isotopic constraints from the Hasvik layered intrusion, Norway. *Journal of Petrology*, *40*(3), 363–380. https://doi.org/10.1093/petrology/40.3.363

Thakurta, J., Ripley, E. M., & Li, C. (2008). Geochemical constraints on the origin of sulfide mineralization in the Duke Island Complex, southeastern Alaska. *Geochemistry, Geophysics*, *Geosystems*, *9*(7), Q07003. https://doi.org/10.1029/2008GC001982

Todesco, M., & Spera, F. J. (1992). Stability of a chemically layered upper mantle. *Physics of the Earth and Planetary Interiors*, *71*(1), 85–99. https://doi.org/10.1016/0031-9201(92)90031-P

van der Molen, I., & Paterson, M. S. (1979). Experimental deformation of partially-melted granite. *Contributions to Mineralogy and Petrology*, *70*(3), 299–318. https://doi.org/10.1007/BF00375359

Vollmer, R. (1976). Rb-Sr and U-Th-Pb systematics of alkaline rocks: The alkaline rocks from Italy. *Geochimica et Cosmochimica Acta*, *40*(3), 283–295. https://doi.org/10.1016/0016-7037(76)90205-2

Walker, B. A. Jr., Miller, C. F., Claiborne, L. L., Wooden, J. L., & Miller J. S. (2007). Geology and geochronology of the Spirit Mountain batholith, southern Nevada: Implications for timescales and physical processes of batholith construction. *Journal of Volcanology and Geothermal Research*, *167*(1–4), 239–262. https://doi.org/10.1016/j.jvolgeores.2006.12.008

Wilcox, R. E. (1954). Petrology of Paricutin volcano, Mexico. *Geological Survey Bulletin*, *965*(C), 281–353. https://doi.org/10.3133/b965C

Wilcox, R. E. (1999). The idea of magma mixing: History of a struggle for acceptance. *The Journal of Geology*, *107*(4), 421–432. https://doi.org/10.1086/314357

Part III
Timescales of Magma Dynamics

8

Elemental Diffusion Chronostratigraphy: Time-Integrated Insights Into the Dynamics of Plumbing Systems

Chiara Maria Petrone[1] and Martin F. Mangler[1,2]

ABSTRACT

Time-related information of pre-eruptive magmatic processes is locked in the chemical profile of compositionally zoned minerals and can be retrieved by means of elemental diffusion chronometry. However, only the timescale of the outermost rim is commonly resolved, limiting our knowledge of timescales to those directly preceding the eruption. A major obstacle is the need to accurately constrain the temperatures at which diffusion occurred. Elemental diffusion chronostratigraphy can be fully resolved for crystals that have spent their lifetime in hot storage. Under this condition, crystals will be kept at the temperature of the eruptible magma(s), and diffusion timescales approximate the storage of the crystal in question in different melt environments. Hot storage conditions are typical of open-conduit systems in steady state and are driven by the regular supply of fresh hot magmas determining the constant presence of eruptible magma. Fe–Mg interdiffusion in pyroxene crystals from Stromboli and Popocatépetl are used to reconstruct elemental diffusion chronostratigraphies of single crystals and to discuss their implications for magma dynamics. Uncertainties introduced by temperature estimates and other input data, including experimentally derived values for the activation energy E and the pre-exponential factor D_0, have large effects on the accuracy of modeled timescales, which need to be evaluated and mitigated. Elemental diffusion chronostratigraphy is an extremely powerful tool for obtaining time-related temporal information on the dynamics and histories of volcanic plumbing systems, providing in-depth knowledge of the magmatic system far beyond late-stage pre-eruptive processes.

8.1. INTRODUCTION

It has long been known that minerals preserve information about the environment they grew in, representing a valuable archive of geological information (e.g.,Cooper, 2017; Streck, 2008). In the case of igneous minerals, crystallized from a magma, a range of information regarding pre-eruptive or pre-emplacement processes is locked in the mineral's compositional profile. Pressure and temperature of crystallization can be unlocked by using barometers and thermometers (e.g., Putirka, 2008). Compositional zoning is commonly linked to magma mixing processes, although they also reflect variations in physical conditions (e.g., P, T, fO_2, and H_2O), particularly but not exclusively in plagioclase (e.g., Anderson, 1984;

---

[1] *Department of Earth Sciences, The Natural History Museum, London, United Kingdom*

[2] *Department of Earth Sciences, Durham University, Durham, United Kingdom*

Crustal Magmatic System Evolution: Anatomy, Architecture, and Physico-Chemical Processes, Geophysical Monograph 264, First Edition.
Edited by Matteo Masotta, Christoph Beier, and Silvio Mollo.

DOI: 10.1002/9781119564485.ch8

Giacomoni et al., 2014; Streck, 2008). Isotope variability from different portions of the crystal can reveal crustal contamination alongside magma mixing processes (e.g., Davidson et al., 2007). Minerals can also provide time-related information. Radiometric dating techniques have long been used to provide the absolute ages of minerals' crystallization (e.g., Cooper, 2019, and references therein), whereas diffusive timescales provide constraints on the time crystals might have spent in crustal magma reservoirs relative to pre-eruption processes (e.g., Mangler et al., 2020; Zellmer et al.,1999). In the last decade, following pioneering studies of timescales of metamorphic processes (e.g., Ayres & Vance, 1997; Ganguly et al., 1996; O'Brien & Vrána, 1995), elemental diffusion modeling has proved an invaluable instrument to infer the timescales of pre-eruptive magmatic processes, such as the timing of magma injections into shallow reservoirs, magma mush remobilization, and ascent rate (e.g., Costa et al., 2008; Dohmen et al., 2017; Petrone et al., 2016, 2018; Turner & Costa, 2007).

The radiometric clock starts at temperatures below the closure temperature of the relative radiometric system, which in most cases corresponds to the age of the crystal growth (i.e., absolute crystallization age) constraining the longevity of a magmatic system (Cooper, 2019, and references therein). The diffusive chronometer starts upon the formation of a chemical gradient. Temperature strongly controls the rate of the diffusive smoothing of the chemical gradient even after the compositional boundary has been isolated from the melt (i.e., overgrowth of a further external crystal's portion). On the contrary, the radiometric clock is insensitive to changes in temperatures subsequent to crystal growth, unless the temperature rises above the closure temperature where the radiometric clock will reset. Radiometric ages are a mixed record from different portion of crystals (i.e., old cores and rims) spanning a large range (10^4–10^5 years) and providing average absolute crystallization ages, which in most cases are unaffected by diffusion, due to the very slow diffusion rate of the elements in question (e.g., U-series; Cooper & Kent, 2014). Elemental diffusion timescales usually record much shorter timescales (hours to 10^3 years; e.g., Cooper & Kent, 2014; Cooper, 2019, and references therein), which are commonly interpreted to represent late-stage, short-lived processes such as final magma mixing and assembly before an eruption. This is due to the intrinsic nature of elemental diffusion processes that requires the presence of a compositional gradient; therefore, the history of an unzoned crystal (or the unzoned portion of a zoned mineral such as the crystal's core) cannot be determined via geospeedometry.

The majority of elemental diffusion models focus on the outermost rim of crystals, yielding time constraints only on the final stage of the crystal's history (e.g., see Cooper, 2019; Costa et al., 2008; and Dohmen et al., 2017, for a review). Recently, however, several authors have attempted to resolve more than one compositional boundary to approach a comprehensive crystal chronostratigraphy (Druitt et al., 2012; Kahl et al., 2011; Petrone et al., 2016, 2018; Rout et al., 2020). When the elemental diffusion profile can be resolved for several compositional boundaries in the same crystal, a closer correspondence between diffusion timescales and radiometric ages tracking the same event can be expected. This allows a more in-depth reconstruction of the dynamics of the plumbing system, alongside a time-constrained sequence of magmatic processes. This information is fundamental in the case of active volcanoes and can be used in combination with monitoring data and other geological, seismic, and petrological constraints to assess volcanic hazard.

The overall goal of this chapter is to explore the potential of geospeedometry in resolving the time-integrated information stored in the stratigraphy of zoned crystals beyond the final pre-eruptive stages, and to highlight the pitfalls related to the approach. We will present examples from Stromboli and Popocatépetl volcanoes, using the recently published non-isothermal step diffusion model (NIDIS, Petrone et al., 2016) as one example of the many possible approaches to resolving single crystal elemental diffusion chronostratigraphy, with the aim of contributing to a better understanding of magmatic system dynamics.

8.2. GEOSPEEDOMETRY: APPROACH AND LIMITATIONS

The possibility of extracting the time elapsed between a magma mixing event and eruption is based on two main assumptions: change in thermodynamic equilibria during the mixing process, leading to the formation of a compositional boundary within a crystal and subsequent elemental diffusion at the boundary; and an elemental diffusion rate close to zero upon eruption. The first assumption is a consequence of the mixing process between two magmas characterized by different physical (i.e., T, fO_2) and chemical composition (including gas and crystal contents) leading to the formation of compositionally zoned crystals. An implicit corollary of this assumption is that the crystal will experience instantaneous growth upon mixing, which might be preceded by dissolution. Normally, crystal growth rates are orders of magnitude higher than elemental diffusion rates, even for relatively fast-diffusing elements such as Fe–Mg in pyroxenes (e.g., Dimanov & Sautter, 2000; Ni et al., 2014). Therefore, in many cases, it is safe to assume instantaneous crystal growth (e.g., Costa et al., 2008; Petrone et al., 2016).

Elemental diffusion is a time (t)- and temperature (T)-dependent process (e.g., Crank, 1975), with the diffusion rate increasing with increasing T. The effect of intracrystal elemental diffusion is to smooth the initial sharp compositional profile at the boundary between two different portions of a compositionally zoned crystal. The diffusive relaxation of the compositional profile is a function of the time spent at magmatic temperature and the rate of diffusion, which is mineral specific and further controlled by temperature, oxygen fugacity, and crystallographic direction (in anisotropic minerals). Upon eruption, the low (i.e., atmospheric) T will drive the diffusion rate for most elements and minerals effectively close to zero, freezing the diffusion profile and therefore preserving the time spent at the high T of the magmatic environment (e.g., Costa et al., 2008; Dohmen et al., 2017). This can be retrieved by means of elemental diffusion modeling. The extent of diffusion in minerals (i.e., the distance affected by diffusion) is a function of the square root of the time (t) over which the diffusion acted and the diffusion coefficient D ($x \cong \sqrt{tD}$ eq. 9, Zhang, 2010). It is therefore clear that in order to calculate the time t related to a diffusion profile, the diffusion coefficient must be known. The diffusion coefficient is a function of T as expressed by the Arrhenius relationship:

$$D = D_0 e^{-E/RT} \tag{8.1}$$

where D_0 is the pre-exponential factor, E the activation energy, R the gas constant, and T the absolute temperature in K. The dependence of D on T means that in order to resolve the diffusion equation and calculate the time t, the temperature at the time of diffusion must also be known. In addition, the exponential relationship means that any error in T can affect the uncertainty on the timescales by orders of magnitude (i.e., from 40% to 20% on clinopyroxene when the error in T decreases from ±15 °C to ±6 °C, Petrone et al., 2016; Scarlato et al., this issue). T and D are the main parameters controlling elemental diffusion in minerals and we shall explore in detail the uncertainties introduced by these parameters in a separate section.

There are many excellent publications about the theoretical framework of diffusion modeling, with published analytical and numerical solutions of the diffusion equations (e.g., Chakraborty, 2006; Costa et al., 2008; Crank, 1975; Dohmen et al., 2017; Petrone et al., 2016; Zhang, 2010). It is not the scope of this paper to repeat those works, but it is important to highlight some of the caveats and assumptions inherent to diffusion models, before exploring in detail the challenges and opportunities offered by resolving crystals' elemental diffusion stratigraphy.

Initial and boundary conditions must be inferred or established before modeling the diffusion profile. The initial zoning profile can be assumed as gradual, abrupt, homogenous, or oscillatory, (Costa et al., 2008) reflecting different magmatic processes and minerals. A common approach for pyroxene is to use slow-diffusing elements to infer the initial profile of fast-diffusing elements (e.g., Allan et al., 2013; Costa et al., 2008; Petrone et al., 2016). For plagioclase, an initial step function profile is assumed, and the fast-diffusing profile of Sr and Mg is inferred from the slow-diffusing profile of CaAl-NaAl (e.g., Costa et al., 2003; Costa et al., 2008; Dohmen et al., 2017). For olivine, the initial profile is considered unzoned (e.g., Costa et al., 2008; Kahl et al., 2011). In the case of sanidine, provided that the Sr distribution mimics Ba, the diffusion of Ba is compared with Sr diffusion modeling to ensure modeling of true diffusive profiles (Chamberlain et al., 2014).

The nature of exchange between the crystal and its surrounding matrix determines the nature of the boundary conditions, which can be open or closed (e.g., Chakraborty & Ganguly, 1991; Costa et al., 2008; Crank, 1975; Mueller et al., 2010). Open boundaries are far more common in magmatic systems than closed boundaries characterized by the absence of diffusive flux of the element of interest in and out of the crystal (i.e., the elements of interest do not significantly partition in the surrounding phase or the diffusion rate in the matrix is much slower than in the mineral; Costa et al., 2008). In the case of open boundaries, there is diffusive communication between the two sides, but depending on the conditions it can result in a variable concentration (e.g., the melt reservoir has limited volume or the ambient conditions change significantly) or fixed concentration (e.g., assuming a diffusive exchange with a large volume of melt). Accordingly, the initial conditions are assumed equal to the maximum and minimum compositions (using concentration plateaus when possible), and the diffusion profile will ultimately equilibrate within the mineral homogenizing at an intermediate level (i.e., a finite reservoir of limited extent). On the contrary, in the case of infinite reservoirs (i.e., the condition mostly characterizing rims), the element concentration will also depend on the partition coefficient between mineral and melt, which will control the final concentration that is fixed at the crystal rim (Mueller et al., 2010). In cases when the initial profile cannot be easily inferred, due to the lack of a clear plateau, an arbitrary maximum value, corresponding to a step function based on the range of natural compositional variation, can be assumed (Petrone et al., 2016; Zellmer et al., 1999).

Non-cubic minerals are anisotropic in terms of elemental diffusion rates, in the same way as their optical properties. This is particularly important for olivine, where elemental diffusion along the c-axis is six times faster than along the a- and b-axes (Dohmen et al., 2017; Tachibana et al., 2013). It is therefore critical to the accuracy of timescales calculated from diffusion models, to precisely identify the crystallographic direction along which the diffusion profile is modeled. This can be satisfactorily approximated for pyroxene and plagioclase on the basis of their optical characteristics. For example, Fe–Mg diffusion profiles have been measured perpendicular to the (100) plane in recent works on pyroxene (Morgan et al., 2006; Petrone et al., 2016, 2018), which can be identified to a certain degree of accuracy under an optical microscope. In other cases where the optical properties cannot help to identify the crystallographic direction, or when there is a need for very precise and accurate information on crystal's orientation, as for example in olivine, electron backscattered diffraction (EBSD) is used to determine the exact crystallographic direction, and the diffusion profile is calculated accordingly to trigonometric rules (Costa et al., 2008; Dohmen et al., 2017; Kahl et al., 2011). A further complication arises from sectioning effects due to the fact that most diffusion models are done in 1D space based on a random 2D thin section of a crystal, with no information on the actual 3D geometry. For example, it is not necessarily possible to infer from a given crystal section whether it cuts through the crystal core or if it is off-centered. Neglecting the effect of 2D and 3D geometry results in a significant mismatch of the modeled timescales (Costa et al., 2003, 2008; Krimer & Costa, 2017; Shea et al., 2015). Some strategies to mitigate this effect such as measuring the diffusion profile along the *b*-axis for pyroxene, using symmetrical profiles (Krimer & Costa, 2017), and comparing the 1D model with the ideal 3-D numerical model (Shea et al., 2015) have been proposed, but the problem is yet to be fully resolved.

8.3. ISOTHERMAL VERSUS NON-ISOTHERMAL APPROACH

Magmatic processes are non-isothermal. Magmas crystallize over a range of temperatures, and the temperature contrast during magma mixing can be as high as 300 °C (e.g., Hawkesworth et al., 2000; Kent et al., 2010). Constraining the range of temperatures from a mineral's compositional profile is not a straightforward task. Pre-eruptive temperatures can be calculated using different types of geothermometers if an equilibrium between mineral and melt or between two coexisting mineral phases can be demonstrated (e.g., Putirka, 2008). A single pre-eruptive temperature, obtained from equilibrium between the crystal's rim and the matrix, is commonly assumed to calculate timescales of pre-eruptive processes (e.g., Allan et al., 2013; Costa et al., 2003; Kilgour et al., 2013; Morgan et al., 2004). However, this temperature in many cases reflects the latest magmatic environment experienced by the crystal prior to the eruption, but it cannot accurately reflect the entire thermal history of the crystal. In fact, as crystals grow from core to rim, their composition changes as a function of temperature and other physicochemical parameters as they move through different magmatic environments. Furthermore, widespread disequilibrium between melt and minerals (e.g., Couch et al., 2001; Sparks & Cashman, 2017) in many volcanic products worldwide indicate that calculated temperatures do not represent the entire magma reservoir during pre-eruptive magma assembly (e.g., Cooper & Kent, 2014). Crystals may not only experience multiple magmatic environments during their lifetime (e.g., antecryst, different portion of zoned crystals; e.g., Fabbro et al., 2013; Kahl et al., 2013; Mangler et al., 2020), but they also spend variable time (i.e., storage) in each environment. This often results in complex zoning patterns reflecting the crystal's history of growth, mixing, and storage in different magmatic environments, at often dramatically different temperatures (e.g., Cooper, 2017; 2019; Di Stefano et al., 2020; Petrone et al., 2018).

In the attempt to resolve with greater accuracy the lifetime history of crystals from their core-to-rim compositional diffusion profile, increasing attention has been devoted to characterizing the different melt environments, moving from an isothermal to a non-isothermal approach. A system analysis approach has been used to reconstruct compositional zoning patterns in olivines derived from different magmatic environments (Kahl et al., 2011). However, only the time spent in the final pre-eruptive magmatic environment has been modeled for most of the olivines (e.g., Kahl et al., 2011, 2013). Using a forward approach with a two-step diffusion model, Druitt et al. (2012) modeled the core-rim diffusion profile of plagioclase from the Santorini volcano assuming equilibrium with two melts of differing compositions and temperatures. More recently, a non-isothermal approach to elemental diffusion (i.e., NIDIS, Petrone et al., 2016) has been proposed to resolve complex core-rim elemental diffusion profiles of clinopyroxene from the Stromboli volcano (Petrone et al., 2016, 2018). Working inward from crystal rim to core, the elemental diffusion stratigraphy profile is deconstructed in single isothermal steps, each one characterized by a specific temperature and diffusion coefficient reflecting the change in magmatic environment, providing the timescales spent in each of those environments. This approach has resulted in a better understanding of the timescales and dynamics of magma mixing, storage, and eruption-trigger events in a steady-state magmatic system (i.e., constant rate of input and output; Petrone et al., 2018). Recently, the NIDIS model was experimentally validated by Rout et al. (2020), who further presented a simplified, mathematically equivalent algorithm yielding reduced propagated errors and therefore improved precision of diffusion timescales.

8.4. THE TEMPERATURE CONUNDRUM

A critical aspect of any elemental diffusion study is the availability of the actual diffusion temperatures at which crystals are stored before eruption. Recently, some authors suggested that magmatic systems spend most of their life in cold storage as almost solid crystal mush, with short and ephemeral bursts of high temperature during remobilization of the mush by mafic magmas, eventually triggering the eruption (e.g., Cooper & Kent, 2014; Cashman & Giordano, 2014). The implication is that the temperature(s) at which crystals spend most of their time is significantly lower than that of the melt from which the crystals grew in and might be difficult to constrain via thermometry (Cooper & Kent, 2014). Therefore, crystal storage times will be much longer than the diffusive timescales modeled from diffusion between magma remobilization and eruption (i.e., the ephemeral hot burst). If the temperature of the cold storage cannot be calculated, then it would be impossible to estimate the time the crystal spent in the cold storage. In this case, diffusive timescales will represent only the final portion of the story, and determining the timescales of multiple events of crystal-rich melt movements between different magmatic environments might be difficult.

However, we argue that if the system is kept at hot storage conditions, which implies the presence of eruptible magma (i.e., <40% crystals, Burgisser & Bergantz, 2011) at temperatures well above the locked crystal mush, crystals will spend their lifetime at the temperature of the eruptible magma in the corresponding magmatic environment. Under this condition, diffusive timescales (from models at the temperatures of the eruptible melt) approximate the storage of the crystals in question (Petrone et al., 2018). Hot storage might be a common condition in open-conduit systems with a frequent input of recharging mafic magma. Hot storage with a continual presence of melt has been suggested for the Soufrière Volcanic Centre (Santa Lucia, Barboni et al., 2016), Popocatépetl (Mangler et al., 2020), and the Laacher See volcano (Rout & Wörner, 2020), and might therefore be a common condition in arc volcanoes. Recent work on the Stromboli volcano has shown agreement between clinopyroxene elemental diffusion timescales (Petrone et al., 2018) and U-Th residence times calculated for the 2–4 km shallow reservoir of Stromboli (Bragagni et al., 2014), suggesting that they are both tracking the residence time at magmatic temperatures of the shallow reservoir, where mixing processes between resident magma, incoming magma, and the mush occur. Considering that according to Bragagni et al. (2014), the mush is made up of a solid portion (i.e., antecrysts) and by an interstitial liquid (i.e., antemelt), and that the antemelt actively contributes to the magma mixing process upon remobilization by the incoming more mafic and hotter magma, we can infer that the mush must be kept at temperatures well above the near-solidus condition for a prolonged time. Therefore, in magmatic systems characterized by hot storage conditions, the storage time of the chemically zoned portion of the crystal can be approximated by the total diffusive timescales occurring at the temperatures of the relative melt environments producing the compositional banding.

On this basis, we argue that hot storage is common for steady-state open-conduit systems, which are often also characterized by a limited whole rock compositional variation over a protracted length of time (e.g., basaltic composition at Stromboli and Etna, Di Renzo et al., 2019; Francalanci et al., 1999; andesitic-dacitic at Popocatépetl, Mangler et al., 2019). Open-conduit conditions associated with a buffered compositional range, which can last several thousands of years (Mangler et al., 2019), indicate that such magmatic systems are controlled by processes that remain constant over a long period of time, and magma hybridization between long-lived end-members is the most probable process (e.g., Di Renzo et al., 2019; Mangler et al., 2019, 2020; Petrone et al., 2018).

If storage time and elemental diffusion timescales can be equated in steady-state open-conduit volcanoes, and if the various magmatic environments (i.e., magma end-members and related hybrid compositions) can be fully characterized using mineral-melt and mineral-mineral geothermometers, then these temperatures can be used to calculate diffusion timescales in each magmatic environment, and to fully reconstruct the crystallization and storage history of individual crystals (Kahl et al., 2011; Petrone et al., 2016, 2018). In the case of Stromboli, where the two end-members have been recognized and fully characterized (e.g., Bragagni et al., 2014; De Carlo et al., 2006; Francalanci et al., 1999; Pichavant et al., 2009), temperatures have been estimated using a combination of experimental data (De Carlo et al., 2006; Pichavant et al., 2009), clinopyroxene-liquid thermometers, and MELTS simulations (Petrone et al., 2018). At Popocatépetl, the equilibrium between ortho- and clinopyroxene, over their entire compositional range has been used to estimate the magmatic temperature corresponding to each portion of a zoned pyroxene (Mangler et al., 2020).

8.5. TWO EXAMPLES: STROMBOLI AND POPOCATÉPETL VOLCANOES

Elemental diffusion stratigraphy has previously been resolved, using the NIDIS approach, for Fe–Mg interdiffusion in clinopyroxene of Stromboli with variously complex compositional zoning (Petrone et al., 2016, 2018). Here we revisit the main findings of those studies and present some further examples of pyroxene crystals from Popocatépetl volcano.

The Stromboli stratovolcano in the Aeolian Islands (Southern Italy) is one of the best-studied volcanoes worldwide. Continuous and moderately explosive, 'Strombolian' activity characterizes at least the last 2,000 years. The typical Strombolian activity is accompanied by periodic lava flows and interposed with more violent eruptions (paroxysm) tapping a deeper reservoir (e.g., Bertagnini et al., 2008; Francalanci et al., 2013). Stromboli has long been recognized as a typical steady-state volcano, with a shallow magmatic reservoir (highly porphyritic or *hp*-magma) refilled continuously and at a constant rate by more mafic deeper magma (low porphyritic or *lp*-magma) and accompanied by mixing, crystallization, and eruption (e.g., Bragagni et al., 2014; Francalanci et al., 1999).

The Popocatépetl stratovolcano is located in central Mexico and is characterized by a wide variety in eruptive styles typical for subduction zone volcanism. Present-day activity was initiated in December 1994 and is characterized by dome-building and -destruction cycles associated with mild to moderate Vulcanian eruptions (Gómez-Vazquez et al., 2016). Past activity included at least six Plinian eruptions in the last ~23.5 ka (Arana-Salinas et al., 2010; Schaaf et al., 2005; Siebe et al., 2017; Sosa-Ceballos et al., 2014) and interplinian emplacement of several voluminous lava flows (Mangler et al., 2019). Popocatépetl lavas and pumices are calc-alkaline andesites and dacites which underwent varying degrees of lower and upper crustal assimilation en route to the surface (Schaaf et al., 2005; Sosa-Ceballos et al., 2014; Mangler et al., 2019). Frequent mixing and hybridization of geochemically distinct magmas effectively buffers whole rock compositions favoring the eruption of a narrow compositional range in the last ~23.5 ka (Mangler et al., 2019, 2020).

We will discuss the general implications for the dynamics of an open-conduit plumbing system arising from the presented examples to illustrate the potential of elemental diffusion chronostratigraphy; however, it is not within the scope of this work to discuss in any detail the specific implications either for Stromboli or for Popocatépetl. It is important to stress that in order to fully understand the dynamics of a specific volcanic system, the crystal cargo needs to be examined and characterized in detail. Such work is fundamental to geospeedometry, because different populations of a mineral phase might represent different magmatic processes and/or multiple generations. Meaningful timescales can only be obtained by modeling a significant number of crystals for each population.

8.6. RESOLVING ELEMENTAL DIFFUSION STRATIGRAPHY

It is well known that igneous rocks contain a complex crystal cargo which preserves information about a variety of processes that occurred over different lengths of time and in different portions of the plumbing system (e.g., Cooper, 2017; Sparks et al., 2019). The simple case of crystals presenting only compositionally zoned rims (Figures 8.1a,b) is the most straightforward to resolve and interpret. In these cases, the obtained timescales indicate the time elapsed from the formation of the rim until the eruption. Therefore, it constrains the time spent in the last magmatic environment before eruption, which can be either more mafic or more evolved than the previous magmatic environment (where the core formed). In the specific example of Stromboli, the mafic rim in the clinopyroxene gives a timescale of around four months from the injection of the mafic magma until the eruption (Figure 8.1a). This suggests a rapid response of the plumbing system to new injections of mafic magmas, which can trigger the eruption over a short timescale. On the contrary, the longer timescale (approximately four years) modeled for the mafic core–evolved rim interface of the orthopyroxene from Popocatépetl (Figure 8.1b) suggests a very different dynamics and origin of the crystal. Texture, composition, and modeled timescale show that the crystal was injected from a mafic into a more evolved magmatic environment (Mangler et al., 2020), where it spent several years before being erupted. In this case, the evolved rim does not show any record of a mafic injection triggering the eruption, which indicates that it was triggered by gas percolation (Bachmann and Bergantz, 2006) and/or second boiling (Cassidy et al., 2018). Alternatively, the crystal might have been erupted without directly interacting with fresh mafic recharge melt, a scenario expected for a significant number of crystals during magma mixing (Cheng et al., 2020). Clearly, a more in-depth study of the crystal cargo populations is necessary to provide adequate context for a firmer answer.

Relatively simply zoned minerals (Figures 8.1c,d) can provide constraints on the timescales spent in different magmatic environments alongside the diffusive storage time and the efficiency of magma dynamics. The NIDIS model (Petrone et al., 2016) facilitates the calculation of a total diffusion residence time (Δt), defined as the time from the (first) injection of the mafic magma to the eruption. Therefore, it does not correspond to the absolute age or the absolute storage time of the crystal, because the formation of the core cannot be accounted for, but it is tracking the timescale of magma injection, storage, and eruption. The diffusion residence time (Δt) is the sum of two partial timescales: the time spent in the last magmatic environment before the eruption (Δt_2 or external timescales) corresponding to the diffusion time of the compositional band–rim boundary (in the case of Figure 8.1c at the lower T of the more evolved magma); and the time spent in contact with the high-T magma (Δt_1 or internal core–compositional band boundary) calculated by the

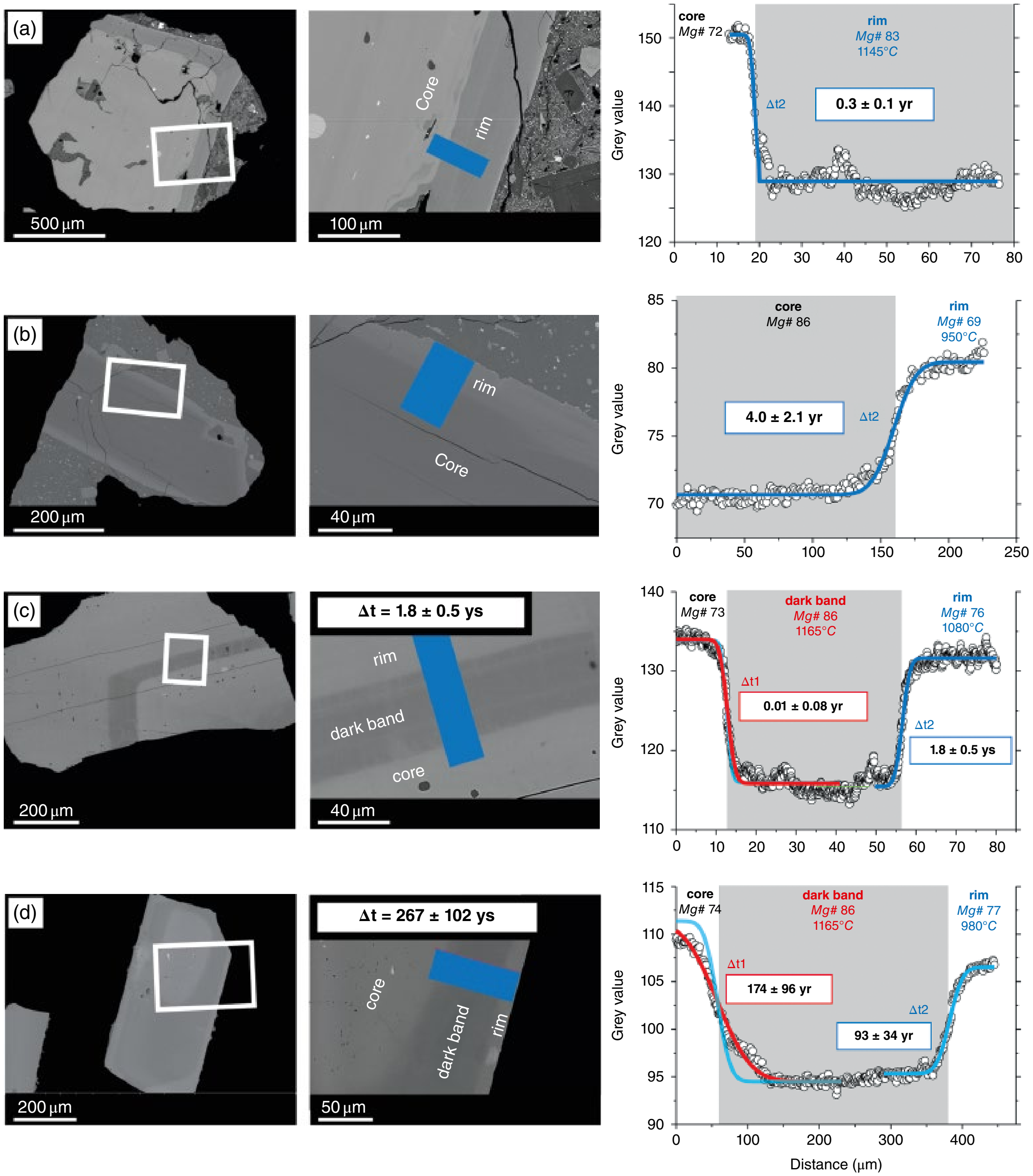

Figure 8.1 Backscattered electron (BSE) images of banded pyroxene phenocrysts from Stromboli (modified from Petrone et al., 2018) and Popocatépetl volcanoes, extracted grayscale profiles, and fits modeled using the MATLAB script `createfit` (Petrone et al., 2016). The blue box in BSE images represents the area the compositional transect is integrated from, using the MATLAB script `greyvalues` (Petrone et al., 2016). External timescales (e.g., core–rim or band–rim) represent the time elapsed between rim formation, in the last magmatic environment, and the eruption (Δt_2, shown in blue). Internal timescales (e.g., core–band) from earlier magmatic environments (Δt_1) are shown in red and represent the time spent at band temperatures, with the effect of diffusion during subsequent storages in different magmatic environments removed (light blue curve). For crystals with both Δt_1 and Δt_2 timescales, the total diffusion residence time ($\Delta t = \Delta t_1 + \Delta t_2$) is given. See Petrone et al. (2016) for a detailed description of the NIDIS model. Mg# and respective equilibrium temperatures are given for each compositional zone (Petrone et al., 2018; Petrone unpublished data). (a) Crystal recording months of storage in the last magmatic environment prior eruption. Stromboli clinopyroxene, STR273_CPX20 (modified from Petrone et al., 2018). (b) Crystal showing years between mixing and eruption. Popocatépetl orthopyroxene, POP-37_OPX1. (c) Crystal recording a rapid, high-*T* mixing process (~4 days) followed by 1.8 yr of storage in a lower-*T* environment. Stromboli clinopyroxene, STR275_CPX16 (modified from Petrone et al., 2018). (d) Crystal showing prolonged storage at high temperatures after mixing, followed by decades at lower temperatures. Popocatépetl clinopyroxene, POP-59Y_OPX36. See text for further explanation. Stromboli pyroxenes are from Petrone et al. (2018). Source: Modified from Petrone et al. (2018).

relaxation of the core–band diffusion profile after taking into account the external timescale Δt_2 (for details, see Petrone et al., 2016, 2018). The external partial timescale (i.e., band–rim Δt_2) constrains the final assemblage of the eruption as in the previous simpler cases (Figures 8.1a,b), whereas the internal timescale (i.e., core–band Δt_1) gives an indication regarding the timescales of crystal transfer from one magmatic environment to the other and/or the efficiency of the magma homogenization process. The most important aspect is that when the two partial timescales are compared together, they provide an important indication of the storage time in different magmatic environments and therefore of the dynamics of the magmatic system. The examples presented are clinopyroxenes from Stromboli (Figure 8.1c) and Popocatépetl (Figure 8.1d), which suggest very different magma dynamics. The Stromboli clinopyroxene shows a short total residence time (1.8±1 yr), and the internal timescale (Δt_1 = 0.01±0.08 yr) is significantly shorter than the external timescale (Δt_2 = 1.8±0.5 yr), which suggests an efficient magma homogenization regime (Petrone et al., 2018). On the other hand, the clinopyroxene from Popocatépetl shows a much longer total residence time (267±102 yr), and it has a Δt_1 (174±96 yr) significantly longer than Δt_2 (93±34 yr). Popocatépetl is characterized by magma hybridization in a long-lived and stable extensive plumbing system (Mangler et al., 2019). This crystal's stratigraphy traces its prolonged path through the complex plumbing system, with 10-100s of years of storage in multiple distinct magmatic environments. Similarly, a mafic Popocatépetl orthopyroxene (Figure 8.2a) records its injection into a more evolved magmatic environment and subsequent storage for several decades (Δt_1 = 84±42 yr), before being rapidly remobilized by a subsequent mafic injection and erupted (Δt_2 = 51±22 days). Although these isolated examples from Popocatépetl can clearly not characterize the full extent of magma dynamics of the volcanic system, they show how elemental diffusion chronostratigraphy can help understand the complexity of magmatic plumbing systems and the heterogeneous nature of magmatic reservoirs. Furthermore, it highlights the importance of modeling a large number of crystals from different populations to reveal the full extent of magma dynamics.

Another example is offered by a Stromboli clinopyroxene (Figure 8.2b) with a low-Mg# core surrounded by three high-Mg# bands alternating with low-Mg# bands. The timescales calculated with the NIDIS model indicate a total residence time of around ten years from the first mafic injection until the eruption, with about five years spent in each of the two older low-Mg# magma environments. This has been interpreted by Petrone et al. (2018) as indication of multiple injections of the high-Mg# magma in the low-Mg# magma accompanied by short storage, followed by the last mafic injection which triggered the eruption. In fact, in some cases, not only can the mafic triggering event be resolved, but also the ongoing hybridization processes (Petrone et al., 2018) up until the eruption, as is evident from the stepped right-hand profile in Figure 8.2c, which, having a less steep slope than the internal core–band boundary, cannot be produced by a diffusion process. Finally, the timescales of crystal mush remobilization can be retrieved by the elemental diffusion stratigraphy alongside further episodes of magma injections (Figure 8.2d). In this Stromboli clinopyroxene, a patchy core surrounded by multiple layers of different compositions has been interpreted by Petrone et al. (2018) as an antecryst remobilized from the crystal mush by the mafic melt recorded by the high-Mg# layer (DB1) immediately surrounding it. The crystal has been then delivered in a low-Mg# melt environment (LB), where it recorded the arrival of another input of more mafic magma (DB2) and was stored for about 2 years before moving to the final low-Mg# environment for some 12 years before eruption.

8.7. UNCERTAINTIES

The examples presented above show that elemental diffusion chronostratigraphy, resolved in this case with the non-isothermal diffusion modeling NIDIS, is a powerful tool to reconstruct pre-eruptive histories of single crystals, and—given a sufficiently large sample set—to constrain timescales of magmatic processes in a given plumbing system, such as magma mixing, crystal transfer and storage, mush remobilization, eruption triggering, and ascent to the surface. However, when it comes to interpreting geospeedometry results, it is important to consider the uncertainties related to the modeled timescales, which are fundamentally controlled by the uncertainty related to the diffusion coefficient D and temperature.

The temperature at which diffusion occurs has exponential influence on the diffusivity [equation 8.1], and thus uncertainties in the temperature strongly affect the calculated timescales. Commonly used geothermometers (see Putirka, 2008 for a review) provide uncertainties in magmatic temperatures on the order of 10–50 °C, which result in uncertainties of up to 60 rel. % in modeled timescales (Figures 8.1 and 8.2). However, in cases where the error on the estimated temperature can be drastically reduced (±6 °C; Scarlato et al., this issue), the corresponding error on the estimated timescales is reduced to 20% (Petrone et al., 2016; Scarlato et al., this issue). Therefore, it is extremely important to minimize uncertainties regarding magmatic temperatures as much as reasonably possible. This requires a detailed knowledge of the magmatic system in question and specific calibration of geothermometers, as that recently calibrated for the

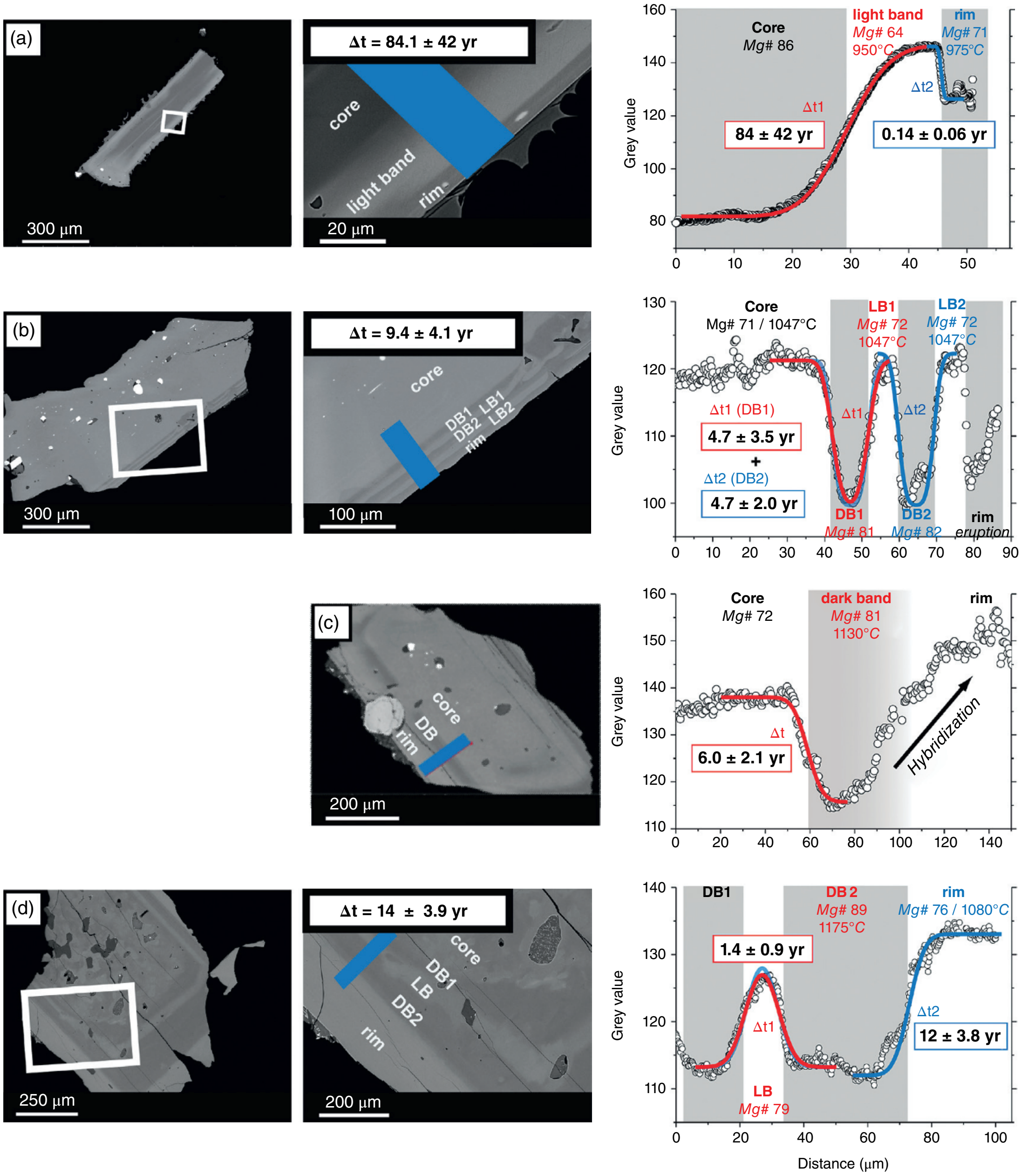

Figure 8.2 Backscattered electron (BSE) images of banded pyroxene phenocrysts from Stromboli (modified Petrone et al., 2018) and Popocatépetl volcanoes, extracted grayscale profiles, and fits modeled using the MATLAB script `createfit` (Petrone et al., 2016). The blue box in BSE images represents the area the compositional transect is integrated from, using the MATLAB script `greyvalues` (Petrone et al., 2016). External timescales (e.g., core–rim or band–rim) represent the time elapsed between rim formation, in the last magmatic environment, and the eruption (Δt_2, shown in blue). Internal timescales (e.g., core–band) from earlier magmatic environments (Δt_1) are shown in red and represent the time spent at band temperatures, with the effect of diffusion during subsequent storages in different magmatic environments removed (light blue curve). For crystals with both Δt_1 and Δt_2 timescales, the total diffusion residence time ($\Delta t = \Delta t_1 + \Delta t_2$) is given. Figures (b) and (d) show finite reservoir models of bands with two diffusing boundaries. See Petrone et al. (2016) for a detailed conceptual discussion. Mg# and respective equilibrium temperatures are given for each compositional zone (Petrone et al., 2018; Mangler et al., 2018). (a) Crystal recording decadal storage at low temperatures (i.e., mush), followed by rapid remobilization and eruption within ~50 days. Popocatépetl orthopyroxene, POP-112_PX23. (b) Crystal recording three high-*T*, mafic injections within 10 yr prior to eruption. Stromboli clinopyroxene, STR273_CPX108 (modified from Petrone et al., 2018). (c) Crystal recording few years of storage in hotter magma and subsequent syn-eruptive ongoing hybridization in the final magmatic environment. Stromboli clinopyroxene, STR276_CPX113 (modified from Petrone et al., 2018). (d) Crystal recording two mafic injections leading to remobilization and eruption of the crystal within decades. Stromboli clinopyroxene, STR275_CPX14. See text for further explanation. Stromboli pyroxenes are from Petrone et al. (2018). Source: Modified from Petrone et al. (2018).

shoshonitic composition of the present-day activity at Stromboli (Scarlato et al., this issue). Even so, gradual and/or minor temperature fluctuations in the magmatic system may not be resolvable, and therefore uncertainties in temperatures to an extent represent the natural variability of a magmatic system.

In addition to the temperature at which diffusion occurs, *D*s depend on various other physico-chemical variables such as pressure, $X_{mineral}$, f_{O_2}, and f_{H_2O} of the host magma (Costa et al., 2008, and references therein). Furthermore, diffusion rates depend on the crystallographic direction, the concentration of the element in question, the diffusion type (e.g., tracer/self vs. chemical diffusion), and the diffusion mechanism (Chakraborty, 1997; Dohmen et al., 2016). Some expressions for *D* allow for variations in other parameters such as composition and f_{O_2} (e.g., Dohmen et al., 2016), but most other variables are commonly accounted for as constant bulk values included in the pre-exponential factor D_0 (e.g., Costa & Chakraborty, 2008). Thus, in addition to *T*, the accuracy and precision of timescales derived from diffusion modeling crucially depend on the accuracy, robustness, and applicability of the pre-exponential factor D_0 and the activation energy *E*. These factors are commonly derived from experiments, and many diffusion modeling studies assume experimentally obtained D_0 and *E* values to be accurate and precise values. However, as we will show for the example of published D_{Fe-Mg} in orthopyroxene, the uncertainties associated with the experimental determination of *D*s are significant and can affect both their precision and accuracy.

Reliable D_{Fe-Mg} in orthopyroxene have proved difficult to obtain experimentally due to the slow diffusivities involved. Therefore, Fe–Mg diffusion rates in orthopyroxene were initially constrained relative to coexisting garnet in granulite facies rocks (Pattison & Bégin, 1994) and mantle xenoliths (Smith & Barron, 1991), and subsequently also relative to coexisting olivine (Klügel, 2001). The first independent D_{Fe-Mg} in orthopyroxene was developed by Ganguly and Tazzoli (1994) based on experimental data on Fe-Mg fractionation between crystallographic sites (Anovitz, Essene, & Dunham, 1988; i.e., order-disorder rates; Besancon, 1981; Molin, Saxena, & Brizi, 1991) and crystallographic constraints. Ganguly and Tazzoli (1994) stated that the standard error in *D*s calculated using their expression is "approximately one order of magnitude," which, if considered in the modeling of timescales, yields greater uncertainties than those introduced by temperature constraints. Ganguly and Tazzoli (1994) identify the dependence of D^{opx}_{Fe-Mg} on the crystallographic direction and oxygen fugacity; however, these factors are not accounted for in their expression, and the given standard error is derived from the scatter in experimental data only. Furthermore, their D^{opx}_{Fe-Mg} is based on experiments conducted at $T \approx 500 - 800\ °C$, $X_{Fe} = 0.1 - 0.5$, and f_{O_2} around the iron-wüstite buffer, which is not representative for many active volcanic systems.

To overcome the theoretical framework required to calculate *D*s, Schwandt, Cygan, and Westrich (1998) directly measured Mg self-diffusion coefficients along the three crystallographic axes in three natural crystals with $En_{88}Fs_{12}$ at four temperatures from 750 to 900 °C at the IW buffer. Linear least squares fitting of the results yielded Arrhenius relationships [equation 8.1] for the three crystallographic axes of orthopyroxene, giving the first direct constraints on *E* and D_0 along the *a*-, *b*-, and *c*-axis in orthopyroxene. Based on their activation energies $E^c < E^b < E^a$, Schwandt et al. (1998) confirmed the diffusion anisotropy $D_0{}^c > D_0{}^b > D_0{}^a$ suggested by Ganguly and Tazzoli (1994). However, large scatter within the dataset resulted in large uncertainties in *E* and D_0 (up to ±70% rel.), to the extent that the respective values for different crystallographic axis are equal within error. This is most apparent for the pre-exponential factors D_0, which become increasingly dominant as the temperature rises, and the activation energy exerts less control on *D* [equation 8.1]. The pre-exponential factors determined by Schwandt et al. (1998) are highest along the *a*-axis and lowest along the *c*-axis, with $D_0{}^a > D_0{}^b > D_0{}^c$. Using these values to extrapolate D_{Fe-Mg} to magmatic temperatures found at arc volcanoes such as Popocatépetl (~950 –1100 °C) result in the paradoxical situation of D^a_{Fe-Mg} being the fastest, and D^c_{Fe-Mg} the slowest diffusion coefficient (Figure 8.3). However, textural evidence unequivocally confirms that diffusion is fastest along the *c*-axis and slowest along the *a*-axis (e.g., Figure 8.2a, where diffusive replacement is most advanced along the *c*-axis). The scatter in experimental data thus results in the imprecise and inaccurate determination of *E* and D_0, which becomes apparent upon extrapolation to magmatic conditions relevant to many volcanoes worldwide. Moreover, Schwandt's *D*s are self-diffusion coefficients that do not inherently consider chemical gradients, which puts into question their suitability for modeling of zoned crystals.

The pioneering works of Ganguly and Tazzoli (1994) and Schwandt et al. (1998) represent cornerstones of diffusion modeling in igneous systems, and they facilitated numerous studies yielding fundamental new insights into the dynamics of magmatic processes. However, uncertainties related to experimental data, crystallographic direction, oxygen fugacity, and extrapolation to actual magmatic conditions are commonly overlooked. We point out the importance of considering such uncertainties when interpreting diffusion modeling results.

New experimental data published by Dohmen, Ter Heege, Becker, and Chakraborty (2016) provide the first expression of D_{Fe-Mg} in orthopyroxene derived from

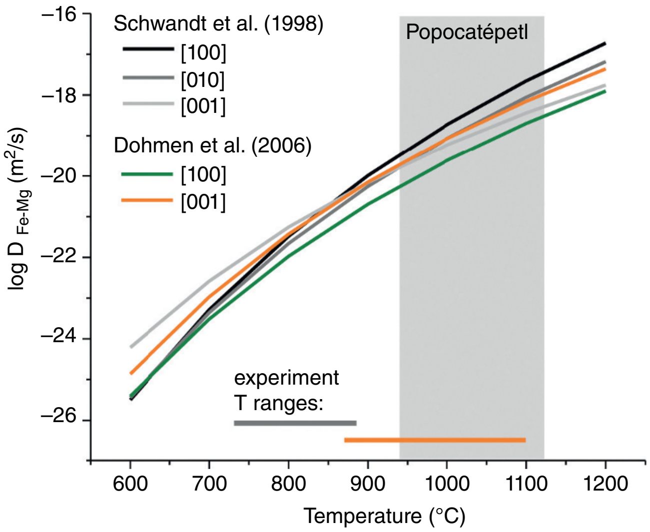

Figure 8.3 log $D_{\text{Fe-Mg}}$ along crystallographic axes in orthopyroxene as determined by Schwandt et al. (1998) and Dohmen et al. (2016). Experimental temperature ranges are also given, log Ds were extrapolated beyond the ranges using given D_0 and dH. Values for Dohmen's Ds assume an oxygen fugacity of $10^{-9.730}$ Pa (Mangler, 2018). The gray area highlights the temperature range of Popocatépetl magmas for reference. Sources: Schwandt et al. (1998); Dohmen et al. (2016).

Fe–Mg interdiffusion under magmatic conditions relevant for many volcanic systems in different tectonic settings. Diffusion in two natural crystals with $En_{98}Fs_1$ and $En_{91}Fs_9$ was measured at T = 870–1100 °C and $f_{O_2} = 10^{-11}$–10^{-7}, and Dohmen et al. (2016) show negligible dependency of D_{Fe-Mg} on the orthopyroxene composition of $Fs_{<50}$. This D_{Fe-Mg} can thus be applied to orthopyroxene in most magmatic systems without the need for extrapolation, and it includes a parameter to account for the dependence of D on the oxygen fugacity. Due to the larger dataset produced by Dohmen et al. (2016), uncertainties in E and D_0 are better constrained than by Schwandt et al. (1998). However, despite significantly improved uncertainties in E (±5 rel.-%) compared to Schwandt et al. (1998; up to 25 rel.-%), uncertainties in D_{Fe-Mg} after Dohmen et al. (2016) introduce a variability of almost two orders of magnitude in the modeled timescales.

This shows that, contrary to common belief, uncertainties introduced by temperature estimates are not necessarily the most significant source of uncertainty on timescales derived from diffusion modeling. Although it is crucial to use accurate and precise input data for diffusion modeling (i.e., T, X, f_{O_2}), the largest—and mostly neglected—sources of uncertainties are those in the experimentally derived values for E and D_0. These uncertainties are intrinsic to the experimental determination of the D used, so producing better experimental constraints on E and D_0 is of utmost importance to increase the accuracy and significance of geospeedometry. Combining diffusion timescales from different minerals and elemental systems can be used to reduce inherent uncertainties and cross-validate diffusion timescales (e.g., Chamberlain et al., 2014; Cooper et al., 2017), and geospeedometry results can be integrated with and cross-checked against timescales derived from other geological techniques such as radiometric dating (Cooper & Kent, 2014; Turner & Costa, 2007). Thus, careful data processing and mindful interpretation of diffusion-derived geological timescales can provide significant and unique insights into magmatic processes, making geospeedometry a powerful geological tool.

8.8. CONCLUSIONS: A WAY FORWARD

Elemental diffusion chronostratigraphy of single crystals preserves time-related information of pre-eruptive magmatic processes, which can be used to reconstruct the histories and dynamics of magma reservoirs. The temporal information can be unlocked via geospeedometry, and in the last decade many studies have modeled timescales of a range of pre-eruptive processes, from magma mixing to magma ascent rate, magma storage, and remobilization in the shallow crust (e.g., Cooper, 2019; Costa et al., 2008; Di Stefano et al., 2020; Dohmen et al., 2017; Petrone et al., 2018). However, in many cases, only the timescale of the last compositional boundary has been resolved, limiting our knowledge of pre-eruptive timescales to those directly preceding the eruption. Therefore, information relative to the lifetime of the crystal might be limited, and the time-related histories of magmatic reservoirs might not be easy to reconstruct. A major obstacle to modeling timescales beyond the outermost rim is the need to accurately constrain the temperatures at which diffusion occurred. This is particularly critical when more than one compositional boundary is present, pointing to multiple compositional and physical changes during the lifetime of a crystal. Recent models (Cooper & Kent, 2014) have suggested cold storage conditions, where the mush is locked at near-solidus condition; therefore, timescales calculated at the pre-eruptive magmatic temperature do not reflect storage timescales but only the final mixing and assemblage of magma shortly before eruption.

Here, we argue that hot storage conditions are typical of magmatic systems characterized by open-system conduits in steady state, where repeated injections of hotter mafic magma determine the continuous presence of eruptible magma at temperatures well above the locked crystal mush. Crystals will spend their lifetime at the temperature of the eruptible magma in the corresponding magmatic environment, and under this condition, the derived diffusion timescales approximate the storage of the crystal in question, as shown by recent work on Stromboli (Di Stefano et al., 2020; Petrone et al., 2018). In fact, in these systems, hybridization processes are controlled by long-lived end-members with relatively constant composition kept at relatively constant temperature (e.g., Bragagni et al., 2014; Di Renzo et al., 2019; Mangler et al., 2019; Petrone et al., 2018).

Providing a careful and detailed study of the petrology of a given magmatic system, it is possible to fully resolve the elemental diffusion chronostratigraphy, as we have shown using Fe–Mg interdiffusion in pyroxenes from Stromboli and Popocatépetl as examples. The possibility of retrieving meaningful timescales from diffusion stratigraphy is linked to an in-depth knowledge of the mineralogy and geochemistry of the crystal cargo and the melt involved, accurate estimates of magmatic temperatures for each environment, and good statistic of the modeled crystals. Uncertainties introduced by temperature estimates and other input data for diffusion modeling (i.e., X, f_{O2}) have large effects on the accuracy of the modeled timescales, and they can be mitigated to a degree by accurate determination of T. Furthermore, intrinsic sources of uncertainties related to experimentally derived values for the activation energy E and the pre-exponential factor D_0 need to be considered when evaluating diffusion timescales. Intrinsic uncertainties can be reduced by calculating independent diffusion timescales for different minerals and diffusion systems, and the results can be cross-related to and checked against other geologically derived timescales (i.e., radiometric ages, monitoring time series). Further reduction of uncertainties related to experimentally derived diffusion coefficients should be considered a priority in order to advance and improve elemental diffusion modeling data.

Elemental diffusion chronostratigraphy has been reconstructed using the backward approach of the NIDIS model (Petrone et al., 2016, 2018), which deconstructs the complex diffusion profile in single isothermal steps providing the crystal diffusive residence time from mafic injection(s) to eruption alongside timescales of storage in different magmatic environments. These timescales, although not equal to absolute crystal ages, provide insights into the time-integrated dynamics of mixing processes, storage, mush mobilization, and eruption triggering events during the lifetime of a single crystal. Using examples from Stromboli and Popocatépetl, we have shown that different dynamics of magmatic systems (e.g., short vs. long storage; mafic injections triggering eruption vs. absence of correlation between mafic injection and eruption; efficient magma homogenization and/or crystal transfer to different magmatic environments) can be resolved by geospeedometry applied to the different portions of complex chemically zoned crystals. Elemental diffusion chronostratigraphy is an extremely powerful tool for obtaining time-related temporal information on the dynamics and histories of volcanic plumbing systems. Combined with monitoring data and other petrological, geological, and geophysical constraints at active volcanoes, they can greatly enhance our capability to inform volcanic hazard assessments.

ACKNOWLEDGMENTS

The authors would like to thank L. Francalanci for the Stromboli samples. The in-depth reviews of S. Tommasini and K. Chamberlain greatly improved the manuscript. We are also grateful to S. Mollo and M. Masotta for the careful editorial handling of the manuscript. The work was financially supported by NERC grant NE/M014584 to CMP, and by Royal Society-Newton Fund International Exchanges Grant IE140605 to CMP.

REFERENCES

Allan, A. S. R., Morgan, D. J., Wilson, C. J. N., & Millet, M.-A. (2013). From mush to eruption in centuries: assembly of the super-sized Oruanui magma body. *Contributions to Mineralogy and Petrology*, *166*(1), 143–164. doi:10.1007/s00410-013-0869-2.

Anderson, A. T. (1984). Probable relations between plagioclase zoning and magma dynamics, Fuego Volcano, Guatemala. *American Mineralogist*, *69*(7–8), 660–676.

Anovitz, L. M., Essene, E. J., & Dunham, W. R. (1988). Order-disorder experiments on orthopyroxenes; implications for the orthopyroxene geospeedometer. *American Mineralogist*, *73*, 1060–1073.

Arana-Salinas, L., Siebe, C., & Macías, J. L. (2010). Dynamics of the ca. 4965yr 14C BP "Ochre Pumice" Plinian eruption of Popocatépetl volcano, México. *Journal of Volcanology and Geothermal Research*, *192*(3–4), 212–231. doi: 10.1016/j.jvolgeores.2010.02.022.

Ayres, M., & Vance, D. (1997). A comparative study of diffusion profiles in Himalayan and Dalradian garnets: Constraints on diffusion data and the relative duration of the metamorphic events. *Contributions to Mineralogy and Petrology*, *128*(1), 66–80. doi: 10.1007/s004100050294.

Bachmann, O., & Bergantz, G. W. (2006). Gas percolation in upper-crustal silicic crystal mushes as a mechanism for upward heat advection and rejuvenation of near-solidus magma bodies. *Journal of Volcanology and Geothermal research*, *149*(1-2), 85–102. doi: 10.1016/j.jvolgeores.2005.06.002.

Barboni, M., Boehnke, P., Schmitt, A. K., Harrison, T. M., Shane, P., Bouvier, A. S., & Baumgartner, L. (2016). Warm storage for arc magmas. *Proceedings of the National Academy of Sciences*, *113*(49), 13959–13964. doi: 10.1073/pnas.1616129113.

Bertagnini, A., Métrich, N., Francalanci, L., Landi, P., Tommasini, S., & Conticelli, S. (2008). Volcanology and magma geochemistry of the present-day activity: Constraints on the feeding system. *The Stromboli Volcano, An integrated study of the 2002-2003 eruption, AGU Geophysical Monographic Series, Washington DC*, *182*, 19–38. doi: 10.1029/182GM04

Besancon, J. R. (1981). Rate of cation disordering in orthopyroxenes. *American Mineralogist*, *66*, 965–973.

Bragagni, A., Avanzinelli, R., Freymuth, H., & Francalanci, L. (2014). Recycling of crystal mush-derived melts and short magma residence times revealed by U-series disequilibria at Stromboli volcano. *Earth and Planetary Science Letters*, *404*, 206–219. doi:10.1016/j.epsl.2014.07.028.

Burgisser, A., & Bergantz, G. W. (2011). A rapid mechanism to remobilize and homogenize highly crystalline magma bodies. *Nature*, *471*(7337), 212. doi: 10.1038/nature09799.

Cashman, K. V., & Giordano, G. (2014). Calderas and magma reservoirs. *Journal of Volcanology and Geothermal Research*, *288*, 28–45. doi: 10.1016/j.jvolgeores.2014.09.007.

Cassidy, M., Manga, M., Cashman, K., & Bachmann, O. (2018). Controls on explosive-effusive volcanic eruption styles. *Nature communications*, *9*(1), 2839. doi: 10.1038/s41467-018-05293-3.

Chakraborty, S., & Ganguly, J. (1991). Compositional zoning and cation diffusion in garnets. *Diffusion, Atomic Ordering, and Mass Transport*, *8*, 120–175.

Chakraborty, S. (1997). Rates and mechanisms of Fe-Mg interdiffusion in olivine at 980°–1300° C, *Journal of Geophysical Research: Solid Earth*, *102*, 12317–12331. doi: 10.1029/97JB00208

Chakraborty, S. (2006). Diffusion modeling as a tool for constraining timescales of evolution of metamorphic rocks. *Mineralogy and Petrology*, *88*(1–2), 7–27. doi:10.1007/s00710-006-0152-6.

Chamberlain, K. J., Morgan, D. J., & Wilson, C. J. (2014). Timescales of mixing and mobilisation in the Bishop Tuff magma body: perspectives from diffusion chronometry. *Contributions to Mineralogy and Petrology*, *168*(1), 1034. doi: 10.1007/s00410-014-1034-2.

Cheng, L., Costa, F., & Bergantz, G. (2020). Linking fluid dynamics and olivine crystal scale zoning during simulated magma intrusion. *Contributions to Mineralogy and Petrology*, *175*(6). doi: 10.1007/s00410-020-01691-3

Cooper, G. F., Morgan, D. J., & Wilson, C. J. (2017). Rapid assembly and rejuvenation of a large silicic magmatic system: Insights from mineral diffusive profiles in the Kidnappers and Rocky Hill deposits, New Zealand. *Earth and Planetary Science Letters*, *473*, 1–13. doi: 10.1016/j.epsl.2017.05.036.

Cooper, K. M. (2019). Time scales and temperatures of crystal storage in magma reservoirs: implications for magma reservoir dynamics. *Philosophical Transactions of the Royal Society A: Mathematical, Physical and Engineering Sciences*, *377*(2139), 20180009. doi:10.1098/rsta.2018.0009.

Cooper, K. M. (2017). What does a magma reservoir look like? The "crystal's-eye" view. *Elements*, *13*(1), 23–28, doi: 10.2113/gselements.13.1.23

Cooper, K. M., & Kent, A. J. R. (2014). Rapid remobilization of magmatic crystals kept in cold storage. *Nature*, *506*(7489), 480–18. doi:10.1038/nature12991.

Costa, F., Dohmen, R., & Chakraborty, S. (2008). Time scales of magmatic processes from modeling the zoning patterns of crystals. *Reviews in Mineralogy and Geochemistry*, *69*(1), 545–594. doi:10.2138/rmg.2008.69.14.

Costa, F., Chakraborty, S., & Dohmen, R. (2003). Diffusion coupling between trace and major elements and a model for calculation of magma residence times using plagioclase. *Geochimica et Cosmochimica Acta*, *67*(12), 2189–2200. doi:10.1016/S0016-7037(02)01345-5.

Couch, S., Sparks, R. S. J., & Carroll, M.R. (2001). Mineral disequilibrium in lavas explained by convective self-mixing in open magma chambers. *Nature*, *411*, 1037. doi: 10.1038/35082540

Crank, J. (1979). The mathematics of diffusion (2nd edn, 414 pp). *Oxford University Press, New York* (*1975*).

Davidson, J. P., Morgan, D. J., Charlier, B. L. A., Harlou, R., & Hora, J. M. (2007). Microsampling and isotopic analysis of igneous rocks: Implications for the study of magmatic systems. *Annual Review of Earth and Planetary Sciences*, *35*(1), 273–311. doi:10.1146/annurev.earth.35.031306.140211.

Dimanov, A., & Sautter, V. (2000). "Average" interdiffusion of (Fe, Mn)-Mg in natural diopside. *European Journal of Mineralogy*, *12*(4), 749–760. doi: 10.1127/0935-1221/2000/0012-0749.

Di Renzo, V., Corsaro, R. A., Miraglia, L., Pompilio, M., & Civetta, L. (2019). Long and short-term magma differentiation at Mt. Etna as revealed by Sr-Nd isotopes and geochemical data. *Earth Science Reviews*, *190*, 112–130. doi:10.1016/j.earscirev.2018.12.008.

Di Stefano, F., Mollo, S., Ubide, T., Petrone, C. M., Caulfiled, J., Scarlato, P., et al. (2020). Mush cannibalism and disruption recorded by clinopyroxene crystals at Stromboli volcano: new insights from recent 2003-207 activity. *Lithos*, *360–361*. doi:10.1016/j.lithos.2020.105440

Dohmen, R., Ter Heege, J. H., Becker, H. W., & Chakraborty, S. (2016). Fe-Mg interdiffusion in orthopyroxene. *American Mineralogist*, *101*(10), 2210–2221. doi: 10.2138/am-2016-5815.

Dohmen, R., Faak, K., & Blundy, J. D. (2017). Chronometry and Speedometry of Magmatic Processes using Chemical Diffusion in Olivine, Plagioclase and Pyroxenes. *Reviews in Mineralogy and Geochemistry*, *83*(1), 535–575., doi:10.2138/rmg.2017.83.16.

Druitt, T. H., Costa, F., Deloule, E., Dungan, M., & Scaillet, B. (2012). Decadal to monthly timescales of magma transfer and reservoir growth at a caldera volcano. *Nature*, *482*(7383), 77–80.

Fabbro, G. N., Druitt, T. H., & Scaillet, S. (2013). Evolution of the crustal magma plumbing system during the build-up to the 22-ka caldera-forming eruption of Santorini (Greece). *Bulletin of Volcanology*, *75*(12), 767. doi: 10.1007/s00445-013-0767-5.

Francalanci, L., Tommasini, S., Conticelli, S., & Davies, G. R. (1999). Sr isotope evidence for short magma residence time for the 20th century activity at Stromboli volcano, Italy. *Earth and Planetary Science Letters*, *167*(1–2), 61–69. doi: 10.1016/S0012-821X(99)00013-8.

Francalanci, L., Lucchi, F., Keller, J., De Astis, G., & Tranne, C. A. (2013). Eruptive, volcano-tectonic and magmatic history of the Stromboli volcano (north-eastern Aeolian archipelago). *Geological Society, London, Memoirs*, *37*(1), 397–471.

Ganguly, J., & Tazzoli, V. (1994). Fe2+-Mg interdiffusion in orthopyroxene: Retrieval from the data on intracrystalline exchange reaction. *American Mineralogist*, *79*(9–10), 930–937.

Ganguly, J., Chakraborty, S., Sharp, T. G., & Rumble, D. (1996). Constraint on the time scale of biotite-grade metamorphism during Acadian Orogeny from a natural garnet-garnet diffusion couple. *American Mineralogist*, *81*(9–10), 1208–1216. doi: 10.2138/am-1996-9-1019.

Giacomoni, P. P., Ferlito, C., Coltorti, M., Bonadiman, C., & Lanzafame, G. (2014). Plagioclase as archive of magma ascent dynamics on "open conduit" volcanoes: the 2001–2006 eruptive period at Mt. Etna. *Earth-science reviews*, *138*, 371–393. doi: 10.1016/j.earscirev.2014.06.009.

Gómez-Vazquez, A., De la Cruz-Reyna, S., & Mendoza-Rosas, A. T. (2016). The ongoing dome emplacement and destruction cyclic process at Popocatépetl volcano, Central Mexico. *Bulletin of Volcanology*, *78*(9), 58. doi: 10.1007/s00445-016-1054-z.

Hawkesworth, C. J., Blake, S., Evans, P., Hughes, R., Macdonald, R., Thomas, L. E., & Turner, S. P. (2000). Time scales of crystal fractionation in magma chambers – Integrating physical, isotopic and geochemical perspectives, *Journal of Petrology*, *41*(7), 991–1006. doi:10.3749/canmin.50.4.1095.

Kahl, M., Chakraborty, S., Costa, F., & Pompilio M. (2011). Dynamic plumbing system beneath volcanoes revealed by kinetic modeling, and the connection to monitoring data: An example from Mt. Etna. *Earth and Planetary Science Letters*, *308*(1–2), 11–22. doi:10.1016/j.epsl.2011.05.008.

Kahl, M., Chakraborty, S., Costa, F., Pompilio, M., Liuzzo, M., & Viccaro, M. (2013). Compositionally zoned crystals and real-time degassing data reveal changes in magma transfer dynamics during the 2006 summit eruptive episodes of Mt. Etna. *Bulletin of Volcanology*, *75*(2), 692. doi:10.1007/s00445-013-0692-7.

Kent, A. J., Darr, C., Koleszar, A. M., Salisbury, M. J., & Cooper, K. M. (2010). Preferential eruption of andesitic magmas through recharge filtering. *Nature Geoscience*, *3*(9), 631. *3*(9), 631–636, doi:10.1038/ngeo924.

Kilgour, G., Blundy, J., Cashman, K., & Mader, H. M. (2013). Small volume andesite magmas and melt–mush interactions at Ruapehu, New Zealand: Evidence from melt inclusions. *Contributions to Mineralogy and Petrology*, *166*(2), 371–392. doi:10.1007/s00410-013-0880-7.

Klügel, A. (2001). Prolonged reactions between harzburgite xenoliths and silica-undersaturated melt: implications for dissolution and Fe-Mg interdiffusion rates of orthopyroxene. *Contributions to Mineralogy and Petrology*, *141*, 1–14. doi: 10.1007/s004100000222.

Krimer, D., & Costa, F. (2017). Evaluation of the effects of 3d diffusion, crystal geometry, and initial conditions on retrieved time-scales from Fe–Mg zoning in natural oriented orthopyroxene crystals. *Geochimica et Cosmochimica Acta*, *196*, 271–288, doi: 10.1016/j.gca.2016.09.037.

Mangler, M. F. (2018), *Evolution and dynamics of the plumbing system of Popocatépetl volcano, Mexico* (Doctoral Dissertation). Imperial College London.

Mangler, M. F., Prytulak, J., Gisbert, G., Delgado-Granados, H., & Petrone, C.M. (2019). Interplinian effusive activity at Popocatépetl volcano, Mexico: New insights into evolution and dynamics of the plumbing system. *Volcanica 2*(1), 45–72. doi: 10.30909/vol.02.01.4572.

Mangler, M. F., Petrone, C. M., Hill, S., Delgado-Granados, H., & Prytulak, J. (2020). A pyroxenic view on magma hybridization and crystallization at Popocatépet Volcano, Mexico. *Frontiers in Earth Science*, *8*, 362. doi: 10.3389/feart.2020.00362

Molin, G., Saxena, S., & Brizi, E. (1991). Iron-magnesium order-disorder in an orthopyroxene crystal from the Johnstown meteorite. *Earth and Planetary Science Letters*, *105*, 260–265. doi: 10.1016/0012-821X(91)90135-5.

Morgan, D. J., Blake, S., Rogers, N. W., De Vivo, B., Rolandi, G., & Davidson, J. P. (2006). Magma chamber recharge at Vesuvius in the century prior to the eruption of AD 79. *Geology*, *34*(10), 845–848. doi:10.1130/G22604.1.

Morgan, D. J., Blake, S., Rogers, N. W., De Vivo, B., Rolandi, G., Macdonald, R., & Hawkesworth, C. J. (2004). Time scales of crystal residence and magma chamber volume from modelling of diffusion profiles in phenocrysts: Vesuvius 1944. *Earth and Planetary Science Letters*, *222*(3–4), 933–946. doi:10.1016/j.epsl.2004.03.030.

Mueller, T., Watson, E. B., & Harrison, T. M. (2010). Applications of diffusion data to high-temperature earth systems. *Reviews in Mineralogy and Geochemistry*, *72*(1), 997–1038. doi:10.2138/rmg.2010.72.23.

Ni, H., Keppler, H., Walte, N., Schiavi, F., Chen, Y., Masotta, M., & Li, Z. (2014). In situ observation of crystal growth in a basalt melt and the development of crystal size distribution in igneous rocks. *Contributions to Mineralogy and Petrology*, *167*(1003). doi:10.1007/s00410-014-1003-9.

O'Brien, P. J., & Vrána, S. (1995). Eclogites with a short-lived granulite facies overprint in the Moldanubian Zone, Czech Republic: Petrology, geochemistry and diffusion modelling of garnet zoning. *Geologische Rundschau*, *84*(3), 473–488. doi: 10.1007/BF00284515

Pattison, D., & Bégin, N. (1994). Zoning patterns in orthopyroxene and garnet in granulites: Implications for geothermometry. *Journal of Metamorphic Geology. 12*, 387–410. doi: 10.1111/j.1525-1314.1994.tb00031.x.

Petrone, C. M., Braschi E., Francalanci L., Casalini M., & Tommasini S. (2018). Rapid mixing and short storage timescale in the magma dynamics of a steady-state volcano. *Earth and Planetary Science Letters*, *492*, 206–221. doi:10.1016/j.epsl.2018.03.055.

Petrone, C. M., Bugatti G., Braschi E., & Tommasini S. (2016). Pre-eruptive magmatic processes re-timed using a non-isothermal approach to magma chamber dynamics. *Nature Communications*, *7*(1), 12946. doi:10.1038/ncomms12946.

Putirka, K. D. (2008). Thermometers and Barometers for Volcanic Systems. *Reviews in Mineralogy and Geochemistry*, *69*(1), 61–120. doi:10.2138/rmg.2008.69.3.

Rout, S. S., & Wörner, G. (2020). Constraints on the pre-eruptive magmatic history of the Quaternary Laacher See volcano (Germany). *Contributions to Mineralogy and Petrology*, *175*(8), 1–22.

Rout, S. S., Schmidt, B. C., & Wörner, G. (2020). Constraints on non-isothermal diffusion modeling: An experimental analysis and error assessment using halogen diffusion in melts. *American Mineralogist*, *105*(2), 227–238.

Scarlato, P., Mollo, S., Petrone, C.M., Ubide, T., & Di Stefano, F. (2019). Interpreting magma dynamics through a statistically refined thermometer: implication for clinopyroxene Fe-Mg diffusion modelling and sector zoning at Stromboli. *AGU Monograph on Crustal Magmatic System Evolution: Anatomy, Architecture, and Physico- Chemical Processes (Mollo, S.and Masotta, M., Edts), this issue*.

Schaaf, P., Stimac, J., Siebe, C., & Macias, J. L. (2005). Geochemical evidence for mantle origin and crustal processes in volcanic rocks from Popocatépetl and surrounding monogenetic volcanoes, central Mexico. *Journal of Petrology*, *46*(6), 1243–1282. doi: 10.1093/petrology/egi015.

Schwandt, C. S., Cygan, R. T., & Westrich, H. R. (1998). Magnesium self-diffusion in orthoenstatite. *Contributions to Mineralogy and Petrology*, *130*(3–4), 390–396. doi: 10.1007/s004100050373.

Shea, T., Lynn, K. J., & Garcia, M. O. (2015). Cracking the olivine zoning code: Distinguishing between crystal growth and diffusion. *Geology*, *43*(10), 935–938. doi: 10.1130/G37082.1.

Siebe, C., Salinas, S., Arana-Salinas, L., Macías, J. L., Gardner, J., & Bonasia, R. (2017). The~ 23,500 y 14 C BP White Pumice Plinian eruption and associated debris avalanche and Tochimilco lava flow of Popocatépetl volcano, México. *Journal of Volcanology and Geothermal Research*, *333*, 66–95. doi: 10.1016/j.jvolgeores.2017.01.011

Sosa-Ceballos, G., Gardner, J. E., & Lassiter, J. C. (2014). Intermittent mixing processes occurring before Plinian eruptions of Popocatepetl volcano, Mexico: insights from textural–compositional variations in plagioclase and Sr–Nd–Pb isotopes. *Contributions to Mineralogy and Petrology*, *167*(2). doi: 10.1007/s00410-014-0966-x.

Smith, D., & Barron, B. R. (1991). Pyroxene-garnet equilibration during cooling in the mantle. *American Mineralogist*, *76*, 1950–1963.

Sparks, R. S. J., & Cashman, K. V. (2017). Dynamic magma systems: Implications for forecasting volcanic activity, *Elements*, *13*(1), 35–40. doi: 10.2113/gselements.13.1.35.

Sparks, R. S. J., Annen, C., Blundy, J. D., Cashman, K. V., Rust, A. C., & Jackson, M. D. (2019). Formation and dynamics of magma reservoirs. *Philosophical Transactions of the Royal Society A*, *377*(2139), 20180019. doi:10.1098/rsta.2018.0019.

Streck, M. J. (2008). Mineral textures and zoning as evidence for open system processes. *Reviews in Mineralogy and Geochemistry*, *69*(1), 595–622. doi: 10.2138/rmg.2008.69.15

Tachibana, S., Tamada, S., Kawasaki, H., Ozawa, K., & Nagahara, H. (2013). Interdiffusion of Mg–Fe in olivine at 1,400–1,600° C and 1 atm total pressure. *Physics and Chemistry of Minerals*, *40*(6), 511–519. doi: 10.1007/s00269-013-0588-2.

Turner, S., & Costa, F. (2007). Measuring timescales of magmatic evolution. *Elements*, *3*(4), 267–272. doi: 10.2113/gselements.3.4.267.

Zellmer, G. F., Blake, S., Vance, D., Hawkesworth, C., & Turner, S. (1999). Plagioclase residence times at two island arc volcanoes (Kameni Islands, Santorini, and Soufriere, St. Vincent) determined by Sr diffusion systematics. *Contributions to Mineralogy and Petrology*, *136*(4), 345–357. doi:10.1007/s004100050543.

Zhang, Y. (2010). Diffusion in minerals and melts: Theoretical Background. *Reviews in Mineralogy and Geochemistry*, *72*(1), 5–59. doi:10.2138/rmg.2010.72.2.

9

Interpreting Magma Dynamics Through a Statistically Refined Thermometer: Implications for Clinopyroxene Fe–Mg Diffusion Modeling and Sector Zoning at Stromboli

Piergiorgio Scarlato[1], Silvio Mollo[1,2], Chiara Maria Petrone[3], Teresa Ubide[4], and Flavio Di Stefano[2]

ABSTRACT

We present a more accurate clinopyroxene-only thermometer for shoshonite melts calibrated through the statistical analysis of both experimental and thermodynamically derived compositions. The calibration data set refers to the compositions of magmas at Stromboli, one of the most studied volcanoes in Italy and of broad significance as the type locality for Strombolian activity. The predictive power of the clinopyroxene-only thermometer is potentially very high, with an uncertainty of only ±6 °C for crystallization conditions of 10–900 MPa, 1,000–1,200 °C, 1–5 wt.% H_2O, and −1.66 to 1.27 NNO. For compositions extremely different from those of Stromboli magmas (i.e., trachytic and phonolitic melts), the error of estimate may increase up to ±30 °C but is still a relatively low uncertainty with respect to other thermometers from the literature. The strong linear correlation between T and $Mg\#^{melt}$ allows to test for equilibrium between natural clinopyroxene compositions and their host magmas, supporting the use of the clinopyroxene-only thermometer with alkaline eruptive products to minimize the error of temperature. We illustrate the potential of this integrated approach by modeling temperature changes for clinopyroxene compositional zoning caused by recharge episodes of mafic magmas at Stromboli. With respect to previous thermometric equations, the percentage error on diffusion timescales decreases from ±510% to ±21%. Owing to its high accuracy, the thermometer is also suitable for estimating the crystallization temperature of hourglass sector-zoned clinopyroxenes, where kinetic effects induce differential elemental partitioning into {100} and {−111} sectors.

9.1. INTRODUCTION

The crystallization temperature of magmas is one of the most important intensive variables governing eruptive dynamics and controlling the geochemical evolutionary path of volcanic systems in terms of mineral and melt compositions. Clinopyroxene is a common phase of volcanic products with an extensive saturation surface encompassing mantle depths and shallow crustal levels (e.g., Putirka, 2008). For this reason, thermometers, barometers, oxygen barometers, hygrometers, and equilibrium models are frequently calibrated using clinopyroxene components (Armienti et al., 2013; France et al., 2010; Masotta et al., 2013; Mollo & Masotta, 2014; Mollo et al., 2010, 2013a, 2018; Neave & Putirka, 2017; Nimis & Taylor, 2000; Perinelli et al., 2016; Putirka, 1999, 2008; Putirka et al., 1996, 2003), and a gamut of clinopyroxene-based partitioning equations are developed to track the

---

[1] *Istituto Nazionale di Geofisica e Vulcanologia, Rome, Italy*

[2] *Department of Earth Sciences, Sapienza – University of Rome, Rome, Italy*

[3] *Department of Earth Sciences, The Natural History Museum, London, United Kingdom*

[4] *School of Earth and Environmental Sciences, The University of Queensland, Brisbane, Australia*

Crustal Magmatic System Evolution: Anatomy, Architecture, and Physico-Chemical Processes, Geophysical Monograph 264, First Edition.
Edited by Matteo Masotta, Christoph Beier, and Silvio Mollo.

DOI: 10.1002/9781119564485.ch9

differentiation of magma during clinopyroxene fractionation (Bédard, 2005, 2014; Blundy et al., 1995; Dygert et al., 2014; Hill et al., 2011; Liang, 2015; Liang et al., 2013; Mollo et al., 2016, 2017, 2020; Sun & Liang, 2012, 2017; Wood & Blundy, 1997, 2001, 2002).

For the specific case of thermometers, the examination of previous works shows that the calibration error derived by regression analysis of experimental data is quite variable: ±30 °C (Eqn. 17) for Nimis and Taylor (2000); ±27 °C (Eqn. T1), ±24 °C (Eqn. T2), ±37 °C (Eqn. T3), and ±28 °C (Eq. T4) for Putirka et al. (1996); ±51 °C (Eqn. 3.8) for Putirka (1999); ±34 °C (Eqn. B) for Putirka et al. (2003); ±58 °C (Eqn. 32d), ±45 °C (Eqn. 33), and ±45 °C (Eqn. 34) for Putirka (2008); ±32 °C (Eqn. Talk1), ±31 °C (Eqn. Talk2), ±34 °C (Eqn. Talk3), ±34 °C (Eqn. Talk4), ±24 °C (Eqn. Talk33), and ±18 °C (Eqn. Talk2012) for Masotta et al. (2013); and ±28 °C (Eqn. 33MAM) and ±20 °C (Eqn. 34MAM) for Mollo et al. (2018). As a general feature, the global calibration of all the experimental compositions available in literature leads to errors of estimate much greater (e.g., ±27-58 °C, Putirka, 2008) than the regression analysis of a more restricted *P*-*T*-*X* range (e.g., ±18–20 °C; Masotta et al., 2013; Mollo et al., 2018). Despite the fact that this latter approach has the advantage of increasing the model accuracy, any application of these defined thermometers outside their calibration bounds may cause errors of estimate up to ±300 °C (cf. Masotta et al., 2013).

One interesting point of clinopyroxene-based thermometers is the wide spectrum of regression parameters employed for their calibration (i.e., a variety of clinopyroxene and/or melt components), with the result of *P*-dependent (or *P*-independent) clinopyroxene–melt, clinopyroxene-only, and melt-only thermometers. The accuracy (±45–58 °C) of models based on one single phase (clinopyroxene or melt) is generally lower than that of clinopyroxene–melt thermometers (±18–34 °C) (Putirka, 2008). The main source of error during the regression analysis of a thermometric equation is due to the low quality of the experimental data or to their provenance from different laboratories, as well as the different analytical conditions used for the chemical analysis of crystals and glasses (Neave & Putirka, 2017; Putirka, 2008). A prerequisite for global thermometers applicable to a broad range of mantle to crustal conditions is the knowledge of *P* to effectively describe the variance of the calibration data set. Unfortunately, this calibration scheme has the collateral effect of introducing further uncertainties due to the estimate of clinopyroxene saturation pressure (Mollo et al., 2018). In the absence of a unique experimental-analytical data set from the same laboratory, it seems more promising to minimize the uncertainty of thermometric equations by selecting restricted crystallization conditions and magma compositions, with the ambition of excluding *P* from the model calibration (Masotta et al., 2013; Mollo et al., 2018).

The calibration error of clinopyroxene-based thermometers can be relatively higher than the pre-eruptive temperature changes associated with magma dynamics and determining complex crystal zoning (Druitt et al., 2012; Kent et al., 2010; Petrone et al., 2016; Tecchiato et al., 2018; Ubide & Kamber, 2018). Some authors overcome this limitation by providing additional temperature constraints from thermodynamic simulations, equilibrium partitioning equations, and experimental investigations (e.g., Armienti et al., 2013; Casetta et al., 2018; Del Bello et al., 2014; Giacomoni et al., 2016, 2018; Iezzi et al., 2009, 2014a, 2014b; Lanzafame et al., 2013, 2017; Masotta et al., 2018; Mollo et al., 2011, 2015a; Petrone et al., 2016, 2018; Scarlato et al., 2017; Ubide et al., 2019). However, during eruption and abundant microlite crystallization, it is extremely difficult to identify the melt composition in equilibrium with each single isolated sector of a chemically zoned clinopyroxene phenocryst (cf. Armienti et al., 2013). For example, the Fe–Mg exchange between clinopyroxene and melt points to an equilibrium value of 0.28 from the most recent calculation of Putirka (2008). However, 0.28 is the weighted arithmetic mean of a much broader equilibrium range of 0.04–0.68 obtained by phase equilibrium experiments. A similar oversimplification applies to other tests for equilibrium based on clinopyroxene components (Putirka, 1999; Mollo et al., 2013a). These models are able to detect the attainment of near-equilibrium conditions for clinopyroxene but, within their calibration uncertainty, are unable to univocally isolate and identify the melt composition feeding the crystal growth.

In view of the above observations, we illustrate how multivariate analysis (i.e., calculation of correlations and covariances between variables to construct a multiple regression model) and statistical tests conducted on experimental and thermodynamically derived clinopyroxene compositions may help to correctly identify the most powerful compositional predictors for the calibration of highly accurate clinopyroxene-only thermometers. This approach ensures that the number and type of multiple linear regression parameters yield high degrees of temperature correlation and sensitivity, but do not cause data overfitting and multicollinearity. The model applicability has been referred to the crustal conditions and magma compositions typical of the Stromboli volcano (Aeolian Islands, Italy). The choice of this specific volcanic setting arises from the following considerations: (a) Stromboli is one of the most famous and best-studied volcanoes in the world because of its typical Strombolian-eruption style (e.g., Del Bello et al., 2015); (b) paroxysm eruptions are continuously monitored and sampled for their implications for flank instability phenomena and tsunami waves (e.g., Di Traglia et al., 2014); (c) a great number of mineral and bulk rock compositions have been analyzed over the last decades, providing a broad data set for the entire (from ~85 ka to present) eruptive history of the volcano (e.g., Francalanci et al., 2013); (d) the present-day activity is characterized by the persistent eruption of shoshonitic basalts whose crystallization conditions have been well constrained (e.g., Di Carlo et al, 2006); (e) clinopyroxene intra-crystal compositional variations record a complex history reflecting different melt domains and magma mixing timescales (e.g., Petrone et al., 2018); and (f) there are no thermometers in literature relevant to Stromboli magmas and suitable for decoding the intricate features of clinopyroxene zoning.

Results from our calibration and test analyses conducted on the clinopyroxene-only thermometer indicate that the crystallization temperature of Stromboli magmas may be accurately (error of ±6 °C) estimated for each single compositional layer of multi-zoned clinopyroxene phenocrysts, thus minimizing the uncertainties related to temperature estimates. For the sake of completeness, we emphasize that the purpose of this work is not to improve our understanding of the Stromboli plumbing system and pre-eruptive magmatic processes. This has been the topic of a great number of previous investigations (e.g., Bertagnini et al., 2003; Di Stefano et al., 2020; Francalanci et al., 1999, 2004, 2012, 2013, 2014; Landi et al., 2004, 2009; Métrich et al., 2010; Petrone et al., 2018; Ubide et al., 2019). However, some applications of the clinopyroxene-only thermometer may have important ramifications for future studies focusing on magma dynamics at Stromboli. This notion is illustrated through two different representative cases. The first case demonstrates that the thermometric model may dramatically reduce the uncertainty in diffusion chronometry modeling based on the non-isothermal nature of Fe–Mg exchange. The second case points out that the prism sector {100} and basal sector {−111} of hourglass-zoned clinopyroxenes may provide new insight into the temperature-dependent crystallization path of Stromboli magmas.

9.2. CALIBRATION AND TEST DATA SETS

With the aim of deriving a new thermometer applicable to Stromboli magmas, 37 experimental clinopyroxene compositions from Di Carlo et al. (2006) and Pichavant et al. (2009) have been selected from the literature. The isothermal experiments were conducted on a primitive K-basalt (PST-9; ~50 wt.% SiO_2 and ~4 wt.% Na_2O+K_2O; on anhydrous basis) erupted in the period 800–1600 CE. Clinopyroxenes were equilibrated at 0.1–417 MPa, 1,050–1,180 °C, 0–5 wt.% H_2O and −1.5–3.8 NNO (Supplementary Material). However, the coexisting experimental melts (~50–54 wt.% SiO_2 and ~4–6 wt.% Na_2O+K_2O) do not reproduce in full the whole rock compositions of the 12 lithosomes identified in the geological map of Stromboli at 1:10,000 scale (Lucchi et al., 2013) through the integrated use of different rock-stratigraphic units (unconformity-bounded units, lithostratigraphic units, and geometric features): Strombolicchio, Paleostromboli I (PSTI), Paleostromboli II (PSTII), Paleostromboli III (PSTIII), Scari, Vancori, Roisa, Neostromboli, Recent Sciara Volcano, San Bartolo, Active Craters, and Dikes. The lithosome termed Active Craters includes the products of the Sciara del Fuoco Formation developed during the Present-day activity of Stromboli (<1.2 ka; Rosi et al., 2013). The TAS (total alkali vs. silica; Le Bas et al., 1986) classification diagram (Figure 9.1a) shows that the compositional variability (~49–62 wt.% SiO_2 and ~4–8 wt.% Na_2O+K_2O) of Stromboli products ranges from sub-alkaline to weakly alkaline. The K_2O versus SiO_2 diagram (Peccerillo & Taylor, 1976) is also useful to discriminate four magmatic series (Figure 9.1b): calc-alkaline (CA), high-K calc-alkaline (HKCA), shoshonitic (SHO), and potassic (K) (Francalanci et al., 2013). Notably, the most recent products of the Active Craters are persistently buffered to the composition of shoshonitic basalts (i.e., ~49–52 wt.% SiO_2, ~4–5 wt.% Na_2O+K_2O, and ~2 wt.% K_2O) similar to PST-9. In order to obtain a further calibration data set more representative of the natural compositions and independent of experiments from the literature, the rhyolite-MELTS code (v.1.2.0; Gualda et al., 2012) was also adopted to perform thermodynamic simulations based on the detection of phase saturation and energy convergence by Gibbs free energy minimization. Using as starting composition the same K-basalt (PST-9) adopted for the experiments, 131 clinopyroxene compositions (Supplementary Material) were equilibrated at the P-T-H_2O-fO_2 conditions inferred for the plumbing system of Stromboli volcano: 10–900 MPa, 1,000–1,200 °C, 1–5 wt.% H_2O, and −1.66–1.27 NNO (Aiuppa et al., 2009, 2010; Di Carlo et al., 2006; Francalanci et al., 2014; Landi et al., 2009;

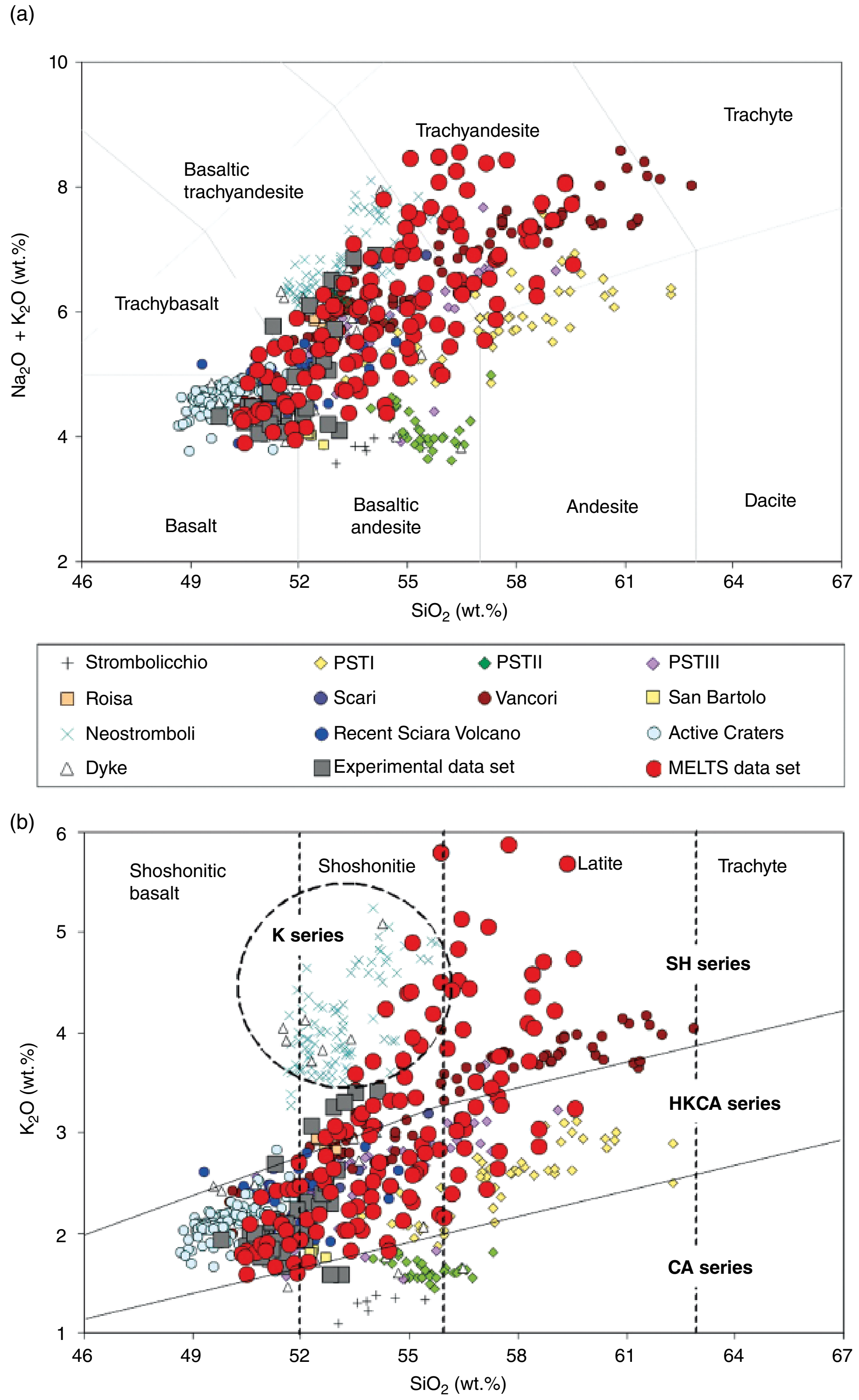

Figure 9.1 Bulk rock analyses (on anhydrous basis) of Stromboli eruptions reported in Francalanci et al. (2013) are plotted in (a) the TAS (total alkali vs. silica; Le Bas et al., 1986) classification diagram and (b) in the K_2O versus SiO_2 diagram (Peccerillo & Taylor, 1976). The data are classified into calc-alkaline (CA), high-K calc-alkaline (HKCA), shoshonitic (SHO), and potassic (K) compositions. Source: Based on Peccerillo and Taylor (1976); Francalanci et al. (2013); Le Bas et al. (1986); Peccerillo and Taylor (1976).

Métrich et al., 2010; Pichavant et al., 2009). The use of this approach makes possible to overcome some important experimental limitations that may reduce the predictive power of the thermometer, such as (a) the paucity of experimental data referring to Stromboli magmas and their underrepresentation in the calibration data set of the model and (b) the potential lack of crystal–melt bulk equilibrium in isothermal experiments, mostly due to substantial FeO loss (see below). The rhyolite-MELTS code includes also some numerical algorithms that remarkably improve the computational stability, especially for hydrous crystallization paths. This makes the code suitable for modeling mineral-melt compositions under variable P-T-H_2O conditions, the only exception being near-solidus or sub-solidus phase equilibria and intermediate systems dominated by the presence of hornblende or biotite (Gualda et al., 2012).

The accuracy of the thermometer has been tested following the same strategy reported in Putirka (2008). Before the regression analysis, ~20% of clinopyroxene compositions were randomly subtracted from the calibration data set (Supplementary Material). The residual ~80% of clinopyroxene compositions were used to calibrate the thermometer, whose accuracy was then verified through the subtracted compositions. Despite the empirical or semi-empirical parameterization approaches frequently reported in literature, one of the most important limitations of mineral-melt multiple linear regression equations is represented by the compositional bounds of the calibration data set (Masotta et al., 2013; Mollo & Masotta, 2014; Mollo et al., 2015b; Putirka, 2008). It has been observed that the estimated error of clinopyroxene-based thermometers may be very large when the equations are extrapolated to compositions not included in the regression analysis of the data (e.g., Mollo et al., 2018, and references therein). A similar uncertainty applies to mineral-melt equilibria derived by regression fits relating liquidus temperatures to melt compositions (Nielsen & Dungan, 1983). Therefore, to assess the extent of this limitation, the thermometer was tested outside its calibration bounds by using thermodynamically derived clinopyroxene compositions in equilibrium with trachytic and phonolitic melts (Supplementary Material). These data were obtained through rhyolite-MELTS simulations conducted by Mollo et al. (2015b) on compositions representative of magmatism at the Phlegraean Fields (Italy) that were equilibrated at 150–200 MPa, 1,067–850 °C, 2.0–4.7 wt.% H_2O, and NNO+0.5 buffer.

9.3. PARAMETERIZATION OF THE THERMOMETER

The statistical algorithm of Statgraphics Centurion has been used to calculate the Pearson product moment correlation coefficient (Pearson's r) between T and the clinopyroxene chemistry expressed as follows (Figure 9.2): X_i (cation fraction of the element of interest i), $Mg\#^{cpx}$ [molar Mg / (Mg+$\mathrm{Fe_{tot}}$) where $\mathrm{Fe_{tot}}$ refers to total Fe^{2+}], Di (diopside), Hd (hedenbergite), En (enstatite), Fs (ferrosilite), Jd (jadeite), CaTs (Ca-Tschermak), CaTiTs (CaTi-Tschermak), CaFeTs (CaFe-Tschermak), and *a*En (activity of En as derived by Putirka, 2008). The value of Pearson's r ranges between −1 (highest negative correlation) and +1 (highest positive correlation), measuring the strength of the linear relationship between two quantitative variables. The experimental clinopyroxene compositions are weakly correlated with T, yielding extremely low Pearson's r values between −0.40 and 0.38 (Figure 9.2a). By contrast, MELTS compositions are highly correlated with T, showing more reliable Pearson's r values up to 0.97 (Figure 9.2b). The multivariate analysis conducted with Statgraphics Centurion also computes the *p-value* as a test of the statistical significance of the estimated correlations (Figure 9.2). A *p-value* < 0.05 indicates statistically significant nonzero correlations at the 95% confidence level, attesting to the validity of the linear regression analysis. It is found that *p-values* computed for both clinopyroxene cation fractions and components from the experimental data set are remarkably high (from 0.06 to 0.99; Figure 9.2a), the only exceptions being the most reliable X_{Ti} (0.01) and X_{Mg} (0.02). Conversely, results for MELTS variables are systematically equal to zero (Figure 9.2b), demonstrating the strong dependence of clinopyroxene chemistry on T. The very low statistics obtained for the experimental data set may be related to the ubiquitous occurrence of clinopyroxene as the liquidus phase under either H_2O-undersaturated or H_2O-saturated experimental conditions. This is quite surprising because the stability field of olivine expands at the expense of clinopyroxene and plagioclase with increasing H_2O dissolved in mafic alkaline melts (Métrich & Rutherford, 1998, and references therein). It has been argued that PST-9 behaves like an ultra-calcic (ankaramitic) melt where the clinopyroxene saturation curve may overstep the olivine crystallization (Di Carlo et al., 2006; Pichavant et al., 2009). However, the CaO/Al_2O_3 ratio (0.81) of PST-9 is very similar to that (0.82) of other mafic alkaline magmas early-saturated with olivine (Métrich & Rutherford, 1998). In addition, MELTS thermodynamic simulations confirm that olivine is the liquidus phase at 10–300 MPa and 1–3 wt.% H_2O, as well as at 600 MPa and 3 wt.% H_2O, thus reproducing much better the crystallization sequence of natural products at Stromboli (cf. Landi et al., 2009). On the other hand, chemical states of partial equilibrium (i.e., homogeneous crystal chemistry) have been identified in the isothermal experiments conducted on Stromboli magmas that, however, are not accompanied by crystal–melt bulk equilibria. This is primarily caused by substantial FeO loss in the experimental capsules quantified between 3.6% and

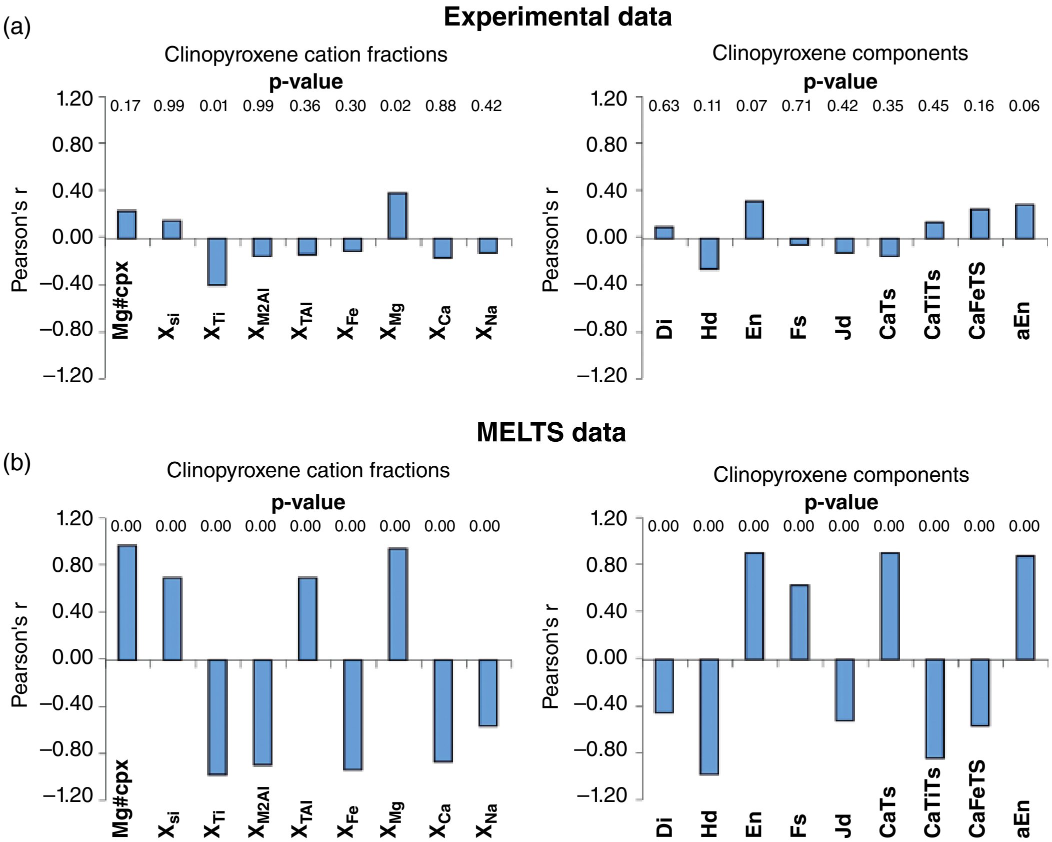

Figure 9.2 Results from statistical analysis conducted on (a) the experimental data set and (b) MELTS data set. The Pearson product moment correlation coefficient (Pearson's *r*) is calculated between *T* and the clinopyroxene cation fractions and components. The *p-value* is a test of the statistical significance of the estimated correlations.

29.4% (Di Carlo et al., 2006). As a consequence, results from crystal–melt mass-balance calculations provide sums of residuals that are generally very high and may increase up to 7.12 (Di Carlo et al., 2006).

According to the above considerations, the multiple linear regression analysis of the experimental data set can be bounded to only X_{Ti} and $X_{Mg,}$ as the most reliable independent variables for the temperature prediction identified by Pearson's *r* and *p-value* statistics. However, the regression fit of the data yields correlation coefficients (*R*) and standard errors of estimate (*SEE* or model uncertainty) indicative of a very low model accuracy, with R^2 = 0.14–0.17 and *SEE* = ±35.12–43.13 °C. Further, any attempt to integrate these experimental compositions with the MELTS data set produces statistically unstable thermometric equations with respect to those obtained by using only the thermodynamic simulations. Due to the lack of bulk equilibrium conditions in most of the isothermal experiments (Di Carlo et al., 2006), some scattering effects are evident during multiple linear regression analysis. For example, the sign of X_{Mg} as predictor for *T*, changes from positive to negative, causing an implausible negative dependency of $X_{Mg,}$ with the saturation temperature of clinopyroxene. This is a typical suppression effect where the variance of the calibration data set is not properly described during multiple linear regression analysis for one or more regression coefficients (Hair et al., 1995). Moreover, strong model mis-calibrations are obtained when permutation tests are conducted on clinopyroxene predictors different from X_{Ti} and X_{Mg}, thus ignoring the Pearson's *r* and *p-value* restrictions for the experimental data set. In other words, any global regression fit in which the number of predictors is greater than X_{Ti} and X_{Mg} suffers from bias-variance trade-off effects due to data overfitting and multicollinearity (cf. Mollo et al., 2015b).

On the other hand, statistical analysis of the MELTS data set shows that clinopyroxene cation fractions and components may be suitable predictors for *T* (Figure 9.2b). In multiple linear regression analysis, however, some variables may closely describe the variance of the data set, whereas some others may generate a set of predictions with low degrees of freedom that lead to strong data overfitting. Therefore, variables that do not improve the fit must be identified and removed from a model. Through an algorithm based on the Mallows' Cp statistic (Hair et al., 1995), we have performed systematic permutations of a number of independent variables relative to the dependent variable T, to capture the best explanatory predictors for the clinopyroxene crystallization temperature. Mallows' Cp is expressed as $Cp = RSS_k/RSS_p - n + 2p$, where RSS_k is the ratio of the residual sum of squares of all predictors k, RSS_p is the residual sum of squares of only p of the k predictors, and n is the number of observations. Mallows' Cp is therefore a measure of the bias in a model. If the type and number of selected predictors p (including the constant term in the linear regression) are sufficient to provide a good description of the data, then Cp has values as close as possible to p (Hair et al., 1995). Results from calculations are listed in Table 9.1, showing that the difference (in absolute value) between Cp and p measured for clinopyroxene cation fractions is much lower than that of clinopyroxene components. Indeed, clinopyroxene components are calculated by the arithmetical combination of cation fractions, leading to potential mis-calibration due to data overfitting and multicollinearity. It is apparent from Table 9.1 that the use of *Di*, *Hd*, *En*, *Jd*, *CaTs*, and *CaTi* as predictors for T may ensure the highest correlation coefficient ($R^2 = 98.41$) and the lowest mean squared error ($MSE = 33.34$). However, under such circumstances, the Mallows' Cp statistic highlights that the variance of the clinopyroxene components is inflated by linear interdependence (i.e., multicollinearity) where Cp is much higher than p (i.e., $|p - Cp| = 4.53$; Table 9.1). Taking these considerations into account, we have regressed X_{Si}, X_{Ti}, X_{M1Al}, X_{Mg}, X_{Ca}, and X_{Na}, as the most suitable predictors for T (i.e., $|p - Cp| = 0.65$; Table 9.1), in order to calibrate the following thermometer:

$$\begin{aligned} T = {} & 723.99 - 96.82X_{Si} - 2410.44X_{Ti} + 946.18X_{M1Al} \\ & + 435.61X_{Mg} + 291.75X_{Ca} - 774.94X_{Na} \end{aligned} \tag{9.1}$$

The regression statistics ($R^2 = 0.98$ and $SEE = \pm 6.35\text{-}6.43$ °C) derived for this model are extremely high and virtually identical for both the calibration (Figure 9.3a) and test (Figure 9.3b) data sets, thus strengthening the reliability of the model estimates.

Although models relying on thermodynamic principles can be realistically extrapolated to a broad range of P-T-X conditions (c.f. Blundy & Wood, 2003, and references therein), it is apparent that empirical equations cannot be applied to clinopyroxene–melt systems that are not included in the calibration data sets (e.g., Masotta et al., 2013; Mollo et al., 2018). Therefore, the magnitude of the error caused by the accidental use of compositions outside the calibration bounds has been quantified through an additional test data set designed specifically for trachytic and phonolitic melts (Mollo et al., 2015b). This test data set consists of compositions with $Mg\#^{melt}$ ranging from 12 to 44, which are rather more differentiated than Stromboli products ($Mg\#^{melt} = 44$–77). Figure 9.4a illustrates that the regression fit of predicted versus observed temperatures provides low statistics ($R^2 = 0.69$ and $SEE = \pm 30$ °C), with overestimates up to one order of magnitude higher than the $SEE = \pm 6$ °C of the thermometric model from this study. However, it must be noted that the retrieved $SEE = \pm 30$ °C is statistically more significant than the internal calibration error (±58 °C) of the clinopyroxene-only thermometer (equation 32d) of Putirka (2008). The lower ability prediction of the thermometer reflects the different paragenesis and crystallization temperatures of trachy-phonolitic systems (e.g., Forni et al., 2016, 2018). Clinopyroxene (mineral mass<10%) readily saturates the melt as liquidus phase, but its formation is accompanied by increasing feldspar crystallization (mineral mass up to 35%), especially at low thermal conditions ($T < 950$ °C). Therefore, great care must be exercised in applying the thermometers presented in this study to compositions and conditions far from those of the Stromboli magmas. Bearing in mind that melt compositional effects may lead to erroneous temperature estimates and interpretations, we have regressed $Mg\#^{melt}$ as a function of clinopyroxene chemistry, in order to provide more robust constraints on the equilibrium conditions between natural clinopyroxenes and their host magmas. Considering the strong codependency ($R^2 = 0.91$) between $Mg\#^{melt}$ and T, the thermometric equation has been reappraised in the following predictive form ($R^2 = 0.96$ and $SEE = \pm 0.39$ $Mg\#^{melt}$; Figure 9.4b):

$$\begin{aligned} Mg\#^{melt} = {} & -100.23 + 25.05X_{Si} + 68.71X_{Ti} + 83.42X_{M1Al} \\ & + 65.51X_{Mg} + 56.32X_{Ca} + 46.66X_{Na} \end{aligned} \tag{9.2}$$

9.4. IMPLICATIONS FOR MAGMA DYNAMICS AT STROMBOLI

9.4.1. Modeling Magma Storage Timescales

The timescales of pre-eruptive magmatic processes are increasingly recognized as one of the most important parameters governing magmatic processes and eruption triggers (Allan et al., 2013; Costa et al., 2008; Morgan et al., 2004). Chemical zoning in clinopyroxene may reflect substantial temperature differences during magma mixing (Ubide & Kamber, 2018, and references therein), which need to be considered when calculating crystal lifetime histories by elemental diffusion chronometry (Petrone et al., 2016, 2018). The Non-Isothermal Diffusion Incremental Step (NIDIS) model is a recent diffusion-based code accounting for Fe-Mg compositional zoning profiles in clinopyroxene, providing robust

Table 9.1 Statistics Obtained for the MELTS Data Set

Independent variables	p	MSE	R^2	Adjusted R^2	Cp	|p – Cp|
Clinopyroxene cation fractions						
X_{Ti} - X_{M1Al} - X_{Mg} - X_{Ca} - X_{Na}	6	40.13	98.07	97.99	5.35	0.65
X_{Si} - X_{Ti} - X_{M1Al} - X_{Mg} - X_{Ca} - X_{Na}	7	40.34	98.07	97.98	7.00	0.98
X_{Si} - X_{Ti} - X_{M1Al} - X_{Mg} - X_{Ca}	6	40.74	98.04	97.96	7.24	1.24
X_{Ti} - X_{M1Al} - X_{Mg} - X_{Ca}	5	40.84	98.02	97.96	6.59	1.59
X_{Si} - X_{Ti} - X_{M1Al} - X_{Mg} - X_{Na}	6	43.74	97.90	97.81	16.55	10.55
X_{Ti} - X_{M1Al} - X_{Mg} - X_{Na}	5	43.78	97.88	97.81	15.75	10.75
X_{Ti} - X_{M1Al} - X_{Na}	4	43.98	97.85	97.80	15.47	11.47
X_{Si} - X_{Ti} - X_{M1Al} - X_{Na}	5	43.98	97.87	97.80	16.40	11.40
X_{Ti} - X_{M1Al} - X_{Ca} - X_{Na}	5	44.08	97.86	97.79	16.70	11.70
X_{Si} - X_{Ti} - X_{M1Al} - X_{Ca} - X_{Na}	6	44.15	97.88	97.79	17.80	11.80
X_{Si} - X_{Ti} - X_{M1Al} - X_{Mg}	5	45.63	97.79	97.72	21.55	16.55
X_{M1Al} - X_{Mg} - X_{Ca}	4	45.79	97.76	97.71	21.16	17.16
X_{Si} - X_{Ti} - X_{M1Al}	4	45.80	97.76	97.71	21.22	17.22
X_{Si} - X_{M1Al} - X_{Mg} - X_{Ca} - X_{Na}	6	45.99	97.79	97.70	23.51	17.51
X_{Ti} - X_{M1Al} - X_{Ca}	4	46.51	97.73	97.67	23.42	19.42
X_{Ti} - X_{M1Al} - X_{Mg}	4	46.57	97.72	97.67	23.64	19.64
X_{Ti} - X_{M1Al}	3	46.80	97.69	97.66	23.50	20.50
X_{Si} - X_{Ti}	3	50.67	97.50	97.46	35.80	32.80
X_{Ti} - X_{Ca}	3	61.78	96.96	96.91	71.04	68.04
X_{Ti} - X_{Na}	3	62.39	96.93	96.88	72.99	69.99
X_{Ti} - X_{Mg}	3	70.26	96.54	96.48	97.96	94.96
X_{Ti}	2	71.72	96.44	96.41	102.37	100.37
X_{Mg}	2	230.33	88.56	88.47	609.60	607.60
X_{M1Al}	2	407.03	79.79	79.63	1174.72	1172.72
X_{Ca}	2	501.67	75.09	74.89	1477.38	1475.38
X_{Si}	2	1045.89	48.06	47.66	3217.86	3215.86
Clinopyroxene components						
Di - Hd - En - Jd - CaTs - CaTi	7	33.34	98.41	98.33	11.53	4.53
Di - Hd - En - Jd - CaTs - aEn	7	33.45	98.40	98.33	11.95	4.95
Di - Hd - En - Jd - CaTs	6	33.60	98.38	98.32	11.57	5.57
Di - Hd - En - Jd - CaTs - CaFeTs	7	33.70	98.39	98.31	12.91	5.91
Di - Hd - En - Fs - Jd - CaTs	7	33.73	98.39	98.31	13.03	6.03
Hd - Fs - CaTs - CaTi - CaFeTs - aEn	7	37.00	98.23	98.15	25.64	18.64
Di - Fs - CaTi - CaFeTs - aEn	6	38.00	98.17	98.10	28.66	22.66
Di - En - Fs - CaTi - CaFeTs	6	38.12	98.17	98.09	29.14	23.14
Fs - CaTs - CaTi - CaFeTs - aEn	6	38.75	98.14	98.06	31.59	25.59
En - Fs - CaTs - CaTi - CaFeTs	6	38.76	98.13	98.06	31.62	25.62
En - CaTs - CaTi - aEn	5	39.32	98.09	98.03	33.04	28.04
Di - En - CaTi - aEn	5	39.33	98.09	98.03	33.06	28.06
En - Fs - CaTi - aEn	5	39.99	98.06	98.00	35.65	30.65
Hd - En - CaTi - aEn	5	40.13	98.05	97.99	36.20	31.20
En - Jd - CaTi - aEn	5	40.31	98.04	97.98	36.88	31.88
En - CaTi - aEn	4	40.35	98.03	97.98	36.32	32.32
Hd - CaTi - CaFeTs	4	45.27	97.79	97.73	55.74	51.74
CaTs - CaTi - CaFeTs	4	48.90	97.61	97.55	70.07	66.07
Fs - CaTi - CaFeTs	4	49.24	97.59	97.54	71.41	67.41
Jd - CaTi - CaFeTs	4	49.96	97.56	97.50	74.24	70.24
CaTi - CaFeTs	3	50.05	97.53	97.50	74.14	71.14
Hd - CaFeTs	3	58.23	97.13	97.09	106.69	103.69
Hd - CaTs	3	61.06	96.99	96.94	117.99	114.99
Hd - aEn	3	61.37	96.98	96.93	119.19	116.19
Hd - CaTs	3	62.71	96.91	96.86	124.53	121.53
Hd	2	65.80	96.73	96.71	136.89	134.89
En	2	388.79	80.69	80.54	1432.13	1430.13
CaTs	2	390.82	80.59	80.44	1440.29	1438.29
aEn	2	477.24	76.30	76.12	1786.84	1784.84
CaTi	2	564.07	71.99	71.77	2135.07	2133.07

Mallows' *Cp* is expressed as $Cp = RSS_k/RSS_p - n + 2p$, where RSS_k is the ratio of the residual sum of squares of all predictors *k*, RSS_p is the residual sum of squares of only *p* of the *k* predictors, and *n* is the number of observations. R^2 and *MSE* are the correlation coefficient and the mean squared error, respectively. Adjusted R^2 refers to the number of predictors used for the model.

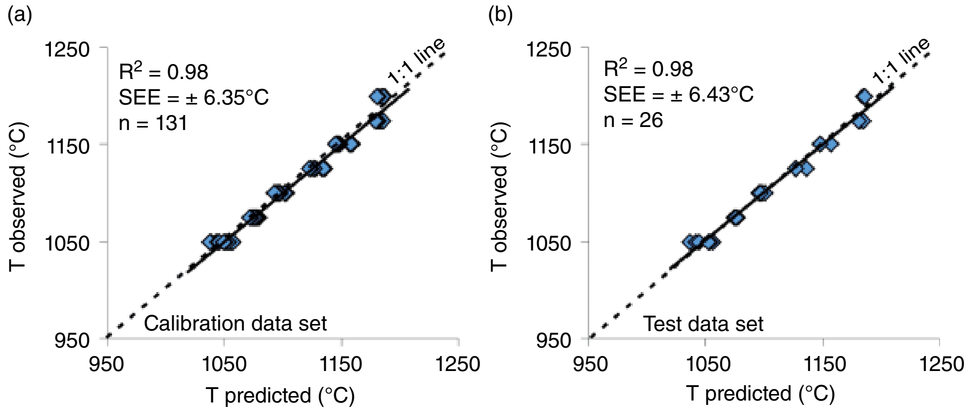

Figure 9.3 Temperatures predicted by the thermometric equation derived for Stromboli magmas are plotted versus those from the (a) calibration and (b) test data sets.

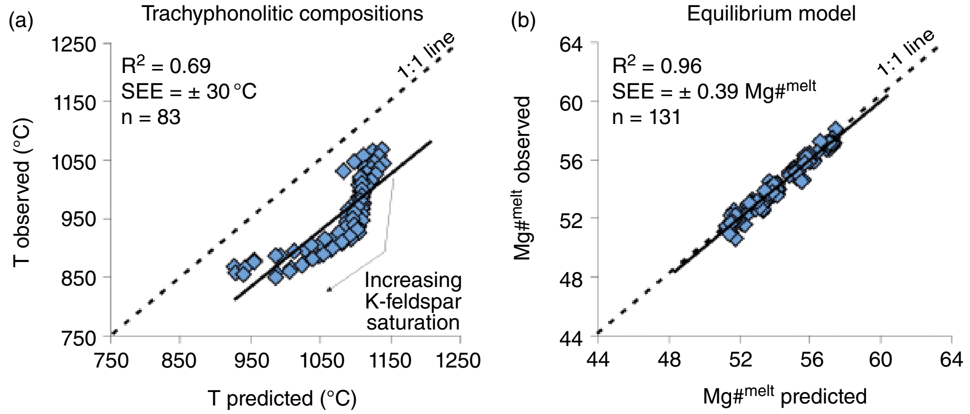

Figure 9.4 (a) Temperatures predicted by the thermometric equation derived for Stromboli magmas are plotted versus those from the test data set referring to trachytic and phonolitic compositions. (b) Equilibrium model derived for Stromboli magmas using the MELTS data set.

constraints on crystal residence times along with the possibility of determining timescales of melt homogenization and eruption triggering events (Petrone et al., 2016, 2018). The NIDIS model resolves the cation diffusion equation across a semi-infinite plane sheet (Crank, 1975) by deconstructing the entire core-rim *Mg#* diffusion profile into distinct isothermal steps reflecting the change in magmatic environment. The Fe–Mg diffusion coefficient is greatly controlled by temperature, as the cation mobility in minerals is a thermally activated process (Dimanov & Sautter, 2000). For the purpose of NIDIS and of any elemental diffusion modeling, the reconstructed residence time and its related uncertainty are strictly dependent on the cation diffusion, thus requiring an accurate estimate of the temperature at which the Fe–Mg exchange takes place (Petrone et al., 2016). For example, an error of ±20 °C (2*sd*, where *sd* refers to the standard deviation) on the temperature translates into a propagated error of 45%–55% (2*sd*) on the estimated residence times (Petrone et al., 2018). This is most relevant for very short timescales from magma recharge to eruption in active volcanoes, on the order of days to a few years (e.g., Druitt et al., 2012; Kent et al., 2010).

To better illustrate the importance of a reliable temperature estimate in reconstructing the pathways and timescales of magma recharge events, two natural clinopyroxene compositions from Stromboli (i.e., Cpx10 and Cpx16; Supplementary Material) have been used as test data for the thermometers from this study and NIDIS. These clinopyroxenes come from two rock samples belonging to the Post-Pizzo activity (sample STR276, Chiappe Lisce Formation) and Active Craters (sample STR275, Sciara del Fuoco Formation), as reported in Petrone et al. (2016, 2018). Sample STR276 is a shoshonite collected from the base of the Post-Pizzo (PP; 1.5-1.7 ka) pyroclastic sequence, whereas sample STR275 is a typical shoshonitic basalt erupted during one of the Early Paroxysms (EP; ~0.35 ka) of the present-day

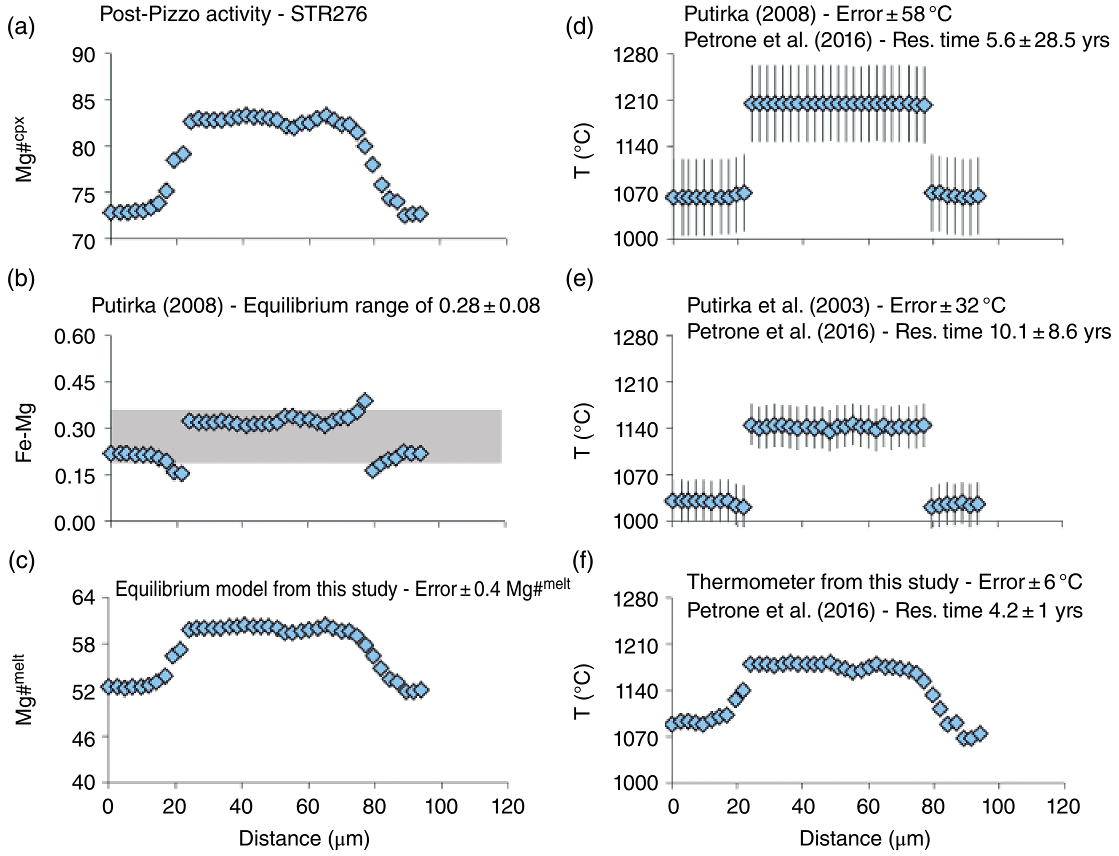

Figure 9.5 (a) $\text{Mg\#}^{\text{cpx}}$ data from Post-Pizzo (PP) activity (sample STR276). (b) Fe–Mg exchange between clinopyroxene compositions and the mafic bulk rock of *lp* magma and the more differentiated matrix glass analysis, as described in Petrone et al. (2018). (c) $\text{Mg\#}^{\text{melt}}$ obtained by applying the equilibrium model from this study and using as input data the composition of clinopyroxene. (d) Application of the clinopyroxene-only thermometer (Eqn. 32d with error of ±58 °C) of Putirka (2008). (e) The clinopyroxene–melt thermometer (Eqn. B with error of ±34 °C) of Putirka et al. (2003) and (f) the thermometer from this study (Eqn. 1 with error of ±6 °C) specific to Stromboli magmas. The Non-Isothermal Diffusion Incremental Step (NIDIS) model of Petrone et al. (2016) is employed to estimate crystal residence times using as input data the temperatures predicted by each different thermometer. Sources: Modified from Petrone et al. (2016, 2018); Based on Putirka (2008); Putirka et al. (2003).

activity. Clinopyroxene phenocrysts are characterized by chemical zoning with high-$Mg\#^{cpx}$ (83-87) diopsidic bands alternating with low-$Mg\#^{cpx}$ (73-76) augitic cores and rims (Figures 9.5a and 9.6a). According to Petrone et al. (2016, 2018), high-$Mg\#^{cpx}$ intra-crystal bands testify to recurrent recharge episodes with more mafic and hotter magmas, driving the plumbing system toward a more primitive character from PP to EP periods. Indeed, PP and EP clinopyroxenes exhibit comparable textural and compositional zoning, suggesting crystallization under the effects of similar recharge mechanisms and similar dynamics of the plumbing system (Petrone et al., 2018). During paroxysm events related to the Present-day activity, primitive, volatile-rich and crystal-poor magmas from depth are injected into the shallower, more degassed, and crystal-rich reservoir (Bragagni et al., 2014; Di Stefano et al., 2020; Francalanci et al., 1999, 2004; Ubide et al., 2019). The paroxysms frequently erupt variable proportions of resident volatile-poor high-porphyritic (*hp*) black scoriae intermingled with low-porphyritic (*lp*) light pumices, attesting to the complex hybridization process related to *lp*–*hp* magma interaction (Francalanci et al., 1999, 2004).

By applying the Fe–Mg exchange equation (Figures 9.5b and 9.6b), it is found that high-$Mg\#^{cpx}$ and low-$Mg\#^{cpx}$ zones in PP and EP clinopyroxenes fall within the equilibrium range of 0.28 ± 0.08 (Putirka, 2008) when compared with the mafic bulk rock composition of *lp* magma and the more differentiated matrix glass analysis, respectively (cf. Petrone et al., 2018). The role played by magma mixing on clinopyroxene evolution is also corroborated by the equilibrium model from this study showing that $Mg\#^{cpx}$ of 83–87 and 73–76 are in equilibrium with $Mg\#^{melt}$ of 60–63 and 52–53, respectively (Figures 9.5c

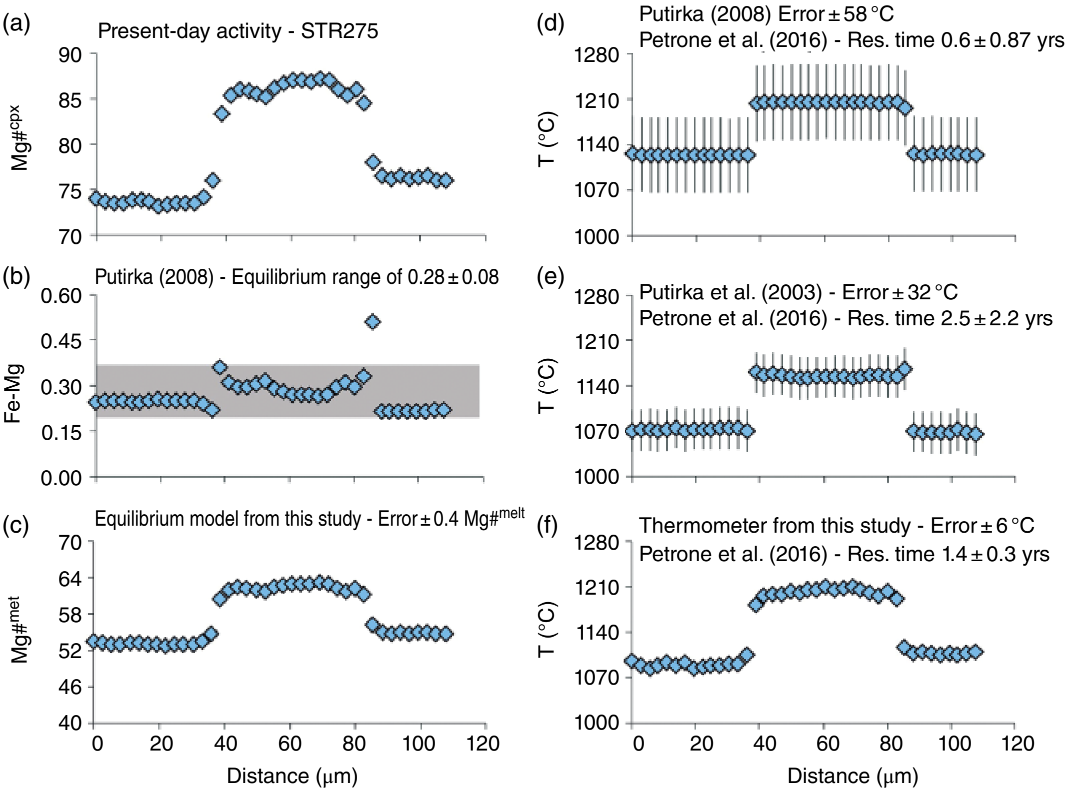

Figure 9.6 (a) Mg#^{cpx} data from Active Craters and Early Paroxysm (EP) activity (sample STR275). (b) Fe–Mg exchange between clinopyroxene compositions and the mafic bulk rock of *lp* magma and the more differentiated matrix glass analysis, as described in Petrone et al. (2018). (c) Mg#^{melt} obtained by applying the equilibrium model from this study and using as input data the composition of clinopyroxene. (d) Application of the clinopyroxene-only thermometer (Eqn. 32d with error of ±58 °C) of Putirka (2008), (e) the clinopyroxene–melt thermometer (Eqn. B with error of ±34 °C) of Putirka et al. (2003), and (f) the thermometer from this study (Eqn. 1 with error of ±6 °C) specific to Stromboli magmas. The Non-Isothermal Diffusion Incremental Step (NIDIS) model of Petrone et al. (2016) is employed to estimate crystal residence times using as input data the temperatures predicted by each different thermometer. Sources: Modified from Petrone et al. (2016, 2018); Based on Putirka (2008); Putirka et al. (2003).

and 9.6c). Having assessed a (near-)equilibrium crystallization condition for PP and EP magmas, three different clinopyroxene-based thermometers have been used to estimate the temperature of the crystal zoning formation: (a) the clinopyroxene-only thermometer (i.e., Eqn. 32d with error of ±58 °C; Figures 9.5d and 9.6d) of Putirka (2008) that is a refined expression of the original activity model of Nimis and Taylor (2000), (b) the clinopyroxene–melt thermometer (i.e., Eqn. B with error of ±34 °C; Figures 9.5e and 9.6e) of Putirka et al. (2003), and (c) the clinopyroxene-only thermometer from this study derived (i.e., Eqn. 1 with error of ±6 °C; Figures 9.5f and 9.6f). Temperatures recovered for the PP activity are ~1,206 (high-$Mg\#^{cpx}$)–1064 (low-$Mg\#^{cpx}$) °C from Eqn. 32d (Figure 9.5d), ~1,143 (high-$Mg\#^{cpx}$)–1,026 (low-$Mg\#^{cpx}$) °C from Eqn. B (Figure 9.5e) and ~1,180 (high-$Mg\#^{cpx}$)–1,090 (low-$Mg\#^{cpx}$) °C from Eqn. 1 (Figure 9.5f). Conversely, the crystallization of EP magma yields temperatures of ~1,206 (high-$Mg\#^{cpx}$)–1,123 (low-$Mg\#^{cpx}$) °C from Eqn. 32d (Figure 9.6d), ~1,154 (high-$Mg\#^{cpx}$)–1,070 (low-$Mg\#^{cpx}$) °C from Eqn. B (Figure 9.6e), and ~1,150 (high-$Mg\#^{cpx}$)–1,090 (low-$Mg\#^{cpx}$) °C from Eqn. 1 (Figure 9.6f). Considering the calibration errors of Eqns. 32d (±58 °C), B (±34 °C), and 2 (±6 °C), all the model estimates tend to overlap.

In the NIDIS model, the Fe–Mg diffusion coefficient is calculated by solving the exponential Arrhenius equation in which the pre-exponential factor and the activation energy are treated as constants (Dimanov & Sautter, 2000). The crystallization temperature of clinopyroxene is the only variable controlling the Fe–Mg diffusion coefficient, and the residence time varies as a function of T. The accurate estimate of T is well known to affect elemental diffusion studies, and points to the significance of the calculated timescales, which can only be evaluated in the context of the larger picture of the studied magmatic system. The parameter $\sqrt{4Dt}$ is used in NIDIS for the calculation of diffusion timescales and, given the diffusion coefficient D from the Arrhenius equation, the value of $\sqrt{4Dt}$ that best fits the data allows one to determine the residence time t of the crystal ($\sqrt{4Dt}$ Petrone et al., 2016). A specific script included in the NIDIS code calculates the error propagation on the crystal residence time relative to the error of the temperature estimate, also accounting for the uncertainty in the fitting parameter $\sqrt{4Dt}$ ($\sqrt{4Dt}$ Petrone et al., 2016, 2018). For the PP magma, the estimated residence times are 5.6 ± 28.5 yr (percentage error of ±510%), 10.1 ± 8.6 yr (percentage error of ±90%), and 4.2 ±1 yr (percentage error of ±21%) relative to Eqn. 32d (±58 °C), Eqn. B (±34 °C), and equation 9.1 (±6 °C), respectively (Figures 9.5d–f). Similarly, the error associated with the residence time of EP magma varies by applying Eqns. 32d, Eqn. B, and Eqn. 1, yielding 0.6 ± 0.8 yr (percentage error of ±130%), 2.5 ± 2.2 yr (percentage error of ±90%), and 1.4 ±0.3 yr (percentage error of ±23%), respectively (Figure 9.6d–f). Overall, the error propagation on the $\sqrt{4Dt}$ parameter (i.e., assuming no error in T) ranges from 40% to 20% for PP and is 10% for EP. Coherently, the very low calibration uncertainty associated with our MELTS thermometer minimizes the percentage error (±21–23%) of NIDIS timescales, providing the most accurate results.

9.4.2. Interpreting Hourglass Sector Zoning

Several eruptive products at Stromboli are characterized by the presence of hourglass sector-zoned clinopyroxene phenocrysts (Bertagnini et al., 2003; Di Stefano et al., 2020; Francalanci et al., 2012, 2014; Landi et al., 2004; Métrich et al., 2010; Ubide et al., 2019), attesting to the role played by complex magma dynamics (i.e., magma recharge, mixing and undercooling) in the evolutionary behavior of the plumbing system (Ubide et al., 2019). Figure 9.7a shows the overall compositions of {100} and {−111} sectors analyzed from core and mantle portions of three clinopyroxene phenocryst sections (profiles Cpx31_1, Cpx31_C_1, and Cpx34_2; see Supplementary Material for further details) belonging to the eruptive activity of Recent Sciara del Fuoco (Pizzo lithosome; Francalanci et al., 2013). By applying the charge balance equation of Lindsley (1980), it is calculated that {100} sectors are enriched in Al^{3+}, Ti^{4+}, and Fe^{3+} and depleted in Si^{4+}, Mg^{2+}, and Fe^{2+}, whereas the opposite occurs for {−111} sectors. In general, such a cation redistribution is controlled by charge balance requirements caused by substitution of [Si^{4+}] for [Al^{3+}] in the tetrahedral site and replacement of [Mg^{+2} + Fe^{2+}] for [Ti^{4+} + Fe^{3+}] in the octahedral sites (Mollo et al., 2013a, 2013b, 2018; Mollo and Hammer, 2017; Ubide et al., 2019). For the case of sector-zoned clinopyroxenes, the kinetically controlled cation exchange $[\mathrm{Si}^{4+} + \mathrm{Mg}^{2+} + \mathrm{Fe}^{2+}]_{\{-111\}} \leftrightarrow [\mathrm{Al}^{3+} + \mathrm{Ti}^{4+} + \mathrm{Fe}^{3+}]_{\{100\}}$ (Ubide et al., 2019) has been documented in laboratory at relatively low degrees of undercooling between 13 and 45 °C (Kouchi et al., 1983). Eruptive products at Stromboli contain millimeter-sized clinopyroxene phenocrysts and abundant glass (in the form of both matrix glass and melt inclusions; Francalanci et al., 2014), testifying to low degrees of undercooling in growth-dominated regimes (Mollo & Hammer, 2017).

Figures 9.7b and 9.7c show result from the clinopyroxene–melt thermometer of Putirka et al. (2003) and the clinopyroxene-only thermometer of Putirka (2008), respectively. We used the matrix glass analysis of the natural products as input melt composition for the clinopyroxene–melt thermometer of Putirka et al. (2003). Two distinct $T\text{-}Mg\#^{cpx}$ trends are depicted by the thermometers, as the models rely on very different calibration strategies and regression parameters, such as the activity of enstatite in clinopyroxene for the thermometer of Putirka (2008). Obviously, these trends reflect an apparent relationship determined by the kinetic cation exchange $[\mathrm{Si}^{4+} + \mathrm{Mg}^{2+} + \mathrm{Fe}^{2+}]_{\{-111\}} \leftrightarrow [\mathrm{Al}^{3+} + \mathrm{Ti}^{4+} + \mathrm{Fe}^{3+}]_{\{100\}}$, rather than the true crystallization temperature of the system. Considering the high temperature estimates (~1,130–1,170 °C) and calibration error (±58 °C) of the thermometer of Putirka (2008), the overall thermal paths of the two models overlap, despite the fact that the clinopyroxene–melt thermometer of Putirka et al. (2003) shows a much more restricted T interval (~1,080–1,110 °C) for both {100} and {−111} sectors. This suggests that thermometric models calibrated using both clinopyroxene and melt parameters are more suitable for estimating the saturation T of sector-zoned crystals. Evidently, the integration of melt components as regression parameters minimizes the effects of crystal growth kinetics and cation redistributions in the clinopyroxene crystal lattice. However, the thermometer from this study (Figure 9.7d) recovers T (~1,060–1,120 °C) estimates very similar to those obtained by the best predictive clinopyroxene–melt thermometer of Putirka et al. (2003), showing high precision when sectoral partitioning develops in clinopyroxenes from Stromboli eruptions.

Putirka (1999) proposed a test for equilibrium based on the difference (Δ) between Di + Hd (*DiHd*) components predicted for clinopyroxene via regression analysis of clinopyroxene–melt pairs in equilibrium conditions, and those measured in the analyzed natural phenocrysts. According to this model, the theoretical equilibrium condition is achieved when the value of $\Delta DiHd$ equals zero. In a more recent study, Mollo et al. (2013a) refined the equilibrium model of Putirka (1999), observing that kinetically controlled cation exchanges between crystal and melt causes $\Delta DiHd > 0.1$ (cf. Mollo & Masotta, 2014). By contrast, slow crystal growth conditions and

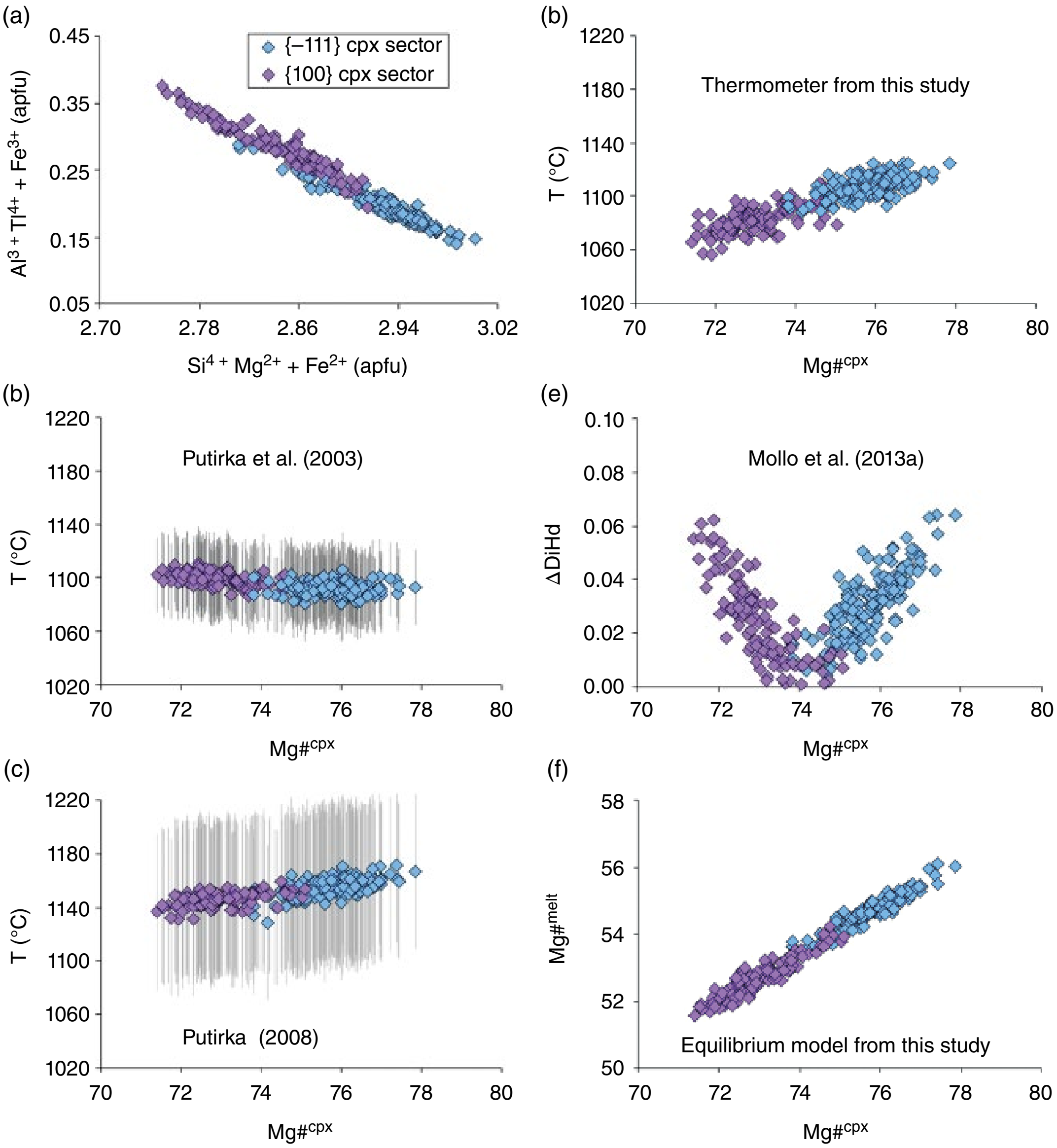

Figure 9.7 (a) Cation proportions of {100} and {−111} clinopyroxene sectors from products erupted during the activity of Recent Sciara volcano. (b) Application of the clinopyroxene–melt thermometer (Eqn. B with error of ±34 °C) of Putirka et al. (2003), (c) clinopyroxene-only thermometer (Eqn. 32d with error of ±58 °C) of Putirka (2008), and (d) the thermometer from this study (Eqn. 1 with error of ±6 °C) specific to Stromboli magmas. (e) Test for equilibrium based on the difference (Δ) between Di + Hd (DiHd) components predicted for clinopyroxene via regression analysis of clinopyroxene–melt pairs in equilibrium conditions, and those measured in the analyzed natural phenocrysts (Putirka, 1999; Mollo et al., 2013a). (f) Test for equilibrium from this study. Sources: Based on Putirka et al. (2003); Putirka (2008); Mollo et al. (2013).

near-equilibrium major and trace element partitioning yield $\Delta DiHd \leq 0.1$ (cf. Mollo et al., 2013a, 2013b, 2017, 2018). The model of Mollo et al. (2013a) has been used to test for equilibrium between the matrix glass and both {100} and {−111} sectors (Figure 9.7e). The relative low values (≤0.06) calculated for $\Delta DiHd$ indicate near-equilibrium cation redistributions at the crystal–melt interface, possibly due to low degrees of magma undercooling within the plumbing system of Stromboli (Bertagnini et al., 2003; Di Stefano et al., 2020; Francalanci et al., 2012, 2014; Landi et al., 2004; Métrich et al., 2010; Ubide et al., 2019). However, the $\Delta DiHd$ versus $Mg\#^{cpx}$ diagram displays two opposite trajectories for {100} and {−111} sectors (Figure 9.7e). The origin of this V-shaped trend (with a minimum at $\Delta DiHd \leq 0.02$) is related to the theoretical prediction that high-$Mg\#^{cpx}$

{−111} sectors are in equilibrium with melts more primitive then those feeding the growth of low-$Mg\#^{cpx}$ {100} sectors, and vice versa. Under such circumstances, intermediate clinopyroxene compositions between {100} and {−111} likely return a more restricted $\Delta DiHd$ range (≤0.06), translating to more reliable T estimates. Hence, the intermediate clinopyroxene compositions should provide the best estimate of crystallization temperature for sector-zoned crystals. This phenomenon can be better appreciated through the application of the equilibrium model from this study that allows one to identify the hypothetical composition of the melt in equilibrium with a specific clinopyroxene sector (Figure 9.7f). The "true" melt (i.e., the melt next to the advancing crystal surface) feeding the growth of both {100} and {−111} sectors at the time of clinopyroxene crystallization shows $Mg\#^{melt}$ variable from ~52 to ~56. This melt compositional variation, although small, conforms to the growth mechanism documented for sector-zoned clinopyroxenes and ascribed to the geometrical control of the structural sites on cation incorporations (Brophy et al., 1999; Dowty, 1976; Dunworth et al., 2001; Duncan & Preston, 1980; Ferguson, 1973; Giuliani et al., 2020 Harkins & Hollister, 1977; Hollister & Garcanz, 1971; Kouchi et al., 1983; Leung, 1974; Nakamura, 1973; Wass, 1973; Shimizu, 1981; Skulski et al., 1994; Watson & Liang, 1995; Ubide et al., 2019). Indeed, the different types of cation substitutions in the sectors reflect the variable spatial structural distributions of M and T sites as a function of the growth velocity of the crystal surface. At low degrees of undercooling, the growth of the {−111} sector is faster than that of {100}. The internal atomic arrangement of the {−111} sector involves single layers of M2 sites alternating with double layers of M1 sites. In this two-dimensional atomic arrangement, both M and T sites are exposed simultaneously, requiring the attachment of divalent cations and silicate tetrahedra (Leung, 1974; Nakamura, 1973). The melt adjacent to the fast-advancing {−111} sector is readily depleted in Si^{4+}, Mg^{2+}, and Fe^{2+}, as these cations are much more suitable for the clinopyroxene structure than Al^{3+}, Ti^{4+}, and Fe^{3+}. Thus, the remaining melt becomes enriched in highly charged incompatible cations that are subsequently incorporated in the slow-growing {100} sector, as its internal structure consists of alternating layers of M and T sites favorable for Al^{3+}, Ti^{4+}, and Fe^{3+} attachment (Downes, 1974; Dowty, 1976; Ferguson, 1973; Hollister & Gancarz, 1971; Kouchi et al., 1983; Leung, 1974; Nakamura, 1973; Nishizawa et al., 1972; Skulski et al., 1994). Referring to models from this study, the comparison between predicted values for T (Figure 9.7d) and $Mg\#^{melt}$ (Figure 9.7f) indicates that the partial overlap between {100} and {−111} data provides the most reasonable T (~1,100 °C) of the magma from which sector-zoned clinopyroxenes crystallized by cation incorporation at near-equilibrium proportions, also minimizing the value of $\Delta DiHd$ to values lower than 0.02 (Figure 9.7e).

9.5. FINAL REMARKS

In this study, we have shown that multivariate analysis and statistical tests may significantly help calibrate clinopyroxene-only thermometers specific to shoshonitic magmas, such as those erupted at Stromboli volcano. The thermometric model is derived by linear regression analysis of temperature-composition data from thermodynamic simulations. The thermodynamic approach allows one to calibrate an extremely powerful predictive equation (error of ±6 °C) that is also independent of P, H$_2$O, and melt composition. However, the clinopyroxene-only thermometer is less suitable for trachytic and phonolitic compositions remarkably different from those erupted at Stromboli volcano and leading to uncertainty up to ±30 °C. The application of the model to natural shoshonitic products may have important implications for correctly interpreting the role played by magma recharge events on intra-crystal zoning at Stromboli. The high accuracy of the thermometer makes it possible to dramatically decrease the error of estimate associated with magma recharge timescales obtained by Fe–Mg diffusion chronometry. With appropriate caution, the model is also suitable for identifying the thermal path driving crystal growth kinetics responsible for the formation of sector-zoned clinopyroxene phenocrysts.

ACKNOWLEDGMENTS

L. Francalanci is acknowledged for her kind help in providing the overall bulk rock analyses of products erupted at Stromboli volcano.

REFERENCES

Aiuppa, A., Federico, C., Giudice, G., Giuffrida, G., Guida, R., Gurrieri, S., et al. (2009). The 2007 eruption of Stromboli volcano: Insights from real-time measurements of the volcanic gas plume CO$_2$/SO$_2$ ratio. *Journal of Volcanology and Geothermal Research*, *182*, 221–230.

Aiuppa, A., Bertagnini, A., Métrich, N., Moretti, R., Di Muro, A., Liuzzo, M., & Tamburello, G. (2010). A model of degassing for Stromboli volcano. *Earth and Planetary Science Letters*, *295*, 195–204.

Allan, A. S. R., Morgan, D. J., Wilson, C. J. N., & Millet, M. A. (2013). From mush to eruption in centuries: Assembly of the super-sized Oruanui magma body. *Contributions to Mineralogy and Petrology*, *166*, 143–164.

Armienti, P., Perinelli, C., & Putirka, K. D. (2013). A new model to estimate deep-level magma ascent rates, with applications to Mt. Etna (Sicily, Italy). *Journal of Petrology*, *54*, 795–813.

Bédard, J. H. (2005). Partitioning coefficients between olivine and silicate melts. *Lithos*, *83*, 394–419.

Bédard, J. H. (2014). Parameterizations of calcic clinopyroxene – Melt trace element partition coefficients. *Geochemistry, Geophysics, Geosystems*, *15*, 303–336.

Bertagnini, A., Métrich, N., Landi, P., & Rosi, M. (2003). Stromboli volcano (Aeolian Archipelago, Italy): An open window on the deep-feeding system of a steady state basaltic volcano. *Journal of Geophysical Research: Solid Earth*, *108*.

Blundy, J. D., Falloon, T. J., Wood, B. J., & Dalton, J. A. (1995). Sodium partitioning between clinopyroxene and silicate melts. *Journal of Geophysical Research: Solid Earth*, *100*, 15501–15515.

Blundy, J. D., & Wood, B. J. (2003). Partitioning of trace elements between crystals and melts. *Earth and Planetary Science Letters*, *210*, 383–397.

Bragagni, A., Avanzinelli, R., Freymuth, H., & Francalanci, L. (2014). Recycling of crystal mush-derived melts and short magma residence times revealed by U-series disequilibria at Stromboli volcano. *Earth and Planetary Science Letters*, *404*, 206–219.

Brophy, J. G., Whittington, C. S., & Park, Y.-R. (1999). Sector-zoned augite megacrysts in Aleutian high alumina basalts: Implications for the conditions of basalt crystallization and the generation of calc-alkaline series magmas. *Contributions to Mineralogy and Petrology*, *135*, 277–290.

Casetta, F., Coltorti, M., Ickert, R. B., Bonadiman, C., Giacomoni, P. P., & Ntaflos, T. (2018). Intrusion of shoshonitic magmas at shallow crustal depth: T–P path, H_2O estimates, and AFC modeling of the Middle Triassic Predazzo Intrusive Complex (Southern Alps, Italy). *Contributions to Mineralogy and Petrology*, *173*, 57.

Costa, F., Dohmen, R., & Chakraborty, S. (2008). Time scales of magmatic processes from modeling the zoning patterns of crystals. *Reviews in Mineralogy and Geochemistry*, *69*, 545–594.

Crank, J. (1975). *The mathematics of diffusion*. Oxford Science Publications.

Del Bello, E., Mollo, S., Scarlato, P., von Quadt, A., Forni, F., & Bachmann, O. (2014). New petrological constraints on the last eruptive phase of the Sabatini Volcanic District (central Italy): Clues from mineralogy, geochemistry, and Sr–Nd isotopes. *Lithos*, *205*, 28–38. http://dx.doi.org/10.1016/j.lithos.2014.06.015.

Del Bello, E., Lane, S. J., James, M. R., Llewellin, E. W., Taddeucci, J., Scarlato, P., & Capponi, A. (2015). Viscous plugging can enhance and modulate explosivity of strombolian eruptions. *Earth and Planetary Science Letters*, *423*, 210–218.

Di Carlo, I., Pichavant, M., Rotolo, S. G., & Scaillet, B. (2006). Experimental crystallization of a high-K arc basalt: The golden pumice, Stromboli volcano (Italy). *Journal of Petrology*, *47*(7), 1317–1343.

Di Stefano, F., Mollo, S., Ubide, T., Petrone, C. M., Caulfield, J., Scarlato, P., Nazzari, M., Andronico, D., & Del Bello, E. (2020). Mush cannibalism and disruption recorded by clinopyroxene phenocrysts at Stromboli volcano: new insights from recent 2003-2017 activity. *Lithos*, *360–361*, 105440.

Di Traglia, F., Intrieri, E., Nolesini, T., Bardi, F., Del Ventisette, C., Ferrigno, F., Frangioni, S., Frodella, W., Gigli, G., Lotti, A., Tacconi Stefanelli, C., Tanteri, L., Leva, D., and Casagli, N. (2014) The ground-based InSAR monitoring system at Stromboli volcano: Linking changes in displacement rate and intensity of persistent volcanic activity. *Bulletin of volcanology*, *76*, 786.

Dimanov, A., & Sautter, V. (2000). “Average” interdiffusion of (Fe, Mn)-Mg in natural diopside. *European Journal of Mineralogy*, *12*(4), 749–760.

Downes, M. J. (1974). Sector and oscillatory zoning in calcic augites from M. Etna, Sicily. *Contributions to Mineralogy and Petrology*, *47*, 187–196.

Dowty, E. (1976). Absorption optics of low-symmetry crystals—application to Titanian clinopyroxene spectra. *Physics and Chemistry of Minerals*, *3*(2), 173–181.

Druitt, T. H., Costa, F., Deloule, E., Dungan, M., & Scaillet, B. (2012). Decadal to monthly timescales of magma transfer and reservoir growth at a caldera volcano. *Nature*, *482*(7383), 77.

Duncan, A. M., & Preston, R. M. F. (1980). Chemical variation of clinopyroxene phenocrysts from the trachybasaltic lavas of Mount Etna, Sicily. *Mineral Magazine*, *43*, 765–770.

Dunworth, E., Neumann, E. R., & Rosenbaum, J. (2001). The Skien lavas, Oslo Rift: Petrological disequilibrium and geochemical evolution. *Contributions to Mineralogy and Petrology*, *140*(6), 701–719.

Dygert, N., Liang, Y., Sun, C., & Hess, P. (2014). An experimental study of trace element partitioning between augite and Fe-rich basalts. *Geochimica et Cosmochimica Acta*, *132*, 170–186.

Ferguson, A. K. (1973). On hour-glass sector zoning in clinopyroxene. *Mineralogical Magazíne*, *39*(303), 321–325.

Forni, F., Degruyter, W., Bachmann, O., De Astis, G., & Mollo, S. (2018). Long-term magmatic evolution reveals the beginning of a new caldera cycle at Campi Flegrei. *Science Advances*, *4*(11), eaat9401. doi: 10.1126/sciadv.aat9401.

Forni, F., Bachmann, O., Mollo, S., De Astis, G., Gelman, S. E., & Ellis, B. S. (2016). The origin of a zoned ignimbrite: Insights into the Campanian Ignimbrite magma chamber (Campi Flegrei, Italy). *Earth and Planetary Science Letters*, *449*, 259–271. doi: http://dx.doi.org/10.1016/j.epsl.2016.06.003.

Francalanci, L., Braschi, E., Di Salvo, S., Lucchi, F., & Petrone, C. M. (2014). When magmas do not interact: Paired Roman-age activity revealed by tephra studies at Stromboli volcano. *Bulletin of Volcanology*, *76*, 884. https://doi.org/10.1007/s00445-014-0884-9.

Francalanci, L., Lucchi, F., Keller, J., De Astis, G., & Tranne, C. A. (2013). Eruptive, volcano-tectonic and magmatic history of the Stromboli volcano (north-eastern Aeolian archipelago). In: *Geological Society, London, Memoirs*, (Vol. 37, pp. 397–471, Chapter 13).

Francalanci, L., Avanzinelli, R., Nardini, I., Tiepolo, M., Davidson, J. P., & Vannucci, R. (2012). Crystal recycling in the steady-state system of the active Stromboli volcano: A 2.5-ka story inferred from in situ Sr-isotope and trace element data. *Contribution to Mineralogy and Petrology*, *163*, 109–131.

Francalanci, L., Tommasini, S., & Conticelli, S. (2004). The volcanic activity of Stromboli in the 1906–1998 A.D. period: Mineralogical, geochemical and isotope data rel-evant to the understanding of plumbing system. *Journal of Volcanology and Geothermal Research*, *131*, 179–211.

Francalanci, L., Tommasini, S., Conticelli, S., & Davies, G. R. (1999). Sr isotope evidence for short magma residence time for the 20th century activity at Stromboli volcano, Italy. *Earth and Planetary Science Letters*, *167*, 61–69.

France, L., Koepke, J., Ildefonse, B., Cichy, S. B., & Deschamps, F. (2010) Hydrous partial melting in the sheeted dike complex at fast spreading ridges: Experimental and natural observations. *Contributions to Mineralogy and Petrology*, *160*(5), 683–704.

Giacomoni, P. P., Coltorti, M., Bryce, J. G., Fahnestock, M. F., & Guitreau, M. (2016). Mt. Etna plumbing system revealed by combined textural, compositional, and thermobarometric studies in clinopyroxenes. *Contributions to Mineralogy and Petrology*, *171*, 34.

Giacomoni, P. P., Coltorti, M., Mollo, S., Ferlito, C., Braiato, M., & Scarlato, P. (2018). The 2011-2012 paroxysmal eruptions at Mt. Etna volcano: Insights on the vertically zoned plumbing system. *Journal of Volcanology and Geothermal Research*, *349*, 370–391.

Giuliani, L., Iezzi, G., & Mollo, S. (2020). Dynamics of volcanic systems: Physical and chemical models applied to equilibrium versus disequilibrium solidification of magmas. In F. Vetere, A. Fiege (Eds.), *Dynamic Magma Evolution*. Geophysical Monograph Series, Wiley.

Gualda, G. A., Ghiorso, M. S., Lemons, R. V., & Carley, T. L. (2012). Rhyolite-MELTS: A modified calibration of MELTS optimized for silica-rich, fluid-bearing magmatic systems. *Journal of Petrology*, *53*(5), 875–890.

Hair, J. F., Jr., Anderson, R. E., Tatham, R. L., & Black, W. C. (1995). *Multivariate Data Analysis* (3rd edn., 742 pp.). Macmillan, New York.

Harkins, E., & Hollister, L. S. (1977). Sector zoning of clinopyroxene from a weakly metamorphosed diabase. *American Mineralogist*, *62*(3–4), 390–394.

Hill, E., Blundy, J. D., and Wood, B. J. (2011). Clinopyroxene-melt trace element partitioning and the development of a predictive model for HFSE and Sc. *Contribution to Mineralogy and Petrology 161*, 423–438. http://dx.doi.org/10.1007/s00410-010-0540-0.

Hollister, L. S., & Gancarz, A. J. (1971). Conpositional sextorzoning in clinopyroxene from the narce area, Italy. *American Mineralogist: Journal of Earth and Planetary Materials*, *56*(5–6), 959–979.

Iezzi, G., Caso, C., Ventura, G., Vallefuoco, M., Cavallo, A., Behrens, H., et al. (2014a). First documented deep submarine explosive eruptions at the Marsili Seamount (Tyrrhenian Sea, Italy): A case of historical volcanism in the Mediterranean Sea. *Gondwana Research*, *25*, 764–775. http://dx.doi.org/10.1016/j.gr.2013.11.001.

Iezzi, G., Mollo, S., Shaini, E., Cavallo, A., & Scarlato, P. (2014b). The cooling kinetics of plagioclase revealed by electron microprobe mapping. *American Mineralogist*, *99*, 898–907. http://dx.doi.org/10.2138/am.2014.4626.

Iezzi, G., Mollo, S., & Ventura, G. (2009). Solidification behaviour of natural silicate melts and volcanological implications. In N. Lewis, A. Moretti, (Eds.), *Volcanoes: Formation, Eruptions and Modelling* (pp. 127–151). New York, Nova Science Publishers, 379 pp., ISBN: 978-1-61728-597-4.

Kent, A. J., Darr, C., Koleszar, A. M., Salisbury, M. J., & Cooper, K. M. (2010). Preferential eruption of andesitic magmas through recharge filtering. *Nature Geoscience*, *3*(9), 631.

Kouchi, A., Sugawara, Y., Kashima, K., & Sunagawa, I. (1983). Laboratory growth of sector zoned clinopyroxenes in the system $CaMgSi_2O_6$-$CaTiAl_2O_6$. *Contributions to Mineralogy and Petrology*, *83*(1–2), 177–184.

Kushiro, I., & Walter, M. J. (1998). Mg-Fe partitioning between olivine and mafic-ultramafic melts. *Geophysical Research Letters*, *25*(13), 2337–2340.

Landi, P., Métrich, N., Bertagnini, A., & Rosi, M. (2004). Dynamics of magma mixing and degassing recorded in plagioclase at Stromboli (Aeolian Archipelago, Italy). *Contributions to Mineralogy and Petrology*, *147*(2), 213–227.

Landi, P., Corsaro, R. A., Francalanci, L., Civetta, L., Miraglia, L., Pompilio, M., & Tesoro, R. (2009). Magma dynamics during the 2007 Stromboli eruption (Aeolian Islands, Italy): Mineralogical, geochemical and isotopic data. *Journal of Volcanology and Geothermal Research*, *182*(3), 255–268.

Lanzafame, G., Iezzi, G., Mancini, L., Lezzi, F., Mollo, S., & Ferlito, C. (2017). Solidification and Turbulence (Non-laminar) during Magma Ascent: Insights from 2D and 3D analyses of bubbles and minerals in an Etnean Dyke. *Journal of Petrology*, *58*, 1511–1533. https://doi.org/10.1093/petrology/egx063.

Lanzafame, G., Mollo S., Iezzi, G., Ferlito, C., & Ventura, G. (2013). Unraveling the solidification path of a pahoehoe "cicirara" lava from Mount Etna volcano. *Bulletin of Volcanology*, *75*, 703–719, 10.1007/s00445-013-0703-8.

Le Bas, M., Le Maitre, R., Streckeisen, A., Zanettin, B., & IUGS Subcommission on the Systematics of Igneous Rocks. (1986). A chemical classification of volcanic rocks based on the total alkali-silica diagram. *Journal of Petrology*, *27*(3), 745–750.

Leung, I. S. (1974). Sector-zoned titanaugites: Morphology, crystal chemistry, and growth. *American Mineralogist: Journal of Earth and Planetary Materials*, *59*(1–2), 127–138.

Liang, Y., Sun, C., and Yao, L. (2013). A REE-in-two-pyroxene thermometer for mafic and ultramafic rocks. *Geochimica et Cosmochimica Acta*, *102*, 246–260.

Liang, Y. (2015). A simple model for closure temperature of a trace element in cooling bi-mineralic systems. *Geochimica et Cosmochimica Acta*, *165*, 35–43.

Lindsley, D. H. (1980). Phase equilibria of pyroxenes at pressures >1 atmosphere. In C. T. Prewitt (Ed.), *Pyroxenes (Reviews of Mineralogy)* (Vol. 7, pp. 289–308). Mineralogical Society of America, Washington DC.

Lucchi, F., Santo, A. P., Tranne, C. A., Peccerillo, A., & Keller, J. (2013). Volcanism, magmatism, volcano-tectonics and sea-level fluctuations in the geological history of Filicudi (western Aeolian archipelago). *Geological Society, London, Memoirs*, *37*(1), 113–153. *Geology*, *211*, 185–215. http://dx.doi.org/10.1016/j.chemgeo.2004.06.032.

Masotta, M., Mollo, S., Nazzari, M., Tecchiato, V., Scarlato, P., Papale, P., & Bachmann, O. (2018). Crystallization and partial melting of rhyolite and felsite rocks at Krafla volcano: A comparative approach based on mineral and glass chemistry of natural and experimental products. *Chemical Geology*, *483*, 603–618. https://doi.org/10.1016/j.chemgeo.2018.03.031.

Masotta, M., Mollo, S., Freda, C., Gaeta, M., & Moore, G. (2013). Clinopyroxene–liquid thermometers and barometers specific to alkaline differentiated magmas. *Contributions to Mineralogy and Petrology*, *166*, 1545–1561. doi: 10.1007/s00410-013-0927-9.

Métrich, N., Bertagnini, A., & Di Muro, A. (2010). Conditions of magma storage, degassing and ascent at Stromboli: New insights into the volcano plumbing system with inferences on the eruptive dynamics. *Journal of Petrology*, *51*, 603–626.

Métrich, N., & Rutherford, M. J. (1998). Low pressure crystallization paths of H_2O-saturated basaltic–hawaiitic melts from Mt Etna: Implications for open-system degassing of basaltic volcanoes. *Geochimica et Cosmochimica Acta*, *62*, 1195–1205.

Mollo, S., Blundy, J., Scarlato, P., Vetere, F., Holtz, F, Bachmann, O., & Gaeta, M. (2020). A review of the lattice strain and electrostatic effects on trace element partitioning between clinopyroxene and melt: Applications to magmatic systems saturated with Tschermak-rich clinopyroxenes. *Earth-Science Reviews*, *210*, 103351. https://doi.org/10.1016/j.earscirev.2020.103351.

Mollo, S., & Hammer, J. E. (2017). Dynamic crystallization in magmas. In W. Heinrich, R. Abart (Eds.), *Mineral reaction kinetics: Microstructures, textures, chemical and isotopic signatures*. *EMU Notes in Mineralogy*, Vol. 16 (2016), Chapter 7, 1–46. Published by the European Mineralogical Union and the Mineralogical Society of Great Britain & Ireland. Doi: 10.1180/EMU-notes.16.12.

Mollo, S., & Masotta, M. (2014). Optimizing pre-eruptive temperature estimates in thermally and chemically zoned magma chambers. *Chemical Geology*, *368*, 97–103. 10.1016/j.chemgeo.2014.01.007.

Mollo, S., Blundy, J. D., Scarlato, P., De Cristofaro, S. P., Tecchiato, V., Di Stefano, F., et al. (2018). An integrated P-T-H_2O-lattice strain model to quantify the role of clinopyroxene fractionation on REE+Y and HFSE patterns of mafic alkaline magmas: Application to eruptions at Mt. Etna. *Earth-Science Reviews*, *185*, 32–56. https://doi.org/10.1016/j.earscirev.2018.05.014.

Mollo, S., Blundy, J. D., Giacomoni, P., Nazzari, M., Scarlato, P., Coltorti, M., et al. (2017). Clinopyroxene-melt element partitioning during interaction between trachybasaltic magma and siliceous crust: Clues from quartzite enclaves at Mt. Etna volcano. *Lithos*, *284–285*, 447–461. https://doi.org/10.1016/j.lithos.2017.05.003.

Mollo, S., Forni, F., Bachmann, O., Blundy, J. D., De Astis, G., & Scarlato, P. (2016). Trace element partitioning between clinopyroxene and trachy-phonolitic melts: A case study from the Campanian ignimbrite (Campi Flegrei, Italy). *Lithos*, *252–253*, 160–172. doi:10.1016/j.lithos.2016.02.024.

Mollo, S., Giacomoni, P. P., Andronico, D., & Scarlato, P. (2015a). Clinopyroxene and titanomagnetite cation redistributions at Mt. Etna volcano (Sicily, Italy): Footprints of the final solidification history of lava fountains and lava flows. *Chemical Geology*, *406*, 45–54. http://dx.doi.org/10.1016/j.chemgeo.2015.04.017.

Mollo, S., Masotta, M., Forni, F., Bachmann, O., De Astis, G., Moore, G., & Scarlato, P. (2015b). A K-feldspar-liquid hygrometer specific to alkaline differentiated magmas. *Chemical Geology*, *392*, 1–8, 10.1016/j.chemgeo.2014.11.010.

Mollo, S., Putirka, K. D., Misiti, V., Soligo, M., & Scarlato, P. (2013a). A new test for equilibrium based on clinopyroxene-melt pairs: Clues on the solidification temperatures of Etnean alkaline melts at post-eruptive conditions. *Chemical Geology*, *352*, 92–100, doi: 10.1016/j.chemgeo.2013.05.026.

Mollo, S., Blundy, J. D., Scarlato, P., Iezzi, G., & Langone, A. (2013b). The partitioning of trace elements between clinopyroxene and trachybasaltic melt during rapid cooling and crystal growth. *Contributions to Mineralogy and Petrology*, *166*, 1633–1654, doi: 10.1007/s00410-013-0946-6.

Mollo, S., Lanzafame, G., Masotta, M., Iezzi, G., Ferlito, C., & Scarlato, P. (2011). Cooling history of a dike as revealed by mineral chemistry: A case study from Mt. Etna volcano. *Chemical Geology*, *283*, 261–273. doi:10.1016/j.chemgeo.2011.06.016.

Mollo, S., Del Gaudio, P., Ventura, G., Iezzi, G., & Scarlato, P. (2010). Dependence of clinopyroxene composition on cooling rate in basaltic magmas: Implications for thermobarometry. *Lithos*, *118*, 302–312. doi:10.1016/j.lithos.2010.05.006.

Morgan, D. J., Blake, S., Rogers, N. W., DeVivo, B., Rolandi, G., Macdonald, R., & Hawkesworth, C. J. (2004). Time scales of crystal residence and magma chamber volume from modelling of diffusion profiles in phenocrysts: Vesuvius 1944. *Earth and Planetary Science Letters*, *222*(3–4), 933–946.

Nakamura, Y. (1973). Origin of sector-zoning of igneous clinopyroxenes. *American Mineralogist: Journal of Earth and Planetary Materials*, *58*(11–12), 986–990.

Neave, D. A., & Putirka, K. D. (2017). A new clinopyroxene-liquid barometer, and implications for magma storage pressures under Icelandic rift zones. *American Mineralogist*, *102*(4), 777–794.

Nielsen, R. L., & Dungan, M. A. (1983). Low pressure mineral-melt equilibria in natural anhydrous mafic systems. *Contributions to Mineralogy and Petrology*, *84*(4), 310–326.

Nimis, P., & Taylor, W. R. (2000). Single clinopyroxene thermobarometry for garnet peridotites. Part I. Calibration and testing of a Cr-in-Cpx barometer and an enstatite-in-Cpx thermometer. *Contributions to Mineralogy and Petrology*, *139*(5), 541–554.

Nishizawa, J. I., Terasaki, T., & Shimbo, M. (1972). Layer growth in silicon epitaxy. *Journal of Crystal Growth*, *13*, 297–301.

Peccerillo, A., & Taylor, S. R. (1976). Geochemistry of Eocene calc-alkaline volcanic rocks from the Kastamonu area, northern Turkey. *Contributions to Mineralogy and Petrology*, *58*(1), 63–81.

Perinelli, C., Mollo, S., Gaeta, M., De Cristofaro, S. P., Palladino, D. M., Armienti, P., et al. (2016) An improved clinopyroxene-based hygrometer for Etnean magmas and implications for eruption triggering mechanisms. *American Mineralogist*, *101*(12), 2774–2777.

Petrone, C. M., Braschi, E., Francalanci, L., Casalini, M., & Tommasini, S. (2018). Rapid mixing and short storage timescale in the magma dynamics of a steady-state volcano. *Earth and Planetary Science Letters*, *492*, 206–221.

Petrone, C. M., Bugatti, G., Braschi, E., & Tommasini, S. (2016). Pre-eruptive magmatic processes re-timed using a non-isothermal approach to magma chamber dynamics. *Nature Communications*, *7*, 12946.

Pichavant, M., Di Carlo, I., Le Gac, Y., Rotolo, S. G., & Scaillet, B. (2009). Experimental constraints on the deep magma feeding system at Stromboli volcano, Italy. *Journal of Petrology*, *50*(4), 601–624.

Putirka, K. D. (2016). Rates and styles of planetary cooling on Earth, Moon, Mars, and Vesta, using new models for oxygen fugacity, ferric-ferrous ratios, olivine-liquid Fe-Mg exchange, and mantle potential temperature. *American Mineralogist*, *101*, 819–840. https://doi.org/10.2138/am-2016-5402.

Putirka, K. D. (2008). Thermometers and barometers for volcanic systems. *Reviews in Mineralogy and Geochemistry*, *69*(1), 61–120.

Putirka, K. D. (1999). Clinopyroxene+liquid equilibria to 100 kbar and 2450 K. *Contribution to Mineralogy and Petrology*, *135*, 151–163. http://dx.doi.org/10.1007/s004100050503.

Putirka, K. D., Mikaelian, H., Ryerson, F., & Shaw, H. (2003). New clinopyroxene-liquid thermobarometers for mafic, evolved, and volatile-bearing lava compositions, with applications to lavas from Tibet and the Snake River Plain, Idaho. *American Mineralogist*, *88*(10), 1542–1554.

Putirka, K., Johnson, M., Kinzler, R., Longhi, J., & Walker, D. (1996). Thermobarometry of mafic igneous rocks based on clinopyroxene-liquid equilibria, 0–30 kbar. *Contributions to Mineralogy and Petrology*, *123*(1), 92–108.

Rosi, M., Pistolesi, M., Bertagnini, A., Landi, P., Pompilio, M., & Di Roberto, A. (2013). Stromboli volcano, Aeolian Islands (Italy): Present eruptive activity and hazards. *Geological Society, London, Memoirs*, *37*(1), 473–490.

Scarlato, P., Mollo, S., Del Bello, E., von Quadt, A., Richard, J. B., Gutierrez, E., et al. (2017). The 2013 eruption of Chaparrastique volcano (El Salvador): Effects of magma storage, mixing, and decompression. *Chemical Geology*, *448*, 110–122. http://dx.doi.org/10.1016/j.chemgeo.2016.11.015.

Shimizu, N. (1981). Trace element incorporation into growing augite phenocryst. *Nature*, *289*, 575–577.

Skulski, T., Minarik, W., & Watson, E. B. (1994). High-pressure experimental trace-element partitioning between clinopyroxene and basaltic melts. *Chemical Geology*, *117*(1–4), 127–147.

Sun, C., & Liang, Y. (2017). A REE-in-plagioclase–clinopyroxene thermometer for crustal rocks. *Contributions to Mineralogy and Petrology*, *172*(4), 24.

Sun, C., & Liang, Y. (2012). Distribution of REE between clinopyroxene and basaltic melt along a mantle adiabat: Effects of major element composition, water, and temperature. *Contributions to Mineralogy and Petrology*, *163*(5), 807–823.

Tecchiato, V., Gaeta, M., Mollo, S., Bachmann, O., von Quadt, A., & Scarlato, P. (2018). Snapshots of primitive arc magma evolution recorded by clinopyroxene textural and compositional variations: The case of hybrid crystal-rich enclaves from Capo Marargiu Volcanic District (Sardinia, Italy). *American Mineralogist*, *103*, 899–910. https://doi.org/10.2138/am-2018-6446.

Ubide, T., & Kamber, B. S. (2018). Volcanic crystals as time capsules of eruption history. *Nature Communications*, *9*(1), 326.

Ubide, T., Mollo, S., Zhao, J.-X., Nazzari, M., & Scarlato, P. (2019). Sector-zoned clinopyroxene as a recorder of magma history, eruption triggers, and ascent rates. *Geochimica et Cosmochimica Acta*, *251*, 265–283.

Ubide, T., Caulfield, J., Brandt, C., Bussweiler, Y., Mollo, S., Di Stefano, F., Nazzari, M., & Scarlato, P. (2019). Deep Magma Storage revealed by Multi-Method Elemental Mapping of Clinopyroxene Megacrysts at Stromboli Volcano. *Frontiers in Earth Science*, *7*:239.

Wass, S. Y. (1973). The origin and petrogenetic significance of hour-glass zoning in titaniferous clinopyroxenes. *Mineral Magazine*, *39*(302), 133–144.

Watson, E. B., & Liang, Y. (1995). A simple model for sector zoning in slowly grown crystals: Implications for growth rate and lattice diffusion, with emphasis on accessory minerals in crustal rocks. *American Mineralogist*, *80*(11–12), 1179–1187.

Wood, B. J., & Blundy, J. D. (2002). The effect of H_2O on crystal-melt partitioning of trace elements. *Geochimica et Cosmochimica Acta*, *66*(20), 3647–3656.

Wood, B. J., & Blundy, J. D. (2001). The effect of cation charge on crystal–melt partitioning of trace elements. *Earth and Planetary Science Letters*, *188*(1–2), 59–71.

Wood, B. J., & Blundy, J. D. (1997). A predictive model for rare earth element partitioning between clinopyroxene and anhydrous silicate melt. *Contributions to Mineralogy and Petrology*, *129*(2–3), 166–181.

10

Insights Into Processes and Timescales of Magma Storage and Ascent From Textural and Geochemical Investigations: Case Studies From High-Risk Neapolitan Volcanoes (Italy)

Lucia Pappalardo[1] and Gianmarco Buono[1,2]

ABSTRACT

The mechanisms and timescales of magmatic evolution during storage in crustal reservoirs and ascent in the volcanic conduit exert an important control on both the evolution of precursory phenomena recorded during volcanic crises as well as the style and intensity of the impending eruption. Improving our knowledge on this topic is therefore of paramount importance for better assessment of hazard for active high-risk volcanoes. The densely populated Neapolitan volcanic area (Italy) is one of the places most at risk of volcanic disaster in Europe. To reconstruct the magma plumbing system and its evolution toward critical conditions close to eruption, we employed petrological data on past eruptive products representative of the entire volcanic history. Our results are consistent with the possible existence of a long-term magmatic sill-shaped storage zone beneath the whole Neapolitan volcanic area, with its maximum volume under the Campi Flegrei supervolcano, where the largest eruptions occurred in the last 40 ka. Moreover, slow magma transfer, an open degassing regime, and stasis at a shallow level (ephemeral storage zones) characterize magma ascent during small-scale events, whereas fast magma rise and a continuous closed degassing mechanism drive violent large-scale eruptions. These distinctive dynamics could imply different time-depth patterns of precursory unrest.

10.1. INTRODUCTION

The size and frequency of volcanic eruptions mostly depend on the mechanisms and timescales of magmatic evolution during storage in crustal reservoirs as well as on ascent in the volcanic conduit.

In recent decades, the great development of geophysical exploration techniques, such as seismic tomography, allowed the detection of partially melted horizons within the crust, whereas advanced monitoring networks provided warnings of variations in volcano dynamics at depth (e.g., Roman & Cashman, 2019); however, a further crucial step is the consistent interpretation of geophysical events and geochemical signals in terms of magma transfer from reservoirs toward the surface and its influence on the eruptive style.

A powerful tool to investigate the evolution of magma plumbing systems at active volcanoes is the study of petrological (textural and geochemical) features of natural volcanic rocks representative of the entire volcano history. In particular, the obtained information on the depth, shape, and chemico-physical conditions of the volcano magma supply systems is essential for forecasting the future behavior of high-risk volcanoes. Moreover, these studies, applied to the products of recent well-monitored eruptions, have revealed crucial relationships between the petrology of emitted rocks and the pre-/syn-eruptive geophysical signals (e.g., Cashman & McConnell, 2005;

---

[1] *Istituto Nazionale di Geofisica e Vulcanologia, Sezione di Napoli-Osservatorio Vesuviano, Naples, Italy*

[2] *Dipartimento di Scienze della Terra, dell'Ambiente e delle Risorse, Università degli Studi di Napoli Federico II, Naples, Italy*

Crustal Magmatic System Evolution: Anatomy, Architecture, and Physico-Chemical Processes, Geophysical Monograph 264, First Edition.
Edited by Matteo Masotta, Christoph Beier, and Silvio Mollo.

DOI: 10.1002/9781119564485.ch10

Hammer et al., 1999; Pappalardo et al., 2014; Preece et al., 2013; Saunders et al., 2012).

In this chapter, we select as a case study the Campi Flegrei caldera and Somma-Vesuvius volcanic complex, situated in the densely populated Naples metropolitan area (Italy), one of the places most at risk of natural disaster in Europe. Combining new and previous evaluations of available petrological data, we reconstruct the conditions of magma chambers and volcanic conduits prior to and during eruptions, to obtain new constraints on the possible state of the current plumbing system and on its possible evolution toward critical state.

In the Neapolitan area, geophysical anomalies as well as petrological evidence indicate the presence of a laterally extensive magma source beneath the Campi Flegrei volcanic district and the Somma-Vesuvius volcano. However, the conditions leading to magma chamber opening, conduit propagation, and eruption remain poorly constrained and debated in the recent literature (e.g., Chiodini et al., 2016; Di Vito et al., 2016; Kilburn et al., 2017; Liedl et al., 2019; Lima et al., 2009; Vanorio & Kanitpanyacharoen, 2015). This knowledge is crucial for improving prediction of future eruptive activity, and thus, it is essential for the mitigation of volcanic risk in the densely urbanized metropolitan area of Naples.

10.2. VOLCANOLOGICAL BACKGROUND OF NEAPOLITAN AREA

The Naples metropolitan area is situated between two active volcanoes: the Campi Flegrei (CF) volcanic district, including also the volcanic islands of Ischia and Procida-Vivara, to the west and the Somma-Vesuvius stratovolcano (SV) to the east (Figure 10.1).

The volcanism in this area started about 1.5 Ma with a widespread effusive activity characterized by calc-alkaline andesitic and basaltic compositions as revealed by geothermal boreholes drilled NW of the Campi Flegrei caldera (Barbieri et al., 1979). Subsequently, from about 300 ka, new volcanic activity, fed by alkaline magmas, has generated the CF and SV volcanic complexes (Figure 10.2).

The substructure of these two volcanoes has been investigated through several geophysical surveys (e.g., De Natale et al., 2006a, 2006b, and references therein). Geophysical data, constrained by deep boreholes (Brocchini et al., 2001; Di Renzo et al., 2007; Rosi & Sbrana, 1987), showed that the deep structure of this volcanic area comprises 1.5–3 km of interbedded lavas and volcanoclastic, marine, and fluvial sedimentary rocks of the Pleistocene age. These sequences overlie the Mesozoic carbonate sequences that extend from 2–4 to roughly 8–11 km depth (Berrino et al., 1998, 2008; Improta & Corciulo, 2006) on the Ercinian crystalline basement. The Moho discontinuity occurs at about 30 and 25 km depth beneath SV and CF, respectively (e.g., De Natale et al., 2006b; Nunziata, 2010); whereas a low-velocity layer, interpreted as the top of a magmatic body, was detected by seismic tomography at 7–8 km depth beneath the Campi Flegrei caldera and the neighboring Vesuvius volcano (Auger et al., 2001; Zollo et al., 2008).

The CF caldera produced at least six large-scale explosive eruptions in the last 250 ka (e.g., Albert et al., 2019; De Vivo et al., 2001) at intervals of 20,000–60,000 years. The largest of these events are the two large ignimbrite eruptions of the Campanian Ignimbrite (CI, 300 km^3 DRE, 40 ka, Gebauer et al., 2014) and the Neapolitan Yellow Tuff (40 km^3, 14.9 ka, Deino et al., 2004) that caused the collapse of the 12-km-wide Campi Flegrei caldera. In the last 15 ka, this nested collapse structure was the site of a monogenetic volcanic activity producing about 70 eruptions (with variable Volcanic Explosivity Index, VEI, spanning from 0 to 5), until the last Monte Nuovo event (VEI 2) occurred in 1538 AD. After a long period of subsidence following this last event, the caldera showed signs of potential reactivation characterized by episodes of ground uplift, shallow seismicity, significant increase in hydrothermal degassing, and changes in fluid-geochemistry. A first inversion of the subsidence occurred between 1950 and 1953 (0.5 m of uplift), followed by the two main bradyseismic crises of 1970–1972 and 1982–1984 (1.7 and 1.8 m of uplift, respectively), which led to a total elevation of the ground of about 3.5 m in the central sector of the caldera. An ongoing unrest phase started in 2005, prompted the Civil Protection to move the Campi Flegrei volcano from the base level (green) to the warning (yellow) alert level since the end of 2012.

The volcanic activity of SV was, on the contrary, mostly polygenetic and characterized by the shift from a quiescent (closed-conduit) state, generally interrupted by large-explosive eruptions (at least tens of VEI 4 or 5 eruptions staggered with minor events occurred in the last 22 ka), to open-conduit periods producing mixed effusive/low-explosivity events. The latest of these periods started after the sub-Plinian 1631 eruption and lasted ca. 300 years until the last eruption on March 1944. Since that time, the volcano has entered a new state of closed-conduit repose, with very modest fumarolic activity, low-magnitude seismicity, and rare earthquakes swarms. The volcano is at its base level of alert (green) due to the absence of variation in monitored parameters.

10.3. MAGMA EVOLUTION IN CRUSTAL RESERVOIRS

Deciphering the mechanisms and timescales of the generation of magmas rich in silica and volatile constituents, which in turn drive the style and frequency of the eruptions, remains a major challenge for igneous petrology. In the last few decades, ideas on the architecture and

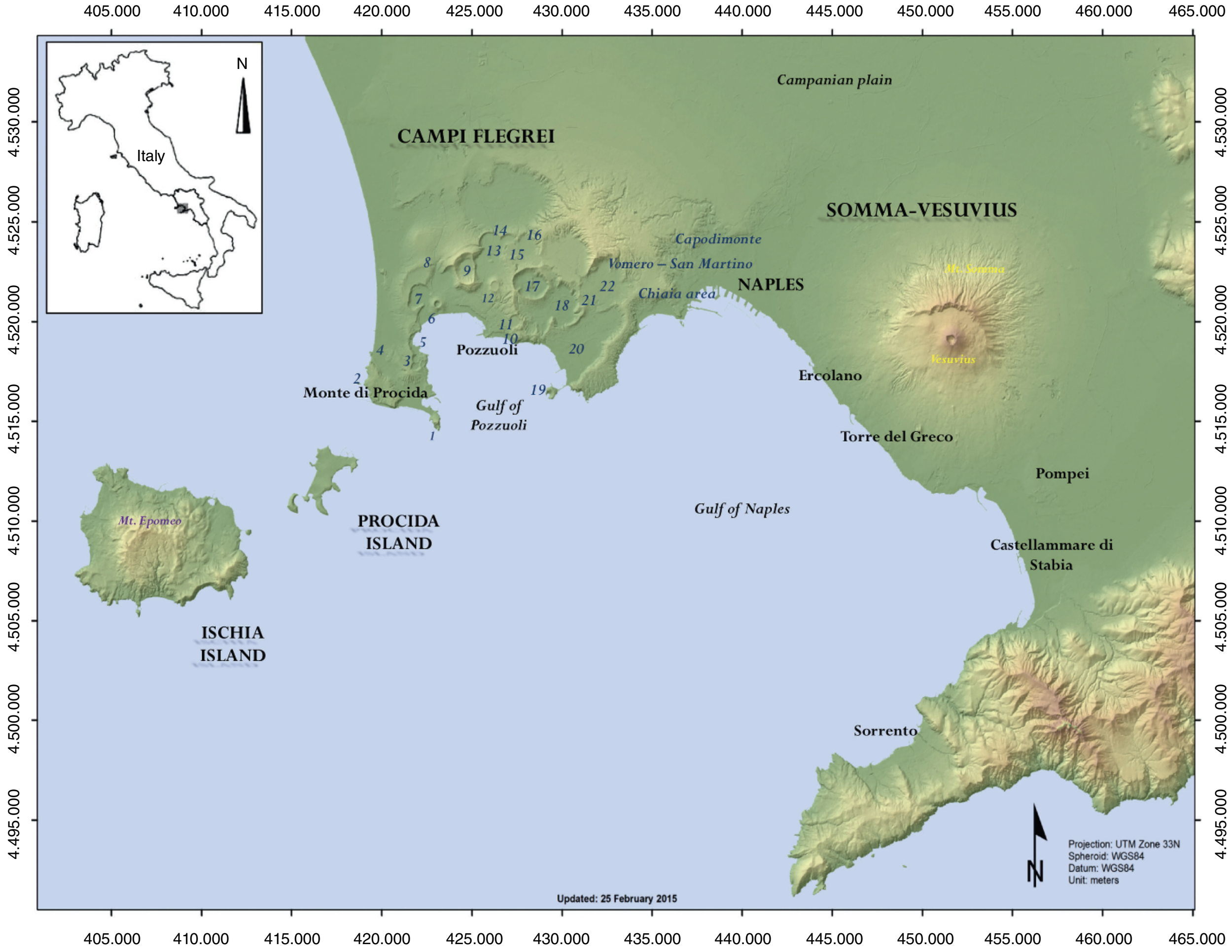

Figure 10.1 The Neapolitan volcanic area (Campi Flegrei district and Somma-Vesuvius complex). Numbers refer to some of the well-preserved craters in CF: (1) Capo Miseno, (2) Acqua Morta, (3) Fondi di Baia, (4) Torregaveta, (5) Baia, (6) Mt. Nuovo, (7) Averno, (8) Fondo Riccio, (9) Gauro, (10) Accademia, (11) Solfatara, (12) Cigliano, (13) S. Martino, (14) Montagna Spaccata, (15) Fossa Lupara, (16) Pisani, (17) Astroni, (18) Agnano, (19) Nisida, (20) S. Teresa, (21) Mt. S. Angelo, (22) Minopoli. Source: LGT INGV OV (2015). © 2015, Vesuvian Observatory - National Institute of Geophysics and Volcanology.

evolution of magmatic systems were profoundly modified, partly due to the significant progresses in analytical techniques as well as geophysical exploration methods (e.g., Marsh 1989, 2015). Several hypotheses have been advocated during time: (a) settling of crystals was shown to play a significant role in the generation of continuous chemical zoning (Bowen, 1928); (b) convective fractionation at the chamber walls in a crystallizing double-diffusive boundary layer (e.g., McBirney et al., 1985; Spera et al., 1995) was proposed to explain the decrease in liquid density at the top of magma chambers; (c) extraction of silicic melts from a crystal-rich mush derived by the in situ crystallization of parental liquid was suggested to justify the abrupt chemico-physical gap observed in some volcanic series (e.g., Brophy, 1991; Hildreth & Wilson, 2007; Marsh, 2002); (d) periodic rejuvenation of previously intruded high-crystallinity (>50% crystals) magma bodies, possibly subject to rapid heating and remobilization (Andersen et al., 2017; Cooper & Kent, 2014); hypothesis (d) could explain the lack of geophysical evidence of extended magma-rich portions in the current upper crust beneath some volcanic systems in the world (e.g., Bachmann & Bergantz, 2003, 2004, 2008a , 2008b, 2008c); (e) incremental assembly of magmatic bodies (e.g., Annen, 2009; Gelman et al., 2013) has been proposed to maintain magma reservoirs in a mush state for long periods (several hundreds of thousands of years). A most recent view considers the development of magma reservoirs by stacking of sill-like magma intrusions that correspond to crustal heterogeneities (e.g., density, rigidity and/or rheology contrasts; stress concentration); the progression of this mechanism could lead to the formation of a large layered intrusion complex in the crust (e.g., Bachmann & Huber, 2016; Cashman & Giordano, 2014;

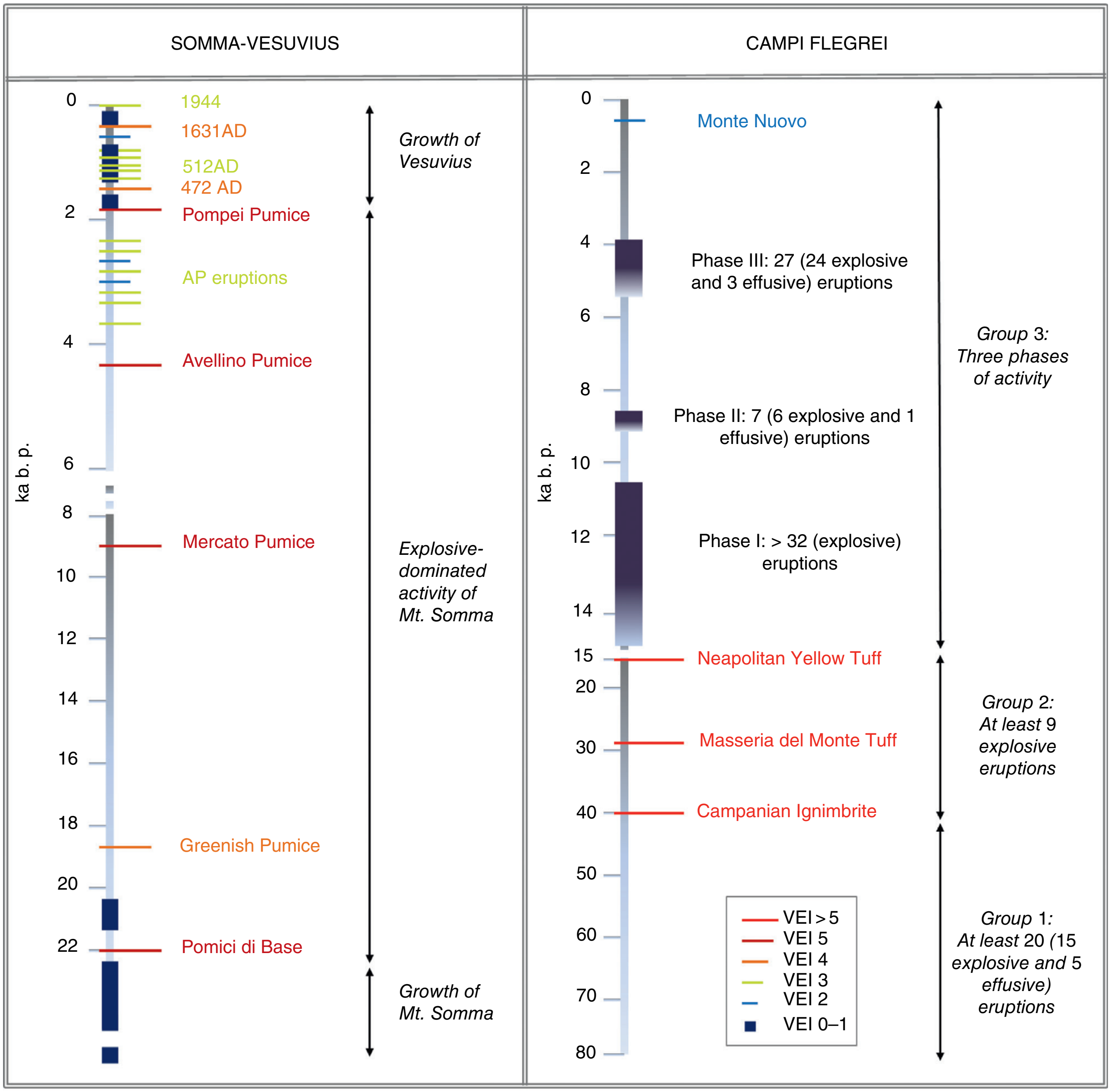

Figure 10.2 Schematic chronograms of volcanic activity as recorded by stratigraphic successions.

Edmonds et al., 2019; Holness et al., 2019; Sparks et al., 2019). In fact, geophysical data have recently shown fast sill propagation before eruptive events in different geodynamic contexts (e.g., Rubin et al., 1998; Sigmundsson et al., 2015) as well as the presence of a large sill containing a significant amount of melt beneath active calderas (e.g., Somma-Vesuvius volcano, Auger et al., 2001; Campi Flegrei caldera, Fedi et al., 2018; Nunziata, 2010; Zollo et al., 2008; Toba caldera, Jaxybulatov et al., 2014; Long Valley caldera, Flinders et al., 2018).

A variety of different approaches (e.g., zircon dating of silicic plutons and volcanic rocks, crystal size distributions theory, diffusion modeling of chemical gradients in minerals) have yielded timescales for magmatic processes on the order of 10^1–10^6 years depending on the evolution mechanism as well as the size and shape of the system (e.g., Annen & Zellmer, 2008; Cooper, 2019; Cooper & Kent, 2014; Hawkesworth et al., 2000, 2004; Morgan & Blake, 2006; Turner et al., 2000; Zellmer et al., 2005). This apparent discrepancy in age determination actually mirrors the difference between the radiometrically determined absolute ages of crystals and the time interval that the crystals spend at high temperature, recorded by diffusion and crystal growth (e.g., Till et al., 2015).

10.3.1. Magma Storage Processes and Timescales for Neapolitan Volcanoes

The volcanic products emitted from Neapolitan volcanoes belong to the potassic series of Central-Southern Italy Province. Slightly silica-undersaturated rocks, ranging in composition from trachybasalt to trachyphonolite, were erupted throughout the whole history of Campi Flegrei volcanic district as well as at Somma-Vesuvius from 25 to 9 ka. Moderately to strongly undersaturated rocks, from leucite-bearing foidites to phonotephrites to phonolites, were erupted at SV between 9 ka and 79 AD and after 79 AD, respectively (Figure 10.3).

The magmatic system architecture of the Neapolitan volcanoes has been explored by petrological studies on products from past eruptions representative of the whole volcanic history (e.g., Di Renzo et al., 2007; Forni et al., 2018; Pappalardo & Mastrolorenzo, 2010, 2012; Pappalardo et al., 2002, 2004, 2008; Santacroce et al., 2008; Stock et al., 2018).

The MELTS (Ghiorso & Sack, 1995) thermodynamic approach (e.g., CF: Fowler et al., 2007; Pappalardo et al., 2008; SV: Pappalardo & Mastrolorenzo, 2010), geothermobarometry (e.g., CF: Forni et al., 2018; Masotta et al., 2013; Mollo & Masotta, 2014; SV: Balcone-Boissard et al., 2016) as well as phase-equilibrium experiments (e.g., CF: Fabbrizio & Carroll, 2008; SV: Dolfi & Trigila, 1978; Pichavant et al., 2014; Scaillet et al., 2008) were used to estimate temperature, pressure, and volatile content conditions during the crystallization of mafic and sialic melts (Table 10.1).

Generally, volatile content measured in melt inclusions is a key tool used to provide information on initial volatile content and crystal equilibration pressure during

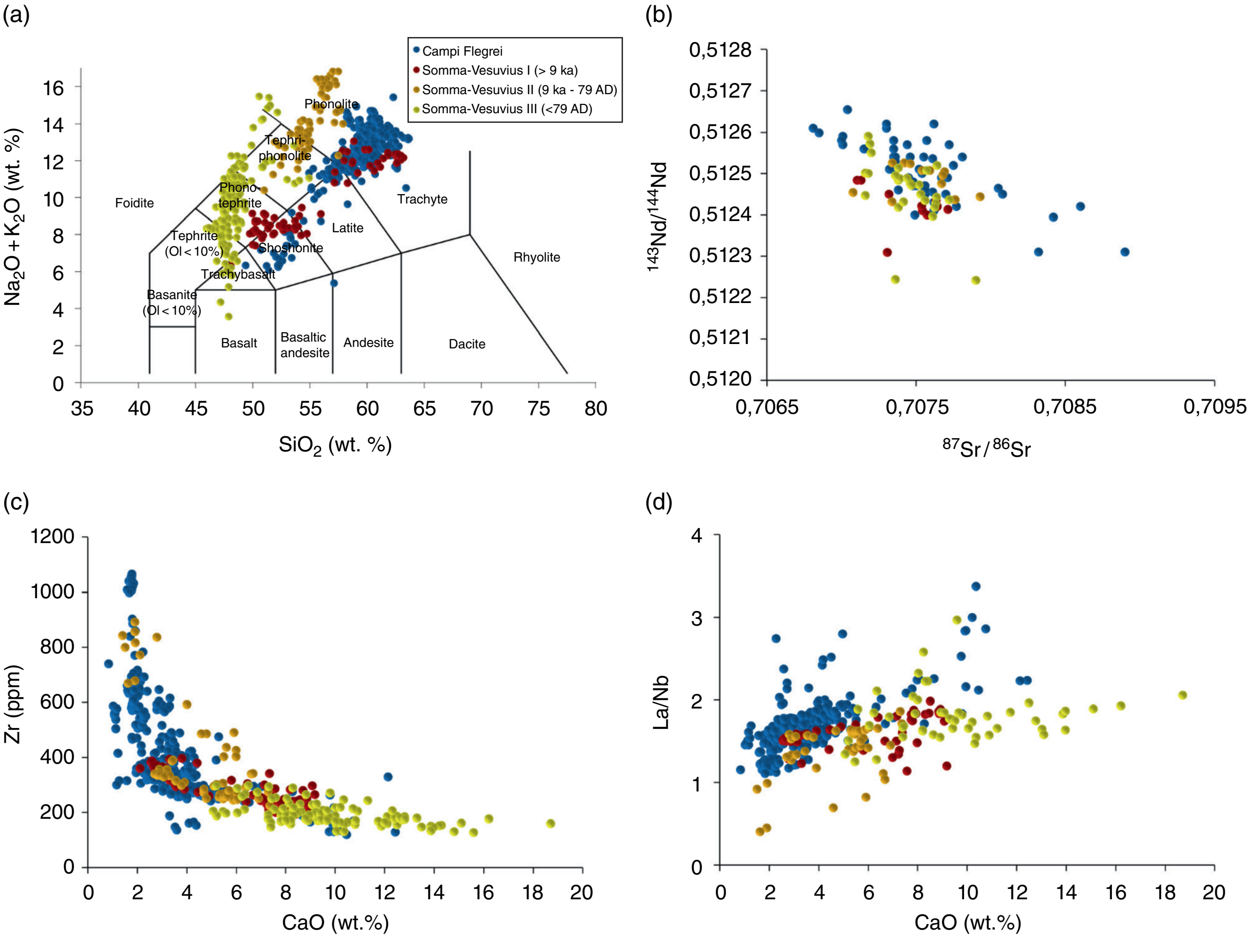

Figure 10.3 (A) Plot of total alkalis versus silica (TAS), (B) Sr and Nd isotopic ratios, (C) and (D) examples of variation diagrams of Campi Flegrei and Somma-Vesuvius volcanic bulk rocks. Data from: Peccerillo (2017) and references therein. Source: Data from Peccerillo (2017).

magma storage, when post-entrapment modification can be excluded. In addition, the inclusion-bearing crystals can have a wide range of origins and ages, further complicating the interpretation of magmatic processes (Ruth et al., 2018). Data summarized in Figure 10.4 demonstrate that in many studied cases melt inclusions entrapped in phenocrysts of Campi Flegrei and Somma-Vesuvius samples (CF: Arienzo et al., 2010; Cannatelli et al., 2007; Esposito et al., 2018; Fourmentraux et al., 2012; Lima et al., 2017; Mangiacapra et al., 2008; Marianelli et al., 2006; Signorelli & Carroll, 2002; SV: Balcone-Boissard et al., 2008, 2012, 2016; Lima et al., 2003; Marianelli et al., 1999, 2005; Webster & De Vivo, 2002) have similar volatile contents to the corresponding degassed matrix glasses. This suggests that melt inclusions volatile content does not univocally record pre-eruptive storage depth (horizontal trends characterized by constant values of Cl buffered concentration, despite a strong variation in CaO content) but can follow syn-eruption degassing paths (vertical trends with a variation in Cl content following pressure decrement versus constant values of CaO concentration) (Figure 10.4).

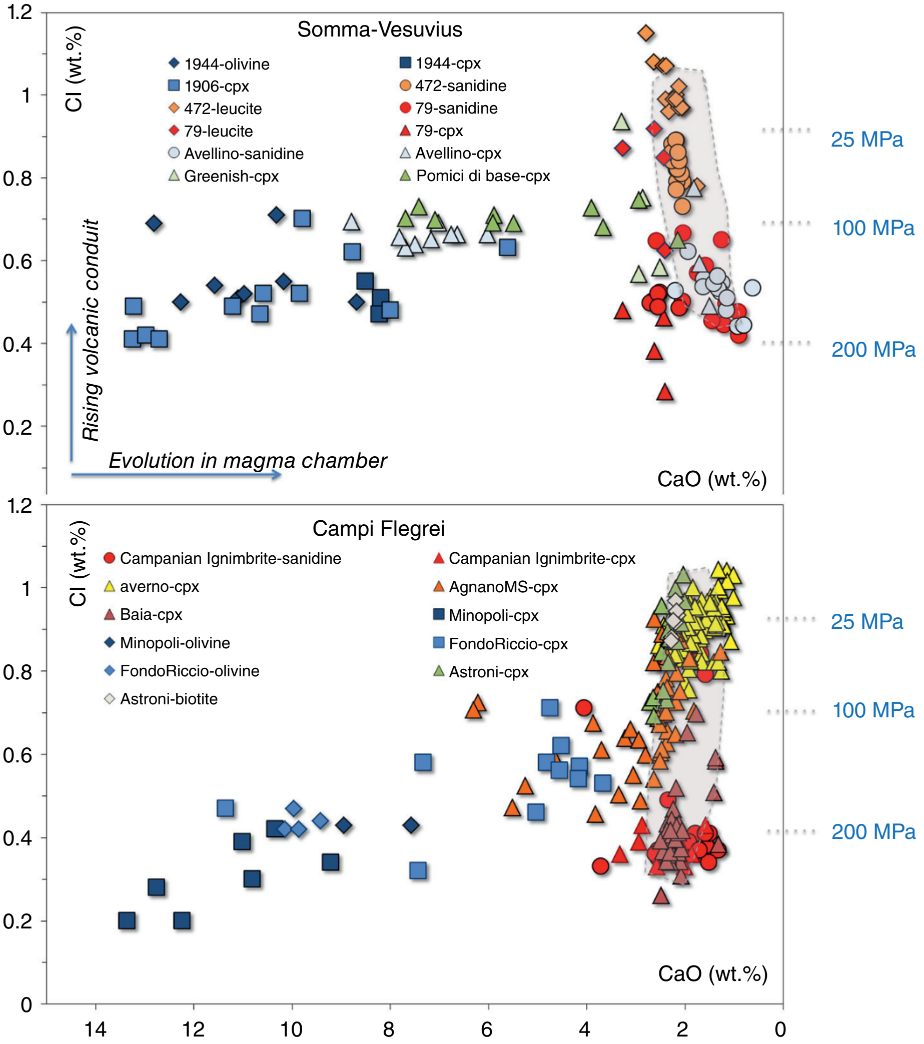

Figure 10.4 Cl versus CaO content of melt inclusions in mineral phases. Horizontal lines on the right axis denote saturation pressure for different Cl contents (solubility model by Signorelli & Carroll, 2002). Fields represent degassed matrix glass composition. Data from: CF: Arienzo et al. (2010), Cannatelli et al. (2007), Esposito et al. (2018) Fourmentraux et al. (2012), Lima et al. (2017), Mangiacapra et al. (2008), Marianelli et al. (2006), Signorelli & Carroll (2002); SV: Balcone-Boissard et al. (2008, 2012, 2016), Lima et al. (2003), Marianelli et al. (1999, 2005), Webster & De Vivo (2002). Sources: Data from Arienzo et al. (2010); Cannatelli et al. (2007); Esposito et al. (2018); Fourmentraux et al. (2012); Lima et al. (2017); Lima et al. (2003); Mangiacapra et al. (2008); Marianelli et al. (2006); Signorelli and Carroll (2002); Balcone-Boissard et al. (2016); Webster and De Vivo (2002).

The existence of two main magma storage depths active under CF and SV volcanoes have been postulated based on the complete petrological results (Table 10.1 and Figure 10.4), (Pappalardo & Mastrolorenzo, 2010, 2012): a deeper mafic (liquidus T ~ 1200 °C, viscosity ~ 10^0–10^1 Pa s at saturation condition, volatile content ~ 5–9 wt. %) reservoir at a pressure of >200–400 MPa (>8–16 km depth) extended toward the Moho discontinuity (25–30 km) and a shallower (150–200 MPa, 6–8 km depth) felsic (liquidus T ~1000 °C, viscosity ~ 10^2–10^3 Pa s at saturation condition, volatile content ~4.5–6 wt. %) magma layer at the inferred carbonatic/metamorphic rocks transition.

The geochemical variations of major, trace, and volatile elements (Figures 10.3 and 10.4) on separated minerals, glass, as well as melts inclusions define systematic trends, suggesting a cogenetic nature of the various magmas at different degree of evolution. However, Sr-Nd isotopic variations indicate that contamination with host rocks and mixing/mingling processes occurred at different depths and timescales (e.g., Dallai et al., 2011; Pappalardo et al., 2004; Piochi et al., 2006). Diffusion chronometry yields mixing timescale on the order of several tens of years before the eruptions (Iovine et al., 2017; Morgan et al., 2006). Furthermore, Iacono Marziano et al. (2008) indicated that the massive Ca-rich clinopyroxene crystallization induced by progressive carbonate assimilation may explain the transition from slightly (CF and SV rocks older than 9 ka) to moderately (SV rocks erupted between 9 ka and 79 AD) and to strongly silica-undersaturated (SV rocks younger than 79 AD) residual melts observed on Neapolitan magmas. It has also been proposed that fast magma–limestone interaction, accompanied by the generation of CO_2 fluid phases, could be an important process in controlling the eruption explosivity (e.g., Buono et al., 2020b; Jolis et al., 2013, 2015; Pappalardo et al., 2018).

Pappalardo and Mastrolorenzo (2010, 2012) applied crystal size distribution theory (Marsh, 1988) on phenocrysts included in the Somma-Vesuvius and Campi Flegrei rocks, and obtained a relatively short crystallization time on the order of few hundred years, in agreement with the pre-eruptive crystal residence time obtained by uranium decay series data for zircon and garnet (Gebauer et al., 2014; Wotzlaw et al., 2019; Wu et al., 2015). This suggests that alkaline magmas could evolve toward a critical state of explosive behavior over a relatively short time span comparable to the repose time of most volcanic systems.

The similar pressure and temperature conditions estimated, as well as the consistent timescale of residence time between the magmatic systems of the two Neapolitan volcanic districts, suggest the existence of a wide sill-shaped magmatic chamber (Pappalardo & Mastrolorenzo, 2012) consisting mainly of crystal-poor melts and fed by a deeper storage zone of mafic crystal-rich magmas (Figure 10.5).

A unique magmatic source for the two Neapolitan volcanic areas is also supported by the similarity in the Sr and Nd isotopic compositions in both silicic and mafic rocks of Campi Flegrei volcanic district and Somma-Vesuvius (Figure 10.3B). Whereas the increase in the degree of magma/wall rock interaction with time (Iacono Marziano et al., 2008) explains the growth of silica undersaturation and precipitation of leucite in younger SV melts. Gebauer et al. (2014) have hypothesized that the development of a crystalline carapace at the boundary magma/crustal rocks during CI supereruption isolated the subsequent CF magmas by extensive assimilation of country rocks (Figure 10.5).

Some authors suggested that the absence of Mesozoic carbonate succession beneath CF caldera is due to the lack of calcareous lithic clasts in the Phlegraean stratigraphic volcanic successions (e.g., D'Antonio, 2011). However, we observe that the CF caldera is located toward the center of the Campanian graben, close to its maximum depression, where possibly the Mesozoic carbonate series is dislocated at a deeper level (>4 and <8–11 km according to geophysical data; e.g., Zollo et al., 2008) compared to the Somma-Vesuvius, placed toward the eastern border of the graben (where the carbonatic succession is reached by boreholes at a depth of 1–2 km; Brocchini et al., 2001). This condition implies that the depth of limestone at CF is always below the surface of magmatic fragmentation (1–2 km, Pappalardo & Mastrolorenzo, 2012) at which the main production of lithic clasts is expected (Macedonio et al., 1994) (Figure 10.5).

The occurrence of ancient (>40 ka) volcanic centers in the heart of the city of Naples, identified in the Chiaia area (Scarpati et al., 2012), halfway between the two volcanoes, might be evidence for the long-lived nature of a unique magmatic source for the two Neapolitan volcanic areas. However, its persistence today can be postulated on the basis of the heat flow distribution showing a single positive anomaly (>100 mW/m^2) extended below the entire Neapolitan area, with the maximum value corresponding to the Phlegraean supervolcano (600 mW/m^2, Carlino et al., 2012; Della Vedova et al., 2013), where most of the magma volume is probably stored (the CF caldera emitted ca. 400 km^3 of magmas in the last 40 ka compared to the ca. 50 km^3 erupted in the last 25 ka at Somma-Vesuvius).

10.4. MAGMA ASCENT IN VOLCANIC CONDUIT

Degassing and crystallization mechanisms and timescales accompanying magma ascent in the volcanic conduit exert an important control on both the evolution of geochemical and geophysical signals recorded during volcanic crises as well as on the style and intensity of the impending eruption.

Table 10.1 Magmatic Intensive Variables for Campi Flegrei and Somma-Vesuvius Reservoirs

		Campi Flegrei				
Methods	**References**	**Composition**	**Pressure**	**Liquidus T**	**Initial water content**	**CO_2 content**
MELTS						
	Fowler et al., 2007	Trachyte	150 MPa	1235 °C	3 wt%	—
	Pappalardo et al., 2008	Trachyte	250 MPa	1199 °C	4 wt%	—
GEOTHERMOBAROMETRY						
cpx-melt thermometers and barometers	Masotta et al., 2013	Trachyte	127–58 MPa	> 884–983 °C	—	—
cpx-melt thermometry and K-feld-melt hygrometry	Forni et al., 2018	Trachyte	200 MPa	1100 °C	4 wt%	—
PHASE-EQUILIBRIUM EXP						
	Fabbrizio & Carroll, 2008	Trachyte	150–200 MPa	> 800°C	satutation condition	—
	Perinelli et al., 2019	Trachybasalt	0.6–0.9 GPa	1400–1200 °C	—	—

		Somma-Vesuvius				
Methods	**References**	**Composition**	**Pressure**	**Liquidus T**	**Initial water content**	**CO_2 content**
MELTS						
	Pappalardo & Mastrolorenzo, 2010	Tephrite	400–350 MPa	1212 °C	5 wt%	—
	Pappalardo & Mastrolorenzo, 2010	Phonolite	250–200 MPa	986 °C	7.7 wt%	—
	Pappalardo et al., 2014	Tephrite	400 MPa	1150 °C	saturation	—
GEOTHERMOBAROMETRY						
cpx-melt thermometers and barometers	Masotta et al., 2013	Phonolite	157–186 MPa	800–770 °C	—	—
	Balcone-Boissard et al., 2016	Phonolite	200–180 MPa	—	5.1 wt%	—
PHASE-EQUILIBRIUM EXPERIMENT						
	Scaillet et al., 2008	Phonolite	200 MPa	815–785 °C	6 wt%	—
	Pichavant et al., 2014	Trachybasalt	300–<200 MPa	1200 °C	1.5–4.5 wt%	600–4500 ppm

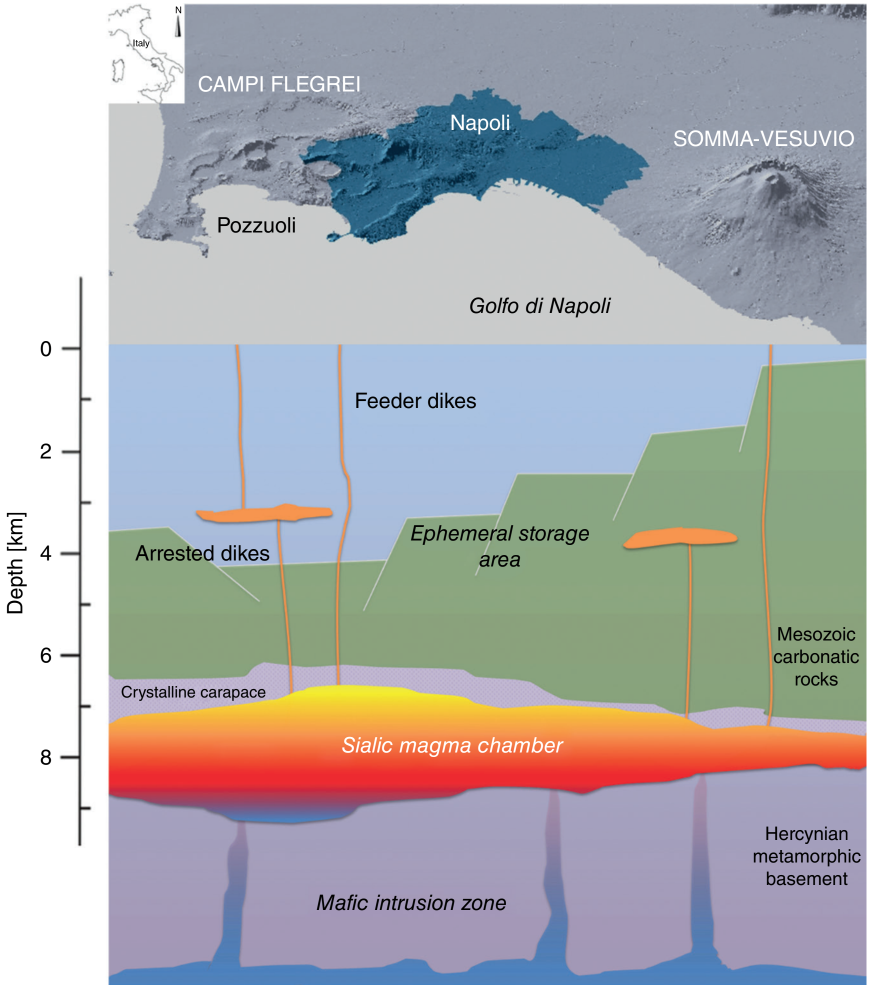

Figure 10.5 Geological model of the deep structure of the Neapolitan volcanoes based on both petrological and geophysical data.

In particular, decompression during magma ascent is associated with a decrease in pressure-dependent solubility, thus causing exsolution of volatiles (mainly H_2O and CO_2) forming a separated gas phase (i.e., bubbles). Exsolution in ascending melts increases the magmas liquidus temperature and may trigger extensive crystallization of microlites (i.e., crystals smaller than about 50–100 μm). As a consequence, decompression-induced degassing and crystallization cause significant changes in the chemistry and physical properties of the ascending magma with drastic effects on the eruptive behavior (e.g., Gonnermann & Manga, 2007, and references therein).

Generally, high-intensity explosive activity is expected to result from rapid (average) magma decompression and ascent (>0.1 m/s; Cassidy et al., 2018) during which the gas remains trapped in the melt (closed-system degassing), causing magma expansion and leading to explosive fragmentation through volatile overpressure in bubbles, high-strain rates due to rapid acceleration, or at a critical vesicularity threshold. On the other hand, low-intensity volcanic activity is associated with slow magma ascent (<0.1 m/s; Cassidy et al., 2018), which gives sufficient time for the gas to escape (open-system degassing) and microlites to grow (Rutherford & Gardner, 2000).

Classically, it is considered that volatile exsolution follows solubility laws (near-equilibrium condition) in low-viscosity melts regardless of the decompression rate, whereas bubble–melt equilibrium is not maintained (disequilibrium degassing) in highly viscous melts at a rapid ascent rate (e.g., Couch et al., 2003; Mangan & Sisson, 2000; Mangan et al., 2004; Mourtada-Bonnefoi & Laporte, 2004). However, several observations do not fit easily in such a simple model (e.g., Larsen & Gardner, 2004; Iacono Marziano et al., 2007; Mastrolorenzo & Pappalardo, 2006) suggesting a more complex relationship between the degassing regime and melts composition and/or ascent rate. In fact, how the different internal (pre-eruptive volatile content, magma injection, magma rheology, etc.) and external (tectonic regime, stress field, conduit and vent geometry, flanks collapse of volcanic edifice, CO_2 liberation by limestone ingestion, magma/water interaction, etc.) factors interact to control the speed of magma ascent is still poorly constrained (e.g., Cassidy et al., 2018; Gonnermann & Houghton, 2012; Rust & Cashman, 2011).

A powerful tool for reconstructing magma decompression history is the 2D and 3D textural characterization of natural volcanic rocks. In particular, in the last decades, 3D textural investigation (e.g., X-ray microtomography; μCT) has become an increasingly important tool for both qualitative and quantitative assessment of rock textures in three dimensions, thus entirely avoiding the mathematical corrections needed for measurements made in conventional 2D techniques. Many recent studies have demonstrated the power of μCT in the understanding complex textures, such as those of pyroclasts produced during explosive eruptions. In fact, μCT allows the direct observation and accurate quantification of important textural parameters (such as the content, number, orientation, shape, and distributions of the crystals and vesicles, as well as of their degree of connectivity and permeability) that strongly influence nucleation, growth, and coalescence of gas bubbles, magma fragmentation, and crystallization (e.g., Baker et al., 2012; Degruyter et al., 2010a, 2010b; Gurioli et al., 2015; Lanzafame et al., 2017; Liedl et al., 2019; Pappalardo et al., 2018; Polacci et al., 2014, 2018; Voltolini et al., 2011).

To be specific, vesicle number densities (VNDs; i.e., the number of vesicles per unit melt or bulk volume) of natural volcanic rocks are generally correlated with the intensity of the examined eruptions as well as with the decompression rate simulated by experiments (Mangan et al., 2004; Mourtada-Bonnefoi & Laporte, 2004) and numerical models (Toramaru, 2006). In general, high VND values are associated with a high rate of decompression; low values are related to slow, or staged ascent (e.g., Cashman & Mangan, 1994). Shea et al. (2010a) reported VND values between 10^{11} to 10^{12} m^{-3} for slow ascent magmas (VEI from 0 to 2) and up to 10^{16} m^{-3} for fast ascent magmas (e.g., Vesuvius 79 AD VEI 6 Plinian eruption).

Vesicle size distributions (VSDs; i.e., the number of vesicles in each size class per unit melt or bulk volume) and vesicle volume distributions (VVDs; i.e., the volume fraction of the vesicles at their equivalent volume) are used commonly to infer kinematics of bubble nucleation and growth rate. In particular, cumulative VSDs (CVSDs) log-log plots have been observed to follow either exponential or power law distributions both in natural and experimental samples. Generally, pumices generated by purely magmatic processes show CVSDs that follow power law distributions for larger vesicles and exponential trends for the smallest bubble sizes (e.g., Carey et al., 2009; Klug et al., 2002); these trends are interpreted as representing the bubble populations generated by continuous nucleation events and/or growth and coalescence during ascent (Blower et al., 2003; Gaonac'h et al., 1996) and by a last nucleation event, respectively (Gonnermann & Houghton, 2012; Rotella et al., 2014).

An additional important parameter is the vesicle-to-melt volume ratio (Vg/Vl after Gardner et al., 1996; i.e., the ratio between the volume of vesicles corrected for phenocrysts, Vg, and the volume of melt and microlites, Vl). In particular, following Stovall et al. (2011), different vesiculation processes impart a characteristic signature on a plot of Vg/Vl versus VND. New nucleation of small bubbles leads to increased VND and only a slight increase in Vg/Vl. Bubble growth by diffusion and/or gas expansion leads to increased Vg/Vl at constant VND. Bubble coalescence causes a decrease in VND while Vg/Vl increases, and bubbles collapse leads to a reduction in both parameters. Intermediate trends on the diagram reflect combinations of more than one of these processes. Moreover, the plot of Vg/Vl versus H_2O content dissolved in the matrix glass of volcanic rocks can be indicative of different degassing regime (open- versus closed-system regime; e.g., Villemant & Boudon, 1998).

Vesicularity and permeability are further important parameters that may have a considerable impact on the characteristics of a volcanic eruption. Theoretically, a vesicularity threshold (percolation threshold) exists because bubbles at low volume fractions are sufficiently distant from one another to prevent pervasive coalescence; however, results of numerical simulations and experiments as well as measurements on natural samples indicate that the percolation threshold can range largely from 30% to 78% with no unique relationship with other compositional or textural parameters (e.g., Giachetti et al., 2019, and references therein).

Similarly, crystal content, number density (CND), size (CSD), and volume (CVD) distribution as well as the shape of microlites are strictly related to the mechanisms and time of magma decompression in volcanic conduits (e.g., Befus et al., 2014; Clarke et al., 2007; Couch et al., 2003; Hammer et al., 1999; Kennedy et al., 2005; Noguchi et al., 2006; Martel, 2012). In particular, decompression experiments (e.g., Blundy & Cashman, 2008; Martel et al., 2017) demonstrated that under conditions of rapid ascent, due to high rate of undercooling (defined as the difference between the liquidus temperature and that of the magma), the crystallization is controlled by nucleation of new sites (nucleation-dominated regime), thus resulting in many tiny skeletal (e.g., hopper, shallow-tail, acicular shape) microlites (e.g., Browne & Gardner, 2006; Couch et al., 2003; Geschwind & Rutherford, 1995; Hammer & Rutherford, 2002;

Hammer et al., 2002; Martel & Schmidt, 2003; Rutherford & Hill, 1993). On the contrary, in slow ascending magmas, growth of existing crystals prevails (growth-dominated regime) over nucleation due to the reduction over time of the degree of undercooling, thus resulting in fewer but larger (e.g., tabular, prismatic) microlites. Moreover, recent studies (Brugger & Hammer, 2010a, 2010b; Melnik et al., 2011) have determined that during decompression at high pressure, crystallization occurs under a growth-dominated regime, whereas at low-pressure decompression crystal nucleation prevails. It is worth noting that decompression experiments show the absence of microlites in the groundmass of pumices from highly explosive eruptions, thus indicating that the magma decompression time was too short (up to tens of hours) to generate microlites (e.g., Couch et al., 2003; Martel, 2012).

10.4.1. Degassing and Crystallization of Ascending Alkaline Neapolitan Magmas

Degassing and crystallization processes and timescales during magma ascent in volcanic conduits for Neapolitan volcanoes have been investigated by several authors measuring textural and geochemical features on natural sialic and mafic rocks (e.g. Cioni et al., 2011; D'Oriano et al., 2005; Mastrolorenzo & Pappalardo, 2006; Mastrolorenzo et al., 2001; Pappalardo & Mastrolorenzo, 2010, 2012; Pappalardo et al., 2008, 2014, 2018; Piochi et al., 2005, 2008; Pistolesi et al., 2017; Shea et al., 2012; Zdanowicz et al., 2018) as well as through decompression experiments (e.g. trachyte: Arzilli et al., 2016; Calzolaio et al., 2010; Mastrolorenzo & Pappalardo 2006; Preuss et al., 2016; phonolite: Allabar & Nowak, 2018; Iacono Marziano et al., 2007; Larsen, 2008; Marxer et al., 2015; Preuss et al., 2016; Shea et al., 2010b). Significant differences are apparent between natural rocks from high-explosive events respect to those from moderately explosive/effusive eruptions (e.g., Mastrolorenzo & Pappalardo, 2006), reflecting different conditions of magma ascent. The only exception is the VND, whose value in natural samples ranges from ca. 10^{10} to 10^{15} m^{-3} (Mastrolorenzo and Pappalardo, 2006; Mastrolorenzo et al., 2001) apparently regardless of the eruptive style and composition, almost consistently with VND values from decompression experiments produced by heterogeneous nucleation in Neapolitan trachytes (7.2×10^{12}–2.9×10^{14} m^{-3}, Mastrolorenzo & Pappalardo, 2006) and phonolites (4.3×10^{13}–3.8×10^{14} m^{-3}, Larsen, 2008; 3.6×10^{14}–9.9×10^{15} m^{-3}, Shea et al., 2010b) as well as by homogeneous nucleation in alkaline melts (3.0×10^{9} –1.3×10^{14}, Marxer et al., 2015; 6.8×10^{13}–2.5×10^{14}, Allabar & Nowak, 2018, and references therein) during experiments at different decompression rates.

Moreover, residual water contents measured on trachytic and phonolitic samples obtained by decompression experiments (Larsen, 2008; Larsen & Gardner, 2004; Marxer et al., 2015; Mastrolorenzo & Pappalardo, 2006; Shea et al., 2010b) suggest that ascending alkaline water-saturated magmas generally follow a degassing path controlled by near-equilibrium solubility in a wide range of ascent rates. On the other hand, water undersaturated (Allabar & Nowak, 2018; Iacono Marziano et al., 2007; Preuss et al., 2016) experiments on phonolitic compositions indicate that degassing can deviate from equilibrium solubility trends.

We recently proposed a further, extensive discussion of experimental and numerical data on degassing in (H_2O- and CO_2-rich) evolved alkaline (trachytic and phonolitic) magmas in Buono et al. (2020c).

In general, trachytic to phonolitic pumice samples (e.g., Mastrolorenzo & Pappalardo, 2006) from large-explosive eruptions have a highly vesicular glassy matrix (60%–80%) and moderate to high residual water content (1–2 wt.%). These clasts have abundant small spherical vesicles and coalesced large vesicles in microlite-poor (feldspar) to microlite-free (0–5 vol.%) groundmass glass (Figure 10.6). Crystal size distributions on microlites are steep (−~300 mm^{-1}) with high intercept values (~18 mm^{-4}). Textural (vesicularity, Vg/Vl, CSDs, CNDs) and geochemical (water content) features of pumices indicate rapid decompression (hours to days) and degassing under closed-system condition, producing explosive fragmentation possibly when the volume of expanding bubbles reaches a fixed vesicularity threshold (70%–80%) at a inferred fragmentation pressure of 10–30 MPa.

The only case of a high-explosive event mainly fueled by mafic magmas in the Neapolitan area is the caldera-forming Pomici di Base Plinian eruption that occurred at 22 ka at Somma-Vesuvius. Recent 3D textural and geochemical studies (Buono et al., 2020a and b; Pappalardo et al., 2018) hypothesized that the explosive character of this mostly shoshonitic-latitic eruption was linked to the rapid release of CO_2, due to the interaction of hot mafic ascending magmas with the limestone substratum. The CVSDs (Figure 10.7) in the scoriae erupted during this Vesuvian event suggest a double degassing episode correlated to both water exsolution in a deeper part of the conduit (first vesiculation event) and subsequent CO_2 liberation (second event of vesiculation) at a shallow level.

By contrast, low-explosive and effusive eruptions (e.g., the 1538 AD Monte Nuovo eruption from Campi Flegrei and the 1944 eruption from Somma-Vesuvius) produced scoriae and/or lavas characterized by moderate vesicularity (40%–60%), moderate to high microcrystalline groundmass (30%–40 vol.%), and low glass water content (below 1 wt.%). Scoriae show large vesicles with

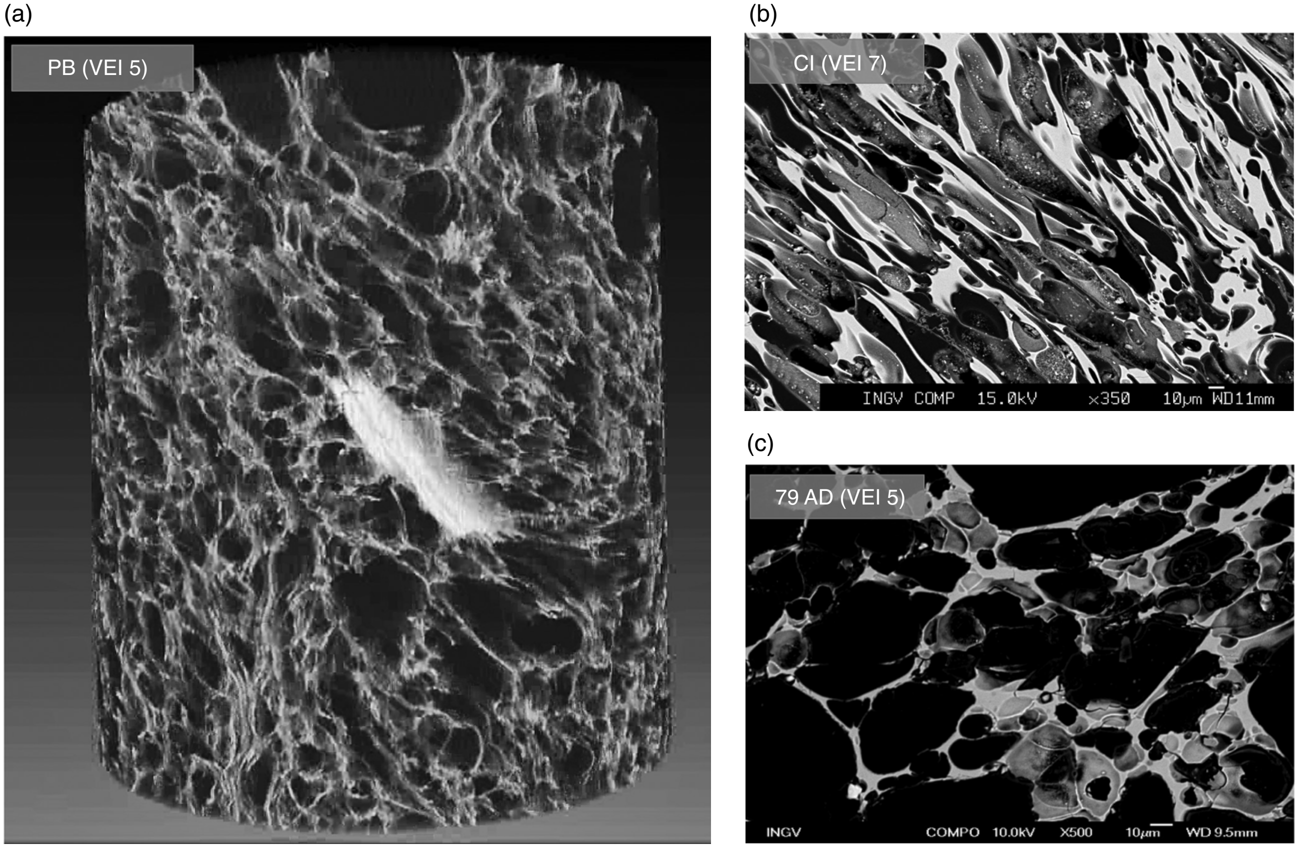

Figure 10.6 Example of volume rendering obtained by computed X-ray microtomography (Carl Zeiss Xradia Versa-410) at INGV-NA laboratory and backscattered electron images of selected rocks, performed at INGV-Rome laboratory, showing the high vesicular and microlite-free texture of pumices from high-explosive eruptions of Campi Flegrei and Somma-Vesuvius. (A) Pomici di Base Plinian eruption (22 ka) from SV, diameter of cylinder = 1mm; (B) Campanian Ignimbrite supereruption from CF; (C) Pompeii Plinian eruption (79 AD) from SV.

polylobate and convoluted shapes, reflecting coalescence in variable directions. Evidence of flattening is also present possibly as a consequence of vesicle collapse and reduction of vesicularity during permeable outgassing (Figure 10.8). CSDs on microlites show gentle slope (between -80 and -25 mm^{-1}) and low intercept values (15–12 mm^{-4}) and in most cases distinct inflections (hyperbolic CSDs) that are interpreted as different crystal populations growing in distinct magma ascent steps (Figure 10.8). The textural and geochemical features of rocks indicate moderate to long magma ascent times (days to months) that favor permeable outgassing (open-system degassing) and in turn bubble collapse as well as extensive degassing-induced microlite crystallization (Figure 10.8). Hyperbolic crystal size distributions data reveal that in the case of small eruptions, magma ascent occurred by steps, and thus melts can reside at a shallower level (ephemeral shallower storage zone) for short periods before erupting or cooling/crystallizing (plug development) in the case of failed eruption.

An example of this behavior is represented by the last CF Monte Nuovo eruption, which occurred in 1538 AD after a quiescent period that lasted ca. 3 ka. This eruption, although of low magnitude (VEI 2), was preceded by a long period of unrest, which became more intense a few months before the eruption as inferred by the description of historical chronicles (Di Vito et al., 2016; Guidoboni & Ciuccarelli, 2011). A recent study Liedl et al. (2019) revealed that the ground deformations and earthquakes that preceded the eruption could be the result of recurrent magma migrations from a long-lived deep source (6–8 km) toward a shallower (3–4 km) temporary storage area (Figure 10.5). The progression of this process possibly caused the weakening (heating) of the crustal rocks, thus favoring the subsequent propagation of fractures toward the surface, triggering the eruption.

Eruptive style transitions have been frequently documented in past eruptions of Neapolitan volcanoes (e.g., Mastrolorenzo et al., 2017, and references therein). Figure 10.9 shows Vg/Vl versus water content

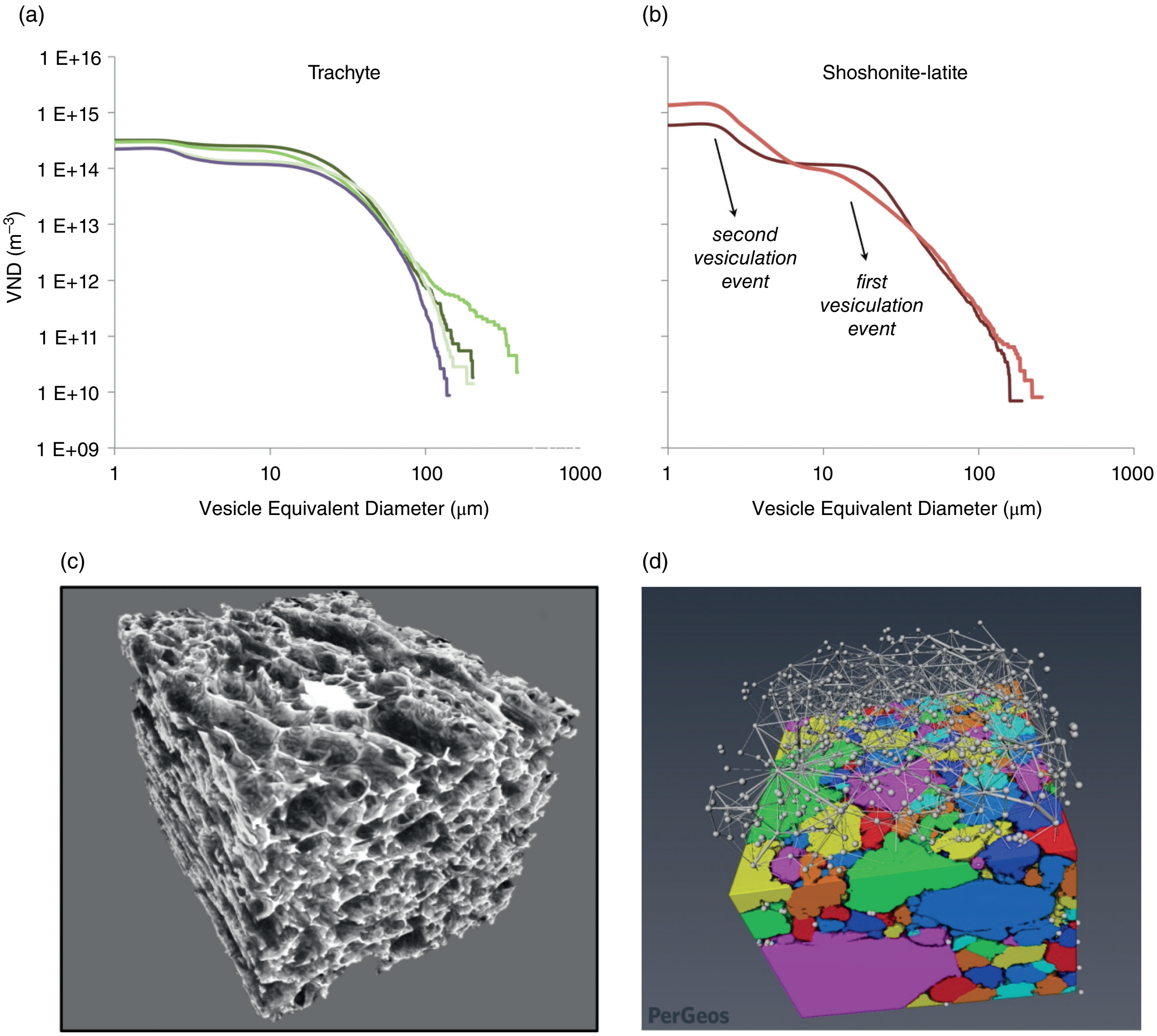

Figure 10.7 Example of volume distributions (CVSDs) of cumulative vesicles for (A) trachytic and (B) shoshonitic-latitic Somma-Vesuvius rocks. CVSDs of trachytic pumices show a curved continuous trend characterized by exponential distribution for the smaller bubbles and power law distribution for the larger bubbles, indicating a continuous nucleation process. On the other hand, CVSDs of scoria latitic samples show irregular trends formed by multiple curved segments, suggesting discrete vesiculation events attributed to multiple nucleation pulses driven by fast CO_2 release during the ongoing decarbonation process (see text for further explanation). (C) Example of 3D micro-CT image (INGV-NA laboratory) of Somma-Vesuvius trachyte. Cube side: 300 pixels (pixel=1 micron). (D) Example of Pore Network Model obtained by Avizo FEI software. A PNM is composed of branching or end-points of the network called pores (or vesicles for volcanic rocks) and lines connecting pores called throats. Pores are displayed using spheres, and throats are displayed using cylinders. Cube side: 300 pixels (pixel=1 micron). Data from Pappalardo et al. (2018). Source: Data from Pappalardo et al. (2018).

(Figure 10.9A) and vesicularity versus permeability (Figure 10.9B) for the two case studies representative of small-scale (Monte Nuovo Strombolian eruption) and high-intensity (Pomici di Base Plinian eruption) events fed by alkaline Campanian magmas. Textural data show values of increase permeability at about 55%–60% of vesicularity at the passage from scoriae- to pumice-bearing layers, marking the transition from closed- (Vg/Vl and water content near equilibrium conditions; Figure 10.9B) to open-system degassing (low Vg/Vl and water content; Figure 10.9B). The highest vesicularity and permeability values are observed in the pumice-forming

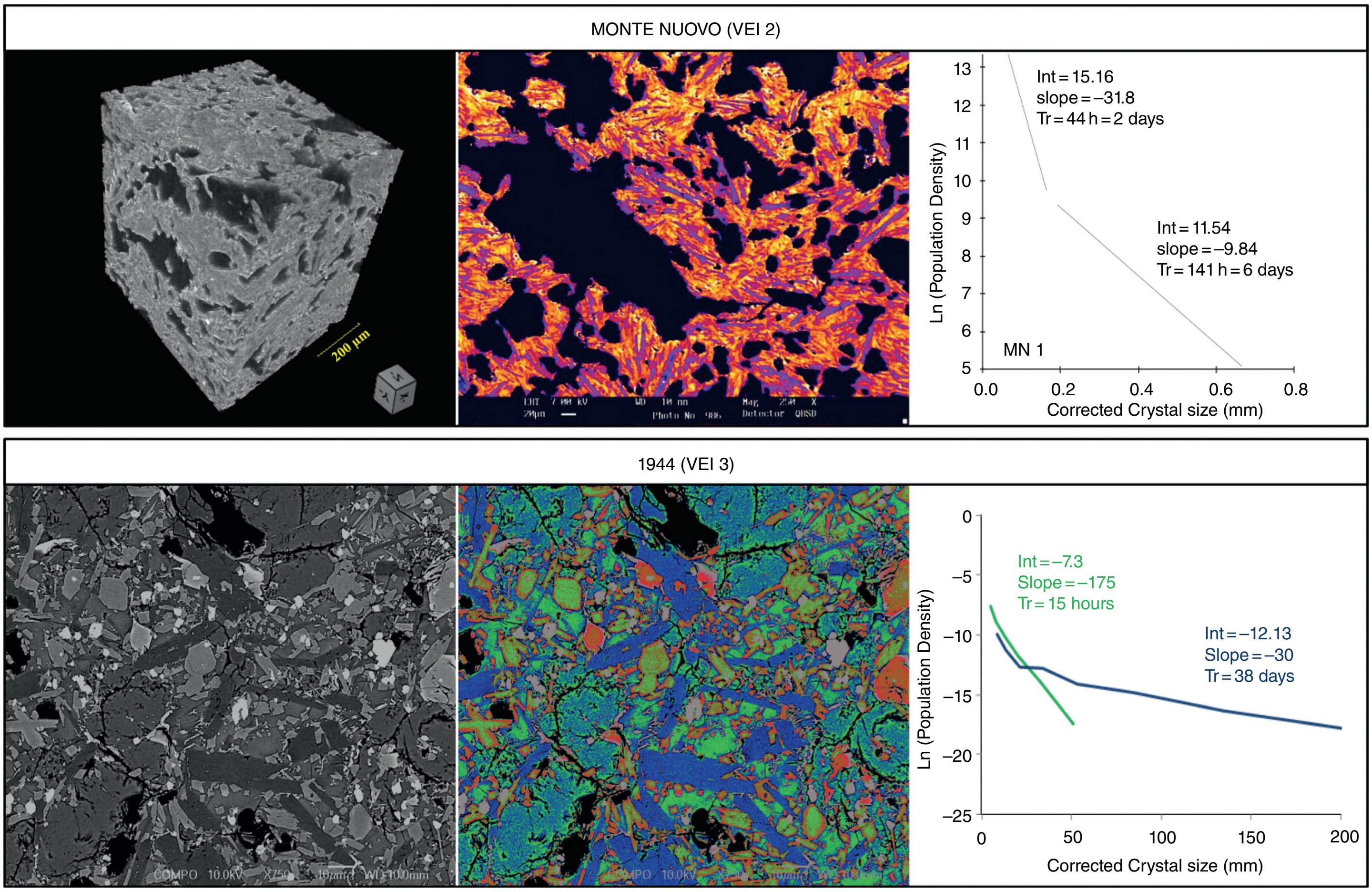

Figure 10.8 3D micro-CT image (INGV-NA laboratory) and 2D backscattered electron images (INGV-Rome laboratory) of selected rocks from small-scale/effusive eruptions of Campi Flegrei and Somma-Vesuvius and corresponding CSD curves obtained by plotting population density (number of crystals per unit volume) versus crystal size (maximum length). In the upper panels, samples from the (phreatomagmatic) opening phase of the last CF Monte Nuovo eruption (1538 AD, VEI 2), in violet: sanidine microlite; data from Piochi et al. (2005). In the lower panels, sample from the (effusive) opening phase of the last SV eruption (1944 AD, VEI 2), data from Pappalardo et al. (2014). CSDs show hyperbolic trend characterized by distinct inflections that are interpreted as different crystal populations growing in distinct magma ascent steps during conduit opening and propagation. In blue: plagioclase microlite; in green: cpx microlite. Source: Data from Piochi et al. (2005); Pappalardo et al. (2014).

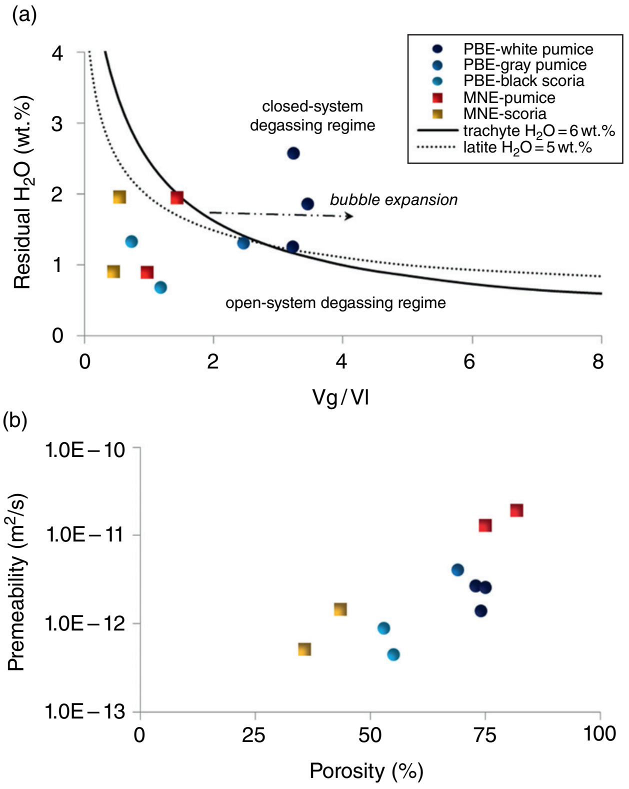

Figure 10.9 (A) Vg/Vl versus H_2O content and (B) vesicularity versus permeability for small-scale Monte Nuovo eruption and for Vesuvian Plinian Pomici di Base eruption. Data from: Pappalardo et al. (2018) for PBE; Liedl et al. (2019), Piochi et al. (2005) for MNE. Sources: Data from Pappalardo et al. (2018); Liedl et al. (2019); Piochi et al. (2005).

phase of MN eruption, possibly as a consequence of a sudden depressurization event driven by magma–water interaction characterizing the opening phase of this event.

10.5. CONCLUSIONS: IMPLICATIONS FOR FUTURE HAZARDS

In this chapter, we used new and previous evaluation of available petrological (geochemical and textural) data of volcanic rocks representative of the eruptive history of Neapolitan volcanoes to reconstruct the architecture of their plumbing system and its evolution toward critical conditions close to eruption.

The results show the possible existence of a wide sill-like felsic magma layer beneath the whole Neapolitan volcanic area with the top at 6–8 km depth (at the transition between sedimentary and metamorphic successions) fed by a deeper (>8–10 km) mafic reservoir extending toward the Moho discontinuity (25–30 km of depth). Generally the shallow chamber fueled mainly intermediate and highly explosive eruptions, whereas the deep mafic magma reservoir was the source of less violent eruptions. Crystal Size Distribution data on feldspar phenocrysts (Pappalardo & Mastrolorenzo, 2010; 2012) reveal that primitive magmas can evolve, during the migration in the upper part of the reservoir, toward less-dense felsic liquids in a relatively short time span comparable with the hundreds of years of a volcano's repose. This plumbing system could represent a long-term magmatic sills intrusion and storage zone, with its maximum volume under the CF supervolcano (where a huge volume of magmas was erupted in the last 40 ka and the maximum value of heat flux is currently measured).

Textural data (e.g., high vesicularity, vesicle size distribution trends, absence of microlites) of rocks erupted during highly explosive eruptions indicate a single-stage volatile degassing under closed-system conditions during fast magma ascent in the volcanic conduit. These features could be indicative of rapid conduit propagation, thus suggesting short, and possibly initially, deep (in proximity of the inferred magma chamber top) precursory signals.

By contrast, textural characters of volcanic rocks erupted from small-scale eruptions show evidence of degassing under open-system conditions during slow magma migration and storage at shallower depth (ephemeral storage zones) where it resided until erupting or cooling (failed eruption), thus indicating slow conduit propagation and a long period of unrest characterized by shallow earthquakes, ground deformation, and gas emission.

ACKNOWLEDGMENTS

We thank Francesca Forni and an anonymous reviewer for comments that greatly improved the manuscript. We gratefully acknowledge the critical reading of the manuscript by Chris Harris. This work is part of the research project LOVE-CF financed by INGV.

REFERENCES

Albert, P. G., Giaccio, B., Isaia, R., Costa, A., Niespolo, E. M., Nomade, S., et al. (2019). Evidence for a large-magnitude eruption from Campi Flegrei caldera (Italy) at 29 ka. *Geology*, *47*(7), 595–599. doi: https://doi.org/10.1130/G45805.1

Allabar, A., & Nowak, M. (2018). Message in a bottle: Spontaneous phase separation of hydrous Vesuvius melt even at low decompression rates. *Earth and Planetary Science Letters*, *501*, 192–201. https://doi.org/10.1016/j.epsl.2018.08.047

Andersen, N. L., Jicha, B. R., Singer, B. S., & Hildreth, W. (2017). Incremental heating of Bishop Tuff sanidine reveals preeruptive radiogenic Ar and rapid remobilization from cold storage. *Proceedings of the National Academy of Sciences*, *114*(47), 12407–12412. https://doi.org/10.1073/pnas.1709581114

Annen, C. (2009). From plutons to magma chambers: Thermal constraints on the accumulation of eruptible silicic magma in the upper crust. *Earth and Planetary Science Letters*, *284*, 409–416. https://doi.org/10.1016/j.epsl.2009.05.006

Annen, C., & Zellmer, G. F. (2008). *Dynamics of crustal magma transfer, storage and differentiation*. Geological Society, London. https://doi.org/10.1144/SP304

Arienzo, I., Moretti, R., Civetta, L., Orsi, G., & Papale, P. (2010). The feeding system of Agnano-Monte Spina eruption (Campi Flegrei, Italy): Dragging the past into present activity and future scenarios. *Chemical Geology*, *270*(1–4), 135–147. https://doi.org/10.1016/j.chemgeo.2009.11.012

Arzilli, F., Piochi, M., Mormone, A., Agostini, C., & Carroll, M. R. (2016). Constraining pre-eruptive magma conditions and unrest timescales during the Monte Nuovo eruption (1538 AD; Campi Flegrei, Southern Italy): integrating textural and CSD results from experimental and natural trachy-phonolites. *Bulletin of Volcanology*, *78*(10), 72. https://doi.org/10.1007/s00445-016-1062-z

Auger, E., Gasparini, P., Virieux, J., & Zollo, A. (2001). Seismic evidence of an extended magmatic sill under Mt. Vesuvius. *Science*, *294*(5546), 1510–1512. https://doi.org/10.1126/science.1064893

Bachmann, O., & Bergantz, G. W. (2003). Rejuvenation of the Fish Canyon magma body: A window into the evolution of large-volume silicic magma systems. *Geology*, *31*(9), 789–792. https://doi.org/10.1130/G19764.1

Bachmann, O., & Bergantz, G. W. (2004). On the origin of crystal-poor rhyolites: Extracted from batholithic crystal mushes. *Journal of Petrology*, *45*(8), 1565–1582. https://doi.org/10.1093/petrology/egh019

Bachmann, O., & Bergantz, G. W. (2008a). Deciphering magma chamber dynamics from styles of compositional zoning in large silicic ash flow sheets. *Reviews in Mineralogy and Geochemistry*, *69*(1), 651–674. https://doi.org/10.2138/rmg.2008.69.17

Bachmann, O., & Bergantz, G. W. (2008b). Rhyolites and their source mushes across tectonic settings. *Journal of Petrology*, *49*(12), 2277–2285. https://doi.org/10.1093/petrology/egn068

Bachmann, O., & Bergantz, G. W. (2008c). The magma reservoirs that feed supereruptions. *Elements*, *4*(1), 17–21. https://doi.org/10.2113/GSELEMENTS.4.1.17

Bachmann, O., & Huber, C. (2016). Silicic magma reservoirs in the Earth's crust. *American Mineralogist*, *101*(11), 2377–2404. https://doi.org/10.2138/am-2016-5675

Baker, D. R., Mancini, L., Polacci, M., Higgins, M. D., Gualda, G. A. R., Hill, R. J., & Rivers, M. L. (2012). An introduction to the application of X-ray microtomography to the three-dimensional study of igneous rocks. *Lithos*, *148*, 262–276. https://doi.org/10.1016/j.lithos.2012.06.008

Balcone-Boissard, H., Boudon, G., Cioni, R., Webster, J. D., Zdanowicz, G., Orsi, G., & Civetta, L. (2016). Chlorine as a geobarometer for alkaline magmas: Evidence from a systematic study of the eruptions of Mount Somma-Vesuvius. *Scientific Reports*, *6*, 21726. https://doi.org/10.1038/srep21726

Balcone-Boissard, H., Boudon, G., Ucciani, G., Villemant, B., Cioni, R., Civetta, L., & Orsi, G. (2012). Magma degassing and eruption dynamics of the Avellino pumice Plinian eruption of Somma-Vesuvius (Italy). Comparison with the Pompeii eruption. *Earth and Planetary Science Letters*, *331–332*, 257–268. https://doi.org/10.1016/j.epsl.2012.03.011

Balcone-Boissard, H., Villemant, B., Boudon, G., & Michel, A. (2008). Non-volatile vs volatile behaviours of halogens during the AD 79 plinian eruption of Mt. Vesuvius, Italy. *Earth and Planetary Science Letters*, *269*(1–2), 66–79. https://doi.org/10.1016/j.epsl.2008.02.003

Barbieri, M., Di Girolamo, P., Locardi, E., Lombardi, G. & Stanzione, D. (1979). Petrology of the calc-alkaline volcanics of the Parete 2 well (Campania, Italy). *Periodico di Mineralogia*, *48*, 53–74

Befus, K. S., Zinke, R. W., Jordan, J. S., Manga, M., & Gardner, J. E. (2014). Pre-eruptive storage conditions and eruption dynamics of a small rhyolite dome: Douglas Knob, Yellowstone volcanic field, USA. *Bulletin of Volcanology*, *76*(3), 1–12. https://doi.org/10.1007/s00445-014-0808-8

Berrino, G., Corrado, G., & Riccardi, U. (1998). Sea gravity data in the Gulf of Naples: a contribution to delineating the structural pattern of the Vesuvian area. *Journal of Volcanology and Geothermal Research*, *82*(1–4), 139–150. https://doi.org/10.1016/S0377-0273(97)00061-9

Berrino, G., Corrado, G., & Riccardi, U. (2008). Sea gravity data in the Gulf of Naples. A contribution to delineating the structural pattern of the Phlegraean Volcanic District. *Journal of Volcanology and Geothermal Research*, *175*(3), 241–252. https://doi.org/10.1016/j.jvolgeores.2008.03.007

Blower, J. D., Keating, J. P., Mader, H. M., & Phillips, J. C. (2003). The evolution of bubble size distributions in volcanic eruptions. *Journal of Volcanology and Geothermal Research*, *120*(1–2), 1–23. https://doi.org/10.1016/S0377-0273(02)00404-3

Blundy, J. D., & Cashman, K. V. (2008). Petrologic reconstruction of magmatic system variables and processes. *Reviews in Mineralogy and Geochemistry*, *69*(1), 179–239. https://doi.org/10.2138/rmg.2008.69.6

Bowen, N. L. (1928). *Evolution of the igneous rocks*. Dover Publications, New York.

Brocchini, D., Principe, C., Castradori, D., Laurenzi, M. A., & Gorla, L. (2001). Quaternary evolution of the southern sector of the Campanian Plain and early Somma-Vesuvius activity: Insights from the Trecase 1 well. *Mineralogy and Petrology*, *73*(1–3), 67–91. https://doi.org/10.1007/s007100170011

Brophy, J. G. (1991). Composition gaps, critical crystallinity, and fractional crystallization in orogenic (calc-alkaline) magmatic systems. *Contributions to Mineralogy and Petrology*, *109*(2), 173–182. https://doi.org/10.1007/BF00306477

Browne, B. L., & Gardner, J. E. (2006). The influence of magma ascent path on the texture, mineralogy, and formation of hornblende reaction rims. *Earth and Planetary Science Letters*, *246*(3–4), 161–176. https://doi.org/10.1016/j.epsl.2006.05.006

Brugger, C. R., & Hammer, J. E. (2010a). Crystal size distribution analysis of plagioclase in experimentally decompressed hydrous rhyodacite magma. *Earth and Planetary Science Letters*, *300*(3–4), 246–254. https://doi.org/10.1016/j.epsl.2010.09.046

Brugger, C. R., & Hammer, J. E. (2010b). Crystallization kinetics in continuous decompression experiments: Implications for interpreting natural magma ascent processes. *Journal of Petrology*, *51*(9), 1941–1965. https://doi.org/10.1093/petrology/egq044

Buono, G., Pappalardo, L., & Petrosino, P. (2020a). Magma storage and ascent during the largest eruption of Somma-Vesuvius volcano: Pomici di Base (22 ka) plinian event. *Bollettino Di Geofisica Teorica e Applicata*, *61*, 23–40. https://doi.org/10.4430/bgta0294.

Buono, G., Pappalardo, L., Harris, C., Edwards, B. R., & Petrosino, P. (2020b). Magmatic stoping during caldera-forming Pomici di Base eruption (Somma-Vesuvius, Italy) as a fuel of eruption explosivity. *Lithos*, *370–371*, 105628. https://doi.org/10.1016/j.lithos.2020.105628

Buono, G., Fanara, S., Macedonio, G., Palladino, D. M., Petrosino, P., Sottili, G., & Pappalardo, L. (2020c). Dynamics of degassing in evolved alkaline magmas: Petrological, experimental and theoretical insights. *Earth-Science Reviews*, *211*, 103402. https://doi.org/10.1016/j.earscirev.2020.103402

Calzolaio, M., Arzilli, F., & Carroll, M. R. (2010). Growth rate of alkali feldspars in decompression-induced crystallization experiments in a trachytic melt of the Phlegraean Fields (Napoli, Italy). *European Journal of Mineralogy*, *22*(4), 485–493. https://doi.org/10.1127/0935-1221/2010/0022-2012

Cannatelli, C., Lima, A., Bodnar, R. J., De Vivo, B., Webster, J. D., & Fedele, L. (2007). Geochemistry of melt inclusions from the Fondo Riccio and Minopoli 1 eruptions at Campi Flegrei (Italy). *Chemical Geology*, *237*(3–4), 418–432. https://doi.org/10.1016/j.chemgeo.2006.07.012

Carey, R. J., Houghton, B. F., & Thordarson, T. (2009). Abrupt shifts between wet and dry phases of the 1875 eruption of Askja Volcano: Microscopic evidence for macroscopic dynamics. *Journal of Volcanology and Geothermal Research*, *184*(3–4), 256–270. https://doi.org/10.1016/j.jvolgeores.2009.04.003

Carlino, S., Somma, R., Troise, C., & De Natale, G. (2012). The geothermal exploration of Campanian volcanoes: Historical review and future development. *Renewable and Sustainable Energy Reviews*, *16*(1), 1004–1030. https://doi.org/10.1016/j.rser.2011.09.023

Cashman, K. V., & Giordano, G. (2014). Calderas and magma reservoirs. *Journal of Volcanology and Geothermal Research*, *288*, 28–45. https://doi.org/10.1016/j.jvolgeores.2014.09.007

Cashman, K. V., & Mangan, M. T. (1994). Physical aspects of magmatic degassing: II. Constraints on vesiculation processes from textural studies of eruptive products. *Reviews in Mineralogy*, *30*, 447–478

Cashman, K. V., & McConnell, S. M. (2005). Multiple levels of magma storage during the 1980 summer eruptions of Mount St. Helens, WA. *Bulletin of Volcanology*, *68*, 57–75. https://doi.org/10.1007/s00445-005-0422-x

Cassidy, M., Manga, M., Cashman, K. V., & Bachmann, O. (2018). Controls on explosive-effusive volcanic eruption styles. *Nature Communications*, *9*(1), 2839. https://doi.org/10.1038/s41467-018-05293-3

Chiodini, G., Paonita, A., Aiuppa, A., Costa, A., Caliro, S., De Martino, P., et al. (2016). Magmas near the critical degassing pressure drive volcanic unrest towards a critical state. *Nature Communications*, *7*, 13712. https://doi.org/10.1038/ncomms13712

Cioni, R., Bertagnini, A., Andronico, D., Cole, P. D., & Mundula, F. (2011). The 512 AD eruption of Vesuvius: Complex dynamics of a small scale subplinian event. *Bulletin of Volcanology*, *73*(7), 789–810. https://doi.org/10.1007/s00445-011-0454-3

Clarke, A. B., Stephens, S., Teasdale, R., Sparks, R. S. J., & Diller, K. (2007). Petrologic constraints on the decompression history of magma prior to Vulcanian explosions at the Soufrière Hills volcano, Montserrat. *Journal of Volcanology and Geothermal Research*, *161*(4), 261–274. https://doi.org/10.1016/j.jvolgeores.2006.11.007

Cooper, K. M. (2019). Time scales and temperatures of crystal storage in magma reservoirs: implications for magma reservoir dynamics. *Philosophical Transactions of the Royal Society A: Mathematical, Physical and Engineering Sciences*, *377*(2139), 20180009. https://doi.org/10.1098/rsta.2018.0009

Cooper, K. M., & Kent, A. J. R. (2014). Rapid remobilization of magmatic crystals kept in cold storage. *Nature*, *506*(7489), 480–483. https://doi.org/10.1038/nature12991

Couch, S., Sparks, R. S. J., & Carroll, M. R. (2003). The kinetics of degassing-induced crystallization at Soufriere Hills Volcano, Montserrat. *Journal of Petrology*, *44*(8), 1477–1502. https://doi.org/10.1093/petrology/44.8.1477

Dallai, L., Cioni, R., Boschi, C., & D'Oriano, C. (2011). Carbonate-derived CO_2 purging magma at depth: Influence on the eruptive activity of Somma-Vesuvius, Italy. *Earth and Planetary Science Letters*, *310*(1–2), 84–95. https://doi.org/10.1016/j.epsl.2011.07.013

D'Antonio, M. (2011). Lithology of the basement underlying the Campi Flegrei caldera: Volcanological and petrological constraints. *Journal of Volcanology and Geothermal Research*, *200*(1–2), 91–98. https://doi.org/10.1016/j.jvolgeores.2010.12.006

Degruyter, W., Bachmann, O., & Burgisser, A. (2010a). Controls on magma permeability in the volcanic conduit during the climactic phase of the Kos Plateau Tuff eruption (Aegean Arc). *Bulletin of Volcanology*, *72*(1), 63–74. https://doi.org/10.1007/s00445-009-0302-x

Degruyter, W., Burgisser, A., Bachmann, O., & Malaspinas, O. (2010b). Synchrotron X-ray microtomography and lattice Boltzmann simulations of gas flow through volcanic pumices. *Geosphere*, *6*(5), 470–481. https://doi.org/10.1130/ges00555.1

Deino, A. L., Orsi, G., de Vita, S., & Piochi, M. (2004). The age of the Neapolitan Yellow Tuff caldera-forming eruption (Campi Flegrei caldera - Italy) assessed by 40Ar/39Ar dating method. *Journal of Volcanology and Geothermal Research*, *133*(1–4), 157–170. https://doi.org/10.1016/S0377-0273(03)00396-2

Della Vedova, B., Bellani, S., Pellis, G., & Squarci, P. (2013). Deep temperatures and surface heat flow distribution. In G. B. Vai, L. P. Martini (Eds.), *Anatomy of an Orogen: the Apennines and adjacent Mediterranean basins* (pp. 65–76). Springer, Dordrecht. https://doi.org/10.1007/978-94-015-9829-3_7

De Natale, G., Troise, C., Pingue, F., Mastrolorenzo, G., & Pappalardo, L. (2006a). The Somma-Vesuvius volcano (Southern Italy): Structure, dynamics and hazard evaluation. *Earth-Science Reviews*, *74*(1–2), 73–111. https://doi.org/10.1016/j.earscirev.2005.08.001

De Natale, G., Troise, C., Pingue, F., Mastrolorenzo, G., Pappalardo, L., Battaglia, M., & Boschi, E. (2006b). The

Campi Flegrei caldera: unrest mechanisms and hazards. *Geological Society, London, Special Publications*, *269*(1), 25–45. https://doi.org/10.1144/gsl.sp.2006.269.01.03

De Vivo, B., Rolandi, G., Gans, P. B., Calvert, A., Bohrson, W. A., Spera, F. J., & Belkin, H. E. (2001). New constraints on the pyroclastic eruptive history of the Campanian volcanic Plain (Italy). *Mineralogy and Petrology*, *73*, 47– 65. https://doi.org/10.1007/s007100170010

Di Renzo, V., Di Vito, M. A., Arienzo, I., Carandente, A., Civetta, L., D'Antonio, M., et al. (2007). Magmatic history of Somma-Vesuvius on the basis of new geochemical and isotopic data from a deep borehole (Camaldoli della Torre). *Journal of Petrology*, *48*(4), 753–784. https://doi.org/10.1093/petrology/egl081

Di Vito, M. A., Acocella, V., Aiello, G., Barra, D., Battaglia, M., Carandente, A., et al. (2016). Magma transfer at Campi Flegrei caldera (Italy) before the 1538 AD eruption. *Scientific Reports*, *6*, 32245. https://doi.org/10.1038/srep32245

Dolfi, D., & Trigila, R. (1978). The role of water in the 1944 Vesuvius eruption. *Contributions to Mineralogy and Petrology*, *67*(3), 297–304. https://doi.org/10.1007/BF00381457

D'Oriano, C., Poggianti, E., Bertagnini, A., Cioni, R., Landi, P., Polacci, M., & Rosi, M. (2005). Changes in eruptive style during the A.D. 1538 Monte Nuovo eruption (Phlegrean Fields, Italy): The role of syn-eruptive crystallization. *Bulletin of Volcanology*, *67*(7), 601–621. https://doi.org/10.1007/s00445-004-0397-z

Edmonds, M., Cashman, K. V., Holness, M., & Jackson, M. (2019). Architecture and dynamics of magma reservoirs. *Philosophical Transactions of the Royal Society A: Mathematical, Physical and Engineering Sciences*, *377*(2139), 20180298. https://doi.org/10.1098/rsta.2018.0298

Esposito, R., Badescu, K., Steele-MacInnis, M., Cannatelli, C., De Vivo, B., Lima, A., et al. (2018). Magmatic evolution of the Campi Flegrei and Procida volcanic fields, Italy, based on interpretation of data from well-constrained melt inclusions. *Earth-Science Reviews*, *185*, 325–356. https://doi.org/10.1016/j.earscirev.2018.06.003

Fabbrizio, A., & Carroll, M. R. (2008). Experimental constraints on the differentiation process and pre-eruptive conditions in the magmatic system of Phlegraean Fields (Naples, Italy). *Journal of Volcanology and Geothermal Research*, *171*(1–2), 88–102. https://doi.org/10.1016/j.jvolgeores.2007.11.002

Fedi, M., Cella, F., D'Antonio, M., Florio, G., Paoletti, V., & Morra, V. (2018). Gravity modeling finds a large magma body in the deep crust below the Gulf of Naples, Italy. *Scientific Reports*, *8*(1), 8229. https://doi.org/10.1038/s41598-018-26346-z

Flinders, A. F., Shelly, D. R., Dawson, P. B., Hill, D. P., Tripoli, B., & Shen, Y. (2018). Seismic evidence for significant melt beneath the Long Valley Caldera, California, USA. *Geology*, *46*(9), 799–802. https://doi.org/10.1130/G45094.1

Forni, F., Degruyter, W., Bachmann, O., De Astis, G., & Mollo, S. (2018). Long-term magmatic evolution reveals the beginning of a new caldera cycle at Campi Flegrei. *Science Advances*, *4*(11), eaat9401. https://doi.org/10.1126/sciadv.aat9401

Fourmentraux, C., Métrich, N., Bertagnini, A., & Rosi, M. (2012). Crystal fractionation, magma step ascent, and syn-eruptive mingling: The Averno 2 eruption (Phlegraean Fields, Italy). *Contributions to Mineralogy and Petrology*, *163*(6), 1121–1137. https://doi.org/10.1007/s00410-012-0720-1

Fowler, S. J., Spera, F. J., Bohrson, W. A., Belkin, H. E., & De Vivo, B. (2007). Phase equilibria constraints on the chemical and physical evolution of the campanian ignimbrite. *Journal of Petrology*, *48*(3), 459–493. https://doi.org/10.1093/petrology/egl068

Gaonac'h, H., Lovejoy, S., Stix, J., & Scherzter, D. (1996). A scaling growth model for bubbles in basaltic lava flows. *Earth and Planetary Science Letters*, *139*(3–4), 395–409. https://doi.org/10.1016/0012-821X(96)00039-8

Gardner, J. E., Thomas, R. M. E., Jaupart, C., & Tait, S. (1996). Fragmentation of magma during Plinian volcanic eruptions. *Bulletin of Volcanology*, *58*(2–3), 144–162. https://doi.org/10.1007/s004450050132

Gebauer, S. K., Schmitt, A. K., Pappalardo, L., Stockli, D. F., & Lovera, O. M. (2014). Crystallization and eruption ages of Breccia Museo (Campi Flegrei caldera, Italy) plutonic clasts and their relation to the Campanian ignimbrite. *Contributions to Mineralogy and Petrology*, *167*(1), 1–18. https://doi.org/10.1007/s00410-013-0953-7

Gelman, S. E., Gutierrez, F. J., & Bachmann, O. (2013) On the longevity of large upper crustal silicic magma reservoirs. *Geology*, *41*, 759–762. https://doi.org/10.1130/G34241.1

Geschwind, C. H., & Rutherford, M. J. (1995). Crystallization of microlites during magma ascent: the fluid mechanics of 1980-1986 eruptions at Mount St Helens. *Bulletin of Volcanology*, *57*(5), 356–370. https://doi.org/10.1007/BF00301293

Ghiorso, M. S., & Sack, R. O. (1995). Chemical mass transfer in magmatic processes IV. A revised and internally consistent thermodynamic model for the interpolation and extrapolation of liquid-solid equilibria in magmatic systems at elevated temperatures and pressures. *Contributions to Mineralogy and Petrology*, *119*(2–3), 197–212. https://doi.org/10.1007/BF00307281

Giachetti, T., Gonnermann, H. M., Gardner, J. E., Burgisser, A., Hajimirza, S., Earley, T. C., et al. (2019). Bubble coalescence and percolation threshold in expanding rhyolitic magma. *Geochemistry, Geophysics, Geosystems*, *20*, 1054– 1074. https://doi.org/10.1029/2018GC008006

Gonnermann, H. M., & Houghton, B. F. (2012). Magma degassing during the Plinian eruption of Novarupta, Alaska, 1912. *Geochemistry, Geophysics, Geosystems*, *13*(10), Q10009. https://doi.org/10.1029/2012GC004273

Gonnermann, H. M. & Manga, M. (2007). The Fluid Mechanics Inside a Volcano. *Annual Review of Fluid Mechanics*, *39*, 321–356. https://doi.org/10.1146/annurev.fluid.39.050905.110207

Guidoboni, E., & Ciuccarelli, C. (2011). The Campi Flegrei caldera: Historical revision and new data on seismic crises, bradyseisms, the Monte Nuovo eruption and ensuing earthquakes (twelfth century 1582 AD). *Bulletin of Volcanology*, *73*(6), 655–677. https://doi.org/10.1007/s00445-010-0430-3

Gurioli, L., Andronico, D., Bachelery, P., Balcone-Boissard, H., Battaglia, J., Boudon, G., et al. (2015). MeMoVolc consensual document: a review of cross-disciplinary approaches to characterizing small explosive magmatic eruptions. *Bulletin of Volcanology*, *77*(6), 49. https://doi.org/10.1007/s00445-015-0935-x

Hammer, J. E., Cashman, K. V., Hoblitt, R. P., & Newman, S. (1999). Degassing and microlite crystallization during pre-climactic events of the 1991 eruption of Mt. Pinatubo, Philippines. *Bulletin of Volcanology*, *60*(5), 355–380. https://doi.org/10.1007/s004450050238

Hammer, J. E., & Rutherford, M. J. (2002). An experimental study of the kinetics of decompression-induced crystallization in silicic melt. *Journal of Geophysical Research: Solid Earth*, *107*(B1), ECV 8-1-ECV 8-24. https://doi.org/10.1029/2001jb000281

Hammer, J. E., Rutherford, M. J., & Hildreth, W. (2002). Magma storage prior to the 1912 eruption at Novarupta, Alaska. *Contributions to Mineralogy and Petrology*, *144*(2), 144–162. https://doi.org/10.1007/s00410-002-0393-2

Hawkesworth, C., Blake, S., Evans, P., Hughes, R., Macdonald, R., Thomas, L. E., et al. (2000). Time scales of crystal fractionation in magma chambers-integrating physical, isotopic and geochemical perspectives. *Journal of Petrology*, *41*(7), 991–1006. https://doi.org/10.1093/petrology/41.7.991

Hawkesworth, C., George, R., Turner, S., & Zellmer, G. (2004). Time scales of magmatic processes. *Earth and Planetary Science Letters*, *218*(1–2), 1–16. https://doi.org/10.1016/S0012-821X(03)00634-4

Hildreth, W., & Wilson, C. J. N. (2007). Compositional zoning of the Bishop Tuff. *Journal of Petrology*, *48*(5), 951–999. https://doi.org/10.1093/petrology/egm007

Holness, M. B., Stock, M. J., & Geist, D. (2019). Magma chambers versus mush zones: constraining the architecture of subvolcanic plumbing systems from microstructural analysis of crystalline enclaves. *Philosophical Transactions of the Royal Society A: Mathematical, Physical and Engineering Sciences*, *377*(2139), 20180006. https://doi.org/10.1098/rsta.2018.0006

Iacono Marziano, G., Gaillard, F., & Pichavant, M. (2008). Limestone assimilation by basaltic magmas: An experimental re-assessment and application to Italian volcanoes. *Contributions to Mineralogy and Petrology*, *155*(6), 719–738. https://doi.org/10.1007/s00410-007-0267-8

Iacono Marziano, G., Schmidt, B. C., & Dolfi, D. (2007). Equilibrium and disequilibrium degassing of a phonolitic melt (Vesuvius AD 79 “white pumice”) simulated by decompression experiments. *Journal of Volcanology and Geothermal Research*, *161*(3), 151–164. https://doi.org/10.1016/j.jvolgeores.2006.12.001

Improta, L., & Corciulo, M. (2006). Controlled source nonlinear tomography: A powerful tool to constrain tectonic models of the Southern Apennines orogenic wedge, Italy. *Geology*, *34*(11), 941–944. https://doi.org/10.1130/G22676A.1

Iovine, R. S., Fedele, L., Mazzeo, F. C., Arienzo, I., Cavallo, A., Wörner, G., et al. (2017). Timescales of magmatic processes prior to the ~4.7 ka Agnano-Monte Spina eruption (Campi Flegrei caldera, Southern Italy) based on diffusion chronometry from sanidine phenocrysts. *Bulletin of Volcanology*, *79*(2), 18. https://doi.org/10.1007/s00445-017-1101-4

Jaxybulatov, K., Shapiro, N. M., Koulakov, I., Mordret, A., Landès, M., & Sens-Schönfelder, C. (2014). A large magmatic sill complex beneath the Toba caldera. *Science*, *346*(6209), 617–619. https://doi.org/10.1126/science.1258582

Jolis, E. M., Freda, C., Troll, V. R., Deegan, F. M., Blythe, L. S., McLeod, C. L., & Davidson, J. P. (2013). Experimental simulation of magma-carbonate interaction beneath Mt. Vesuvius, Italy. *Contributions to Mineralogy and Petrology*, *166*(5), 1335–1353. https://doi.org/10.1007/s00410-013-0931-0

Jolis, E. M., Troll, V. R., Harris, C., Freda, C., Gaeta, M., Orsi, G., & Siebe, C. (2015). Skarn xenolith record crustal CO_2 liberation during Pompeii and Pollena eruptions, Vesuvius volcanic system, central Italy. *Chemical Geology*, *415*, 17–36. https://doi.org/10.1016/j.chemgeo.2015.09.003

Kennedy, B., Spieler, O., Scheu, B., Kueppers, U., Taddeucci, J., & Dingwell, D. B. (2005). Conduit implosion during Vulcanian eruptions. *Geology*, *33*(7), 581–584. https://doi.org/10.1130/G21488.1

Kilburn, C. R. J., De Natale, G., & Carlino, S. (2017). Progressive approach to eruption at Campi Flegrei caldera in southern Italy. *Nature Communications*, *8*, 15312. https://doi.org/10.1038/ncomms15312

Klug, C., Cashman, K. V., & Bacon, C. (2002). Structure and physical characteristics of pumice from the climactic eruption of Mount Mazama (Crater Lake), Oregon. *Bulletin of Volcanology*, *64*(7), 486–501. https://doi.org/10.1007/s00445-002-0230-5

Lanzafame, G., Iezzi, G., Mancini, L., Lezzi, F., Mollo, S., & Ferlito, C. (2017). Solidification and Turbulence (Non-laminar) during magma ascent: Insights from 2D and 3D analyses of bubbles and minerals in an Etnean dyke. *Journal of Petrology*, *58*(8), 1511–1534. https://doi.org/10.1093/petrology/egx063

Larsen, J. F. (2008). Heterogeneous bubble nucleation and disequilibrium H 2 O exsolution in Vesuvius K-phonolite melts. *Journal of Volcanology and Geothermal Research*, *175*(3), 278–288. https://doi.org/10.1016/j.jvolgeores.2008.03.015

Larsen, J. F., & Gardner, J. E. (2004). Experimental study of water degassing from phonolite melts: implications for volatile oversaturation during magmatic ascent. *Journal of Volcanology and Geothermal Research*, *134*, 109–124. https://doi.org/10.1016/j.jvolgeores.2004.01.004

Liedl, A., Buono, G., Lanzafame, G., Dabagov, S. B., Della Ventura, G., Hampai, D., et al. (2019). A 3D imaging textural characterization of pyroclastic products from the 1538 AD Monte Nuovo eruption (Campi Flegrei, Italy). *Lithos*, *340–341*, 316–331. https://doi.org/10.1016/j.lithos.2019.05.010

Lima, A., Danyushevsky, L. V., De Vivo, B., & Fedele, L. (2003). A model for the evolution of the Mt. Somma-Vesuvius magmatic system based on fluid and melt inclusion investigations. *Developments in Volcanology*, *5*(C), 227–249. https://doi.org/10.1016/S1871-644X(03)80032-3

Lima, A., De Vivo, B., Spera, F. J., Bodnar, R. J., Milia, A., Nunziata, C., et al. (2009). Thermodynamic model for uplift and deflation episodes (bradyseism) associated with magmatic-hydrothermal activity at the Campi Flegrei (Italy). *Earth-Science Reviews*, *97*(1–4), 44–58. https://doi.org/10.1016/j.earscirev.2009.10.001

Lima, A., Esposito, R., & De Vivo, B. (2017). Fluid and melt inclusions from subvolcanic to surface environment in the Campi Flegrei (Napoli, Italy) active volcanic system. *Journal of the Geological Society of India*, *90*(5), 515–523. https://doi.org/10.1007/s12594-017-0747-z

Macedonio, G., Dobran, F., & Neri, A. (1994). Erosion processes in volcanic conduits and application to the AD 79 eruption of Vesuvius. *Earth and Planetary Science Letters*, *121*(1–2), 137–152. https://doi.org/10.1016/0012-821X(94)90037-X

Mangan, M. T, & Sisson, T. (2000). Delayed, disequilibrium degassing in rhyolite magma: Decompression experiments and implications for explosive volcanism. *Earth and Planetary Science Letters*, *183*(3–4), 441–455. https://doi.org/10.1016/S0012-821X(00)00299-5

Mangan, M. T., Sisson, T.W., & Hankins, W. B. (2004). Decompression experiments identify kinetic controls on explosive silicic eruptions. *Geophysical Research Letters*, *31*(8), L08605. https://doi.org/10.1029/2004GL019509

Mangiacapra, A., Moretti, R., Rutherford, M., Civetta, L., Orsi, G., & Papale, P. (2008). The deep magmatic system of the Campi Flegrei caldera (Italy). *Geophysical Research Letters*, *35*(21), L21304. https://doi.org/10.1029/2008GL035550

Marianelli, P., Métrich, N., & Sbrana, A. (1999). Shallow and deep reservoirs involved in magma supply of the 1944 eruption of Vesuvius. *Bulletin of Volcanology*, *61*(1–2), 48–63. https://doi.org/10.1007/s004450050262

Marianelli, P., Sbrana, A., Métrich, N., & Cecchetti, A. (2005). The deep feeding system Vesuvius involved in recent violent strombolian eruptions. *Geophysical Research Letters*, *32*(2), 1–4. https://doi.org/10.1029/2004GL021667

Marianelli, P., Sbrana, A., & Proto, M. (2006). Magma chamber of the Campi Flegrei supervolcano at the time of eruption of the Campanian Ignimbrite. *Geology*, *34*(11), 937–940. https://doi.org/10.1130/G22807A.1

Marsh, B. D. (1988). Crystal size distribution (CSD) in rocks and the kinetics and dynamics of crystallization I. Theory. *Contributions to Mineralogy and Petrology*, *99*(3), 277–291. https://doi.org/10.1007/BF00375362

Marsh, B. D. (1989). Magma Chambers. *Annual Review of Earth and Planetary Sciences*, *17*(1), 439–474. https://doi.org/10.1146/annurev.earth.17.1.439

Marsh, B. D. (2002). On bimodal differentiation by solidification front instability in basaltic magmas, part 1: Basic mechanics. *Geochimica et Cosmochimica Acta*, *66*(12), 2211–2229. https://doi.org/10.1016/S0016-7037(02)00905-5

Marsh, B. D. (2015). Magma Chambers. In H. Sigurdsson, B. Houghton, S. R. McNutt, H. Rymer, J. Stix (Eds.), *The Encyclopedia of Volcanoes* (2nd edn., pp. 185–201). Academic Press, London. https://doi.org/10.1016/B978-0-12-385938-9.00008-0

Martel, C. (2012). Eruption dynamics inferred from microlite crystallization experiments: Application to plinian and dome-forming eruptions of Mt. Pelée (martinique, lesser antilles). *Journal of Petrology*, *53*(4), 699–725. https://doi.org/10.1093/petrology/egr076

Martel, C., Brooker, R. A., Andújar, J., Pichavant, M., Scaillet, B., & Blundy, J. D. (2017). Experimental Simulations of Magma Storage and Ascent. In J. Gottsmann, J. Neuberg, B. Scheu (Eds.), *Volcanic unrest* (pp. 101–110). Springer, Cham. https://doi.org/10.1007/11157_2017_20

Martel, C., & Schmidt, B. C. (2003). Decompression experiments as an insight into ascent rates of silicic magmas. *Contributions to Mineralogy and Petrology*, *144*(4), 397–415. https://doi.org/10.1007/s00410-002-0404-3

Marxer, H., Bellucci, P., & Nowak, M. (2015). Degassing of H_2O in a phonolitic melt: A closer look at decompression experiments. *Journal of Volcanology and Geothermal Research*, *297*, 109–124. https://doi.org/10.1016/j.jvolgeores.2014.11.017

Masotta, M., Mollo, S., Freda, C., Gaeta, M., & Moore, G. (2013). Clinopyroxene-liquid thermometers and barometers specific to alkaline differentiated magmas. *Contributions to Mineralogy and Petrology*, *166*(6), 1545–1561. https://doi.org/10.1007/s00410-013-0927-9

Mastrolorenzo, G., Brachi, L., & Canzanella, A. (2001). Vesicularity of various types of pyroclastic deposits of Campi Flegrei volcanic field: Evidence of analogies in magma rise and vesiculation mechanisms. *Journal of Volcanology and Geothermal Research*, *109*(1–3), 41–53. https://doi.org/10.1016/S0377-0273(00)00303-6

Mastrolorenzo, G., Palladino, D. M., Pappalardo, L. & Rossano, S. (2017) Probabilistic-numerical assessment of pyroclastic current hazard at Campi Flegrei and Naples city: Multi-VEI scenarios as a tool for "full-scale" risk management. *PLoS ONE*, *12*(10), e0185756. https://doi.org/10.1371/journal.pone.0185756

Mastrolorenzo, G., & Pappalardo, L. (2006). Magma degassing and crystallization processes during eruptions of high-risk Neapolitan-volcanoes: Evidence of common equilibrium rising processes in alkaline magmas. *Earth and Planetary Science Letters*, *250*(1–2), 164–181. https://doi.org/10.1016/j.epsl.2006.07.040

McBirney, A. R., Baker, B. H., & Nilson, R. H. (1985). Liquid fractionation. Part I: Basic principles and experimental simulations. *Journal of Volcanology and Geothermal Research*, *24*(1–2), 1–24. https://doi.org/10.1016/0377-0273(85)90026-5

Melnik, O. E., Blundy, J. D., Rust, A. C., & Muir, D. D. (2011). Subvolcanic plumbing systems imaged through crystal size distributions. *Geology*, *39*(4), 403–406. https://doi.org/10.1130/G31691.1

Mollo, S., & Masotta, M. (2014). Optimizing pre-eruptive temperature estimates in thermally and chemically zoned magma chambers. *Chemical Geology*, *368*, 97–103. https://doi.org/10.1016/j.chemgeo.2014.01.007

Morgan, D. J., & Blake, S. (2006). Magmatic residence times of zoned phenocrysts: Introduction and application of the binary element diffusion modelling (BEDM) technique. *Contributions to Mineralogy and Petrology*, *151*(1), 58–70. https://doi.org/10.1007/s00410-005-0045-4

Mourtada-Bonnefoi, C. C., & Laporte, D. (2004). Kinetics of bubble nucleation in a rhyolitic melt: An experimental study of the effect of ascent rate. *Earth and Planetary Science Letters*, *218*(3–4), 521–537. https://doi.org/10.1016/S0012-821X(03)00684-8

Noguchi, S., Toramaru, A., & Shimano, T. (2006). Crystallization of microlites and degassing during magma ascent: Constraints on the fluid mechanical behavior of magma during the Tenjo Eruption on Kozu Island, Japan. *Bulletin of Volcanology*, *68*(5), 432–449. https://doi.org/10.1007/s00445-005-0019-4

Nunziata, C. (2010). Low shear-velocity zone in the Neapolitan-area crust between the Campi Flegrei and Vesuvio volcanic areas. *Terra Nova*, *22*(3), 208–217. https://doi.org/10.1111/j.1365-3121.2010.00936.x

Pappalardo, L., Buono, G., Fanara, S., & Petrosino, P. (2018). Combining textural and geochemical investigations to explore the dynamics of magma ascent during Plinian eruptions: A Somma–Vesuvius volcano (Italy) case study. *Contributions to Mineralogy and Petrology*, *173*(7), 61. https://doi.org/10.1007/s00410-018-1486-x

Pappalardo, L., Civetta, L., De Vita, S., Di Vito, M., Orsi, G., Carandente, A., & Fisher, R. V. (2002). Timing of magma extraction during the Campanian Ignimbrite eruption (Campi Flegrei Caldera). *Journal of Volcanology and Geothermal Research*, *114*(3–4), 479–497. https://doi.org/10.1016/S0377-0273(01)00302-X

Pappalardo, L., D'Auria, L., Cavallo, A., & Fiore, S. (2014). Petrological and seismic precursors of the paroxysmal phase of the last Vesuvius eruption on March 1944. *Scientific Reports*, *4*, 6297. https://doi.org/10.1038/srep06297

Pappalardo, L. & Mastrolorenzo, G. (2010). Short residence times for alkaline Vesuvius magmas in a multi-depth supply system: Evidence from geochemical and textural studies. *Earth and Planetary Science Letters*, *296*(1–2), 133–143. https://doi.org/10.1016/j.epsl.2010.05.010

Pappalardo, L. & Mastrolorenzo, G. (2012). Rapid differentiation in a sill-like magma reservoir: A case study from the campi flegrei caldera. *Scientific Reports*, *2*, 712. https://doi.org/10.1038/srep00712

Pappalardo, L., Ottolini, L., & Mastrolorenzo, G. (2008). The Campanian Ignimbrite (southern Italy) geochemical zoning: Insight on the generation of a super-eruption from catastrophic differentiation and fast withdrawal. *Contributions to Mineralogy and Petrology*, *156*(1), 1–26. https://doi.org/10.1007/s00410-007-0270-0

Pappalardo, L. Piochi, M., & Mastrolorenzo, G. (2004). The 3550 year BP-1944 A.D. magma-plumbing system of Somma-Vesuvius: Constraints on its behaviour and present state through a review of Sr-Nd isotope data. *Annals of Geophysics*, *47*(4), 1471–1483. https://doi.org/10.4401/ag-3354

Peccerillo, A. (2017). *Cenozoic Volcanism in the Tyrrhenian Sea Region*. Springer, Cham. http://doi.org/10.1007/978-3-319-42491-0

Perinelli, C., Gaeta, M., Bonechi, B., et al. (2019). Effect of water on the phase relations of primitive K-basalts: implications for high-pressure differentiation in the Phlegraean Volcanic District magmatic system. *Lithos*, *342–343*, 530–541.

Pichavant, M., Scaillet, B., Pommier, A., Iacono-Marziano, G., & Cioni, R. (2014). Nature and Evolution of Primitive Vesuvius Magmas: an Experimental Study. *Journal of Petrology*, *55*(11), 2281–2310. https://doi.org/10.1093/petrology/egu057

Piochi, M., Ayuso, R. A., De Vivo, B., & Somma, R. (2006). Crustal contamination and crystal entrapment during polybaric magma evolution at Mt. Somma-Vesuvius volcano, Italy: Geochemical and Sr isotope evidence. *Lithos*, *86*(3–4), 303–329. https://doi.org/10.1016/j.lithos.2005.05.009

Piochi, M., Mastrolorenzo, G., & Pappalardo, L. (2005). Magma ascent and eruptive processes from textural and compositional features of Monte Nuovo pyroclastic products, Campi Flegrei, Italy. *Bulletin of Volcanology*, *67*(7), 663–678. https://doi.org/10.1007/s00445-005-0410-1

Piochi, M., Polacci, M., De Astis, G., Zanetti, A., Mangiacapra, A., Vannucci, R., & Giordano, D. (2008). Texture and composition of pumices and scoriae from the Campi Flegrei caldera (Italy): Implications on the dynamics of explosive eruptions. *Geochemistry, Geophysics, Geosystems*, *9*(3), Q03013. https://doi.org/10.1029/2007GC001746

Pistolesi, M., Bertagnini, A., Di Roberto, A., Isaia, R., Vona, A., Cioni, R., & Giordano, G. (2017). The Baia–Fondi di Baia eruption at Campi Flegrei: stratigraphy and dynamics of a multi-stage caldera reactivation event. *Bulletin of Volcanology*, *79*(9), 67. https://doi.org/10.1007/s00445-017-1149-1

Polacci, M., Arzilli, F., La Spina, G., Le Gall, N., Cai, B., Hartley, M. E., et al. (2018). Crystallisation in basaltic magmas revealed via in situ 4D synchrotron X-ray microtomography. *Scientific Reports*, *8*(1), 8377. https://doi.org/10.1038/s41598-018-26644-6

Polacci, M., Bouvet de Maisonneuve, C., Giordano, D., Piochi, M., Mancini, L., Degruyter, W., & Bachmann, O. (2014). Permeability measurements of Campi Flegrei pyroclastic products: An example from the Campanian Ignimbrite and Monte Nuovo eruptions. *Journal of Volcanology and Geothermal Research*, *272*, 16–22. https://doi.org/10.1016/j.jvolgeores.2013.12.002

Preece, K., Barclay, J., Gertisser, R. & Herd, R. A. (2013). Textural and micro-petrological variations in the eruptive products of the 2006 dome-forming eruption of Merapi volcano, Indonesia: Implications for sub-surface processes. *Journal of Volcanology and Geothermal Research*, *261*, 98–120. https://doi.org/10.1016/j.jvolgeores.2013.02.006

Preuss, O., Marxer, H., Ulmer, S., Wolf, J., & Nowak, M. (2016). Degassing of hydrous trachytic Campi Flegrei and phonolitic Vesuvius melts: Experimental limitations and chances to study homogeneous bubble nucleation. *American Mineralogist*, *101*(4), 859–875. https://doi.org/10.2138/am-2016-5480

Roman, D. C. & Cashman, K. V. (2018) Top–Down Precursory Volcanic Seismicity: Implications for 'Stealth' Magma Ascent and Long-Term Eruption Forecasting. *Frontiers in Earth Science*, *6*, 124. https://doi.org/10.3389/feart.2018.00124

Rosi, M., & Sbrana, A. (1987). *The Phlegraean fields*. CNR Quaderni della Ricerca Scientifica, Roma.

Rotella, M. D., Wilson, C. J. N., Barker, S. J., Cashman, K. V., Houghton, B. F., & Wright, I. C. (2014). Bubble development in explosive silicic eruptions: Insights from pyroclast vesicularity textures from Raoul volcano (Kermadec arc). *Bulletin of Volcanology*, *76*(8), 1–24. https://doi.org/10.1007/s00445-014-0826-6

Rubin, A. M., Gillard, D., & Got, J.-L. (1998). A reinterpretation of seismicity associated with the January 1983 dike intrusion at Kilauea Volcano, Hawaii. *Journal of Geophysical Research: Solid Earth*, *103*(B5), 10003–10015. https://doi.org/10.1029/97jb03513

Rust, A. C., & Cashman, K. V. (2011). Permeability controls on expansion and size distributions of pyroclasts. *Journal of Geophysical Research: Solid Earth*, *116*(11), B11202. https://doi.org/10.1029/2011JB008494

Ruth, D. C. S., Costa, F., Bouvet De Maisonneuve, C., Franco, L., Cortés, J. A., & Calder, E. S. (2018). Crystal and melt inclusion timescales reveal the evolution of magma migration before eruption. *Nature Communications*, *9*(1), 2657. https://doi.org/10.1038/s41467-018-05086-8

Rutherford, M. J., & Gardner, J. E. (2000). Rates of Magma Ascent. In H. Sigurdsson, B. Houghton, H. Rymer, J. Stix, S. R. McNutt (Eds.), *The encyclopedia of volcanoes* (pp. 207–218). Academic Press, London.

Rutherford, M. J., & Hill, P. M. (1993). Magma ascent rates from amphibole breakdown: An experimental study applied to the 1980-1986 Mount St. Helens eruptions. *Journal of Geophysical Research: Solid Earth*, *98*(B11), 19667–19685. https://doi.org/10.1029/93jb01613

Santacroce, R., Cioni, R., Marianelli, P., Sbrana, A., Sulpizio, R., Zanchetta, G., et al. (2008). Age and whole rock-glass compositions of proximal pyroclastics from the major explosive eruptions of Somma-Vesuvius: A review as a tool for distal tephrostratigraphy. *Journal of Volcanology and Geothermal Research*, *177*(1), 1–18. https://doi.org/10.1016/j.jvolgeores.2008.06.009

Saunders, K. E., Blundy, J. D., Dohmen, R. G. & Cashman, K. V. (2012). Linking petrology and seismology at an active volcano. *Science*, *336*(6084), 1023–1027. https://doi.org/10.1126/science.1220066

Scaillet, B., Pichavant, M., & Cioni, R. (2008). Upward migration of Vesuvius magma chamber over the past 20,000 years. *Nature*, *455*(7210), 216–219. https://doi.org/10.1038/nature07232

Scarpati, C., Perrotta, A., Lepore, S., & Calvert, A. (2012). Eruptive history of Neapolitan volcanoes: Constraints from 40Ar-39Ar dating. *Geological Magazine*, *150*(3), 412–425. https://doi.org/10.1017/S0016756812000854

Shea, T., Gurioli, L., & Houghton, B. F. (2012). Transitions between fall phases and pyroclastic density currents during the AD 79 eruption at Vesuvius: Building a transient conduit model from the textural and volatile record. *Bulletin of Volcanology*, *74*(10), 2363–2381. https://doi.org/10.1007/s00445-012-0668-z

Shea, T., Gurioli, L., Larsen, J. F., Houghton, B. F., Hammer, J. E., & Cashman, K. V. (2010b). Linking experimental and natural vesicle textures in Vesuvius 79AD white pumice. *Journal of Volcanology and Geothermal Research*, *192*(1–2), 69–84. https://doi.org/10.1016/j.jvolgeores.2010.02.013

Shea, T., Houghton, B. F., Gurioli, L., Cashman, K. V., Hammer, J. E., & Hobden, B. J. (2010a). Textural studies of vesicles in volcanic rocks: An integrated methodology. *Journal of Volcanology and Geothermal Research*, *190*(3–4), 271–289. https://doi.org/10.1016/j.jvolgeores.2009.12.003

Sigmundsson, F., Hooper, A., Hreinsdóttir, S., Vogfjörd, K. S., Ófeigsson, B. G., Heimisson, E. R., et al. (2015). Segmented lateral dyke growth in a rifting event at Bárðarbunga volcanic system, Iceland. *Nature*, *517*(7533), 191–195. https://doi.org/10.1038/nature14111

Signorelli, S., & Carroll, M. R. (2002). Experimental study of Cl solubility in hydrous alkaline melts: Constraints on the theoretical maximum amount of Cl in trachytic and phonolitic melts. *Contributions to Mineralogy and Petrology*, *143*(2), 209–218. https://doi.org/10.1007/s00410-001-0320-y

Sparks, R. S. J., Annen, C., Blundy, J. D., Cashman, K. V., Rust, A. C., & Jackson, M. D. (2019). Formation and dynamics of magma reservoirs. *Philosophical Transactions of the Royal Society A: Mathematical, Physical and Engineering Sciences*, *377*(2139), 20180019. https://doi.org/10.1098/rsta.2018.0019

Spera, F. J., Oldenburg, C. M., Christensen, C., & Todesco, M. (1995). Simulations of convection with crystallization in the system KAlSi2O6-CaMgSi2O6: Implications for compositionally zoned magma bodies. *American Mineralogist*, *80*(11–12), 1188–1207. https://doi.org/10.2138/am-1995-11-1210

Stock, M. J., Humphreys, M. C. S., Smith, V. C., Isaia, R., Brooker, R. A., & Pyle, D. M. (2018). Tracking volatile behaviour in sub-volcanic plumbing systems using apatite and glass: Insights into pre-eruptive processes at Campi Flegrei, Italy. *Journal of Petrology*, *59*(12), 2463–2492. https://doi.org/10.1093/petrology/egy020

Stovall, W. K., Houghton, B. F., Gonnermann, H., Fagents, S. A., & Swanson, D. A. (2011). Eruption dynamics of Hawaiian-style fountains: The case study of episode 1 of the Kilauea Iki 1959 eruption. *Bulletin of Volcanology*, *73*(5), 511–529. https://doi.org/10.1007/s00445-010-0426-z

Till, C. B., Vazquez, J. A., & Boyce, J. W. (2015). Months between rejuvenation and volcanic eruption at Yellowstone caldera, Wyoming. *Geology*, *43*, 695–698. https://doi.org/10.1130/G36862.1

Toramaru, A. (2006). BND (bubble number density) decompression rate meter for explosive volcanic eruptions. *Journal of Volcanology and Geothermal Research*, *154*(3–4), 303–316. https://doi.org/10.1016/j.jvolgeores.2006.03.027

Turner, S. P., George, R. M. M., Evans, P. J., Hawkesworth, C. J., & Zellmer, G. F. (2000). Time-scales of magma formation, ascent and storage beneath subduction-zone volcanoes. *Philosophical Transactions of the Royal Society A: Mathematical, Physical and Engineering Sciences*, *358*(1770), 1443–1464. https://doi.org/10.1098/rsta.2000.0598

Vanorio, T., & Kanitpanyacharoen, W. (2015). Rock physics of fibrous rocks akin to Roman concrete explains uplifts at Campi Flegrei caldera. *Science*, *349*(6248), 617–621. https://doi.org/10.1126/science.aab1292

Villemant, B., & Boudon, G. (1998). Transition from dome-forming to plinian eruptive styles controlled by H_2O and Cl degassing. *Nature*, *392*(6671), 65–69. https://doi.org/10.1038/32144

Voltolini, M., Zandomeneghi, D., Mancini, L., & Polacci, M. (2011). Texture analysis of volcanic rock samples: Quantitative study of crystals and vesicles shape preferred orientation from X-ray microtomography data. *Journal of Volcanology and Geothermal Research*, *202*(1–2), 83–95. https://doi.org/10.1016/j.jvolgeores.2011.02.003

Webster, J. D., & De Vivo, B. (2002). Experimental and modeled solubilities of chlorine in aluminosilicate melts, consequences of magma evolution, and implications for exsolution of hydrous chloride melt at Mt. Somma-Vesuvius. *American Mineralogist*, *87*(8–9), 1046–1061. https://doi.org/10.2138/am-2002-8-902

Wotzlaw, J. F., Guillong, M., Balashova, A., Fornia, F., Dunkl, I., Mattssona, H. B., & Bachmann, O. (2019). In-situ garnet 238U-230Th geochronology of Holocene silica-undersaturated volcanic tuffs at millennial-scale precision. *Quaternary Geochronology*, *50*, 1–7. https://doi.org/10.1016/j.quageo.2018.10.004

Wu, W. N., Schmitt, A. K., & Pappalardo, L. (2015). U-Th baddeleyite geochronology and its significance to date the emplacement of silica undersaturated magmas. *American Mineralogist*, *100*(10), 2082–2090. https://doi.org/10.2138/am-2015-5274

Zdanowicz, G., Boudon, G., Balcone-Boissard, H., Cioni, R., Mundula, F., Orsi, G., et al. (2018). Geochemical and textural constraints on degassing processes in sub-Plinian eruptions: Case-study of the Greenish Pumice eruption of Mount Somma-Vesuvius. *Bulletin of Volcanology*, *80*(4), 38. https://doi.org/10.1007/s00445-018-1213-5

Zellmer, G. F., Annen, C., Charlier, B. L. A., George, R. M. M., Turner, S. P., & Hawkesworth, C. J. (2005). Magma evolution and ascent at volcanic arcs: Constraining petrogenetic processes through rates and chronologies. *Journal of Volcanology and Geothermal Research*, *140*(1–3), 171–191. https://doi.org/10.1016/j.jvolgeores.2004.07.020

Zollo, A., Maercklin, N., Vassallo, M., Dello Iacono, D., Virieux, J., & Gasparini, P. (2008). Seismic reflections reveal a massive melt layer feeding Campi Flegrei caldera. *Geophysical Research Letters*, *35*(12), L12306. https://doi.org/10.1029/2008GL034242

INDEX

Page numbers in *italics* refer to figures, those in **bold** refer to tables

---

Crustal Magmatic System Evolution: Anatomy, Architecture, and Physico-Chemical Processes, Geophysical Monograph 264, First Edition.
Edited by Matteo Masotta, Christoph Beier, and Silvio Mollo.

DOI: 10.1002/9781119564485